TWO-DIMENSIONAL RIVER MODELING PACKAGE

FESWMS-2DH

Property of
Control District of MC Library
Return to
Tucson, AZ 85709

Finite Element Surface-Water Modeling System: Two-Dimensional Flow in a Horizontal Plane

Support Literature

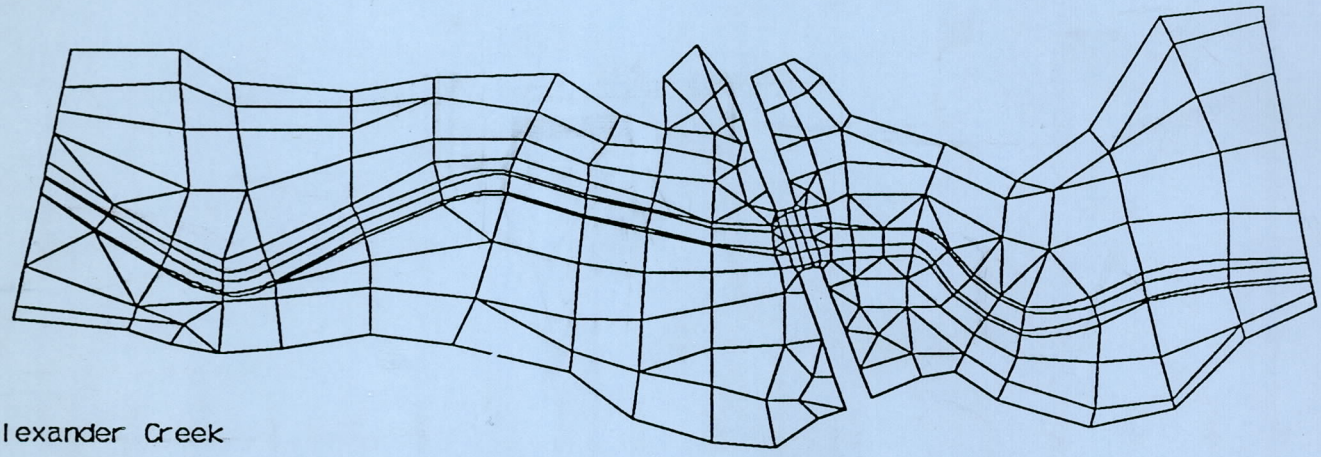

Alexander Creek

WEST Consultants, Inc.
2111 Palomar Airport Road • Suite 180 • Carlsbad, California 92009-1419 • (619) 431-8113

Property of
Flood Control District of MC Library
Please Return to
2801 W. Durango
Phoenix, AZ 85009

TWO-DIMENSIONAL RIVER MODELING PACKAGE

FESWMS-2DH

Finite Element Surface-Water Modeling System: Two-Dimensional Flow in a Horizontal Plane

Support Literature

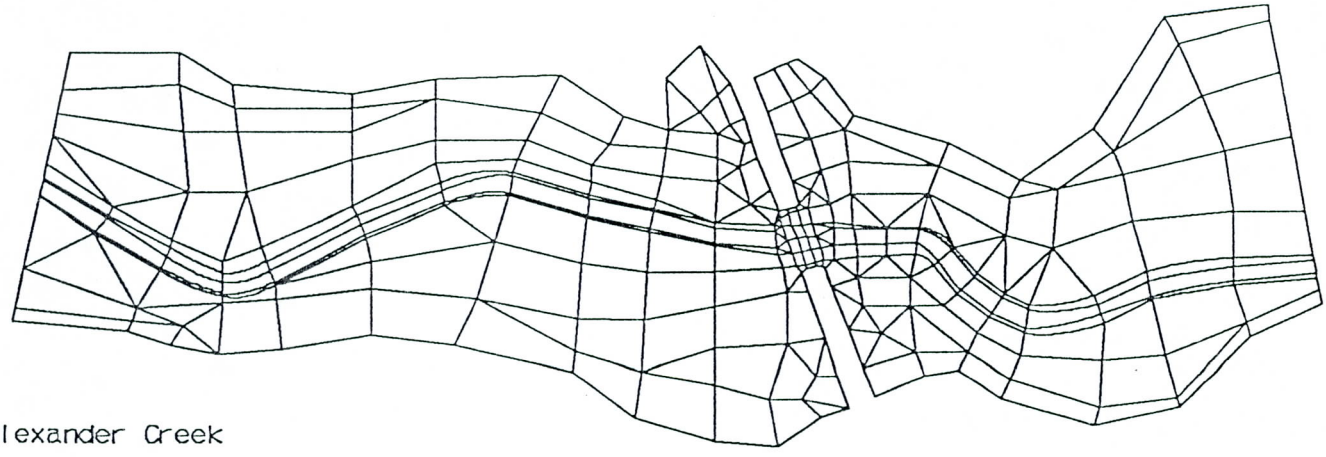

Alexander Creek

WEST Consultants, Inc.
2111 Palomar Airport Road • Suite 180 • Carlsbad, California 92009-1419 • (619) 431-8113

A TWO-DIMENSIONAL FINITE-ELEMENT MODEL STUDY OF BACKWATER AND FLOW DISTRIBUTION AT THE I-10 CROSSING OF THE PEARL RIVER NEAR SLIDELL, LOUISIANA

By Jonathan K. Lee, David C. Froehlich,

J. J. Gilbert, and Gregg J. Wiche

U.S. GEOLOGICAL SURVEY

Water-Resources Investigations Report 82-4119

Prepared in cooperation with the

LOUISIANA DEPARTMENT OF TRANSPORTATION

AND DEVELOPMENT, OFFICE OF HIGHWAYS,

and the UNITED STATES DEPARTMENT OF TRANSPORTATION,

FEDERAL HIGHWAY ADMINISTRATION

NSTL Station, Mississippi

1983

UNITED STATES DEPARTMENT OF THE INTERIOR

JAMES G. WATT, Secretary

GEOLOGICAL SURVEY

Dallas L. Peck, Director

For additional information
write to:

U.S. Geological Survey, WRD
Gulf Coast Hydroscience Center
Building 2101
NSTL Station, MS 39529

Copies of this report
can be purchased from:

Open-File Services Section
Western Distribution Branch
U.S. Geological Survey
Box 25425, Federal Center
Lakewood, CO 80225
(Telephone: (303) 234-5888)

TWO-DIMENSIONAL RIVER MODELING OF BUCKHORN CREEK NEAR SHILOH ALABAMA

by

James Thompson

WEST Consultants, Inc.
2111 Palomar Airport Road, Suite 180
Carlsbad, California 92009-1419

and

Dr. Wesley P. James

Department of Civil Engineering
Texas A&M University
College Station, Texas 77843

ABSTRACT: The flow velocities and water surface elevations at a highway crossing of heavily vegetated flood plain were investigated using a two-dimensional numerical model. The results of the simulation using FESWMS-2DH, the Finite Element Surface-Water Modeling System were compared to field observations and to a one-dimensional simulation using the U.S. Army Corps of Engineers backwater program HEC-2. Both the one-dimensional and two-dimensional simulations were performed on a microcomputer. The results of the two-dimensional showed better agreement with observed data than the results of the one-dimensional simulation. The two-dimensional model simulated the flow more completely and more accurately than the one-dimensional model.

TWO-DIMENSIONAL RIVER MODELING OF BUCKHORN CREEK NEAR SHILOH ALABAMA

INTRODUCTION

A two-dimensional Finite Element Surface Water Modeling System (FESWMS-2DH) was used to simulate steady flow at a bridge crossing of a heavily vegetated flood plain at the State Highway 130 crossing of Buckhorn Creek near Shiloh, Alabama. The flow field and water surface elevations near the bridge opening were of particular interest. Results of the two-dimensional analysis were compared to field observations and to the results of a one-dimensional analysis using HEC-2.

FESWMS-2DH was developed for the U.S. Federal Highways Administration by the Water Resources Division of the U.S. Geological Survey. The modeling system is able to simulate complex flow conditions which are essentially two-dimensional in the horizontal plane. The FESWMS-2DH modeling system may be applied to a broad range of flow conditions such as flow at a multiple opening bridge crossing, flow around islands, or flow over an irregular flood plain. Steady or unsteady flow may be modeled although the following application considers only steady flow.

The two-dimensional model uses the complete St. Venant equations where two equations describe the conservation of momentum and one equation describes the conservation of mass. Frictional losses may be modeled using the Chezy or Manning equation. Turbulence is modeled using the Boussinesq eddy viscosity concept. The value of the kinematic eddy viscosity may be determined as a function of the shear velocity and flow depth. Optionally the effects of wind stress and the Coriolis force may be included. A Galerkin finite element method is used to solve the resulting system of differential equations. The solution method is described by Lee, Froehlich, Gilbert, and Wiche (1983).

The study shows that FESWMS-2DH is capable of simulating the significant features of the flow in this irregular flood plain with particular detail near the bridge opening. The two-dimensional model is able to reproduce the water surface elevations and velocity field near the bridge opening more completely and more accurately than the one-dimensional model.

DESCRIPTION OF THE STUDY AREA

The site is located at the State Highway 130 crossing of Buckhorn Creek near Shiloh, Alabama as shown in Figure 1. The flood plain is 850 feet wide just upstream of the

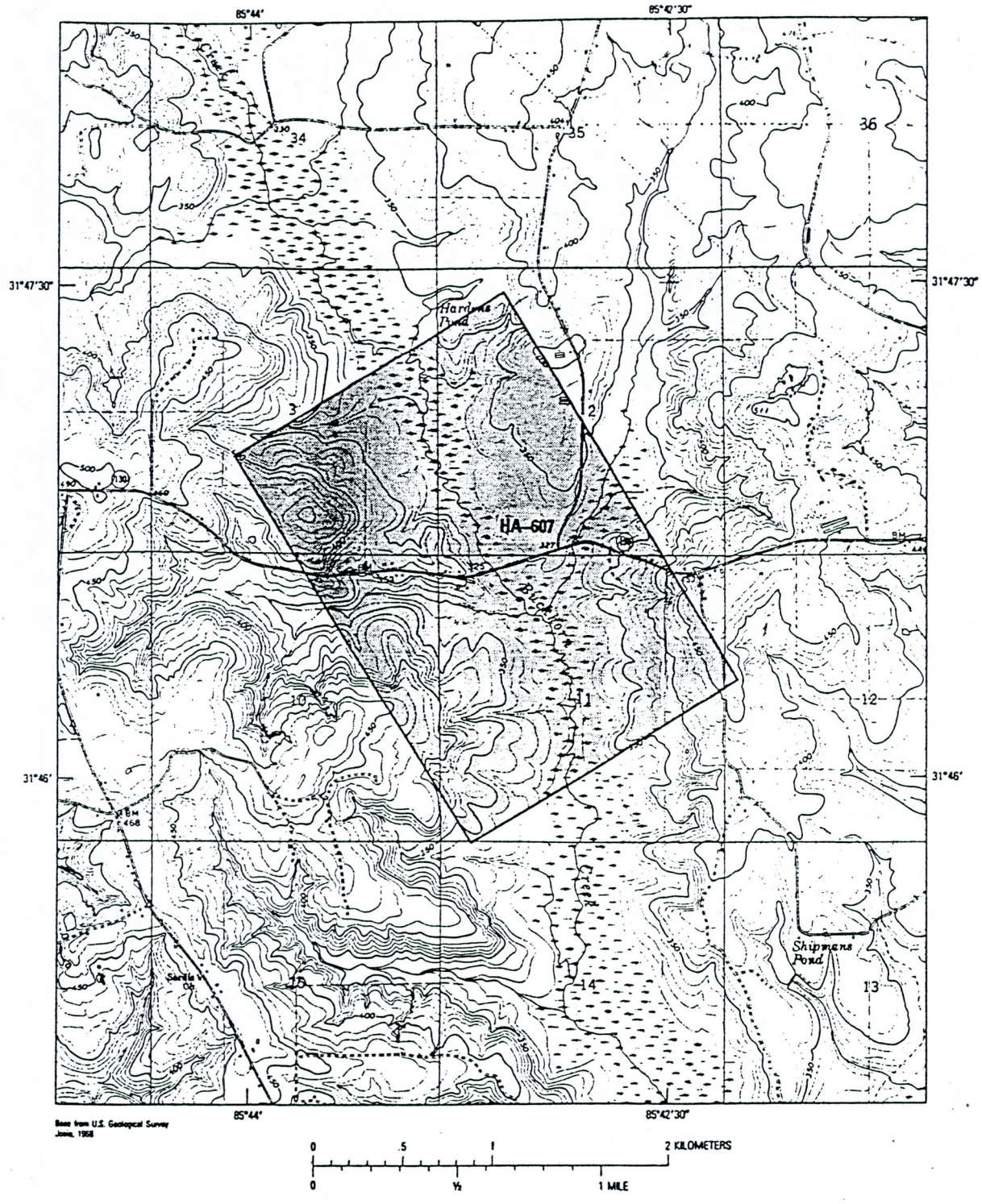

from Hydrologic Investigations Atlas HA-607

Figure 1. Site Location

embankment and 1150 feet wide just downstream of the embankment. The bridge has spillthrough type abutments and has a span of 256 ft. The flood plain is heavily vegetated and relatively flat. Moderate slopes which border the flood plain help restrict the extent of the flooding.

DATA

The data for Buckhorn Creek were taken from the Hydrologic Investigations Atlas as presented by Ming, Colson, and Arcement (1973). This data was collected by the U.S Geological Survey in cooperation with the U.S. Federal Highway Administration and the Alabama State Highway Department. Information provided by the Hydrologic Investigations Atlas included topographic maps, surveyed cross-section data, bridge geometry, discharge measurements, observed high-water marks, and other data.

The event analyzed in this study was the flood of December 21, 1972 which had a peak flow rate of 4150 cfs and an estimated return period of 28 years (Hains 1973). The peak stage at the bridge was below the lower chord therefore pressure flow or weir flow at the bridge crossing was not considered.

Cross section data for the one-dimensional model were taken from nine surveyed sections and from bridge details. Ground surface elevations used in the two-dimensional model were taken from the seven cross-sections located within the network boundary as shown in Figure 2. The extent of flooding which defined the lateral boundaries of the network was taken from the Hydrologic Investigations Atlas.

Observed water surface elevations from the Hydrologic Investigations Atlas were recovered from identified high water marks along the cross sections and survey baselines and from standard survey stakes set along the highway embankment during discharge measurements. The local variation among the observed water surface elevations was as much as 0.95 ft.

The one-dimensional model used a single value for Manning's n of 0.15 based on an investigation by Shearman (1986). The two-dimensional model used the same single value of 0.15 for Manning's n. Variation of Manning's n between elements of the two-dimensional model was not attempted as a color-infrared aerial photograph showed a fairly uniform cover of dense vegetation over the entire flood plain. Expansion and contraction coefficients used by the one-dimensional model were based on accepted values from the HEC-2 user's manual. Expansion and contraction coefficients are not required by the two-dimensional model.

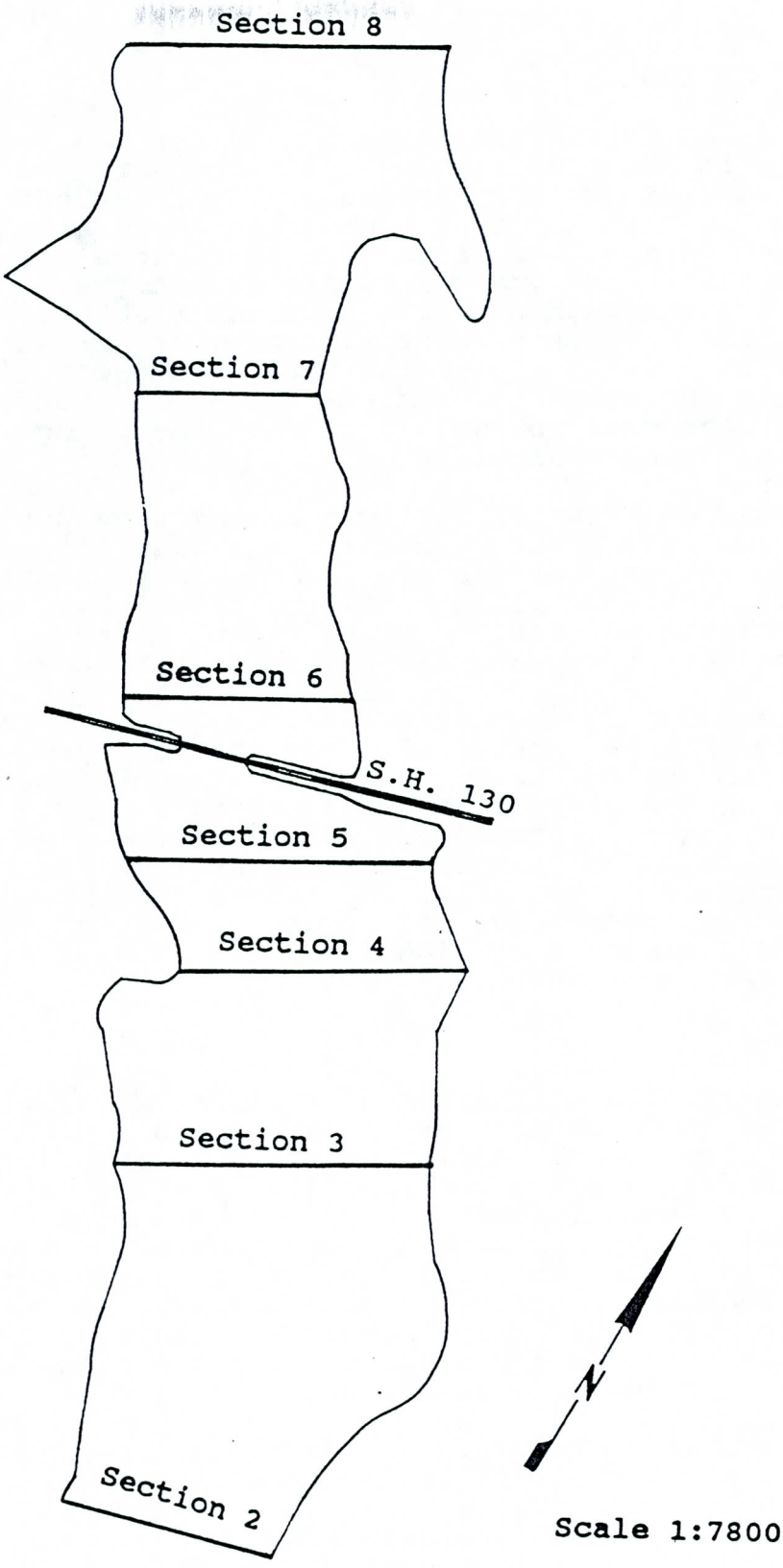

Figure 2. Cross Section Locations

NETWORK DESIGN

The finite element network used for the two-dimensional analysis is shown in Figure 3. The network was extended at least two valley widths upstream and downstream of the crossing so that the open boundaries would have little influence on the flow field near the bridge opening. In general, nine-node quadrilateral elements were used for most of the network with six-node triangular shapes being used at transitions between element sizes and at irregular boundaries. Smaller elements were used where high velocity gradients were expected and at changes in the ground slope. As such, the greatest detail is near the bridge opening and along the creek channel.

Observed water surface elevations were used as the downstream open boundary condition. Slip flow was specified so that flow was parallel to the closed boundaries at the edges of the flood plain and along the highway embankment. The discharge was divided among the upstream boundary nodes based on the conveyance along this open boundary.

The time required to design the grid for the two-dimensional model, input the data and run the initial simulation was one week. A finite element network containing 338 elements and 1345 nodes was used to describe the study area. Eight iterations were required for convergence. The criteria for convergence was a change in water surface elevation at any node of not more than 0.001 feet between successive iterations. About ten minutes was required for each iteration on an 80386 based microcomputer with a math coprocessor.

RESULTS

The results of the two-dimensional simulation are presented in terms of the velocity field and the water surface elevations. A plot of the velocity field for the entire model is presented in Figure 4. The magnitude of the velocity at each computational node is indicated by the length of the vector symbol. The density of the vector symbols indicates only the density of the computational nodes, that is, closely spaced symbols do not necessarily indicate higher velocity. Typical velocities within the flood plain are on the order of 2 ft/s or less as may be expected with dense vegetation.

The maximum velocity at the bridge opening is 3 ft/s. Figure 5 shows a detail of the flow field near the bridge. Upstream of the bridge opening lateral flow is apparent within a distance of approximately one bridge opening. Downstream of the bridge opening the flow is fully expanded within a distance of about one valley width. One-dimensional modeling techniques suggest that in this case

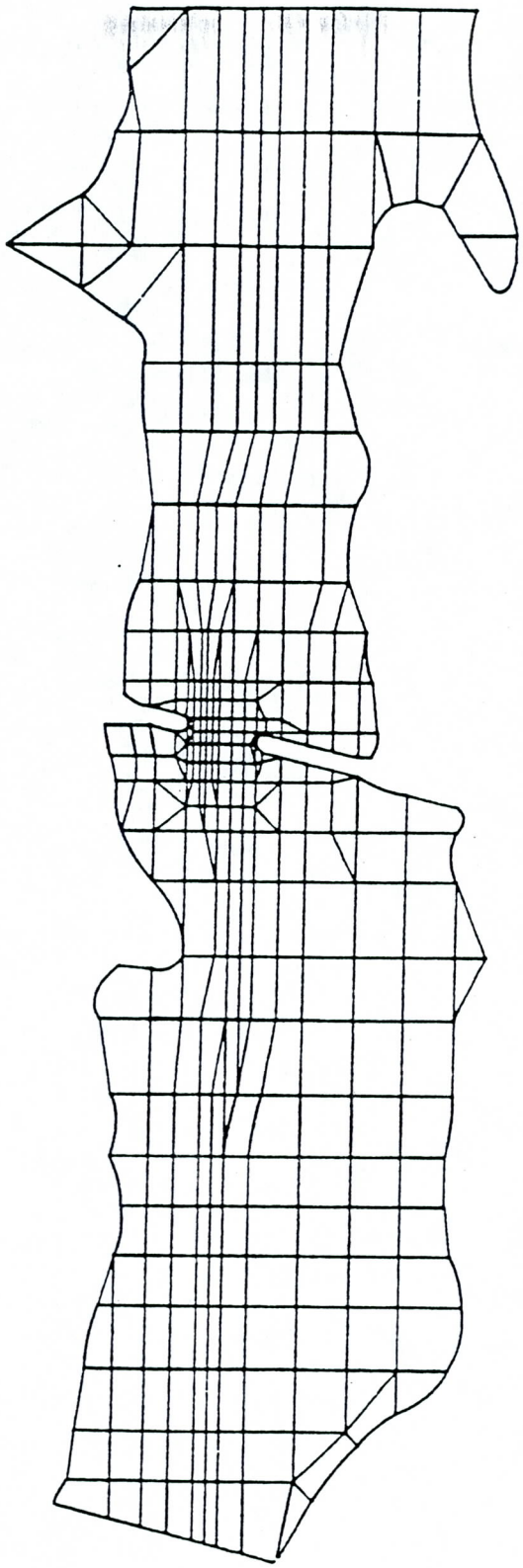

Scale 1:7800

Figure 3. Finite Element Network

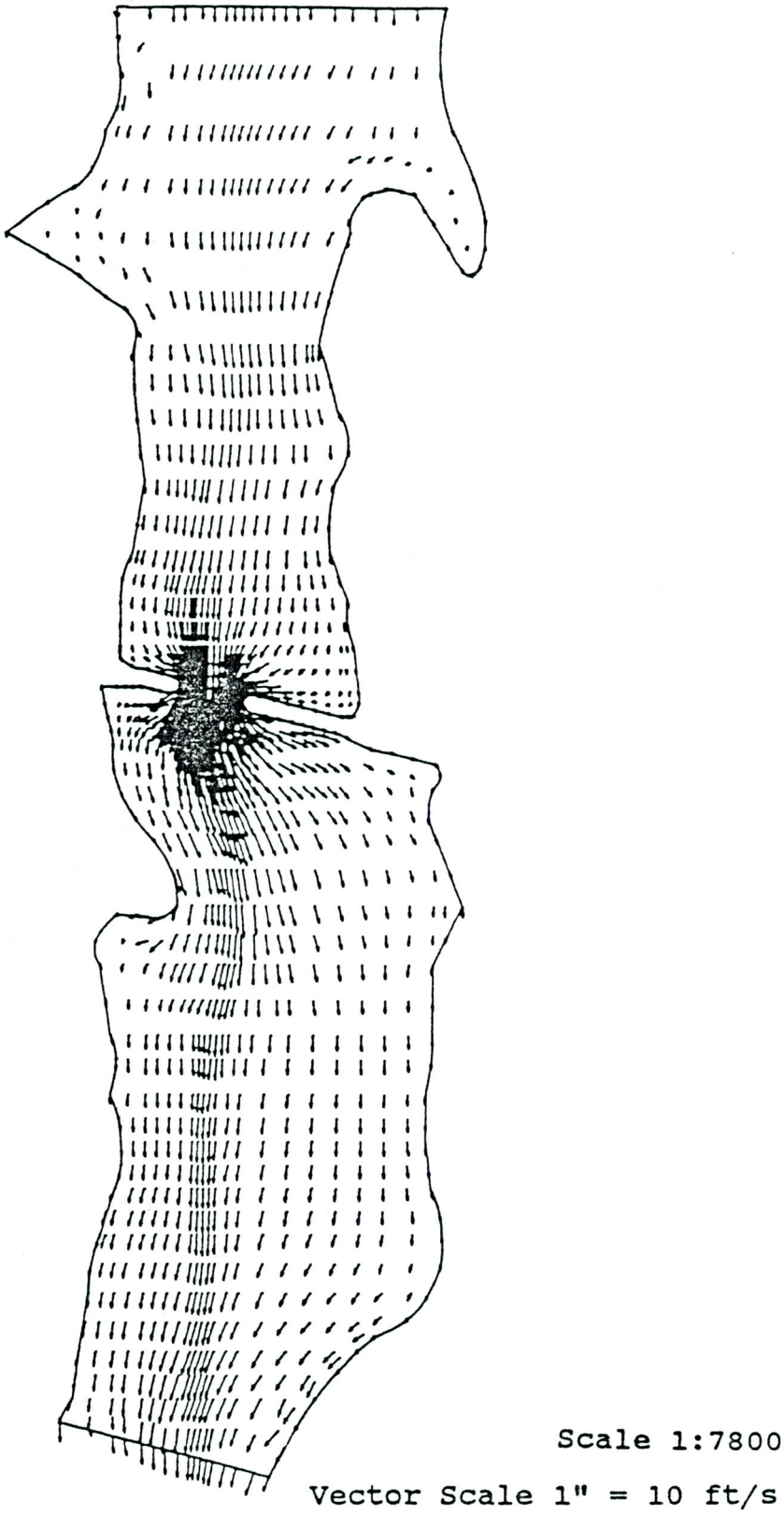

Figure 4. Velocity Field for Network

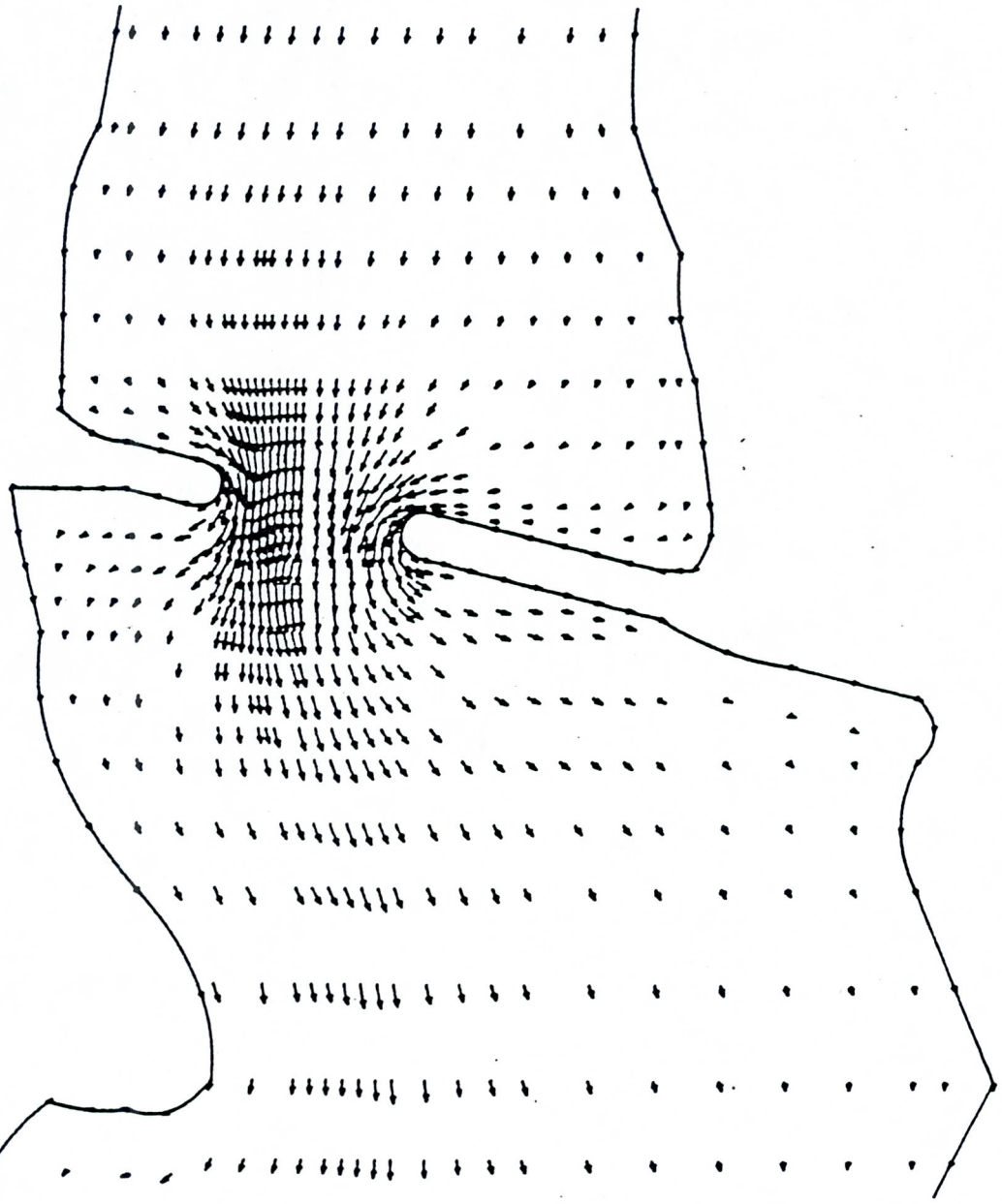

Vector Scale 1" = 15 ft/s

Scale 1:3000

Figure 5. Detail of Velocity Field Near Bridge

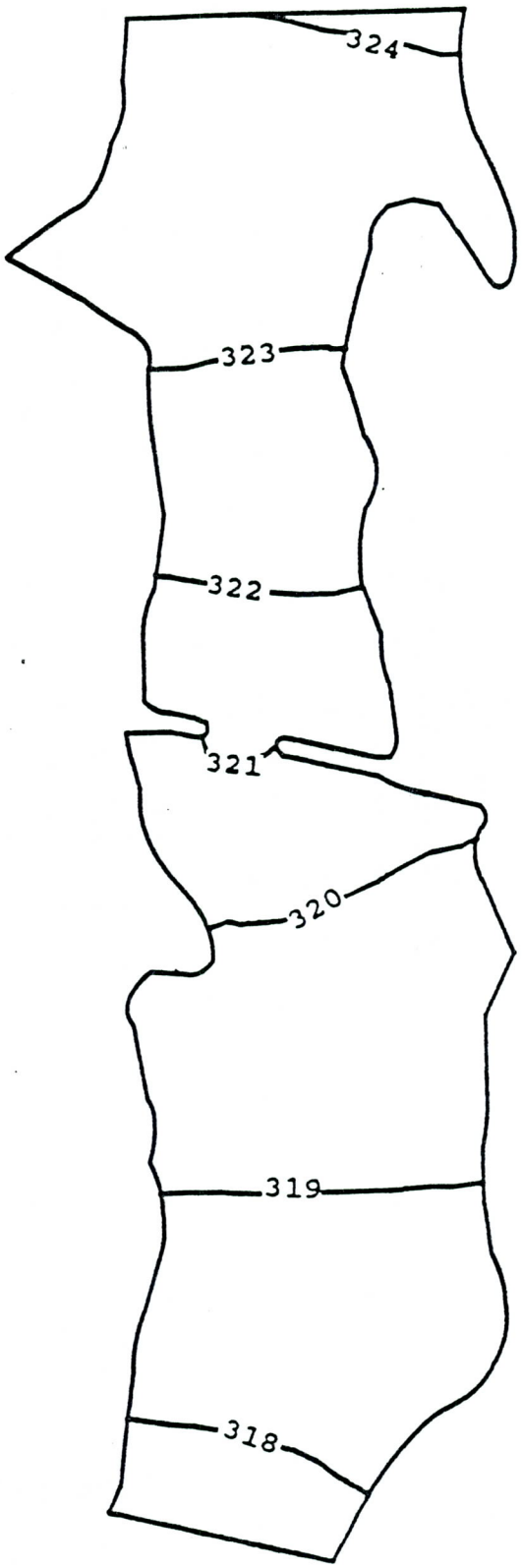

Scale 1:7800

Figure 6. Water Surface Contours

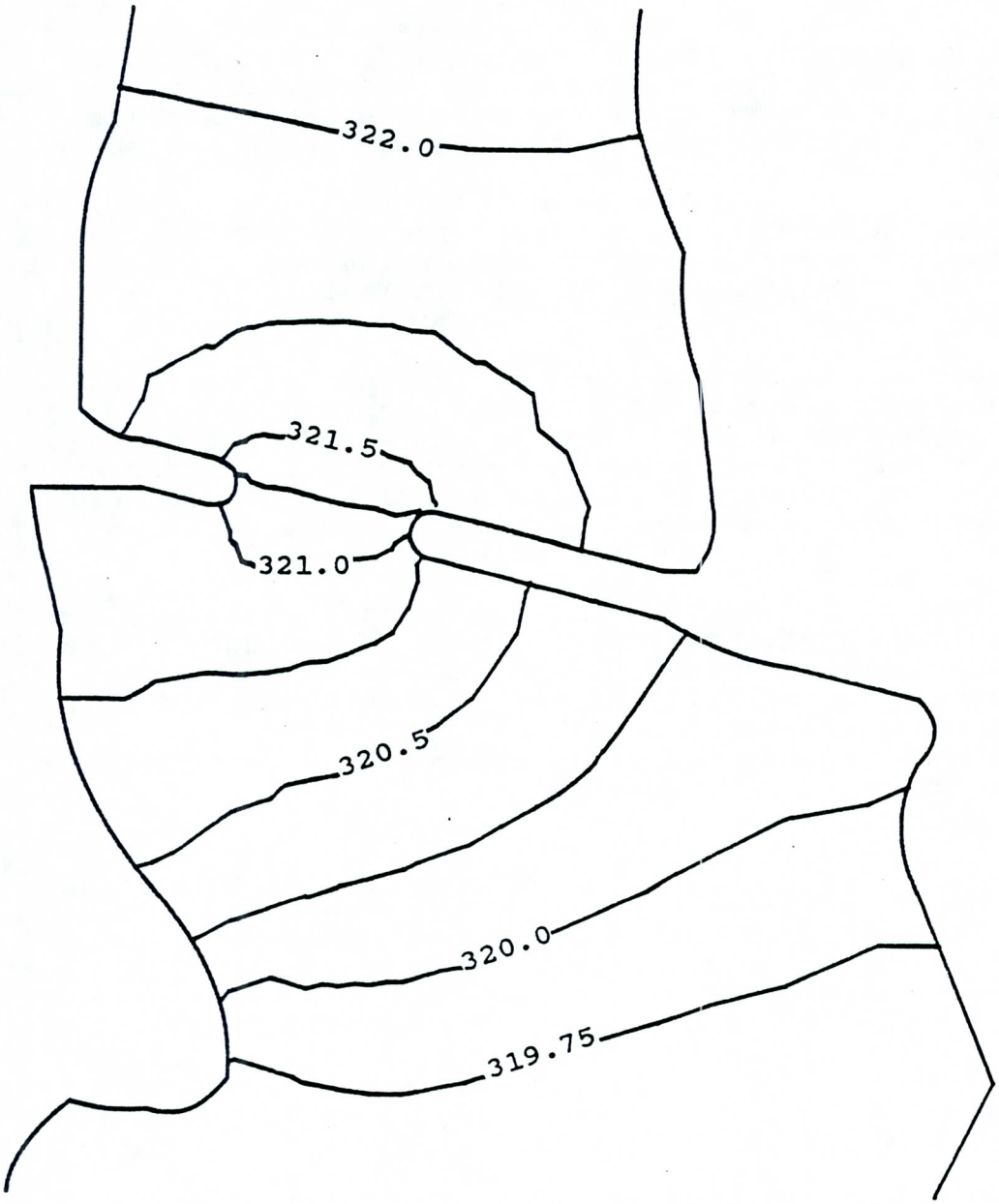

Scale 1:3000

Figure 7. Detail of Water Surface Contours Near Bridge

the flow would not be fully expanded until more than two valley widths downstream. The flow field shows no apparent recirculation at the bridge opening. Potentially, recirculation may cause higher head losses and increased scour.

The water surface elevation contours for the entire model are shown in Figure 6. The bank-to-bank variation of the water surface is most apparent where the water surface contours are curved such as near the bridge opening as shown in Figure 7.

The observed water surface elevations are compared to the water surface elevations predicted by the one-dimensional and two-dimensional models in Table 1 and plotted as a water surface profiles in Figure 8.

The one-dimensional model was calibrated to provide overall quantitative agreement with the observed along-stream data although it was incapable of reproducing cross-stream variations. HEC-2 tends to overpredict the water surface elevation downstream of a contraction, consequently the agreement with the observed data was poor near the bridge.

The agreement between the two-dimensional model and the observed data was good, particularly near the bridge opening. The observed water surface elevations near the bridge opening were generally higher on the right bank than on the left bank, a feature reproduced in the two-dimensional model. Left and right refer to the orientation of a viewer facing downstream.

Table 1. Comparison of Water Surface Elevations

X-SECT	DISTANCE (ft)	LB Obs (ft)	RB Obs (ft)	HEC-2 (ft)	LB 2-D (ft)	RB 2-D (ft)
2	1025	317.25	317.55	317.46	317.26	317.55
3	2340	319.10	318.94	319.23	319.11	319.12
4	3030		320.00	320.31	319.75	319.70
4	3030		319.80	320.31	319.75	319.70
BRIDGE DS	3710	320.30	321.73	321.49	320.48	320.90
BRIDGE DS	3710	320.54	320.92	321.49	320.48	320.90
BRIDGE US	3736	321.69	321.76	321.97	321.66	321.66
BRIDGE US	3736		321.18	321.97	321.66	321.66
6	3938	321.84	321.94	322.01	321.78	321.80
6	3938	321.81	321.83	322.01	321.78	321.80
7	4988	323.10	323.09	323.12	322.75	322.98
7	4988	322.78	322.14	323.12	322.75	322.98
8	6238	324.48	324.11	323.97	324.09	323.96
8	6238	324.06	324.05	323.97	324.09	323.96

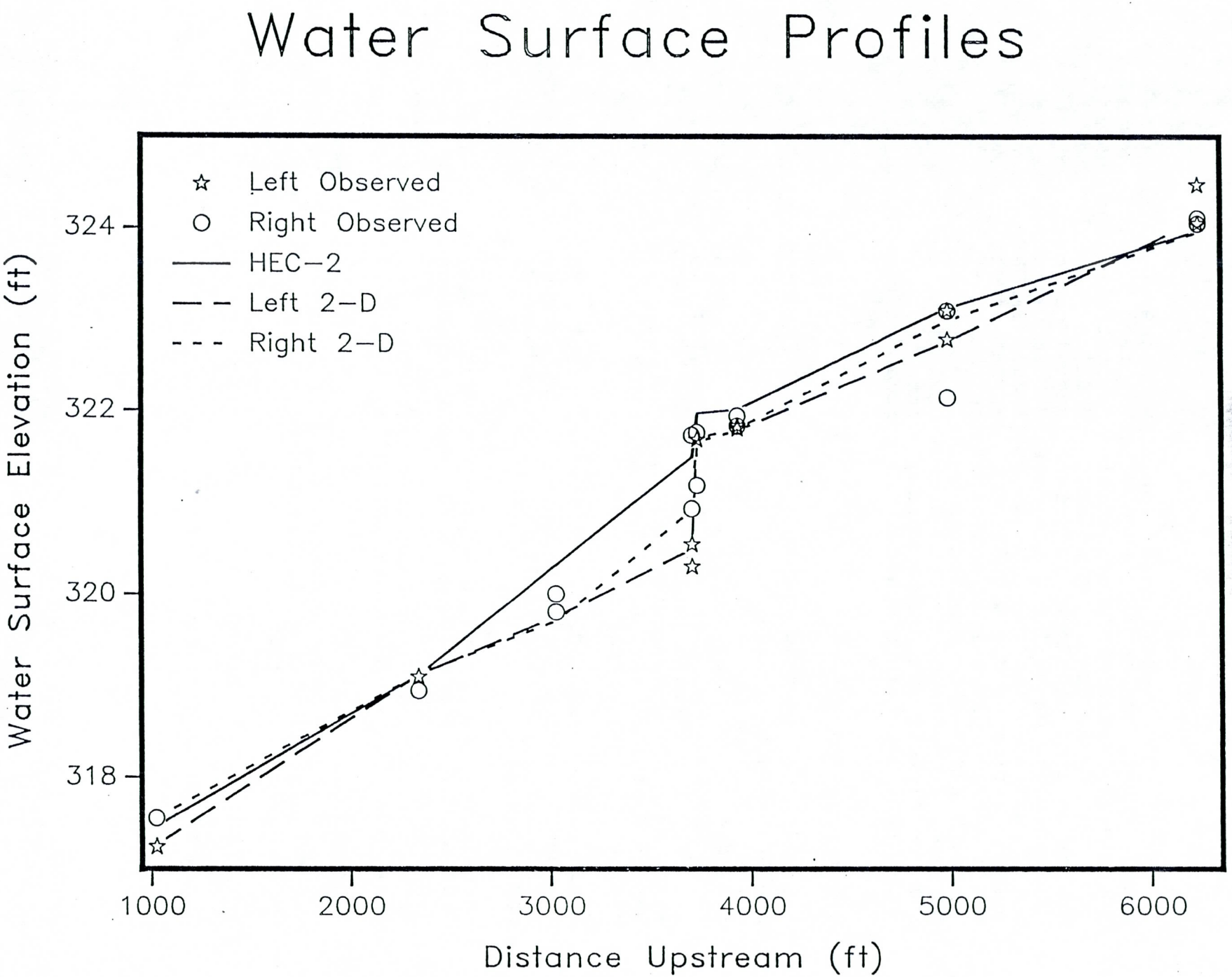

Figure 8. Comparison of Water Surface Profiles

SUMMARY

While the overall agreement between the one-dimensional model, HEC-2, and the observed water surface elevations was acceptable, water surface elevations near the bridge opening could not be accurately predicted. Fundamentally the one-dimensional model cannot represent lateral components of the flow velocity or evaluate the cross-stream variation of the water surface. The two-dimensional model, FESWMS-2DH, was able to reproduce the significant features of the observed water surface elevations and determine the two-dimensional velocity field with particular detail near the bridge opening. In essence, the two-dimensional model performed more completely and more accurately than the one-dimensional model near the bridge opening and throughout the floodplain.

REFERENCES

Froehlich, D.C., "U.S. Geological Survey Open-File Report," Reston, Virginia, 1988.

Lee, J.K., Froehlich, D.C., Gilbert, J.J., and Wiche, G.J., "A Two-Dimensional Finite-Element Model Study of Backwater and Flow Distribution at the I-10 Crossing of the Pearl River Near Slidell, Louisiana," U.S. Geological Survey Water- Resources Investigations Report 82-4119, NSTL Station, Mississippi, 1983.

Ming, C.O., Colson, B.E., and Arcement, G.J., "Backwater at Bridges and Densely Wooded Flood Plains, Buckhorn Creek Near Shiloh Alabama," U.S. Geological Survey Hydrologic Atlas HA-607, 1979.

Schneider, V.R., Board, J.W., Colson, B.E., Lee, F.N., and Druffel, L., "Computation of Backwater and Discharge at Width Constrictions of Heavily Vegetated Flood Plains," U.S. Geological Survey Water-Resources Investigations Report 76-129, NSTL Station, Mississippi, 1976.

Shearman, J.O., Kirkby, W.H., Schneider, V.R., and Flippo, H.N., "Bridge Waterways Analysis Model: Research Report," Federal Highways Administration Report FHWA/RD-86/108, Reston, Virginia, 1986.

U.S. Army Corps of Engineers Water Resources Support Center, "HEC-2 Water Surface Profiles Users Manual," Hydrologic Engineering Center, Davis, California, 1984.

A TWO-DIMENSIONAL FINITE-ELEMENT MODEL STUDY OF BACKWATER AND FLOW DISTRIBUTION AT THE I-10 CROSSING OF THE PEARL RIVER NEAR SLIDELL, LOUISIANA

By Jonathan K. Lee, David C. Froehlich,
J. J. Gilbert, and Gregg J. Wiche

U.S. GEOLOGICAL SURVEY

Water-Resources Investigations Report 82-4119

Prepared in cooperation with the
LOUISIANA DEPARTMENT OF TRANSPORTATION
AND DEVELOPMENT, OFFICE OF HIGHWAYS,
and the UNITED STATES DEPARTMENT OF TRANSPORTATION,
FEDERAL HIGHWAY ADMINISTRATION

NSTL Station, Mississippi

1983

UNITED STATES DEPARTMENT OF THE INTERIOR

JAMES G. WATT, Secretary

GEOLOGICAL SURVEY

Dallas L. Peck, Director

For additional information
write to:

U.S. Geological Survey, WRD
Gulf Coast Hydroscience Center
Building 2101
NSTL Station, MS 39529

Copies of this report
can be purchased from:

Open-File Services Section
Western Distribution Branch
U.S. Geological Survey
Box 25425, Federal Center
Lakewood, CO 80225
(Telephone: (303) 234-5888)

CONTENTS

	Page
Abstract	1
Introduction	2
Model description	3
Flow equations	4
Numerical solution of the flow equations	5
Description of the study area	6
Pearl River basin	6
Study reach	8
Hydrology of the Pearl River basin	11
Flood data	11
Flood frequency	16
Simulation of the April 2, 1980, flood	16
Data collection and analysis	16
Steady-state assumption	18
Network design	18
Model adjustment	21
Boundary conditions	21
Aspects of model adjustment	24
Preliminary model calibration	26
Adjustment of model boundary conditions, network detail, and ground-surface elevations	29
Final model calibration	30
Comparison of computed and observed water-surface elevations and discharges	31
Additional results of the simulation	37
Simulation of the April 2, 1980, flood without the I-10 embankments in place	49
Network modifications	49
Results of the simulation	50
Backwater and drawdown caused by the I-10 embankments	53
Discussion	53
Summary and conclusions	58
References	58

ILLUSTRATIONS

Page

Figure 1. Map showing lower Pearl River basin, Louisiana and Mississippi---------- 7
2. Map showing study reach of the lower Pearl River basin near Slidell---------- 9
3. Photographs showing flooding near Slidell during April 1980---------- 12
4. Photograph showing overtopped north lane of I-10 between Slidell and Bay St. Louis during the April 2, 1980, flood---------- 14

Figures 5-16. Graphs showing:
5. Water-surface elevations at Pearl River and Pearlington from March 31 to April 4, 1980---------- 19
6. Prototype and model channel cross sections at section A-A'---------- 22
7. Computed and measured unit discharge at the I-10 bridge opening at the Pearl River---------- 38
8. Computed and measured unit discharge at the I-10 bridge opening at the Middle River---------- 39
9. Computed and measured unit discharge at the I-10 bridge opening at the West Pearl River---------- 40
10. Computed water-surface elevations for the Pearl River with and without the I-10 embankments in place--------- 41
11. Computed water-surface elevations for the West Pearl River with and without the I-10 embankments in place---------- 42
12. Computed water-surface elevations at the east edge of the flood plain with and without the I-10 embankments in place---------- 43
13. Computed water-surface elevations at the west edge of the flood plain with and without the I-10 embankments in place---------- 44
14. Computed channel discharge for the Pearl River with and without the I-10 embankments in place---------- 47
15. Computed channel discharge for the West Pearl River with and without the I-10 embankments in place--------- 48
16. Computed backwater and drawdown for the Pearl and West Pearl Rivers------- 54

PLATES

Page

Plate 1. Map showing finite-element network and element types with the I-10 embankments in place for the flood of April 2, 1980, on the Pearl River near Slidell, La. (2 sheets)-------In pocket

2. Map showing computed velocity field and water-surface elevations and observed high-water marks with the I-10 embankments in place for the flood of April 2, 1980, on the Pearl River near Slidell, La. (2 sheets)-------------In pocket

3. Map showing computed velocity field and water-surface elevations without the I-10 embankments in place for the flood of April 2, 1980, on the Pearl River near Slidell, La. (2 sheets)-------In pocket

4. Map showing backwater and drawdown caused by I-10 for the flood of April 2, 1980, on the Pearl River near Slidell, La. (2 sheets)-------------In pocket

TABLES

Page

Table 1. Discharges measured during the 1961, 1979, and 1980 floods on the lower Pearl River-------- 15

2. Flood frequency data for the Pearl River at Bogalusa and Pearl River---------- 17

3. Distribution of discharge at the upstream model boundary---------- 23

4. Water-surface elevations at the downstream model boundary---------- 25

5. Values of Chézy coefficients used to simulate the April 2, 1980, flood---------- 27

6. Elevations of the computed water surface and observed high-water marks for the April 2, 1980, flood---------- 33

7. Computed and measured discharges at the I-10 bridge openings---------- 36

8. Computed discharges at the Highway 90 bridge openings with and without the I-10 embankments in place---------- 46

9. Computed discharges at I-10 with and without the I-10 embankments in place---------- 52

10. Computed water-surface elevations with and without the I-10 embankments in place and backwater or drawdown---------- 55

CONVERSION FACTORS

Factors for converting inch-pound units to the International System of Units (SI) are shown to four significant figures.

Multiply inch-pound unit	By	To obtain SI unit
foot (ft)	3.048×10^{-1}	meter (m)
foot to the one-sixth power ($ft^{1/6}$)	8.204×10^{-1}	meter to the one-sixth power ($m^{1/6}$)
foot to the one-half power per second ($ft^{1/2}/s$)	5.521×10^{-1}	meter to the one-half power per second ($m^{1/2}/s$)
foot per second (ft/s)	3.048×10^{-1}	meter per second (m/s)
foot per square second (ft/s^2)	3.048×10^{-1}	meter per square second (m/s^2)
cubic foot per second (ft^3/s)	2.832×10^{-2}	cubic meter per second (m^3/s)
mile (mi)	1.609	kilometer (km)
square mile (mi^2)	2.590	square kilometer (km^2)
foot per mile (ft/mi)	1.894×10^{-1}	meter per kilometer (m/km)
slug per cubic foot ($slug/ft^3$)	5.154×10^{2}	kilogram per cubic meter (kg/m^3)
pound second per square foot ($lb \cdot s/ft^2$)	4.787×10^{2}	pascal second (Pa·s)

National Geodetic Vertical Datum of 1929 (NGVD of 1929): A geodetic datum derived from a general adjustment of the first-order level nets of both the United States and Canada, called NGVD of 1929, is referred to as sea level in this report.

A TWO-DIMENSIONAL FINITE-ELEMENT MODEL STUDY OF BACKWATER AND FLOW DISTRIBUTION AT THE I-10 CROSSING OF THE PEARL RIVER NEAR SLIDELL, LOUISIANA

By Jonathan K. Lee, David C. Froehlich,
J. J. Gilbert, and Gregg J. Wiche

ABSTRACT

A two-dimensional finite-element surface-water flow modeling system based on the shallow-water equations was used to study the effect of Interstate Highway 10 (I-10) on water-surface elevations and flow distribution during the flood of April 2, 1980, on the Pearl River near Slidell, Louisiana. The model can be used to simulate both lateral and longitudinal velocities and variations in water-surface elevation, highly variable flood-plain topography and vegetative cover, and geometric features such as highway embankments, dikes, and channel bends. Geometric features of widely varying sizes are easily accommodated within a single finite-element network.

A finite-element network was designed to represent the topography and vegetative cover of the study reach. Hydrographic data collected for the April 1980 flood were used to calibrate the flow model. The finite-element network was then modified to represent conditions without I-10 in place, and the hydraulic impact of I-10 was determined by comparing results with and without I-10.

Model results show that, without I-10 in place, much of the flow shifts from the west side of the flood plain to the east side upstream from the site of I-10. With I-10 in place, this flow shift occurs somewhat farther upstream than it does without the roadway in place. Upstream from the roadway, maximum backwater at the west edge of the flood plain is 1.5 feet, and maximum backwater at the east edge is 1.1 feet, but backwater extends farther upstream along the east edge of the flood plain than along the west edge. Backwater ranging from 0.6 to 0.2 foot extends more than a mile downstream from the Pearl River bridge opening in I-10 at the east edge of the flood plain, and drawdown of 0.2 foot or more occurs along approximately 2 miles of the west edge of the flood plain downstream from I-10.

The capability of the modeling system to simulate the significant features of steady-state flow in a complex multichannel river-flood-plain system with variable topography and vegetative cover was successfully demonstrated in this study. These features included lateral variations in discharge distribution and backwater or drawdown.

INTRODUCTION

In April 1979 and April 1980, major flooding on the lower Pearl River caused extensive damage to homes located on the flood plain in the Slidell, La., area. Many persons were forced from their homes until the flood waters receded. Property damages in the Slidell area due to the 1980 flood, the largest flood of record in the area, were estimated to be $12.275 million (U.S. Army Corps of Engineers, 1981, p. 76). The 1980 flood forced the closing of the I-10 crossing of the Pearl River flood plain between Slidell and Bay St. Louis, Miss., for several hours while the flood crest passed. Many local residents attributed part of the 1979 and 1980 flooding in the Slidell area to backwater caused by the I-10 embankments.

The U.S. Geological Survey, in cooperation with the Louisiana Department of Transportation and Development, Office of Highways, and the U.S. Department of Transportation, Federal Highway Administration, undertook to determine the effect of the highway crossing on water-surface elevations and flow distribution during the April 2, 1980, flood for three reasons: (1) there was much interest in the impact of I-10; (2) the April 1980 flood was a large flood, which partially inundated the I-10 crossing; and (3) the study offered the opportunity to test a two-dimensional finite-element flow modeling system in a multichannel flood plain.

The two-dimensional finite-element surface-water flow modeling system FESWMS was used to study the effect of I-10 during the 1980 flood. The width of the Pearl River flood plain, constrictions created by highway embankments, and other physical features of the flood plain caused significant lateral variations in water-surface elevation and flow distribution during the 1980 flood. Thus, use of a two-dimensional model was warranted in order to obtain a more precise evaluation of water-surface elevations and flow distribution near the I-10 crossing than could be obtained by one-dimensional backwater and conveyance techniques.

An earlier version of the modeling system FESWMS was used to study the impact of a proposed highway crossing on flood stages of the Congaree River near Columbia, S.C. (Lee, 1980; Lee and Bennett, 1981). In the Congaree River study, it was demonstrated that the model can be used to simulate both lateral and longitudinal velocities and variations in water-surface elevation. Highly variable flood-plain topography and vegetative cover and geometric features such as highway embankments, dikes, and channel bends can be readily accounted for in a finite-element network. Moreover, geometric features of widely varying sizes are easily accommodated within a network. In order to demonstrate that FESWMS can be used effectively to analyze steady-state flow in large multichannel flood plains, the Geological Survey used the model to determine the effect of the I-10 crossing on water-surface elevations and flow distribution during the April 1980 flood on the Pearl River.

This report presents the application of FESWMS to the Pearl

River and illustrates the usefulness of the two-dimensional model in analyzing steady-state flow with both lateral and longitudinal variations. The report begins with a brief description of the modeling system FESWMS, a description of the study area, and a discussion of the hydrology of the Pearl River basin. Data collection, network design, and model adjustment for the 1980 flood with I-10 in place are described. Results of the simulation of the 1980 flood both with and without I-10 in place are presented, and backwater and drawdown caused by the roadway are discussed.

The assistance of the following individuals and organizations in making available data for this study is gratefully acknowledged: William T. Jack, Jr., Louisiana Department of Transportation and Development, Office of Highways; and Harold V. Doyal and Michael W. Peterson, U.S. Army Corps of Engineers, Mobile District. The support of the U.S. Department of Transportation, Federal Highway Administration, is also gratefully acknowledged. Computer work was done on an IBM 3033[1/] at Johns Hopkins University's Applied Physics Laboratory.

Throughout this report, the words "right" and "left" refer to positions that would be reported by an observer facing downstream. The words "backwater" and "drawdown" denote an increase and a decrease, respectively, in water-surface elevation caused by a flood-plain constriction. Backwater may occur both upstream and downstream from the constriction. Elevations refer to the National Geodetic Vertical Datum (NGVD) of 1929, called sea level in this report. A list of factors for converting inch-pound units to SI units is provided at the front of the report. All data supporting the conclusions of this report are available in the files of the Louisiana District office of the Geological Survey at Baton Rouge, La.

MODEL DESCRIPTION

The core of the modeling system FESWMS, which is under development by the Geological Survey, is a two-dimensional finite-element surface-water flow model based on the work of Norton and King (Norton and King, 1973; Norton and others, 1973; Tseng, 1975; King and Norton, 1978). Around this core, the Geological Survey has developed pre- and postprocessing programs which make the system accessible to the user. Preprocessing programs place input data in an appropriate form for the flow model and plot maps of finite-element networks and associated data. Postprocessing programs plot maps of velocity vectors, water-surface contour lines, lines of equal backwater and drawdown, discharge at specified cross sections, and observed high-water marks.

The formulation and development of the flow model have been reported elsewhere; therefore, only the equations solved and a brief outline of the technique used to solve them are presented here.

1/The use of brand names in this report is for identification purposes only and does not imply endorsement by the U.S. Geological Survey.

Flow Equations

Under the usual assumptions (for example, hydrostatic pressure and momentum correction factors of unity), two-dimensional surface-water flow in the horizontal plane is described by three nonlinear partial-differential equations, two for conservation of momentum and one for conservation of mass (Pritchard, 1971):

$$\frac{\partial u}{\partial t} + u\frac{\partial u}{\partial x} + v\frac{\partial u}{\partial y} + g\frac{\partial h}{\partial x} + g\frac{\partial z_o}{\partial x} - \frac{1}{\rho h}\left[\frac{\partial}{\partial x}\left(\varepsilon_{xx} h \frac{\partial u}{\partial x}\right) + \frac{\partial}{\partial y}\left(\varepsilon_{xy} h \frac{\partial u}{\partial y}\right)\right]$$

$$- 2\omega v \sin\varphi + \frac{gu}{C^2 h}(u^2 + v^2)^{1/2} - \frac{\zeta}{h} V_a^2 \cos\psi = 0, \qquad (1)$$

$$\frac{\partial v}{\partial t} + u\frac{\partial v}{\partial x} + v\frac{\partial v}{\partial y} + g\frac{\partial h}{\partial y} + g\frac{\partial z_o}{\partial y} - \frac{1}{\rho h}\left[\frac{\partial}{\partial x}\left(\varepsilon_{yx} h \frac{\partial v}{\partial x}\right) + \frac{\partial}{\partial y}\left(\varepsilon_{yy} h \frac{\partial v}{\partial y}\right)\right]$$

$$+ 2\omega u \sin\phi + \frac{gv}{C^2 h}(u^2 + v^2)^{1/2} - \frac{\zeta}{h} V_a^2 \sin\psi = 0, \qquad (2)$$

and

$$\frac{\partial h}{\partial t} + \frac{\partial}{\partial x}(uh) + \frac{\partial}{\partial y}(vh) = 0, \qquad (3)$$

where x, y = Cartesian coordinates in the positive east and north directions, respectively (feet),
t = time (seconds),
u, v = depth-averaged velocity components in the x- and y-directions, respectively (feet per second),
h = depth (feet),
z_o = bed elevation (feet),
ρ = density of water (assumed constant) (slugs per cubic foot),
ω = rate of the Earth's angular rotation (per second),
φ = latitude (degrees),
g = gravitational acceleration (feet per square second),
C = Chézy coefficient (feet to the one-half power per second),
ε_{xx}, ε_{xy}, ε_{yx}, ε_{yy} = eddy viscosities (pound second per square foot),
ζ = water-surface resistance coefficient (nondimensional),
V_a = local wind velocity (feet per second), and
ψ = angle between the wind direction and the x-axis (degrees).

The two-dimensional surface-water flow equations account for energy losses through two mechanisms: bottom friction and turbulent stresses. The Chézy equation for bottom friction in open-channel flow is extended to two dimensions for use in equations 1 and 2. Equations 1 and 2 also use Boussinesq's eddy-viscosity concept, which assumes the turbulent stresses to be proportional to the mean-velocity gradients.

Boundary conditions consist of the specification of flow components or water-surface elevations at open boundaries and zero flow components or zero normal flow (tangential flow) at all other boundaries, called lateral boundaries. For a time-dependent problem, initial conditions must also be specified. Equations 1 through 3, together with properly specified initial and boundary conditions, constitute a well-posed initial-boundary-value problem.

Numerical Solution of the Flow Equations

Quadratic basis functions are used to interpolate velocity components, and linear basis functions are used to interpolate depth on triangular, six-node, isoparametric elements (mixed interpolation). Model topography is defined by assigning a ground-surface elevation to each element vertex and requiring the ground surface to vary linearly within an element.

The finite-element model requires the specification of a constant Chézy coefficient, C, and a constant symmetric turbulent-exchange, or eddy-viscosity, tensor, ε, over each element. Nonisotropic turbulent stresses can be simulated by assigning different values to the components of the eddy-viscosity tensor. The eddy-viscosity terms in the momentum equations suppress nonlinear instabilities generated by the convective terms, and nonzero eddy-viscosity values are necessary for convergence of the numerical method to a solution. The eddy-viscosity values can influence the results of a simulation; however, optimum values are difficult to determine. In general, increased values serve to increase water-surface slopes. It is also known that eddy-viscosity values should increase with element size.

Flow components are specified at inflow boundary nodes, and water-surface elevations are specified at outflow boundary nodes. In this study, zero normal flow was specified at all lateral boundaries. Isoparametric elements permit the use of smooth, curved lateral boundaries. The improvement in accuracy obtained by using such boundaries, together with the specification of zero normal flow (tangential flow) there, has been documented by Gee and MacArthur (1978), King and Norton (1978), and Walters and Cheng (1978, 1980) for the mixed-interpolation formulation of the surface-water flow equations.

Galerkin's method of weighted residuals, a Newton-Raphson iteration scheme, numerical integration using seven-point Gaussian quadrature (Zienkiewicz, 1977, p. 200-201), and a frontal solution algorithm using out-of-core storage (Hood, 1976, 1977) are used to

solve for the nodal values of the velocity components and depth. The time derivatives are handled by an implicit finite-difference scheme; in the application reported here, however, only the steady-state forms of the equations were solved.

If a finite-element network is not well designed, errors in conservation of mass can be significant because there are only approximately half as many equations for conservation of mass as there are for conservation of momentum in either the x- or y-direction. For a well-designed network, however, errors in mass conservation are small. The model has the capability of integrating the discharge across a line following element sides and beginning and ending at element vertices. Thus, conservation of mass can be checked (King and Norton, 1978).

The interested reader may consult the books by Pinder and Gray (1977) and Zienkiewicz (1977) for additional information on the finite-element method.

DESCRIPTION OF THE STUDY AREA

Pearl River Basin

The Pearl River basin is about 240 mi long and 50 mi wide. The basin drains a large part of Mississippi and part of southeastern Louisiana. The basin is bounded on the north by the Tombigbee River basin, on the east by the Pascagoula River basin, on the south by Lake Borgne and the Mississippi Sound, and on the west by the Mississippi River basin and several coastal streams in southeastern Louisiana. The basin lies within the Gulf Coastal Plain. Elevations within the basin range from sea level along the coast to about 650 ft above sea level in the north-central hills.

The Pearl River originates in Neshoba County, Miss., at the confluence of Nanawaya and Tallahaga Creeks. From its origin, it flows southwestward for 130 mi to the vicinity of Jackson, Miss., then southeastward for another 281 mi to empty into Lake Borgne. Most of the low-water flow of the Pearl is transferred to the West Pearl River through Holmes Bayou 28 mi above the West Mouth of the West Pearl at the Rigolets (fig. 1). Cardwell and others (1967, p. 43) have described this westward shift of flow:

> The bottom lands...are laced by cross-connecting channels which distribute flow across these bottoms during periods of high river stage. In the vicinity of Picayune, Miss., the main channel of the Pearl River begins to shift westward to become the West Pearl River. A small cross channel, Farr Slough, leaves the main channel near Picayune and joins Hobolochitto Creek. The channel, known downstream as the "Pearl River," begins at this confluence. There is evidence that this eastern channel was once the major channel of the lower Pearl River system and that a portion of the old channel near Picayune became filled when the flow shifted to the west... It is estimated that during times

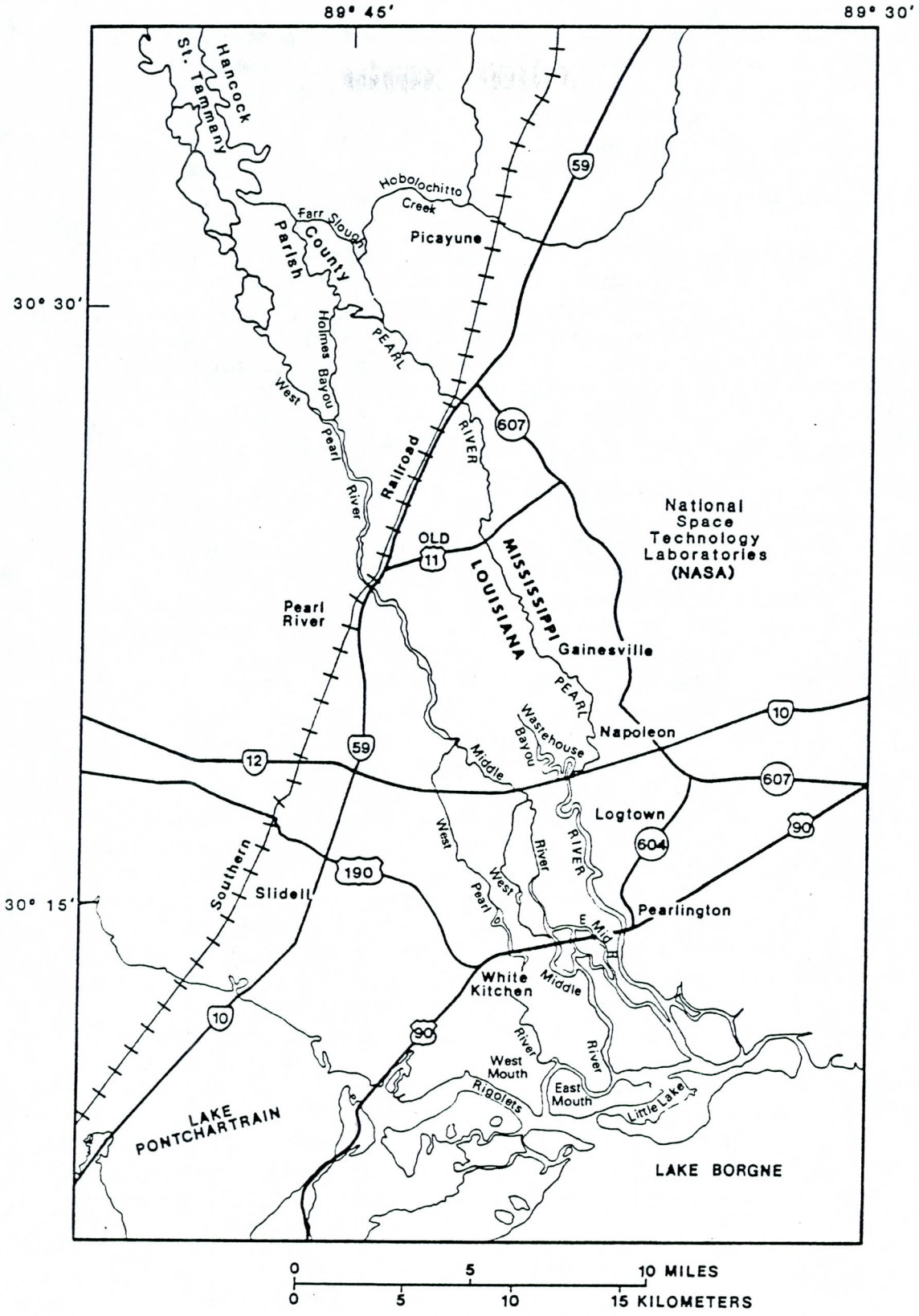

Figure 1.--Lower Pearl River basin, Louisiana and Mississippi.

of minimum flow in the system, less than 5 percent of the flow in the main channel flows through Farr Slough to continue in the eastern channel and the remainder flows through the western channel. At maximum flood stages there is considerable flow across the flood plain, and the eastern channel carries the greater part of the flow in the system.

From the confluence of Holmes Bayou and the West Pearl River, the main river channels continue generally southward and south-southeastward to the mouths of the Pearl River system. The Pearl River flows into Lake Borgne; the West Middle River, a distributary channel, and the East Mouth of the West Pearl River flow into Little Lake; and the West Mouth of the West Pearl River flows into the Rigolets (fig. 1). The drainage area of the Pearl Rivers is 8,670 mi^2 at the mouths of the system (Shell, 1981, p. 232).

The major tributaries to the Pearl River are Lobutcha and Tuscolameta Creeks and the Yockanookany, Strong, and Bogue Chitto Rivers. The main channel of the Pearl River has a slope of about 1 ft/mi and varies in width from about 100 to about 1,000 ft. The channel meanders within the flood plain and is obstructed in many places by sand bars, brush, and fallen and overhanging trees. The Ross Barnett Reservoir, put into operation in 1961, is located upstream from Jackson on the Pearl River and is the only major reservoir within the basin.

Study Reach

The reach of the Pearl River flood plain studied in this report is shown in figure 2. Ground-surface contour lines within the study area are shown on plate 1. The study reach is located in the lower part of the basin between river miles 9.0 and 26.3 on the Pearl River and river miles 7.9 and 21.9 on the West Pearl River. (River miles are defined for each of the channels modeled in detail in this study and are shown in fig. 2 and on all plates. In each case, river mile zero is defined as the channel mouth. The Geological Survey assigned all river miles except those for the West Pearl River, which were assigned by the Corps of Engineers.) The study reach, approximately 12 mi long, is bounded on the north by old U.S. Highway 11 and Interstate Highway 59 (I-59) and on the south by U.S. Highway 90. (Old Highway 11 is used only for access to the flood-plain forests because the bridge across the Pearl River has been destroyed.) The eastern and western boundaries are the natural bluffs at the edges of the flood plain, where ground-surface elevations rise abruptly to 15 to 25 ft above sea level in the northern part of the study reach and to 5 to 15 ft above sea level in the southern part. Within the study reach, the axis of the flood plain is aligned in a north-northwest-to-south-southeast direction, and the flood plain varies in width from about 3 to about 7 mi.

The major channels in the study reach are the Pearl (known locally as the East Pearl), East Middle, Middle, West Middle, and

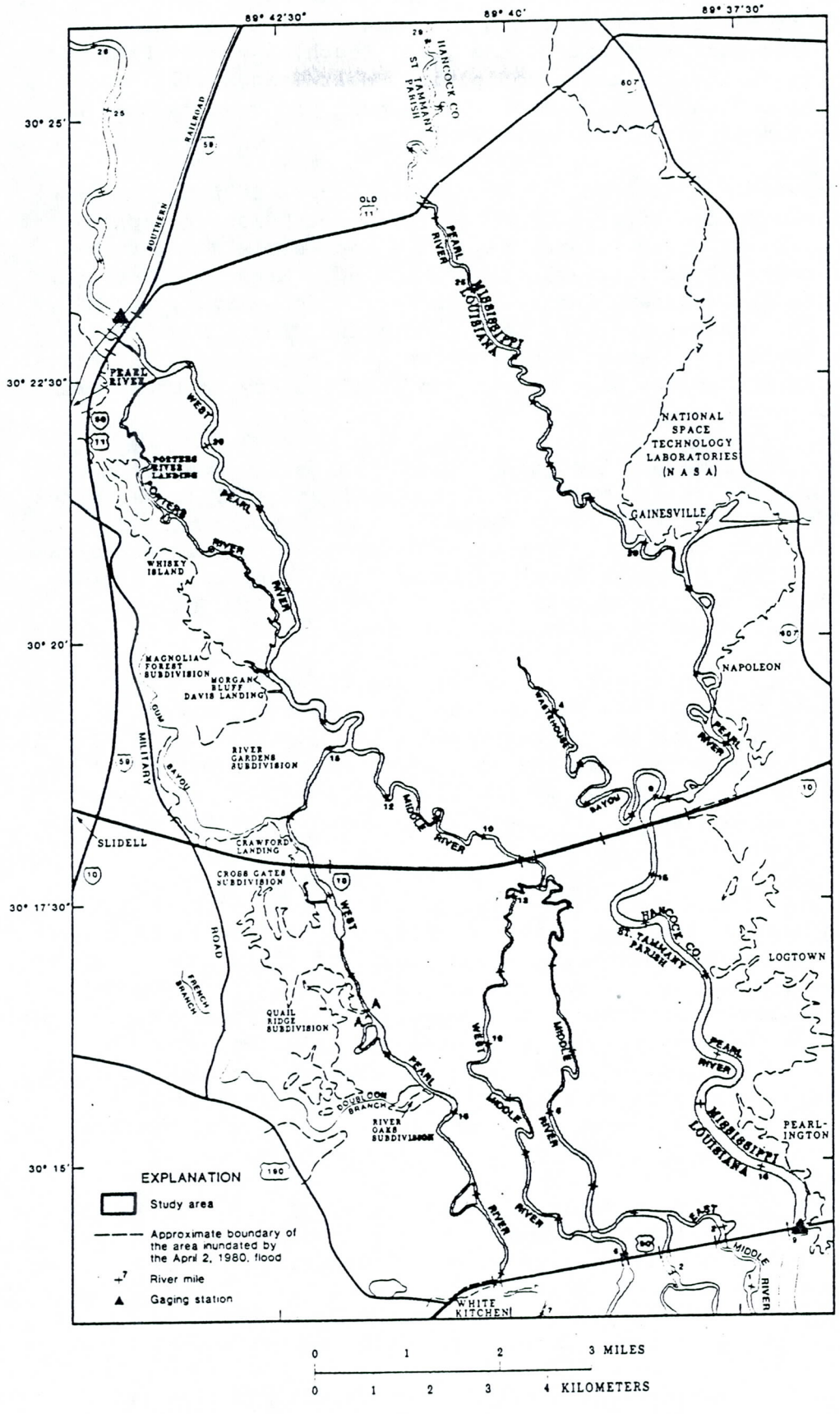

Figure 2.--Study reach of the lower Pearl River basin near Slidell. Cross section A-A' is shown in figure 6.

West Pearl Rivers, and Wastehouse Bayou. The Pearl flows along the east side of the flood plain, and the West Pearl along the west side. In the northern part of the study reach, the West Pearl is the largest channel in the flood plain. Near Gainesville, Miss., the channel of the Pearl becomes the largest and remains the largest to the mouths of the river system.

At river mile 15.2 on the West Pearl River, a distributary channel, the Middle River, forms and flows southeastward approximately 3.9 mi, where it divides into the Middle and West Middle Rivers. Approximately 6.3 mi farther south, the Middle River divides again, and another distributary channel, the East Middle River, forms. South of the study reach, the East Middle and Middle Rivers flow into the Pearl River about 1.3 mi north of Little Lake. Wastehouse Bayou forms within the flood plain and is tributary to the Pearl River just north of I-10.

There are numerous less significant channels in the flood plain within the study area. For example, Porters River, a branch of the West Pearl River, forms south of I-59 at river mile 21.4 and rejoins the West Pearl at river mile 17.4. Among the small streams which flow into the Pearl River system in the study reach are Gum Bayou and Doubloon Branch, which are tributary to the West Pearl River at river miles 14.0 and 10.5, respectively.

Flood-plain ground-surface elevations range from 1 ft above sea level in the southern part of the study area to 15 ft above sea level in the northwestern part. Between the upstream boundary and I-10, ground-surface elevations are higher near the West Pearl River than on the east side of the flood plain. Low natural levees border most of the channels in the study reach. The flood plain has a slope of about 1 ft/mi.

The streambeds and flood plain generally consist of alluvial soils and sands. The vegetative cover of the study area is shown on plate 1. Except near Highway 90, the flood plain is covered by dense woods, mixed with underbrush in many places. The flood-plain forests consist of bottomland hardwoods and bald-cypress tupelo-gum swamps. Near Highway 90, coastal marsh predominates, with dense grass 5 to 10 ft high. The taller grass borders the channels, and the shorter grass is found away from the channels. A small marsh area is located just downstream from the I-10 bridge across the Pearl River at the left edge of the flood plain.

Flow enters the study reach through the old Highway 11 bridge opening at the Pearl River, through the I-59 opening at the West Pearl River, and through numerous small openings in the old Highway 11 embankments. The I-59 opening at the West Pearl River is 2,630 ft long, and the old Highway 11 opening at the Pearl River is 570 ft long. The deck of the old Highway 11 bridge has been destroyed.

The I-10 crossing, about 4.4 mi long, spans the flood plain in an east-to-west direction in the middle of the study reach. There are bridges at the Pearl, Middle, and West Pearl Rivers, with

lengths of 4,980, 770, and 2,240 ft, respectively. The embankment between the Pearl and Middle Rivers is about 0.8 mi long, and the embankment between the Middle and West Pearl Rivers is about 2.1 mi long. The embankments are about 300 ft wide, and the elevation of the roadway is between 12 and 13 ft above sea level.

Natural flood-plain elevations near I-10 range from 1 to 3 ft above sea level. Spoil from bridge construction increased these natural elevations by as much as 3 ft on the right overbank at the Pearl River bridge opening, by as much as 2 ft on both overbanks at the Middle River opening, and by as much as 6 to 7 ft on the left overbank at the West Pearl River opening. In addition, there is a large knoll adjacent to the southeast corner of the West Pearl River bridge that protrudes into the flow-expansion zone downstream from the bridge. This knoll was apparently created during construction of the highway embankments. The vegetation beneath the three bridges was removed during construction, but brush of varying density has grown back in the openings.

A short distance downstream from the West Pearl River bridge, between river miles 12.4 and 13.2, there is a relatively shallow reach of the West Pearl River, where the channel was artificially widened by the removal of earth fill during construction of the highway embankments.

Flow leaves the study reach through five openings in the Highway 90 embankments. The bridge at the Pearl River is 960 ft long; at the East Middle River, 630 ft long; at the Middle River, 580 ft long; at the West Middle River, 580 ft long, and at the West Pearl River, 570 ft long. During the April 1980 flood, there was a small amount of flow out of the study area over the top of the U.S. Highway 190 embankment.

HYDROLOGY OF THE PEARL RIVER BASIN

Flood Data

During the months of April 1979 and April 1980, extreme flooding on the Pearl River caused extensive property damage in subdivisions located on the flood plain in the Bogalusa (about 30 mi upstream from the study area) and Slidell, La., areas (fig. 3). Many persons were forced from their homes until the flood waters receded. The factors influencing the magnitude of these two floods have been discussed by Wax and Tingle (1980) and Lee and Arcement (1981).

The April 1979 flood was caused by heavy rainfall over the upper part of the basin, where as much as 19.6 in. of rain fell during one 2-day storm. This was the largest flood in the Jackson, Miss., area during the period of record (June 1901 to the current year, 1982) and the largest in the Bogalusa area during the period of record (October 1938 to the current year, 1982) (U.S. Geological Survey, 1981, p. 147; 1982, p. 23).

The April 1980 flood was caused by precipitation amounts

Figure 3.--Flooding near Slidell during April 1980. Upper photograph: Flooded homes. Lower photograph: Flooded business establishment. Photographs from the Slidell "Daily Times," 1980.

ranging from 8.6 to 15.0 in. over the entire Pearl River basin. This was the largest flood at Pearl River, La., near Slidell during the period of record (October 1899 to the current year, 1982). The approximately simultaneous arrival of the peak discharges of the Pearl and Bogue Chitto Rivers at their confluence caused a larger flood peak to occur near Slidell than would have been expected on the basis of the peak discharge recorded at Bogalusa. Urban property damage was estimated by the Corps of Engineers to be $12.275 million in the Slidell area alone (U.S. Army Corps of Engineers, 1981, p. 76). The April 1980 flood forced the closing of I-10 between Slidell and Bay St. Louis, Miss., for several hours while the flood crest passed (fig. 4).

Gage-height records have been collected at the Geological Survey gaging station, Pearl River near Bogalusa, La., from October 1938 to the current year, 1982. Water-surface elevations have ranged from about 59.8 to about 78.2 ft above sea level (April 24, 1979) during the 43-year period of record. At Bogalusa, maximum annual discharges between 1947 and 1981 have ranged in magnitude from 13,200 ft^3/s in 1952 to 129,000 ft^3/s in 1979 (April 24). (See U.S. Geological Survey, 1982, p. 23.)

Gage-height records have been collected at the Geological Survey gaging station, Pearl River at Pearl River, La. (fig. 2), from October 1899 to the current year, 1982. Water-surface elevations have ranged from about 1.5 to about 19.7 ft above sea level (from flood mark, April 1, 1980) during the 82-year period of record. A historical maximum of 20.2 ft above sea level occurred in 1874. At Pearl River, maximum annual discharges between 1947 and 1981 have ranged in magnitude from 17,700 ft^3/s in 1952 to 174,000 ft^3/s in 1980 (April 1). (See U.S. Geological Survey, 1982, p. 52.)

Gage-height records have been collected at the Corps of Engineers gaging station, Pearl River at Pearlington, Miss. (fig. 2), from December 1961 to the current year, 1982. Water-surface elevations have ranged from about 2.0 ft below to about 8.4 ft above sea level (September 10, 1965) during the 20-year period of record (U.S. Army Corps of Engineers, written commun., 1982). The maximum water-surface elevation during the April 1980 flood was 5.3 ft above sea level on April 2.

During the 1961, 1979, and 1980 floods, discharge measurements were made at or near peak flow at various highway crossings of the study reach. Each of these discharge measurements and the date it was made are given in table 1.

Approximately 200 high-water marks within and near the study area were located and flagged by the Geological Survey as the April 1980 flood waters receded. The Corps of Engineers ran a level loop around the study area to permit all high-water marks to be evaluated with respect to sea level. No high-water mark was located more than a mile from the nearest temporary bench mark on the level loop. Differential leveling from the temporary bench marks to the high-water marks was used by Geological Survey personnel to determine

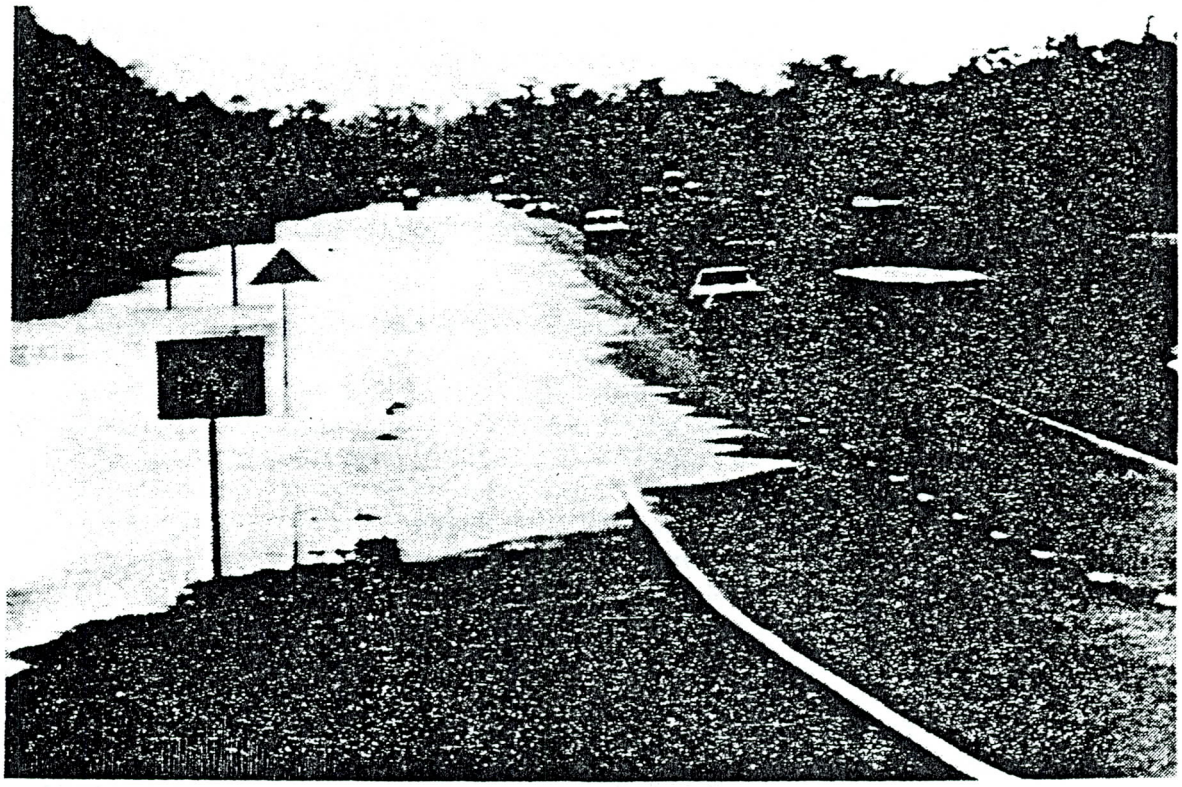

Figure 4.--Overtopped north lane of I-10 between Slidell and Bay St. Louis during the April 2, 1980, flood.

Table 1.--Discharges measured during the 1961, 1979, and 1980 floods on the lower Pearl River

Date	Discharge, in cubic feet per second								
	I-59 bridge opening[1/]								
	1 (Pearl River)	2	3	4	5	6	7	8 (West Pearl River)	Total
4-24-79	14,800	2,790	5,510	9,110	4,270	5,140	9,620	91,000	142,000
4-26-79	17,700	3,640	7,360	11,200	5,420	5,800	11,600	92,000	155,000

	I-10 bridge opening			
	Pearl River	Middle River	West Pearl River	Total
2-27-61	--	--	--	[2/] 106,000
4-26-79	88,600	29,000	33,800	151,000
5-01-79	55,000	16,600	18,700	90,000
4-02-80	103,000	30,000	40,800	174,000

	Highway 90 bridge opening					
	Pearl River	East Middle River	Middle River	West Middle River	West Pearl River	Total
4-22-80	51,900	11,800	16,700	16,600	6,830	104,000

1/ The bridge openings are numbered from left to right as an observer faces downstream.
2/ This measurement was made prior to the construction of I-10.

the elevations of the high-water marks. These elevations are accurate to within ±0.1 ft.

Flood Frequency

After the 1980 flood, the Geological Survey and the Corps of Engineers carried out a coordinated flood-frequency analysis for eight gaging stations on the Pearl River (U.S. Geological Survey, written commun., 1980). Discharges for specified recurrence intervals at two of these stations, Bogalusa and Pearl River, are given in table 2 (Lee and Arcement, 1981, p. 35). The values in the table were developed using procedures described by the U.S. Water Resources Council (1977). Skew values and historical flood data used in the analysis were mutually agreed upon by both agencies. The discharge of 174,000 ft^3/s measured at I-10 on April 2, 1980, is about 3 percent greater than the 50-year discharge at Pearl River.

SIMULATION OF THE APRIL 2, 1980, FLOOD

The two-dimensional finite-element surface-water flow modeling system FESWMS was used to determine the effect of I-10 on Pearl River flooding during the April 2, 1980, flood. Hydrographic and topographic data were collected and analyzed. These data were used to verify the assumption that a steady-state analysis is valid, define the region to be modeled, represent it as an equivalent finite-element network, and establish model boundary conditions. The initial finite-element network included the I-10 embankments. The hydrographic data were then used in calibrating the flow model to simulate the April 1980 flood as closely as possible.

Next, the finite-element network was modified to represent conditions without I-10 in place, and the hydraulic impact of I-10 was determined by comparing model results with and without I-10. Modeling the April 2, 1980, flood with the highway embankments in place is discussed in this section; modeling the flood without the embankments in place is discussed in the next section.

Data Collection and Analysis

A large amount of hydrographic and topographic data was collected and analyzed for use in modeling the April 2, 1980, flood. High-water marks recovered after the flood were examined for validity and grouped for use in establishing model boundary conditions and calibrating the model. Discharge measurements made by the Geological Survey and the Corps of Engineers at old Highway 11, I-59, I-10, and Highway 90 during the 1980 and earlier floods were assembled for the same purposes.

Detailed topographic information for the significant channels and their overbanks was obtained to ensure that model topography accurately represented prototype topography. A fathometer was used to obtain longitudinal profiles of the channels of the Pearl, East Middle, Middle, West Middle, and West Pearl Rivers, and Wastehouse

Table 2.--Flood frequency data for the Pearl River at Bogalusa and Pearl River

Station name	Drainage area, in square miles	Discharge, in cubic feet per second, for indicated recurrence interval, in years							
		2	5	10	25	50	100	200	500
Bogalusa	6,630	42,500	62,600	77,200	97,000	113,000	129,000	147,000	172,000
Pearl River.	8,590	56,500	87,400	111,000	143,000	169,000	198,000	228,000	272,000

Bayou, approximately 50 mi in all. Each profile was referenced in the field to outstanding topographic features.

On the basis of these profiles, sites were selected for 73 representative and special-purpose cross-section surveys needed to define channel geometry. A fathometer was used to establish channel-bottom elevations, and differential leveling with the water surface as a temporary benchmark was used to establish overbank elevations. The stadia method was used to measure distances. The water-surface elevation at a cross-section location was determined from upstream and downstream water-surface elevations established for the time that the cross section was being surveyed. During the time that this work was being done, flows were assumed steady except near Highway 90, where water-surface elevations were affected by tidal fluctuations of about 0.5 ft. Staff-gage readings were taken at frequent intervals, and the water-surface elevation at each cross section was adjusted for tidal fluctuations. Good control was maintained to ensure that computed water-surface elevations were accurate to within about ±0.25 ft.

Detailed topographic data at and near bridge openings were obtained from special topographic maps and highway-crossing plans provided by the Office of Highways. Additional field observations were made as the study progressed to describe conditions more adequately in problem areas. The collected data were supplemented by historic hydrologic data and Geological Survey topographic maps.

Infrared aerial photographs of the study area were obtained for use in determining vegetation type and density. Field observations of vegetation type and density were made to assist in estimating initial values of Chézy coefficients.

Steady-State Assumption

Water-surface elevations at the upper and lower ends of the study reach are plotted in figure 5 as a function of time for the period March 31 to April 4, 1980. These elevations were obtained from gage-height records at Pearl River and Pearlington. The peak water-surface elevation at Pearl River occurred before 6 a.m. on April 1, and the peak elevation at Pearlington occurred before midnight on April 2. At the time of the downstream peak, the upstream water-surface elevation had fallen less than 0.5 ft from its maximum value.

On the basis of this observation, it was assumed for modeling purposes that the flow was steady. This implies that the maximum discharge of 174,000 ft^3/s measured at I-10 was constant along the study reach and that all the high-water marks were attained by the water surface at the same time.

Network Design

The first task in applying the model to the April 2, 1980, flood was to define the boundaries of the area to be modeled and

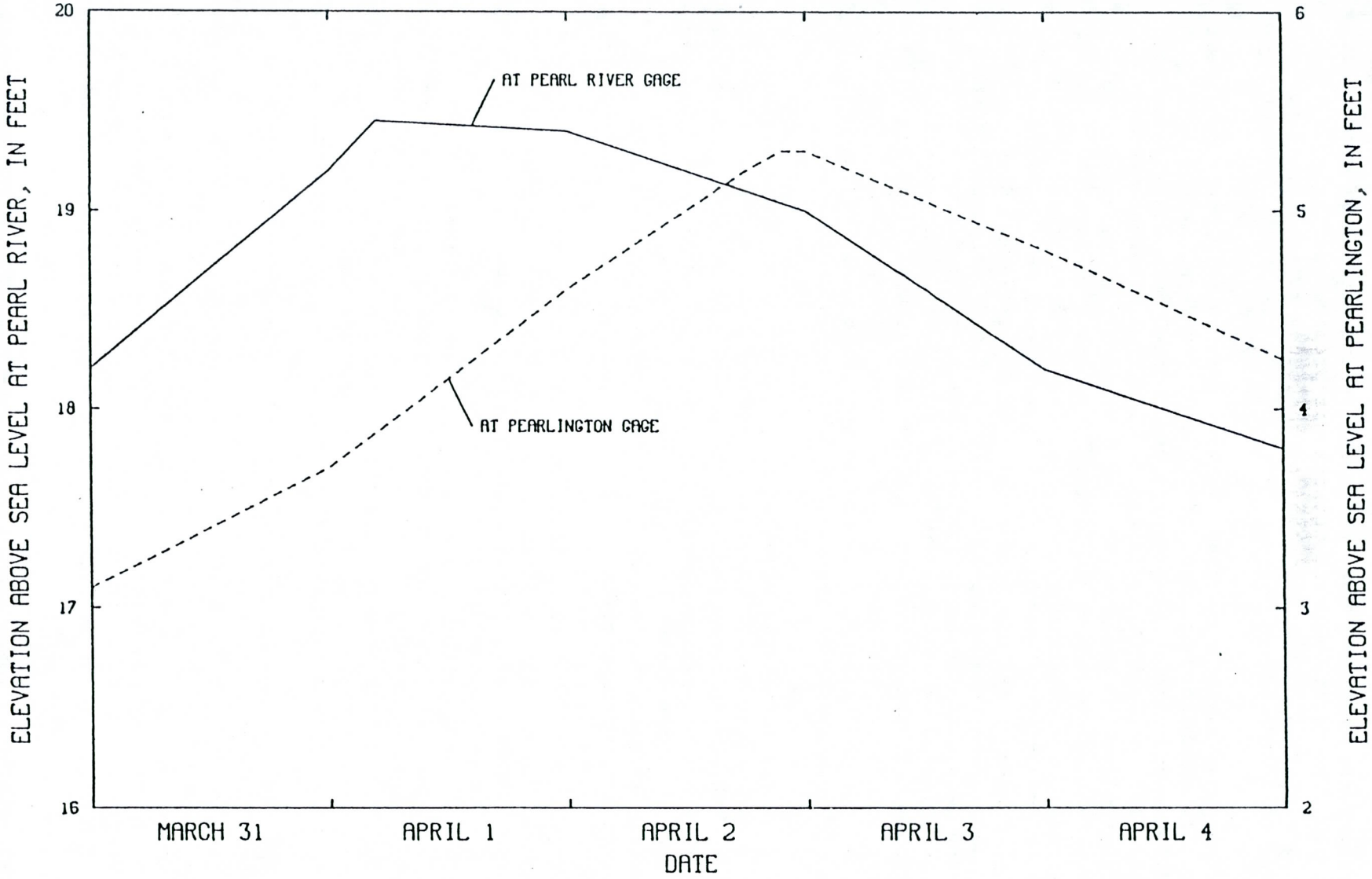

Figure 5.--Water-surface elevations at Pearl River and Pearlington from March 31 to April 4, 1980.

then represent the study area as an equivalent network of triangular elements. The finite-element network was prepared directly on Geological Survey topographic maps of the study area enlarged to a scale of 1 to 6,000.

The network, shown on plate 1, was designed to closely represent the highly nonuniform boundary of the area inundated by the 1980 flood. The upstream model boundary was located just downstream from and parallel to old Highway 11 and I-59, where inflows could be approximated on the basis of earlier discharge measurements. The downstream model boundary was located just upstream from and parallel to Highway 90, and outflows were placed at the five bridge openings, where water-surface elevations could be estimated on the basis of nearby high-water marks. Because both the upstream and downstream model boundaries were located at least one flood-plain width distant from the I-10 crossing, modifications made to the model near the highway crossing were assumed to have little effect on the boundary conditions. Smooth, curved-sided elements were used along all lateral boundaries, at which tangential flow was specified. The edges of the I-10 embankments and the adjoining knoll at the West Pearl River were also treated as tangential-flow boundaries.

After the boundaries were defined, the study area was subdivided into an equivalent network of triangular elements. Careful placement of nodes and elements was necessary to adequately represent prototype topography and vegetative cover. Subdivision lines between elements were located where abrupt changes in vegetative cover or topography occurred. Each element was designed to represent an area of nearly homogeneous vegetative cover.

It was found that water-depth changes of more than about 1,000 percent across an element often caused local inconsistencies in the solution. Occasionally, smaller depth changes caused problems. Hence, large prototype ground-surface gradients, such as those between overbanks and channel bottoms, required the use of additional network detail. In areas where velocity and water-surface gradients were expected to be relatively large, such as near bridge openings, network detail was increased to facilitate better simulation of the large gradients by the flow model. The use of curved-sided elements to define channel bends facilitated the design of a more realistic network.

The use of elements with aspect ratios greater than unity made it possible to design the network with fewer elements than would have been required otherwise. The element aspect ratio is defined as the ratio of the largest element dimension to the smallest. The optimum aspect ratio for a particular element depends largely on the local velocity and depth gradients. If these gradients can be estimated beforehand, it is possible to align the smallest element dimension with the largest variable change and the largest dimension with the smallest change.

Elements with large aspect ratios were used primarily in defining river channels. During network design, the longest element side was aligned with the channel axis, along which velocity and

depth changes would typically be small. Element aspect ratios were kept to a maximum of about 10. In channel reaches with significant curvature, however, it was often necessary to use a much smaller value to avoid an unrealistic solution.

The complex geometry of the flood plain of the Pearl River was modeled in detail. Most prototype lengths and widths were realistically represented in the model; however, in order to reduce the number of elements in the finite-element network, several approximations were made. First, only relatively large channels, those of the Pearl, East Middle, Middle, West Middle, and West Pearl Rivers, and Wastehouse Bayou, were included in the network. Less important channels, such as Porters River, were not included in the model. Second, prototype channel cross sections were represented in the model by either triangular or trapezoidal cross sections with cross-sectional areas equal to the measured areas. A triangular model cross section and the prototype cross section to which it corresponds are shown in figure 6. Third, some meandrous channel reaches with relatively small flows were replaced with artificially straightened, but hydraulically equivalent, reaches (pl. 1). Hydraulic equivalence was obtained by decreasing the value of the Chézy coefficient of a straightened channel, as explained in detail on page 26. Lastly, the width of simulated stream channels was kept to a minimum of 200 ft.

Because of the large number of elements required to simulate prototype hydraulics accurately, the model was initially developed in three sections to reduce the cost of design and preliminary calibration. The study reach was divided approximately 2 mi above and 1 mi below I-10. The three sections of the network were designed simultaneously with coordinated effort. Estimated boundary conditions were used at the upstream and downstream boundaries of each of the sections to calibrate each of the sections on a preliminary basis. The three sections were then combined to perform final calibration and subsequent analysis.

In its complete state, the finite-element network contained a total of 5,224 triangular elements and 10,771 computational node points requiring the simultaneous solution of 23,697 nonlinear algebraic equations. The element areas ranged in size from 0.000116 to 0.438 mi^2 and covered a total area of 60.0 mi^2. Ground-surface elevations used in the model ranged from a minimum of 58.5 ft below sea level to a maximum of 15.0 ft above sea level.

Model Adjustment

After network design was complete, boundary conditions were determined, and the model was adjusted to simulate the April 2, 1980, flood as closely as possible.

Boundary Conditions

The discharge distribution at the upstream boundary (table 3) was based on the peak discharge of 174,000 ft^3/s measured at I-10

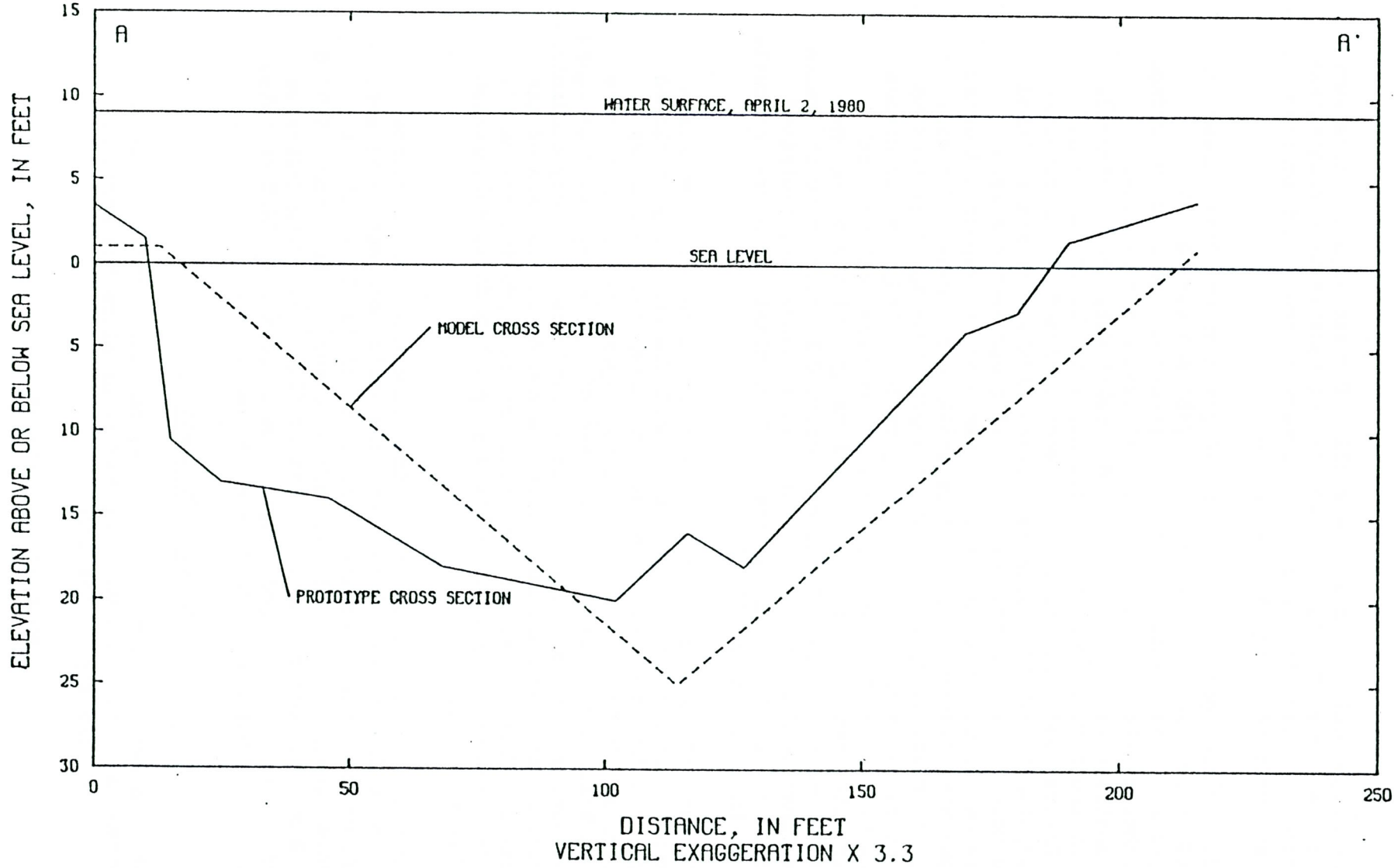

Figure 6.--Prototype and model channel cross sections at section A-A' (fig. 2).

Table 3.--Distribution of discharge at the upstream model boundary

Section of upstream boundary	Discharge, in cubic feet per second	Discharge, as percent of total discharge
Flood plain between east edge of flood plain and Pearl River.	22,100	12.7
Pearl River bridge opening	22,000	12.6
Flood plain between Pearl and West Pearl Rivers.	32,900	18.9
West Pearl River channel	69,100	39.7
Flood plain between West Pearl River and west edge of flood plain.	28,200	16.2
Total	174,000	100

and on previous discharge measurements at the bridge openings in old Highway 11 and I-59. Inflow was concentrated at the old Highway 11 bridge across the Pearl River and at the I-59 bridge across the West Pearl River. Flow into the study reach through numerous small openings in old Highway 11 was represented as continuous inflow between the east edge of the flood plain and the Pearl River and between the Pearl and West Pearl Rivers. Water-surface elevations at the downstream boundary (table 4) were based on high-water marks near the five bridge openings in Highway 90. Other minor inflows and outflows along the boundary of the modeled flood plain (for example, inflows from Gum Bayou and Doubloon Branch and outflow across Highway 190) were considered negligible and were not included in the simulation. In running each of the three network sections, intermediate downstream boundary conditions were estimated from nearby high-water marks, and intermediate upstream boundary conditions were obtained from the adjacent upstream section.

Aspects of Model Adjustment

The model-adjustment process consisted of two parts: the adjustment of empirical model coefficients (model calibration) and the adjustment of model boundary conditions, network detail, and ground-surface elevations on the basis of additional information obtained during the study.

The two-dimensional surface-water flow model is based on the formulation and solution of equations which simulate a complex physical flow situation. Since no physical flow system can be completely described or understood, the mathematical formulation involves some level of approximation. Three-dimensional topographic features are represented by two-dimensional elements, and the physics of flow is assumed to obey differential equations in which empirical hydraulic coefficients appear. Model calibration is the process of adjusting the values of the empirical coefficients so that the model simulates an observed flow as closely as possible. In this study, model calibration, performed by trial and error, was based on observed high-water marks and discharges obtained during the April 2, 1980, flood. This aspect of model adjustment will be discussed in detail.

The second aspect of the model-adjustment process involved the correction of deficiencies in the model boundary conditions and the representation of flood-plain topography. Although extensive data-collection work was done earlier, there were gaps in the data used to estimate model boundary conditions, design the model network, and assign model ground-surface elevations. During model adjustment, it occasionally became apparent that these data gaps were causing the model to fail to simulate correctly certain observed features of the 1980 flood. A review of existing data or additional data collection was necessary in these instances. Then boundary conditions, network detail, or ground-surface elevations were adjusted on the basis of the additional information. This aspect of model adjustment also will be discussed in detail.

Table 4.--Water-surface elevations at the downstream model boundary

Highway 90 bridge opening	Water-surface elevation above sea level, in feet
Pearl River	5.8
East Middle River	5.7
Middle River	5.7
West Middle River	5.8
West Pearl River	5.9

Preliminary Model Calibration

On the basis of previous finite-element simulations, the values of all components of the eddy-viscosity tensor were initially set at 100 lb·s/ft^2 for all elements in the network. Numerical experiments indicated that once the values of these coefficients were set high enough to ensure convergence, the solution was much less sensitive to changes in their values than to changes in the values of the Chézy coefficients. Because of a lack of information about their correct values and to avoid convergence problems, the values of all components of the eddy-viscosity tensor were maintained at 100 lb·s/ft^2 throughout the study for all elements in the network.

Once the values of the eddy viscosities were fixed, preliminary calibration work focused on determining the values of Chézy coefficients. Nominal values were selected for initial use with each of the three separate network sections on the basis of the infrared aerial photographs of the flood plain and field inspection. In making both the initial estimates of the Chézy values and subsequent modifications to them, care was taken to ensure that the assigned values were reasonable and mutually consistent. Areas to which different Chézy values were assigned are shown on plate 1, and the final values are given in table 5.

The Chézy value assigned to a channel element in an artificially straightened reach was derived from the value for the corresponding natural or unstraightened reach on the basis of the equation

$$C_s = C_n \sqrt{\frac{L_s}{L_n}}, \qquad (4)$$

where C is the value of the Chézy coefficient (feet to the one-half power per second), L is the length of the reach (feet), and the subscripts s and n denote straightened- and natural-channel-reach values, respectively. Equation 4 is obtained directly from the Chézy equation.

A series of simulations with each of the three network sections was conducted to determine the relative effect on water-surface elevations of changes in the values of the Chézy coefficients of both overbank and channel elements. Computed water-surface elevations were most sensitive to changes in the value of the Chézy coefficient of the wooded flood plain. Changes in the Chézy values of channel elements had little or no effect on computed water-surface elevations except for channel reaches carrying a significant percentage of the total flow. Such reaches included the Pearl River between I-10 and Highway 90 and reaches located a few thousand feet upstream and downstream from bridge openings. Computed water-surface elevations were also moderately sensitive to the values of the Chézy coefficients of the overbank areas under the three I-10 bridges.

Table 5.--Values of Chézy coefficients used to simulate the April 2, 1980, flood

Element description or location	Chézy coefficient[1/] ($ft^{1/2}/s$)
Flood plain	
Woods	22
Low marsh grass in southern part of study reach	35
High marsh grass in southern part of study reach	28
Marsh grass and brush downstream from I-10 bridge across Pearl River.	30
Brush and trees south of preceding marsh-grass area	21
Grass and scattered brush on left overbank under I-10 bridge across Pearl River.	40 (22)
Grass and brush on right overbank under I-10 bridge across Pearl River.	30 (22)
Brush and trees under I-10 bridge across Middle River	21 (22)
Grass and scattered brush under I-10 bridge across West Pearl River.	40 (22)
Pearl River	
Natural channel between river miles 9.0 and 15.9	105
Natural channel between river miles 15.9 and 19.2	85
Straightened channel between river miles 19.2 and 20.3	[2/]85
Natural channel between river miles 20.3 and 20.9	85
Straightened channel between river miles 20.9 and 26.3	[2/]85
Wastehouse Bayou	
Straightened channel between river miles 0.0 and 4.4	59

Table 5.--Values of Chézy coefficients used to simulate the April 2, 1980, flood --Continued

Element description or location	Chézy coefficient[1/] ($ft^{1/2}/s$)
East Middle River	
Natural channel between river miles 1.8 and 2.7	85
Middle River	
Natural channel between river miles 2.3 and 5.4	85
Straightened channel between river miles 5.4 and 9.0	66
Natural channel between river miles 9.0 and 10.0	85
Straightened channel between river miles 10.0 and 12.9	68
West Middle River	
Natural channel between river miles 5.9 and 8.0	85
Straightened channel between river miles 8.0 and 12.7	75
West Pearl River	
Natural channel between river miles 7.9 and 14.9	85
Straightened channel between river miles 14.9 and 15.9	51
Natural channel between river miles 15.9 and 19.4	100
Straightened channel between river miles 19.4 and 20.4	94
Natural channel between river miles 20.4 and 21.4	100
Natural channel between river miles 21.4 and 21.9	115

[1/]Values in parentheses were used in the simulation without I-10 in place.
[2/]No correction factor was applied to the value of the Chézy coefficient for this straightened reach of the Pearl River.

Preliminary calibration consisted of matching as closely as possible all observed high-water marks as well as measured discharges at the three bridge openings in I-10.

Adjustment of Model Boundary Conditions, Network Detail, and Ground-Surface Elevations

Appropriate adjustments to the values of the Chézy coefficients gave close agreement between computed and observed data in most cases. In several areas, however, discrepancies between model results and observations made it necessary to obtain additional data or review previously obtained data. Additional field work was occasionally necessary to check the location and elevation of high-water marks and study previously overlooked topographic features. On the basis of the results of the early simulations and the additional observations, modifications were made to model boundary conditions, network detail, and model ground-surface elevations.

The upstream inflow at the West Pearl River was initially estimated by linear extrapolation of the discharge measured there on April 26, 1979, under the assumption that the percentage of the total discharge at the West Pearl opening was the same in 1979 and 1980 (table 1). A discharge of 103,000 ft^3/s was calculated by this procedure and used in early simulations with the upper model section. Inflows across the remaining sections of the upstream boundary were estimated on the basis of the April 26, 1979, discharge measurements at I-59 and earlier measurements at old Highway 11. With the resulting discharge distribution, the computed water-surface elevation was much higher than high-water-mark elevations near the West Pearl River bridge at location 1 (pl. 2, sheet 1) for any reasonable choice of the values of the Chézy coefficients.

A comparison of discharge measurements made on April 24 and April 26, 1979, indicates that the percentage of flow through the I-59 opening at the West Pearl River decreases as the total discharge increases (table 1). On the basis of this observation and to improve the agreement between the computed and observed water-surface elevations near the West Pearl opening in I-59, the model discharge there was decreased to 97,300 ft^3/s. Inflows across the rest of the upstream boundary were increased to maintain a total discharge of 174,000 ft^3/s. The final values for the different sections of the upstream boundary are given in table 3. Lowering the discharge at the West Pearl River opening improved the computed water-surface elevation at location 1 but still did not give adequate agreement between the computed and observed values.

During this adjustment, it was observed that computed water-surface elevations along the upstream boundary were quite sensitive to changes in the upstream discharge distribution. This sensitivity decreased rapidly with distance downstream. For example, as a result of the change discussed previously, the water-surface elevation at the upstream boundary increased by more than 0.2 ft in the Pearl River and decreased by more than 0.3 ft in the West Pearl

River. Less than 3 mi downstream, the maximum increase in water-surface elevation in the Pearl River was less than 0.05 ft, and the maximum decrease in the West Pearl River was less than 0.1 ft.

During the effort to identify the causes of the disagreement between the computed and observed water-surface elevations at location 1, a short earthen dike was discovered along the left bank of the West Pearl River approximately 0.1 mi downstream from I-59. The error at location 1 was caused in part by the omission of this dike from the original finite-element network. The inclusion of the dike in the network resulted in satisfactory agreement between the computed and observed water-surface elevations at location 1.

In early simulations, a lack of agreement was noted between the computed and observed discharges at the three I-10 bridge openings. Additional field observations indicated that the ground-surface elevations of the overbank areas within the highway right-of-way at the three I-10 bridge openings had been increased by the addition of fill during construction. Also, a check of the topographic data showed that flood-plain ground-surface elevations for about 2 mi upstream from the highway embankment between the Middle and West Pearl Rivers had been set 1 to 2 ft too high in the model. Correcting model ground-surface elevations at and near I-10 resulted in a better discharge distribution at I-10. In particular, decreasing the flood-plain ground-surface elevations upstream from the bridge opening at the West Pearl River increased the computed discharge at that opening.

Final Model Calibration

When satisfactory agreement between simulated and observed water-surface elevations and discharges was obtained, the three network sections were combined, and further calibration was performed. Minor adjustments to the values of the Chézy coefficients were needed for final calibration of the full-reach model. The final Chézy values were 22 $ft^{1/2}/s$ for the wooded flood plain, 28 to 35 $ft^{1/2}/s$ for the marsh-grass areas, 21 to 40 $ft^{1/2}/s$ for the overbank areas under the three I-10 bridges, and 85 to 115 $ft^{1/2}/s$ for the unstraightened channels. A more detailed listing of the final values of the Chézy coefficients is given in table 5. Computed element-averaged flow depths range from 2 to 23 ft for the wooded flood plain, from 4 to 10 ft for the marsh-grass areas, from 4 to 9 ft for the overbank areas under the I-10 bridges, and from 5 to 47 ft for the unstraightened channels. On the basis of these depths and the well-known relationship between the Manning roughness coefficient, n, and the Chézy coefficient (Chow, 1959, p. 100), Manning values corresponding to the final Chézy values are found to range from 0.077 to 0.114 $ft^{1/6}$ for the wooded flood plain, from 0.055 to 0.074 $ft^{1/6}$ for the marsh-grass areas, from 0.046 to 0.098 $ft^{1/6}$ for the overbank areas under the I-10 bridges, and from 0.021 to 0.033 $ft^{1/6}$ for the unstraightened channels.

In both this and earlier applications of FESWMS, the values of the Manning n required for model calibration are generally somewhat

smaller than the values required to calibrate a one-dimensional model of the same reach. Several factors contribute to this situation. Wherever lateral flow is significant, streamlines are not parallel to the axis of the flood plain. Thus, flow paths are generally longer in a two-dimensional model than in a one-dimensional model, and it is possible to account for a given loss of energy with a smaller roughness coefficient than is needed in a one-dimensional model. In addition, some energy loss is accounted for by the turbulent-stress terms in the two-dimensional momentum equations. This loss must be accounted for by bottom friction in a step-backwater analysis.

Computed flow depths in the calibrated model average about 21 ft in the channels and about 8 ft on the flood plain. Most cross-sectional average channel velocities are between 1 and 3 ft/s. Somewhat higher velocities occur at several of the bridge openings. The average velocity on the flood plain is about 0.7 ft/s.

Comparison of Computed and Observed Water-Surface Elevations and Discharges

How well the model reproduces an observed flow depends on the approximations made in the model and on the calibration data. Calibrated model results represent a best fit to the available calibration data.

Network design and adjustment is a process of approximating hydraulically important topographic and vegetative-cover features with a finite number of homogeneous elements. The quality of the approximation depends on the amount and quality of the available topographic and vegetative-cover data. Further approximations are made in assigning model boundary conditions. In addition, the model equations describe the prototype flow process in an approximate way. The quality of this approximation depends in part on how well such assumptions as steady flow and the eddy-viscosity concept reflect prototype conditions. This approximation also depends on the values of the model's empirical coefficients, determined during calibration. Hence, velocities and water-surface elevations obtained from the calibrated model are approximate values, responses of approximate equations to approximate boundary conditions, topography, and vegetative cover.

Realistic and mutually consistent values of empirical parameters are chosen during calibration to bring model results into as close agreement as possible with observed data. If there is a major discrepancy between model results and observed data, then the approximations made in constructing the model are in error or the observed calibration data are not accurate or are not representative of the general hydraulic situation. The capability of a model to reproduce observed flows and subsequently predict the outcome of future or hypothetical flows depends largely on the amount and quality of the topographic, vegetative-cover, boundary-condition,

and calibration data that are available. Thus, improvements in observed data can lead to more accurate simulation.

Plate 2 is a plot of the velocity field and water-surface contour lines for the calibrated model. Points lying on a specific water-surface contour line were located by interpolation between nodal water-surface elevations. The contour line was then obtained by drawing a smooth curve through the points. The locations of the high-water marks used in calibration are also shown on plate 2. Table 6 contains a list of the location reference numbers, computed water-surface elevations, observed high-water-mark elevations, and differences between the computed and observed elevations.

At many of the locations listed in table 6, several high-water marks were observed. In general, hydrologic field data reflect the dominant features simulated by the model; however, they also reflect local variation that is not represented in the model. For this reason, several observations of water-surface elevation near a particular location, giving a range of values or an average value, are more useful than a single observation for model calibration.

At most of the locations shown on plate 2, the computed water-surface elevation is in close agreement with the elevation of the observed high-water mark or marks at that location. It is not possible to determine how much of the difference between the computed and observed water-surface elevations is due to model error and how much is due to error in the elevations of the high-water marks. The mean absolute difference between the computed and observed values is 0.12 ft, and the root mean square difference is 0.18 ft. (Because the marks at locations 19, 20, and 21 were used to establish downstream boundary conditions, they were not used in computing the mean differences.) The computed water-surface elevations are within ±0.3 ft of the elevations of the high-water marks at all but four locations, and at these four locations, the computed elevations are within ±0.5 ft of the observed values.

The discharge measurements made at the I-10 bridge openings on April 2, 1980, were also used in model calibration. The computed and measured discharges for the left overbank, the channel, and the right overbank at each of the three openings are given in table 7. The computed discharges given in table 7 were obtained from continuity checks along the line of nodes closest to the south edge of the eastbound lane, where the measured discharges were obtained. The errors in computed discharge at the bridge openings at the Pearl, Middle, and West Pearl Rivers, as a percent of the measured discharge at each opening, are 7, -10, and -7, respectively. The sum of the computed discharges at the three openings is 175,000 ft^3/s. The cause of the small discrepancy between the total computed discharge at I-10 and the total upstream inflow is discussed on page 6. (Continuity checks were used to compute the total discharge at numerous cross sections along the study reach. The maximum difference between the computed discharge and the inflow is about 6 percent of the inflow.)

Table 6.--Elevations of the computed water surface and observed high-water marks for the April 2, 1980, flood

Location reference number[1]	Elevation above sea level of computed water surface, in feet	Elevation above sea level of observed high-water mark(s)[2], in feet	Computed water-surface elevation minus observed high-water mark[3], in feet
1	13.5	17.9 - 18.0 (3)	0.5
2	17.4	17.2 (3)	0.2
3	16.6	16.7 (2)	-0.1
4	16.6	16.4 (2)	0.2
5	15.8	15.6 (1)	0.2
6	15.7	15.4 (1)	0.3
7	15.3	15.7 - 15.8 (2)	-0.4
8	15.2	15.2 (3)	0.0
9	15.1	15.0 - 15.1 (3)	0.0
10	13.4	13.5 (1)	-0.1
11	13.1	13.1 - 13.2 (2)	0.0
12	12.3	12.2 - 12.3 (3)	0.0
13	12.0	11.8 - 11.9 (4)	0.1
14	10.9	10.8 - 10.9 (6)	0.0
15	9.2	8.9 (1)	0.3
16	9.4	9.4 (1)	0.0
17	8.7	8.6 - 8.7 (2)	0.0
18	6.2	6.2 (1)	0.0
19	5.7	[4]5.7 (1)	0.0
20	5.8	[4]5.8 (1)	0.0
21	5.8	[4]5.8 (1)	0.0

Table 6.--Elevations of the computed water surface and observed high-water marks for the April 2, 1980, flood--Continued

Location reference number[1]	Elevation above sea level of computed water surface, in feet	Elevation above sea level of observed high-water mark(s)[2], in feet	Computed water-surface elevation minus observed high-water mark[3],
22	7.3	7.1 (1)	0.2
23	7.1	6.9 (1)	0.2
24	7.5	7.3 (1)	0.2
25	7.7	7.4 (1)	0.3
26	8.3	8.2 (1)	0.1
27	8.6	8.6 (1)	0.0
28	8.6	8.4 (1)	0.2
29	8.6	8.6 (1)	0.0
30	8.6	8.5 (3)	0.1
31	11.6	11.1 - 11.2 (2)	0.4
32	11.8	11.6 - 11.9 (5)	0.0
33	12.6	12.4 - 12.7 (4)	0.0
34	12.8	12.4 - 12.8 (3)	0.0
35	12.8	12.8 - 12.9 (4)	0.0
36	14.1	14.1 - 14.3 (4)	0.0
37	14.7	14.7 - 14.8 (2)	0.0
38	15.7	15.2 - 15.6 (3)	0.1
39	11.8	11.5 - 11.6 (4)	0.2
40	11.8	11.7 (1)	0.1
41	10.3	10.1 - 10.5 (2)	0.0
42	12.7	12.5 - 12.8 (3)	0.0

Table 6.--Elevations of the computed water surface and observed high-water marks for the April 2, 1980, flood--Continued

Location reference number[1]	Elevation above sea level of computed water surface, in feet	Elevation above sea level of observed high-water mark(s)[2], in feet	Computed water-surface elevation minus observed high-water mark[3],
43	10.0	12.5 - 12.8 (3)	0.0
44	12.7	12.7 - 12.8 (4)	0.0
45	10.0	10.3 (3)	-0.3
46	12.6	12.6 - 12.7 (3)	0.0
47	10.5	10.8 - 10.9 (2)	-0.3
48	12.2	11.5 - 11.8 (2)	0.4

[1] Location reference numbers are shown on plate 2.
[2] The number of marks at a location is given in parentheses.
[3] The observed value nearest the computed value is used in computing the difference.
[4] This high-water mark was used to establish downstream boundary conditions and was not used in computing the mean differences.

Table 7.--Computed and measured discharges at the I-10 bridge openings

Opening section	Computed discharge, in cubic feet per second	Measured discharge, in cubic feet per second
	Pearl River	
Left overbank	23,600	21,500
Channel	50,200	52,000
Right overbank	36,100	29,600
Total	110,000	103,000
	Middle River	
Left overbank	3,810	1,920
Channel	17,800	20,400
Right overbank	5,360	7,670
Total	27,000	30,000
	West Pearl River	
Left overbank	10,000	11,300
Channel	16,900	19,700
Right overbank	11,000	9,800
Total	37,900	40,800

Discharge per unit distance or unit discharge, both computed and measured, is plotted as a function of distance at each of the three bridge openings in figures 7, 8, and 9. At each opening, the computed profile is shown along the line of nodes used to compute the discharges given in table 7. In general, there is good agreement between the computed and observed profiles, especially for the overbank areas. The profiles based on field observations are more variable than the computed profiles due to debris, flow around piers and fenders, and local variations in topography and vegetative cover. Because the main-channel fenders at the Pearl and West Pearl Rivers were not modeled in this study, the peak unit discharges at those openings are underestimated by the model.

Additional Results of the Simulation

The water-surface contour lines and the velocity field, shown on plate 2, together with the continuity checks used at numerous locations along the study reach, give additional information about water-surface elevations and flow distribution for the April 2, 1980, flood. Computed water-surface elevation is plotted as a function of river mile for the channels of the Pearl and West Pearl Rivers in figures 10 and 11, respectively. In addition, computed water-surface elevation is plotted for the east and west edges of the flood plain in figures 12 and 13, respectively. (As one moves downstream along either edge of the flood plain, there are short sections where the north-south coordinate increases rather than decreases due to the meandering boundary of the flood plain. This causes the multivalued behavior of the graphs plotted in figures 12 and 13.)

Between the upstream boundary and I-10, there is a movement of water from the west to the east side of the flood plain. At the upstream boundary, 56 percent of the inflow was estimated to pass through the bridge opening at the West Pearl River (table 3), but at I-10, 63 percent of the computed discharge passes through the bridge opening at the Pearl River (table 7). (Table 1 shows that 59 percent of the measured discharge passed through the Pearl River opening at I-10.) The velocity field in this reach is aligned in a generally southeastward direction.

The 15.5- to 20.5-foot water-surface contour lines (pl. 2, sheet 1) form a "mound" downstream from the I-59 bridge opening at the West Pearl River. At the upstream boundary, the water surface is more than 3 ft higher on the west side of the flood plain than on the east side. Downstream from the West Pearl River bridge opening, the water surface drops sharply both in the downstream direction and towards the east side of the flood plain. However, 2 mi downstream, the water surface remains 1 ft higher on the west side of the flood plain than on the east side. Between 3 and 4 mi downstream, the alignment and spacing of the contour lines, as well as the direction and magnitude of the velocity vectors, indicate that the flow has become uniformly distributed across the flood plain and parallel to the flood-plain axis.

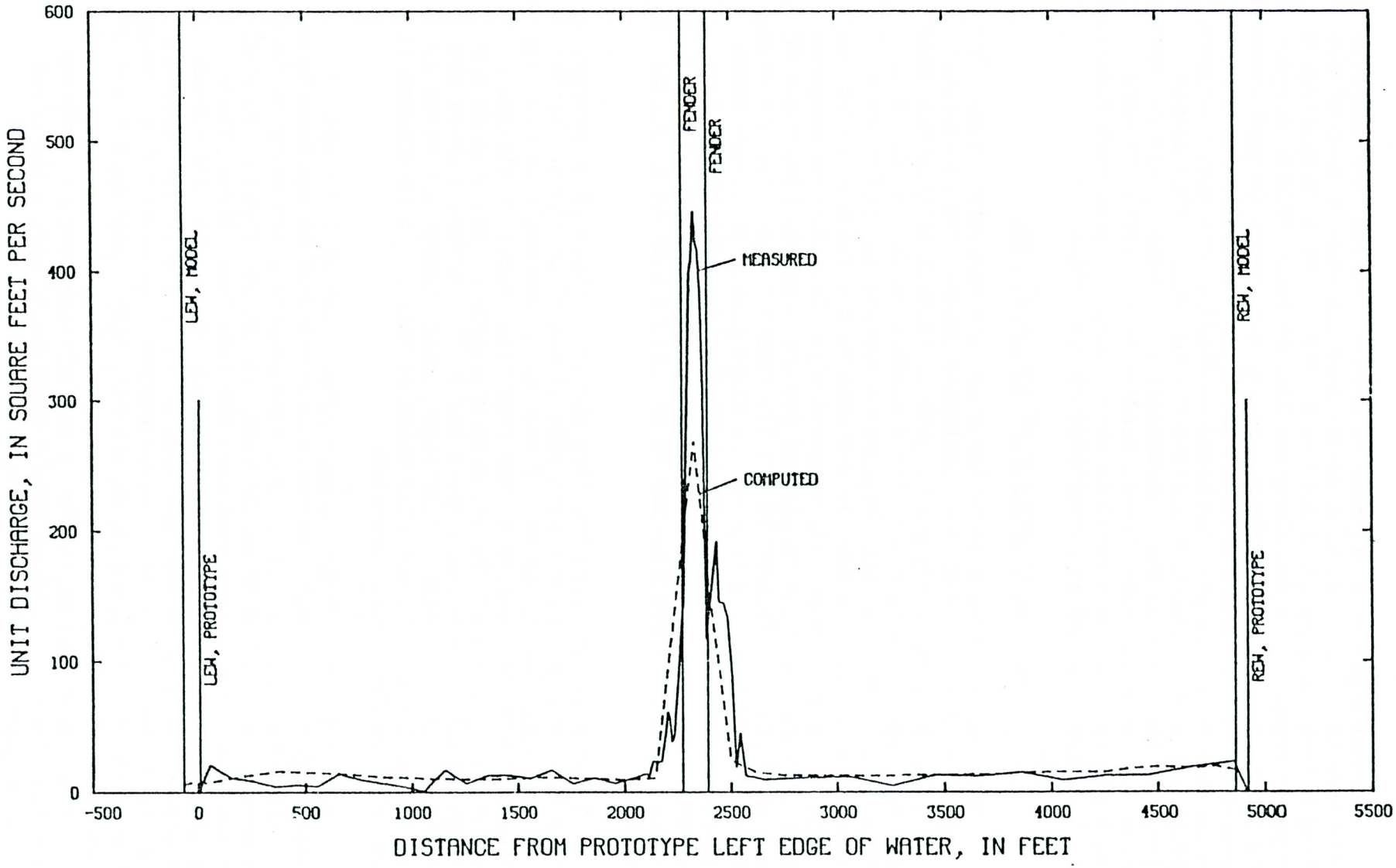

Figure 7.--Computed and measured unit discharge at the I-10 bridge opening at the Pearl River.

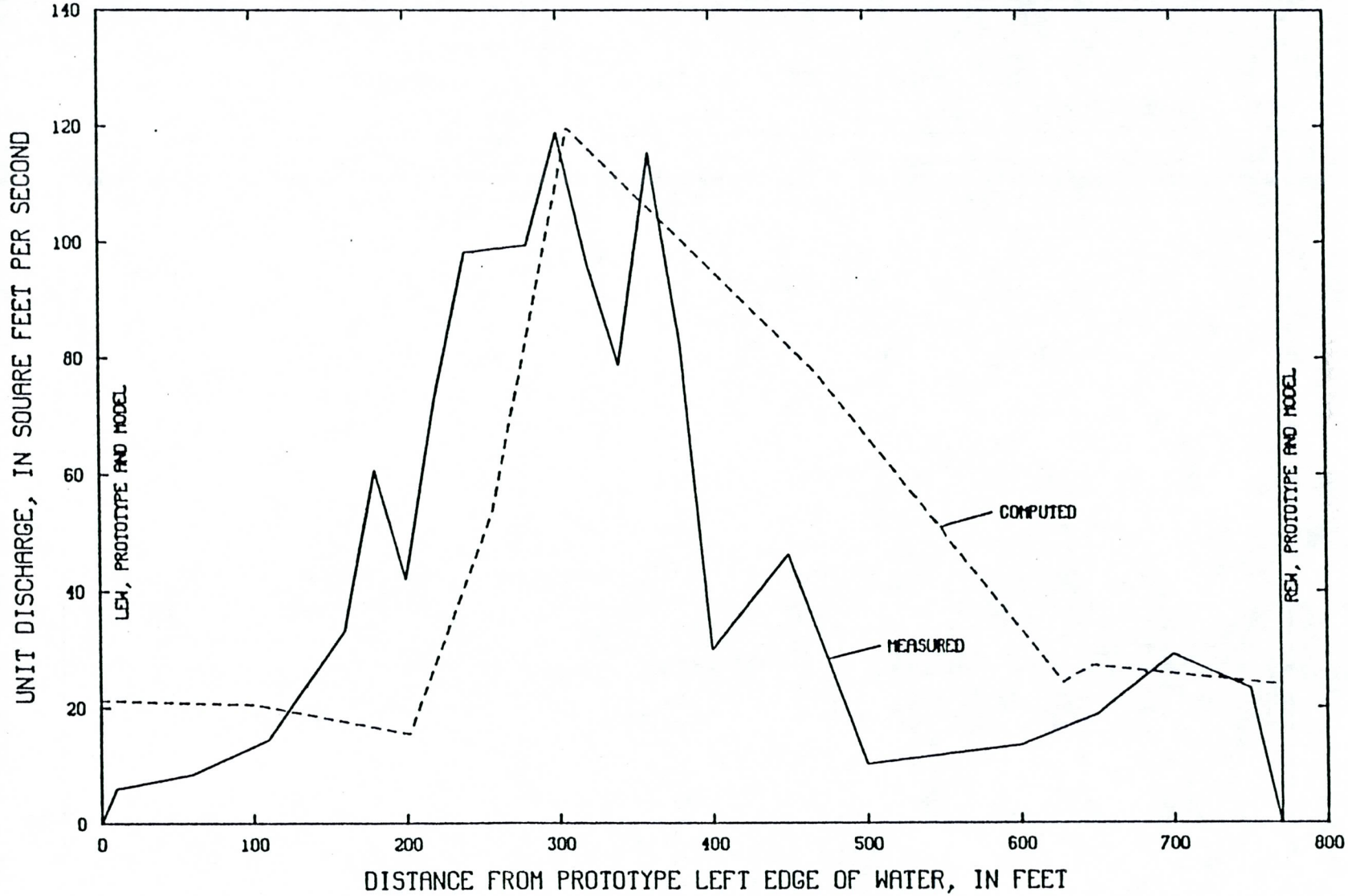

Figure 8.--Computed and measured unit discharge at the I-10 bridge opening at the Middle River.

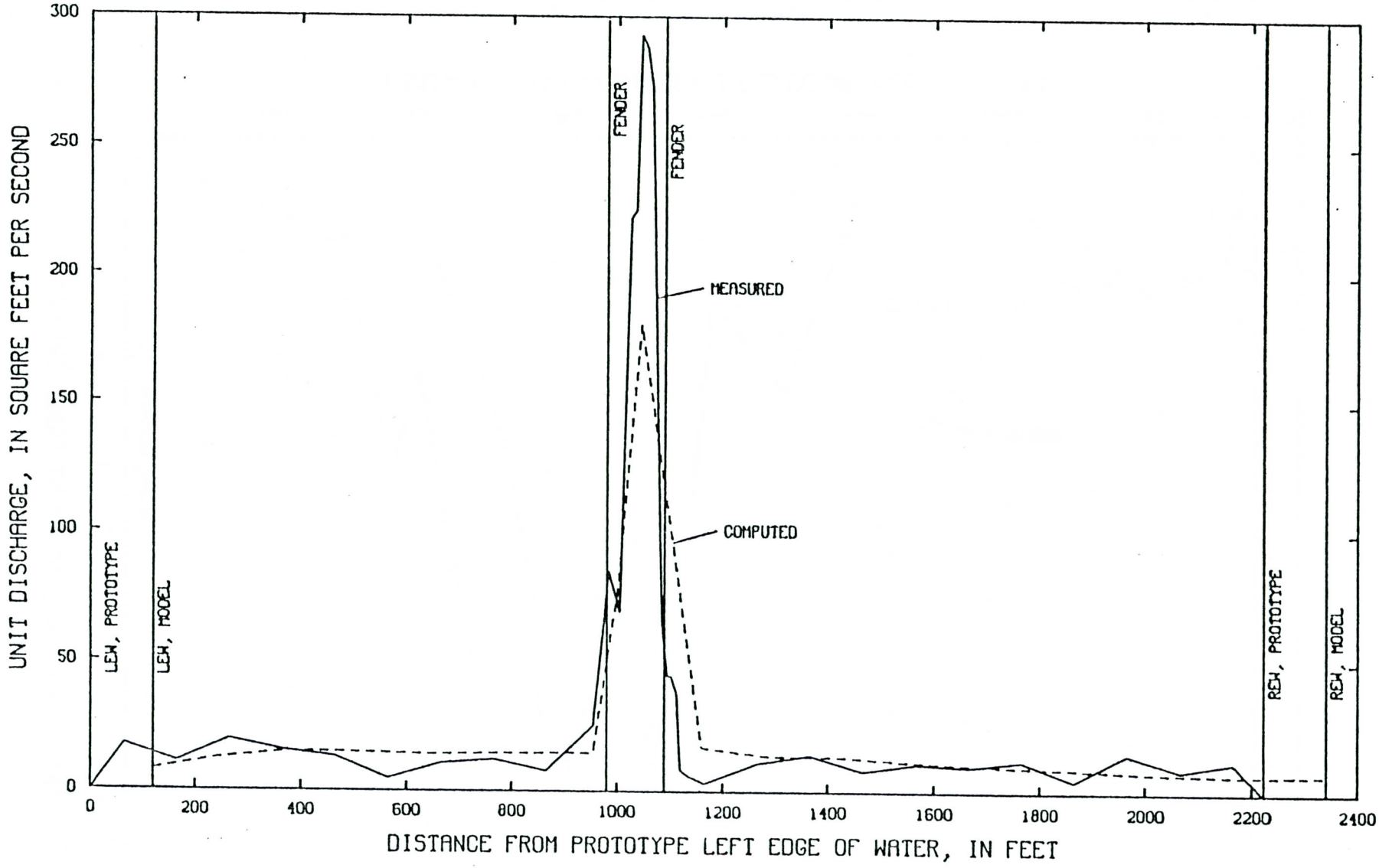

Figure 9.--Computed and measured unit discharge at the I-10 bridge opening at the West Pearl River.

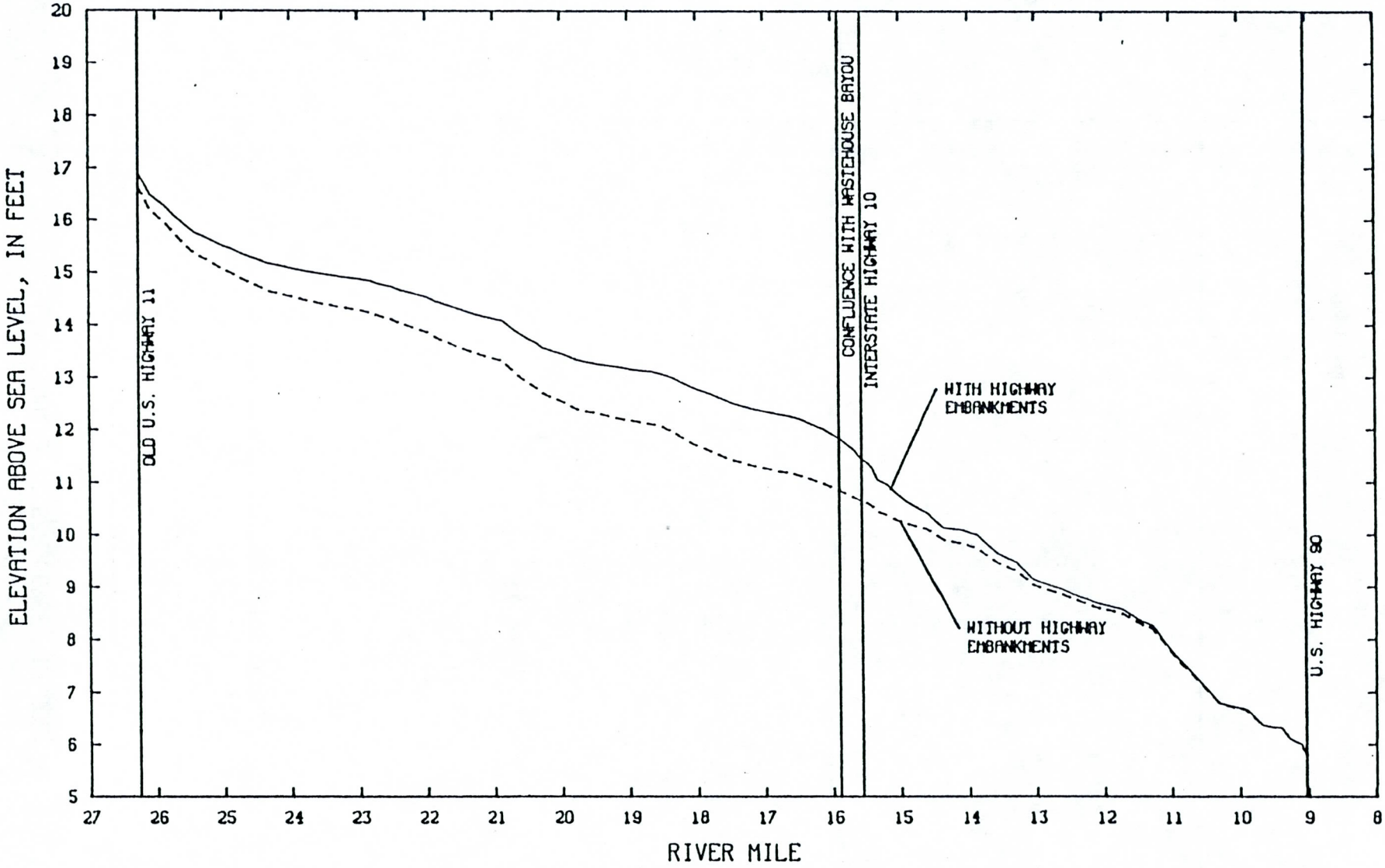

Figure 10.--Computed water-surface elevations for the Pearl River with and without the I-10 embankments in place.

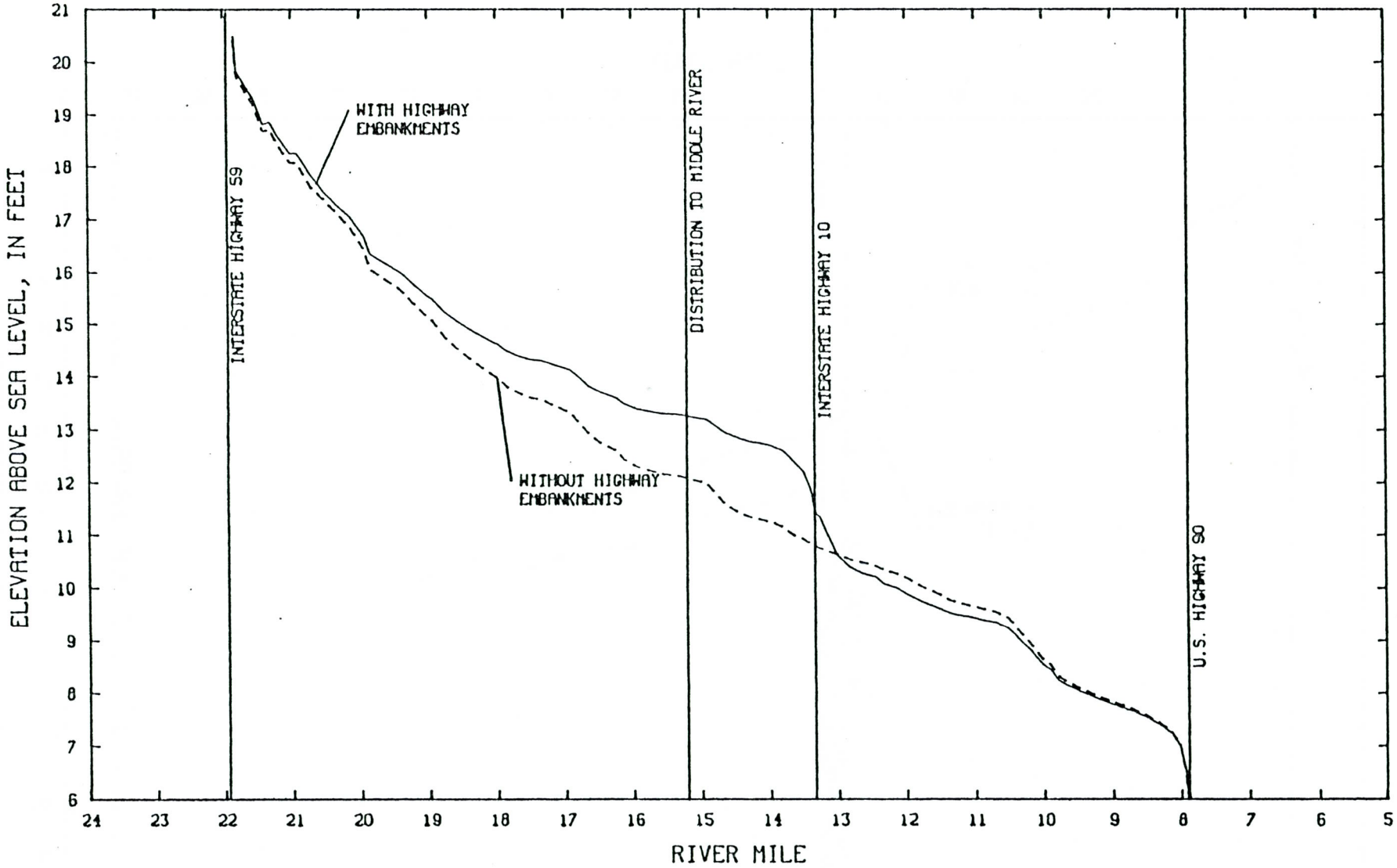

Figure 11.--Computed water-surface elevations for the West Pearl River with and without the I-10 embankments in place.

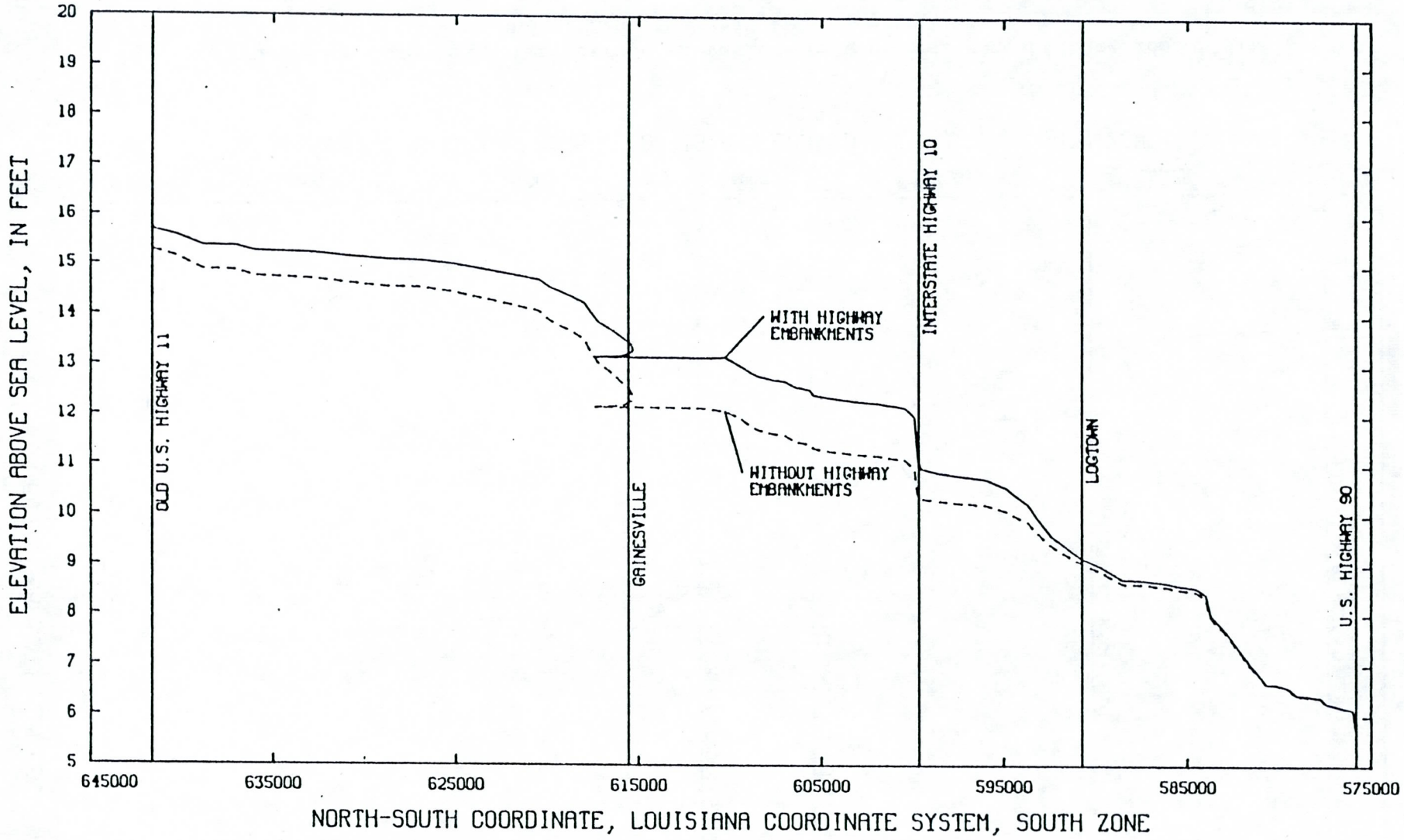

Figure 12.--Computed water-surface elevations at the east edge of the flood plain with and without the I-10 embankments in place.

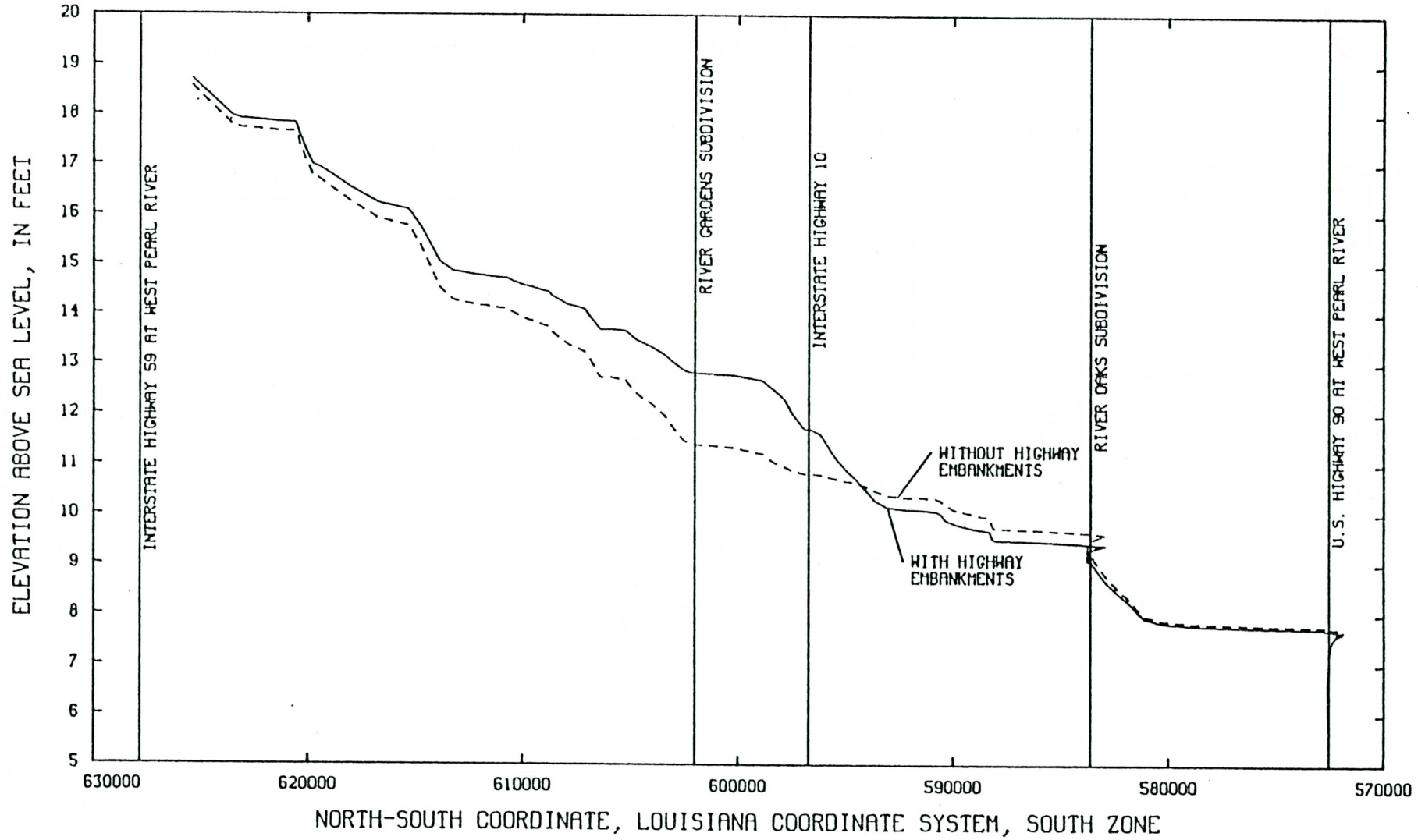

Figure 13.--Computed water-surface elevations at the west edge of the flood plain with and without the I-10 embankments in place.

Within a 3-mile-long reach centered about I-10, the flow converges toward and passes through the three bridge openings and then diverges back onto the flood plain. Along the upstream side of the I-10 embankments, the flow divides at approximately 71 percent of the way from the Pearl River to the Middle River and at approximately 64 percent of the way from the Middle River to the West Pearl River. Just downstream from I-10, the water surface is somewhat higher on the east side of the flood plain than on the west side. For example, 1 mi downstream from the roadway, the difference is about half a foot. Approximately 1.5 mi downstream from the highway crossing, the flow is again uniformly distributed across the flood plain, and the velocity field is aligned with the axis of the flood plain in a south-southeastward direction.

In an approximately mile-and-a-half-long reach upstream from Highway 90, the flow turns away from the flood-plain axis and moves in a southeastward direction. Along the upstream side of the Highway 90 embankments, the flow divides at approximately 60 percent of the way from the Pearl River to the East Middle River, at approximately 44 percent of the way from the East Middle River to the Middle River, at approximately 59 percent of the way from the Middle River to the West Middle River, and at approximately 63 percent of the way from the West Middle River to the West Pearl River. The water surface is about 1.5 ft higher at the west end of the Highway 90 crossing than at the east end. The computed discharges at the bridge openings in Highway 90 are given in table 8.

The contour lines shown on plate 2 indicate that water-surface gradients are largest at natural and man-made constrictions of the flood plain. Upstream from I-10, the slope of the water-surface in the direction of the axis of the flood plain is larger on the west side of the flood plain than on the east side. At I-10, the water-surface gradient is larger at the Middle River and West Pearl River openings than at the Pearl River opening. Downstream from I-10, the water-surface slope is generally larger on the east side of the flood plain than on the west side. At Highway 90, the water-surface gradient is much larger at the West Pearl River opening than at the other four openings.

Computed channel discharge for the Pearl and West Pearl Rivers is plotted as a function of river mile in figures 14 and 15, respectively. Throughout the study reach, except near the bridges, most of the discharge is in the flood plain. At the upstream boundary (river mile 26.3), the discharge in the channel of the Pearl River, with the I-10 embankments in place, is 22,000 ft^3/s. The discharge drops sharply downstream from old Highway 11 to a low of 2,760 ft^3/s at river mile 23.0. The discharge in the channel of the West Pearl River, with the I-10 embankments in place, drops from 69,100 ft^3/s at the upstream boundary (river mile 21.9) to 20,800 ft^3/s at river mile 20.9 and to 7,380 ft^3/s at river mile 18.2.

At the upstream boundary, 52 percent of the total discharge is in the channels of the Pearl and West Pearl Rivers. Less than 1.5 mi

Table 8.--Computed discharges at the Highway 90 bridge openings with and without the I-10 embankments in place

Bridge opening	With highway embankments		Without highway embankments	
	Discharge, in cubic feet per second	Discharge, as percent of total discharge	Discharge, in cubic feet per second	Discharge, as precent of total discharge
Pearl River	60,500	34.6	59,800	34.4
East Middle River	25,200	14.4	25,000	14.4
Middle River	27,600	15.8	27,500	15.8
West Middle River	32,000	18.3	32,100	18.4
West Pearl River	29,600	16.9	29,900	17.2
Total[1/]	175,000	100	174,000	100

1/The reason for the discrepancy between the total computed discharge and the total inflow is discussed on page 6.

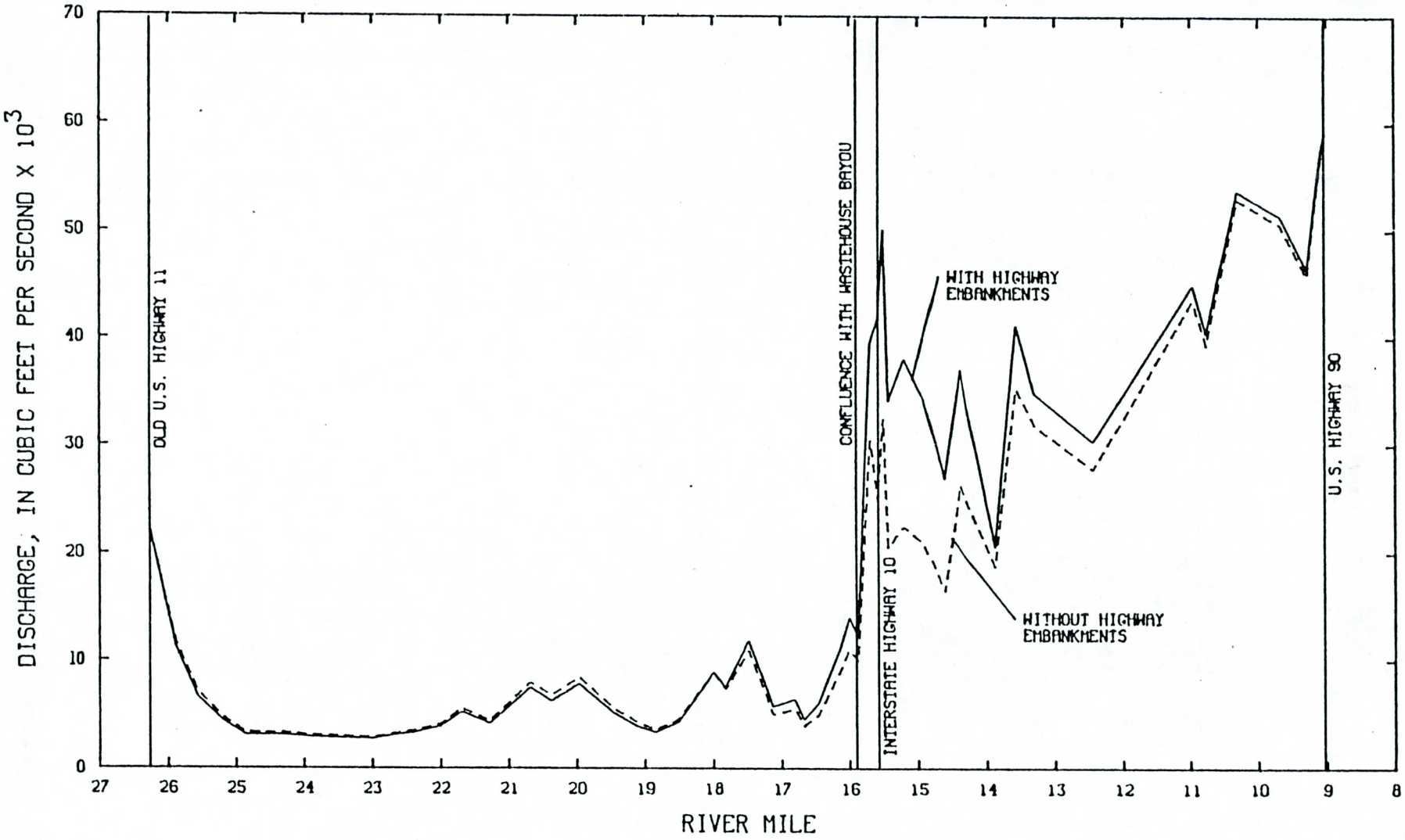

Figure 14.--Computed channel discharge for the Pearl River with and without the I-10 embankments in place.

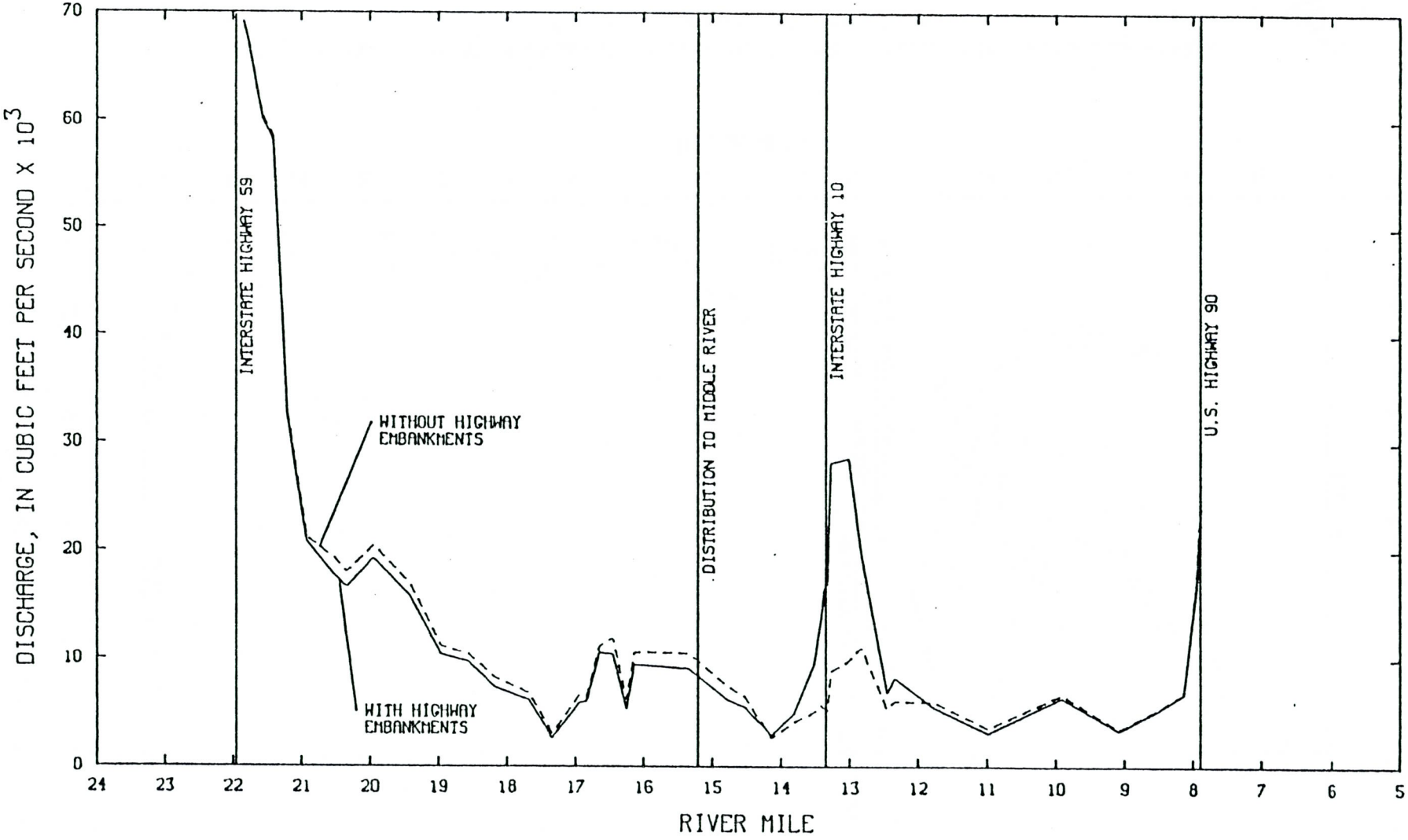

Figure 15.--Computed channel discharge for the West Pearl River with and without the I-10 embankments in place.

downstream, only 14 percent of the discharge is in the channels, and approximately halfway between the upstream boundary and I-10, only 6 percent of the discharge is in the channels. This value increases to 12 percent about a mile upstream from I-10 due to the increase in the number of channels from two to four. About 500 ft north of I-10, 36 percent of the discharge is in the three channels, and at the crossing, 49 percent of the computed discharge is in the channels. (Table 7 shows that 53 percent of the measured discharge was in the channels at I-10.)

In the reach from I-10 to Highway 90, between 25 and 41 percent of the discharge is in the channels. The increased channel discharge is due to both the increase in the size of the channel of the Pearl River downstream from Wastehouse Bayou and the increase in the number of channels. The discharge in the channel of the West Pearl River drops sharply at the downstream end of the widened reach between river miles 12.4 and 13.2. At the center of the reach (river mile 12.8), the channel discharge is 19,800 ft^3/s; at the downstream end, it is 6,920 ft^3/s. At Highway 90, 90 percent of the total discharge is in the five channels.

SIMULATION OF THE APRIL 2, 1980, FLOOD

WITHOUT THE I-10 EMBANKMENTS IN PLACE

The finite-element network used to simulate the April 2, 1980, flood was modified to represent conditions without I-10 in place, and the hydraulic impact of the I-10 embankments was determined by comparing results with and without I-10.

It should be noted that conditions with I-10 were compared to conditions without I-10, not to conditions prior to the construction of I-10. Thus, the reach of the West Pearl River between river miles 12.4 and 13.2, which was widened during construction, was not restored to its original width and depth in the simulation without I-10. However, because of the relatively small flow in the channel of the West Pearl River without I-10 in place, the difference with respect to backwater between conditions without I-10 and conditions prior to the construction of I-10 is almost certainly negligible.

Network Modifications

Elements were added in the areas occupied in the original network by the highway embankment between the Pearl and Middle Rivers, the embankment between the Middle and West Pearl Rivers, the 200-foot embankment at the left edge of the flood plain, and the knoll southeast of the West Pearl River bridge opening. Elsewhere, the two networks were identical.

Model ground-surface elevations at and near the highway embankments were changed where it was decided that they had been substantially altered during construction. Elevations ranging from 2.2 to 4.6 ft above sea level within the highway right-of-way on the right overbank at the Pearl River were lowered to 1.5 ft above

sea level. No changes were made to ground-surface elevations on the left overbank. Elevations ranging from 2.5 to 4.0 ft above sea level on both overbanks at the Middle River were lowered to 2.0 ft above sea level. Ground-surface elevations on the right overbank at the West Pearl River were not changed, but elevations ranging from 4.0 to 9.0 ft above sea level on the left overbank were lowered to 2.5 ft above sea level. Elevations at and near the knoll southeast of the West Pearl River opening were lowered to the elevation of the surrounding flood plain, 1.5 to 3.0 ft above sea level, and elevations ranging from 5.0 to 8.0 ft above sea level between the knoll and the West Pearl River were lowered to between 3.0 and 5.0 ft above sea level. Natural levees along the channel banks were left in place.

The Chézy coefficients corresponding to the new elements and the elements formerly located in overbank areas under the I-10 bridges were assigned the value 22 $ft^{1/2}/s$, the value used in both simulations for the wooded flood plain (table 5). Upstream and downstream boundary conditions were the same as those used in the simulation with the highway embankments in place.

Results of the Simulation

The velocity field and water-surface contour lines for the simulation without I-10 in place are shown on plate 3. Computed water-surface elevation is plotted as a function of river mile for the channels of the Pearl and West Pearl Rivers in figures 10 and 11, respectively, and computed water-surface elevation is plotted for the east and west edges of the flood plain in figures 12 and 13, respectively.

Flow patterns in the upper and lower parts of the study reach are similar to those computed with the highway embankments in place. The discharges at the Highway 90 bridge openings are given in table 8. Throughout the middle part of the study reach, the flow is uniformly distributed across the flood plain and parallel to the flood-plain axis. In the reach extending from about 2 mi upstream from the site of I-10 to about a mile and a half upstream from Highway 90, the velocity field is aligned in a southward to south-southeastward direction.

As expected, water-surface elevations upstream from the I-10 site are lower without the highway embankments in place. Downstream from the roadway site, the water surface is lower on the east side of the flood plain and higher on the west side than it is with I-10 in place. There is no noticeable difference between water-surface elevations on opposite sides of the flood plain just downstream from the roadway site. Backwater caused by the I-10 embankments is discussed in detail in the next section.

Computed channel discharge for the Pearl and West Pearl Rivers is plotted as a function of river mile in figures 14 and 15, respectively. Throughout most of the reach upstream from the site

of I-10, there is slightly more flow in the channels without the roadway in place. This is due to the lower water-surface elevations without the roadway. A decrease in water-surface elevations reduces cross-sectional flow areas more rapidly on the flood plain than in the channels. Only near the site of the highway crossing are channel discharges significantly lower. Approximately halfway between the upstream boundary and the site of I-10, 7 percent of the discharge is in the channels, compared with 6 percent with the roadway in place. About 500 ft north of the I-10 site, 22 percent of the discharge is in the channels, compared with 36 percent with the roadway present, and at the roadway site, 23 percent of the discharge is in the channels, compared with 49 percent with the roadway present. The percentages near the site of I-10 are larger than upstream values due to the increase in the size of the channel of the Pearl River downstream from Wastehouse Bayou and the increase in the number of channels.

Discharges in the three channels near the highway crossing were compared with and without the embankments in place. The discharge with the roadway in place is at least 30 percent higher than the discharge without the roadway in place from about 1,000 ft upstream from the crossing to about 7,000 ft downstream from the crossing in the channel of the Pearl River, from about 4,000 ft upstream to about 3,000 ft downstream in the channel of the Middle River, and from about 2,000 ft upstream to about 5,000 ft downstream in the channel of the West Pearl River.

Computed discharges at the site of I-10 with and without the highway embankments in place are given in table 9. Without the highway embankments in place, flow is reduced 41 percent at the Pearl River bridge opening, 80 percent at the Middle River opening, and 67 percent at the West Pearl River opening. Without the roadway in place, the computed discharge across that part of the flood plain that is occupied by the embankments with the roadway present is 95,200 ft^3/s. With the roadway in place, 48 percent of this discharge is added to the discharge at the Pearl River opening, 23 percent to the discharge at the Middle River opening, and 27 percent to the discharge at the West Pearl River opening. (The 2-percent discrepancy is due to a conservation-of-mass error, which occurs for the reason discussed on page 6.) Thus, without I-10 in place, the flow shift from the west side of the flood plain to the east side is reduced upstream from the site of I-10.

In the reach downstream from the site of I-10, between 20 and 41 percent of the discharge is in the channels. The discharge at the widened reach of the West Pearl between river miles 12.4 and 13.2 drops from 11,100 ft^3/s at the center of the reach (river mile 12.8) to 5,420 ft^3/s at the downstream end. From a mile downstream from the site of I-10 to Highway 90, the discharge in the channel of the West Pearl River is virtually the same with and without the highway embankments in place. At Highway 90, 91 percent of the total discharge is in the channels.

Table 9.--Computed discharges at I-10 with and without the I-10 embankments in place

Subsection	Discharge with highway embankments, in cubic feet per second	Discharge without highway embankments, in cubic feet per second
Embankment between left edge of flood plain and Pearl River.	0	833
Pearl River, left overbank	23,600	13,800
Pearl River, channel	50,200	32,500
Pearl River, right overbank	36,100	18,100
Pearl River, total	110,000	64,400
Embankment between Pearl and Middle Rivers.	0	29,900
Middle River, left overbank	3,810	916
Middle River, channel	17,800	3,320
Middle River, right overbank	5,360	1,100
Middle River, total	27,000	5,340
Embankment between Middle and West Pearl Rivers.	0	64,500
West Pearl River, left overbank	10,000	3,560
West Pearl River, channel	16,900	5,260
West Pearl River, right overbank	11,000	3,580
West Pearl River, total	37,900	12,400
Total[1/]	175,000	177,000

1/The reason for the discrepancy between the total computed discharge and the total inflow is discussed on page 6.

Backwater and Drawdown Caused by the I-10 Embankments

A map of backwater and drawdown was obtained by subtracting nodal water-surface elevations computed without the roadway in place from the corresponding nodal water-surface elevations computed with the roadway in place. Lines of equal backwater and drawdown are shown on plate 4. Backwater and drawdown are plotted as a function of river mile for the channels of Pearl and West Pearl Rivers in figure 16, and values of backwater or drawdown at locations of interest are given in table 10.

When highway embankments are removed in a flood-plain model, error in the computed water surface due to incorrect simulation of the fall through bridge openings is also removed. Hence, backwater, which is computed by subtracting the water surface without highway embankments in place from the water surface with embankments in place, still contains this error. On the other hand, when highway embankments are removed, error due, for example, to incorrect values of flood-plain Chézy coefficients is still present in the computed water surface. Much of this error cancels when the water surface computed without the highway in place is subtracted from the water surface computed with the highway in place. Thus, error in computed backwater is likely to be less than error in the calibrated water surface computed with highway embankments in place.

The 1.2-foot to 2.0-foot lines form a "mound" north of I-10 between the Pearl River and the west edge of the flood plain. The 0.2-foot to 1.0-foot lines are aligned approximately in a southwest-to-northeast direction. Although maximum backwater at the west edge of the flood plain (1.5 ft) is greater than maximum backwater at the east edge (1.1 ft), backwater decreases more rapidly in the upstream direction along the west edge of the flood plain than along the east edge.

Backwater ranging from 0.6 to 0.2 ft extends more than a mile downstream from the Pearl River bridge opening in I-10 at the east edge of the flood plain. A large area of drawdown extends from the downstream side of the highway embankment between the Middle and West Pearl Rivers to the west edge of the flood plain. Drawdown of 0.2 ft or more occurs along approximately 2 mi of the west edge of the flood plain downstream from I-10.

DISCUSSION

A combination of natural and man-made factors causes most of the flow to enter the study reach on the west side of the flood plain and leave on the east side (tables 1 and 8). The ground-surface contour lines between the upstream model boundary and I-10 show that ground-surface elevations are higher near the West Pearl River than on the east side of the flood plain (pl. 1). At the upstream boundary, the channel of the West Pearl River is larger than the channel of the Pearl River. South of its confluence with Wastehouse Bayou, the channel of the Pearl River is much larger than that of the West Pearl River. The Middle River and Wastehouse

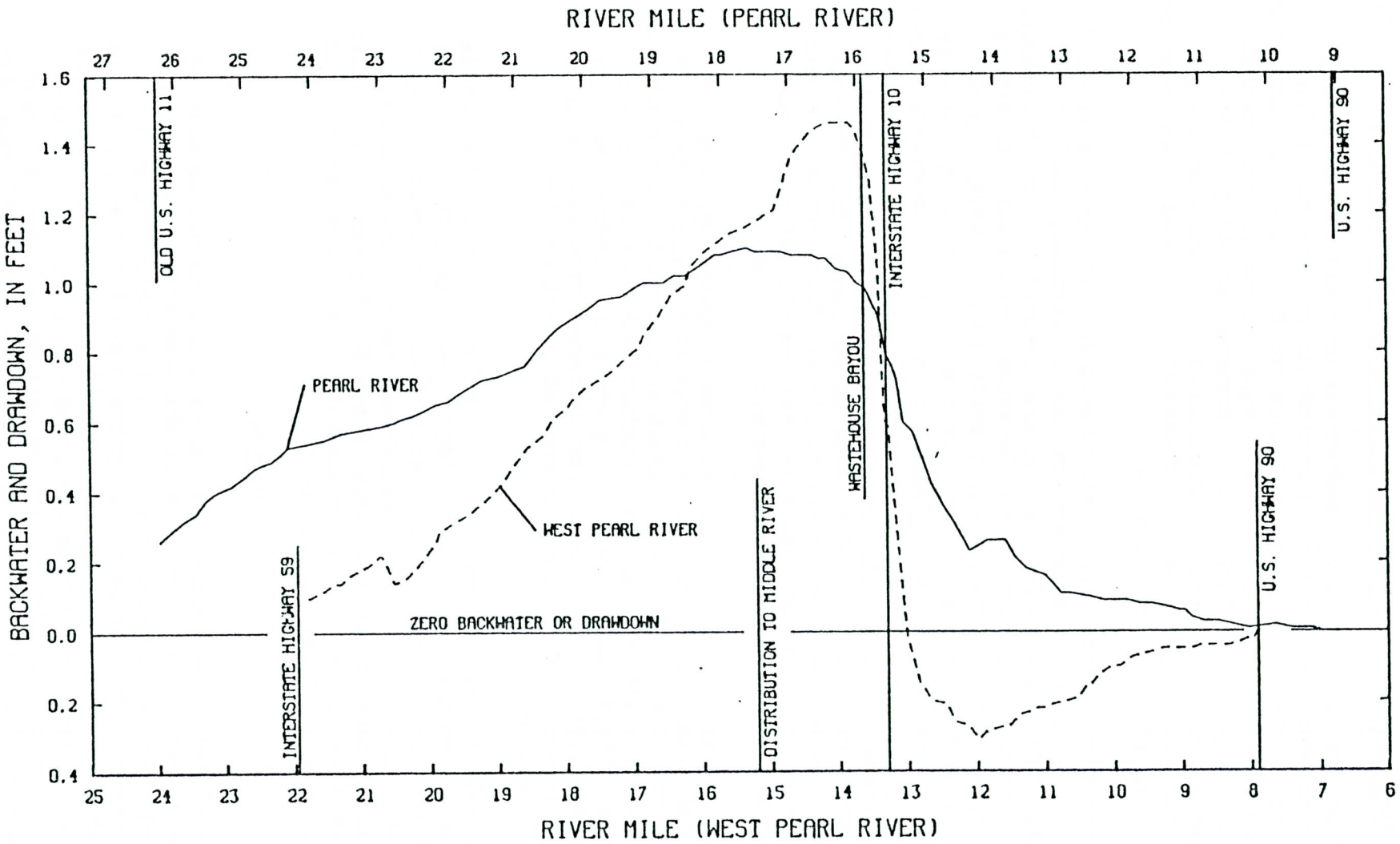

Figure 16.--Computed backwater and drawdown for the Pearl and West Pearl Rivers.

Table 10.--Computed water-surface elevations with and without the I-10 embankments in place and backwater or drawdown

Location reference number[1/]	Location	Water-surface elevation above sea level with highway embankments, in feet	Water-surface elevation above sea level without highway embankments, in feet	Backwater or drawdown[2/], in feet
1	Old Highway 11 at east edge of flood plain.	15.7	15.3	0.4
2	Gainesville	13.3	12.4	0.9
3	Napoleon	12.8	11.7	1.1
4	Location of maximum backwater at east edge of flood plain.	12.6	11.5	1.1
5	Logtown	9.2	9.1	0.1
6	Location of maximum backwater on north side of embankment between Pearl and Middle Rivers.	12.4	10.6	1.8
7	Location of maximum drawdown on south side of embankment between Pearl and Middle Rivers.	10.5	10.6	(0.1)
8	Old Highway 11 at Pearl River.	16.9	16.6	0.3
9	Location of maximum backwater on north side of the embankment between Middle and West Pearl Rivers.	12.7	10.6	2.1
10	Location of maximum drawdown on south side of embankment between Middle and West Pearl Rivers.	10.0	10.7	(0.7)
11	I-59 at West Pearl River.	20.5	20.4	0.1

Table 10.--Computed water-surface elevations with and without the I-10 embankments in place and backwater or drawdown--Continued

Location reference number[1]	Location	Water-surface elevation above sea level with highway embankments, in feet	Water-surface elevation above sea level without highway embankments, in feet	Backwater or drawdown[2], in feet
12	Porters River Landing	17.0	16.8	0.2
13	Magnolia Forest Subdivision, northeast corner.	14.8	14.2	0.6
14	Morgan Bluff	14.2	13.4	0.8
15	Davis Landing	13.8	12.9	0.9
16	River Gardens Subdivision	12.8	11.4	1.4
17	Mouth of Gum Bayou	12.7	11.3	1.4
18	Location of maximum backwater at west edge of flood plain.	12.7	11.2	1.5
19	Location of maximum drawdown at west edge of flood plain.	9.9	10.2	(0.3)
20	Quail Ridge Subdivision	9.8	10.1	(0.3)
21	River Oaks Subdivision, north side.	9.3	9.5	(0.2)

1/Location reference numbers are shown on plate 4.
2/Values of drawdown are given in parentheses.

Bayou cross the flood plain diagonally from west to east. At high stages, these topographic factors cause water to flow across the flood plain from the higher west side to the lower east side either with or without I-10 in place. However, with the roadway in place, the shift of flow from west to east occurs farther upstream. (See pls. 2 and 3.)

Accompanying the roadway-induced shift of flow to the east are higher water-surface elevations downstream from the roadway in the eastern part of the flood plain and lower water-surface elevations downstream in the western part. Upstream from the roadway, maximum backwater at the west edge of the flood plain is greater than maximum backwater at the east edge. However, because of the larger water-surface slope on the west side of the flood plain, backwater decreases more rapidly in the upstream direction along the west edge than along the east edge. (See pl. 4.)

For the three discharge measurements made at I-10 in 1979 and 1980, between 59 and 61 percent of the total discharge was at the Pearl River bridge opening (table 1). For the April 2, 1980, flood, about half of the discharge across the sites of the highway embankments without the roadway in place is diverted to the Pearl River opening when the roadway is in place (table 9). The change in the flow distribution and the lateral variations in backwater and drawdown with I-10 in place are due in part to the greater constriction of the flow in the western part of the flood plain than in the eastern part and in part to the topography of the flood plain.

The results obtained in this study suggest that the parallel I-59 and Southern Railroad embankments just north of the study reach and the Highway 90 embankments at the south end of the study reach may have significant hydraulic effects within and near the study area. The large proportion of the total flow entering the study reach at the West Pearl River (table 1) and the water-surface "mound" just downstream from the I-59 bridge opening at the West Pearl River (pl. 2) suggest that the I-59 and Southern Railroad embankments may contribute to a westward shift of flow upstream from I-59 and may cause backwater downstream from I-59. Observations made while adjusting the upstream discharge distribution and discussed on pages 29 and 30 suggest that such backwater extends no more than 3 or 4 mi downstream from I-59. An upstream extension of the finite-element network of about 5 mi would be needed to quantify the hydraulic effect of I-59 and the Southern Railroad.

Several factors discussed on page 45 suggest that backwater upstream from Highway 90 may be greater on the west side of the flood plain than on the east side: (1) Highway 90 constricts the western part of the flood plain more than the eastern part, (2) there is an eastward flow shift just upstream from the roadway, (3) water-surface elevations are higher at the west end of Highway 90 than at the east end, and (4) the water-surface gradient in the downstream direction is much larger at the West Pearl River bridge opening than at the other openings. A downstream extension of the

finite-element network of about 2 mi would be needed to quantify the hydraulic effect of Highway 90.

SUMMARY AND CONCLUSIONS

The two-dimensional finite-element surface-water flow modeling system FESWMS was used to study the effect of I-10 on water-surface elevations and flow distribution during the April 2, 1980, flood on the Pearl River near Slidell, La. A finite-element network was designed to represent the topography and vegetative cover of the study reach. Hydrographic data collected for the April 2, 1980, flood were used to adjust the flow model to simulate the flood as closely as possible. The finite-element network was then modified to represent conditions without I-10 in place, and the hydraulic impact of I-10 was determined by comparing results with and without I-10.

Without I-10 in place, much of the flow shifts from the west side of the flood plain to the east side upstream from the site of I-10. With I-10 in place, this flow shift occurs farther upstream than it does without the roadway in place. Upstream from the roadway, maximum backwater at the west edge of the flood plain (1.5 ft) is greater than maximum backwater at the east edge (1.1 ft), but backwater decreases more rapidly in the upstream direction along the west edge of the flood plain than along the east edge. Backwater ranging from 0.6 to 0.2 ft extends more than a mile downstream from the Pearl River bridge opening in I-10 at the east edge of the flood plain, and drawdown of 0.2 ft or more occurs along approximately 2 mi of the west edge of the flood plain downstream from I-10.

The results of the study suggest that I-59, the Southern Railroad, and Highway 90 may have significant hydraulic effects in and near the study reach. Further work would be needed to quantify these effects.

The capability of the modeling system FESWMS to simulate the significant features of steady-state flow in a complex multichannel river-flood-plain system with variable topography and vegetative cover was successfully demonstrated in this study. These features included lateral variations in discharge distribution, water-surface elevation, and backwater or drawdown at and near I-10, caused in part by the greater constriction of the flow in the western part of the flood plain and in part by the topography of the flood plain.

REFERENCES

Cardwell, G. T., Forbes, M. J., Jr., and Gaydos, M. W., 1967, Water resources of the Lake Pontchartrain area, Louisiana: Baton Rouge, La., Louisiana Department of Conservation, Geological Survey, and Louisiana Department of Public Works, Water Resources Bulletin No. 12, 105 p.

Chow, V. T., 1959, Open-channel hydraulics: New York, McGraw-Hill, 680 p.

Gee, D. M., and MacArthur, R. C., 1978, Development of generalized free surface flow models using finite element techniques, in Brebbia, C. A., and others, eds., Finite elements in water resources: International Conference on Finite Elements in Water Resources, 2nd, London, 1978, Proceedings: London, Pentech Press, p. 2.61-2.79.

Hood, P., 1976, Frontal solution program for unsymmetric matrices: International Journal for Numerical Methods in Engineering, v. 10, no. 2, p. 379-399.

_____ 1977, Note on frontal solution program for unsymmetric matrices: International Journal for Numerical Methods in Engineering, v. 11, no. 6, p. 1055.

King, I. P., and Norton, W. R., 1978, Recent applications of RMA's finite element models for two dimensional hydrodynamics and water quality, in Brebbia, C. A., and others, eds., Finite elements in water resources: International Conference on Finite Elements in Water Resources, 2nd, London, 1978, Proceedings: London, Pentech Press, p. 2.81-2.99.

Lee, F. N., and Arcement, G. J., 1981, Hydrologic analysis of Pearl River floods, April 1979 and April 1980, in Louisiana and Mississippi: Baton Rouge, La., Louisiana Department of Transportation and Development, Office of Highways, 37 p.

Lee, J. K., 1980, Two-dimensional finite element analysis of the hydraulic effect of highway bridge fills in a complex flood plain, in Wang, S. Y., and others, eds., Finite elements in water resources: International Conference on Finite Elements in Water Resources, 3rd, University, Miss., 1980, Proceedings: University, Miss., University of Mississippi, School of Engineering, p. 6.3-6.23.

Lee, J. K., and Bennett, C. S., III, 1981, A finite-element model study of the impact of the proposed I-326 crossing on flood stages of the Congaree River near Columbia, South Carolina: U.S. Geological Survey Open-File Report 81-1194, 56 p.

Norton, W. R., and King, I. P., 1973, A finite element model for Lower Granite Reservoir. Computer application supplement and user's guide: Walnut Creek, Calif., Water Resources Engineers, Inc., 90 p.

Norton, W. R., King, I. P., and Orlob, G. T., 1973, A finite element model for Lower Granite Reservoir: Walnut Creek, Calif., Water Resources Engineers, Inc., 138 p.

Pinder, G. F., and Gray, W. G., 1977, Finite element simulation in surface and subsurface hydrology: New York, Academic Press, 295 p.

Pritchard, D. W., 1971, Two-dimensional models, in Ward, G. H., Jr., and Espey, W. H., Jr., eds., Estuarine modeling: An assessment: Washington, D.C., Environmental Protection Agency, Water Quality Office, Water Pollution Control Research Ser. 16070DZV, p. 22-33.

Shell, J. D., 1981, Drainage areas in the Pearl River basin, Mississippi-Louisiana. Part 2. Pearl River below Strong River to mouth: U.S. Geological Survey, 232 p.

Tseng, M. T., 1975, Evaluation of flood risk factors in the design of highway stream crossings. V. III. Finite element model for bridge backwater computation: Washington, D.C., Federal Highway Administration, Report No. FHWD-RD-75-53, 176 p.

U.S. Army Corps of Engineers, 1981, Pearl River basin reconnaissance report (stage 1 report): Mobile, Ala., U.S. Army Corps of Engineers, 200 p.

U.S. Geological Survey, 1981, Water resources data for Mississippi: U.S. Geological Survey Water-Data Report MS-79-1, 438 p.

_____ 1982, Water resources data for Louisiana. V. 2. Southern Louisiana: U.S. Geological Survey Water-Data Report LA-81-2, 327 p.

U.S. Water Resources Council, 1977, Guidelines for determining flood flow frequency: Washington, D.C., U.S. Water Resources Council, Hydrology Committee, Revised Bulletin 17A, 163 p.

Walters, R. A., and Cheng, R. T., 1978, A two-dimensional hydrodynamic model of a tidal estuary, in Brebbia, C. A., and others, eds., Finite elements in water resources: International Conference on Finite Elements in Water Resources, 2nd, London, 1978, Proceedings: London, Pentech Press, p. 2.3-2.21.

_____ 1980, Accuracy of an estuarine hydrodynamic model using smooth elements: Water Resources Research, v. 16, no. 1, p. 187-195.

Wax, C. L., and Tingle, J. L., 1980, The Pearl River flood of Easter 1979: A water balance explanation: Mississippi State, Miss., Mississippi State University, Water Resources Research Institute, 27 p.

Zienkiewicz, O. C., 1977, The finite element method (3rd ed.): London, McGraw-Hill, 787 p.

GUIDE FOR SELECTING MANNING'S ROUGHNESS COEFFICIENTS FOR NATURAL CHANNELS AND FLOOD PLAINS

Research, Development, and Technology

Turner-Fairbank Highway Research Center
6300 Georgetown Pike
McLean, Virginia 22101

Report No.
FHWA-TS-84-204

Final Report

April 1984

U.S. Department of Transportation
Federal Highway Administration

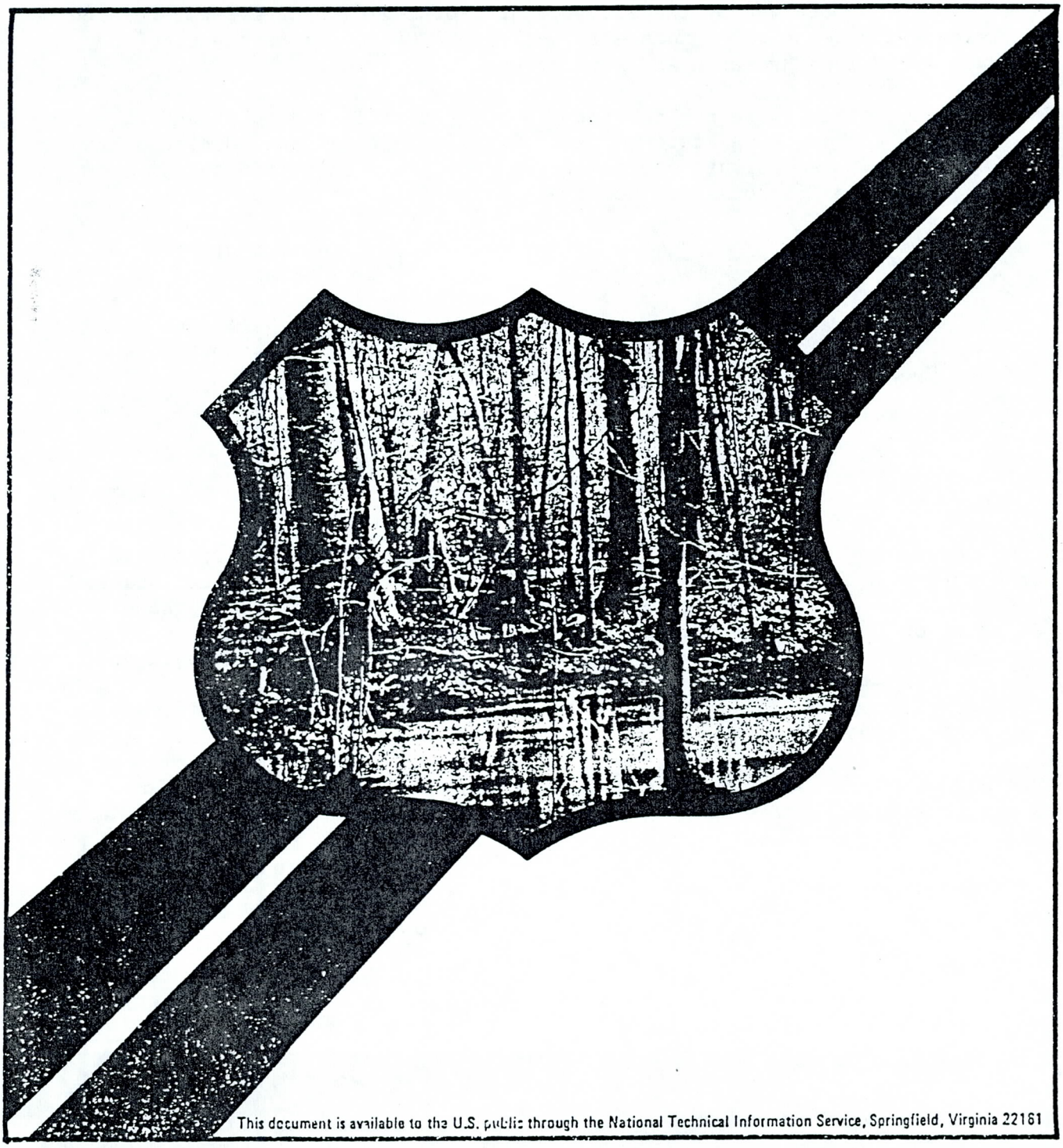

This document is available to the U.S. public through the National Technical Information Service, Springfield, Virginia 22161

FOREWORD

This Technology Sharing Report provides procedures for determining Manning's roughness coefficient for densely vegetated flood plains. The guidelines should be of interest to hydraulic and bridge engineers. Environmental specialists concerned with flood plains and wetlands may also find this report useful.

The report was prepared by the United States Geological Survey, Water Resources Division, with technical guidance from the FHWA Office of Engineering and Highway Operations Research and Development.

Sufficient copies of the publication are being distributed to provide a minimum of one copy to each FHWA region office, division office, and to each State highway agency. Additional copies of the report can be obtained from the National Technical Information Service, Springfield, Virginia 22161.

R. E. Hay
Director, Office of
Engineering and Highway
Operations R&D

R. J. Betsold
Director, Office of
Implementation

NOTICE

This document is disseminated under the sponsorship of the Department of Transportation in the interest of information exchange. The United States Government assumes no liability for its contents or use thereof. The contents of this report reflect the views of the contractor, who is responsible for the accuracy of the data presented herein. The contents do not necessarily reflect the official views or policy of the Department of Transportation. This report does not constitute a standard, specification or regulation.

The United States Government does not endorse products or manufacturers. Trade or manufacturer's names appear herein only because they are considered essential to the object of this document.

Technical Report Documentation Page

1. Report No.	2. Government Accession No.	3. Recipient's Catalog No.
FHWA-TS-84-204		

4. Title and Subtitle

GUIDE FOR SELECTING MANNING'S ROUGHNESS COEFFICIENTS FOR NATURAL CHANNELS AND FLOOD PLAINS

5. Report Date: April 1984

6. Performing Organization Code

8. Performing Organization Report No.

7. Author(s)

G. J. Arcement, Jr., and V. R. Schneider

9. Performing Organization Name and Address

U. S. Geological Survey
Water Resources Division
P.O. Box 66492
Baton Rouge, LA 70896

10. Work Unit No. (TRAIS)

11. Contract or Grant No.

13. Type of Report and Period Covered

Final Report

12. Sponsoring Agency Name and Address

Office of Implementation
Federal Highway Administration
6300 Georgetown Pike
McLean, Virginia 22101

14. Sponsoring Agency Code

15. Supplementary Notes

Co-COTR: John M. Kurdziel
Roy Trent

16. Abstract

Although much research has been done on Manning's roughness coefficients for stream channels, very little has been done on the selection of roughness values for densely vegetated flood plains. A procedure for the determination of Manning's roughness coefficient (n) for channels and flood plains analyzes the different roughness factors that affect the roughness coefficients for channels and flood plains. By determining the value of each factor and combining those values, the n value can be determined. Another procedure deals with densely vegetated flood plains where the major roughness is caused by trees, vines, and brush. The n value for this type of flood plain can be determined by measuring the "vegetation density" of the flood plain.

Photographs of flood plain segments where n values have been verified are presented as a comparison standard to aid in assigning n values to similar flood plains.

17. Key Words	18. Distribution Statement
Roughness Coefficient, Manning Equation, Channels, Stable, Unstable, Channel Flow, Flood Plains, Flow Resistance, Hydraulic Roughness, Hydraulic Friction, Overland Flow, Vegetation Effects	No restrictions. This document is available to the public through the National Technical Information Service, Springfield, Virginia 22161.

19. Security Classif. (of this report)	20. Security Classif. (of this page)	21. No. of Pages	22. Price
Unclassified	Unclassified	68	

TABLE OF CONTENTS

	Page
Introduction	1
Approach	2
Method for assigning n values for channels	3
Selection of base n values (n_b)	4
Adjustment factors for channels	8
Irregularity (n_1)	8
Variation in channel cross section (n_2)	8
Obstructions (n_3)	12
Vegetation (n_4)	12
Meandering (m)	13
Methods for assigning n values for flood plains	13
Modified channel method	13
Adjustment factors for flood plains	16
Surface irregularities (n_1)	16
Obstructions (n_3)	16
Vegetation (n_4)	16
Vegetation density methods	17
Techniques for determining vegetation density	17
Indirect technique	18
Direct technique	18
Photographs of flood plains	23
Procedures for assigning n values	39
Description of steps for assigning n values	39
Channel roughness (steps 3-13)	39
Flood-plain roughness (steps 14-23)	50
Examples of procedures for determining n values	51
Summary	60
Selected references	61

LIST OF FIGURES

		Page
Figure 1.	Graph showing relation of stream power and median grain size to flow regime	6
2.	Forms of bed roughness in sand-bed channels	7
3.	Plot of effective-drag coefficient versus hydraulic radius for wide, wooded flood plains using verified n values	19
4.	Example measurement of vegetation density of representative sample area	21
5.	Example of determination of Manning's n by direct technique of vegetation density	22
6-20.	Photograph showing flood plains having verified n values:	
	6. Cypress Creek near Downsville, La., n=0.10	24
	7. Bayou de Loutre near Farmerville, La., n=0.11	25
	8. Bayou de Loutre near Farmerville, La., n=0.11	26
	9. Bayou de Loutre near Farmerville, La., n=0.11	27
	10. Coldwater River near Red Banks, Miss., n=0.11	28
	11. Coldwater River near Red Banks, Miss., n=0.11	29
	12. Yockanookany River near Thomastown, Miss., n=0.12	30
	13. Yockanookany River near Thomastown, Miss., n=0.12	31
	14. Flagon Bayou near Libuse, La., n=0.13	32
	15. Pea Creek near Louisville, Ala., n=0.14	33
	16. Pea Creek near Louisville, Ala., n=0.14	34
	17. Tenmile Creek near Elizabeth, La., n=0.15	35
	18. Sixmile Creek near Sugartown, La., n=0.13	36
	19. Thompson Creek near Clara, Miss., n=0.20	37
	20. Thompson Creek near Clara, Miss., n=0.20	38
21.	Flow chart of procedures for assigning n values	40
22.	Sample form for computing n values	42
23.	Sketch of a hypothetical cross section showing reaches, segments, and subsections used in assigning n values	47

LIST OF TABLES

Table 1.	Base values of Manning's n	4
2.	Factors that affect roughness of the channel	9
3.	Factors that affect roughness of flood plains	14
4.	Outline and example of procedures for determining n values for a hypothetical channel and flood plain	52

SYMBOLS AND UNITS

Symbol	Definition	Units
A	cross-section area of flow	ft^2
ΣA_i	the total frontal area of vegetation blocking the flow	ft^2
C_*	effective drag coefficient for vegetation	-----
d_{84}	particle diameter that equals or exceeds that of 84 percent of the particles	ft
g	gravitational constant	ft/s^2
h	height of water on flood plain	ft
K	conveyance of a section	ft^3/s
L	length of channel reach being considered	ft
l	length of representative sample area	ft
m	correction factor for meandering of channel or flood plain	-----
n	Manning's roughness coefficient, including boundary and vegetation effects	$ft^{1/6}$
n_b	base value of Manning's roughness coefficient for the surface material of the channel or flood plain	$ft^{1/6}$
$\Sigma n_i d_i$	summation of number of trees in a sample area multiplied by diameter	ft
n_o	Manning's roughness coefficient, excluding the effect of the vegetation	$ft^{1/6}$
n_1	value of Manning's roughness coefficient for the effect of surface irregularity	$ft^{1/6}$
n_2	value of Manning's roughness coefficient for variations in shape and size of channel and flood plain	$ft^{1/6}$
n_3	value of Manning's roughness coefficient for obstructions	$ft^{1/6}$
n_4	value of Manning's roughness coefficient for vegetation	$ft^{1/6}$
n_4'	value of Manning's roughness coefficient used in determining n_o, representing vegetation not accounted for in vegetation density	$ft^{1/6}$

SYMBOLS AND UNITS--Continued

Symbol	Definition	Units
R	hydraulic radius	ft
S_e	slope of energy-grade line	ft/ft
S_w	slope of water-surface profile	ft/ft
SP	stream power	(ft-lbs/s)/ ft^2
V	mean velocity of flow	ft/s
Veg_d	vegetation density	ft^{-1}
Veg_R	vegetation resistivity	ft^{-1}

FACTORS FOR CONVERTING INCH-POUND UNITS TO INTERNATIONAL SYSTEM OF UNITS (SI)

Multiply	By	To obtain
cubic foot per second (ft^3/s)	0.02832	cubic meter per second (m^3/s)
foot (ft)	0.3048	meter (m)
foot per second (ft/s)	0.3048	meter per second (m/s)
foot per second square (ft/s^2)	0.3048	meter per second square (m/s^2)
inch (in.)	25.40	millimeter (mm)
square foot (ft^2)	0.0929	square meter (m^2)
pounds per square foot (lb/ft^2)	4.882	kilograms per square meter (km/m^2)

INTRODUCTION

There has been increasing interest and activity in flood-plain management, flood-insurance studies, and in the design of bridges and highways across flood plains. Hydraulic computations of flow for such studies involve roughness coefficients, which represent the resistance to flood flows in channels and flood plains.

The Manning's formula, frequently used as a part of an indirect computation of streamflow, is

$$V = \frac{1.486}{n} R^{2/3} S_e^{1/2} \qquad (1)$$

in which: V = mean velocity of flow, in feet per second;
R = hydraulic radius, in feet;
S_e = slope of energy grade line;
and n = Manning's roughness coefficient.

When a large number of calculations are necessary in using Manning's formula, it is sometimes convenient to use a conveyance term, where conveyance is defined as

$$K = \frac{1.486}{n} AR^{2/3} \qquad (2)$$

in which: K = conveyance of the channel, in cubic feet per second;
A = cross-sectional area of channel, in square feet;
R = hydraulic radius, in feet;
and n = Manning's roughness coefficient.

The term K is known as the conveyance of the channel section and it is a measure of the carrying capacity of the channel section.

Suggested values for Manning's n, tabulated according to factors that affect roughness, are found in references such as Chow (1959), Henderson (1966), and Streeter (1971). Roughness characteristics of natural channels are given by Barnes (1967). Barnes presents pictorial illustrations of typical rivers and creeks with their respective n values.

It would be impractical to record all that is known about the selection of the Manning's roughness coefficient in this guide, but many textbooks and technique manuals contain discussions of the factors involved in the selection. Three, which could be considered as supplements to this guide, are Barnes (1967), Chow (1959), and Ree (1954).

Although much research has been done to determine roughness coefficients for open-channel flow (Carter and others, 1963), less has been done for densely vegetated flood plains, coefficients that are typically very different from those for channels.

The objective of this guide is to develop procedures to aid engineers in the selection of roughness coefficients for channels and flood plains,

so that flow information needed for highway design might be computed. The guide presents step-by-step procedures that enable determination of Manning's n values for natural channels and flood plains.

This guide builds on the report by Aldridge and Garrett (1973), who attempted to systematize the selection of roughness coefficients for Arizona streams. An attempt is made to broaden the scope of that work, in particular to describe procedures for the selection of roughness coefficients in densely vegetated flood plains.

The n values for channels are determined by evaluating the effects of certain roughness factors in the channels. Two methods are presented to determine the roughness coefficients of flood plains. One method, similar to that for channel roughness, involves the evaluation of the effects of certain roughness factors in the flood plain. The other method involves the evaluation of the vegetation density of the flood plain to determine the n value. This second method is particularly suited to handle roughness for densely wooded flood plains.

There is a tendency to regard the selection of roughness coefficients as either an arbitrary or an intuitive process. This design guide presents specific procedures to determine the values for roughness coefficients in channels and flood plains. Photographs of flood plains with known roughness coefficients are also presented for comparison.

APPROACH

Values of the roughness coefficient, n, may be assigned for conditions that exist at the time of a specific flow event, for average conditions over a range in stage, or for anticipated conditions at the time of a future event.

The procedures described in this report are limited to the selection of roughness coefficients for application to one-dimensional, open-channel flow. Further, in most instances, the values are intended for use in the energy equation as applied to one-dimensional, open-channel flow--such as in a slope-area or step-backwater procedure for determining flow.

The roughness coefficients apply to a longitudinal reach of channel and (or) flood plain. The cross section within the reach may be of regular geometric shape (such as triangular, trapezoidal, or semicircular) or of an irregular shape typical of many natural channels. The flow may be confined to one or more channels; and, especially during floods, the flow may occur both in the channel and in the flood plain. Such cross sections may be termed compound channels, consisting of channel and flood plain subsections. Cross sections are typically divided into subsections at points where major roughness or geometric changes occur. For example, such changes may be at the juncture of dense woods and a pasture or a flood plain and main channel. However, subsections should reflect representative conditions in the reach rather than only at the cross section. Roughness coefficients are determined for each subsection, and the procedures described herein apply to the selection of roughness coefficients for each subsection.

There are several means of compositing the results to obtain an equivalent n value for a stream cross section. These procedures, summarized by Chow (1959, p. 136), involve use of each of the following three assumptions: (1) The mean velocity in each subsection of the cross section is the same; (2) The total force resisting the flow is equal to the sum of the forces resisting the flows in the subdivided areas; and (3) The total discharge of the flow is equal to the sum of the discharges of the subdivided areas. It is also assumed that the slope of the energy grade line is the same for each of the subsections. In some cases it is not necessary to compute the equivalent n value. Instead, the subsection conveyances, which are additive, are computed through assumption (3) to obtain the total conveyance for the cross section.

Roughness values for flood plains can be quite different from values for channels. Therefore, roughness values for flood plains should be determined independently from channels. As in the computation of channel roughness, a base roughness (n_b) is assigned to the flood plain, and adjustments for various roughness factors are made to determine the total n value for the flood plain.

Seasonal variability of roughness coefficients should be considered. Floods often occur during the winter when there is less vegetation. Thus, the field surveys, including photographs, may not be completed until spring when vegetation growth would be more dense. In these instances, a variable roughness coefficient may be needed to account for seasonal changes.

In developing the ability to assign n values, reliance must be on n values that have been verified. A verified n value is one that has been computed where both discharge and cross-section geometry are known.

METHOD FOR ASSIGNING n VALUES FOR CHANNELS

Although several factors affect the selection of an n value for a channel, the most important factors are the type and size of the materials that compose the bed and banks of a channel and the shape of the channel. Cowan (1956) developed a procedure for estimating the effects of these factors to determine the value of n for a channel. In this procedure, the value of n may be computed by

$$n = (n_b + n_1 + n_2 + n_3 + n_4)m \qquad (3)$$

where: n_b = a base value of n for a straight uniform, smooth channel in natural materials;
n_1 = a value added to correct for the effect of surface irregularities;
n_2 = a value for variations in shape and size of the channel cross section;
n_3 = a value for obstructions;
n_4 = a value for vegetation and flow conditions;
and m = a correction factor for meandering of the channel.

Proper values of n_b, n_1 to n_4, and m for various types of channels will be presented in detail in following sections.

Selection of Base n Values (n_b)

In the selection of a base n value for channel subsections, the channel must by classified as a stable channel or as a sand channel.

A stable channel is defined as a channel in which the bed is composed of firm soil, gravel, cobbles, boulders, or bedrock and which remains relatively unchanged through most of the range in flow. Table 1 (Aldridge and Garrett, 1973) lists base n_b values for stable channels and sand channels. The base values of Benson and Dalrymple (1967) generally apply to conditions that are close to average; whereas, Chow's (1959) base values are for the smoothest reach attainable for a given bed material.

Table 1.--Base values of Manning's n

[Modified from Aldridge and Garrett, 1973, table 1]

Channel or flood-plain type	Median size of bed material		Base n value	
	Millimeters	Inches	Benson and Dalrymple (1967) [1/]	Chow (1959) [2/]
Sand channels				
(Only for upper regime flow where grain roughness is predominant.)	0.2	---	0.012	---
	.3	---	.017	---
	.4	---	.020	---
	.5	---	.022	---
	.6	---	.023	---
	.8	---	.025	---
	1.0	---	.026	---
Stable channels and flood plains				
Concrete	---	---	0.012-0.018	0.011
Rock cut	---	---	---	.025
Firm soil	---	---	.025- .032	.020
Coarse sand	1- 2	---	.026- .035	---
Fine gravel	---	---	---	.024
Gravel	2- 64	0.08- 2.5	.028- .035	---
Coarse gravel	---	---	---	.026
Cobble	64-256	2.5 -10.1	.030- .050	---
Boulder	>256	>10.1	.040- .070	---

[1/] Straight uniform channel.
[2/] Smoothest channel attainable in indicated material.

Barnes (1967) catalogued verified n values for stable channels having roughness coefficients ranging from 0.024 to 0.075. In addition to a description of the cross section, bed material, and flow conditions during the measurement, color photographs of the channels were provided.

A sand channel is defined as a channel in which the bed has an unlimited supply of sand. By definition, sand ranges in grain size from 0.062 to 2 mm.

Resistance to flow varies greatly in sand channels because the bed material moves easily and takes on different configurations or bed forms. Bed form is a function of velocity of flow, grain size, bed shear, temperature, and other variables. The flows that produce the bed forms are classified as lower-regime flow and upper-regime flow, according to the relation between depth and discharge. The lower-regime flow occurs with low discharges and the upper-regime flow with high discharges. An unstable discontinuity in the depth-discharge relationship appears between the two regimes and this is called a transitional zone. In lower-regime flow, the bed may have a plane surface and no movement of sediment, or it may be deformed and have small uniform waves or large irregular saw-toothed waves formed by sediment moving downstream. The smaller waves are known as ripples, and the larger waves are known as dunes. In upper-regime flow, the bed may have a plane surface and movement of sediment, or it may have long, smooth sand waves in phase with the surface waves. These waves are known as standing waves and antidunes. Bed forms on dry beds are remnants of the bed forms that existed during receding flows and may not represent bed forms present during flood stages.

The regime is governed by the size of the bed materials and the stream power, which is a measure of energy transfer. Stream power (SP) is computed by the formula,

$$SP = 62\ RS_wV \qquad (4)$$

where: 62 = specific weight of water, in pounds per cubic foot;
R = hydraulic radius, in feet;
S_w = water-surface slope, in feet per foot;
and V = mean velocity, in feet per second.

The n value for a sand channel is assigned for upper-regime flow using table 1, which shows the relation between median-grain size and the n value. The flow regime is checked by computing the velocity and stream power that correspond to the assigned n value. The computed stream power is compared with the value that is necessary to cause upper-regime flow. Figure 1, developed by Simons and Richardson (1966, fig. 28), may be used for this purpose. If the computed stream power is not large enough to produce upper-regime flow (an indication of lower-regime or transitional-zone flow), a reliable value of n cannot be assigned. The evaluation of n due to bed-form drag is complicated and different equations are needed to describe bed forms. The total n value for lower- and transitional-regime flows can vary greatly and depends on the bed forms present at a particular time. Figure 2 illustrates how the total resistance in a channel varies as bed forms progress from one type to another. The n

values for lower- and transitional-regime flows generally are much larger than the values given in table 1 for upper regime flow. Simons, Lee, and Associates (1982), gave a range of n values commonly found for different bed forms.

The values given in table 1 for sand channels are for upper-regime flows and are based on extensive laboratory and field data obtained by the U.S. Geological Survey. In using these values, a check must be made (in the manner previously described) to ensure that the stream power is large enough to produce upper-regime flow (fig. 1). Although the base n values given in table 1 for stable channels are from verification studies, the values have a wide range because the effects of bed roughness are extremely difficult to separate from the effects of other roughness factors. The n values selected from table 1 will be influenced by personal judgment and experience.

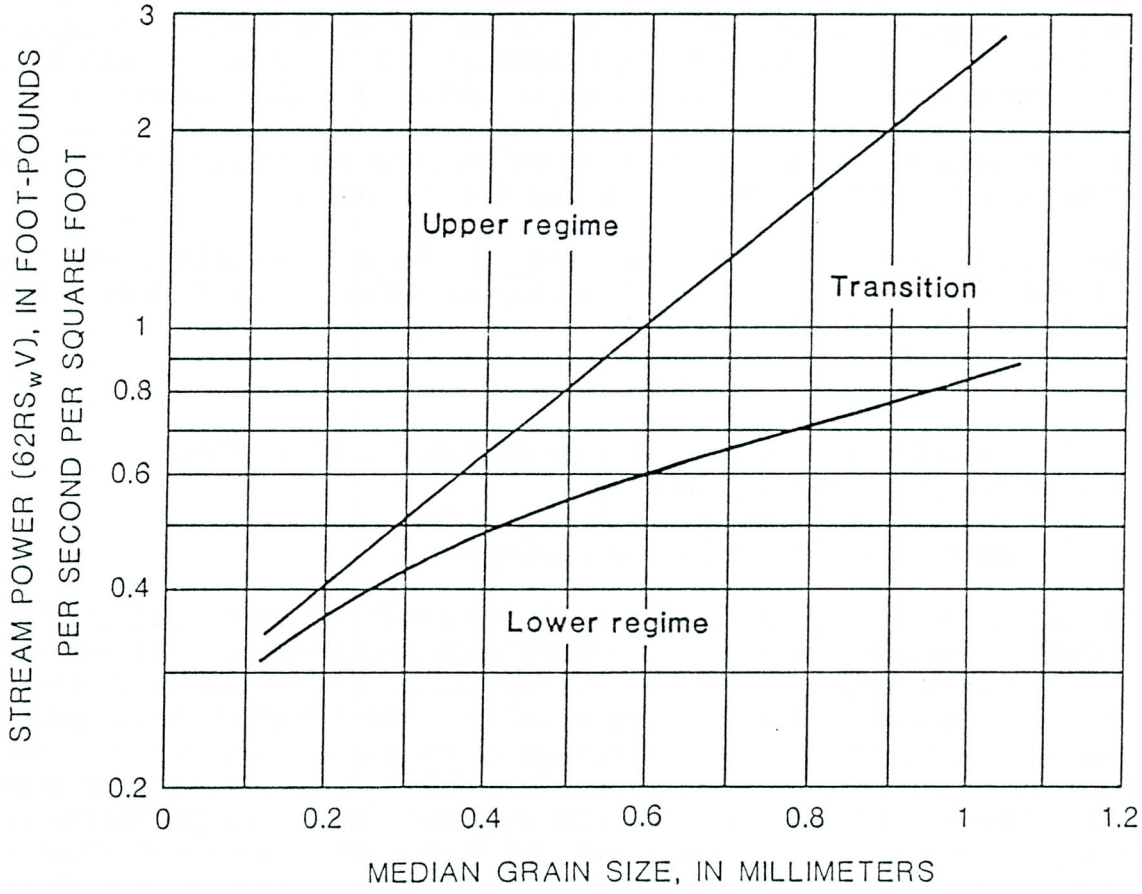

Figure 1.--Relation of stream power and median grain size to flow regime.

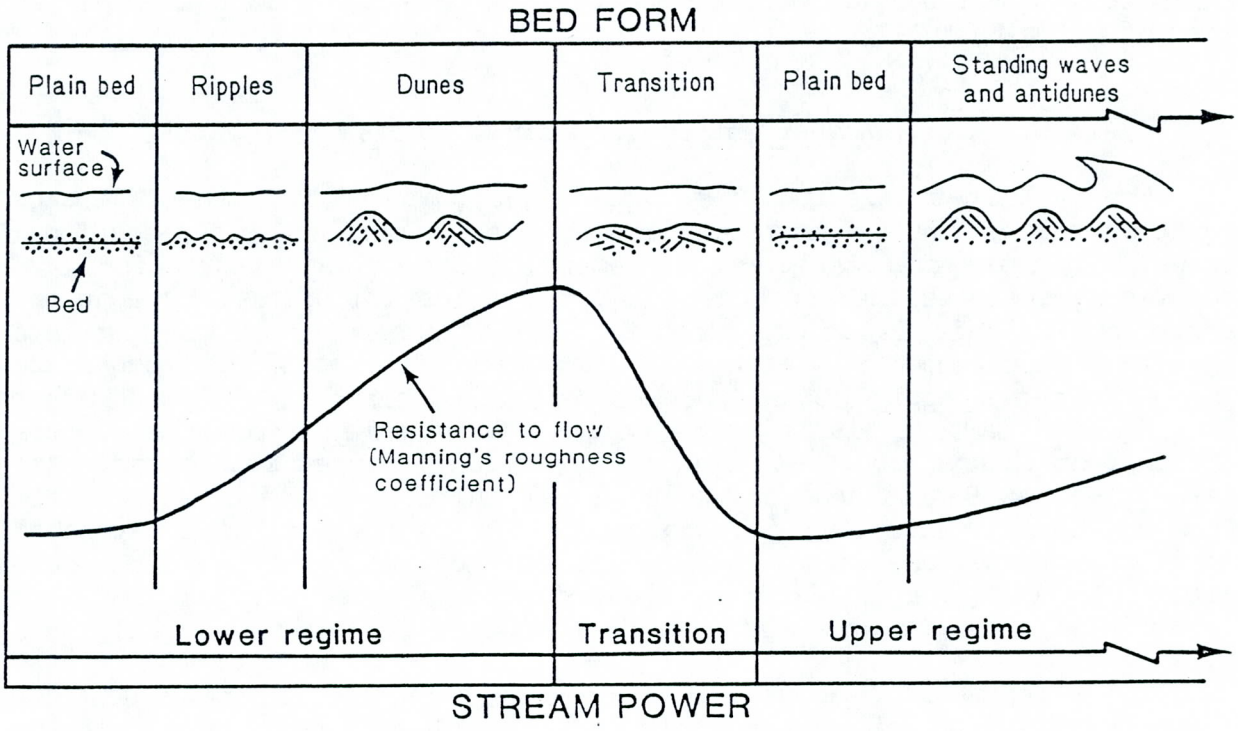

Figure 2.--Forms of bed roughness in sand-bed channels.

Limerinos (1970) related n to hydraulic radius and particle size based on samples from 11 stream channels having bed material ranging from small gravel to medium-size boulders. Particles have three dimensions--length, width, and thickness--and are generally oriented so that length and width are about parallel to the plane of the streambed. Limerinos related n to minimum diameter (thickness) and to intermediate diameter (width); his equation using intermediate diameter appears to be the most useful because this dimension is most easily measured in the field and estimated from photographs.

The equation for n using intermediate diameter, is

$$n = \frac{(0.0926)\,R^{1/6}}{1.16 + 2.0\,\log\left(\frac{R}{d_{84}}\right)} \qquad (5)$$

where: R = hydraulic radius, in feet;
d_{84} = the particle diameter, in feet, that equals or exceeds that of 84 percent of the particles (determined from a sample of about 100 randomly distributed particles).

Limerinos selected reaches having a minimum amount of roughness, other than that caused by bed material, and reaches that correspond to the base values given by Benson and Dalrymple (1967), shown in table 1.

Burkham and Dawdy (1976) showed that equation 5 applies for upper-regime flow in sand channels. If a measured d_{84} is available or can be estimated, equation 5 may be used to obtain a base n for sand channels in lieu of using table 1.

Adjustment Factors for Channels

The n_b values selected from table 1 or computed from the Limerinos equation are for straight channels of nearly uniform cross-sectional shape. Channel irregularities, alinement, obstructions, vegetation, and meandering increase the roughness; and the value for n must by adjusted accordingly. This is accomplished by adding increments of roughness to the base value, n_b, for each condition that increases the roughness. The adjustments apply to stable and to sand channels. Table 2 from Aldridge and Garrett (1973) gives ranges of adjustments for the factors that affect channel roughness for the prevailing channel conditions. The base values of Benson and Dalrymple (1967) in table 1 and those computed from equation 5 generally apply to conditions that are close to average; therefore, those base values require smaller adjustments than do the base values of Chow (1959). Likewise, the adjustments made (using table 2) to base values of Benson and Dalrymple (1967) should be reduced slightly.

The effects of depth of flow on the selection of n values for channels must be considered. If the depth of flow is shallow in relation to the size of the roughness elements, the n value can be large. The n value generally decreases with increasing depth, except where the channel banks are much rougher than the bed or where dense brush overhangs the low-water channel.

Irregularity (n_1)

Where the ratio of width to depth is small, roughness caused by eroded and scalloped banks, projecting points, and exposed tree roots along the banks must be accounted for by fairly large adjustments. Chow (1959) and Benson and Dalrymple (1967) showed that severely eroded and scalloped banks can increase n values by as much as 0.02. Larger adjustments may be required for very large, irregular banks having projecting points.

Variation in Channel Cross Section (n_2)

The value of n is not affected significantly by relatively large changes in the shape and size of cross sections if the changes are gradual and uniform. Greater roughness is associated with alternating large and small sections where the changes are abrupt. The degree of the effect of changes in the size of the channel depends primarily on the number of alternations of large and small sections and secondarily on the

Table 2.--Factors that effect roughness of the channel
[Modified from Aldridge and Garrett, 1973, table 2]

Channel conditions		n value adjustment[1/]	Example
Degree of irregularity (n_1)	Smooth	0.000	Compares to the smoothest channel attainable in a given bed material.
	Minor	0.001-0.005	Compares to carefully dredged channels in good condition but having slightly eroded or scoured side slopes.
	Moderate	0.006-0.010	Compares to dredged channels having moderate to considerable bed roughness and moderately sloughed or eroded side slopes.
	Severe	0.011-0.020	Badly sloughed or scalloped banks of natural streams; badly eroded or sloughed sides of canals or drainage channels; unshaped, jagged, and irregular surfaces of channels in rock.
Variation in channel cross section (n_2)	Gradual	0.000	Size and shape of channel cross sections change gradually.
	Alternating occasionally	0.001-0.005	Large and small cross sections alternate occasionally, or the main flow occasionally shifts from side to side owing to changes in cross-sectional shape.
	Alternating frequently	0.010-0.015	Large and small cross sections alternate frequently, or the main flow frequently shifts from side to side owing to changes in cross-sectional shape.

Table 2.--Factors that effect roughness of the channel--Continued

Channel conditions		n value adjustment[1/]	Example
Effect of obstruction (n_3)	Negligible	0.000-0.004	A few scattered obstructions, which include debris deposits, stumps, exposed roots, logs, piers, or isolated boulders, that occupy less than 5 percent of the cross-sectional area.
	Minor	0.005-0.015	Obstructions occupy less than 15 percent of the cross-sectional area and the spacing between obstructions is such that the sphere of influence around one obstruction does not extend to the sphere of influence around another obstruction. Smaller adjustments are used for curved smooth-surfaced objects than are used for sharp-edged angular objects.
	Appreciable	0.020-0.030	Obstructions occupy from 15 to 50 percent of the cross-sectional area or the space between obstructions is small enough to cause the effects of several obstructions to be additive, thereby blocking an equivalent part of a cross section.
	Severe	0.040-0.050	Obstructions occupy more than 50 percent of the cross-sectional area or the space between obstructions is small enough to cause turbulence across most of the cross section.
Amount of vegetation (n_4)	Small	0.002-0.010	Dense growths of flexible turf grass, such as Bermuda, or weeds growing where the average depth of flow is at least two times the height of the vegetation; supple tree seedlings such as willow, cottonwood, arrowweed, or saltcedar growing where the average depth of flow is at least three times the height of the vegetation.

	Medium	0.010-0.025	Turf grass growing where the average depth of flow is from one to two times the height of the vegetation; moderately dense stemmy grass, weeds, or tree seedlings growing where the average depth of flow is from two to three times the height of the vegetation; brushy, moderately dense vegetation, similar to 1- to 2-year-old willow trees in the dormant season, growing along the banks and no significant vegetation along the channel bottoms where the hydraulic radius exceeds 2 feet.
Amount of vegetation (n_4)-- (continued)	Large	0.025-0.050	Turf grass growing where the average depth of flow is about equal to the height of vegetation; 8- to 10-year-old willow or cottonwood trees intergrown with some weeds and brush (none of the vegetation in foliage) where the hydraulic radius exceeds 2 feet; bushy willows about 1 year old intergrown with some weeds along side slopes (all vegetation in full foliage) and no significant vegetation along channel bottoms where the hydraulic radius is greater than 2 feet.
	Very large	0.050-0.100	Turf grass growing where the average depth of flow is less than half the height of the vegetation; bushy willow trees about 1 year old intergrown with weeds along side slopes (all vegetation in full foliage) or dense cattails growing along channel bottom; trees intergrown with weeds and brush (all vegetation in full foliage).
Degree of meandering[1/] (Adjustment values apply to flow confined in the channel and do not apply where downvalley flow crosses meanders.) (m)	Minor	1.00	Ratio of the channel length to valley length is 1.0 to 1.2.
	Appreciable	1.15	Ratio of the channel length to valley length is 1.2 to 1.5.
	Severe	1.30	Ratio of the channel length to valley length is greater than 1.5.

[1/]Adjustments for degree of irregularity, variations in cross section, effect of obstructions, and vegetation are added to the base n value (table 1) before multiplying by the adjustment for meander.

magnitude of the changes. The effects of sharp bends, constrictions, and side-to-side shifting of the low-water channel may extend downstream for several hundred feet. The n value for a reach below these disturbances may require adjustment, even though none of the roughness-producing factors are apparent in the study reach. A maximum increase in n of 0.003 will result from the usual amount of channel curvature found in designed channels and the reaches of natural channels used to compute discharge (Benson and Dalrymple, 1967).

Obstructions (n_3)

Obstructions--such as logs, stumps, boulders, debris, pilings, and bridge piers--disturb the flow pattern in the channel and increase roughness. The amount of increase depends on the shape of the obstruction; its size in relation to that of the cross section; and the number, arrangement, and spacing of obstructions. The effect of obstructions on the roughness coefficient is a function of the flow velocity. When the flow velocity is high, an obstruction exerts a sphere of influence that is much larger than the obstruction because the obstruction affects the flow pattern for considerable distances on each side. The sphere of influence for velocities that generally occur in channels that have gentle to moderately steep slopes is about 3 to 5 times the width of the obstruction. Several obstructions can create overlapping spheres of influence and may cause considerable disturbance, even though the obstructions may occupy only a small part of a channel cross section. Chow (1959) assigned adjustment values to four degrees of obstruction (table 2).

Vegetation (n_4)

The extent to which vegetation affects n depends on the depths of flow, the percentage of the wetted perimeter covered by the vegetation, the density of vegetation below the high-water line, the degree to which the vegetation is flattened by high water, and the alinement of vegetation relative to the flow. Rows of vegetation that parallel the flow may have less effect than rows of vegetation that are perpendicular to the flow. The adjustment values given in table 2 apply to constructed channels that are narrow in width. In wide channels having small depth-to-width ratios and no vegetation on the bed, the effect of bank vegetation is small, and the maximum adjustment is about 0.005. If the channel is relatively narrow and has steep banks covered by dense vegetation that hangs over the channel, the maximum adjustment is about 0.03. The larger adjustment values given in table 2 apply only in places where vegetation covers most of the channel.

Meandering (m)

In selecting the value of m, the degree of meandering depends on the ratio of the total length of the meandering channel in the reach being considered to the straight length of the channel reach. The meandering is considered minor for ratios of 1.0 to 1.2, appreciable for ratios of 1.2 to 1.5, and severe for ratios of 1.5 and greater. According to Chow (1959), meanders can increase the n values as much as 30 percent where flow is confined within a stream channel. The meander adjustment should only be considered when the flow is confined to the channel. There may be very little flow in a meandering channel when there is flood-plain flow.

METHODS FOR ASSIGNING n VALUES FOR FLOOD PLAINS

As stated earlier, it is usually necessary to determine roughness values for channels and flood plains separately. The makeup of a flood plain can be quite different from that of a channel. The physical shape of a flood plain is different from that of a channel and the vegetation covering a flood plain is typically different from that found in a channel. The procedure given in the following paragraphs is designed for determining an n value for flood plains.

Modified Channel Method

By altering Cowan's (1956) procedure that was developed for estimating n values for channels, the following equation can be used to estimate n values for a flood plain.

$$n = (n_b + n_1 + n_2 + n_3 + n_4)m \qquad (6)$$

where

n_b = a base value of n for the flood plain's natural bare soil surface, with nothing on the surface,
n_1 = a value to correct for the effect of surface irregularities on the flood plain,
n_2 = A value for variations in shape and size of the flood-plain cross section, assumed to equal 0.0,
n_3 = a value for obstructions on the flood plain,
n_4 = a value for vegetation on the flood plain,
m = a correction factor for sinuosity of the flood plain, equal to 1.0.

Using equation 6, the roughness value for the flood plain is determined by selecting a base value of n_b for the natural bare soil surface of the flood plain and adding adjustment factors due to surface irregularity, obstructions, and vegetation. The selection of an n_b value is the same as outlined for channels in the previous section. A description of the major factors follows, and table 3 gives n value adjustments. The adjustment for cross-section shape and size is assumed to be 0.0. The cross

Table 3.--Factors that affect roughness of flood plains

[Modified from Aldridge and Garrett, 1973, table 2]

Flood plain conditions		n value adjustment	Example
Degree of irregularity (n_1)	Smooth	0.000	Compares to the smoothest, flattest flood plain attainable in a given bed material.
	Minor	0.001-0.005	Is a flood plain with minor irregularity in shape. A few rises and dips or sloughs may be visible on the flood plain.
	Moderate	0.006-0.010	Has more rises and dips. Sloughs and hummocks may occur.
	Severe	0.011-0.020	The flood plain is very irregular in shape. Many rises and dips or sloughs are visible. Irregular ground surfaces in pastureland and furrows perpendicular to the flow are also included.
Variation of flood-plain cross section (n_2)		0.0	Not applicable.
Effect of obstructions (n_3)	Negligible	0.000-0.004	A few scattered obstructions, which include debris deposits, stumps, exposed roots, logs, or isolated boulders, occupy less than 5 percent of the cross-sectional area.
	Minor	0.005-0.019	Obstructions occupy less than 15 percent of the cross-sectional area.
	Appreciable	0.020-0.030	Obstructions occupy from 15 to 50 percent of the cross-sectional area.

Amount of vegetation (n_4)	Small	0.001-0.010	Dense growth of flexible turf grass, such as Bermuda, or weeds growing where the average depth of flow is at least two times the height of the vegetation; or supple tree seedlings such as willow, cottonwood, arrowweed, or saltcedar growing where the average depth of flow is at least three times the height of the vegetation.
	Medium	0.011-0.025	Turf grass growing where the average depth of flow is from one to two times the height of the vegetation; or moderately dense stemmy grass, weeds, or tree seedlings growing where the average depth of flow is from two to three times the height of the vegetation; brushy, moderately dense vegetation, similar to 1- to 2-year-old willow trees in the dormant season.
	Large	0.025-0.050	Turf grass growing where the average depth of flow is about equal to the height of vegetation; or 8- to 10-year-old willow or cottonwood trees intergrown with some weeds and brush (none of the vegetation in foliage) where the hydraulic radius exceeds 2 ft; or mature row crops such as small vegetables; or mature field crops where depth of flow is at least twice the height of the vegetation.
	Very large	0.050-0.100	Turf grass growing where the average depth of flow is less than half the height of the vegetation; or moderate to dense brush; or heavy stand of timber with few down trees and little undergrowth with depth of flow below branches; or mature field crops where depth of flow is less than height of the vegetation.
	Extreme	0.100-0.200	Dense bushy willow, mesquite, and saltcedar (all vegetation in full foliage); or heavy stand of timber, few down trees, depth of flow reaching branches.
Degree of meander (m)		1.0	Not applicable.

section of a flood plain is generally subdivided where there are abrupt changes in the shape of the flood plain. The adjustment for meandering is assumed to be 1.0, because there may be very little flow in a meandering channel when there is flood-plain flow. In certain cases where the roughness of the flood plain is caused by trees and brush, the roughness value for the flood plain can be determined by measuring the "vegetation density" of the flood plain rather than directly estimating from table 3. This is discussed under "Vegetation Density Methods".

Adjustment Factors for Flood Plains

Surface Irregularities (n_1).--Irregularity of the surface of a flood plain causes an increase in the roughness of the flood plain. Such physical factors as rises and depressions of the land surface and sloughs and hummocks increase the roughness of the flood plain. A hummock can be defined as a low mound or ridge of earth above the level of an adjacent depression. A slough is a stagnant swamp, marsh, bog, or pond.

Shallow water depths, accompanied by an irregular ground surface in pastureland or brushland and by deep furrows perpendicular to the flow in cultivated fields, can increase the n values by as much as 0.02.

Obstructions (n_3).--The roughness contribution of some obstructions on a flood plain, such as debris deposits, stumps, exposed roots, logs, or isolated boulders, cannot be measured directly but must be considered. Table 3 lists values of roughness for obstructions at different percentages of occurrence.

Vegetation (n_4).--Visual observation, judgment, and experience may be used in selecting adjustment factors for the effects of vegetation from table 3. An adjustment factor for tree trunks and other measureable obstacles is described in the next section. Although it is relatively easy to measure the area occupied by tree trunks and other major vegetation, it is much more difficult to measure the area occupied by vegetation such as low vines, briars, grass, and crops. Adjustments of the roughness factor due to these types of vegetation can be determined by using table 3.

In the case of open fields and cropland on flood plains, several references are available to help determine the roughness factors. Ree and Crow (1977) conducted experiments to determine roughness factors for earthen channels of small slope planted to wheat, sorghum, lespedeza, and grasses. The roughness factors were intended for application to the design of diversion terraces. However, the data can be applied to the design of any terrace, or they can be used to estimate the roughness of flood plains planted to the type of vegetation used.

Chow (1959) presents a table giving minimum, normal, and maximum values of n for flood plains made up of pasture and cultivated crops. These values are helpful as a comparison for roughness values of flood plains having similar vegetation.

Vegetation Density Methods

In cases where a flood plain is wooded, the vegetation-density method can be used as an alternative to the previous method for determining n values for flood plains. In a wooded flood plain, where the tree diameters can be measured, the vegetation density of the flood plain can be determined.

Determining the vegetation density is an effective way of relating plant height and density characteristics, as a function of depth of flow, to the flow resistance of vegetation. Application of the flow-resistance model presented below requires an estimate of the vegetation density as a function of depth of flow. The procedure requires a direct or indirect determination of vegetation density at a given depth. If the change in n value through a range in depth is required, then an estimation of vegetation density through that range is necessary.

Techniques of Determining Vegetation Density

A method of analysis of the "vegetation density" to determine the roughness coefficient for a densely vegetated flood plain was developed by Petryk and Bosmajian (1975). By summing the forces in the longitudinal direction of a reach and substituting in the Manning's formula, the following equation was developed.

$$n = n_o \sqrt{1 + \left(\frac{C_* \Sigma A_i}{2gAL}\right)\left(\frac{1.49}{n_o}\right)^2 R^{4/3}} \qquad (7)$$

where: n_o = Manning's boundary roughness coefficient, excluding the effect of the vegetation (a base n);

C_* = the effective drag coefficient for the vegetation in the direction of flow;

g = the gravitational constant, in feet per second squared;

A = the cross-sectional area of flow, in square feet;

R = the hydraulic radius, in feet;

ΣA_i = the total frontal area of vegetation blocking the flow in the reach, in square feet;

and L = the length of channel reach being considered, in feet.

Equation 7 gives the n value in terms of the boundary roughness, n_o; the hydraulic radius, R; the effective drag coefficient, C_*; and the vegetation characteristics, $\Sigma A_i/AL$. The vegetation density, Veg_d, in the cross section is represented by the expression

$$Veg_d = \frac{\Sigma A_i}{AL} \tag{8}$$

The boundary roughness, n_o, can be determined from the following equation.

$$n_o = n_b + n_1 + n_2 + n_3 + n_4' \tag{9}$$

Equation 9 contains all of the roughness factors of equation 6, which describes the boundary roughness. The definition of the roughness factors n_b and n_1 through n_3 are the same as those in equation 6. The n_4' factor is for vegetation, such as brush and grass, on the surface of the flood plain that could not be measured directly in the Veg_d term. The value for the above roughness factors can be determined using table 3. The n_4' factor would be defined in the small to medium range in table 3 because the tree canopy would prohibit a dense undergrowth in a densely wooded area.

The hydraulic radius, R, is equal to the cross-sectional area of flow divided by the wetted perimeter; therefore, in a wide flood plain the hydraulic radius would be equal to the depth of flow. An effective-drag coefficient for densely wooded flood plains can be selected from figure 3, a plot of effective-drag coefficient versus hydraulic radius for densely wooded flood plains.

Indirect Technique.--A vegetation resistivity value, Veg_R, can be determined through indirect methods (Petryk and Bosmajian, 1975). When flood data that include a measured discharge and depth of flow are available, hydraulic analysis can be made and the roughness coefficients can be determined for a flood plain. By rearranging equation 7 and using the hydraulic radius and n value computed from the discharge measurement and an assumed n_o, the vegetation resistivity for the reported flood can be determined from the following equation:

$$Veg_R = \frac{C_*\Sigma A_i}{AL} = \frac{(n^2-n_o^2)2g}{(1.49)^2 R^{4/3}} \tag{10}$$

The value of Veg_R determined at this known depth of flow can be used to estimate Veg_R for other depths by estimating the change in the density of growth. This can be done from pictorial or physical descriptions of the vegetation. By evaluating the change in Veg_R, an evaluation of the n value as a function of flow depth can be determined.

Direct Technique.--Tree trunks are major contributors to the roughness coefficient in a densely wooded flood plain. Where trees are the major factor, the vegetation density can be easily determined by measuring the number of trees and trunk size in a representative-sample area. The n value as a function of height can be computed using equation 7.

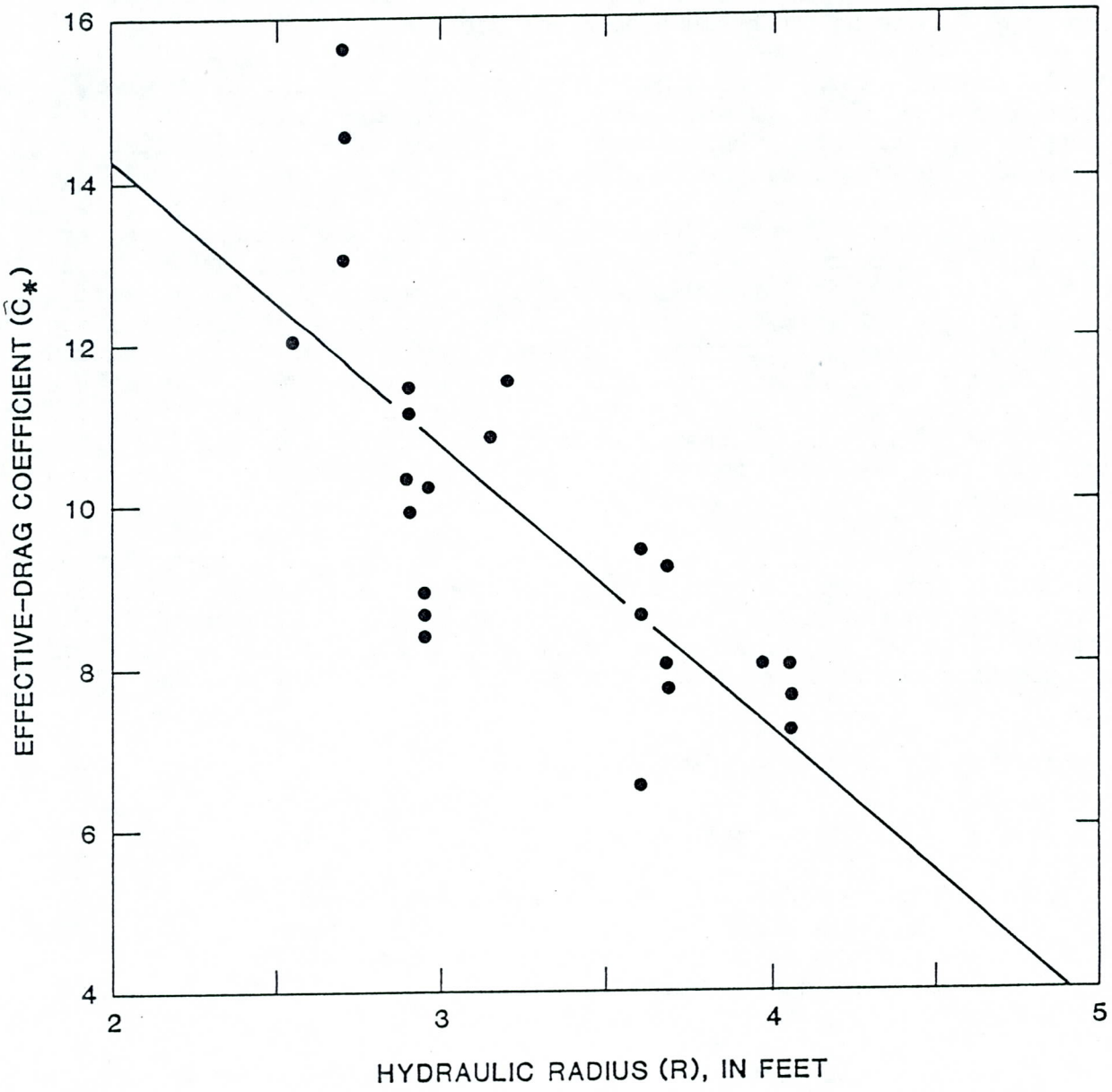

Figure 3.--Plot of effective-drag coefficient versus hydraulic radius for wide, wooded flood plains using verified n values.

Sampling area.--A representative-sample area must be chosen on the cross section to represent the roughness of the cross section accurately. The flood plain can be divided into subsections due to geometric and (or) roughness differences in the cross-section reach. The vegetation density is determined for each subsection.

It is important that the sampling area be representative of the roughness coefficient of the cross section. By examining the cross section closely in the field, a representative-sampling area can be chosen. Another way to better determine the roughness coefficient is to select several representative areas and compare the results. It should be pointed out again that cross sections should be divided into subsections when changes in roughness properties dictate.

All of the trees, including vines, in the sampling area must be counted and the diameter measured to the nearest 0.1 ft. Each tree diameter is measured at a height that will give an average diameter for the expected flow depth of the sample area.

Determining the area of the trees in the sampling area is not very difficult. A sampling area 100 ft along the cross section by 50 ft in the flow direction is generally adequate to determine the vegetation density of an area when the sample area is representative of the flood plain. A 100-ft tape is stretched out perpendicular to the flow direction in the sample area. Every tree within 25 ft along either side of the 100-ft tape is counted. The position of the tree is plotted on a grid system by measuring the distance to each tree from the centerline along the 100-ft tape and the diameter of the tree is recorded on the grid system. (See fig. 4.)

The area, ΣA_i, occupied by trees in the sampling area can be computed from the number of trees, their diameter, and the depth of flow in the flood plain. Once the vegetation area, ΣA_i, is determined, the vegetation density can be computed using equation 8 and the n value for the subsection can be determined using equation 7 with appropriate values for n_o, R, and C*.

Equation 8 can be simplified to

$$Veg_d = \frac{\Sigma A_i}{AL} = \frac{h \, \Sigma n_i d_i}{hwl} \qquad (11)$$

where $\Sigma n_i d_i$ = the summation of number of trees multiplied by tree diameter, in feet;
h = height of water on flood plain, in feet;
w = the sample area width, in feet;
and l = the sample area length, in feet.

Example of use of direct technique.--An example of how to compute n for a flood plain using the direct method for vegetation density is shown in figures 4 and 5. A representative sample area along the cross section is chosen. The Veg_d of the sample area is determined by measuring the number and diameter of trees in the 100 ft by 50 ft area. This is easily done by plotting the location and diameter of the trees, in the sample area on the grid shown in figure 4. The numbers by the dots in figure 4 are the diameters of the trees, in tenths of a foot, except for those numbers underlined. The numbers underlined are the diameters of the trees in feet.

SITE: Poley Creek, cross section 2

DATE: March 14, 1979

DESCRIPTION: Flood plain consists of hardwood trees up to 40 feet tall, including many smaller-diameter trees, and some vines and ground cover. The surface is fairly smooth with a firm soil base.

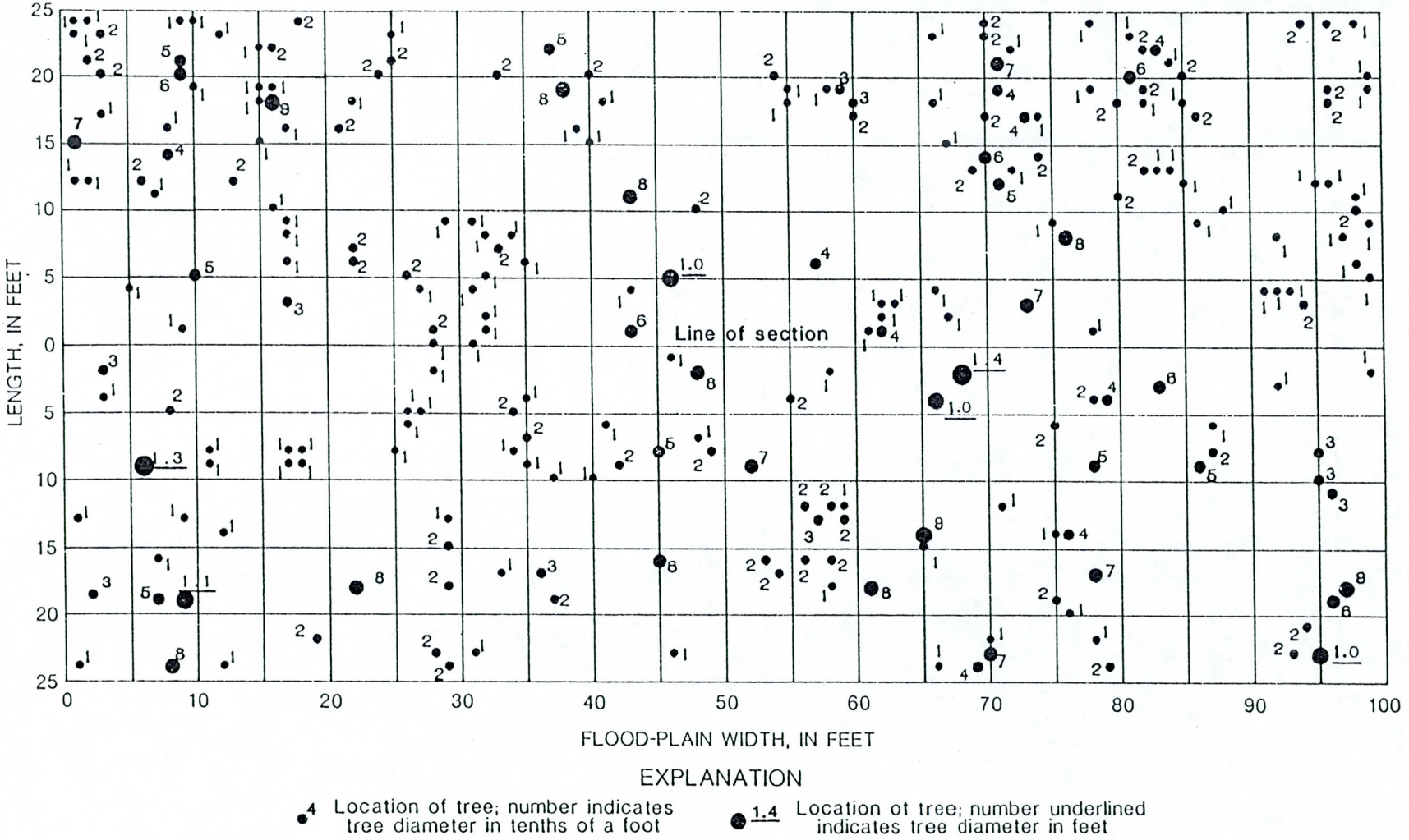

Figure 4.--Example measurement of vegetation density of representative sample area.

SITE: Poley Creek, Cross-Section 2, March 14, 1979

Tree diameter in feet (d_i)	Total number of trees (n_i)	(n_i) (d_i)
0.1	128	12.8
0.2	65	13.0
0.3	10	3.0
0.4	9	3.6
0.5	8	4.0
0.6	7	4.2
0.7	5	3.5
0.8	6	4.8
0.9	2	1.8
1.0	3	3.0
1.1	1	1.1
1.3	1	1.3
1.4	1	1.4
		$\Sigma n_i d_i = 57.5$

$$(Veg_d) = \frac{\Sigma A_i}{AL} = \frac{h\Sigma n_i d_i}{hwl} = \frac{(2.9)\,(57.5)}{(2.9)\,(50)\,(100)} = 0.0115$$

where: $\Sigma n_i d_i$ = summation of number of trees multiplied by diameter, in feet;
h = depth of water on flood plain, in feet;
w = width of sample area, in feet;
and l = length of sample area, in feet.

$R = 2.9$ feet, $C_* = 11.0$, $n_o = 0.025$

$$n = n_o \sqrt{1 + (Veg_d)\,(C_*)\left(\frac{1.49}{n_o}\right)^2\left(\frac{1}{2g}\right)R^{4/3}}$$

$$n = 0.025 \sqrt{1 + (0.0115)\,(11.0)\left(\frac{1.49}{0.025}\right)^2\left(\frac{1}{64.4}\right)(2.9)^{4/3}}$$

$n = 0.136$

Figure 5.--Example of determination of Manning's n by direct technique of vegetation density.

Figure 5 summarizes the number of trees and their diameter; by using this information and equation 11, Veg_d can be determined.

A value for flow depth must be determined for the flood plain, and depth of flow is assumed to equal the hydraulic radius, R, for the flood plain. An effective-drag coefficient is selected from figure 3. The boundary roughness, n_o, is determined for the flood plain using equation 9 and the n for the flood plain is computed using equation 7.

PHOTOGRAPHS OF FLOOD PLAINS

The following series of photographs (figs. 6-20) represent densely vegetated flood plains for which roughness coefficients have been verified. The coefficients for these sites were determined as a part of a study on computation of backwater and discharge at width constrictions of heavily vegetated flood plains by Schneider and others (1976). By using these photographs for comparison with other field situations, n values can be selected in the field. The photographs can then be used to verify n values computed by other methods.

Information included with the photographs are site name and location; n value determined for the area; base roughness, n_o; depth of flow on flood plain; date of flood; and date picture was taken.

Several reports present photographs of channels for which roughness coefficients are known and which would be helpful in determining roughness values of other areas. Barnes (1967) presented photographs of natural, stable channels having known n values ranging from 0.023 to 0.075; a few flood plains were included in the report.

Ree and Crow (1977) conducted experiments to determine friction factors for earthen channels planted with certain crops and grasses. The values that were determined may be used to help estimate the roughness of flood plains planted to the type of vegetation used in their experiments. Photographs and brief descriptions of the vegetation are given, and a tabulation of the hydraulic elements are included.

Aldridge and Garrett (1973) presented photographs of channels and flood plains in Arizona having known roughness coefficients. Included with the photographs are channel geometry and a description of the roughness factors involved in assigning an n value for the site.

Chow (1959) presented photographs of a number of typical channels, accompanied by brief descriptions of the channel conditions and the corresponding n value.

Figure 6.--Cypress Creek near Downsville, La.

Computed roughness coefficient: Manning's n = 0.10

Date of flood - February 21, 1974

Date of picture: February 13, 1979

Depth of flow in flood plain: 2.6 ft

Description of flood plain: The vegetation of flood plain consists mostly of trees including oak, gum, and pine. The base is firm soil that has slight surface irregularities. Obstructions are negligible (a few downed trees and limbs). Ground cover and vines are negligible. Veg_d = 0.0067 and C_* = 12.0. The selected values are n_b = 0.025, n_1 = 0.005, n_3 = 0.005 and n_o = 0.035.

Figure 7.--Bayou de Loutre near Farmerville, La.

Computed roughness coefficient: Manning's n = 0.11

Date of flood: March 18, 1973

Date of picture: February 14, 1979

Depth of flow in flood plain: 3.6 ft

Description of flood plain: The vegetation of the flood plain consists mostly of large, tall trees, including oak, gum, ironwood, and pine. The base is firm soil and is smooth. Obstructions are few and ground cover and undergrowth are sparse. Veg_d = 0.0067 and C_* = 8.8. The selected values are n_b = 0.020, n_1 = 0.002, n_3 = 0.003, and n_o = 0.025.

Figure 8.--Bayou de Loutre near Farmerville, La.

Computed roughness coefficient: Manning's n = 0.11

Date of flood: March 18, 1973

Date of picture: February 14, 1979

Depth of flow in flood plain: 3.7 ft

Description of flood plain: The vegetation of the flood plain consists mostly of large, tall trees including, oak, gum, and ironwood. The base is firm soil that has slight surface irregularities and obstructions caused by downed trees and limbs. Ground cover and undergrowth are negligible. Veg_d = 0.0075 and C_* = 7.7. The selected values are n_b = 0.020, n_1 = 0.002, n_3 = 0.003, and n_o = 0.025.

Figure 9.--Bayou de Loutre near Farmerville, La.

Computed roughness coefficient: Manning's n = 0.11

Date of flood: March 18, 1973

Date of picture: February 14, 1979

Depth of flow in flood plain: 3.7 ft

Description of flood plain: The vegetation of the flood plain consists mostly of trees including oak, gum, ironwood and pine. The base is firm soil that has slight surface irregularities and obstructions caused by downed trees and limbs. Ground cover and undergrowth are negligible. Veg_d = 0.0072 and C_* = 8.0. The selected values are n_b = 0.020, n_1 = 0.002, n_3 = 0.003, and n_o = 0.025.

Figure 10.--Coldwater River near Red Banks, Miss.

Computed roughness coefficient: Manning's n = 0.11

Date of flood: February 22, 1971

Date of picture: April 5, 1979

Depth of flow in flood plain: 3.0 ft

Description of flood plain: The vegetation of the flood plain consists mostly of trees including oak, gum, and ironwood. The base is silty soil that has slight surface irregularities. Few obstructions with some flood debris. Ground cover is short weeds and grass with little undergrowth. Veg_d = 0.0077 and C* = 10.2. The selected value are n_b = 0.020, n_1 = 0.002, n_4' = 0.005, and n_o = 0.027.

Figure 11.--Coldwater River near Red Banks, Miss.

Computed roughness coefficient: Manning's n = 0.11

Date of flood: February 22, 1971

Date of picture: April 5, 1979

Depth of flow on flood plain: 3.0 ft

Description of flood plain: The vegetation of the flood plain consists mostly of trees including oak, gum, and ironwood. The base is silty soil that has slight surface irregularities. Few obstructions with some flood debris. Ground cover is short weeds and grass with little undergrowth. Veg_d = 0.0090 and C_* = 8.6. The selected values are n_b = 0.020, n_1 = 0.003, n_4' = 0.005, and n_o = 0.028.

Figure 12.--Yockanookany River near Thomastown, Miss.

Computed roughness coefficient: Manning's n = 0.12

Date of flood: April 12, 1969

Date of picture: March 28, 1979

Depth of flow on flood plain: 4.0 ft

Description of flood plain: The vegetation of the flood plain consists mostly of trees including oak, gum, and ironwood, and there are many smaller diameter trees. The base is firm soil and the surface has little irregularity. Obstructions are negligible. Ground cover and undergrowth are negligible. Veg_d = 0.0082 and C_* = 7.6. The selected values are n_b = 0.025 and n_o = 0.025.

Figure 13.--Yockanookany River near Thomastown, Miss.

Computed roughness coefficient: Manning's n = 0.12

Date of flood: April 12, 1969

Date of picture: March 28, 1979

Depth of flow on flood plain: 4.0 ft

Description of flood plain: The vegetation of the flood plain consists mostly of trees including oak, gum, and ironwood, and there are many smaller diameter trees. The base is firm soil and the surface has little irregularity. Obstructions are negligible (a few downed trees and limbs). Ground cover and undergrowth are negligible. Veg_d = 0.0082 and C_* = 7.6. The selected values are n_b = 0.025 and n_o = 0.025.

Figure 14.--Flagon Bayou near Libuse, La.

Computed roughness coefficient: Manning's n = 0.13

Date of flood: December 7, 1971

Date of picture: April 10, 1979

Depth of flow on flood plain: 3.2 ft

Description of flood plain: The vegetation of the flood plain consists mostly of a mixture of large and small trees including oak, gum, and ironwood. The base is firm soil that has minor surface irregularities with some rises. Obstructions are negligible (some exposed roots and small trees). Ground cover and undergrowth are negligible. Veg_d = 0.0087 and C_* = 11.5. The selected values are n_b = 0.025, n_1 = 0.003, n_3 = 0.002 and n_o = 0.030.

Figure 15.--Pea Creek near Louisville, Ala.

Computed roughness coefficient: Manning's n = 0.14

Date of flood: December 21, 1972

Date of picture: March 13, 1979

Depth of flow in flood plain: 2.9 ft

Description of flood plain: The vegetation of the flood plain consists mostly of a mixture of large and small trees including oak, gum, and ironwood. The base is firm soil. Minor surface irregularity (some rises and depressions). Obstructions are minor (downed trees and limbs and a buildup of debris). Little ground cover with a small amount of undergrowth made up of small trees and vines. Veg_b = 0.0085 and C_* = 15.6. The selected values are n_b = 0.025, n_1 = 0.005, n_3 = 0.015, n_4' = 0.005, and n_o = 0.050.

Figure 16.--Pea Creek near Louisville, Ala.

Computed roughness coefficient: Manning's n = 0.14

Date of flood: December 21, 1972

Date of picture: March 13, 1979

Depth of flow on flood plain: 2.8 ft

Description of flood plain: The vegetation of the flood plain consists mostly of a mixture of large and small trees including oak, gum, and ironwood. The base is firm soil. Minor surface irregularity (some rises and depressions). Obstructions are minor (downed trees and limbs and a buildup of debris). Ground cover is negligible with a small amount of undergrowth made up of small trees and vines. Veg_d = 0.0102 and C_* = 15.6. The selected values are n_b = 0.025, n_1 = 0.005, n_3 = 0.015, n_4' = 0.005, and n_o = 0.050.

Figure 17.--Tenmile Creek near Elizabeth, La.

Computed roughness coefficient: Manning's n = 0.15

Date of flood: December 7, 1971

Date of picture: April 12, 1979

Depth of flow on flood plain: 4.1 ft

Description of flood plain: The vegetation of the flood plain is covered with a mixture of large and small trees including oak, gum, and ironwood. The base is firm soil that has minor surface irregularities caused by rises and depressions. Obstructions are negligible (some exposed roots). Ground cover is negligible except for a small amount of undergrowth. Veg_d = 0.0067 and C_* = 14.4. The selected values are n_b = 0.025, n_1 = 0.003, n_3 = 0.002, and n_o = 0.030.

Figure 18.--Sixmile Creek near Sugartown, La.

Computed roughness coefficient: Manning's n = 0.18

Date of flood: March 23, 1973

Date of picture: April 11, 1979

Depth of flow on flood plain: 5.0 ft

Description of flood plain: The vegetation of the flood plain is covered with mostly large trees including oak, gum, ironwood and pine. The base is firm soil that has moderate surface irregularities caused by rises and depressions. Obstructions are negligible (a few vines). Ground cover and undergrowth are negligible. Veg_d = 0.0084 and C_* = 13.3. The selected values are n_b = 0.025, n_1 = 0.008, n_3 = 0.002, and n_o = 0.035.

Figure 19.--Thompson Creek near Clara, Miss.

Computed roughness coefficient: Manning's n = 0.20

Date of flood: March 3, 1971

Date of picture: March 29, 1979

Depth of flow on flood plain: 2.9 ft

Description of flood plain: The flood plain is covered by a mixture of large and small trees including oak, gum, and ironwood. The base is firm soil that has minor surface irregularities. Obstructions are minor with some ground cover and a large amount of undergrowth such as vines and palmettos. Veg_d = 0.0115 and C_* = 22.7. The selected values are n_b = 0.025, n_1 = 0.005, n_3 = 0.010, n_4' = 0.015, and n_o = 0.055.

Figure 20.--Thompson Creek near Clara, Miss.

Computed roughness coefficient: Manning's n = 0.20

Date of flood: March 3, 1971

Date of picture: March 29, 1979

Depth of flow on flood plain: 2.9 ft

Description of flood plain: The flood plain is covered with a mixture of large and small trees including oak, gum, and ironwood. The base is firm soil that has minor surface irregularities. Obstructions are minor (some downed trees and limbs). Vegetation is medium with some ground cover and a large amount of undergrowth such as vines and palmettos. Veg_d = 0.0115 and C_* = 22.7. The selected values are n_1 = 0.025, n_2 = 0.005, n_3 = 0.010, n_4' = 0.015 and n_o = 0.055.

PROCEDURES FOR ASSIGNING n VALUES

The procedure given in the following paragraphs is designed to determine n values for a cross section. Parts of the procedure apply only to roughness of channels, and other parts deal with roughness of flood plains.

The procedure involves a series of decisions that are based on the interaction of roughness-causing factors. A flow chart (fig. 21) illustrates the steps in the procedure. A description of each step follows. A form is also provided to help in the computation of the n values. After using the procedure a few times, the user may wish to combine steps or to change the order of the steps. Experienced personnel may perform the entire operation mentally, but the inexperienced user may find the form in figure 22 useful. Steps 3 through 13 apply to channel roughness, and steps 14 through 23 apply to flood-plain roughness. The procedure is adapted from the report by Aldridge and Garrett (1973), but it is extended to include assigning n values for flood plains.

Description of Steps for Assigning n Values

1. Determine the extent of stream reach to which the roughness factor will apply. Although n may be applied to an individual cross section that is typical of a reach, it must take into account the roughness in the reach that encompasses the section. When two or more cross sections are being considered, the reach that applies to any one section is considered to extend halfway to the next section. For example in figure 23, the n value for section 1 represents the roughness in reach A, and the n value for section 2 represents the roughness in reach B. If the roughness is not uniform throughout the reach being considered, n should be assigned for average conditions.

2. If the roughness is not uniform across the width of the cross section, determine where subdivision of the cross section should occur. Determine whether subdivision between channel and flood plain is necessary and whether subdivision of the channel or flood plain is also necessary. If the roughness is not uniform across the width of the channel, determine whether a base n should be assigned to the entire channel cross section or whether a composite n should be derived by weighting values for individual segments of the channel having different amounts of roughness. (See steps 4-10.) When the base value is assigned to the entire channel, the channel constitutes the one segment being considered; and steps 5, 8, 9, and 10 do not apply.

Channel Roughness (Steps 3-13)

3. Determine the channel type--stable channel, sand channel, or a combination--and whether the conditions are representative of those that may exist during the design event being considered. Look especially for evidence of bed movement and excessive amounts of bank scour. If the conditions do not appear to be the same as those that would exist during the flow event, attempt to visualize the conditions that would occur.

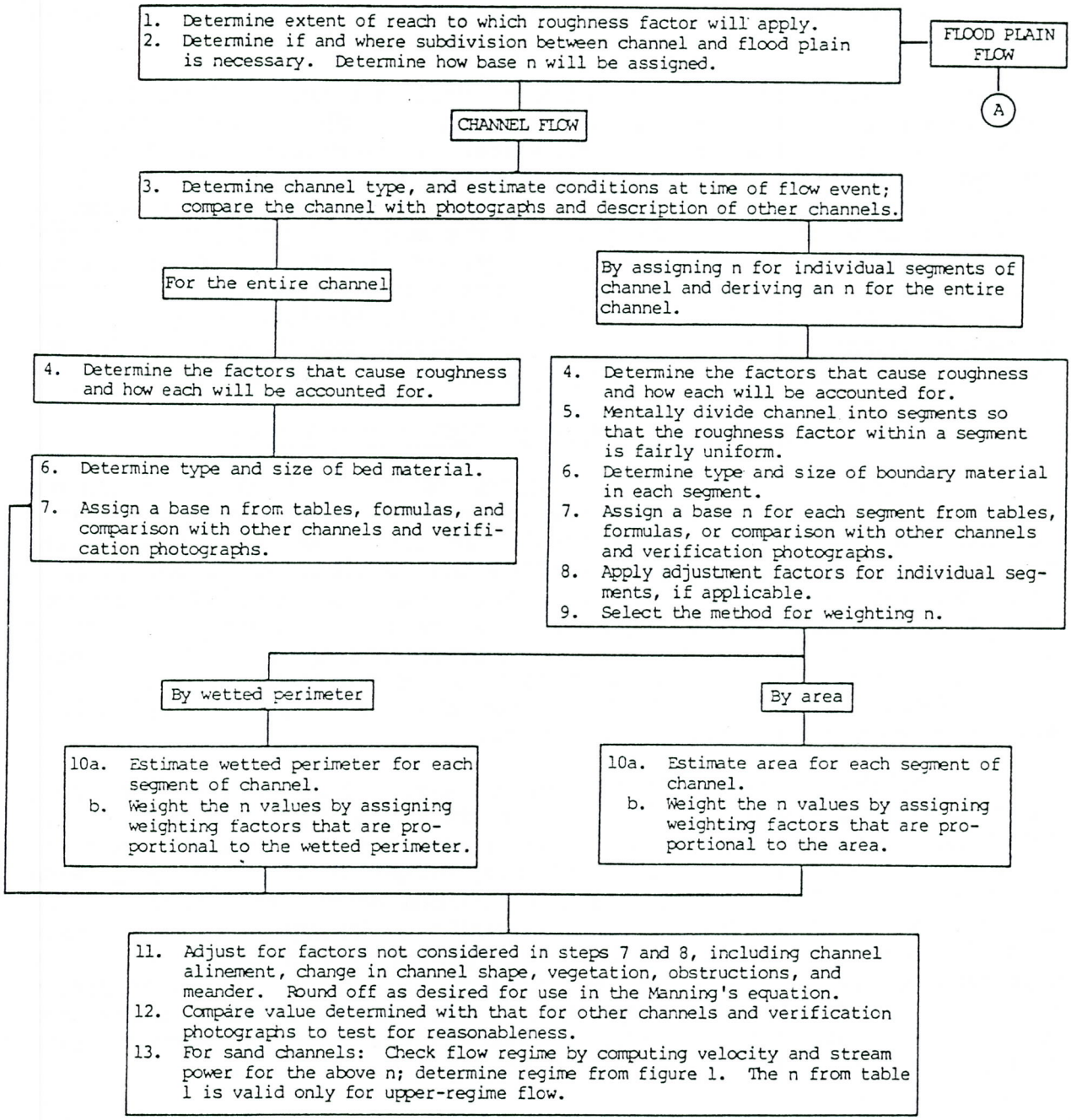

Figure 21.--Flow chart of procedures for assigning n values. (Modified from Aldridge and Garrett, 1973, fig. 3)

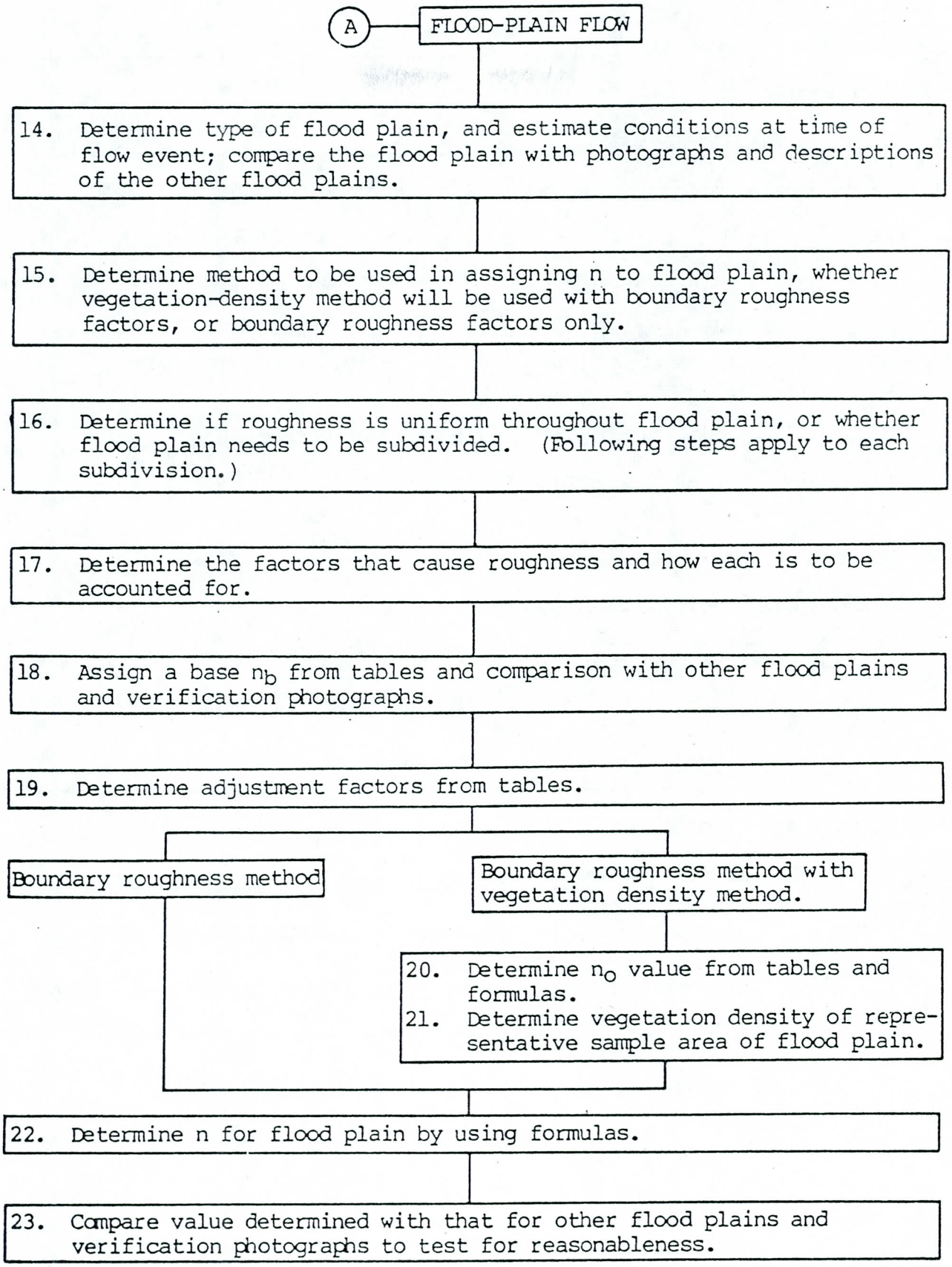

Figure 21.--Flow chart of procedures for assigning n values--Continued.

Stream and location: _____

Reach or section: _____

Event for which n is assigned: _____

1. Is roughness uniform throughout the reach being considered?

   If not, n should be assigned for the average condition of the reach.

2. Is roughness uniformly distributed along the cross section?

   Is a division between channel and flood plain necessary? (Channel roughness uses steps 3-13, flood-plain roughness uses steps 14-23).

   Is roughness uniformly distributed across the channel?

   If not, on what basis should n for the individual segments be weighted?

3. Describe the channel.

   Are present conditions representative of those during the flood?

   If not, describe the probable conditions during the flood.

4. How will the roughness producing effects of the following on the channel be accounted for?

   Bank roughness: _____

   Bedrock outcrops: _____

   Isolated boulders: _____

   Vegetation: _____

   Obstructions: _____

   Meander: _____

Figure 22.--Sample form for computing n values.

(Modified from Aldridge and Garrett, 1973, fig. 4)

5-10. Computation of weighted n for the channel.

Segment number and material	Approximate dimensions, in feet		Wetted perimeter, in feet	Area, in square feet	Median grain size, mm	Base n for segment	Adjust-ments	Adjusted n	Weight factor	Adjusted n x weight factor
	Width	Depth								
								Sum		
								Weighted n =		

Factor	Describe conditions briefly	Adjustment
Irregularity, n_1		
Alinement, n_2		
Obstructions, n_3		
Vegetation, n_4		
Meander, m		
	Weighted n plus adjustments	
	Use n =	

14. Describe the flood plain.

    Are present conditions representative of those during the flood?

    If not describe probable conditions during the flood.

15. Is the roughness coefficient to be determined by roughness factors only or to include vegetation-density method?

16. Is roughness uniformly distributed across the flood plain?

If not, how should the flood plain be subdivided?

17-23. Computation of n for flood plain.

Adjustment factors without vegetation-density method

Subsection	Base n, n_b	Irregularity, n_1	Obstructions, n_3	Vegetation, n_4	Computed n

Adjustment factors including vegetation-density method

Subsection	Base n, n_b	Irregularity, n_1	Obstructions, n_3	Vegetations, n_4	Boundary roughness, n_o	Vegetation density, Veg_d	Effective drag, C*	Hydraulic radius, R	Computed n

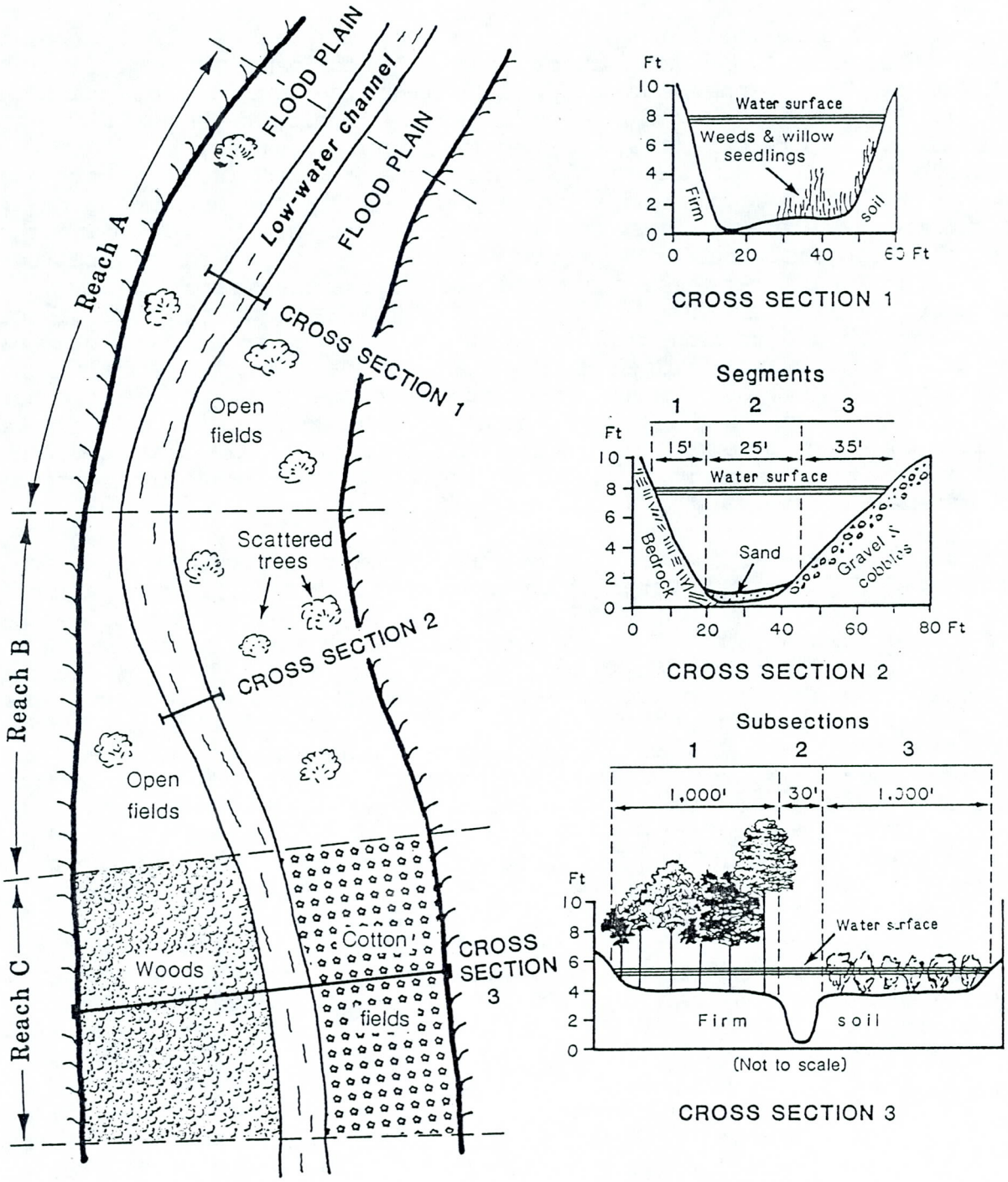

Figure 23.--Hypothetical cross section showing reaches, segments, and subsections used in assigning n values.

Compare the channel with other channels for which n values have been verified or assigned by experienced personnel in order to estimate the possible range in n values. (See photographs in the report by Barnes (1967).)

4. Determine the factors that cause roughness and how each is to be taken into account. Some factors may be predominant in a particular segment of the channel, or they may affect the entire cross section equally. The manner in which each factor is handled depends on how it combines with other factors. A gently sloping bank may constitute a separate segment of the cross section; whereas, a vertical bank may add roughness either to the adjacent segment or to the entire channel. Obstructions, such as debris, may be concentrated in one segment of the channel. Isolated boulders generally should be considered as obstructions; but if boulders are scattered over the entire reach, it may be necessary to consider them in determining the median-particle size of the bed material. Vegetation growing in a distinct segment of the channel may be assigned an n value of its own; whereas, roughness caused by vegetation growing only along steep banks or scattered on the channel bottom will be accounted for by means of an adjustment factor that can be applied to either a segment of the channel or to the entire cross section. If a composite n is being derived from segments, the user should continue with step 5; otherwise step 5 should be omitted.

5. Divide the channel width into segments according to general roughness. If distinct, parallel banks of material of different particle sizes or of different roughness are present, it is fairly easy to define the contact between the types of material. (See fig. 23, section 2.) The dividing line between any two segments should parallel the general flow lines in the stream and should be located so as to represent the average contact between types of material. The dividing line must extend through the entire reach, as defined in step 1, although one of the types of bed material may not be present throughout the reach. If a segment contains more than one type of roughness, it may be necessary to use an average size of bed material. Where sand is mixed with gravel, cobbles, and boulders throughout a channel, it is impractical to divide the main channel.

6. Determine the type of material that occupies and bounds each segment of channel and compute the median-particle size in each segment, using either method a or b (below). If the Limerinos equation (equation 5) is used, the size corresponding to the 84th percentile should be used in the computation.

(a) If the particles can be separated according to size by screening, small samples of the bed material should be collected at 8 to 12 sites in the segment of the reach. The samples are combined, and the composite sample is passed through screens that divide it into a minimum of five size ranges. Either the volume or weight of material in each range is measured and converted to a percentage of the total.

(b) If the material is too large to be screened, a grid system having 50 to 100 intersecting points or nodes per segment is laid out. The width, or intermediate diameter of each particle that falls directly under a node is measured and recorded. The sizes are grouped into a minimum of five ranges. The number of particles in each range is recorded and converted to a percentage of the total sample.

In both of the above sampling methods, the size that corresponds to the 50th percentile (using table 1) or the 84th percentile (using the Limerinos method) is obtained from a distribution curve derived by plotting particle size versus the percentage of sample smaller than the indicated size. Experienced personnel generally can make a fairly accurate estimate of the median-particle size by inspection of the channel, if the range in particle size is small.

7. Determine the base n for each segment of channel using table 1 or equation 5, or the comparison given in step 3. Chow's (1959) base values (table 1) are for the smoothest condition possible for a given material. The values (table 1) of Benson and Dalrymple (1967) are for a straight, uniform channel of the indicated material and are closer to actual field values than are those of Chow. If a composite n is being derived from segments, the user should proceed with step 8. If n is being assigned for the channel as a whole, the user should go to step 11.

8. Add the adjustment factors from table 2 that apply only to individual segments of the channel.

9. Select the basis for weighting n for the channel segments. Wetted perimeter should be used for trapezoidal and V-shaped channels having banks of one material and beds of another material; wetted perimeter also should be used where the depth across the channel is fairly uniform. Area should be used where the depth varies considerably or where dense brush occupies a large and distinct segment of the channel.

10. Estimate the wetted perimeter or area for each segment, and assign a weighting factor to each segment that is proportional to the total wetted perimeter or area. Weight n by multiplying the n for each segment by its weighting factor.

11. Select the adjustment factors from table 2 for conditions that influence n for the entire channel. Do not include adjustment factors for any items used in steps 7 and 8. Consider upstream conditions that may cause a disturbance in the reach being studied. If Chow's (1959) base values are used, the adjustment factors in table 2 may be used directly. If base values are computed from the Limerinos equation or are taken from Benson and Dalrymple (1967), the adjustment factors should be from one-half to three-fourths as large as those given in table 2. If n is assigned on the basis of a comparison with other streams, the adjustment factors will depend on the relative amounts of roughness in the two streams. Add the adjustment factors to the weighted n from step 10 to

derive the overall n for the channel reach being considered. When a multiplying factor for meander is used, it is applied after the other adjustments have been added to the base n. Round the n value as desired. The value obtained is the composite or overall n for the channel reach selected in step 1. When more than one reach is used, repeat steps 1-13 for each reach.

12. Compare the study reach with photographs of other channels found in Barnes (1967) and Chow (1959) to determine if the final values of n obtained in step 11 appear reasonable.

13. Check the flow regime for all sand channels. Use the n from step 11 in the Manning's equation to compute the velocity, which is then used to compute stream power. The flow regime is determined from figure 1. The assigned value of n is not reliable unless the stream power is sufficient to cause upper-regime flow.

Flood-Plain Roughness (Steps 14-23)

14. As in step 1, the n value selected must be representative of the average conditions of the reach being considered. Determine if the flood-plain conditions are representative of those that may exist during the design event being considered. Compare the flood plain with other flood plains for which n values have been determined, or assigned by experienced personnel, in order to estimate the possible range in n values. Compare with photographs in this design guide and in other references.

15. The n value for the flood plain may be determined using the measurement of vegetation density or resistivity; there may be cases where the roughness is determined by a qualitative evaluation of the roughness, using equation 6 and the adjustment factors in table 3. A decision must be made as to which method will be used.

16. If there are abrupt changes in roughness on the flood plain, it will need to be subdivided. A representative sampling area is selected for each subarea of the flood plain.

17. Determine the factors that cause roughness and how each is to be taken into account. Such factors as surface irregularities and obstructions may be accounted for in the boundary roughness, whereas vegetation may be accounted for in the boundary roughness or by using the quantitative method.

18. A base value, n_b, for the flood plain's surface (bare soil without anything protruding on the surface) must be chosen. A value for n_b is chosen from table 1.

19. Select the adjustment factors from table 3 for conditions that influence roughness of the flood-plain subsection.

20. Determine the n_o value by equation 9, using the adjustment factors selected in step 19. The n_4' value is the adjustment factor for vegetation not accounted for by the vegetation-density method.

21. The vegetation density of the sampling area is determined using equation 11 by measuring the cross-sectional area occupied by the trees and undergrowth in the sampling area. An estimate of the depth of flow on the flood plain is necessary to determine vegetation density and the n value. By measuring 2 or 3 sampling areas in a subsection, a more representative value for vegetation density can be determined.

22. The n value for the flood-plain subsection is determined by using equation 6 or 7, depending on which method has been chosen. If the quantitative method is being used, the n value for each subarea of the flood plain is computed, using equation 7 and vegetation-density and boundary-roughness values for each subarea.

23. Compare the study reach with photographs of other flood plains in this report and in other references to determine if the final values of n obtained in step 22 appear to be reasonable.

Examples of procedures for determining n values

A sketch of a hypothetical channel and flood plain is shown in figure 23 and procedures for determining n values are outlined in table 4. The channel and flood plain together are divided into three separate reaches (A, B, C) and each reach has a cross section (1, 2, 3). The shape of each cross section is shown in figure 23.

In section 1, the flow is confined to the channel. The channel is composed of firm soil and no subdivision of the channel is necessary. Steps 1 through 13 in "Procedures for Assigning n Values" are used in the computation of n for this section. These steps apply only to channel conditions.

Flow in section 2 is also confined to the channel, which is composed of three distinct parallel bands of (1) bedrock, (2) sand, (3) gravel and cobbles. The n value for each segment is determined and a composite n for the channel is computed by weighting each segment n value by its wetted perimeter. Again, steps 1 through 13 are used in the computation of n for this section.

The flow in section 3 is channel and flood-plain flow. The cross section is divided into three subsections. Subsection 1 is flood-plain flow through woods, subsection 2 is channel flow, and subsection 3 is flood-plain flow through a cotton field.

In subsection 1, the flood plain is made up of dense woods having little undergrowth. The procedure using the vegetation density of the woods is used to determine the n value for the flood plain. The vegetation density is determined from a representative sample area of the

Table 4.--Outline and example of procedures for determining n values for a hypothetical channel and flood plain

[Modified from Aldridge and Garrett, 1973, table 6]

SECTION 1		
Step	Item to be determined or operation to be performed	Factors on which decisions are based and the results
1	Extent of reach	The reach extends one section width above section 1 to midway between sections 1 and 2. Designated as reach A (fig. 23).
2	Subdivision of cross section	Only channel flow, no overbank flood-plain flow. Assign a base n_b to entire channel.
	Channel Roughness (steps 3-13)	
3	(a) Type of channel	A stable channel made up of firm soil.
	(b) Conditions during flow event	Assume channel conditions are representative of those that existed during the peak flow.
	(c) Comparable streams	None.
4	Roughness factors	Add adjustments for grass and trees in channel and for channel alinement.
5	Divide into segments	Not necessary.
6	Type of channel	Firm soil.
7	Base n_b	Table 1 gives a n_b value for firm soil of 0.020-0.032. Use 0.025.
8	Adjustment factors for segments	None.
9	Basis for weighting n	Not applicable.
10	Weighting factors and weighted n	Not applicable.

Table 4.--Outline and example of procedures for determining n values for a hypothetical channel and flood plain--Continued

SECTION 1--Continued		
Channel Roughness (steps 3-13)--Continued		
Step	Item to be determined or operation to be performed	Factors on which decisions are based and the results
11	Add adjustments for entire channel	Vegetation (n_4)--weeds and supple seedlings along bottom of channel, $n_4 = 0.005$ Meander is minor, m = 1.00 $n = (n_b + n_1 + n_2 + n_3 + n_4)m$ $n = (0.025 + 0 + 0 + 0 + 0.005)1.00$ n = 0.030.
12	Compare with other streams	None.
13	Check flow regime	Not applicable.
SECTION 2		
1	Extent of reach	From midway between sections 1 and 2 to midway between sections 2 and 3. Designated as reach B (fig. 23.)
2	Subdivision of cross section	Flow remains in channel, no overbank flood-plain flow. The channel is composed of distinct bands, each having a different roughness. Derive n by weighting segments.
Channel Roughness (steps 3-13)		
3	(a) Type of channel	Combinations of sand and stable channel. Consider that channel reacts as a stable channel.
	(b) Conditions during flow event	Some movement of sand may have occurred during the peak flow, but assume that channel conditions are representative of those that existed during the peak.
	(c) Comparable streams	None.
4	Roughness factors	(1) Bedrock--may be accounted for by adding an adjustment factor to the n value for the bed or as a separate segment. Use latter.

Table 4.--Outline and example of procedures for determining n values for a hypothetical channel and flood plain--Continued

Channel Roughness (steps 3-13)--Continued		
Step	Item to be determined or operation to be performed	Factors on which decisions are based and the results
		(2) Divide into segments according to type of material. (3) Boulder at head of reach--add as an adjustment factor to composite n.
5	Divide into segments	The channel has three basic types of roughness caused by parallel bands of bedrock, sand, and gravel and cobbles. Each band is a segment.
6	Type of material and grain size	(1) Bedrock--slightly irregular with fairly sharp projections having a maximum height of about 3 in. (2) Sand--determined by sieve analysis, median particle size is 0.8 mm. (3) Gravel and cobbles--as determined by examination, the material is from 2 to 10 in. in diameter. As determined from 100-point grid system, the median particle size is 6 in.
7	Base n_b	(1) Bedrock--table 1 shows that n_b for jagged and irregular rock cut is from 0.035 to 0.050. Assume that the projections have an average cut, n_b for this segment is 0.040. (2) Sand--table 1 gives an n_b value of 0.025. (3) Gravel and cobbles--table 1 shows that the base n_b for cobbles ranges from 0.030 to 0.050. The median diameter is small for the size range. Use a base n_b value of 0.030.

Table 4.--Outline and example of procedures for determining n values for a hypothetical channel and flood plain--Continued

SECTION 2--Continued		
Channel Roughness (steps 3-13)--Continued		
Step	Item to be determined or operation to be performed	Factors on which decisions are based and the results
8	Adjustment factors for segments	None.
9	Basis for weighting n	Use wetted perimeter for basis of weighting n for the channel segments.
10	Weighting factors and weighted n	About 10 ft of the wetted perimeter is bounded by bedrock, about 30 ft by sand, and about 60 ft is bounded by gravel and cobbles. The unadjusted n value is (0.1 X 0.040 + 0.3 X 0.025 + 0.6 X 0.030)/1.0 = 0.030.
11	Add adjustments for entire channel	(1) Boulders at head of reach are slight obstructions, add 0.002 (table 2). (2) The bend near the lower end of reach A (fig. 23) causes slight irregularity; add 0.002 (table 2). $n = (n_b + n_1 + n_2 + n_3 + n_4)m$ $n = (0.030+0.002+0+0.002+0)1.0$ $n = 0.034$.
12	Compare with other streams	None.
13	Check flow regime	Sufficient sand was not present to warrant a check.
SECTION 3		
1	Extent of reach	From midway between sections 2 and 3 to one section width below section 3. Designated as reach C (fig. 23).

Table 4.--Outline and example of procedures for determining n values for a hypothetical channel and flood plain--Continued

SECTION 3--Continued		
Step	Item to be determined or operation to be performed	Factors on which decisions are based and the results
2	Subdivision of cross section	There is overbank flood-plain flow on both sides of the channel. Subsection 1 is flood-plain flow through trees, subsection 2 is channel flow, and subsection 3 is flood-plain flow through a cotton field. Assign a base n_b to each subsection.
	Channel Roughness (steps 3-13) Subsection 2	
3	(a) Type of channel	A stable channel made up of firm soil.
	(b) Conditions during flow event	Assume channel conditions are representative of those that existed during the peak flow.
	(c) Comparable streams	See photographs of similar channels in Barnes (1967, p. 16-17). Channel made up of same type of material. Barnes used n of 0.026 for the channel.
4	Roughness factors	Trees along the bank should be considered as obstruction (n_3) for the channel.
5	Divide into segments	Not necessary.
6	Type of material and grain size	Firm soil (clay).
7	Base n_b	Table 1 gives a base n_b value for firm soil of 0.020 to 0.030. Use 0.025.
8	Adjustment factors for segments	None.
9	Base for weighting n	Not applicable.
10	Weighting factors and weighted n	Not applicable.

Table 4.--Outline and example of procedures for determining n values for a hypothetical channel and flood plain--Continued

Step	Item to be determined or operation to be performed	Factors on which decisions are based and the results
	Channel Roughness (steps 3-13) Subsection 2--Continued	
11	Add adjustments for entire channel	Obstructions (n_3)--negligible--scattered trees and tree roots along edge of channel banks. $n_3 = 0.003$ Meander is minor, m = 1.00 $n = (n_b + n_1 + n_2 + n_3 + n_4)m$ $n = (0.025 + 0 + 0 + 0.003 + 0)1.00$ $n = 0.028$.
12	Compare with other streams	Similar to channel in photographs in Barnes (1967, p. 16-17). The n value reported was 0.026.
13	Check flow regime	Not applicable.
	Flood-Plain Roughness (steps 14-23) Subsection 1 (made up of trees)	
14	(a) Type of flood plain	A slightly irregular flood plain covered with hardwood trees. No undergrowth.
	(b) Conditions during flow event	Assume present conditions are representative of those that existed during the peak flow.
	(c) Comparable flood plains	Flood plain is similar to one shown in fig. 14 of this report.
15	Method to be used in assigning n	Use the "vegetation density" method. Need to determine a value for boundary roughness.
16	Subdivision of flood plain	The flood plain is uniform throughout.
17	Roughness factors	Trees are major roughness factor, surface irregularity and some obstructions are on flood plain.
18	Base n_b	Table 1 gives a base n_b value for firm soil of 0.020-0.030. Use 0.020.

Table 4.--Outline and example of procedures for determining n values for a hypothetical channel and flood plain--Continued

Step	Item to be determined or operation to be performed	Factors on which decisions are based and the results
	Flood-Plain Roughness (steps 14-23)--Continued Subsection 1 (made up of trees)--Continued	
19	Adjustment factors	Irregularity is minor, a few rises and dips across the flood plain. n_1 = 0.005 (table 2). Obstructions are negligible, consisting of scattered debris, exposed roots, and downed trees. n_3 = 0.004 (table 3).
20	n_o	$n_o = (n_b + n_1 + n_2 + n_3 + n_4')m$ $n_o = (0.020+0.005+0+0.004+0)1.0$ $n_o = 0.029$
21	Vegetation density of representative sample area	$Veg_d = 0.0115$ Is an average value from three sampling areas.
22	n for the flood-plain subsection	$R = 2.9$ ft $C_* = 11.0$ $Veg_d = 0.0115$ $n = n_o\sqrt{1 + (Veg_d)(C_*)\left(\frac{1.49}{n_o}\right)^2\left(\frac{1}{2g}\right)R^{4/3}}$ $n = 0.029\sqrt{1 + (.0115)(11.0)\left(\frac{1.49}{.029}\right)^2\left(\frac{1}{64.4}\right)(2.9)^{4/3}}$ $n = 0.137$
23	Compare with other flood plains	Photographs of similar flood plains found in this report (fig. 14).
	Flood-Plain Roughness (steps 14-23) Subsection 3 (cotton field)	
14	(a) Type of flood plain	Flood plain is a cotton field in full growth.
	(b) Conditions during flow event	Conditions are similar to flood event.
	(c) Comparable flood plains	None.

Table 4.--Outline and example of procedures for determining n values for a hypothetical channel and flood plain--Continued

Flood-Plain Roughness (steps 14-23)--Continued Subsection 3 (cotton field)--Continued		
Step	Item to be determined or operation to be performed	Factors on which decisions are based and the results.
15	Method to be used in assigning n	Assign n by evaluation of boundary roughness only.
16	Subdivision of flood plain	No division of flood plain is necessary.
17	Roughness factors	Roughness factors to be considered are surface irregularity and vegetation.
18	Base n_b	Table 1 gives a base n_b value for firm earth of 0.020-0.030. Use 0.025.
19	Adjustment factors	Irregularity is moderate with furrows parallel to flow on flood plain, n_1 = 0.010 (table 3). Vegetation is cotton crop, depth of flow about equal to height of vegetation, n_4 = 0.040 (table 3).
20	n_o	Not applicable.
21	Vegetation density of representative sample area	Not applicable.
22	n for flood plain	$n = (n_b + n_1 + n_2 + n_3 + n_4)m$ $n = (0.025+0.01+0+0+0.040)1.00$ $n = 0.075$
23	Compare with other flood plains	Ree and Crow (1977, p. 39-40) assigned cotton fields an n value of about 0.08.

wooded-flood plain. A boundary roughness, n_o, is determined from equation 9 and the n value is determined using equation 7. Steps 14 through 23 in "Procedures for Assigning n Values" are used in the computation of n for this subsection.

Subsection 2 of this cross section has channel flow. The channel is composed of firm soil, and no subdivision of the channel is necessary. Steps 1 through 13 are used in the computation of n for this subsection.

Subsection 3 is also flood-plain flow. The flood plain is a field planted in cotton. There is no need to subdivide the subsection, and the depth of flow is equal to the height of the vegetation. Steps 14 through 23 are used in the computation of the n for this subsection, and equation 6 is used to determine the n value for the flood plain.

SUMMARY

In this design guide, procedures are presented for assigning reliable n values to channels and flood plains. The roughness coefficient applies to a reach of a channel and should be representative of that entire reach. It may be necessary to divide a channel and flood plain into subsections and to assign n values to each subsection.

In the case of channel roughness, a procedure is presented that involves a series of decisions based on the interaction of roughness-causing factors. A base value is assigned to the channel and adjustments are made for certain roughness-causing factors.

A similar procedure is used to assign n values to flood plains. A base value is determined for the flood plain related to certain roughness factors; then an option, based on the measurement of vegetation density of the flood plain, is used to determine the total roughness of flood-plain subsections. The vegetation density of the flood plain is determined from physical measurements of the vegetation in a representative sample area of a flood-plain subsection.

Photographs of flood plains for which n values are known are presented to aid in the determination of roughness coefficients. The photographs can be used for comparison with field situations to help verify selected n values.

Step-by-step procedures are presented to determine the roughness coefficients for channels and flood plains, and examples showing how to use the procedures are included.

SELECTED REFERENCES

Aldridge, B. N., and Garrett, J. M., 1973, Roughness coefficients for stream channels in Arizona: U.S. Geological Survey open-file report, 49 p.

Barnes, H. H., Jr., 1967, Roughness characteristics of natural channels: U.S. Geological Survey Water-Supply 1849, 213 p.

Benson, M. A., and Dalrymple, Tate, 1967, General field and office procedures for indirect discharge measurements: U.S. Geological Survey Techniques of Water-Resources Investigations, Book 3, Chap. A1, 30 p.

Burkham, D. E., and Dawdy, D. R., 1976, Resistance equation for alluvial-channel flow: Proceedings American Society of Civil Engineers, Journal of the Hydraulic Division, v. 102, no. HY10, p. 1479-1489.

Carter, R. W., Einstein, H. A., Hinds, Julian, Powell, R. W., and Silberman, E., 1963, Friction factors in open channels, progress report of the task force on friction factors in open channels of the Committee on Hydromechanics of the Hydraulic Division: Proceedings American Society of Civil Engineers, Journal of Hydraulics Division, v. 89, no. HY2, pt. 1, p. 97-143.

Chow, V. T., 1959, Open-channel hydraulics: New York, McGraw-Hill Book Company, 680 p.

Cowan, W. L., 1956, Estimating hydraulic roughness coefficients: Agricultural Engineering, v. 37, no. 7, p. 473-475.

Fasken, G. B., 1963, Guide for selecting roughness coefficient n values for channels: Soil Conservation Service, U.S. Department of Agriculture, 45 p.

Henderson, F. M., 1966, Open-channel flow: New York, MacMillan Publishing Co., Inc., 522 p.

Limerinos, J. T., 1970, Determination of the Manning coefficient from measured bed roughness in natural channels: U.S. Geological Survey Water-Supply Paper 1898-B, 47 p.

Petryk, Sylvester, and Bosmajian, George, III, 1975, Analysis of flow through vegetation: Proceedings American Society of Civil Engineers, Journal of the Hydraulics Division, v. 101, no. HY7, p. 871-884.

Ree, W. O., 1954, Handbook of channel design for soil and water conservation: Soil Conservation Service, U.S. Department of Agriculture, SCS-TP-61, 40 p.

Ree, W. O., and Crow, F. R., 1977, Friction factors for vegetated waterways of small slope: Agricultural Research Service, U.S. Department of Agriculture, ARS-S-151, 56 p.

Schneider, V. R., Board, J. W., Colson, B. E., Lee, F. N., and Druffel, Leroy, 1977, Computation of backwater and discharge at width constrictions of heavily vegetated flood plains: U.S. Geological Survey Water-Resources Investigations 76-129, 64 p.

Simons, D. B., and Richardson, E. V., 1966, Resistance to flow in alluvial channels: U.S. Geological Survey Professional Paper 422-J, 61 p.

Simons, D. B., Lee, R. M., and Associates, 1982, Engineering analysis of alluvial systems: Simons, Lee, and Associates, Ft. Collins, Colorado, Chap. 6, p. 11-17.

Streeter, V. L., 1971, Fluid mechanics: New York, McGraw-Hill Book Company, 705 p.

Technical Report Documentation Page

1. Report No.	2. Government Accession No.	3. Recipient's Catalog No.
FHWA/RD-88/146		

4. Title and Subtitle	5. Report Date
TWO-DIMENSIONAL FINITE-ELEMENT HYDRAULIC MODELING OF BRIDGE CROSSINGS: RESEARCH REPORT	April 1989
	6. Performing Organization Code
	8. Performing Organization Report No.
7. Author(s) J. K. Lee and D. C. Froehlich	
9. Performing Organization Name and Address U.S. Geological Survey, WRD 430 National Center 12201 Sunrise Valley Drive Reston, VA 22092	10. Work Unit No. (TRAIS) NCP-3D3-1082
	11. Contract or Grant No. DTFH61-80-Y-3011
12. Sponsoring Agency Name and Address Structures Division Federal Highway Administration 6300 Georgetown Pike McLean, VA 22101-2296	13. Type of Report and Period Covered
	14. Sponsoring Agency Code USDOT, FHWA, RD&T

15. Supplementary Notes
FHWA contract manager (COTR): R. E. Trent (HNR-10)

16. Abstract

This report presents the results of a 6-year project, conducted by the U.S. Geological Survey in cooperation with the Federal Highway Administration (FHWA), to develop an accurate, efficient, easy-to-use finite-element surface-water flow model (FESWMS-2DH) for use in analyzing backwater and flow distribution at highway crossings of rivers and flood plains. When lateral variations in water-surface elevation and flow distribution are significant, a two-dimensional approach has advantages over a one-dimensional approach. The finite-element method is ideally suited to modeling two-dimensional flow over complex topography with spatially variable roughness and allows the user great flexibility in defining flow boundaries, channels, and embankments.

A large number of alternative flow-equation formulations, interpolation and weighting functions, and schemes for solving the large systems of algebraic equations that arise in applying the finite-element method were tested during the project. Features added to FESWMS-2DH include weir flow (roadway overtopping), culvert flow, linear variation of Manning's n with depth, simple and accurate handling of lateral boundaries, automatic network generation and refinement, and extensive error checking.

Sections of the report are devoted to the application of FESWMS-2DH to data from the Geological Survey's Flood Plain Simulation Facility, the use and calibration of FESWMS-2DH, and the use of the model by the highway industry.

17. Key Words	18. Distribution Statement
Bridge backwater, Finite-element method, Hydraulics, Shallow-water equations, Galerkin's method, Flow through contracted opening, Flow through constriction, Model calibration	No restrictions. This document is available to the public through the National Technical Information Service, Springfield, VA 22161.

19. Security Classif. (of this report)	20. Security Classif. (of this page)	21. No. of Pages	22. Price
Unclassified	Unclassified	290	

METRIC (SI*) CONVERSION FACTORS

APPROXIMATE CONVERSIONS TO SI UNITS

Symbol	When You Know	Multiply By	To Find	Symbol
LENGTH				
in	inches	2.54	millimetres	mm
ft	feet	0.3048	metres	m
yd	yards	0.914	metres	m
mi	miles	1.61	kilometres	km
AREA				
in²	square inches	645.2	millimetres squared	mm²
ft²	square feet	0.0929	metres squared	m²
yd²	square yards	0.836	metres squared	m²
mi²	square miles	2.59	kilometres squared	km²
ac	acres	0.395	hectares	ha
MASS (weight)				
oz	ounces	28.35	grams	g
lb	pounds	0.454	kilograms	kg
T	short tons (2000 lb)	0.907	megagrams	Mg
VOLUME				
fl oz	fluid ounces	29.57	millilitres	mL
gal	gallons	3.785	litres	L
ft³	cubic feet	0.0328	metres cubed	m³
yd³	cubic yards	0.0765	metres cubed	m³

NOTE: Volumes greater than 1000 L shall be shown in m³.

TEMPERATURE (exact)

°F	Fahrenheit temperature	5/9 (after subtracting 32)	Celsius temperature	°C

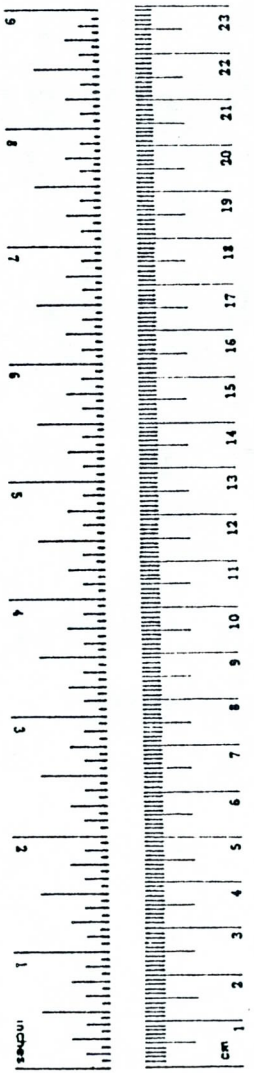

APPROXIMATE CONVERSIONS TO SI UNITS

Symbol	When You Know	Multiply By	To Find	Symbol
LENGTH				
mm	millimetres	0.039	inches	in
m	metres	3.28	feet	ft
m	metres	1.09	yards	yd
km	kilometres	0.621	miles	mi
AREA				
mm²	millimetres squared	0.0016	square inches	in²
m²	metres squared	10.764	square feet	ft²
km²	kilometres squared	0.39	square miles	mi²
ha	hectores (10 000 m²)	2.53	acres	ac
MASS (weight)				
g	grams	0.0353	ounces	oz
kg	kilograms	2.205	pounds	lb
Mg	megagrams (1 000 kg)	1.103	short tons	T
VOLUME				
mL	millilitres	0.034	fluid ounces	fl oz
L	litres	0.264	gallons	gal
m³	metres cubed	35.315	cubic feet	ft³
m³	metres cubed	1.308	cubic yards	yd³

TEMPERATURE (exact)

°C	Celsius temperature	9/5 (then add 32)	Fahrenheit temperature	°F

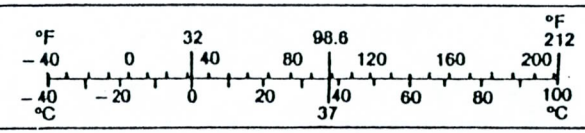

These factors conform to the requirement of FHWA Order 5190.1A.

* SI is the symbol for the International System of Measurements

TABLE OF CONTENTS

	Page
INTRODUCTION	1
EQUATION FORMULATION	10
Conservative and Nonconservative Primitive Formulations	10
Velocity and Unit-Discharge Formulations	14
Initial and Boundary Conditions for Primitive-Equation Formulations	15
Wave-Equation and Vorticity-Stream-Function Formulations	17
Momentum-Correction Coefficients	18
Bed Shear Stress	20
Surface Shear Stress	22
Lateral Stresses	23
Eddy Viscosities	24
Turbulence Models	25
Turbulence Models in FLOMOD	32
Weir Flow and Roadway Overtopping	34
Bridge/Culvert Flow	35
One-Dimensional Bridge/Culvert Flow	36
Two-Dimensional Bridge/Culvert Flow	37
APPLYING THE FINITE-ELEMENT METHOD TO THE SHALLOW-WATER EQUATIONS	40
Interpolation Functions and Elements	41
Solution Methods	50
Numerical Integration	54

TABLE OF CONTENTS (Continued)

	Page
Solution of Nonlinear Algebraic Equations	56
Solution of Linear Algebraic Equations	59
Banded-Storage Solution Scheme	60
Partitioned-Block Skyline-Storage Solution Scheme	61
Frontal Solution Scheme	62
Conjugate-Gradient Solution Scheme	64
Finite-Element Equations	65
Residuals	65
Time Derivatives	69
Application of Boundary and Special Conditions	71
Open boundaries	72
Solid boundaries	75
Total discharge across a boundary	76
FEATURES OF THE MODELING SYSTEM FESWMS-2DH	80
Graphic Output Standard	80
Data Input Module, DINMOD	80
Error Checking	81
Automatic Network Generation	82
Network Refinement	86
Element Resequencing	88
Minimum-frontgrowth method	91
Level-structure method	92

TABLE OF CONTENTS (Continued)

	Page
Depth-Averaged Flow Module, FLOMOD	92
Error Checking	93
Automatic Boundary Adjustment	94
The Continuity Norm	96
Output Analysis Module, ANOMOD	97
APPLYING FESWMS-2DH TO DATA FROM THE FLOOD PLAIN SIMULATION FACILITY	99
Research Facility	99
Data Collection	102
Experiments on Flow through Contracted Openings	104
Data Processing	109
Data Analysis	110
Modeling Flood Plain Simulation Facility Data	118
Model Ground-Surface Elevations	118
Modeling Normal Flows	118
Modeling Constricted Flows	122
Sensitivity Analyses	209
Conclusions from the Application of FESWMS-2DH to Flood Plain Simulation Facility Data	218
USE AND CALIBRATION OF FESWMS-2DH	223
Data Collection and Analysis	224
Network Design	225
Model Adjustment, Including Calibration	233

TABLE OF CONTENTS (Continued)

	Page
USE OF FESWMS--2DH BY THE HIGHWAY INDUSTRY	239
Operational Potential of FESWMS-2DH	239
Training	241
Future Possible Improvements to FESWMS-2DH	243
Software Maintenance	245
SUMMARY AND CONCLUSIONS	247
REFERENCES	250

LIST OF FIGURES

Figure		Page
1	Examples of the types of two-dimensional elements used in FESWMS-2DH: (a) a six-node triangle, (b) an eight-node "serendipity" quadrilateral, and (c) a nine-node "Lagrangian" quadrilateral	43
2	Two-dimensional "mapping" of some elements	43
3	Examples of (a) a region inside of which a finite-element network is to be generated automatically and (b) an initial subdivision of the region into simply connected subregions A and B	83
4	Formation of two new elements by automatic triangulation	84
5	Neighborhood of node i in element k used in Laplacian smoothing of a finite-element network that has been generated automatically	86
6	Example of a network that has been generated automatically: (a) an initial subdivision defined by a series of connected corner nodes and (b) the network generated inside the initial subdivision	87
7	Refinement of (a) a six-node triangular element, (b) an eight-node quadrilateral element, and (c) a nine-node quadrilateral element	89
8	Plan view of the Flood Plain Simulation Facility	101
9	Vertical velocity profile measured 135 feet from the right bank at cross section 1050 during experiment S6810105. The total depth is 1.29 feet	111
10	Velocity correction factor as a function of relative roughness for 1975 vertical velocity profiles	113
11	Velocity correction factor as a function of discharge Froude number for 1975 vertical velocity profiles	114
12	Velocity correction factor as a function of point velocity Froude number for 1975 vertical velocity profiles	115

LIST OF FIGURES (Continued)

Figure		Page
13	Corrected and uncorrected velocity components for experiment S6410085 at cross section 900	117
14	Ground-surface-elevation (GSE) data and model ground-surface representation at cross section 400	119
15	Upstream half of the finite-element network used to model normal-flow experiments	120
16	Observed and computed water-surface elevations (WSE) for experiment S5810015	122
17	Observed and computed water-surface elevations (WSE) for experiment S6410085	123
18	Observed and computed water-surface elevations (WSE) for experiment S7010215	123
19	Observed and computed velocity components at cross section 900 for experiment S5810015	124
20	Observed and computed velocity components at cross section 950 for experiment S5810015	124
21	Observed and computed velocity components at cross section 1050 for experiment S5810015	125
22	Observed and computed velocity components at cross section 1100 for experiment S5810015	125
23	Observed and computed velocity components at cross section 900 for experiment S6410085	126
24	Observed and computed velocity components at cross section 950 for experiment S6410085	126
25	Observed and computed velocity components at cross section 1050 for experiment S6410085	127
26	Observed and computed velocity components at cross section 1100 for experiment S6410085	127
27	Observed and computed velocity components at cross section 900 for experiment S7010215	128

LIST OF FIGURES (Continued)

Figure		Page
28	Observed and computed velocity components at cross section 950 for experiment S7010215	128
29	Observed and computed velocity components at cross section 1050 for experiment S7010215	129
30	Observed and computed velocity components at cross section 1100 for experiment S7010215	129
31	Part of the right half of finite-element network 1 upstream from the constriction. The continuity norm exceeds 0.1 on the shaded elements for the simulation of experiment S7410235 with the calibrated parameters	131
32	Part of the right half of finite-element network 2 upstream from the constriction. The continuity norm exceeds 0.1 on the shaded elements for the simulation of experiment S7410235 with the calibrated parameters	132
33	Part of the right half of finite-element network 3 upstream from the constriction. The continuity norm exceeds 0.1 on the shaded elements for the simulation of experiment S7410235 with the calibrated parameters	133
34	Part of the right half of finite-element network 4 upstream from the constriction. The continuity norm exceeds 0.1 on the shaded elements for the simulation of experiment S7410235 with the calibrated parameters	134
35	Observed and computed water-surface elevations (WSE) for experiment S6210035, calibrated parameters, network 1. The letters U and D refer, respectively, to the upstream side and the downstream side of the constriction	137
36	Observed and computed water-surface elevations (WSE) for experiment S6210035, calibrated parameters, network 2. The letters U and D refer, respectively, to the upstream side and the downstream side of the constriction	137

LIST OF FIGURES (Continued)

Figure		Page
37	Observed and computed water-surface elevations (WSE) for experiment S6210035, calibrated parameters, network 3. The letters U and D refer, respectively, to the upstream side and the downstream side of the constriction	138
38	Observed and computed water-surface elevations (WSE) for experiment S6210035, calibrated parameters, network 4. The letters U and D refer, respectively, to the upstream side and the downstream side of the constriction	138
39	Observed and computed velocity components at cross section 900 for experiment S6210035, calibrated parameters, network 1	139
40	Observed and computed velocity components at cross section 900 for experiment S6210035, calibrated parameters, network 2	139
41	Observed and computed velocity components at cross section 900 for experiment S6210035, calibrated parameters, network 3	140
42	Observed and computed velocity components at cross section 900 for experiment S6210035, calibrated parameters, network 4	140
43	Observed and computed velocity components at cross section 950 for experiment S6210035, calibrated parameters, network 1	141
44	Observed and computed velocity components at cross section 950 for experiment S6210035, calibrated parameters, network 2	141
45	Observed and computed velocity components at cross section 950 for experiment S6210035, calibrated parameters, network 3	142
46	Observed and computed velocity components at cross section 950 for experiment S6210035, calibrated parameters, network 4	142

LIST OF FIGURES (Continued)

Figure		Page
47	Observed and computed velocity components at cross section 1050 for experiment S6210035, calibrated parameters, network 1	143
48	Observed and computed velocity components at cross section 1050 for experiment S6210035, calibrated parameters, network 2	143
49	Observed and computed velocity components at cross section 1050 for experiment S6210035, calibrated parameters, network 3	144
50	Observed and computed velocity components at cross section 1050 for experiment S6210035, calibrated parameters, network 4	144
51	Observed and computed velocity components at cross section 1100 for experiment S6210035, calibrated parameters, network 1	145
52	Observed and computed velocity components at cross section 1100 for experiment S6210035, calibrated parameters, network 2	145
53	Observed and computed velocity components at cross section 1100 for experiment S6210035, calibrated parameters, network 3	146
54	Observed and computed velocity components at cross section 1100 for experiment S6210035, calibrated parameters, network 4	146
55	Partial velocity field for experiment S6210035, calibrated parameters, network 1. A vector 1 inch long represents a velocity of 4 feet per second	148
56	Partial velocity field for experiment S6210035, calibrated parameters, network 2. A vector 1 inch long represents a velocity of 4 feet per second	149
57	Partial velocity field for experiment S6210035, calibrated parameters, network 3. A vector 1 inch long represents a velocity of 4 feet per second	150

Figure		Page
58	Partial velocity field for experiment S6210035, calibrated parameters, network 4. A vector 1 inch long represents a velocity of 4 feet per second ...	151
59	Observed and computed water-surface elevations (WSE) for experiment S6810105, calibrated parameters, network 1. The letters U and D refer, respectively, to the upstream side and the downstream side of the constriction	152
60	Observed and computed water-surface elevations (WSE) for experiment S6810105, calibrated parameters, network 2. The letters U and D refer, respectively, to the upstream side and the downstream side of the constriction	152
61	Observed and computed water-surface elevations (WSE) for experiment S6810105, calibrated parameters, network 3. The letters U and D refer, respectively, to the upstream side and the downstream side of the constriction	153
62	Observed and computed water-surface elevations (WSE) for experiment S6810105, calibrated parameters, network 4. The letters U and D refer, respectively, to the upstream side and the downstream side of the constriction	153
63	Observed and computed velocity components at cross section 900 for experiment S6810105, calibrated parameters, network 1	155
64	Observed and computed velocity components at cross section 900 for experiment S6810105, calibrated parameters, network 2	155
65	Observed and computed velocity components at cross section 900 for experiment S6810105, calibrated parameters, network 3	156
66	Observed and computed velocity components at cross section 900 for experiment S6810105, calibrated parameters, network 4	156

LIST OF FIGURES (Continued)

Figure		Page
67	Observed and computed velocity components at cross section 950 for experiment S6810105, calibrated parameters, network 1	157
68	Observed and computed velocity components at cross section 950 for experiment S6810105, calibrated parameters, network 2	157
69	Observed and computed velocity components at cross section 950 for experiment S6810105, calibrated parameters, network 3	158
70	Observed and computed velocity components at cross section 950 for experiment S6810105, calibrated parameters, network 4	158
71	Observed and computed velocity components at cross section 1050 for experiment S6810105, calibrated parameters, network 1	159
72	Observed and computed velocity components at cross section 1050 for experiment S6810105, calibrated parameters, network 2	159
73	Observed and computed velocity components at cross section 1050 for experiment S6810105, calibrated parameters, network 3	160
74	Observed and computed velocity components at cross section 1050 for experiment S6810105, calibrated parameters, network 4	160
75	Observed and computed velocity components at cross section 1100 for experiment S6810105, calibrated parameters, network 1	161
76	Observed and computed velocity components at cross section 1100 for experiment S6810105, calibrated parameters, network 2	161
77	Observed and computed velocity components at cross section 1100 for experiment S6810105, calibrated parameters, network 3	162

Figure		Page
78	Observed and computed velocity components at cross section 1100 for experiment S6810105, calibrated parameters, network 4	162
79	Partial velocity field for experiment S6810105, calibrated parameters, network 1. A vector 1 inch long represents a velocity of 4 feet per second ...	163
80	Partial velocity field for experiment S6810105, calibrated parameters, network 2. A vector 1 inch long represents a velocity of 4 feet per second ...	164
81	Partial velocity field for experiment S6810105, calibrated parameters, network 3. A vector 1 inch long represents a velocity of 4 feet per second ...	165
82	Partial velocity field for experiment S6810105, calibrated parameters, network 4. A vector 1 inch long represents a velocity of 4 feet per second ...	166
83	Observed and computed water-surface elevations (WSE) for experiment S7410235, calibrated parameters, network 1. The letters U and D refer, respectively, to the upstream side and the downstream side of the constriction	167
84	Observed and computed water-surface elevations (WSE) for experiment S7410235, calibrated parameters network 2. The letters U and D refer, respectively, to the upstream side and the downstream side of the constriction	167
85	Observed and computed water-surface elevations (WSE) for experiment S7410235, calibrated parameters, network 3. The letters U and D refer, respectively, to the upstream side and the downstream side of the constriction	168
86	Observed and computed water-surface elevations (WSE) for experiment S7410235, calibrated parameters, network 4. The letters U and D refer, respectively, to the upstream side and the downstream side of the constriction	168

LIST OF FIGURES (Continued)

Figure		Page
87	Observed and computed velocity components at cross section 900 for experiment S7410235, calibrated parameters, network 1	170
88	Observed and computed velocity components at cross section 900 for experiment S7410235, calibrated parameters, network 2	170
89	Observed and computed velocity components at cross section 900 for experiment S7410235, calibrated parameters, network 3	171
90	Observed and computed velocity components at cross section 900 for experiment S7410235, calibrated parameters, network 4	171
91	Observed and computed velocity components at cross section 950 for experiment S7410235, calibrated parameters, network 1	172
92	Observed and computed velocity components at cross section 950 for experiment S7410235, calibrated parameters, network 2	172
93	Observed and computed velocity components at cross section 950 for experiment S7410235, calibrated parameters, network 3	173
94	Observed and computed velocity components at cross section 950 for experiment S7410235, calibrated parameters, network 4	173
95	Observed and computed velocity components at cross section 1050 for experiment S7410235, calibrated parameters, network 1	174
96	Observed and computed velocity components at cross section 1050 for experiment S7410235, calibrated parameters, network 2	174
97	Observed and computed velocity components at cross section 1050 for experiment S7410235, calibrated parameters, network 3	175

Figure		Page
98	Observed and computed velocity components at cross section 1050 for experiment S7410235, calibrated parameters, network 4	175
99	Observed and computed velocity components at cross section 1100 for experiment S7410235, calibrated parameters, network 1	176
100	Observed and computed velocity components at cross section 1100 for experiment S7410235, calibrated parameters, network 2	176
101	Observed and computed velocity components at cross section 1100 for experiment S7410235, calibrated parameters, network 3	177
102	Observed and computed velocity components at cross section 1100 for experiment S7410235, calibrated parameters, network 4	177
103	Partial velocity field for experiment S7410235, calibrated parameters, network 1. A vector 1 inch long represents a velocity of 4 feet per second	178
104	Partial velocity field for experiment S7410235, calibrated parameters, network 2. A vector 1 inch long represents a velocity of 4 feet per second	179
105	Partial velocity field for experiment S7410235, calibrated parameters, network 3. A vector 1 inch long represents a velocity of 4 feet per second	180
106	Partial velocity field for experiment S7410235, calibrated parameters, network 4. A vector 1 inch long represents a velocity of 4 feet per second	181
107	Observed and computed water-surface elevations (WSE) for experiment S6210035, $\beta = 1.64$, network 3. The letters U and D refer, respectively, to the upstream side and the downstream side of the constriction	183
108	Observed and computed velocity components at cross section 900 for experiment S6210035, $\beta = 1.64$, network 3	184

LIST OF FIGURES (Continued)

Figure		Page
109	Observed and computed velocity components at cross section 950 for experiment S6210035, β = 1.64, network 3	184
110	Observed and computed velocity components at cross section 1050 for experiment S6210035, β = 1.64, network 3	185
111	Observed and computed velocity components at cross section 1100 for experiment S6210035, β = 1.64, network 3	185
112	Partial velocity field for experiment S6210035, β = 1.64, network 3. A vector 1 inch long represents a velocity of 4 feet per second	186
113	Observed and computed water-surface elevations (WSE) for experiment S6810105, β = 1.59, network 3. The letters U and D refer, respectively, to the upstream side and the downstream side of the constriction	187
114	Observed and computed velocity components at cross section 900 for experiment S6810105, β = 1.59, network 3	188
115	Observed and computed velocity components at cross section 950 for experiment S6810105, β = 1.59, network 3	188
116	Observed and computed velocity components at cross section 1050 for experiment S6810105, β = 1.59, network 3	189
117	Observed and computed velocity components at cross section 1100 for experiment S6810105, β = 1.59, network 3	189
118	Partial velocity field for experiment S6810105, β = 1.59, network 3. A vector 1 inch long represents a velocity of 4 feet per second	190

LIST OF FIGURES (Continued)

Figure		Page
119	Observed and computed water-surface elevations (WSE) for experiment S7410235, β = 1.48, network 3. The letters U and D refer, respectively, to the upstream side and the downstream side of the constriction	191
120	Observed and computed velocity components at cross section 900 for experiment S7410235, β = 1.48, network 3	192
121	Observed and computed velocity components at cross section 950 for experiment S7410235, β = 1.48, network 3	192
122	Observed and computed velocity components at cross section 1050 for experiment S7410235, β = 1.48, network 3	193
123	Observed and computed velocity components at cross section 1100 for experiment S7410235, β = 1.48, network 3	193
124	Partial velocity field for experiment S7410235, β = 1.48, network 3. A vector 1 inch long represents a velocity of 4 feet per second	194
125	Observed and computed water-surface elevations (WSE) for experiment S6210035, β = 1.64, Manning's n reduced where velocities exceed 1 foot per second, network 3. The letters U and D refer, respectively, to the upstream side and the downstream side of the constriction	196
126	Observed and computed velocity components at cross section 900 for experiment S6210035, β = 1.64, Manning's n reduced where velocities exceed 1 foot per second, network 3	197
127	Observed and computed velocity components at cross section 950 for experiment S6210035, β = 1.64, Manning's n reduced where velocities exceed 1 foot per second, network 3	197

Figure		Page
128	Observed and computed velocity components at cross section 1050 for experiment S6210035, β = 1.64, Manning's n reduced where velocities exceed 1 foot per second, network 3	198
129	Observed and computed velocity components at cross section 1100 for experiment S6210035, β = 1.64, Manning's n reduced where velocities exceed 1 foot per second, network 3	198
130	Partial velocity field for experiment S6210035, β = 1.64, Manning's n reduced where velocities exceed 1 foot per second, network 3. A vector 1 inch long represents a velocity of 4 feet per second	199
131	Observed and computed water-surface elevations (WSE) for experiment S6810105, β = 1.59, Manning's n reduced where velocities exceed 1 foot per second, network 3. The letters U and D refer, respectively, to the upstream side and the downstream side of the constriction	200
132	Observed and computed velocity components at cross section 900 for experiment S6810105, β = 1.59, Manning's n reduced where velocities exceed 1 foot per second, network 3	201
133	Observed and computed velocity components at cross section 950 for experiment S6810105, β = 1.59, Manning's n reduced where velocities exceed 1 foot per second, network 3	201
134	Observed and computed velocity components at cross section 1050 for experiment S6810105, β = 1.59, Manning's n reduced where velocities exceed 1 foot per second, network 3	202
135	Observed and computed velocity components at cross section 1100 for experiment S6810105, β = 1.59, Manning's n reduced where velocities exceed 1 foot per second, network 3	202

Figure		Page
136	Partial velocity field for experiment S6810105, β = 1.59, Manning's n reduced where velocities exceed 1 foot per second, network 3. A vector 1 inch long represents a velocity of 4 feet per second	203
137	Observed and computed water-surface elevations (WSE) for experiment S7410235, β = 1.48, Manning's n reduced where velocities exceed 1 foot per second, network 3. The letters U and D refer, respectively, to the upstream side and the downstream side of the constriction	204
138	Observed and computed velocity components at cross section 900 for experiment S7410235, β = 1.48, Manning's n reduced where velocities exceed 1 foot per second, network 3	205
139	Observed and computed velocity components at cross section 950 for experiment S7410235, β = 1.48, Manning's n reduced where velocities exceed 1 foot per second, network 3	205
140	Observed and computed velocity components at cross section 1050 for experiment S7410235, β = 1.48, Manning's n reduced where velocities exceed 1 foot per second, network 3	206
141	Observed and computed velocity components at cross section 1100 for experiment S7410235, β = 1.48, Manning's n reduced where velocities exceed 1 foot per second, network 3	206
142	Partial velocity field for experiment S7410235, β = 1.48, Manning's n reduced where velocities exceed 1 foot per second, network 3. A vector 1 inch long represents a velocity of 4 feet per second	207
143	Observed and computed water-surface elevations (WSE) for experiment S6210035, β = 0, network 3. The letters U and D refer, respectively, to the upstream side and the downstream side of the constriction	210

LIST OF FIGURES (Continued)

Figure		Page
144	Observed and computed velocity components at cross section 900 for experiment S6210035, β = 0, network 3	211
145	Observed and computed velocity components at cross section 950 for experiment S6210035, β = 0, network 3	211
146	Observed and computed velocity components at cross section 1050 for experiment S6210035, β = 0, network 3	212
147	Observed and computed velocity components at cross section 1100 for experiment S6210035, β = 0, network 3	212
148	Partial velocity field for experiment S6210035, β = 0, network 3. A vector 1 inch long represents a velocity of 4 feet per second	213
149	Observed and computed water-surface elevations (WSE) for experiment S6810105, β = 0, network 3. The letters U and D refer, respectively, to the upstream side and the downstream side of the constriction	214
150	Observed and computed velocity components at cross section 900 for experiment S6810105, β = 0, network 3	215
151	Observed and computed velocity components at cross section 950 for experiment S6810105, β = 0, network 3	215
152	Observed and computed velocity components at cross section 1050 for experiment S6810105, β = 0, network 3	216
153	Observed and computed velocity components at cross section 1100 for experiment S6810105, β = 0, network 3	216
154	Partial velocity field for experiment S6810105, β = 0, network 3. A vector 1 inch long represents a velocity of 4 feet per second	217

Figure		Page
155	Observed and computed water-surface elevations (WSE) for experiment S7410235, $\beta = 0$, network 3. The letters U and D refer, respectively, to the upstream side and the downstream side of the constriction	218
156	Observed and computed velocity components at cross section 900 for experiment S7410235, $\beta = 0$, network 3	219
157	Observed and computed velocity components at cross section 950 for experiment S7410235, $\beta = 0$, network 3	219
158	Observed and computed velocity components at cross section 1050 for experiment S7410235, $\beta = 0$, network 3	220
159	Observed and computed velocity components at cross section 1100 for experiment S7410235, $\beta = 0$, network 3	220
160	Partial velocity field for experiment S7410235, $\beta = 0$, network 3. A vector 1 inch long represents a velocity of 4 feet per second	221
161	Finite-element network near the I-10 crossing of the Pearl River in southeastern Louisiana (adapted from Wiche and others, 1982, p. 264)	227
162	Finite-element network at a roadway embankment that contains a culvert and is divided into weir segments	232
163	Finite-element network at a bridge where pressure flow within the bridge opening is modeled	234

LIST OF TABLES

Table		Page
1	Model features tried in FESWMS-2DH	4
2	Parent elements and natural-coordinate shape functions	46
3	Summary of 1975 steady-flow experiments on flow through contracted openings	106
4	Values of Manning's n determined in calibration of the model for normal-flow experiments	121
5	Computed discharge at the 14-foot contracted opening for three discharges and four networks	135
6	Outline for a 1-week workshop on finite-element surface-water flow modeling using FESWMS-2DH	242

LIST OF SYMBOLS

Symbol(s)	Definition	Units
a	Vector of nodal values	---
a_i	Approximation of solution vector a at iteration i	---
a_i^o, b_i^o	Coefficients in constraint equation (equation 97) for specified discharge normal to an open boundary	L^2
a_i^s, b_i^s	Coefficients in constraint equation (equation 98) for specified discharge normal to a solid boundary	L^2
a_o	Initial estimate of solution vector a	---
A	Area of element side below water surface	L^2
A	Matrix defined by equation 62	---
A_c	Cross-sectional area of culvert	L^2
A_e	Area of element e	L^2
b	Opening width at contraction	L
B	Basin width at contraction	L
c	Celerity of gravity wave, $(gy)^{1/2}$	L/T
c_b	Bottom-stress coefficient	$M/(L^2T)$
c_f	Dimensionless bed-shear-stress coefficient	---
c_s	Dimensionless surface-shear-stress coefficient	---
c_{s1}, c_{s2}	Dimensionless coefficients in equation for c_s (equation 20)	---
c_β	Dimensionless coefficient in equation for β (equation 13)	---
c_μ	Dimensionless coefficient used in equations 33, 34, and 35	---

LIST OF SYMBOLS (Continued)

Symbol(s)	Definition	Units
c'_μ	Dimensionless coefficient used in equation 32	---
C	Chezy discharge coefficient	$L^{1/2}/T$
C_c	Dimensionless culvert discharge coefficient	---
C_{sub}	Submergence coefficient for weir segment	---
C_w	Discharge coefficient for free flow over weir segment	---
d	Total depth of flow down infinitely wide inclined plane	L
d	Differential	---
f	Force or load vector	---
f_v	Factor to correct $v_{.2}$ to vertically averaged velocity, v	---
f_{1i}, f_{2i}	Residuals of depth-averaged equations of motion at node i	L^4/T^2
f'_{1i}, f'_{2i}	Residuals of depth-averaged equations of motion at node i in tangential and normal directions, respectively	L^4/T^2
f_{3i}	Residual of continuity equation at node i	L^3/T
F_1	Froude number based on discharge	---
F_2	Froude number based on $v_{.2}$	---
g	Gravitational acceleration	L/T^2
H	Total depth of water	L
$\overline{H}$	Average of total depths at nodes 1 and 3	L
H_G	Height of grass in Flood Plain Simulation Facility	L
H_i	Total depth at node i	L

Symbol(s)	Definition	Units
H_i^*	Specified total depth at node i	L
H_1, H_2	Depths used to define linear dependence of Manning's n on depth	L
H_1, H_2, H_3	Total depths at nodes 1, 2, 3, respectively	L
i	Summation index	---
i_{max}	Maximum number of iterations to be performed in quasi-Newton method	---
J	Jacobian or tangent matrix	---
J_o	Jacobian matrix at initial estimate of solution vector a	---
k	Turbulent energy	L^2/T^2
k	Summation index	---
k	Dimensionless relative roughness	---
$\tilde{k}$	Depth-averaged turbulent energy	L^2/T^2
K	Coefficient matrix	---
K	Conveyance through element side	L^3/T
K_c	Culvert coefficient	$L^{5/2}/T$
K_w	Weir coefficient	$L^{3/2}/T$
K_1, K_2, K_3	Conveyance at nodes 1, 2, 3, respectively	L^3/T
ℓ_m	Mixing length	L
ℓn	Natural logarithm	---
ℓ_x, ℓ_y	Direction cosines between outward normal to boundary and x- and y-directions, respectively	---
L	Length scale	L
L_c	Length of culvert barrel	L

LIST OF SYMBOLS (Continued)

Symbol(s)	Definition	Units
L_i	Number of elements connected to node i	---
L_w	Length of weir segment	L
m	Contraction ratio, 1 - b/B	---
M_i	Linear shape function which has value unity at node i and value zero at all other nodes	---
M^{ij}	Mass or capacity matrix	---
n	Manning roughness coefficient	$L^{1/6}$
n	Number of nodes associated with element	---
n	Number of interpolation functions	---
n_c	Manning roughness coefficient of culvert barrel	$L^{1/6}$
n_1, n_2	Values of Manning's n used to define linear dependence of n on depth	$L^{1/6}$
N_i	Shape function which has value unity at node i and value zero at all other nodes	---
$N_i^{(e)}$	Shape function which has value unity at node i in element e and value zero at all other nodes	---
N_i'	Shape function which has value unity at node i and value zero at all other nodes	---
$N_i'^{(e)}$	Shape function which has value unity at node i in element e and value zero at all other nodes, used to define isoparametric transformation	---
N_i*	Basis function defined by equation 63	---
O	Order of	---
P	Pressure head	L
q	Unit discharge	L^2/T

Symbol(s)	Definition	Units
q_{xi}, q_{yi}	Specified unit discharges in x- and y-directions, respectively	L^2/T
Q	Discharge	L^3/T
Q_c	Discharge through culvert	L^3/T
Q_{ci}	Computed discharge through culvert at node i	L^3/T
Q_i^o	Normal discharge across open boundary due to flow at node i	L^3/T
Q_i^s	Normal discharge across solid boundary due to flow at node i	L^3/T
Q_{si}^o	Normal discharge across open boundary due to directly specified flow at node i	L^3/T
Q_{si}^s	Normal discharge across solid boundary due to directly specified flow at node i	L^3/T
Q_w	Discharge over weir segment	L^3/T
Q_{wi}	Computed discharge over weir segment associated with node i	L^3/T
Q_x	Discharge at cross section x in Flood Plain Simulation Facility	L^3/T
Q_{xi}	Portion of total discharge through cross section assigned to node i by procedure discussed on pages 73 through 75	L^3/T
r	Residual load vector	---
r_i	Difference between search direction i and search direction i-1	---
R	Hydraulic radius of element side	L
R	Continuity equation residual	L/T
R_c	Hydraulic radius of culvert barrel	L
S_e	Element surface or boundary	L

LIST OF SYMBOLS (Continued)

Symbol(s)	Definition	Units
S_e^o	Portion of network boundary considered to be open	L
S_e^s	Portion of network boundary considered to be solid	L
t	Time	T
T	As superscript, transposition	---
u	Average flow velocity, q/y	L/T
u, v	Velocity components in the x- and y-directions, respectively	L/T
u*	Shear velocity for flow down infinitely wide inclined plane	L/T
$\tilde{u}^{(e)}$	Approximation of variable u over element e	---
u_i	Velocity component in x_i-direction	L/T
$u_i^{(e)}$	Value of variable u at node i of element e	---
u^n	Variable u at iteration n	---
U	Vector defined by equation 61	---
U, V	Depth-averaged velocity components in x- and y-directions, respectively	L/T
U*	Bed shear velocity, $\sqrt{c_f}\,U$	L/T
U_i, V_i	Depth-averaged velocity components at node i in x- and y-directions, respectively	L/T
U_i^*, V_i^*	Specified depth-averaged velocity components at node i in x- and y-directions, respectively	L/T
U_o	Depth-averaged velocity component in x-direction at beginning of time step	L/T
$\bar{v}$	Vertically averaged velocity in Flood Plain Simulation Facility	L/T

Symbol(s)	Definition	Units
$v_{.2}$	Point velocity measured 0.2 of depth below water surface	L/T
W	Characteristic wind velocity at reference elevation above water surface	L/T
W_{min}	Wind speed below which surface-shear-stress coefficient is constant	L/T
x	Distance	L
x	Cross section number in Flood Plain Simulation Facility	L
(x,y)	Cartesian coordinates in positive east and north directions, respectively	(L,L)
x_i	Cartesian coordinate i	L
(x_i,y_i)	Coordinates of node i to be adjusted by smoothing during automatic triangulation	(L,L)
$(x_i^{(e)},y_i^{(e)})$	Global coordinates of node i of element e	(L,L)
(x_{kj},y_{kj}), $(x_{k\ell},y_{k\ell})$	Coordinates of nodes j and ℓ in element k connected to node i	(L,L)
(x_1,y_1), (x_3,y_3)	Coordinates of corner nodes adjacent to corner node which is to be removed during automatic triangulation	(L,L)
(x_2,y_2)	Coordinates of vertex (corner node) to be removed during automatic triangulation	(L,L)
(x_4,y_4)	Coordinates of new node formed during automatic triangulation	(L,L)
y	Depth of flow	L
y	Distance above bed	L
z	Distance above bed	L
z_b	Bed elevation	L
z_c	Crest elevation of weir segment	L

LIST OF SYBMOLS (Continued)

Symbol(s)	Definition	Units
z_c	Ceiling elevation	L
z_e^h	Headwater energy-head elevation	L
z_{inv}	Invert elevation at culvert inlet	L
z_s^h	Headwater elevation	L
z_s^t	Tailwater elevation	L
α	Coefficient defined in equation 78	1/T
β	Momentum-correction coefficient	---
β_o	Dimensionless coefficient in equation for β (equation 13)	---
β_{uu}, β_{uv}, β_{vu}, β_{vv}	Momentum-correction coefficients	---
β_1	Coefficient defined by equation 79	L/T^2
β_2	Coefficient defined by equation 82	---
β_3	Coefficient defined by equation 83	L/T
γ	Coefficient used in equations 30 and 31	T/L^3
δ	Angle between positive x-direction and tangent to boundary at node i	---
δ_i	Search direction i-1 for solution vector a	---
Δa_i	Change in solution vector a between iteration i and iteration i+1	---
Δa_i	Search direction i for solution vector a	---
Δa_o	Initial search direction for solution vector a	---
ΔH	Difference between total depth at node 3 and total depth at node 1	L
$\Delta \ell$	Length of diagonal of finite-difference cell	L

Symbol(s)	Definition	Units
Δt	Time increment	T
Δu^n	Change in variable u between iteration n and iteration n+1	---
Δx	Grid interval	L
ε	Dissipation rate of turbulent energy	L^2/T^3
ε	Coefficient used to control degree of discontinuity in equation 63	T
$\tilde{\varepsilon}$	Depth-averaged dissipation rate of turbulent energy	L^2/T^3
ζ	Vorticity, defined by equation 7	L/T
ζ	Expression defined on page 74	---
η_o	Dimensionless expression used in table 2, $\eta\eta_i$	---
θ	Weighting coefficient used in equation 76	---
κ	Constant of von Karman	---
ν	Kinematic eddy viscosity	L^2/T
$\tilde{\nu}$	Depth-averaged kinematic eddy viscosity	L^2/T
ν_{ij}	Component (i,j) of kinematic-eddy-viscosity tensor	L^2/T
$\tilde{\nu}_o$	Minimum depth-averaged kinematic eddy viscosity	L^2/T
$\tilde{\nu}_o$	Base depth-averaged kinematic eddy viscosity	L^2/T
ν^v	Kinematic eddy viscosity in vertical direction	L^2/T
$\tilde{\nu}^v$	Average kinematic eddy viscosity in vertical direction	L^2/T

LIST OF SYMBOLS (Continued)

Symbol(s)	Definition	Units
$\tilde{\nu}_{xx}$, $\tilde{\nu}_{xy}$, $\tilde{\nu}_{yx}$, $\tilde{\nu}_{yy}$	Components of depth-averaged-kinematic-eddy-viscosity tensor	L^2/T
(ξ,η)	Local coordinates	---
(ξ_i,η_i)	Local coordinates of node i	---
ξ_o	Dimensionless expression used in table 2, $\xi\xi_i$	---
ρ	Density of water	M/L^3
ρ_a	Density of air	M/L^3
ρ_i	Expression defined by step 4 on page 58	---
σ_t	Turbulent Prandtl number	---
Σ	Summation	---
Σ_e	Summation over all elements	---
τ_x^b, τ_y^b	Components of bottom stress (friction) in x- and y-directions, respectively	$M/(LT^2)$
τ_x^c, τ_y^c	Components of ceiling stress in x- and y-directions, respectively	$M/(LT^2)$
τ_x^s, τ_y^s	Components of surface stress (wind) in x- and y-directions, respectively	$M/(LT^2)$
τ_{xx}, τ_{xy}, τ_{yx}, τ_{yy}	Components of depth-averaged effective-stress tensor	$M/(LT^2)$
ϕ	Latitude	---
ϕ	Coefficient used in equation 17	L/T^2
ψ	Stream function, defined by equation 6	L^3/T
ψ	Angle between direction of wind and positive x-axis	---
ω	Magnitude of angular velocity of Earth	T^{-1}
ω	Vorticity	L/T

Symbol(s)	Definition	Units
ω	Underrelaxation factor	---
ω	Weighting factor used in automatic triangulation	---
Ω	Coriolis parameter, $2\omega\sin\phi$	T^{-1}
Ω	Domain	---
∂	Partial differential	---
$\int$	Integral	---
[ ]	Matrix	---
[ ]	Vector	---
| |	Absolute value	---
| |	Determinant	---
$\sqrt{\ }$	Square root	---

INTRODUCTION

The project "Two-Dimensional Finite-Element Hydraulic Modeling of Bridge Crossings" was conducted by the U.S. Geological Survey in cooperation with the Federal Highway Administration (FHWA) to develop an accurate, efficient, easy-to-use finite-element surface-water flow model for use in analyzing highway crossings of rivers and flood plains. An additional purpose was to develop a model with capabilities greater than those of the two-dimensional finite-element model developed for the FHWA in 1975 (Tseng, 1975a, 1975b).

The two-dimensional finite-element approach to the hydraulic analysis of highway crossings of flood plains has advantages over the more common one-dimensional analysis when lateral variations in water-surface elevation and flow distribution are significant. The finite-element method is ideally suited to simulating two-dimensional flow over complex topography having spatially variable resistance. A two-dimensional finite-element surface-water flow model with depth and vertically averaged velocity components as dependent variables allows the user great flexibility in defining geometric features such as the boundaries of a water body, channels, islands, dikes, and embankments. The user of the model is able to use a fine network in regions where geometric or flow gradients are large and a coarse network in regions where geometry and flow are more nearly uniform. A two-dimensional finite-element surface-water flow model eliminates the need to use empirical coefficients other than bottom-resistance coefficients in simulating flow through

constrictions. In addition, the introduction of boundary conditions is easily handled in the finite-element approach.

This report summarizes the work done in developing the finite-element surface-water modeling system, FESWMS-2DH. FESWMS-2DH consists of three programs: a data-input module, DINMOD; a hydrodynamic flow module, FLOMOD; and an analysis-of-output module, ANOMOD.

The preprocessor, DINMOD, generates a two-dimensional finite-element network for use by FLOMOD. In particular, DINMOD edits input data, plots the finite-element network, and orders elements to permit an efficient solution. DINMOD also is capable of automatic network generation and refinement.

FLOMOD is capable of simulating steady or unsteady two-dimensional flow in the horizontal plane. The vertically integrated equations of motion and continuity are solved for the depth-averaged velocity components and depth at the node points of the finite-element network. The model takes into account bed friction, turbulent stresses, wind stresses, and the Coriolis force. Flow over weirs (such as highway embankments) and through culverts can be simulated. The effects of vertical nonuniformity of the flow may be taken into account by the use of momentum-correction coefficients.

The postprocessor, ANOMOD, uses output from FLOMOD to generate plots of velocity or unit-discharge vectors and ground-surface-elevation or water-surface-elevation contours. ANOMOD also generates time-history plots at node points or cross-section plots at a

specified time of velocity, unit discharge, or water-surface elevation.

A large number of alternative model components were tested during the project. Also, new model features and capabilities were added to FESWMS-2DH. These components and features are listed in table 1.

The following model components are discussed under the heading of equation formulation in this report: conservative and nonconservative primitive formulations, velocity and unit-discharge formulations, initial and boundary conditions for primitive-equation formulations, wave-equation and vorticity-stream-function formulations, momentum-correction coefficients, bed shear stress, surface shear stress, lateral stresses, weir flow and roadway overtopping, and bridge/culvert flow. Under the heading of application of the finite-element method to the shallow-water equations are discussed interpolation functions and elements, solution methods, numerical integration, the solution of nonlinear algebraic equations, the solution of linear algebraic equations, and the finite-element equations. The following features of the modeling system FESWMS-2DH are discussed: the graphic output standard, the data input module DINMOD (error checking, automatic network generation, network refinement, and element resequencing), the depth-averaged flow module FLOMOD (error checking, automatic boundary adjustment, and the continuity norm), and the output analysis module ANOMOD.

Sections of the report are devoted to the application of FESWMS-2DH to data from the Geological Survey's Flood Plain Simulation

Table 1. Model features tried in FESWMS-2DH.

Model feature	Tried	Used	Not used
Conservative formulation	×	×	
Nonconservative formulation	×		×
Velocity formulation	×	×	
Unit-discharge formulation	×		×
Wave-equation formulation	×		×
Vorticity-stream-function formulation	×		×
Momentum-correction coefficients	×	×	
Bed shear stress			
Chezy discharge coefficient	×	×	
Manning's roughness coefficient	×	×	
Bed-slope correction factor	×	×	
Variation with flow depth	×	×	
Surface shear stress	×	×	
Lateral stresses			
Constant eddy viscosity	×	×	
Eddy viscosity function of friction velocity	×	×	
k-ε model	×		×
Weir flow (roadway overtopping)	×	×	
Bridge/culvert flow			
One-dimensional	×	×	
Two-dimensional	×	×	

Table 1. Model features tried in FESWMS-2DH (continued).

Model feature	Tried	Used	Not used
Element types			
Six-node triangles	×	×	
Eight-node quadrilaterals	×	×	
Nine-node quadrilaterals	×	×	
Curved-sided elements	×	×	
Solution methods			
Mixed interpolation	×	×	
Wave-equation approach	×		×
Dissipative Galerkin approach	×		×
Numerical integration			
Gaussian quadrature	×	×	
Nodal integration	×		×
Solution of nonlinear algebraic equations			
Newton iteration	×	×	
Quasi-Newton iteration	×	×	
Solution of linear algebraic equations			
Banded-storage scheme	×		×
Partitioned-block skyline-storage scheme	×		×
Frontal scheme	×	×	
Conjugate-gradient scheme	×		×

Table 1. Model features tried in FESWMS-2DH (continued).

Model feature	Tried	Used	Not used
Finite-element expressions for residuals			
Integration by parts of convective terms	×	×	
Integration by parts of pressure terms	×	×	
Boundary and special conditions			
Essential depth boundary conditions	×	×	
Natural depth boundary conditions	×	×	
Essential velocity boundary conditions	×	×	
Essential unit-discharge boundary conditions	×	×	
Distribution of total discharge on basis of conveyance	×	×	
Slip boundary conditions	×	×	
No-slip boundary conditions	×	×	
Correct computation of zero normal discharge at solid boundaries without smooth boundaries	×	×	
GKS graphics	×	×	
DINMOD features			
Inch-pound or metric units	×	×	
Extensive checking of input data	×	×	
Interpolation of nodal coordinates along straight line segments	×	×	
Automatic network generation	×	×	

Table 1. Model features tried in FESWMS-2DH (continued).

Model feature	Tried	Used	Not used
Automatic network refinement	×	×	
Element resequencing by the minimum frontgrowth method	×	×	
Element resequencing by the level-structure method	×	×	
Plotting of network and ground-surface-elevation contours	×	×	
FLOMOD features			
Inch-pound or metric units	×	×	
Extensive checking of input data	×	×	
Automatic adjustment of network boundary	×	×	
Computation of flow across specified cross sections	×	×	
Computation of continuity norms	×	×	
ANOMOD features			
Inch-pound or metric units	×	×	
Extensive checking of input data	×	×	
Plotting of finite-element network	×	×	
Plotting of velocity or unit-discharge vectors	×	×	
Plotting of ground-surface-elevation contours	×	×	
Plotting of water-surface-elevation contours	×	×	
Plotting of flow-check lines	×	×	

Table 1. Model features tried in FESWMS-2DH (continued).

Model feature	Tried	Used	Not used
Plotting of time-histories	×	×	
Plotting of contours of differences of water-surface elevations	×	×	
Plotting of data at cross sections	×	×	

Facility, the use and calibration of FESWMS-2DH (data collection and analysis, network design, and model adjustment, including calibration), and the use of FESWMS-2DH by the highway industry (operational potential of FESWMS-2DH, training, future possible improvements to FESWMS-2DH, and software maintenance). References are given in a final section.

A list of factors for converting inch-pound units to metric units is provided at the front of the report. In this report, "sea level" refers to the National Geodetic Vertical Datum of 1929 (NGVD of 1929)—a geodetic datum derived from a general adjustment of the first-order level nets of both the United States and Canada, formerly called "Mean Sea Level of 1929." The use of brand names in this report is for identification purposes only and does not imply endorsement by the Federal Highway Administration or the Geological Survey.

EQUATION FORMULATION

Several related sets of equations can be used to describe steady and unsteady two-dimensional surface-water flow in the horizontal plane.

We discuss below several formulations of the flow equations considered during this study. These include the primitive shallow-water equations in conservative and nonconservative form, velocity and unit-discharge formulations, a wave-equation formulation, and a vorticity-stream-function formulation.

Conservative and Nonconservative Primitive Formulations

The equations of two-dimensional surface-water flow in the horizontal plane consist of three nonlinear partial-differential equations. In conservative form, the equations of motion in the x- and y-directions are (Pinder and Gray, 1977, p. 262-269)

$$\frac{\partial}{\partial t}(HU) + \frac{\partial}{\partial x}(\beta_{uu}HUU) + \frac{\partial}{\partial y}(\beta_{uv}HUV) + gH\frac{\partial z_b}{\partial x} + \frac{g}{2}\frac{\partial H^2}{\partial x} - \Omega HV + \frac{1}{\rho}\left[\tau_x^b - \tau_x^s - \frac{\partial}{\partial x}(H\tau_{xx}) - \frac{\partial}{\partial y}(H\tau_{xy})\right] = 0 \qquad (1)$$

and

$$\frac{\partial}{\partial t}(HV) + \frac{\partial}{\partial x}(\beta_{vu}HVU) + \frac{\partial}{\partial y}(\beta_{vv}HVV) + gH\frac{\partial z_b}{\partial y} + \frac{g}{2}\frac{\partial H^2}{\partial y} + \Omega HU + \frac{1}{\rho}\left[\tau_y^b - \tau_y^s - \frac{\partial}{\partial x}(H\tau_{yx}) - \frac{\partial}{\partial y}(H\tau_{yy})\right] = 0 , \qquad (2)$$

respectively, and the continuity equation is

$$\frac{\partial H}{\partial t} + \frac{\partial}{\partial x}(HU) + \frac{\partial}{\partial y}(HV) = 0 \quad , \tag{3}$$

where x, y = Cartesian coordinates in the positive east and north directions, respectively,

t = time,

U, V = depth-averaged velocity components in the x- and y-directions, respectively,

H = total depth of water,

$\beta_{uu}, \beta_{uv}, \beta_{vu}, \beta_{vv}$ = momentum-correction coefficients,

z_b = bed elevation,

ρ = density of water (assumed constant),

$\Omega = 2\omega \sin \phi$ = Coriolis parameter,

ω = magnitude of the angular velocity of the Earth,

ϕ = latitude,

g = gravitational acceleration,

$\tau_{xx}, \tau_{xy}, \tau_{yx}, \tau_{yy}$ = components of depth-averaged effective-stress tensor,

τ_x^s, τ_y^s = components of surface stress (wind) in the x- and y-directions, respectively, and

τ_x^b, τ_y^b = components of bottom stress (friction) in the x- and y-directions, respectively.

Equations 1 through 3 are commonly referred to as the shallow-water equations, and the formulation given in equations 1 through 3

is called the primitive formulation. These equations are obtained from the three-dimensional Reynolds equations for turbulent flow by integrating with respect to the water depth under the assumption of hydrostatic pressure and by making simplifying assumptions regarding the nonlinear terms.

The first three terms of equations 1 and 2 are inertial-force terms, the first of the three representing temporal acceleration and the second and third representing convective acceleration. The momentum-correction coefficients result from the vertical integration of the equations of motion and account for the fact that when the vertical velocity profile is not uniform, the integral of the product of two velocity profiles is not equal to the product of the integrals. The fourth and fifth terms represent the pressure force due to the water-surface gradient. The sixth term represents the Coriolis force, an inertial force representing the effect of the Earth's rotation. The seventh and eighth terms in equations 1 and 2 represent bottom and surface stresses, respectively.

The ninth and tenth terms represent the combined effect of viscous stresses and Reynolds stresses. Many authors assume that the values of the momentum-correction coefficients are unity and include the effect of momentum transfers due to the vertical velocity distribution in these effective-stress terms (Wang and Connor, 1975, p. 64; Lean and Weare, 1979, p. 18). Some authors (Pritchard, 1971, p. 30-32; Schaffranek, 1976, p. 51) ignore the Reynolds-stress terms and handle the effect of the vertical velocity shear in the depth-

averaged equations by using values of the momentum-correction coefficients which are greater than unity.

Many authors express the effective stresses in terms of the mean-flow variables by using Boussinesq's eddy-viscosity concept, which assumes that momentum transfers due to turbulence and, possibly, the vertical nonuniformity of velocity are proportional to the mean-velocity gradients. The coefficients of proportionality are called eddy viscosities.

Equation 3 states that the change in storage in an infinitesimally small control volume accounts for the net flux of mass into or out of the control volume.

Equations 1 and 2 may be converted to nonconservative form by the use of equation 3 and the assumption that the values of the momentum-correction coefficients are unity:

$$\frac{\partial U}{\partial t} + U\frac{\partial U}{\partial x} + V\frac{\partial U}{\partial y} + g\frac{\partial H}{\partial x} + g\frac{\partial z_b}{\partial x} - \Omega V - \frac{1}{\rho H}\left[\frac{\partial}{\partial x}(H\tau_{xx}) + \frac{\partial}{\partial y}(H\tau_{xy}) + \tau_x^s - \tau_x^b\right] = 0 \qquad (4)$$

and

$$\frac{\partial V}{\partial t} + U\frac{\partial V}{\partial x} + V\frac{\partial V}{\partial y} + g\frac{\partial H}{\partial y} + g\frac{\partial z_b}{\partial y} + \Omega U - \frac{1}{\rho H}\left[\frac{\partial}{\partial x}(H\tau_{yx}) + \frac{\partial}{\partial y}(H\tau_{yy}) + \tau_y^s - \tau_y^b\right] = 0 . \qquad (5)$$

The systems of equations 1, 2, and 3, and 4, 5, and 3 were both tested in the flow model, FLOMOD. The first system was found to give slightly better results and is used in the final version of FLOMOD.

Velocity and Unit-Discharge Formulations

A variant of the primitive shallow-water equations based on unit discharges is used by Norton and King (1973), Norton and others (1973), King and Norton (1978), and Withum and others (1979). The dependent variables are the unit discharges, UH and VH, and the depth, H. King and Norton (1978, p. 2.82) state that the advantages of this formulation include ease of representation of discharge boundary conditions and linearization of the continuity equation. Withum and others (1979, p. 703) mention the ease of ensuring the continuity of mass and momentum transfer across interelement boundaries. In general, the use of the dependent variables that vary the least spatially gives the best approximation. Thus, it has been observed by Teeter and McAnally (1981, p. 255) and the writers that a finite-element model using the unit-discharge formulation is much more sensitive to cross-channel depth changes and low eddy-viscosity values than a finite-element model formulated in terms of velocities. In a model with velocities as dependent variables, unit-discharge boundary conditions are easily handled at discharge boundaries by incorporating the equations UH = constant and VH = constant into the process for handling the nonlinearities of the equations. On the basis of these observations and extensive

numerical tests, the velocity formulation was selected as preferable to the unit-discharge formulation for river-flood-plain modeling and is used in FLOMOD.

Initial and Boundary Conditions for Primitive-Equation Formulations

Both initial and boundary conditions must be specified to solve the unsteady shallow-water equations. To obtain a solution to the unsteady equations, both the water depth and the depth-averaged x- and y-velocity components must be specified as initial conditions throughout the entire solution region. Boundary conditions must be specified around the entire boundary for the duration of the simulation. The required boundary information depends on the type of boundary and the flow condition. Two types of boundaries are commonly encountered in surface-water flow problems: the solid, or no-flux, boundary and the open boundary.

Solid boundaries define geometric features such as natural shorelines, highway embankments, jetties, or seawalls. The flow across such boundaries generally must equal zero. In addition, either the tangential velocity or tangential stress must be specified. At open boundaries, flow is allowed to enter or leave the system. Open boundaries usually represent rivers flowing into or out of the area under study or a connection with an open water body such as a lake, bay, or ocean.

For subcritical flow conditions at an open boundary, either the unit discharge (or velocity) normal to the boundary or the

water depth (normal stress), in addition to either the tangential unit discharge (or velocity) or the tangential (shear) stress, must be specified. When the Coriolis term is significant in tidal applications, problems can arise by specifying water-surface elevations across an open boundary. Walters and Cheng (1980, p. 192, 193) and Jamart and Winter (1982, p. 168-172) solve this problem by specifying water-surface elevation at only one point on the open boundary and the direction of the velocity across the entire open boundary. For supercritical flow conditions at an open boundary, both the normal unit discharge (or velocity) and depth must be specified on inflow boundaries along with either the tangential unit discharge (or velocity) or the tangential (shear) stress; on outflow boundaries, only the tangential (shear) stress must be specified.

In FLOMOD, tangential (shear) stresses along open boundaries are assumed to equal zero. Along solid boundaries, either tangential stresses are assumed to equal zero (a slip condition) or the velocity is set to zero (a no-slip condition). When a slip condition is specified along solid boundaries, velocities at boundary nodes are adjusted so that there is zero net flow across the boundary. When a no-slip condition is prescribed, the requirement of zero flow across the boundary is automatically satisfied.

In modeling subcritical riverine flows, the x- and y-direction unit discharges are usually prescribed at inflow boundaries and the water-surface elevation (from which depth is determined by subtracting

the ground-surface elevation) is prescribed at outflow boundaries. Velocity components may also be specified at inflow boundaries. A slip condition is generally prescribed along all solid boundaries.

Wave-Equation and Vorticity-Stream-Function Formulations

Another variant of the system of equations 1 through 3 involves replacing the primitive continuity equation by a wave continuity equation. The reasons for doing this and the numerical results obtained by using wave-equation schemes are discussed on pages 51 through 53.

In the case of steady flow, it is possible to apply a vorticity-stream-function approach to two-dimensional surface-water flow. This is of considerable interest because it is possible to handle as steady state most problems involving flood-plain constrictions. Franques (1971) and Franques and Yannitell (1974) develop such an approach. They define the stream function, ψ, by

$$\frac{\partial \psi}{\partial x} = - HV \text{ and } \frac{\partial \psi}{\partial y} = HU \qquad (6)$$

and the vorticity, ζ, by

$$\zeta = \frac{\partial}{\partial y}(HU) - \frac{\partial}{\partial x}(HV) . \qquad (7)$$

By neglecting the convective term in the vorticity-transport equation, the authors obtain a nonlinear elliptic partial-differential equation

in ψ. Boundary conditions consist of constant values of ψ at solid boundaries and zero values of the normal derivative of ψ at inflow and outflow boundaries, which are assumed to be normal to the flow. Water-surface elevations are obtained from Bernoulli's equation.

Neglecting the convective term in the vorticity-transport equation is equivalent to neglecting the convective terms in the primitive equations of motion. In modeling constricted flow in the Flood Plain Simulation Facility, it was found that neglecting the convective terms in the equations of motion caused significant underestimation of backwater. In addition, the jet and recirculation zones downstream from the constriction do not appear when the convective terms are omitted.

Momentum-Correction Coefficients

The momentum-correction coefficients (β_{uu}, β_{uv}, β_{vu}, β_{vv}) result from the vertical integration of the equations of motion and account for the fact that when the vertical velocity profile is not uniform, the integral of the product of the two velocity profiles is not equal to the product of the integrals. The momentum-correction coefficients are defined as

$$\beta_{uu} = \frac{1}{HUU} \int_{z_b}^{z_b+H} uu \, dz \, , \tag{8}$$

$$\beta_{uv} = \beta_{vu} = \frac{1}{HUV} \int_{z_b}^{z_b+H} uv \, dz \, , \tag{9}$$

and

$$\beta_{vv} = \frac{1}{HVV} \int_{z_b}^{z_b+H} vv \, dz \ , \qquad (10)$$

in which u and v are the velocity components in the x- and y-directions, respectively. These coefficients depend on the velocity profile and are often assumed to equal unity.

If it is assumed that the velocity profile in the vertical plane can be approximately represented by the logarithmic distribution

$$u = \frac{U_*}{\kappa} \ln(z-z_b) + \text{constant} \ , \qquad (11)$$

in which U_* is the bed shear velocity equal to $\sqrt{c_f}\, U$, c_f is a dimensionless coefficient (see p. 20), and κ is von Karman's constant, the resulting momentum-correction coefficients are all equal and are given by

$$\beta = 1 + c_f/\kappa^2 \ . \qquad (12)$$

The momentum-correction coefficient in FLOMOD is computed as

$$\beta = \beta_o + c_\beta c_f \ . \qquad (13)$$

Equations 12 and 13 are equivalent when $\beta_o = 1.0$ and $c_\beta = 1/\kappa^2$. The coefficient κ has been found to equal approximately 0.4, from which $c_\beta = 6.25$. Thus, if $c_f = O(10^{-3})$, the correction $\beta - 1 = O(10^{-2})$. A constant correction factor can be specified by

setting β_o equal to the desired value and setting c_β equal to zero. The default values in FLOMOD for β_o and c_β are 1.0 and 0.0, respectively. Acceptance of these default values by the user means that the effect of any vertical nonuniformities in velocity are ignored.

Bed Shear Stress

The directional components of the bed shear stress are given by

$$\tau_x^b = \rho c_f U(U^2 + V^2)^{1/2} \left[1 + (\partial z_b/\partial x)^2 + (\partial z_b/\partial y)^2\right]^{1/2} \qquad (14)$$

and

$$\tau_y^b = \rho c_f V(U^2 + V^2)^{1/2} \left[1 + (\partial z_b/\partial x)^2 + (\partial z_b/\partial y)^2\right]^{1/2} , \qquad (15)$$

in which c_f is a dimensionless coefficient and the square-root terms involving $\partial z_b/\partial x$ and $\partial z_b/\partial y$ account for the effect of a sloping bed.

The bed-shear-stress coefficient, c_f, is computed as either

$$c_f = \frac{g}{C^2} \qquad (16)$$

or

$$c_f = \frac{gn^2}{\phi H^{1/3}} , \qquad (17)$$

where C is the Chezy discharge coefficient, n is the Manning roughness coefficient, and ϕ is a factor that equals 2.208 when

inch-pound units are being used and 1.0 when metric units are being used.

Manning roughness coefficients can be varied with depth of flow in FLOMOD. This feature is especially important when modeling flows through densely vegetated areas on river flood plains. In such areas the roughness coefficients may either increase or decrease with the depth of flow depending on the ground cover and the type and density of vegetation. Chezy coefficients, on the other hand, are assumed in FLOMOD to remain constant for all flow depths.

Values of the Chezy discharge coefficient and the Manning roughness coefficient for natural and manmade channels as well as flood plains are available in a number of references, such as Chow (1959), Barnes (1967), and Arcement and Schneider (1984). These estimates, however, have been determined under the assumption of one-dimensional flow and implicitly account for the effects of turbulence and deviations from a constant cross-sectional velocity. Since the depth-averaged flow model takes into account the horizontal variation in velocity and considers independently the effect of turbulence, values of c_f computed using coefficients based on one-dimensional-flow assumptions may be somewhat larger than they actually should be (Lee and others, 1983, p. 30-31). Since little information is available on choosing coefficients for purely depth-averaged flows, the user must estimate Chezy or Manning coefficients as best he can on the basis of available references and experience.

Surface Shear Stress

The directional components of the surface shear stress due to wind are given by

$$\tau_x^s = c_s \rho_a W^2 \cos \psi \tag{18}$$

and

$$\tau_y^s = c_s \rho_a W^2 \sin \psi \ , \tag{19}$$

in which c_s is a dimensionless surface-stress coefficient, ρ_a is the density of the air, W is a characteristic wind velocity at a reference elevation above the water surface, and ψ is the angle between the direction of the wind and the positive x-axis.

The surface-stress coefficient, c_s, has been found generally to be a function of wind speed and is computed as

$$c_s = \begin{cases} c_{s1} \times 10^{-3}, \text{ for W less than or equal to } W_{min}, \text{ and} \\ [c_{s1} + c_{s2}(W - W_{min})] \times 10^{-3}, \text{ for W greater than } W_{min} \ . \end{cases} \tag{20}$$

For wind speed in meters per second measured 10 meters above the water surface, Garratt (1977) concludes that $c_{s1} = 1.0$ and $c_{s2} = 0.067$ with $W_{min} = 4.0$ m/s. Wang and Connor (1975, p. 61) compare several relations for c_s as a function of wind speed and decide that $c_{s1} = 1.1$ and $c_{s2} = 0.0536$ with $W_{min} = 0.0$ m/s. Hicks (1972) finds that $c_{s1} = 1.0$ and $c_{s2} = 0.05$ with $W_{min} = 5.0$ m/s.

It must be remembered, however, that factors other than wind velocity may influence the value of the surface-stress coefficient. For example, Hicks and others (1974) show that as water becomes very shallow, less than 2.5 m deep, long period waves are not able to fully develop and the water surface is smoother. Under these conditions, the value of the surface-stress coefficient remains close to 1.0×10^{-3} for all wind speeds. Stratification of the air also effectively reduces the value of the surface-stress coefficient.

Equation 20 is used to compute the surface-stress coefficient in FLOMOD. The coefficients c_{s1} and c_{s2} are supplied by the user. The default values are 1.0 and 0.0, respectively.

Lateral Stresses

The lateral stress terms (τ_{xx}, τ_{xy}, τ_{yx}, τ_{yy}) that appear in the depth-averaged equations of motion include contributions from viscous stresses and turbulent stresses. Viscous stresses are typically quite small in comparison with turbulent stresses and may be safely neglected. Diffusive momentum transport supplied by the lateral stresses is an important factor in inducing horizontal circulation of steady flow. In fact, some writers claim that circulating flow driven by the main flow cannot exist when the lateral stresses are neglected (Flokstra, 1977). Therefore, although cases may exist where lateral stresses may be neglected, in general they are an important feature of depth-averaged flow computations.

Eddy Viscosities

The oldest proposal for modeling the turbulent stresses in the three-dimensional equations of motion was formulated in 1877 by Boussinesq (Schlichting, 1968, p. 544), who assumed the turbulent stresses to be proportional to the gradients of the time-mean velocities. This concept has been extended to the depth-averaged equations of motion to compute the lateral stresses due to turbulence as

$$\tau_{xx} = \rho\tilde{\nu}_{xx}\left(\frac{\partial U}{\partial x} + \frac{\partial U}{\partial x}\right) , \tag{21}$$

$$\tau_{xy} = \tau_{yx} = \rho\tilde{\nu}_{xy}\left(\frac{\partial U}{\partial y} + \frac{\partial V}{\partial x}\right) , \tag{22}$$

and

$$\tau_{yy} = \rho\tilde{\nu}_{yy}\left(\frac{\partial V}{\partial y} + \frac{\partial V}{\partial y}\right) , \tag{23}$$

in which $\tilde{\nu}_{xx}$, $\tilde{\nu}_{xy}$, and $\tilde{\nu}_{yy}$ are directional values of the eddy viscosity. Although not truly depth-averaged quantities in a mathematical sense, these eddy-viscosity coefficients are defined in such a way that they yield the proper depth-averaged turbulent stresses.

Equations 21 through 23 are used to evaluate the turbulent stresses in FLOMOD. Because of the difficulty in determining these directional components, the depth-averaged kinematic eddy viscosity

used in FLOMOD is assumed to be isotropic (that is, $\tilde{\nu}_{xx} = \tilde{\nu}_{xy} = \tilde{\nu}_{yy}$) and is denoted by $\tilde{\nu}$.

Turbulence Models

Unlike the coefficient of molecular viscosity, the eddy-viscosity coefficients are not solely a property of the fluid but depend also on the state of turbulent motion and therefore may vary significantly from one point to another in the flow or with time. If not computed from another, more advanced, model of turbulence, the values of the eddy viscosities must be obtained by measurement or estimated on the basis of experience.

In order to advance the eddy-viscosity concept initiated by Boussinesq, it is necessary to find relations describing the distribution of the eddy viscosity. The first such model was suggested by Prandtl in 1925 (Schlichting, 1968, p. 546-549) and is known as the Prandtl mixing-length hypothesis. By assuming that eddies move around in a fluid very much like molecules in a gas, an expression for two-dimensional shear-layer flows was developed which relates the kinematic eddy viscosity to the local mean-velocity gradient by

$$\nu = \ell_m^2 \left| \frac{du}{dy} \right| , \tag{24}$$

where u is the time-averaged velocity in the x-coordinate direction and ℓ_m is defined as the mixing length. The mixing length is roughly

analogous to the mean free path of a molecule in the kinetic theory of gases. - A result similar to equation 24 was obtained earlier by G. I. Taylor (Schlichting, 1968, p. 550) on the basis of his vorticity-transport theory.

The mixing length is a function of position because it depends on the state of turbulence. Von Karman (Schlichting, 1968, p. 551-553) attempted to relate ℓ_m to the mean-velocity profile by the equation

$$\ell_m = \kappa \left| \frac{du/dy}{d^2u/dy^2} \right| , \tag{25}$$

in which κ is a universal constant. Experiments have shown that κ is not a universal constant but may vary considerably, having an average value of about 0.4. Other investigators have proposed relationships describing the distribution of the mixing length for particular types of flow. However, for flows in general the mixing-length formulation is of restricted usefulness.

The mixing-length hypothesis may be extended to general flows (Rodi, 1980a, p. 18) in the form

$$\nu_{ij} = \ell_m^2 \left[\left(\frac{\partial u_i}{\partial x_j} + \frac{\partial u_j}{\partial x_i} \right) \frac{\partial u_i}{\partial x_j} \right]^{1/2} , \tag{26}$$

where the nonisotropic kinematic eddy viscosity is a function of ℓ_m and the mean-velocity gradients. But this formulation as well has been used infrequently because of the difficulty in specifying ℓ_m

for flows that are more complex than shear layers.

Von Karman's expression for the mixing length in equation 25 may be used to derive the well-known logarithmic velocity distribution. On the basis of this velocity distribution, Elder (1959) considered a flow down an infinitely wide inclined plane and derived the expression

$$\nu^v = \kappa \frac{y}{d}\left(1 - \frac{y}{d}\right) du^* \qquad (27)$$

for the vertical eddy viscosity, ν^v, where κ is von Karman's constant, y is the vertical distance from the plane's surface, d is the total depth of flow, and u* is the shear velocity. Averaging over the depth and taking κ equal to 0.4 leads to the expression

$$\tilde{\nu}^v = 0.067 du^* \qquad (28)$$

for the average kinematic eddy viscosity in the vertical direction. Experiments have shown that a similar relation exists for the transverse mixing of momentum. Values of $\tilde{\nu}/(\sigma_t du^*)$ in straight uniform channels (where σ_t is the turbulent Prandtl number) are found to generally fall between 0.1 and 0.2 (Fischer and others, 1979, p. 107-112), while curves and sidewall irregularities increase the coefficient such that values of $\tilde{\nu}/(\sigma_t du^*)$ in natural streams hardly ever fall below 0.4. For practical purposes,

$$\tilde{\nu}/(\sigma_t du^*) = 0.6 \pm 0.3 \ . \qquad (29)$$

Higher values are likely if the channel has sharp curves or rapid changes in geometry. Lean and Weare (1979) use such a formulation to determine the depth-averaged horizontal eddy viscosity in a finite-difference model of two-dimensional, horizontal flow in a rectangular channel. A similar relation is used by Falconer (1980) in a finite-difference model study of tide-induced circulatory velocity fields within narrow-entranced harbors and estuaries.

Horizontal-eddy-viscosity coefficients based on the theory of two-dimensional flow (Kraichnan, 1967; Leith, 1968) are used by Haney and Wright (1975) in a barotropic model of wind-driven circulation in a closed, rectangular basin. Two-dimensional turbulence has the property that the enstrophy (defined as one-half of the square vorticity) cascades from larger scales to smaller scales. To dissipate local enstrophy in the model, Haney and Wright introduce a nonlinear eddy viscosity of the form

$$\tilde{\nu} = \tilde{\nu}_o \left\{ 1 + \gamma \left[\left(\frac{\partial \omega}{\partial x} \right)^2 + \left(\frac{\partial \omega}{\partial y} \right)^2 \right]^{1/2} (\Delta x)^3 \right\} , \qquad (30)$$

where $\tilde{\nu}_o$ and γ are constants, ω is the vorticity, and Δx is the finite-difference grid interval. The eddy viscosity, $\tilde{\nu}$, is a monotonically increasing function of the magnitude of the vorticity gradient computed on the grid, $\tilde{\nu}_o$ is the minimum value of $\tilde{\nu}$, and γ determines the variation of $\tilde{\nu}$. Leendertse and Liu (1977) adopt a similar model for the eddy viscosity, which is written as

$$\nu = \gamma \left| \frac{\partial \omega}{\partial x} + \frac{\partial \omega}{\partial y} \right| (\Delta \ell)^3 \ , \qquad (31)$$

where $\Delta \ell = (\Delta x^2 + \Delta y^2)^{1/2}$ in which Δx and Δy are the finite-difference grid intervals in the x- and y-coordinate directions, respectively.

One of the main shortcomings of all the previously mentioned models, as pointed out by Rodi (1982, p. 45), is that they are based on the implied assumption that turbulence is in local equilibrium, which means that at each point in the flow, turbulent energy or enstrophy is dissipated at the same rate at which it is produced. Consequently, there is no influence of turbulence production at other points or at other times; the eddy viscosity will be computed to be zero whenever the velocity gradients are zero.

In order to account for transport and history effects, turbulence models have been proposed which employ transport equations for the turbulence quantities in three-dimensional flows. The simplest of these are referred to as <u>one-equation models</u>. One such group of models expresses the eddy-viscosity coefficient as a function of the locally available turbulent energy, k, and a length scale, L, characteristic of the turbulent flow. The governing system of equations is closed by introducing an expression for the transport of k and by specifying the distribution of L. The eddy viscosity is then computed as

$$\nu = c_\mu' \sqrt{k} L \ , \qquad (32)$$

where c_μ' is an empirical constant. This formula is known as the Kolmogorov-Prandtl expression (Rodi, 1980a, p. 21) and relates the eddy viscosity to the velocity scale, $\sqrt{k}$, and the length scale, L, of large-scale turbulent motion. As with the mixing-length model, the length scale must be empirically determined. Examples of various algebraic expressions for the length scale are given by Launder and Spalding (1972, p. 71-89).

One-equation models which do not make use of the eddy-viscosity concept have been devised. Bradshaw and others (1967) solve a differential equation describing the transport of turbulent shear stress in boundary-layer flows. While this equation frees the shear stress from the local mean-velocity gradient, it still requires the specification of a turbulence length scale. Nee and Kovasznay (1969) propose an equation which directly describes the transport of the kinematic eddy viscosity. As in the other one-equation models that have been discussed, a length-scale distribution must still be prescribed.

One-equation models of turbulence have been found to yield acceptable results in turbulent-flow computations, provided that a precise algebraic prescription of the length scale is available. This can rarely be done for any but boundary-layer flows, and, therefore, Prandtl's mixing-length model may often give as good an account of turbulent fluid motion at a much lower cost. The difficulty in finding widely valid equations for calculating the length scale has led to the development of models in which transport effects on

the turbulence length scale are also considered. These two-equation models have shown great promise in the fields of mechanical and aerospace engineering and have recently been used in simulating open-channel flow.

Several two-equation models using various dependent variables have been presented in the literature and are reviewed by Launder and Spalding (1972, 1974), Reynolds (1976), and Rodi (1980a, 1980b). In his state-of-the-art review, Rodi (1980a, p. 33) concludes that the two-equation model in which the dependent variables are the turbulent energy, k, and the dissipation rate of turbulent energy, ε, is perhaps the most universal and is well suited for application to hydraulic flow problems. Since, by dimensional reasoning, the dissipation rate, ε, is proportional to $k^{3/2}/L$, the parameter pair k-ε is equivalent to the pair k-L. Once the parameters k and ε have been computed, the kinematic eddy viscosity can be found (again by dimensional reasoning) as

$$\nu = c_\mu \frac{k^2}{\varepsilon} , \tag{33}$$

where c_μ is an empirically derived constant. The distribution of the parameters k and ε, and thus ν, over the flow field is computed by solving the transport equations for these variables simultaneously with those governing the mean-flow behavior.

McGuirk and Rodi (1978) use the k-ε model in calculating depth-averaged open channel flow and transport. Rastogi and Rodi

(1978) use the k-ε model to simulate both three-dimensional and depth-averaged flow and transport in open channels. Leschziner and Rodi (1979) use the k-ε turbulence model in computing three-dimensional flow in strongly-curved open channels. In adapting the k-ε model for use in computing depth-averaged open-channel flow, McGuirk and Rodi (1978) and Rastogi and Rodi (1978) assume that the local depth-averaged state of turbulence can be characterized by the turbulent energy, $\tilde{k}$, and the dissipation rate, $\tilde{\varepsilon}$, and that the eddy viscosity, $\tilde{\nu}$, used in calculating the depth-averaged turbulent stresses is related to these parameters by

$$\tilde{\nu} = c_\mu \frac{\tilde{k}^2}{\tilde{\varepsilon}} , \tag{34}$$

where, as before, c_μ is an empirical constant. Terms are also added to the transport equations to account for the production and dissipation of turbulence by bottom shear stresses.

Turbulence Models in FLOMOD

The turbulence model used in FLOMOD is based on equation 29 and therefore assumes that turbulence is in local equilibrium (that is, turbulent energy is dissipated at the same rate at which it is produced). Under the assumption that the turbulent exchange of mass and momentum are analogous, the kinematic eddy viscosity in FLOMOD is computed as

$$\tilde{\nu} = \tilde{\nu}_o + c_\mu U_\star H , \tag{35}$$

in which $U_* = \sqrt{c_f}\, U$ and c_μ is a coefficient. With $\tilde{\nu}_o = 0$ in equation 35, the depth-averaged kinematic eddy viscosity with $c_\mu = 0.6 \pm 0.3$ may not be large enough in some cases to ensure computational stability. Therefore, a base kinematic eddy viscosity, $\tilde{\nu}_o$, is included in the formulation to provide a means of increasing the eddy viscosity to a level that will provide a convergent solution. A constant value of $\tilde{\nu}$ can also be specified by setting $c_\mu = 0$ and $\tilde{\nu}_o \geq 0$.

A depth-averaged k–ε turbulence model was added to FLOMOD, and flows in curved channels and a reach of the Kankakee River were simulated. The variation of depth-averaged velocity across the channel was simulated much better by using the k–ε model than by using a constant eddy viscosity.

The k–ε model requires the solution of two additional equations at each node point (one for the transport of turbulent energy, k, and the other for the transport of the dissipation rate of turbulent energy, ε). The resulting system of nonlinear equations was quite difficult to solve. An underrelaxation factor, ω, of 0.1 was used such that at the end of the (n+1)st iteration, the new value of a solution variable, u, was computed as $u^{n+1} = u^n + \omega \Delta u^n$, where $\Delta u^n = u^{n+1} - u^n$. The solution converged quite slowly in all cases. In addition, boundary and initial conditions had a substantial effect on solution convergence.

Although the k-ε model provided good results, the difficulty and cost of obtaining a solution must be considered. FESWMS-2DH has been developed primarily to solve complicated hydraulic problems at bridge crossings. These problems generally do not require extremely accurate simulations of velocity distributions in river channels and through bridge openings. For this reason, the depth-averaged k-ε turbulence model has not been included in FLOMOD. Use of a constant kinematic eddy viscosity or the kinematic eddy viscosity model given by equation 35 has been found to provide excellent solutions to the types of problems for which the modeling system has been developed.

Weir Flow and Roadway Overtopping

Because of the assumptions made in the depth-averaging process, equations 1, 2, and 3 cannot accurately simulate flow over weirs. Instead, flow over weirs or weir-type structures, such as roadway embankments, is computed in a one-dimensional sense by dividing such structures into weir segments, each of which connects two boundary nodes (one on either side of the weir) or allows flow to exit the system at a single boundary node. Flow over each weir segment is computed as

$$Q_w = K_w(z_e^h - z_c)^{3/2} \quad , \tag{36}$$

in which K_w is a weir coefficient, z_e^h is the headwater energy-head elevation, and z_c is the crest elevation of the weir segment (assumed constant along the segment). The weir coefficient is

computed as

$$K_w = C_{sub} C_w L_w \sqrt{g} \quad , \tag{37}$$

in which C_w is a discharge coefficient for free flow over the weir segment, C_{sub} is a coefficient that adjusts for submergence of the weir segment by tailwater, and L_w is the length of the weir segment. The submergence coefficient, C_{sub}, is automatically determined.

Headwater and tailwater elevations are taken from the two boundary nodes connected by the weir with the higher elevation being that of headwater and the lower elevation that of tailwater. Flow is assumed to leave the system at the headwater boundary node and to re-enter the system at the tailwater boundary node. When only one node is connected to the weir segment, free flow is assumed and exits the system at the boundary node.

Bridge/Culvert Flow

Flows through bridges and culverts can be modeled as either one- or two-dimensional flow. If the bridge or culvert is small in relation to the channel or flood plain, it may be more appropriate to model the structure in a one-dimensional sense. If the bridge is very wide with substantial variations in water-surface elevations across the opening, or large lateral velocities, or both, a two-dimensional approach is probably warranted.

One-Dimensional Bridge/Culvert Flow

One-dimensional flow through a small bridge or a culvert is computed using an empirical equation developed for flow through culverts. Each culvert is defined by its physical characteristics and a set of empirical coefficients and is considered either to connect two boundary nodes of the finite-element network or to allow flow to exit the system at a single boundary node.

Discharge through a culvert is computed under the assumption of either type 4 or type 5 flow as described by Bodhaine (1968). In type 4 flow, the culvert is submerged by both headwater and tailwater. In type 5 flow (inlet control), the top edge of the culvert entrance contracts the flow in a manner similar to a sluice gate, and the culvert barrel flows partly full at a depth less than critical. The culvert discharge is computed as

$$Q_c = \begin{cases} K_c(z_s^h - z_s^t)^{1/2}, \text{ for type 4 flow, and} \\ K_c(z_s^h - z_{inv})^{1/2}, \text{ for type 5 flow,} \end{cases} \tag{38}$$

in which K_c is a culvert coefficient that depends on the type of flow, z_s^h is the headwater elevation, z_s^t is the tailwater elevation, and z_{inv} is the invert elevation at the culvert inlet. For type 4 flow,

$$K_c = C_c A_c \left(\frac{2g}{1 + \frac{29\, C_c^2 n_c^2 L_c}{R_c^{4/3}}} \right)^{1/2}, \tag{39}$$

in which C_c is the culvert discharge coefficient, A_c is the cross-sectional area of the culvert, n_c is the Manning roughness coefficient of the culvert barrel, L_c is the length of the culvert barrel, and R_c is the hydraulic radius of the culvert barrel. For type 5 flow, the culvert coefficient is computed as

$$K_c = C_c A_c \sqrt{2g} \quad . \tag{40}$$

Headwater and tailwater elevations are taken from the two boundary nodes connected by the culvert with the headwater elevation the higher of the two. Flow is assumed to leave the system at the headwater boundary node and to re-enter the system at the tailwater boundary node. When only one node is assigned to the culvert, flow is assumed to leave the system at that node and not return.

Two-Dimensional Bridge/Culvert Flow

Two-dimensional flow through a bridge or culvert is modeled exactly as ordinary flow when the water surface is not in contact with the top of the bridge or culvert opening (unconfined flow). When the water surface is in contact with the top of the opening (hereafter referred to as the "ceiling"), confined, or pressure, flow conditions exist. The depth-averaged flow equations are modified at node points where this condition occurs and a pressure head rather than depth is computed. While it is usually not practical to directly model the effect of piles and piers, their effect on flow can be indirectly accounted for by increasing bed-friction coefficients within the bridge opening.

Depth-averaged confined flow through a bridge or culvert is modeled by specifying a "ceiling" elevation at node points within the opening. When the water surface is in contact with the ceiling, pressure flow exists and the governing depth-averaged flow equations are modified to account for this. The equations of motion become

$$H\frac{\partial U}{\partial t} + \frac{\partial}{\partial x}(\beta HUU) + \frac{\partial}{\partial y}(\beta HUV) + g\frac{\partial}{\partial x}(HP-H^2/2) + gP\frac{\partial z_b}{\partial x} - g(P-H)\frac{\partial z_c}{\partial x}$$

$$- \Omega HV + \frac{1}{\rho}\left[\tau_x^b + \tau_x^c - \frac{\partial}{\partial x}(H\tau_{xx}) - \frac{\partial}{\partial y}(H\tau_{xy})\right] = 0 \qquad (41)$$

in the x-direction, and

$$H\frac{\partial V}{\partial t} + \frac{\partial}{\partial x}(\beta HVU) + \frac{\partial}{\partial y}(\beta HVV) + g\frac{\partial}{\partial y}(HP-H^2/2) + gP\frac{\partial z_b}{\partial y} + g(P-H)\frac{\partial z_c}{\partial y}$$

$$+ \Omega HU + \frac{1}{\rho}\left[\tau_y^b + \tau_y^c - \frac{\partial}{\partial x}(H\tau_{yx}) - \frac{\partial}{\partial y}(H\tau_{yy})\right] = 0 \qquad (42)$$

in the y-direction, and the continuity equation becomes

$$\frac{\partial}{\partial x}(HU) + \frac{\partial}{\partial y}(HV) = 0 \ , \qquad (43)$$

in which P is the pressure head, z_c is the ceiling elevation, $H = z_c - z_b$, and τ_x^c and τ_y^c are the components of ceiling shear stress in the x- and y-directions, respectively. The dependent variables in the confined flow case are U, V, and P. The effect of increased frictional resistance due to the contact with the ceiling is described by the ceiling-shear-stress term. The directional components of

ceiling shear stress are computed as

$$\tau_x^c = \bar{\rho} c_f U(U^2 + V^2)^{1/2} \left[1 + (\partial z_c/\partial x)^2 + (\partial z_c/\partial y)^2\right]^{1/2} \qquad (44)$$

and

$$\tau_y^c = \rho c_f V(U^2 + V^2)^{1/2} \left[1 + (\partial z_c/\partial x)^2 + (\partial z_c/\partial y)^2\right]^{1/2} , \qquad (45)$$

in which c_f is considered to be the same dimensionless friction coefficient used to model the bed shear stress. The bracketed term involving $\partial z_c/\partial x$ and $\partial z_c/\partial y$ accounts for the increased resistance due to a sloping ceiling. Note that when confined flow exists, surface stress due to wind is not considered.

APPLYING THE FINITE-ELEMENT METHOD TO THE SHALLOW-WATER EQUATIONS

The finite-element method is a numerical procedure for solving the differential equations encountered in problems of physics and engineering. Although it was originally devised to analyze structural systems, the finite-element method has developed into an effective tool for evaluating a wide range of problems in the field of continuum mechanics. This development has been encouraged primarily by the continued advancement of high-speed digital computers, which provide a means of rapidly performing the many calculations involved in applying the method. Although application of the finite-element method to surface-water flow problems has been relatively recent, a significant amount of literature on the subject has already emerged. A detailed review of literature on the finite-element solution of the equations of two-dimensional surface-water flow in the horizontal plane is presented by Lee and Froehlich (1986).

FESWMS-2DH uses the Galerkin finite-element method to solve the system of differential equations governing two-dimensional surface-water flow in the horizontal plane. The time derivatives in the flow equations are handled by an implicit finite-difference scheme. In the finite-element approach, the physical region of interest is divided into a finite number of subregions called elements. An element may be either a triangle or a quadrilateral and is defined by a finite number of nodal points situated along its boundary or in its interior. Values of the dependent variables are uniquely defined within each element in terms of their values at the element's

node points by a set of interpolation functions.

The method of weighted residuals is then applied to the governing differential equations to form a set of finite-element equations for each element. Approximations of the dependent variables in terms of the interpolation functions and nodal unknowns are substituted into the governing equations, which are generally not satisfied exactly, to form residuals. The residuals are required to vanish in a weighted-average sense over the entire solution domain. In Galerkin's method, the weighting functions are chosen to be the same as those used to interpolate values of the dependent variables within each element. By requiring the weighted residuals to vanish over the entire solution domain, the finite-element equations take on an integral form. Coefficients are integrated numerically, and all the element, or local, contributions are assembled to obtain the complete, or global, set of equations. This set of algebraic equations is solved simultaneously for the nodal values of the dependent variables. Additional details on the finite-element method can be found in Pinder and Gray (1977), Zienkiewicz (1977), Becker and others (1981), Carey and Oden (1983), Lee and Froehlich (1986, p. 5-10), and the FESWMS-2DH users manual.

Interpolation Functions and Elements

The interpolation functions used in the finite-element method are typically low-order polynomials and depend on the type of elements used to represent the solution domain. The most commonly used two-

dimensional elements are triangles and quadrilaterals. The linear variation of a quantity within such an element can be expressed in terms of the values of the quantity at the corners (vertices) of the element. The quadratic variation of a quantity can be expressed in terms of the values of the quantity at the element vertices and at points along the sides of the element (usually at the midway points between the corner nodes) and possibly also at the center of the element in the case of the quadrilateral. For these elements, the interpolated quantity is continuous between elements and is said to have C^o-continuity. If the first derivatives are continuous, the interpolated quantity is said to have C^1-continuity (Carey and Oden, 1983, p. 5, 6, 25, 36). Such higher order interpolation is sometimes useful.

The model FESWMS-2DH allows the use of six-node triangles, eight-node "serendipity" quadrilaterals, and nine-node "Lagrangian" quadrilaterals for representing velocity components (fig. 1). Depth is represented using linear triangles or bilinear quadrilaterals. In general, nine-node quadrilaterals are preferred to eight-node quadrilaterals for reasons of accuracy.

At times, it may be more convenient to represent relatively complex geometric features with elements having curved sides. The essential idea underlying the concept of curved-sided elements is the mapping or transformation of a simple "parent" element defined in a local-coordinate system to the desired curved shape in the global coordinate system as shown in figure 2. The transformation

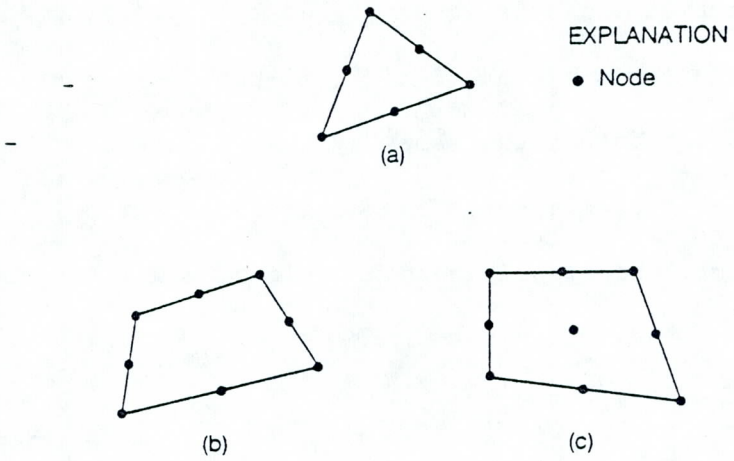

Figure 1. Examples of the types of two-dimensional elements used in FESWMS-2DH: (a) a six-node triangle, (b) an eight-node "serendipity" quadrilateral, and (c) a nine-node "Lagrangian" quadrilateral.

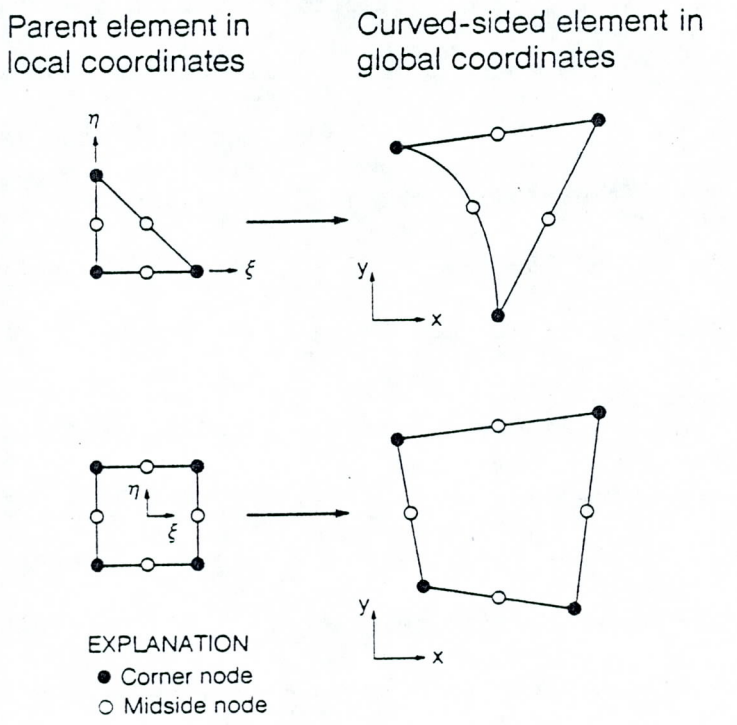

Figure 2. Two-dimensional "mapping" of some elements.

from straight to curved sides is accomplished by expressing the global (x,y)-coordinates in terms of the local (ξ,η)-coordinates using shape or interpolation functions in the same way that a dependent variable is interpolated within an element. Such a transformation is called isoparametric. Thus, the global coordinates can be written as

$$x = \sum_{i=1}^{n} N_i'^{(e)} x_i^{(e)} \tag{46}$$

and

$$y = \sum_{i=1}^{n} N_i'^{(e)} y_i^{(e)} \ , \tag{47}$$

in which n is the number of nodes associated with the element, $N_i'^{(e)} = N_i'^{(e)}(\xi,\eta)$ is the shape or interpolation function which has the value unity at node i in element e and the value zero at all other nodes, and $(x_i^{(e)},y_i^{(e)})$ are the global coordinates of node i of element e. In FESWMS-2DH, $N_i'^{(e)}$ is a quadratic shape function for the particular type of element being transformed.

The local coordinates (ξ,η) used in defining the shape functions depend on whether the element is a triangle or a quadrilateral. A local-coordinate system that relies on the element geometry for its definition and whose coordinates range in absolute value from zero to unity within an element is known as a natural-coordinate system. Natural-coordinate systems for the parent elements corresponding to triangular and quadrilateral global elements are

shown in table 2 along with their appropriate shape functions. Both linear and quadratic shape functions are listed for each element because mixed interpolation is used in FESWMS-2DH in solving the shallow-water equations; that is, linear functions are used to interpolate flow depth and quadratic functions are used to approximate the depth-averaged horizontal velocities.

The finite-element equations involve derivatives of the nodal variables with respect to the global Cartesian coordinates x and y. Therefore, the derivatives of the shape functions with respect to x and y must be defined, since, for example,

$$\frac{\partial \tilde{u}^{(e)}}{\partial x} = \frac{\partial}{\partial x}\left[\Sigma\, N_i^{(e)} u_i^{(e)}\right] = \Sigma\, \frac{\partial N_i^{(e)}}{\partial x}\, u_i^{(e)} \quad , \tag{48}$$

in which $\tilde{u}^{(e)} = \sum_{i=1}^{n} N_i^{(e)} u_i^{(e)}$ is the approximation of the variable u over the element e, $N_i^{(e)}$ is the shape function which has the value unity at node i in element e, and $u_i^{(e)}$ is the value of the variable u at node i of element e. Because the shape functions are given in terms of the local coordinates of an element, it is necessary to transform the global derivatives to local derivatives. By the rules of partial differentiation,

$$\frac{\partial N_i}{\partial x} = \frac{\partial N_i}{\partial \xi}\frac{\partial \xi}{\partial x} + \frac{\partial N_i}{\partial \eta}\frac{\partial \eta}{\partial x} \tag{49}$$

and

Table 2. Parent elements and natural-coordinate shape functions.

Parent element	Natural-coordinate shape functions ($\xi_o = \xi\xi_i$, $\eta_o = \eta\eta_i$)
Triangular elements	
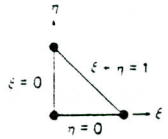 Linear	All nodes $N_i = \xi_o + \eta_o + (1-\xi-\eta)\,(1-\xi_i)\,(1-\eta_i)$
Quadratic	Corner nodes $N_i = \xi_o\,(2\xi-1) + \eta_o\,(2\eta-1)$ $+ (1-\xi-\eta)\,(1-2\xi-2\eta)\,(1-\xi_i)\,(1-\eta_i)$ Midside nodes $N_i = 16\,\xi_o\eta_o + 8\,(\eta_o+\xi_o)\,(1-\xi-\eta)$
"Serendipity" quadrilateral elements	
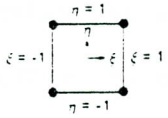 Linear	All nodes $N_i = 1/4\,(1+\xi_o)\,(1+\eta_o)$
Quadratic	Corner Nodes $N_i = 1/4\,(1+\xi_o)\,(1+\eta_o)\,(\xi_o+\eta_o-1)$ Midside Nodes $N_i = 1/2\,(1-\xi^2)\,(1+\eta_o);\ \xi_i = 0$ $N_i = 1/2\,(1-\eta^2)\,(1+\xi_o);\ \eta_i = 0$

Table 2. Parent elements and natural-coordinate shape functions (continued).

Parent element	Natural-coordinate shape functions ($\xi_o = \xi\xi_i$, $\eta_o = \eta\eta_i$)
"Lagrangian" quadrilateral elements	
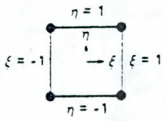 Linear	All Nodes $N_i = 1/4\ (1+\xi_o)\ (1+\eta_o)$
Quadratic	Corner Nodes $N_i = 1/4\ \xi_o\eta_o\ (1+\xi_o)\ (1+\eta_o)$ Midside Nodes $N_i = 1/2\ \eta_o\ (1-\xi^2)\ (1+\eta_o);\ \xi_i = 0$ $N_i = 1/2\ \xi_o\ (1-\eta^2)\ (1+\xi_o);\ \eta_i = 0$ Center Node $N_i = (1-\xi^2)\ (1-\eta^2)$

$$\frac{\partial N_i}{\partial y} = \frac{\partial N_i}{\partial \xi}\frac{\partial \xi}{\partial y} + \frac{\partial N_i}{\partial \eta}\frac{\partial \eta}{\partial y}, \tag{50}$$

where the superscript (e) has been dropped. However, explicit expressions for ξ and η in terms of x and y are usually not readily available. Thus, it is necessary to first consider N_i to be a function of x and y. Writing the derivatives of $N_i^{(e)}$ with respect to ξ and η and dropping the superscript (e) yields, in matrix form,

$$\begin{bmatrix} \frac{\partial N_i}{\partial \xi} \\ \frac{\partial N_i}{\partial \eta} \end{bmatrix} = \begin{bmatrix} \frac{\partial x}{\partial \xi} & \frac{\partial y}{\partial \xi} \\ \frac{\partial x}{\partial \eta} & \frac{\partial y}{\partial \eta} \end{bmatrix} \begin{bmatrix} \frac{\partial N_i}{\partial x} \\ \frac{\partial N_i}{\partial y} \end{bmatrix} = [J] \begin{bmatrix} \frac{\partial N_i}{\partial x} \\ \frac{\partial N_i}{\partial y} \end{bmatrix}, \tag{51}$$

where [J] is the Jacobian matrix, which can be found explicitly in terms of the local coordinates using equations 46 and 47. Thus

$$[J] = \begin{bmatrix} \Sigma \frac{\partial N_i'}{\partial \xi} x_i & \Sigma \frac{\partial N_i'}{\partial \xi} y_i \\ \Sigma \frac{\partial N_i'}{\partial \eta} x_i & \Sigma \frac{\partial N_i'}{\partial \eta} y_i \end{bmatrix}, \tag{52}$$

where N_i' is the shape function defining the coordinate transformation. The global derivatives may then be found as

$$\begin{bmatrix} \frac{\partial N_i}{\partial x} \\ \frac{\partial N_i}{\partial y} \end{bmatrix} = [J]^{-1} \begin{bmatrix} \frac{\partial N_i}{\partial \xi} \\ \frac{\partial N_i}{\partial \eta} \end{bmatrix} \tag{53}$$

or

$$\frac{\partial N_i}{\partial x} = \frac{1}{|J|}\left(\frac{\partial y}{\partial \eta}\frac{\partial N_i}{\partial \xi} - \frac{\partial y}{\partial \xi}\frac{\partial N_i}{\partial \eta}\right) \tag{54}$$

and

$$\frac{\partial N_i}{\partial y} = \frac{1}{|J|}\left(-\frac{\partial x}{\partial \eta}\frac{\partial N_i}{\partial \xi} + \frac{\partial x}{\partial \xi}\frac{\partial N_i}{\partial \eta}\right) , \tag{55}$$

where $|J|$ is the determinant of $[J]$ and is computed as

$$|J| = \frac{\partial x}{\partial \xi}\frac{\partial y}{\partial \eta} - \frac{\partial x}{\partial \eta}\frac{\partial y}{\partial \xi} . \tag{56}$$

In addition to transforming the global derivatives to local derivatives in the element equations, the area of the element must be expressed in terms of ξ and η. It can be shown (Sokolnikoff and Redheffer, 1966, p. 355) that

$$dx\, dy = |J|\, d\xi\, d\eta . \tag{57}$$

The operations indicated in equations 53 through 55 depend on the existence of $[J]^{-1}$ for each element of the network. By the inverse function theorem, the inverse mapping $[J]^{-1}$ exists if and only if the mapping defined by equations 46 and 47 is one-to-one. Also, $[J]^{-1}$ exists if and only if the determinant of $[J]$, $|J|$, does not vanish within the element.

Solution Methods

Many researchers solving the shallow-water equations by finite-element methods have used the same order of interpolation for both the velocity components and the depth (Lee and Froehlich, 1986, p. 10). However, the use of equal-order interpolation results in solutions that are plagued with short-wavelength noise (Lee and Froehlich, 1986, p. 10). The reasons for these problems are discussed by Gray and Lynch (1979) and Platzman (1981).

A widely used approach for eliminating oscillations in the water-surface elevation is the use of mixed interpolation, in which a lower order of interpolation is used for depth than for the velocity components. Quadratic interpolation for velocity components and linear interpolation for depth or water-surface elevation on triangles is used by Norton and King (1973), Norton and others (1973), Tseng (1975a, 1975b), King and Norton (1978), Walters and Cheng (1978, 1980), Norton (1980), and Gee and MacArthur (1982). This approach has been adopted in FLOMOD. Additionally, the FLOMOD user has the option of using quadratic interpolation for velocity components and bilinear interpolation for depth on eight-node quadrilateral elements or biquadratic interpolation for velocity components and bilinear interpolation for depth on nine-node quadrilateral elements.

Although primitive models using mixed interpolation do not exhibit spurious surface-elevation modes (they do, however, exhibit

velocity modes), they suffer from a ratio of discrete continuity equations to discrete momentum equations that is much less than the continuum ratio of 0.5. This can cause significant errors in mass conservation. Increasing network detail is effective in reducing these mass-conservation errors (Gee and MacArthur, 1978).

In another approach, the primitive continuity equation 3 is replaced by the second-order wave continuity equation (Lynch and Gray, 1979, 1980):

$$\frac{\partial^2 H}{\partial t^2} + \frac{c_b}{\rho H}\frac{\partial H}{\partial t} - \frac{\partial}{\partial x}\left[\frac{\partial}{\partial x}(HU^2) + \frac{\partial}{\partial y}(HVU) + gH\frac{\partial H}{\partial x} + gH\frac{\partial z_b}{\partial x} - \Omega HV - \frac{\tau_x^s}{\rho}\right] - \frac{\partial}{\partial y}\left[\frac{\partial}{\partial x}(HUV) + \frac{\partial}{\partial y}(HV^2) + gH\frac{\partial H}{\partial y} + gH\frac{\partial z_b}{\partial y} + \Omega HU - \frac{\tau_y^s}{\rho}\right] - \frac{HU}{\rho}\frac{\partial}{\partial x}\left(\frac{c_b}{\rho}\right) - \frac{HV}{\rho}\frac{\partial}{\partial y}\left(\frac{c_b}{\rho}\right) = 0 \quad . \tag{58}$$

In deriving equation 58 from equations 1, 2, and 3, the stress terms τ_{xx}, τ_{xy}, τ_{yx}, and τ_{yy} are set to zero, and the substitution

$$\tau_x^b = c_b u \text{ and } \tau_y^b = c_b v \tag{59}$$

is made, in which c_b is a bottom-stress coefficient.

Use of a wave-equation model requires that steady-state solutions be obtained by dynamic relaxation (time stepping) rather than directly unless Fourier transformation is used to transform

the equations from the time domain to the frequency domain. In this case, the steady-state solution can be obtained for zero frequency (Walters, 1986).

An advantage of a wave-equation scheme is that equal-order interpolation can be used for both depth and velocity components without the spurious oscillations in water-surface elevation that plague solutions based on equal-order interpolation and the primitive shallow-water equations, thus providing a ratio of discrete continuity equations to discrete momentum equations that is closer to the continuum ratio of 0.5 than that obtained with mixed interpolation. Consequently, better mass conservation might be expected for a wave-equation solution. Another advantage of a wave-equation scheme is that the depth solution can be separated from the velocity solution.

Extensive tests were performed with two wave-equation models. The first model, WAVETL (Lynch and Gray, 1980), is explicit in time and uses linear triangular elements. Element nodes are used as integration points (nodal integration). This causes the matrices multiplying the time derivatives to be diagonal, thus eliminating the need for solving large systems of linear equations at each time step. A second model, QUIET (Gray and Kinnmark, 1982), uses nine-node isoparametric quadrilaterals and is explicit in time. Nodal integration is also used in QUIET. Thus, the matrices generated are diagonal. It was found to be very difficult to obtain stable solutions in tests with both hypothetical and real-world cases. For this reason, further attempts to use a wave-equation scheme

were abandoned.

Another technique which can be used to eliminate spurious oscillations when equal-order interpolation is used is upwinding. This involves the use of discontinuous weighting functions. An upwinding scheme called the dissipative Galerkin scheme is presented by Katapodes (1984, p. 451). The equations of one-dimensional flow in a prismatic channel of rectangular cross section are written in matrix form as

$$\frac{\partial U}{\partial t} + A \frac{\partial U}{\partial x} = 0 \ , \tag{60}$$

in which

$$U = \begin{bmatrix} y \\ q \end{bmatrix} \tag{61}$$

and

$$A = \begin{bmatrix} 0 & 1 \\ c^2-u^2 & 2u \end{bmatrix} \ , \tag{62}$$

in which t is time, x is distance, y is depth of flow, q is unit discharge, u is average flow velocity, $c = (gy)^{1/2}$, and g is gravitational acceleration. Katapodes (1984, p. 455) proposes the following weighting function:

$$N_{i*} = N_i + \varepsilon A^T \frac{\partial N_i}{\partial x} \ , \tag{63}$$

in which N_i is the linear basis function which has the value unity at node i and the superscript T denotes transposition. The degree of discontinuity is controlled by the choice of ε. A second-order-accurate time-stepping scheme is used.

Numerical tests by the writers indicated that this weighting function provides effective damping of short-wavelength oscillations for dynamic solutions to unsteady one-dimensional flow problems when ε is optimized to damp short wavelengths and when the value of the Courant number, $c\Delta t/\Delta x$, is approximately unity or less. A least squares scheme is a special case of the dissipative Galerkin scheme for $\varepsilon = \Delta t/2$.

For obtaining direct steady-state solutions, the writers found that the weighting function $\partial N_i/\partial x$ worked best. In this case, boundary conditions were simply superimposed on the finite-element equations at boundary nodes. The resulting scheme is just the four-point implicit (Preissmann) finite-difference scheme. An effort was made, but without success, to generalize this direct steady-state approach to two dimensions.

Numerical Integration

Numerical integration is used in FLOMOD to evaluate the terms of the equation residuals and the Jacobian matrix. Fifth-order integration (nine-point for quadrilaterals and seven-point for triangles) is used.

In transient finite-element analyses, the matrix multiplying the time derivative (also called the mass or capacity matrix) is

$$M^{ij} = \int_{\Omega} N_i N_j \ , \tag{64}$$

where N_i, $i = 1, 2, \ldots, n$, are the interpolation functions and Ω is the discretized domain. It has been noted that the use of element nodes as integration points increases the sparsity and diagonal dominance of the time matrix and, under appropriate conditions, yields a diagonal matrix.

As stated above, nodal integration is used in the explicit wave-equation models WAVETL and QUIET. Thus, diagonal time matrices are obtained. The difficulty in obtaining stable solutions with these models was discussed above. Moreover, even if stable steady-state solutions could be obtained, in a simulation involving thousands of elements, the time step would be restricted by the smallest element size in the network. Thus, such a large number of time steps would be required to obtain a steady-state solution that the approach would not be competitive with a direct steady-state solution that may require the solution of a system of linear equations at each iteration.

Nodal integration was tried in FLOMOD for evaluating both the equation residuals and the terms of the Jacobian matrix. Because an implicit time-stepping scheme is used in FLOMOD, the use of nodal integration does not result in diagonal time matrices. Use of nodal integration to evaluate residuals was found to decrease

solution accuracy somewhat. Use of nodal integration to evaluate the terms of the Jacobian matrix was found to increase slightly the sparsity of the matrix but not enough to affect the time required to solve the system of equations. Thus, there is no advantage to using nodal integration in FLOMOD.

Solution of Nonlinear Algebraic Equations

The depth-averaged equations of motion and continuity which describe shallow surface-water flow are, in their complete form, a coupled system of nonlinear partial-differential equations. The many alternatives for numerically solving the system of nonlinear algebraic equations which results from the finite-element discretization of the governing partial-differential equations present such a wide choice that it is difficult to know which technique is best. Processes which are economical in one context may be uneconomical or divergent in another.

The numerical solution of the nonlinear equation system represents the major part of the cost in obtaining a finite-element solution to fluid-flow problems. Computational efficiency in terms of both time and storage space dictates that a symmetric equation system be solved if possible. The coefficient matrix that is formed, however, is nonsymmetric due to the presence of the nonlinear inertia and bottom-friction terms.

The finite-element formulation leads to a set of global discretized equations of motion and continuity in the form

$$K(a)a = f \ , \tag{65}$$

in which the K is the matrix of assembled element coefficients, a is the vector of unknown nodal values, and f is the global force or load vector. This simultaneous nonlinear system of equations is solved in FLOMOD using a strategy that combines both full-Newton and quasi-Newton iteration.

In full-Newton iteration, the (i+1)st iterate, a_{i+1}, is given in terms of the ith iterate, a_i, as

$$a_{i+1} = a_i - J(a_i)^{-1} r(a_i) \ , \tag{66}$$

in which $J(a_i)$ is the Jacobian, or tangent, matrix computed from a_i and $r(a_i) = K(a_i)a_i - f$ is the residual load vector. In practice, this iteration is performed as

$$J(a_i)\Delta a_i = - r(a_i) \tag{67}$$

with

$$a_{i+1} = a_i + \Delta a_i \ . \tag{68}$$

The process usually converges quite rapidly in the vicinity of the solution; however, if the initial estimate is not sufficiently close, divergence can occur.

The LU factorization of the Jacobian (the factorization of the Jacobian into lower and upper triangular matrices) that is formed during the full-Newton iteration can, optionally, be updated in a

relatively simple manner rather than be recomputed completely at each iteration. Such a procedure is known as a quasi-Newton method. Broyden's update procedure in inverse form is used (Engelman and others, 1981).

Given an initial solution estimate, a_o, the LU factorization of its Jacobian, J_o, and the initial search direction, Δa_o, the quasi-Newton algorithm proceeds as follows:

For i = 1 to i_{max}

1. Form $\delta_i = \Delta a_{i-1}$
2. Compute $\Delta a_i = - J_o^{-1} r(a_i)$
3. For j = 1 to i-1

   Compute $\Delta a_i = \Delta a_i - \rho_j(\delta_j + r_j)\delta_i^T \Delta a_i$

   Next j
4. Form $r_i = \Delta a_i - \delta_i$

   $\rho_i = 1/\delta_i^T r_i$
5. Compute $\Delta a_i = \Delta a_i - \rho_i(\delta_i + r_i)\delta_i^T \Delta a_i$

Next i

Each iteration requires the solution of a single linear system for which the triangular factors of the coefficient matrix are already known, plus the vector operations needed to update the matrix. Two updating vectors (δ_i and r_i) are created at each iteration and are kept and reused in subsequent iterations up to a limit imposed by the user. When the upper limit is reached, the updating vectors are shifted one position downward (thus the first pair is lost) and computations continue. If the limiting number of updates is set to

zero, then the coefficient matrix is not updated and modified-Newton iteration results.

The user is thus provided with a choice of solution strategies. A typical solution will combine both full- and quasi-Newton iterations in an attempt to achieve the fastest solution possible. Generally, at least two or three full-Newton iterations are required when starting cold (that is, initially with velocities set to zero and a constant water-surface elevation) or after having made substantial changes to boundary conditions or the geometry of the finite-element network. These initial iterations can then be followed by one or more quasi-Newton iterations or by a combination of quasi- and full-Newton iterations.

The optimal number of update vectors to use in a quasi-Newton iteration is largely problem dependent. Beyond a limit, the updating procedure becomes uneconomical. Maintaining more than about five sets of update vectors in memory has been found to result in wasted computational effort. Therefore, the number of update vectors used in FLOMOD is limited to a maximum of five.

Solution of Linear Algebraic Equations

At each iteration a system of linear algebraic equations of the form

$$Ka = f \tag{69}$$

must be solved, where K is the square coefficient matrix, a is the

column vector of nodal unknowns, and f is the column vector of nodal forces, or loads.

The system of equations represented by equation 69 can be solved either directly or iteratively. Direct methods are based on Gaussian elimination and are direct in the theoretical sense that if rounding errors are ignored, the exact answer will be found in a finite number of steps. Iterative methods, on the other hand, consist of a series of successive corrections to an initial estimate of the unknowns, the process being performed repetitively until the size of the corrections becomes sufficiently small. Although convergence of iterative methods can often be assured, the amount of computation required to reach a sufficiently accurate solution is not known in advance.

Several solution algorithms were tried in the development of FLOMOD: (1) a banded-storage solution, (2) a partitioned-block skyline-storage solution scheme, (3) a frontal solution scheme, and (4) a conjugate-gradient solution scheme. The first three solution strategies are direct methods, and the last is an iterative solution scheme. The use of these methods to solve the shallow-water equations is discussed in the following sections.

Banded-Storage Solution Scheme

The coefficient matrix, K, that is found in the finite-element solution process is generally quite sparse (that is, a preponderant number of the coefficients are zero). The nodal unknowns in the

column vector, a, can be arranged so that the nonzero coefficients in the matrix K are within a band running parallel to the diagonal of K. The width of this band can often be made quite small compared with the number of unknowns, and a significant savings in storage can be achieved by storing only those terms within this band.

A banded-storage solution scheme was initially used in FLOMOD. This scheme employed direct triangular decomposition. No pivoting was used in the factorization although a partial-pivoting strategy could have been employed.

Partitioned-Block Skyline-Storage Solution Scheme

It is possible to reduce the required storage and computational effort even further by using a skyline-storage scheme in which the lower triangular part of the coefficient matrix is stored by rows and the upper triangular part by columns (or vice versa). It is necessary to store and compute only within the nonzero profile of the equations. This method has advantages over a banded-storage solution scheme since it never requires more storage and coefficients are arranged so that all multiplications can be performed as very fast dot-product operations.

The partitioned-block skyline-storage scheme presented by Hasbani and Engelman (1979) was modified for use in FLOMOD. In this algorithm, the coefficient matrix is partitioned into blocks which are temporarily stored in a disk file during equation solution. This storage scheme

allows extremely large systems of equations to be solved.

The partitioned-block skyline-storage solution scheme was faster than either the banded-storage or the frontal solution schemes but has the disadvantage of not allowing pivoting. Walters (1980, p. 268) states that the lack of pivoting is not a severe problem when solving the shallow-water equations using the finite-element method since the assembled system exhibits strong diagonal dominance.

In order to simulate flow over weirs (highway embankments) and through culverts and also pressure flow through bridges when the water-surface is in contact with the underside of the bridge deck, some of the shallow-water equations are replaced by others containing a zero diagonal coefficient. Also, flows along boundaries of the finite-element network are treated in such a way that under certain conditions a zero diagonal coefficient might be formed. For these reasons, the skyline-storage algorithm cannot always be used.

Frontal Solution Scheme

The frontal solution technique is a direct solution scheme which is closely connected to the finite-element method. It is designed to minimize core-storage requirements as well as the number of arithmetic operations needed to solve the system of equations. The main idea of the frontal method is to assemble and eliminate the element equations at the same time. As soon as an equation is completely formed from the contributions of all relevant

elements, it is reduced and then eliminated from the "active" coefficient matrix, being written to a buffer and, eventually, an auxiliary storage device. Therefore, the coefficient matrix is usually never formed in its entirety. The active matrix contains, at any given instant, only those equations which have been partly assembled or are complete but have not yet been eliminated.

The number of unknowns in the front at any particular time is called the frontwidth and will generally change continually during the assembly/elimination process. The maximum frontwidth determines the required size of the active coefficient matrix and is determined by the order in which the elements are assembled. When assembly is complete, the upper triangular matrix will have been formed and will be ready for backsubstitution.

The frontal solution scheme presented by Hood (1976, 1977) was modified and added to FLOMOD. Modifications were made to eliminate unnecessary computations and to save both the upper and lower triangular matrix decompositions if a quasi-Newton solution is to be performed. Also, eliminated equations are stored in a buffer (the size of which depends on available computer storage and storage-device limitations), which is written to an off-line storage device when full or nearly full. Data-transfer time decreases as the size of the equation buffer is increased. A diagonal-pivoting strategy is used in which the equations that are complete in the active coefficient matrix and ready for elimination are scanned and the one with the largest value on the diagonal is

eliminated next. A minimum number of completed equations may be maintained in the active coefficient matrix, thus ensuring a choice of pivotal elements.

The frontal solution algorithm contained in FLOMOD has been tested on small to extremely large problems and has been proven quite successful in all cases. It is faster than the banded-storage scheme and generally needs much less core-storage space.

Conjugate-Gradient Solution Scheme

The process of solving a set of n simultaneous equations is similar to that of minimizing an error function defined over an n-dimensional space. In each step of a conjugate-gradient solution, a trial set of values is used to determine a new set of values with a correspondingly smaller value of the error function. The conjugate-gradient method is thus an iterative solution technique. The convergence of the method, even if it can be assured, can be very slow and thus the amount of computation required to obtain an acceptable solution is not very predictable.

A conjugate-gradient solution scheme was tested in FLOMOD. For each conjugate-gradient iteration performed, equations at each node are assembled and residuals computed. The computational effort at each iteration is thus quite large. Convergence is very slow. Although others (see Lee and Froehlich, 1986, p. 40) have successfully employed the conjugate-gradient method for the solution of finite-element problems, use of this solution technique in

FLOMOD was found to be much slower than direct solution schemes. Although the core-storage requirement of the conjugate-gradient solution scheme is less than that of direct methods, the tradeoff between computer memory and computer time does not seem to be an advantage. Therefore, the conjugate-gradient method has not been included in FLOMOD as an equation-solution scheme.

Finite-Element Equations

The method of weighted residuals with Galerkin weighting is applied to the governing depth-averaged flow equations to form the finite-element equations. Because the system of equations is nonlinear, Newton's iterative method (see, for example, Atkinson, 1978) is used to obtain a solution. At each iteration, the residuals are formed. In addition, the Jacobian, or tangent, matrix, a matrix of derivatives with respect to each of the independent variables for each of the residuals, is required. The finite-element expressions for the residuals written at the ith node point and a discussion of the application of boundary and other "special" conditions are presented in the following sections. The elements of the Jacobian matrix may be found in the FESWMS-2DH users manual.

Residuals

The finite-element expressions for the residuals of the depth-averaged flow equations written at node i are

$$f_{1i} = \sum_e \int_{A_e} \{ N_i \left[H \frac{\partial U}{\partial t} + U \frac{\partial H}{\partial t} + gH \frac{\partial z_b}{\partial x} - \Omega HV - \frac{\rho_a}{\rho} c_s W^2 \cos\psi \right.$$

$$\left. + c_f U (U^2 + V^2)^{1/2} \left(1 + (\partial z_b/\partial x)^2 + (\partial z_b/\partial y)^2\right)^{1/2} \right]$$

$$+ \frac{\partial N_i}{\partial x} \left[-\beta HUU - \frac{g}{2} H^2 + \tilde{\nu} H \left(\frac{\partial U}{\partial x} + \frac{\partial U}{\partial x} \right) \right]$$

$$+ \frac{\partial N_i}{\partial y} \left[-\beta HUV + \tilde{\nu} H \left(\frac{\partial U}{\partial y} + \frac{\partial V}{\partial x} \right) \right] \} \, dA_e$$

$$+ \sum_e \int_{S_e} N_i \left[\left(\beta HUU + \frac{g}{2} H^2 \right) \ell_x + \beta HUV \, \ell_y \right] dS_e$$

$$- \sum_e \int_{S_e} N_i \left[\tilde{\nu} H \left(\frac{\partial U}{\partial x} + \frac{\partial U}{\partial x} \right) \ell_x + \tilde{\nu} H \left(\frac{\partial U}{\partial y} + \frac{\partial V}{\partial x} \right) \ell_y \right] dS_e \qquad (70)$$

for the equation of motion in the x-direction,

$$f_{2i} = \sum_e \int_{A_e} \{ N_i \left[H \frac{\partial V}{\partial t} + V \frac{\partial H}{\partial t} + gH \frac{\partial z_b}{\partial y} + \Omega HU - \frac{\rho_a}{\rho} c_s W^2 \sin\psi \right.$$

$$\left. + c_f V (U^2 + V^2)^{1/2} \left(1 + (\partial z_b/\partial x)^2 + (\partial z_b/\partial y)^2\right)^{1/2} \right]$$

$$+ \frac{\partial N_i}{\partial x} \left[-\beta HVU + \tilde{\nu} H \left(\frac{\partial U}{\partial y} + \frac{\partial V}{\partial x} \right) \right]$$

$$+ \frac{\partial N_i}{\partial y} \left[-\beta HVV - \frac{g}{2} H^2 + \tilde{\nu} H \left(\frac{\partial V}{\partial y} + \frac{\partial V}{\partial y} \right) \right] \} \, dA_e$$

$$+ \sum_e \int_{S_e} N_i \left[\beta HUV \, \ell_x + \left(\beta HVV + \frac{g}{2} H^2 \right) \ell_y \right] dS_e$$

$$- \sum_e \int_{S_e} N_i \left[\tilde{\nu} H \left(\frac{\partial U}{\partial y} + \frac{\partial V}{\partial x} \right) \ell_x + \tilde{\nu} H \left(\frac{\partial V}{\partial y} + \frac{\partial V}{\partial y} \right) \ell_y \right] dS_e \qquad (71)$$

for the equation of motion in the y-direction, and

$$\underline{f}_{3i} = \sum_e \int_{A_e} M_i \left[\frac{\partial H}{\partial t} + H \frac{\partial U}{\partial x} + U \frac{\partial H}{\partial x} + H \frac{\partial V}{\partial y} + V \frac{\partial H}{\partial y} \right] dA_e \qquad (72)$$

for the continuity equation, where $\sum_e$ indicates a summation over all elements, A_e is an element area, S_e is an element surface (or boundary), N_i is a quadratic shape function which has the value unity at node i and the value zero at all other nodes, M_i is a linear shape function which has the value unity at node i and zero at all other nodes, and ℓ_x and ℓ_y are the direction cosines between the outward normal to the boundary and the x- and y-directions, respectively. All second-derivative terms in the momentum equations have been integrated by parts through application of Green's theorem to reduce the order of the equations and allow the use of quadratic shape functions for velocities. The convective and pressure terms have also been integrated by parts. Integration by parts of the convective terms simplifies the finite-element-equation formulation, and integration by parts of the pressure terms facilitates the application of normal-stress boundary conditions. The last boundary integral in the two equations of motion represents the lateral stress due to the transport of momentum by turbulence.

When two-dimensional flow through a bridge is in contact with the ceiling, pressure flow exists, and the pressure, P, replaces the flow depth, H, as the solution variable at the relevant node points. In the case of pressure flow, the finite-element expressions

for the residuals of the depth-averaged flow equations written at node i are

$$f_{1i} = \sum_e \int_{A_e} \{ N_i \left[H \frac{\partial U}{\partial t} + gP \frac{\partial z_b}{\partial x} - g(P-H) \frac{\partial z_c}{\partial x} - \Omega HV \right.$$

$$+ c_f U (U^2 + V^2)^{1/2} \left(1 + (\partial z_b/\partial x)^2 + (\partial z_b/\partial y)^2\right)^{1/2}$$

$$\left. + c_f U (U^2 + V^2)^{1/2} \left(1 + (\partial z_c/\partial x)^2 + (\partial z_c/\partial y)^2\right)^{1/2} \right]$$

$$+ \frac{\partial N_i}{\partial x} \left[-\beta HUU - g(HP - H^2/2) + \tilde{\nu} H \left(\frac{\partial U}{\partial x} + \frac{\partial U}{\partial x} \right) \right]$$

$$+ \frac{\partial N_i}{\partial y} \left[-\beta HUV + \tilde{\nu} H \left(\frac{\partial U}{\partial y} + \frac{\partial V}{\partial x} \right) \right] \} \, dA_e$$

$$+ \sum_e \int_{S_e} N_i \left[(\beta HUU + g(HP - H^2/2)) \ell_x + \beta HUV \ell_y \right] dS_e$$

$$- \sum_e \int_{S_e} N_i \left[\tilde{\nu} H \left(\frac{\partial U}{\partial x} + \frac{\partial U}{\partial x} \right) \ell_x + \tilde{\nu} H \left(\frac{\partial U}{\partial y} + \frac{\partial V}{\partial x} \right) \ell_y \right] dS_e \quad (73)$$

for the equation of motion in the x-direction,

$$f_{2i} = \sum_e \int_{A_e} \{ N_i \left[H \frac{\partial V}{\partial t} + gP \frac{\partial z_b}{\partial y} - g(P-H) \frac{\partial z_c}{\partial y} + \Omega HU \right.$$

$$+ c_f V (U^2 + V^2)^{1/2} \left(1 + (\partial z_b/\partial x)^2 + (\partial z_b/\partial y)^2\right)^{1/2}$$

$$\left. + c_f V (U^2 + V^2)^{1/2} \left(1 + (\partial z_c/\partial x)^2 + (\partial z_c/\partial y)^2\right)^{1/2} \right]$$

$$+ \frac{\partial N_i}{\partial x} \left[-\beta HVU + \tilde{\nu} H \left(\frac{\partial U}{\partial y} + \frac{\partial V}{\partial x} \right)\right]$$

$$- + \frac{\partial N_i}{\partial y} \left[-\beta HVV - g(HP-H^2/2) + \tilde{\nu} H \left(\frac{\partial V}{\partial y} + \frac{\partial V}{\partial y} \right)\right] \Big\} \, dA_e$$

$$+ \sum_e \int_{S_e} N_i \left[\beta HUV \, \ell_x + (\beta HVV + g(HP-H^2/2)) \, \ell_y\right] dS_e$$

$$- \sum_e \int_{S_e} N_i \left[\tilde{\nu} H \left(\frac{\partial U}{\partial y} + \frac{\partial V}{\partial x} \right) \ell_x + \tilde{\nu} H \left(\frac{\partial V}{\partial y} + \frac{\partial V}{\partial y} \right) \ell_y\right] dS_e \quad (74)$$

for the equation of motion in the y-direction, and

$$f_{3i} = \sum_e \int_{A_e} M_i \left[H \frac{\partial U}{\partial x} + U \frac{\partial H}{\partial x} + H \frac{\partial V}{\partial y} + V \frac{\partial H}{\partial y}\right] dA_e \quad (75)$$

for the continuity equation where $H = z_c - z_b$.

Time Derivatives

Equations 70, 71, and 72 apply to a particular instant in time. If a steady-state solution is desired, all the time derivatives are equal to zero and do not need to be evaluated. If the solution is time dependent, however, these equations must be integrated with respect to time as well as space. This is accomplished by using an implicit scheme in which the time derivatives are approximated by a finite-difference expression. For example, the derivative of U with respect to time at the end of a time step is given by

$$\frac{\partial U}{\partial t} = \frac{1}{\theta \Delta t} (U - U_o) - \frac{(1 - \theta)}{\theta} \left(\frac{\partial U}{\partial t} \right)_o , \quad (76)$$

where θ is a weighting coefficient ranging between 0.5 and 1, Δt is the length of the time step, and the subscript o indicates known values at the start of the time step. Note that if θ equals unity the integration scheme is linear, and if θ equals 0.5 a trapezoidal integration scheme results. A value of θ equal to 0.67 has been found to produce a stable solution even for relatively large time steps while also providing a high degree of accuracy (King and Norton, 1978, p. 2.82, 2.83). R. A. Walters (written commun., 1987) observes that for a value of θ equal to unity, the solution is damped; for a value of θ equal to 0.5, there is peaking in amplitude near the grid cutoff (for wavelengths close to twice the grid spacing); and for a value of θ equal to 0.67, the solution response is nearly optimal.

Equation 76 can be rearranged as

$$\frac{\partial U}{\partial t} = \alpha U - \beta_1 \ , \tag{77}$$

in which

$$\alpha = \frac{1}{\theta \Delta t} \tag{78}$$

and

$$\beta_1 = \alpha U_o + \frac{(1 - \theta)}{\theta} \left(\frac{\partial U}{\partial t} \right)_o \ , \tag{79}$$

where β_1 contains only known quantities. Similarly, time derivatives

of V and H can be written as

$$\frac{\partial V}{\partial t} = \alpha V - \beta_2 \tag{80}$$

and

$$\frac{\partial H}{\partial t} = \alpha H - \beta_3 \ , \tag{81}$$

where

$$\beta_2 = \alpha V_o + \frac{(1 - \theta)}{\theta} \left(\frac{\partial V}{\partial t} \right)_o \tag{82}$$

and

$$\beta_3 = \alpha H_o + \frac{(1 - \theta)}{\theta} \left(\frac{\partial H}{\partial t} \right)_o \ . \tag{83}$$

Application of Boundary and Special Conditions

The Galerkin finite-element formulation allows complicated boundary conditions to be automatically satisfied as natural conditions of the problem. Natural boundary conditions are treated by moving terms involving the relevant variables to the right-hand side of the finite-element equations. Those boundary conditions that must be explicitly imposed are known as forced, or essential, conditions. These boundary values are prescribed by modifying the finite-element equations governing the relevant variables so that the boundary

conditions are explicitly satisfied. In addition, special boundary conditions imposed by one-dimensional flow at culverts and weirs can be easily applied.

Open boundaries

In FLOMOD, velocities and depth may be applied as essential boundary conditions at any node point on an open boundary as long as the system of equations does not become overconstrained. These prescribed nodal variables are introduced by replacing the residuals at node i by

$$f_{1i} = U_i^* , \tag{84}$$

$$f_{2i} = V_i^* , \tag{85}$$

and

$$f_{3i} = H_i^* , \tag{86}$$

where U_i^*, V_i^*, and H_i^* are the specified values at node i. Unit discharges are applied in a similar manner by replacing the motion-equation residual expressions by

$$f_{1i} = U_i H_i - q_{xi} \tag{87}$$

and

$$f_{2i} = V_i H_i - q_{yi} , \tag{88}$$

where q_{xi} and q_{yi} are specified unit discharges in the x- and y-

directions, respectively, at node i. The derivative equations corresponding to equations 84 through 88 are given in the FESWMS-2DH users manual.

Depth may also be specified as a natural boundary condition of the problem. This is done by using the specified value of depth at node i, H_i^*, when evaluating the boundary-integral terms in the momentum residual expressions 70 and 71. When computing derivatives of the momentum residuals with respect to H_i^*, contributions from the boundary-integral terms are taken as zero. When depth is specified as a natural boundary condition, global mass conservation is ensured, and total inflow equals total outflow in steady-state simulations. However, depths computed at nodes where the water-surface elevation is applied as a natural boundary condition may differ slightly from the specified values. When depth is specified as an essential boundary condition, the total outflow may differ slightly from the total inflow in steady-state simulations.

If the total discharge through a cross section forming part of the open boundary of a finite-element network is specified, a constant energy slope along the section is assumed and the total discharge is divided among the node points on the basis of conveyance. The cross section is composed of a list of node points which form a connected series of element sides. Each element side is composed of three nodes (1, 2, and 3) with nodes 1 and 3 being corner nodes and node 2 a midside node. The conveyance through each element

side is computed as

$$K = A\sqrt{\frac{gR}{c_f}} , \tag{89}$$

in which R is the hydraulic radius (area divided by wetted perimeter) of the element side and A is the area of the element side below the water surface. The conveyance for the total cross section is computed as the sum of the conveyances of each element side forming the section.

The conveyance through each element side is distributed among the three nodes forming the side as follows:

$$K_1 = K(1 - \zeta)/6 , \tag{90}$$

$$K_2 = 2K/3 , \tag{91}$$

and

$$K_3 = K(1 + \zeta)/6 , \tag{92}$$

in which $\zeta = 5\Delta H/12\bar{H}$ where $\Delta H = H_3 - H_1$, $\bar{H} = (H_1 + H_3)/2$, H_1 is the depth at node 1, and H_3 is the depth at node 3. Total discharge normal to the open boundary at each node forming the cross section is then based on the ratio of conveyance assigned to each node to the total conveyance computed for the cross section. The velocities and depth computed at each node are required to satisfy the condition that the net discharge across the open boundary due to flow at the node will equal the assigned portion of the total cross-section

discharge. The procedure used to ensure that this condition is satisfied is described in the section "Total discharge across a boundary."

Solid boundaries

Solid boundaries define such features as natural shorelines, jetties, or seawalls. For viscous fluids, the velocity at a solid boundary is actually zero. This is commonly referred to as the "no-slip" boundary condition. A no-slip condition can be specified by applying x- and y-velocities of zero as essential boundary conditions. Near a boundary at which a no-slip condition has been imposed, a relatively dense network of elements is required in order to resolve the lateral boundary layer. For practical purposes, however, a "slip" condition is usually applied whereby flow is allowed to move tangentially along a solid boundary. Imposing a slip condition along solid boundaries reduces the total number of elements needed in the network and thus decreases the number of computations in the solution. Slip conditions are applied at a solid-boundary node by first transforming the x- and y-equations of motion that are associated with that node into the tangential and normal equations. The equation of motion in the normal direction is then replaced by a constraint equation that requires the net discharge across the solid boundary due to flow at the node point to equal zero. This procedure is described in the following section.

Total discharge across a boundary

Total discharge across a boundary (normal discharge) due to flow at node i may be specified in several ways. The normal discharge across an open boundary due to flow at node i is computed as

$$Q_i^o = Q_{si}^o + Q_{xi} \quad , \tag{93}$$

where Q_{si}^o is the open-boundary normal discharge due to directly specified flow at node i and Q_{xi} is the portion of the total discharge through a cross section assigned to node i (by the procedure discussed on pages 73 through 75). The normal discharge across a solid boundary due to flow at node i is computed as

$$Q_i^s = Q_{si}^s + Q_{wi} + Q_{ci} \quad , \tag{94}$$

where Q_{si}^s is the solid-boundary normal discharge due to directly specified flow at node i, Q_{wi} is the computed discharge over a weir (roadway embankment) segment associated with node i, and Q_{ci} is the computed discharge through a culvert at node i.

Along a boundary (either open or solid) where the normal discharge is to be prescribed, the residuals of the x- and y-equations of motion are first transformed into tangential and normal residuals. At node point i, this transformation is written as

$$f_{1i}' = f_{1i} \cos \delta + f_{2i} \sin \delta \tag{95}$$

and

$$f'_{2i} = - f_{1i} \sin \delta + f_{2i} \cos \delta \ , \qquad (96)$$

where f'_{1i} and f'_{2i} are the transformed motion-equation residuals in the tangential and normal directions, respectively, and δ is the angle between the positive x-direction and the tangent to the boundary at node i.

If discharge normal to an open boundary at node i is specified, the equation of motion for flow tangential to the boundary is replaced by

$$f_{1i} = a_i^o U_i + b_i^o V_i - Q_i^o = 0 \ . \qquad (97)$$

If discharge normal to a solid boundary at node i is specified, the equation of motion for flow normal to the boundary is replaced by

$$f_{2i} = a_i^s U_i + b_i^s V_i - Q_i^s = 0 \ . \qquad (98)$$

The terms a_i^o, b_i^o and a_i^s, b_i^s in equations 97 and 98 are coefficients that are found by requiring the computed discharge across the open or solid boundary due to flow at node i to equal the specified discharge. These conditions are written as

$$U_i \sum_e \int_{S_e^o} N_i H \ell_x \, dS_e^o + V_i \sum_e \int_{S_e^o} N_i H \ell_y \, dS_e^o - Q_i^o = 0 \qquad (99)$$

and

$$U_i \sum_e \int_{S_e^s} N_i H \ell_x \, dS_e^s + V_i \sum_e \int_{S_e^s} N_i H \ell_y \, dS_e^s - Q_i^s = 0 \ , \qquad (100)$$

where N_i is the interpolation function for velocity at node i, S_e^o is that portion of the network boundary considered to be open, and S_e^s is that portion of the network boundary considered to be solid. Comparing equation 97 with equation 99 and equation 98 with equation 100, it is readily seen that

$$a_i^o = \sum_e \int_{S_e^o} N_i H \ell_x \, dS_e^o , \tag{101}$$

$$b_i^o = \sum_e \int_{S_e^o} N_i H \ell_y \, dS_e^o , \tag{102}$$

$$a_i^s = \sum_e \int_{S_e^s} N_i H \ell_x \, dS_e^s , \tag{103}$$

and

$$b_i^s = \sum_e \int_{S_e^s} N_i H \ell_y \, dS_e^s . \tag{104}$$

The derivatives of the constraints for total discharge across open and solid boundaries are given in the FESWMS-2DH users manual.

Along all solid boundaries, the normal discharge is required to equal zero unless otherwise specified. This is accomplished by setting Q_i^s to zero in equation 98 and requiring the normal-flow constraint to be satisfied at all solid-boundary nodes.

In the finite-element model developed by Norton (1980), a continuous tangent along a slip boundary is assumed to ensure zero mass flux through the boundary if the velocity is forced to be tangential to the boundary. This is true when the dependent variables

are the velocity components, U and V. As shown by Gray (1984), the appropriate normal and tangential directions depend on the depth, H, and thus depend on time in unsteady flows. As shown above, the FLOMOD code ensures zero normal mass flux along slip boundaries without the need to use a smoothly varying boundary. This significantly simplifies the user's task in setting up model input data.

FEATURES OF THE MODELING SYSTEM FESWMS-2DH

Graphic Output Standard

FESWMS-2DH programs generate graphic output through calls to American National Standards Institute Graphical Kernal System (ANSI GKS) subroutines. Use of the GKS standard (1) makes the graphics programs very portable (that is, they will be able to run on any system provided the necessary interface software is available), (2) provides the ability to transport graphical information from one place to another (for example, by means of magnetic tapes or floppy diskettes), and (3) enables long-term storage of graphical information. The ANSI GKS has been adopted as a Federal Information Processing Standard (FIPS) effective November 3, 1986 (National Bureau of Standards, 1986).

Data Input Module, DINMOD

The data input module, DINMOD, can be used to develop a new finite-element network or to refine or modify an existing network. The capabilities of DINMOD include the following:

- Input of all geometric data required to define the finite-element network. Input data are read from data records and, optionally, from a previously generated geometric data file.
- Use of either U.S. Customary (inch-pound) units or International System (metric) units in all computations.
- Checking of all input data for compatibility with array dimensions and, optionally, for strict geometric consistency and completeness, which is useful when developing a new network or making extensive revisions to an existing network.

- Interpolation of nodal coordinates along straight-line segments of the finite-element network.
- Automatic generation of all or part of the finite-element network including element connectivity lists, nodal locations, and interpolation of nodal ground-surface elevations.
- Refinement of the network.
- Development of an element-assembly sequence that will result in an efficient frontal solution of the system of finite-element equations.
- Output of the processed geometric data to a file for input to other FESWMS-2DH programs.
- Plotting of the finite-element network and ground-surface elevation contours.

Error Checking

In order to assist the model user in developing or modifying a finite-element network, numerous error checks have been included in the data input module. Among the checks for geometric consistency and completeness of the finite-element network that have been added are the following:

- All node, element, element-sequence, and property-type numbers are checked for compatibility with the appropriate array dimensions and other program limits.
- Nodal coordinates are checked to be sure they are within the appropriate range.
- Each corner node is checked to be sure its coordinates are specified.
- Within an element, a check is made for different nodes with the same coordinates.
- DINMOD checks for consistency of element sides common to two elements.

- A check is made to see that each node is used only as a corner node, a midside node, or a center node (if any).
- DINMOD notes when the Jacobian determinant is negative or zero at a Gaussian integration point within an element. This is caused by a poorly formed element.

The geometric data file should not be considered free of errors until a network plot and a contour plot of ground-surface elevations are carefully inspected.

Automatic Network Generation

In order to use the finite-element method to solve surface-water-flow problems, a model must be constructed describing the geometry, physical properties, and boundary conditions of the system under study. For elementary problems, the required input data may be conveniently computed and assembled by hand, then keypunched or typed into a file. For moderate to large problems, manual preparation of the finite-element network data becomes a tedious and expensive task which is prone to errors.

Automatically developing all or part of the finite-element network is accomplished in DINMOD by first subdividing the area or areas for which elements are to be generated into one or more subareas of relatively simple shape. A second-level subdivision is then imposed on each of the initial regions to develop an orderly assemblage of elements and node points. DINMOD employs a triangulation technique (Tracy, 1976) in combination with a final smoothing procedure to automatically construct six-node triangular elements during the second-level subdivision.

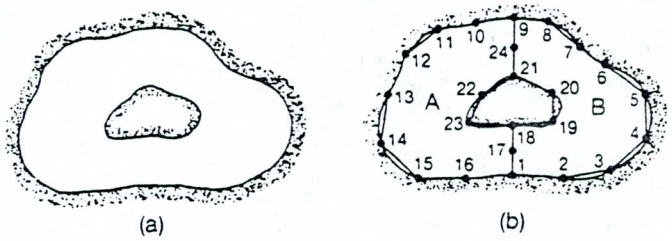

Figure 3. Examples of (a) a region inside of which a finite-element network is to be generated automatically and (b) an initial subdivision of the region into simply connected subregions A and B.

Initial subdivisions typically define areas of similar topography and surface cover in which solution gradients (that is, the horizontal rates of change of depth and velocity) are relatively constant. An initial region is described by a list of the corner nodes that form its boundary. These points are recorded starting at any node and proceeding around the boundary in a counterclockwise direction.

An initial region must be simply connected; that is, the entire boundary must be formed by a continuous line. If a network is to be automatically generated for a region such as that shown in figure 3(a), the region must be divided into at least two initial subregions, A and B, as shown in figure 3(b).

The polygon formed by the list of corner nodes defining the initial region is next filled in with six-node triangular elements. These elements are formed by cutting off sharp corners of the polygon

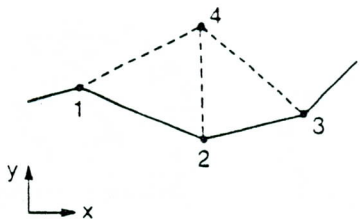

Figure 4. Formation of two new elements by automatic triangulation.

and replacing selected nodes on the boundary of the polygon with new nodes in the interior of the region.

The automatic triangulation begins by removing each vertex (corner node) of the polygon having an internal angle less than 90 degrees by connecting the two adjacent corner nodes to form a triangle. Then, starting at any vertex with an internal angle less than 180 degrees, two new triangles are formed by adding a corner node to the interior of the polygon based on the coordinates of the corner nodes adjacent to the vertex. The x- and y-coordinates of the new node are computed as

$$x_4 = \frac{1}{2}(x_1+x_3) + \omega(y_1-y_3) \tag{105}$$

and

$$y_4 = \frac{1}{2}(y_1+y_3) + \omega(x_3-x_1) \ , \tag{106}$$

where the subscripts refer to the numbered node points shown in figure 4 and ω is a weighting factor. The default value of ω in

DINMOD is 1/3; however, other values can be used to generate slightly different networks. If any vertices are created with internal angles less than 90 degrees, they are immediately removed by connecting the two adjacent vertices to form a new element. This process continues until there are only three nodes remaining in the polygon list, thus defining the last element.

Since there is the possibility of generating some overlapping elements that would eventually cause computational problems, a smoothing procedure is used to refine the shape of the elements formed in the triangulation process. The smoothing procedure used is the Laplacian scheme described by Buell and Bush (1973). This scheme requires the coordinates of the newly created node points to satisfy the equations

$$x_i = \frac{1}{2L_i} \sum_{k=1}^{L_i} (x_{kj} + x_{k\ell}) \tag{107}$$

snd

$$y_i = \frac{1}{2L_i} \sum_{k=1}^{L_i} (y_{kj} + y_{k\ell}) \ , \tag{108}$$

in which L_i is the number of elements connected to node i, and (x_{kj},y_{kj}) and $(x_{k\ell},y_{k\ell})$ are the coordinates of nodes in neighboring element k, as shown in figure 5. Since equations 107 and 108 are nonlinear, they are solved by an indirect iterative technique. Convergence is usually achieved within five iterations.

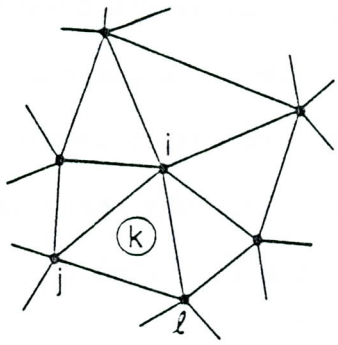

Figure 5. Neighborhood of node i in element k used in Laplacian smoothing of a finite-element network that has been generated automatically.

Element connectivity lists and the coordinates of newly created nodes are automatically computed. Ground-surface elevations of the corner nodes must be entered by hand.

An example of a region inside which elements are to be automatically generated is shown in figure 6(a). The generated network is shown in figure 6(b).

Network Refinement

In many instances, the user will not be sure just what level of discretization is required in a finite-element network to provide a desired solution accuracy. If this is the case, one way to proceed is to develop an initial network using fairly large elements in order to minimize computational effort and computer storage requirements. If the results indicate that a network with smaller elements is

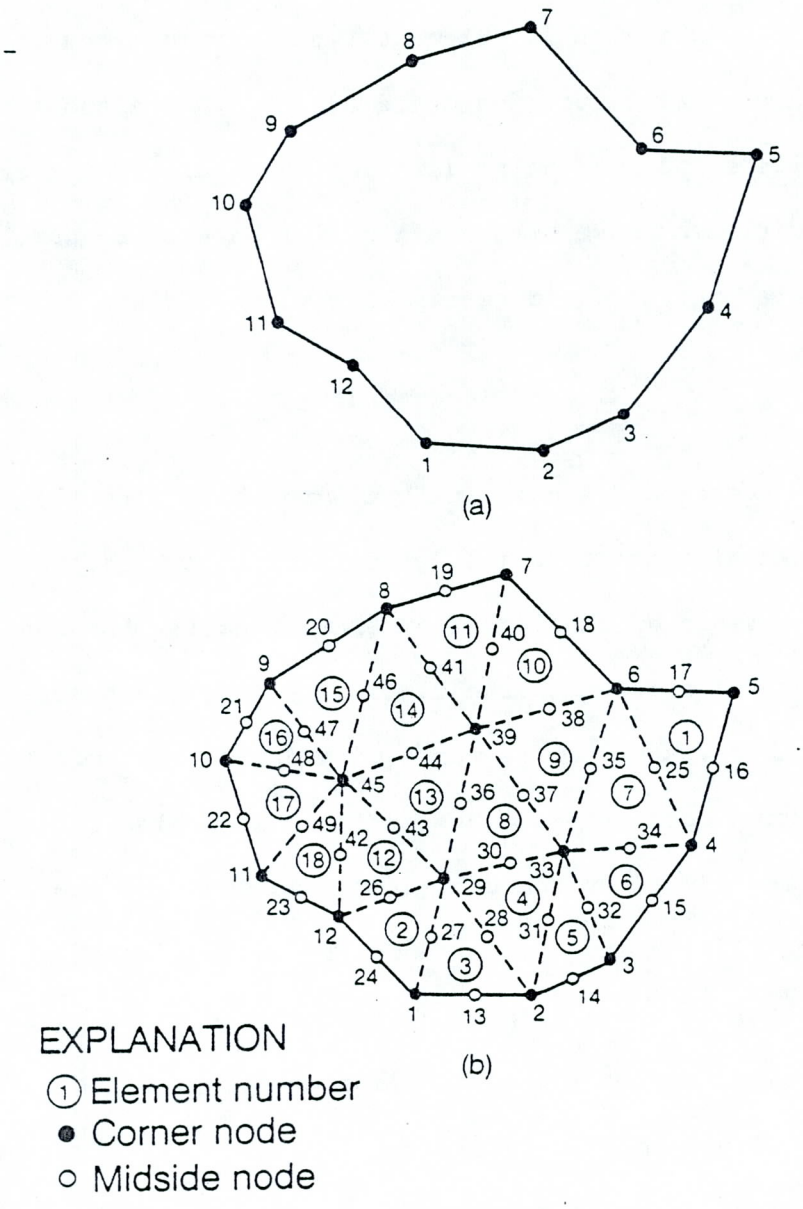

Figure 6. Example of a network that has been generated automatically: (a) an initial subdivision defined by a series of connected corner nodes and (b) the network generated inside the initial subdivision.

needed, a feature of DINMOD can be used to quickly refine the entire network by dividing all the elements into four similar elements as shown in figure 7. Elements with curved sides will be transformed into similar curved-sided elements. New element connectivity lists and node point data are automatically generated. However, a new element assembly sequence will have to be developed by using the element resequencing capability of DINMOD.

Element Resequencing

A frontal technique is used in FLOMOD to solve directly the system of finite-element equations. This technique assembles and reduces the equations on an element-by-element basis. As soon as the coefficients of a particular equation are completely assembled from the contributions of all elements adjacent to the node to which the equation corresponds, the partially assembled set of equations can be reduced by the completed equation, and the completed equation can be eliminated and stored out of core. Therefore, the entire global coefficient matrix is never completely formed in core. At any given instant, the equations contained in core are those that are either not yet complete (are only partially assembled) or those that have just been completed but have not yet been eliminated.

The degrees of freedom associated with the equations in core are called the wavefront, or simply the front, because the line of nodes corresponding to these active degrees of freedom generally moves through the network like a wave as the elements are assembled

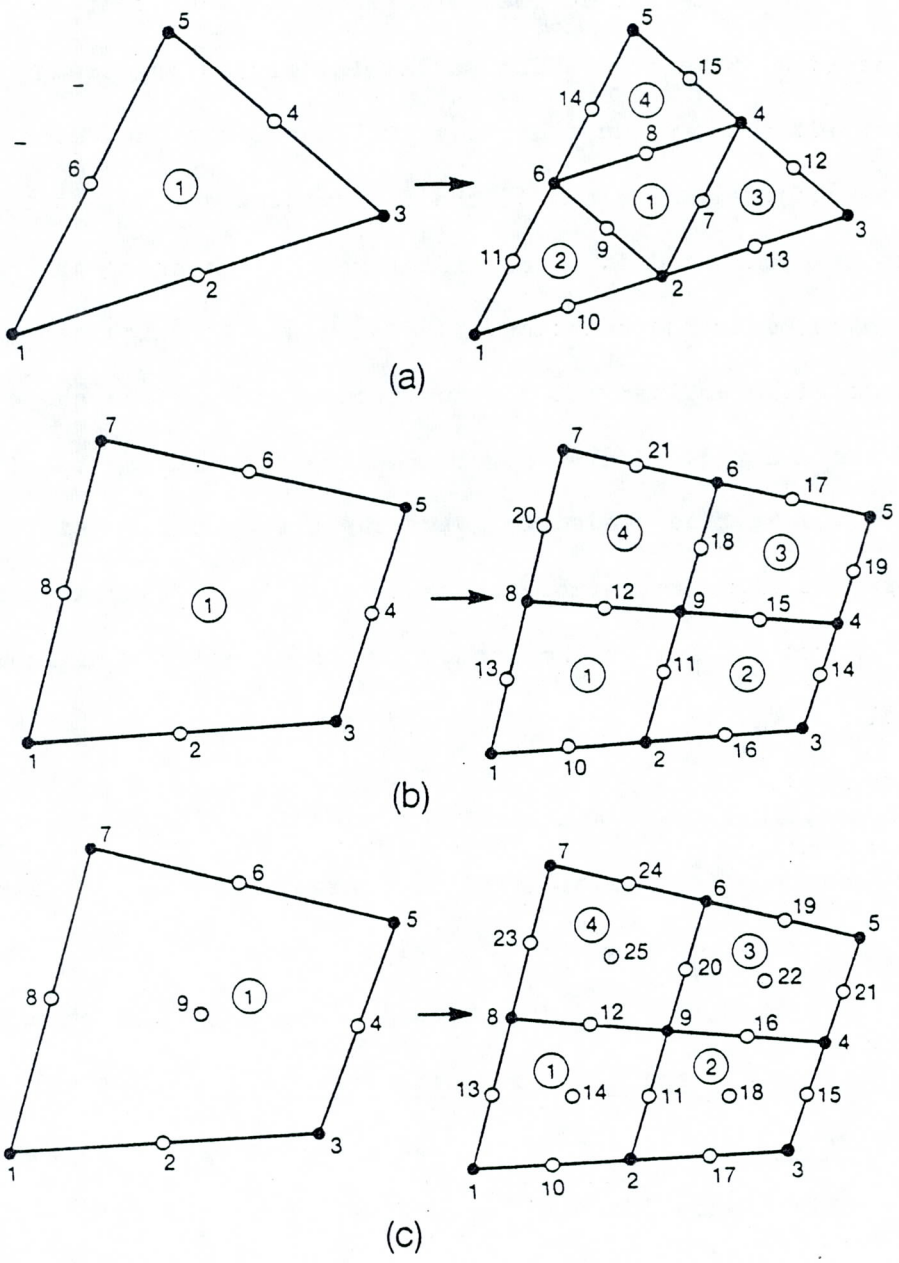

Figure 7. Refinement of (a) a six-node triangular element, (b) an eight-node quadrilateral element, and (c) a nine-node quadrilateral element.

in order. The number of degrees of freedom in the front is called the frontwidth. The frontwidth varies in size during equation solution, and the maximum frontwidth will determine how much core memory is required. The sum of the frontwidths squared as each equation is eliminated is proportional to the number of arithmetic operations used in the solution. The sequence in which the elements are assembled determines the maximum frontwidth and the sum of the frontwidths squared and thus determines the core memory requirements and the computer time needed to solve the system of equations. Therefore, an element-assembly sequence that keeps the maximum frontwidth and the sum of the frontwidths squared to a minimum is essential.

For small networks, a manual determination of an optimal element-assembly sequence is possible, but for large networks the task quickly becomes quite tedious and uneconomical to perform by hand. Two methods are available in DINMOD to automatically develop an efficient element-assembly sequence: the minimum-frontgrowth method and the level-structure method. Since it is virtually impossible to investigate all the combinations of element sequences, these algorithms attempt to provide good, but not necessarily the best, assembly sequences based on various solution strategies.

Both resequencing methods require an initial list of elements containing at least one element with which to begin the resequencing. From this starting list, assembly sequences for the remaining elements are determined. For both methods, several different

starting element lists should be attempted before a final element-assembly sequence is accepted. A good initial starting list consists of all or just some of the elements running across the narrowest edge of the network.

Minimum-frontgrowth method

The minimum-frontgrowth method tries to maintain the smallest possible frontwidth at all times. The initial wavefront is determined from the starting element list and is defined in terms of nodes rather than degrees of freedom. The nodes forming the wavefront are those that are attached both to elements that are assembled and to elements that have not yet been assembled. A list of unassembled elements lying along this front is formed. The element contained in this adjacent-element list that gives the smallest frontwidth upon its assembly is chosen to be the next element assembled. If more than one element gives the same minimum frontwidth, various tie-breaking strategies are used to choose between them. Once the element is assembled, the wavefront is modified and the adjacent-element list is updated. This process continues until all elements have been resequenced.

Sometimes an element in the adjacent-element list is passed over for assembly a great number of times. This can lead to excessively large frontwidths. In order to avoid this situation, a parameter that controls the maximum length of stay of an element in the adjacent-element list is included. An appropriate value

for this parameter has to be determined by trial and error, but a value equal to about twice the expected maximum frontwidth (in terms of nodes) is a good first try. The maximum frontwidth can be estimated as the number of nodes in a line across the widest part of the network when the network is aligned lengthwise.

Level-structure method

The level-structure method uses a simple layer-by-layer resequencing strategy and is much faster than the minimum-frontgrowth method, especially for large networks. As in the previous scheme, a starting element list is given, and the wavefront as well as a list of elements adjacent to the wavefront is formed. Then, the first element in the adjacent-element list is assembled, and the unassembled elements adjacent to it are added to the adjacent-element list while the first element is removed. This process continues until all elements have been assembled.

Depth-Averaged Flow Module, FLOMOD

The depth-averaged flow module, FLOMOD, solves the equations of steady or unsteady two-dimensional surface-water flow in the horizontal plane. The capabilities of FLOMOD include the following:

- Input of geometric, initial, boundary, wind, and element-property data.
- Use of either U.S. Customary (inch-pound) units or International System (metric) units in all computations.
- Checking of input data for compatibility with array dimensions.

- Solution of the flow equations.
- Automatic adjustment of the network boundary to allow "dry" nodes to exist in the network.
- Automatic computation of unit discharge along a section of a network boundary where total discharge across the section is specified as a boundary condition.
- Computation of the flow across specified cross sections and the computation of continuity norms.
- Printing of results at selected iterations or times. Writing of a solution output file.

Error Checking

Numerous error checks have been included in the flow module. These include the following:

- All node, element, element-sequence, and property-type numbers are checked for compatibility with the appropriate array dimensions and other program limits.
- Values of Manning's n and the Chezy C are checked to be sure they are positive.
- A check is made to determine that depths prescribed at boundaries are positive.
- When a ceiling elevation is given, it is checked to make sure that it is greater than the ground-surface elevation.
- A check is made to be sure that weir and culvert nodes are boundary nodes.
- The maximum frontwidth and the maximum number of equations are checked for consistency with the appropriate array dimensions and other program limits.
- An error message is written if a zero pivot is found in solving the finite-element equations.

Automatic Boundary Adjustment

A feature has been added to FLOMOD to allow elements that are not fully covered by water to exist in the finite-element network. Previously, the extent of the submerged area had to be known (or guessed) in advance, and the finite-element network had to be designed so that all elements would be completely covered by water during the simulation. If the depth of water at a node became negative, computational problems arose.

A conceptually simple scheme to automatically solve the problem of defining the boundary of the finite-element network has been added as an option to FLOMOD. This is done by excluding from the computations those elements that are at least partially dry.

To explain how the algorithm determines whether or not an element should be included in the computations, some terms must be defined. An element is said to be "on" if it is included in the computation and is said to be "off" if it is not included. A "dry" element is one that has at least one node at which the flow depth is not positive. A "wet" element is one in which all nodes have positive flow depths.

At the beginning of each iteration, each element that is currently on is checked to see if it is dry. If found to be dry, that element is turned off. In addition, each element that is currently off is checked to see if it should be turned on.

The decision to turn on an element is based on the minimum flow depth and maximum ground-surface elevation at the element's node points. If the minimum water-surface elevation is greater than the maximum ground-surface elevation plus some small depth tolerance, the element is turned on. The need for a depth tolerance is twofold. First, there will probably be some change in the water-surface elevation across the element when it is turned on because of energy losses. Second, the element condition (wet or dry) may oscillate between iterations resulting in a slowly convergent or a divergent solution. A depth tolerance of 0.5 feet has been found to provide good results and is used in FLOMOD; however, this value will depend on the size of the elements in the finite-element network and the flow conditions.

It is possible that an element that would actually be wet is turned off in the final solution. However, the depth of flow in such an element would be small, and the effect of not including it in the computational network would be negligible. The possibility of this occurring can be minimized by constructing smaller elements in areas where the computation network boundary is expected to occur.

The automatic boundary-adjustment feature allows a finite-element network to be designed without too much concern for the location of boundaries. However, one must still be very careful in specifying ground-surface elevations within the network. If the automatic boundary-adjustment feature is being used and a high node point

(located on a channel bank in the middle of a flood plain, for example) becomes dry, all the elements containing that node point will be turned off for the next iteration. This could significantly affect the solution unless all the elements turned off were quite small.

Either slip or no-slip conditions (as specified by the user) are automatically applied at all existing or newly created boundary nodes. However, if a velocity, unit discharge, or depth condition is specified at a node point that is eliminated from the computation network, and this node is later readmitted for computation, the boundary condition that was specified at that node will not be specified again. Therefore, if a velocity, unit discharge, or water-surface elevation is specified at a node, the user must be certain that the node will not be removed from the computation network even temporarily during the automatic boundary-adjustment process.

The Continuity Norm

A potential problem with mixed interpolation is that mass conservation is not well enforced because the ratio of discrete continuity constraints to discrete momentum equations is much smaller than the continuum ratio of 0.5.

Computing the mass flux at model cross sections in steady-state simulations is one method for determining whether mass-conservation errors are within acceptable limits. At cross sections where the

mass flux differs substantially from the inflow, the finite-element network can be refined to reduce the errors. An even better method for determining parts of the network which should be refined to improve mass conservation is the computation of the continuity norm for each element in the network.

Letting R denote the continuity-equation residual,

$$R = \frac{\partial H}{\partial t} + H\frac{\partial U}{\partial x} + U\frac{\partial H}{\partial x} + H\frac{\partial V}{\partial y} + V\frac{\partial H}{\partial y}, \tag{109}$$

the continuity norm is defined by

$$\left(\frac{1}{A_e}\int_{A_e} R^2\, dA_e\right)^{1/2}, \tag{110}$$

where A_e is the element area. The continuity norm will be large for those elements in which mass-conservation errors are large. Computation of the continuity norm has been added as an option to FLOMOD. Norms greater than a user-defined value are flagged with an asterisk. The network can then be refined in areas where the continuity norms are large.

Output Analysis Module, ANOMOD

The output analysis module, ANOMOD, is the modeling-system postprocessor. Its capabilities include the following:

- Plotting of the finite-element network.
- Plotting of velocity or unit-discharge vectors.

- Plotting of ground-surface-elevation contours.
- Plotting of water-surface-elevation contours.
- Plotting of flow-check lines.
- Plotting of time-histories of velocity, unit discharge, or water-surface elevation at a node point.
- Plotting of contours of the difference between water-surface elevations from two different simulations. This capability can be used to plot lines of equal backwater.
- Plotting of ground-surface elevation, water-surface elevation, velocity, or unit discharge at a cross section.
- Checking of all node and element numbers, time-history node numbers, the number of flow-check lines, and the number of element sides for compatibility with appropriate array dimensions and other program limits.

APPLYING FESWMS-2DH TO DATA FROM THE FLOOD PLAIN SIMULATION FACILITY

FESWMS-2DH was used to simulate normal and contracted steady flows in the Flood Plain Simulation Facility at the Gulf Coast Hydroscience Center near Bay St. Louis, Miss.

This application was designed to answer several questions. First, how well can the backwater and discharge distribution associated with steady flow through a constriction in the Flood Plain Simulation Facility be modeled under the assumptions of a simple representation of the kinematic eddy viscosity, a momentum-correction-coefficient value of unity, and a single linear representation of Manning's n as a function of depth determined during normal flow at the same discharge? Second, can a fairly coarse network be used to accurately simulate backwater and flow distribution throughout the flow domain? Can such a network be used to accurately simulate the jet and recirculation downstream from the opening? Third, can the flux-computation and continuity-norm options in FLOMOD be used to selectively refine a network to achieve improved accuracy? The information obtained in answering these questions suggests that FESWMS-2DH should be an effective tool for solving prototype problems involving the design and analysis of complex highway crossings of flood plains.

Research Facility

The Flood Plain Simulation Facility (FPSF) is an L-shaped basin approximately 300 ft wide with a straight reach approximately 2,690

ft long upstream from a right-angle bend to the left and a straight reach approximately 1,020 ft long downstream from the bend. The bend has a centerline radius of curvature of 450 ft. A trapezoid-shaped low-water channel is located in the center of the basin and is approximately 1 ft deep with a bottom width of 10 ft and side slopes of 2:1 (H:V). Both edges of the flow basin are bounded by levees of sufficient height to permit depths of flow up to 3 ft.

The basin was constructed with a uniform downstream design slope of 0.0004 and with both overbank flow areas sloping toward the low-water channel with a design slope of 0.00067 to facilitate drainage. Roughness consists of a fairly dense cover of coastal Bermuda grass. A diagram of the basin is shown in figure 8.

A constriction that consists of bottom-mounted, movable, hinged plates is located 1000 ft downstream from the upstream end of the basin. The hinged plates, each about 3.4 in thick, are arranged so that when they are raised and fastened into place, a vertical flat-plate constriction is formed. Except for the plates in the low-water channel, each plate is about 2.8 ft high, and except for four smaller transition plates, each is about 10 ft long. Thus, the opening width can be adjusted in 10-foot increments. The location of the constriction is shown in figure 8.

Inflow to the basin is through an open-reservoir-type head basin from three constant-discharge pumps. Each pump has a design capacity of 70 ft^3/s. Water is pumped from a freshwater canal

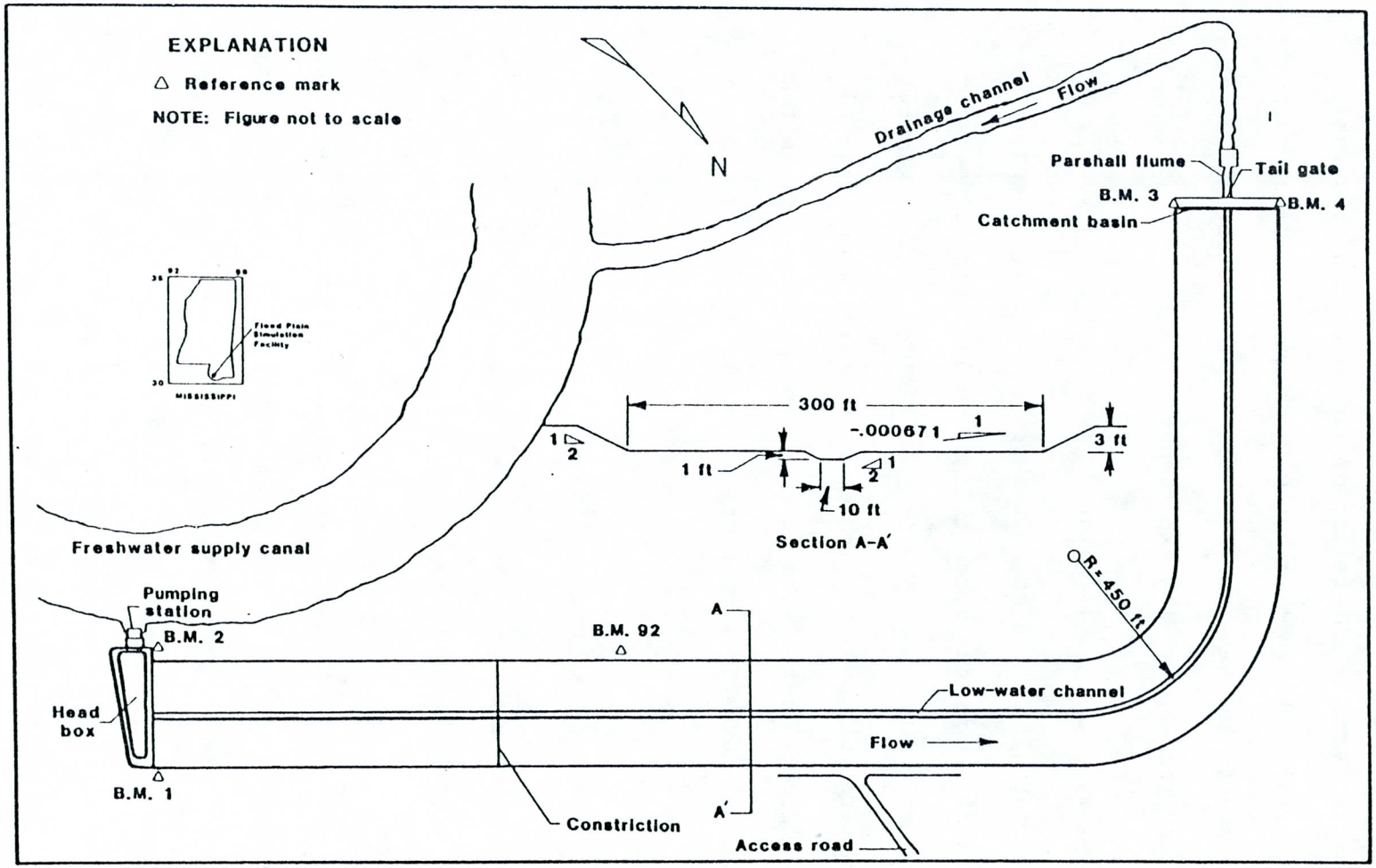

Figure 8. Plan view of the Flood Plain Simulation Facility.

adjacent to the facility. Gate valves were installed in two 3-foot bypass pipes to regulate the return of flow from the head basin back to the canal. The gate valves were rated in place by current-meter measurements and were set manually to obtain some of the flow rates used for the steady-flow experiments.

The water-surface elevation at the downstream end of the facility is controlled by a movable sharp-crested weir that is located in a 35-foot-wide concrete-lined outlet channel downstream of a concrete-lined catchment basin 300 ft wide and approximately 10 ft long. The outflow weir was set to minimize backwater and drawdown. Current-meter discharge measurements were made in the drainage channel downstream from the outlet gates for each of the steady-flow experiments.

Data Collection

Water-surface elevation data were collected using 165 dual-line-type bubble gages located in 15 basin cross sections with 11 points per cross section. In addition, 55 additional depth sensors were located near the constriction between cross sections 750 and 1200. (Cross-section values refer to the distance in feet from the upstream end of the basin.) The depth-collection system was operated on a 6-minute record cycle for all steady-flow experiments, and approximately 13 records were collected for each steady-flow experiment. Water-surface elevations also were obtained from manual measurements using the 35 staff and crest-stage gages located

along the right bank of the facility and 34 staff and crest-stage gages located along the left bank. Also, data were collected at staff gages located on the upstream and downstream sides of each plate forming the constriction. At least two complete sets of staff-gage and crest-stage-gage readings were collected for each steady-flow experiment. Both manually and automatically collected water-surface-elevation data are accurate to within ± 0.02 ft.

Point velocity data were collected automatically at four cross sections (900, 950, 1050, and 1100) during each steady-flow experiment. Twenty six current meters (Price pygmy- or AA-type meters) were located in each cross section. Each current meter was positioned on a stationary rod at 0.2 of the depth below the water surface because of grass interference with the bucket wheels at lower depths and distortion of the velocity profiles. Overhead wires connected the current meters to the data assemblers. Velocities were obtained from the current-meter time and revolution data by the use of a standard rating for the appropriate meter type.

Vertical velocity profiles were collected on both of the overbanks and in the low-water channel to define the vertical velocity distribution. The point and profile current-meter data are accurate to within 5 percent.

The flow direction at each velocity-measurement point was determined by attaching a short thread to the back of each current meter and determining the angle of deflection from the basin's longitudinal axis. A tag line was set at each cross section to help in the alignment of the angle reader. The angle data are considered accurate to within 5 degrees.

Experiments on Flow through Contracted Openings

From October to December 1975, data were collected in 33 steady-flow experiments on flow over uniform grass roughness with concentric contracted openings. These experiments involved five discharges and four contraction ratios. For each discharge, both normal and contracted water-surface profiles were measured. Throughout this series of experiments, the coastal Bermuda grass covering the basin was approximately 10 in high.

Before the experimental season began, ground-surface-elevation data were obtained by differential leveling. Data were collected every 50 ft longitudinally and every 10 ft laterally. More frequent lateral measurements were made where necessary to define breaks in cross-section geometry. In addition, the elevations of the sensor heads and the elevations of the zeroes of the staff gages, including those on the constriction plates, and the crest-stage gages were found.

The experiments are summarized in table 3. All experiments are numbered using an eight-character alphanumeric numbering system.

The first character, S, refers to steady flow. The second two digits are the experiment number. The next four digits record the month and date of the experiment. The last digit is the last digit of the calendar year. The experiment number is given in the first column of table 3. The design and measured discharges are recorded in the third and fourth columns of the table. The design discharges ranged from 50 to 210 ft^3/s. The grass height is given in the fifth column. Whether the flow was normal (N) or contracted (C) is recorded in the sixth column. The contraction ratio, m, is given in the seventh column. This ratio is defined as

$$m = 1 - \frac{b}{B}, \tag{111}$$

where b is the opening width and B is the total basin width, in this case 300 ft. The four contraction ratios used were 0.42, 0.62, 0.82, and 0.95, corresponding to opening widths of 174, 114, 54, and 14 ft, respectively.

During a given week of data collection, the discharge was held fixed. During the first week, the design discharge was 50 ft^3/s; during the second week, it was increased to 70 ft^3/s; and so forth. For a fixed discharge, a normal-flow experiment was conducted first. Then a concentric contraction was formed by raising the hinged plates. The opening size was decreased as the week progressed. The final experiment for each discharge was another normal-flow experiment. During the final week of the

Table 3. Summary of 1975 steady-flow experiments on flow through contracted openings.

Experiment number	Discharge, in cubic feet per second		Grass height, in inches	Experiment type (Normal or Contracted)	Contraction ratio
	Design	Measured			
S5810015	50	47.9	9.8	N	
S5910015	50	47.9	9.8	C	0.42
S6010025	50	48.5	9.8	C	0.62
S6110025	50	48.5	9.8	C	0.82
S6210035	50	47.1	9.8	C	0.95
S6310035	50	47.1	9.8	N	
S6410085	70	67.8	9.5	N	
S6510085	70	67.8	9.5	C	0.42
S6610095	70	68.1	9.5	C	0.62
S6710095	70	68.1	9.5	C	0.82
S6810105	70	66.6	9.5	C	0.95
S6910105	70	66.6	9.5	N	
S7010215	110	109	10.5	N	
S7110215	110	109	10.5	C	0.42
S7210225	110	111	10.5	C	0.62
S7310225	110	111	10.5	C	0.82
S7410235	110	111	10.5	C	0.95
S7510235	110	111	10.5	N	
S7610295	160	160	10.0	N	

Table 3. Summary of 1975 steady-flow experiments on flow through contracted openings (continued).

Experiment number	Discharge, in cubic feet per second		Grass height, in inches	Experiment type (Normal or Contracted)	Contraction ratio
	Design	Measured			
S7710295	160	160	10.0	C	0.42
S7810305	160	159	10.0	C	0.62
S7910305	160	159	10.0	C	0.82
S8010315	160	160	10.0	N	
S8111045	210	210	10.0	N	
S8211045	210	210	10.0	C	0.42
S8311055	210	218	10.0	C	0.62
S8411055	210	218	10.0	C	0.82
S8511065	210	213	10.0	N	
S9812155	50	51.7	10.5	N	
S9912155	70	68.0	10.5	N	
S0112165	110	105	10.5	N	
S0212165	160	160	10.5	N	
S0312175	210	217	10.5	N	

season, normal-flow experiments were repeated for all five discharges.

For a given week of experiments, the appropriate discharge was set at the headbox, and steady flow was established with all the constriction plates down. The outflow weir was adjusted to minimize backwater and drawdown and establish steady, uniform flow.

The current meters were positioned in the vertical 0.2 of the depth below the water surface. As the current meters were positioned, the direction of flow at the meter was recorded.

Early in each experiment day, a discharge measurement was made in the outflow channel. As the automatically collected depth and current-meter measurements were being recorded, the manually collected gage and vertical-velocity data were collected. During 22 of 33 experiments, an average of 6.4 vertical velocity profiles were obtained. (No vertical velocity profiles were obtained during 11 of the experiments.)

After the normal-flow experiment was completed, plates were raised to form the first constriction. When the flow had become steady, the current meters were repositioned and the angles of flow recorded. Automatic and manual data were collected as before. The test cycle continued with constriction changes, meter repositioning, and data collection until the test series for the week was complete.

Data Processing

All manually and automatically collected water-surface-elevation data were grouped into one composite record for each experiment. The manually collected data were checked for incorrect elevations, and a mean elevation was determined from the two readings. These elevations were assumed to be the true elevation. The automatically collected elevation data required small corrections to account for friction losses in the bubble-gage system. The corrections were determined by comparing the manually collected data to the automatically collected data for normal-flow experiments. For these experiments, the water surface at a cross section was known to be horizontal, and the elevations from the bubble gages could be compared to the elevations from the staff gages to determine the corrections necessary to make the water surface at that cross section horizontal. This correction was then applied to all automatically collected elevation data from both normal-flow and contracted-flow experiments.

The corrected elevation files were merged to form one water-surface-elevation file for each experiment. The elevation data include data obtained from the automatic bubble-gage sensors, the staff gages, including those on the constriction plates, and the crest-stage gages.

The automatically collected velocity data were in the form of elapsed time and meter revolutions for each current meter. Bad

data, usually caused by a fouled meter, were deleted, and a mean for each meter was computed using the remaining data. The mean time and revolutions for each current meter were converted to velocities using standard ratings. After conversion, the velocities were checked to ensure that they were reasonable. No attempt was made to correct or estimate apparently faulty velocities. Such values were deleted. The final velocity file for each experiment contains the longitudinal and lateral position of each meter, the total depth, the fraction of the total depth the meter was located below the water surface, the flow angle, and the flow speed.

The vertical-velocity-profile data were processed in the field. The data include the location of the profile observation, the flow direction, the point velocities, and the depths at which the velocities were obtained.

Data Analysis

To use the velocity data collected in the FPSF for calibrating and verifying two-dimensional, vertically averaged models required the conversion of the point velocities measured 0.2 of the depth below the water surface to vertically averaged velocities.

A correction factor was developed on the basis of the vertical velocity profiles. A total of 140 vertical velocity profiles were obtained during the 1975 steady-flow experiments. The total included 34 at the design discharge of 70 ft^3/s, 53 at 110 ft^3/s, 31 at 160 ft^3/s, and 22 at 210 ft^3/s.

from the profile.

Using the data for the 140 profiles, an equation for the correction factor, f_v, was obtained by multiple linear regression. The regression equation is given in terms of three dimensionless variables: a relative roughness,

$$k = \frac{H}{H_G} , \tag{112}$$

in which H is the depth at the profile location and H_G is the height of the grass for the experiment; a Froude number,

$$F_1 = \frac{Q}{HB\sqrt{gH}} , \tag{113}$$

in which Q is the measured discharge for the experiment and B is the width of the basin (300 ft); and a second Froude number,

$$F_2 = \frac{v_{.2}}{\sqrt{gH}} , \tag{114}$$

in which $v_{.2}$ is the point velocity measured 0.2 of the depth below the water surface. Because there was little variation in the height of the grass during the experimental series, a constant value of H_G equal to 10 in was used in equation 112. The correction factor is plotted against each of these three dimensionless variables in figures 10 through 12. It is evident that there is significant scatter in the data and that, consequently, not all the variation

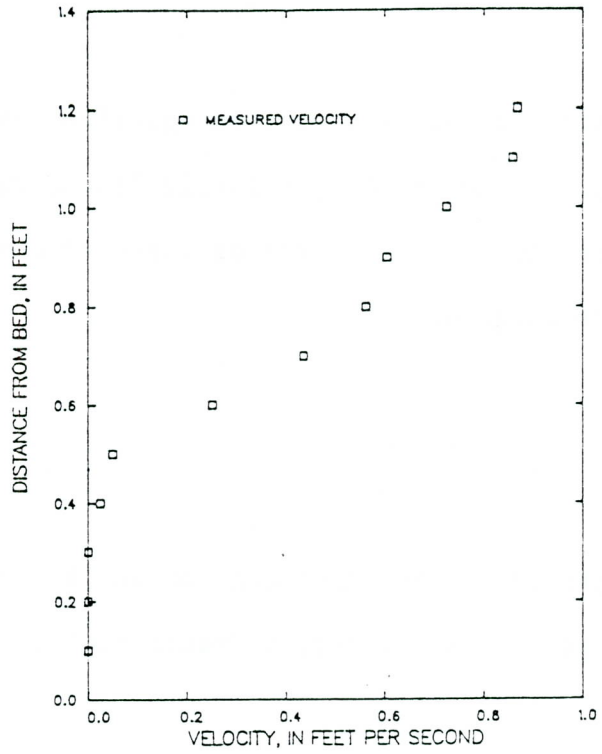

Figure 9. Vertical velocity profile measured 135 feet from the right bank at cross section 1050 during experiment S6810105. The total depth is 1.29 feet.

To compute the average velocity corresponding to each profile, the profile was integrated under the assumptions that the velocity is linear between measured values, the velocity at the bed is zero, and the velocity at the water surface can be obtained by linear extrapolation from the two velocities immediately below the water surface. One of the profiles is shown in figure 9. The average velocity was computed by dividing the integral of the velocity profile by the total depth. The correction factor for the profile was then calculated by dividing the average velocity by the velocity at 0.2 of the depth below the water surface, obtained by interpolation

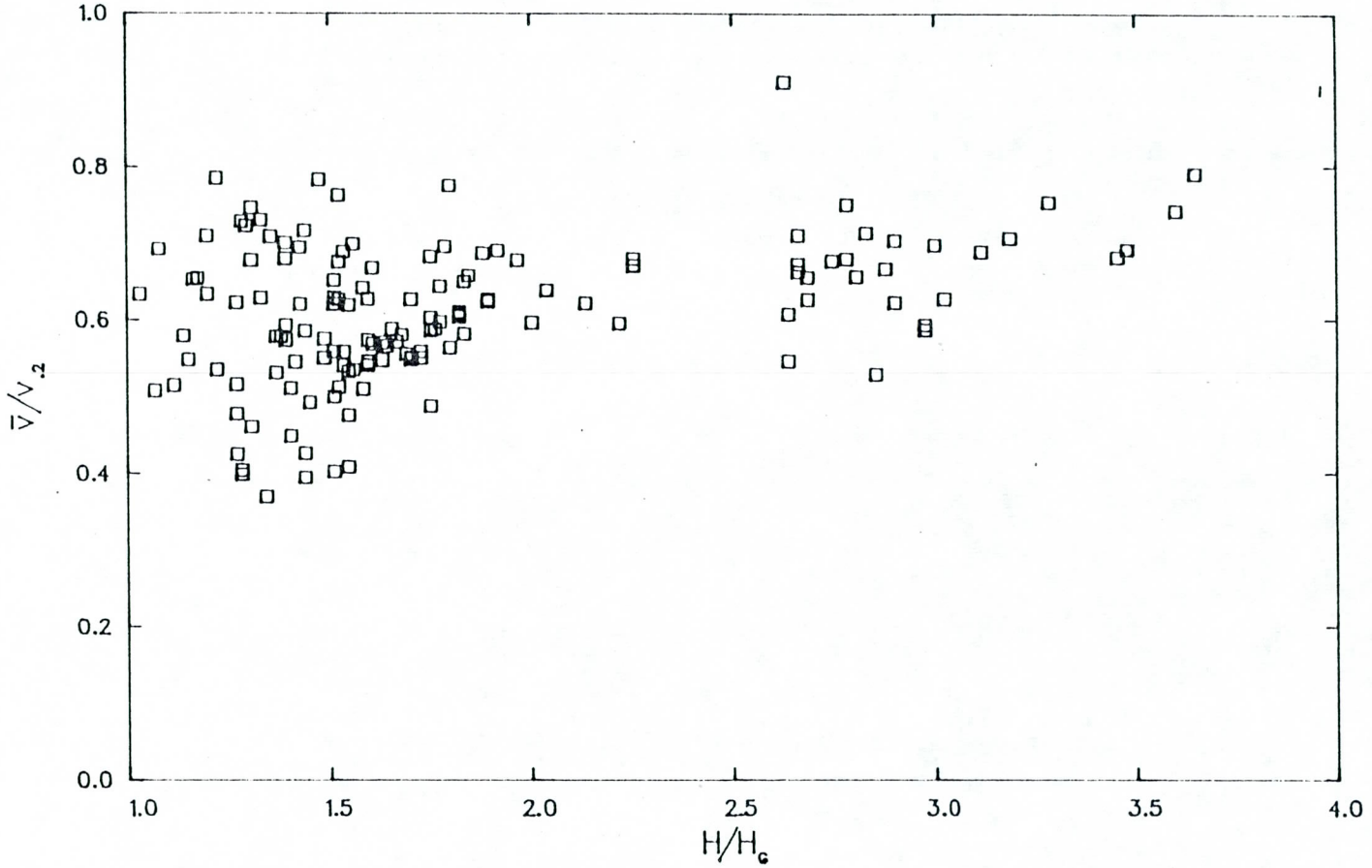

Figure 10. Velocity correction factor as a function of relative roughness for 1975 vertical velocity profiles.

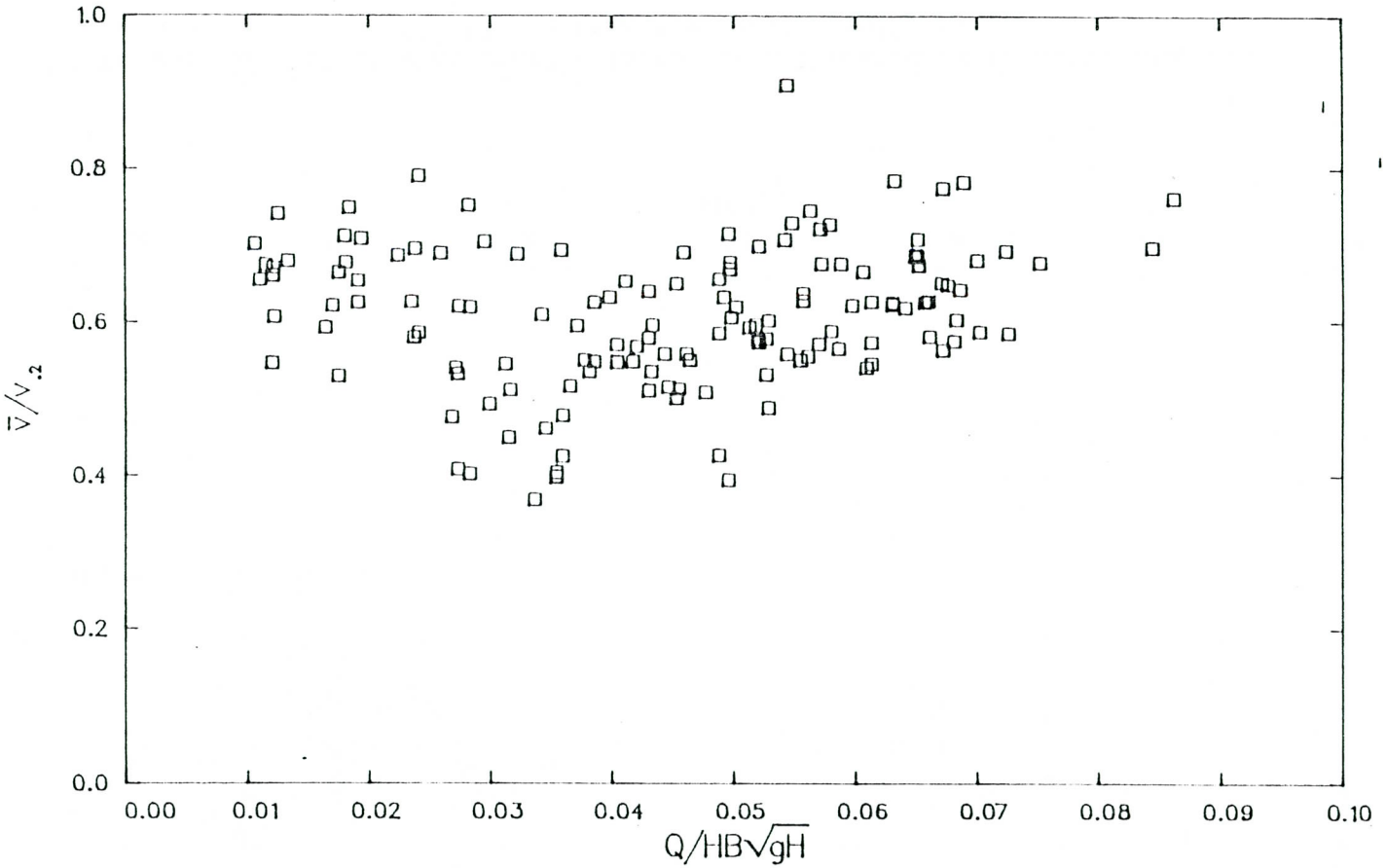

Figure 11. Velocity correction factor as a function of discharge Froude number for 1975 vertical velocity profiles.

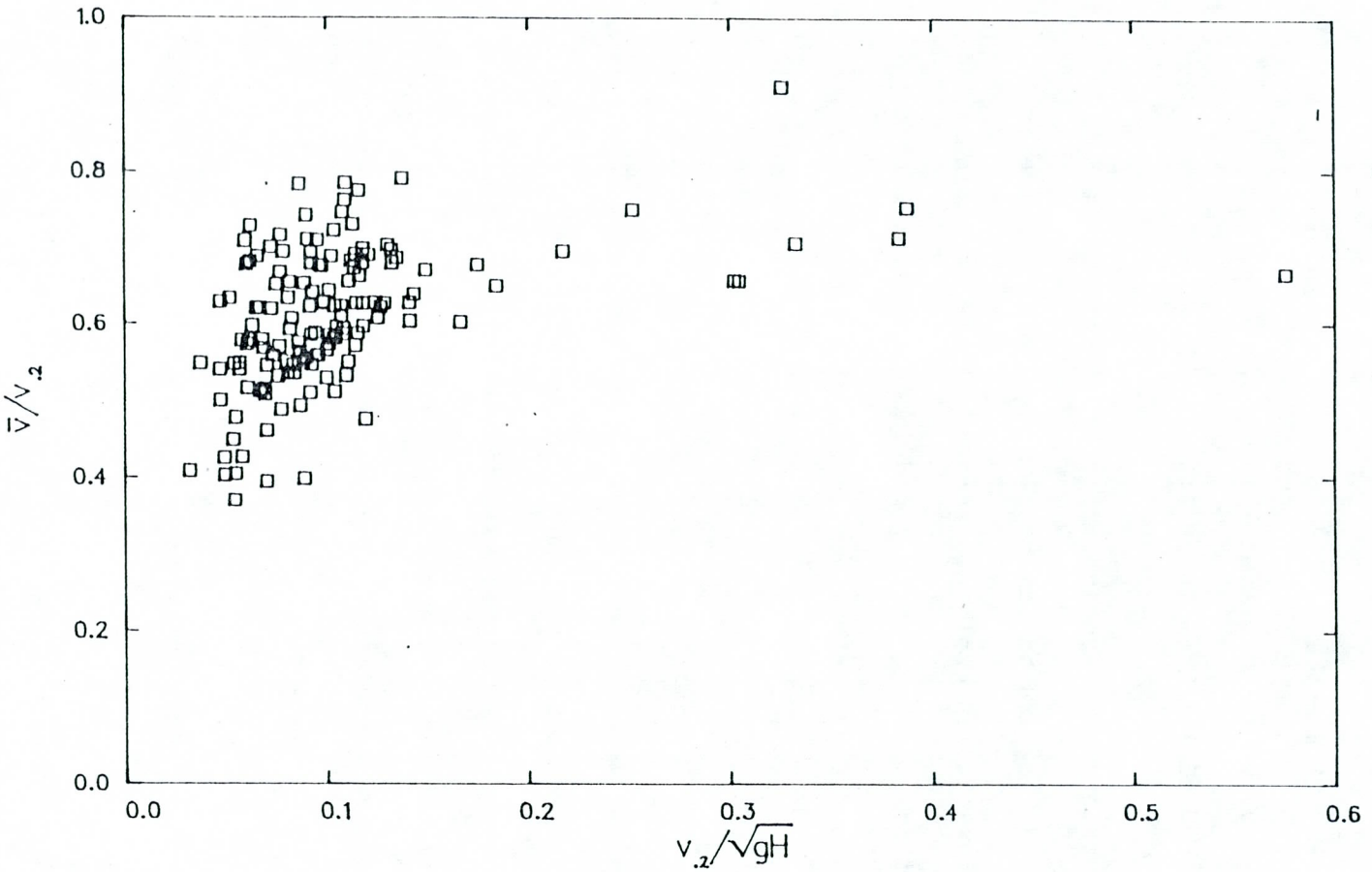

Figure 12. Velocity correction factor as a function of point velocity Froude number for 1975 vertical velocity profiles.

in the correction factor can be explained by the regression equation. The regression equation for the correction factor, f_v, is

$$\bar{f}_v = -0.1173 + 0.2063\,k + 15.26\,F_1 + 1.869\,F_2 - 5.354\,kF_1 + 0.1606\,kF_2 - 4.678\,F_1F_2 + 0.007451\,k^2 - 30.60\,F_1^2 - 1.959\,F_2^2 \quad . \qquad (115)$$

Various combinations of these and other dimensionless variables were tried in the regression analysis, but no other choice of three or fewer variables explained as much of the variation in the correction factor as do the three given in equations 112 through 114. About 54 percent of the variation in f_v is explained by this regression equation.

All 1975 velocity data were multiplied by the correction factor, f_v. Next, using the corrected point velocities, a discharge, Q_x, was computed at each of the four cross sections where velocity data were collected. All corrected point velocities in a cross section were multiplied by the ratio Q/Q_x to yield the final vertically averaged velocities. Thus, a vertically averaged velocity, $\bar{v}$, can be represented as

$$\bar{v} = \frac{Qf_v v_{.2}}{Q_x} \quad . \qquad (113)$$

Typical corrected velocity components are compared with velocity components which have been corrected only by multiplication by the factor Q/Q_x (called "uncorrected" velocity components in the figure

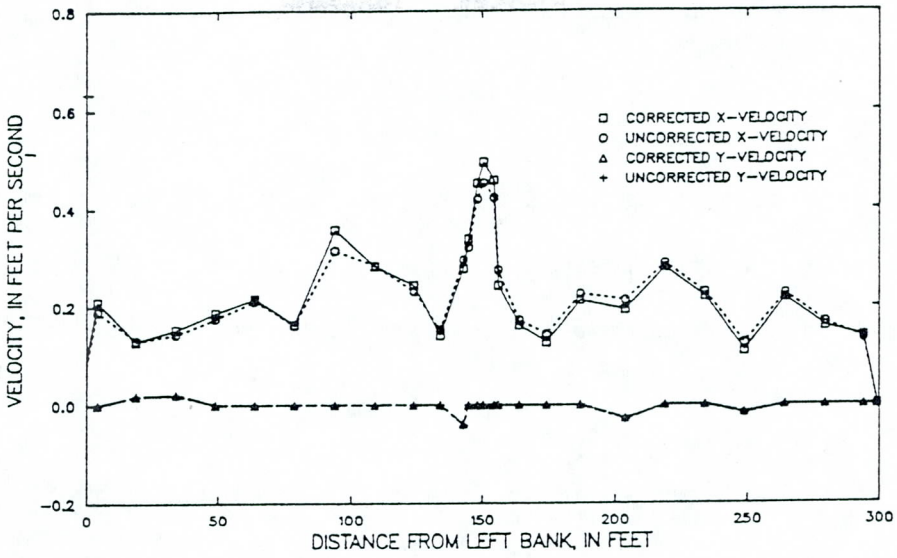

Figure 13. Corrected and uncorrected velocity components for experiment S6410085 at cross section 900.

explanation) in figure 13. Although multiplication by the factor f_v increases some overbank velocities and decreases others, peak values in the low-water channel are consistently larger after correction.

A second approach for obtaining vertically averaged velocities was tried in which separate regression correction factors were obtained for the low-water channel and the overbanks. After these corrections were applied to the point velocities, the cross-sectional velocities were corrected as in the first method. Because the difference between the two approaches was negligible, and because the first approach was simpler, it was used throughout this study.

Modeling Flood Plain Simulation Facility Data

Model Ground-Surface Elevations

All finite-element networks developed in this study extended 600 ft upstream and downstream from the constriction. Elements were located so that the trapezoid-shaped low-water channel could be modeled accurately.

The ground-surface-elevation data at cross sections 50 ft apart were used to represent the bed at each cross section as a series of linear segments. By linear regression, straight lines were fit to the ground-surface-elevation data on each overbank and on the bottom of the low-water channel. Then the overbanks were connected by straight line segments to the channel bottom so that the entire cross section was represented by five line segments. The data points and the resulting five-segment representation for cross section 400 are shown in figure 14. Ground-surface elevations for all finite-element networks were obtained by linear interpolation between cross sections where ground-surface-elevation data were available using values from these five-segment representations.

Modeling Normal Flows

A network was developed first to model the normal-flow experiments (fig. 15). Most elements in this network were 20-foot-by-20-foot squares except along the low-water channel, where smaller rectangles were used to define the channel.

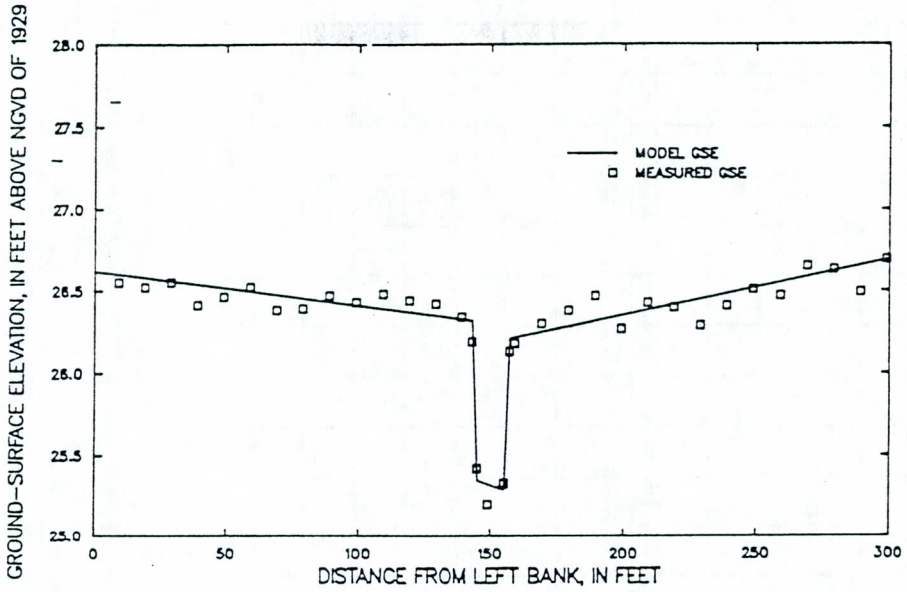

Figure 14. Ground-surface-elevation (GSE) data and model ground-surface representation at cross section 400.

For each normal-flow experiment modeled, the downstream model water surface was assumed to be horizontal, and its elevation was taken as the average observed water-surface elevation there. In all cases, a natural boundary condition was used at the downstream end. The upstream unit-discharge distribution was chosen to approximate the unit-discharge distributions at the four cross sections where observed velocity data were available and to give the correct total measured discharge. At all solid boundaries, a slip boundary condition was used.

The flow model was calibrated separately for each of the normal-flow experiments S5810015 (47.9 ft^3/s), S6410085 (67.8 ft^3/s), S7010215 (109 ft^3/s), S7610295 (160 ft^3/s), and S8111045 (210 ft^3/s) by adjusting Manning's n, represented as a linear function of depth,

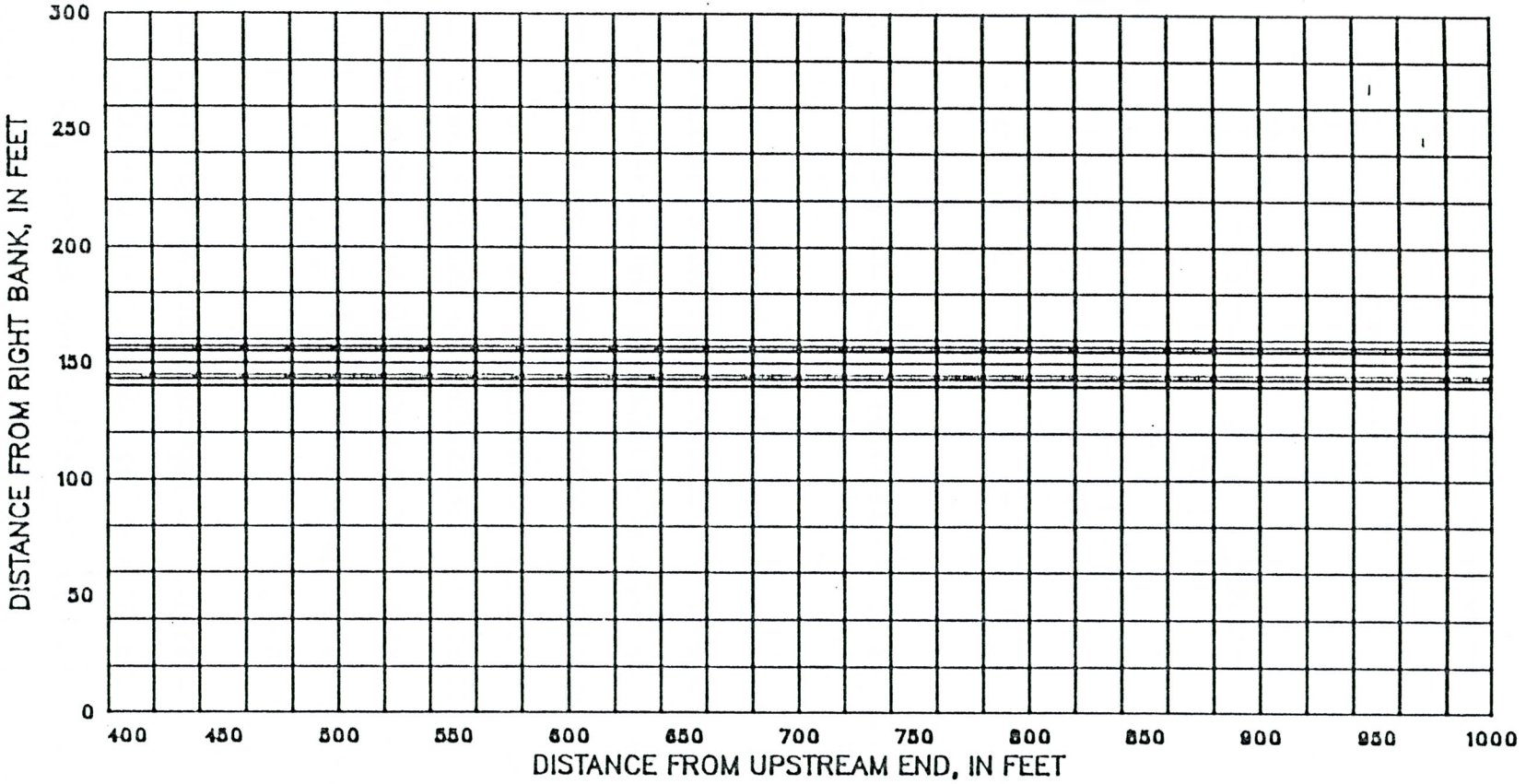

Figure 15. Upstream half of the finite-element network used to model normal-flow experiments.

Table 4. Values of Manning's n determined by calibration of the model for normal-flow experiments.

Experiment number	Manning's n, n_1	Depth, H_1, in feet	Manning's n, n_2	Depth, H_2, in feet
S5810015	0.263	0.5	0.049	2.5
S6410035	0.206	0.5	0.066	2.5
S7010215	0.139	0.5	0.067	2.5
S7610295	0.116	0.5	0.063	2.5
S8111045	0.114	0.5	0.040	3.0

Note: Manning's n is interpolated linearly for depths greater than H_1 and less than H_2. The value n_1 is used wherever the depth is less than or equal to H_2; the value n_2 is used wherever the depth is greater than or equal to H_2.

until the upstream water-surface elevation was correct and the computed velocities at the four data cross sections approximately matched the observed values. In all computer simulations, the kinematic eddy viscosity, $\tilde{\nu}$, was assigned the value $0.6U_*H$, where U_* is the shear velocity (see p. 19) and H is the total depth. The momentum-correction coefficient was assigned the value unity.

The values of Manning's n determined by calibration are shown in table 4. Manning's n is interpolated linearly for depths greater than H_1 and less than H_2. For depths less than or equal to H_1, the value n_1 is used, and for depths greater than or equal to H_2, the value n_2 is used. Computed and observed water-surface elevations for experiments S5810015, S6410035, and S7010215 are shown in

figures 16 through 18, and the computed and observed velocity components for the same three experiments are shown in figures 19 through 30.

Modeling Constricted Flows

Flows through the 14-foot contracted opening were modeled next. In these experiments, the entire flow was forced into the low-water channel at cross section 1000. All three experiments conducted at this contraction ratio were simulated: S6210035, S6810105, and S7410235. Because of the large contraction ratio (0.95), flow conditions vary greatly in a short distance and the convective terms in the equations of motion are significant. Thus, modeling these three experiments with a range of coarse to fine networks illustrates the relationship between the degree of network refinement

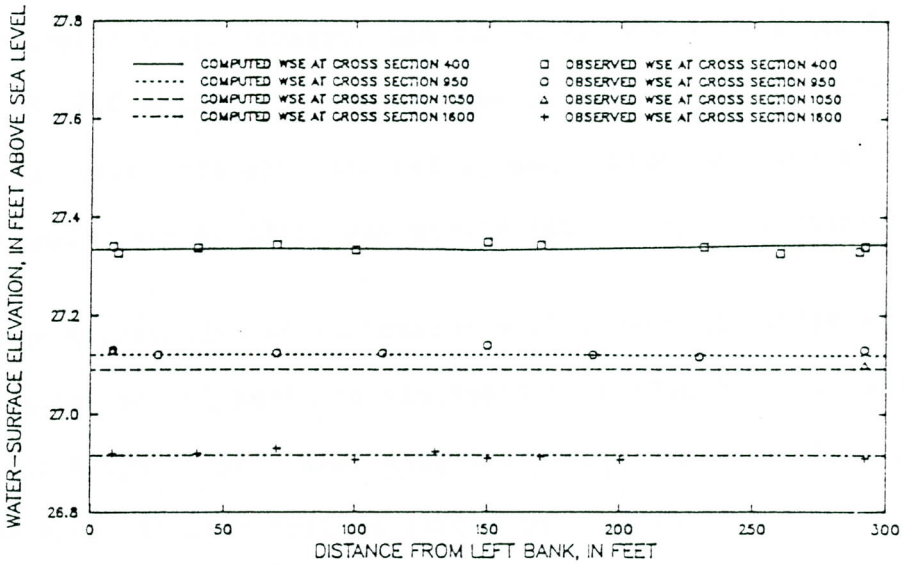

Figure 16. Observed and computed water-surface elevations (WSE) for experiment S5810015.

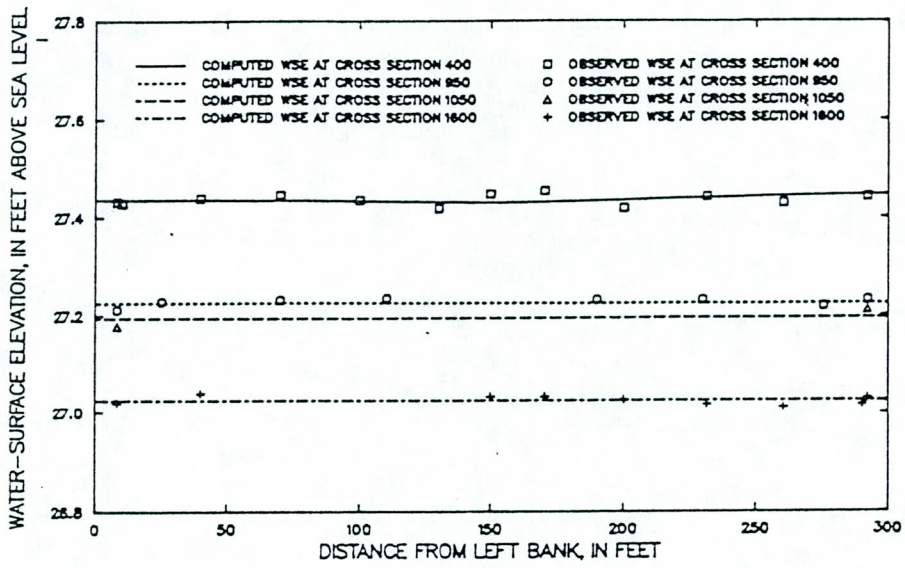

Figure 17. Observed and computed water-surface elevations (WSE) for experiment S6410085.

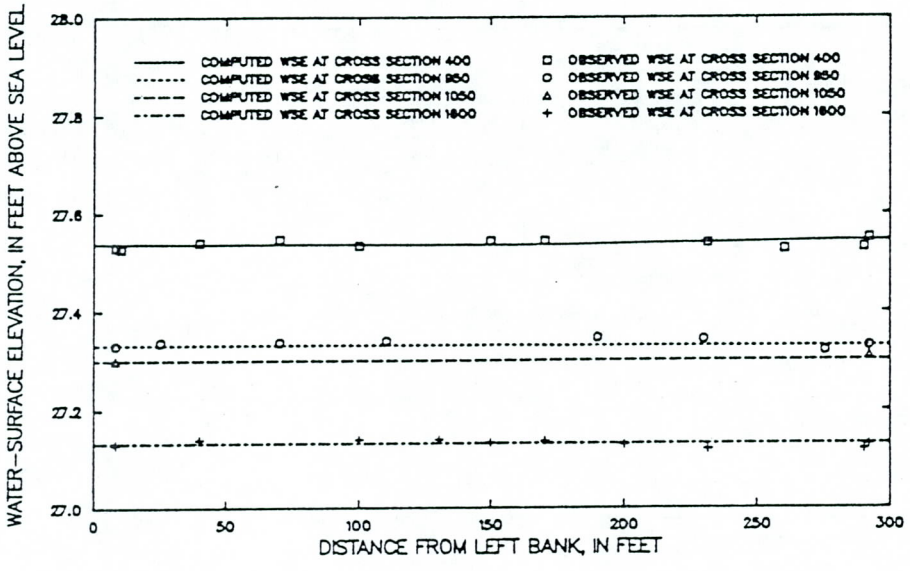

Figure 18. Observed and computed water-surface elevations (WSE) for experiment S7010215.

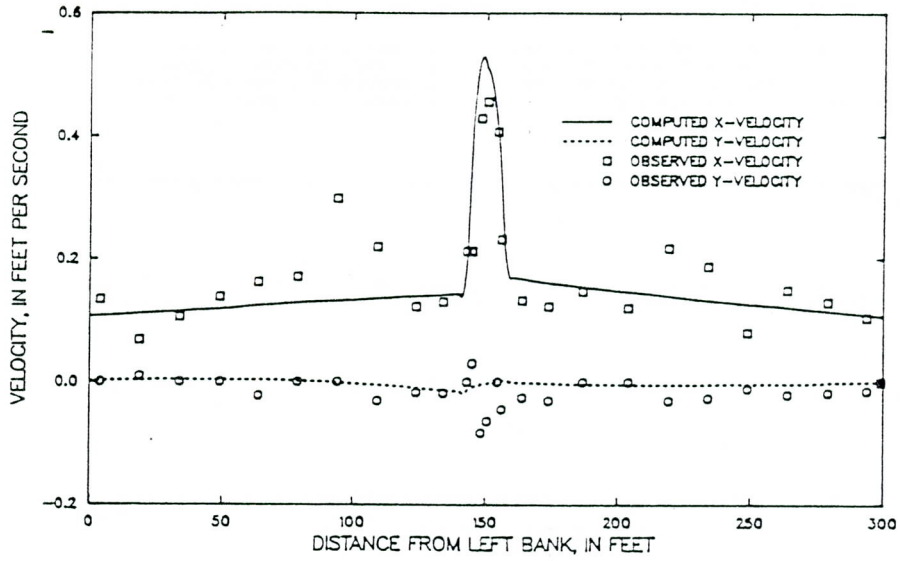

Figure 19. Observed and computed velocity components at cross section 900 for experiment S5810015.

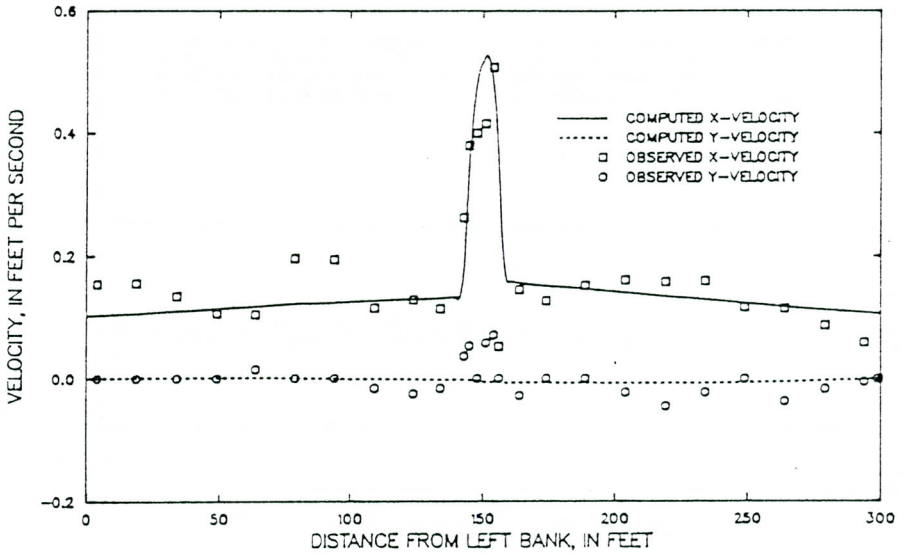

Figure 20. Observed and computed velocity components at cross section 950 for experiment S5810015.

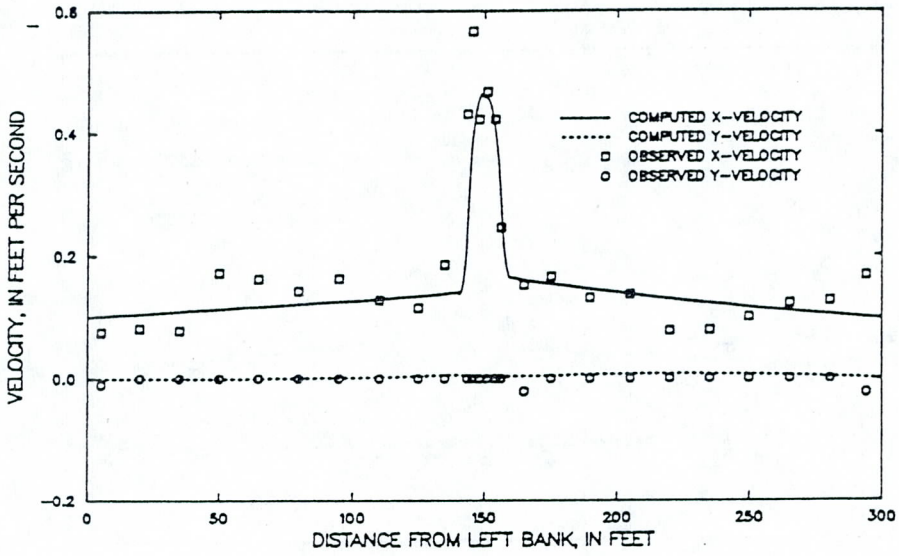

Figure 21. Observed and computed velocity components at cross section 1050 for experiment S5810015.

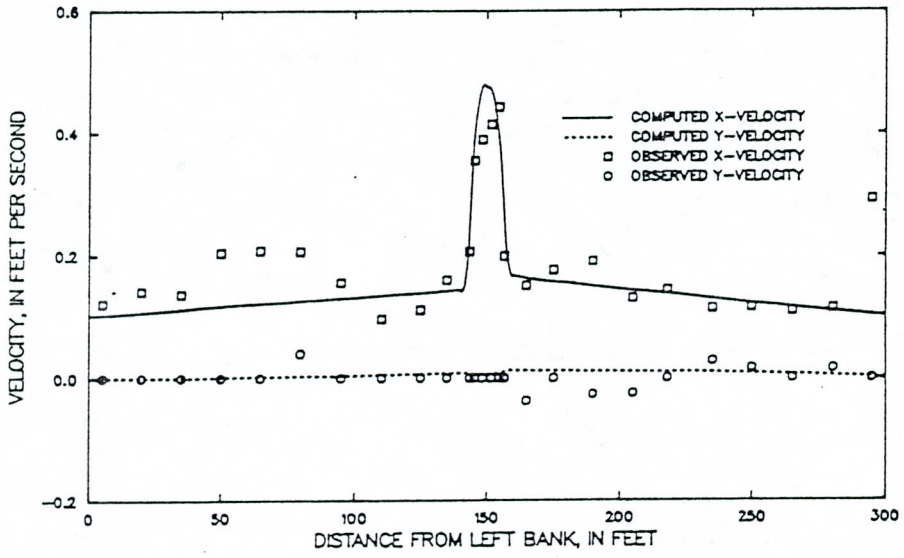

Figure 22. Observed and computed velocity components at cross section 1100 for experiment S5810015.

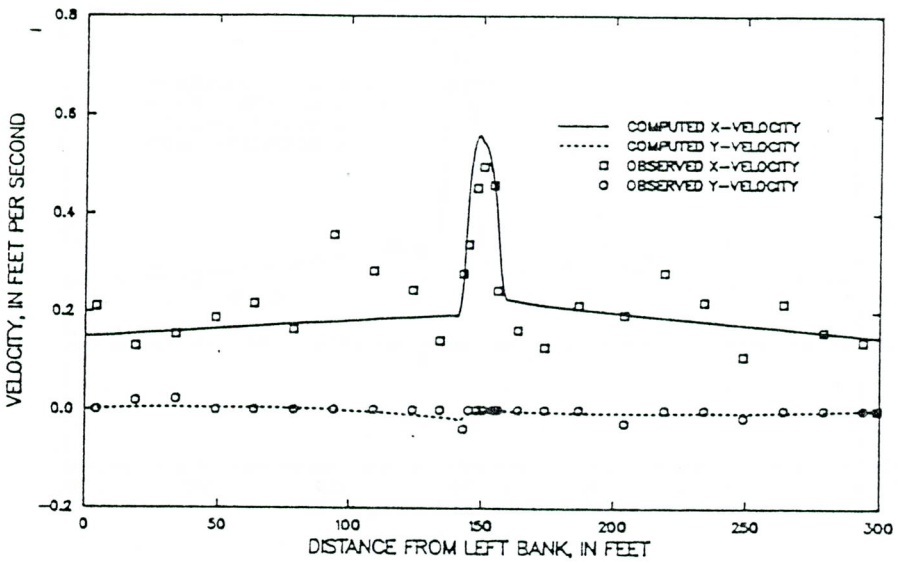

Figure 23. Observed and computed velocity components at cross section 900 for experiment S6410085.

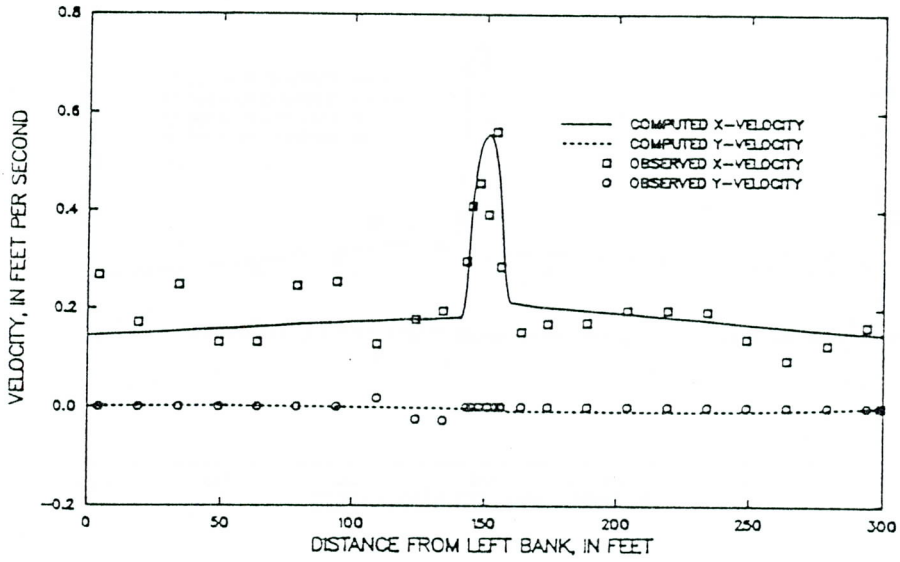

Figure 24. Observed and computed velocity components at cross section 950 for experiment S6410085.

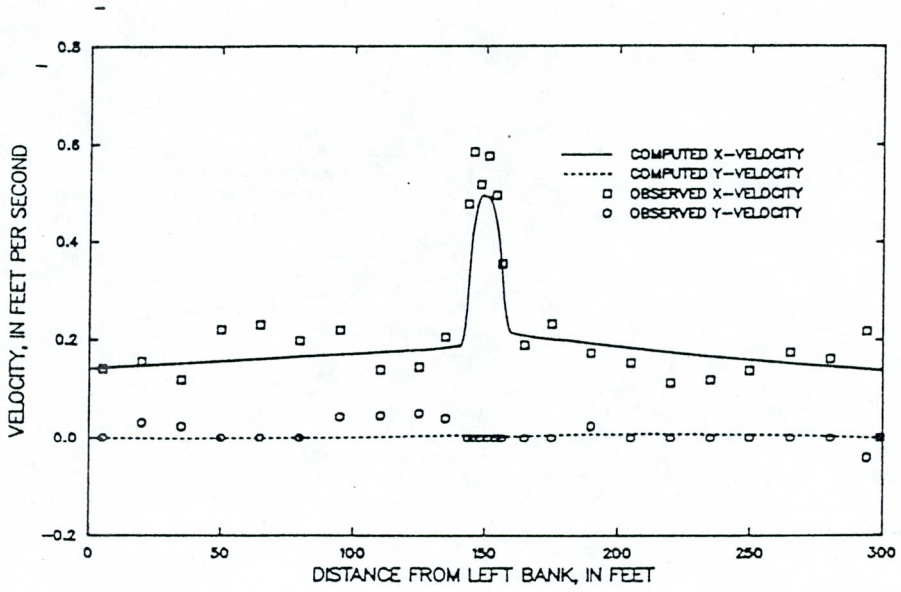

Figure 25. Observed and computed velocity components at cross section 1050 for experiment S6410085.

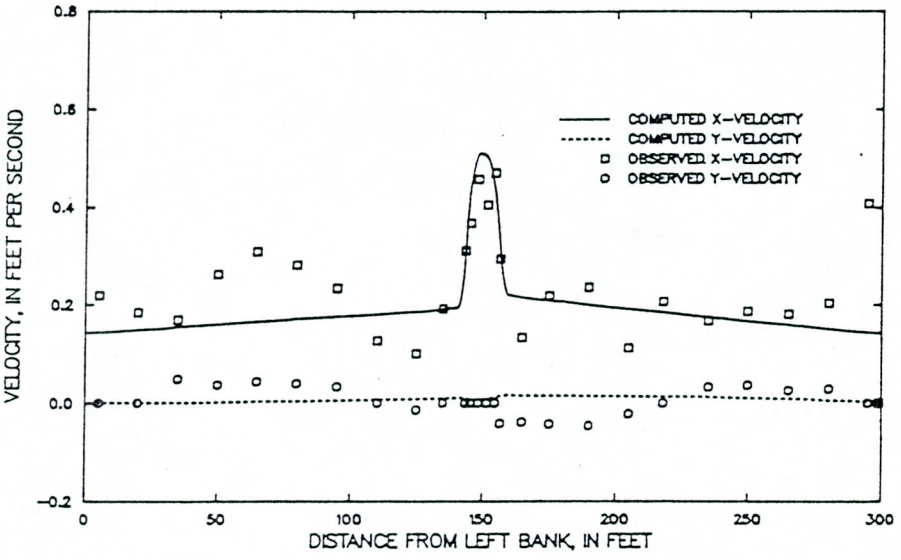

Figure 26. Observed and computed velocity components at cross section 1100 for experiment S6410085.

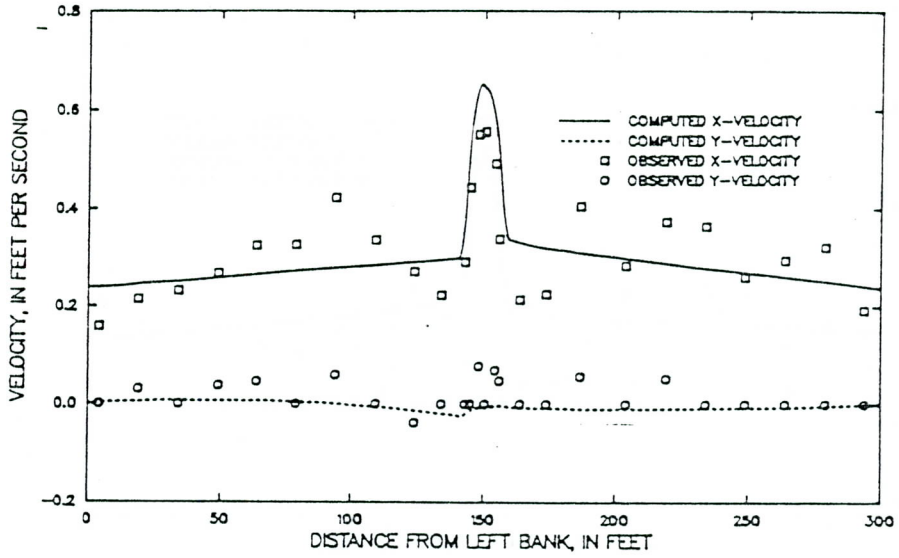

Figure 27. Observed and computed velocity components at cross section 900 for experiment S7010215.

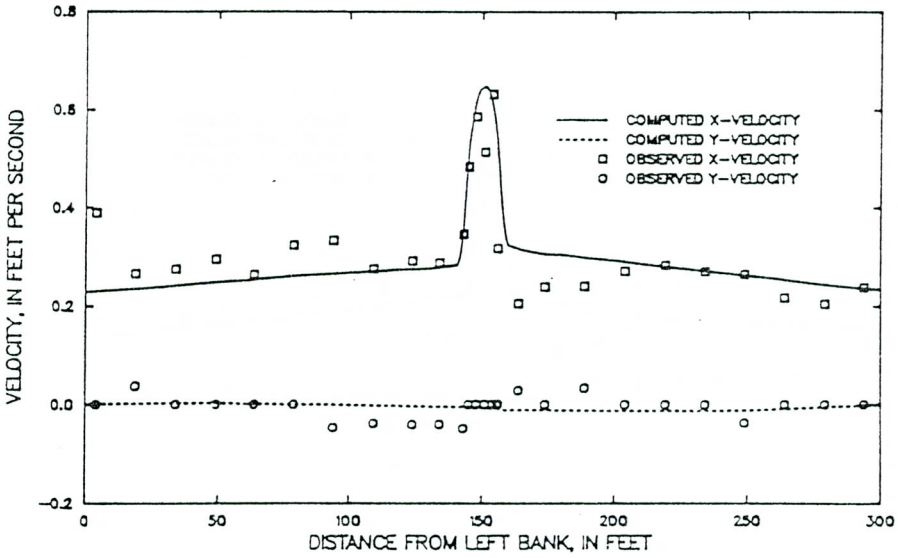

Figure 28. Observed and computed velocity components at cross section 950 for experiment S7010215.

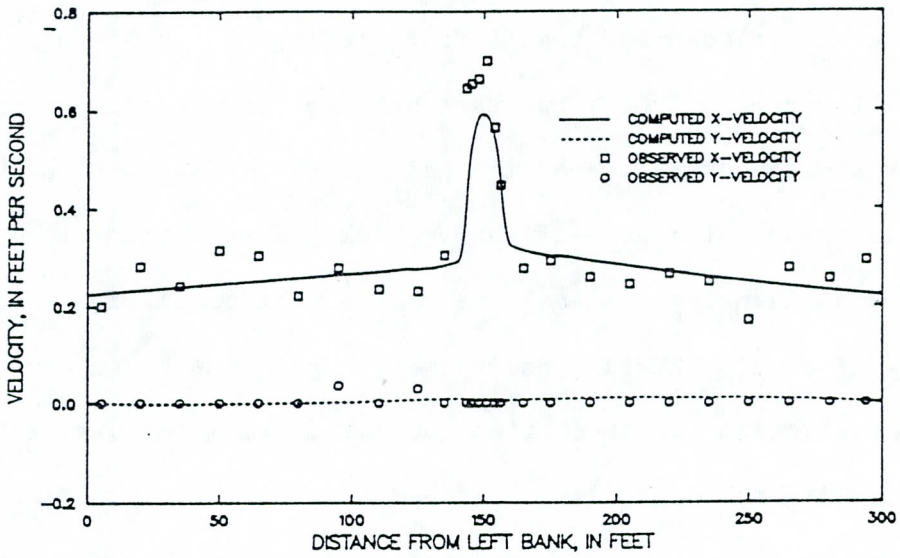

Figure 29. Observed and computed velocity components at cross section 1050 for experiment S7010215.

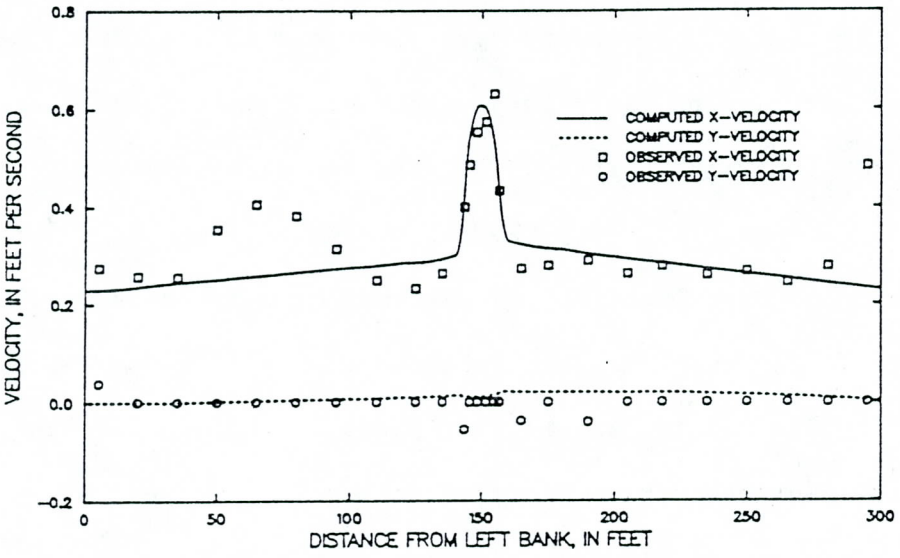

Figure 30. Observed and computed velocity components at cross section 1100 for experiment S7010215.

and solution accuracy when nonlinear effects are important.

To test the dependence of the solution on network detail, four networks were developed for the 14-foot opening. They are shown in figures 31 through 34. Only the part of each network between the right bank and the basin centerline and between cross sections 900 and 1000 is shown. The part of the network upstream from cross section 900 is identical to the same part of the normal-flow network (fig. 15). Each network is symmetric about both the basin centerline and the constriction (cross section 1000). In each network, the constriction is represented as a plate of zero thickness. Each of the four has successively greater detail at and near the opening. In network 1, four elements are used to span the opening; in networks 2 and 3, eight elements; and in network 4, 12 elements.

The values of the mass flux at model cross sections and the values of the element continuity norm were used in the development of these networks. The mass-conservation error at the contracted opening for each of the three experiments and each of the four networks is shown in table 5. The refinement of the network at and near the opening was effective in reducing the mass-conservation errors there. Elements for which the continuity norm for experiment S7410235 exceeded 0.1 are shaded in figures 31 through 34. The value of the continuity norm was used as a guide to where the addition of network detail would be most effective in reducing errors.

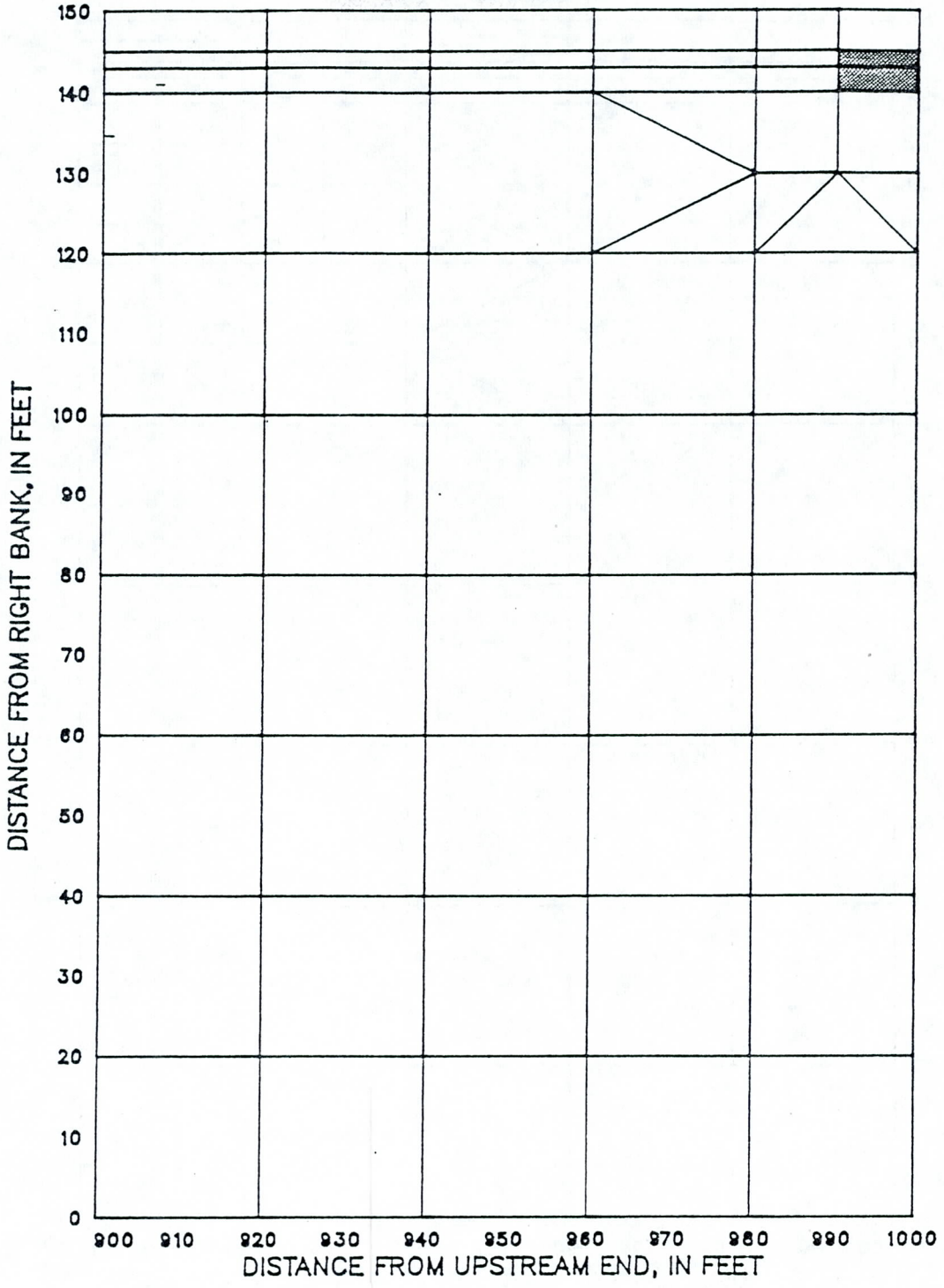

Figure 31. Part of the right half of finite-element network 1 upstream from the constriction. The continuity norm exceeds 0.1 on the shaded elements for the simulation of experiment S7410235 with the calibrated parameters.

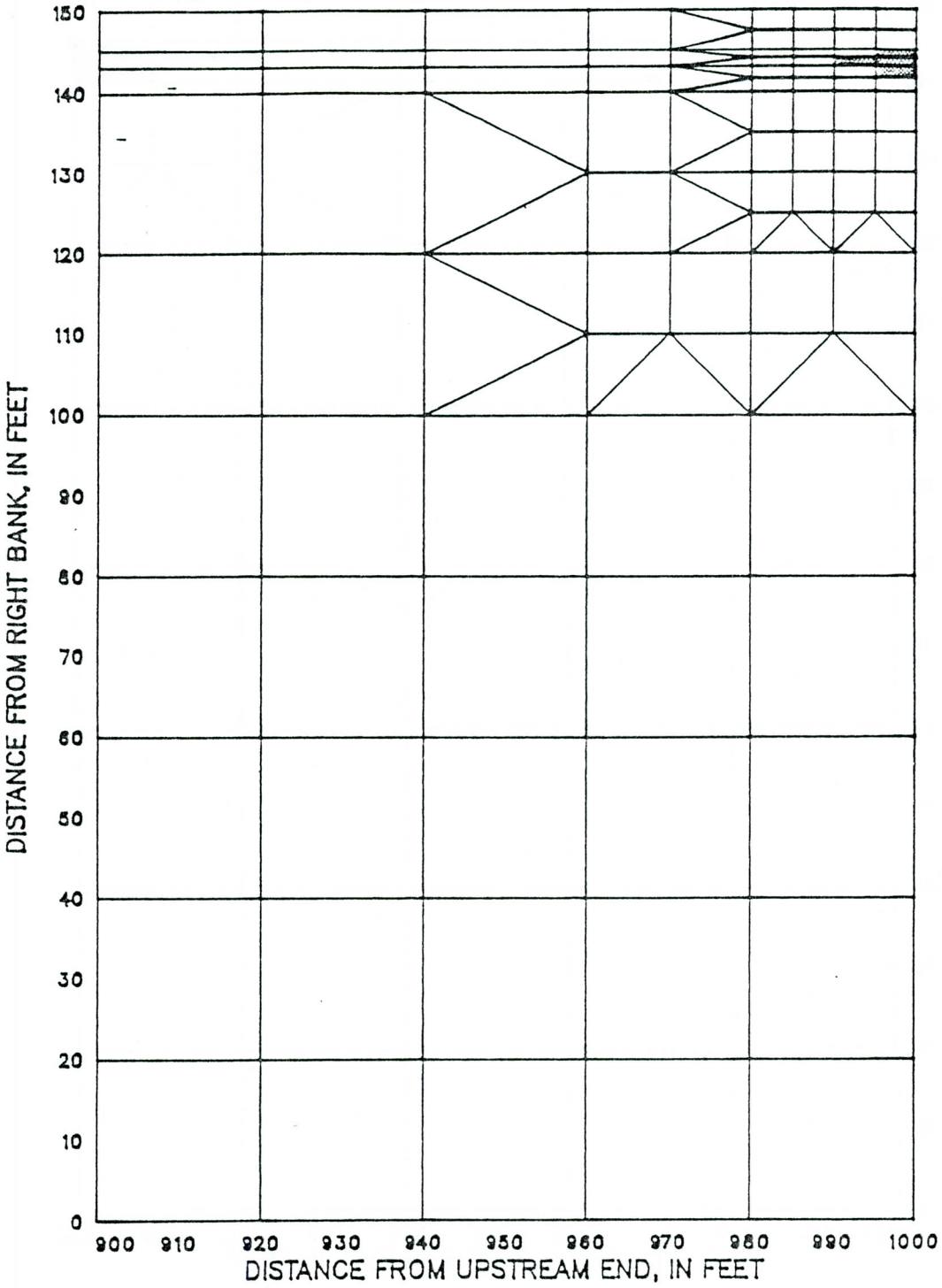

Figure 32. Part of the right half of finite-element network 2 upstream from the constriction. The continuity norm exceeds 0.1 on the shaded elements for the simulation of experiment S7410235 with the calibrated parameters.

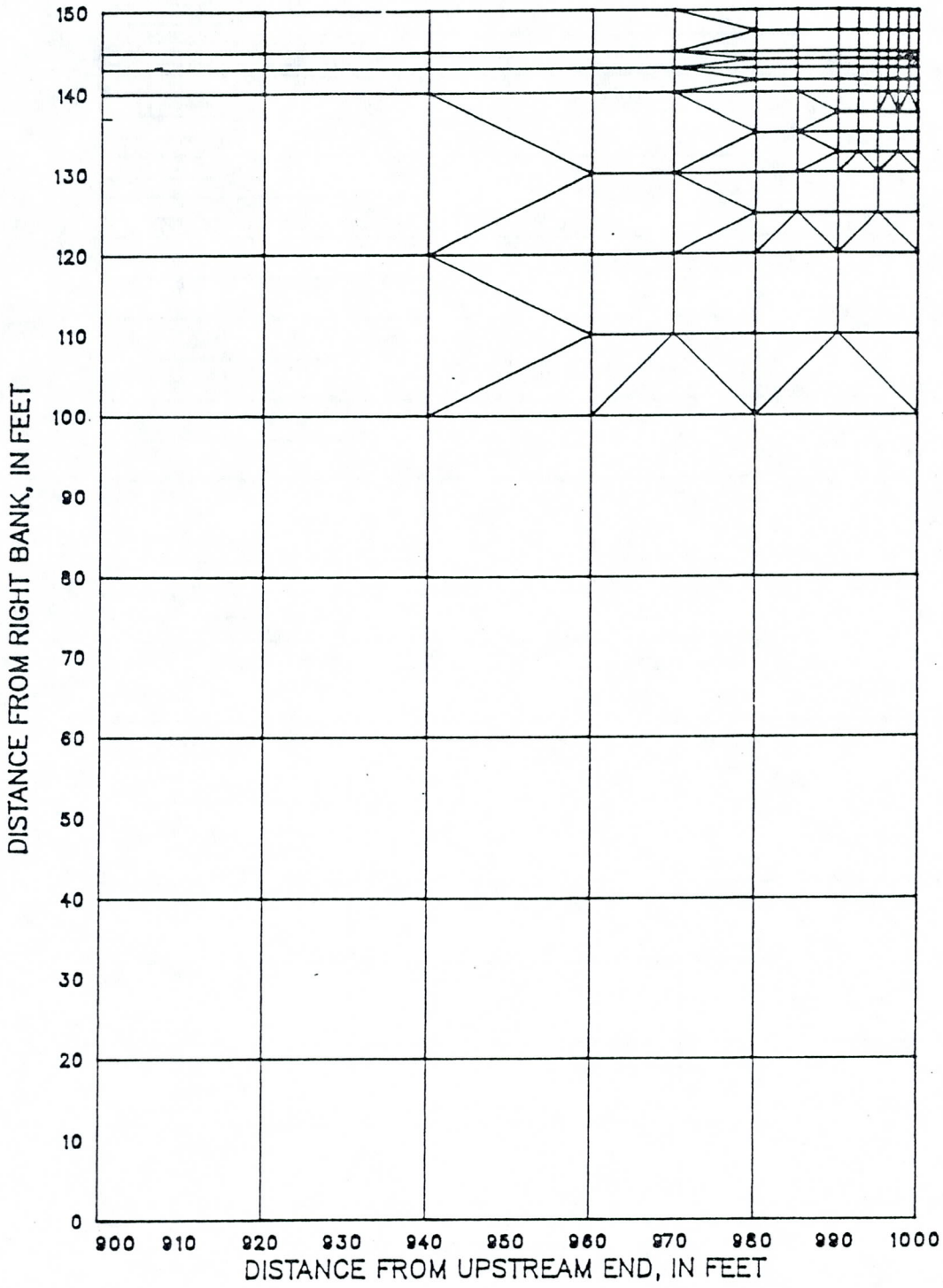

Figure 33. Part of the right half of finite-element network 3 upstream from the constriction. The continuity norm exceeds 0.1 on the shaded elements for the simulation of experiment S7410235 with the calibrated parameters.

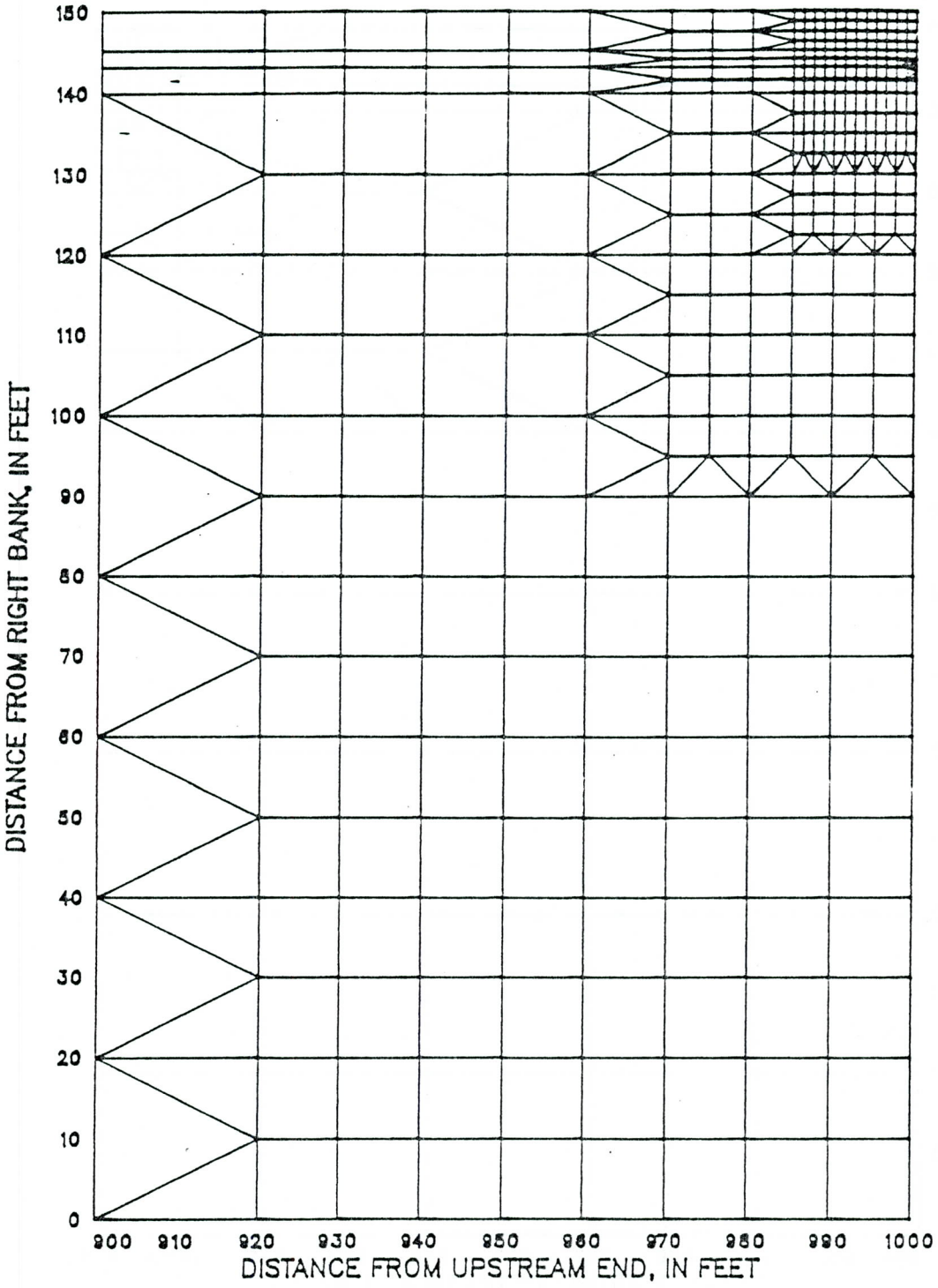

Figure 34. Part of the right half of finite-element network 4 upstream from the constriction. The continuity norm exceeds 0.1 on the shaded elements for the simulation of experiment S7410235 with the calibrated parameters.

Table 5. Computed discharge at the 14-foot contracted opening for three discharges and four networks.

Experiment number	Discharge at contracted opening, as percent of total inflow			
	Network 1	Network 2	Network 3	Network 4
S6210035	85.7	91.9	97.7	97.7
S6810105	82.2	89.8	97.4	97.4
S7410235	78.4	87.2	96.9	96.9

For each simulation, the downstream model water surface was assumed to be horizontal, and its elevation was taken as the average observed water-surface elevation there. As before, a natural boundary condition was used. For a given design discharge, the upstream unit-discharge distribution used in the corresponding normal-flow simulation was multiplied by a constant factor to give the upstream discharge distribution used in the contracted-opening simulation. This factor was chosen to give the correct total measured discharge. A slip boundary condition was used along all solid boundaries except at the four corners formed by the the intersection of the constriction with the left and right banks, where the values of both components of velocity were set to zero. Where the ends of the constriction met the top of the low-water channel, the velocity was forced to be tangential to the constriction boundary.

In each simulation involving a given design discharge, the linear representation of Manning's n was used that was determined in the calibration simulation for that design discharge. As in the normal-flow simulations, the kinematic eddy viscosity, $\tilde{\nu}$, was assigned the value $0.6U_*H$ and the momentum-correction coefficient, β, was assigned the value unity.

Water-surface elevations are shown for experiment S6210035 in figures 35 through 38 for the four networks. The differences among the four sets of computed elevations are quite small. Only a minor improvement was achieved by using the finer networks. Near the opening, the observed backwater was computed fairly well for networks 1 and 2 and very accurately for networks 3 and 4. Away from the opening in the lateral direction, computed water-surface elevations are up to 0.02 ft lower than observed water-surface elevations on the upstream side of the constriction. On the downstream side, computed water-surface elevations are up to 0.04 ft lower than the observed values.

Computed and observed velocity profiles at cross sections 900, 950, 1050, and 1100 for the four networks are shown in figures 39 through 54. Again, differences among the results for the four networks are minor. In all cases, the computed profiles upstream are very accurate. Downstream from the constriction, the computed peak velocity in the low-water channel is 32 percent lower than the observed peak velocity at cross section 1050 and 17 to 18 percent lower at 1100. The profiles at cross section 1050 show

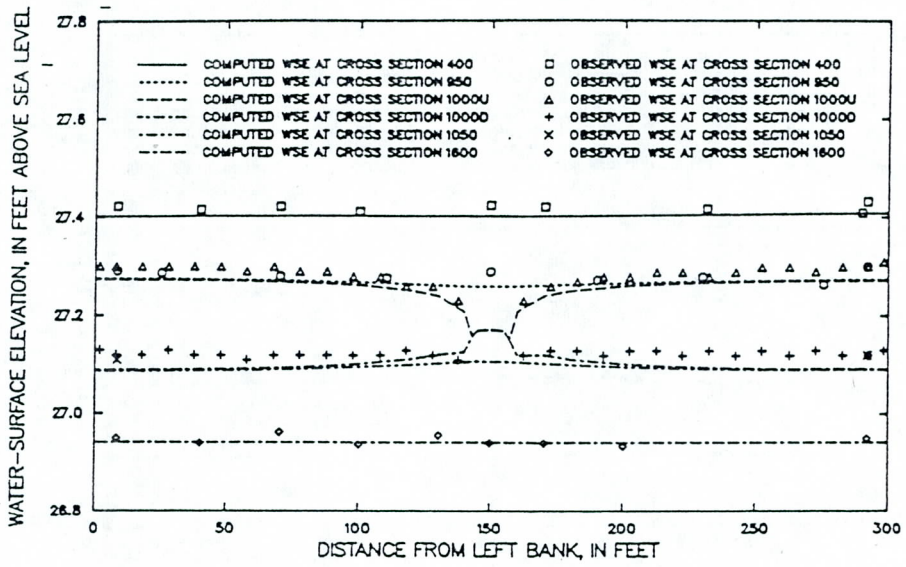

Figure 35. Observed and computed water-surface elevations (WSE) for experiment S6210035, calibrated parameters, network 1. The letters U and D refer, respectively, to the upstream side and the downstream side of the constriction.

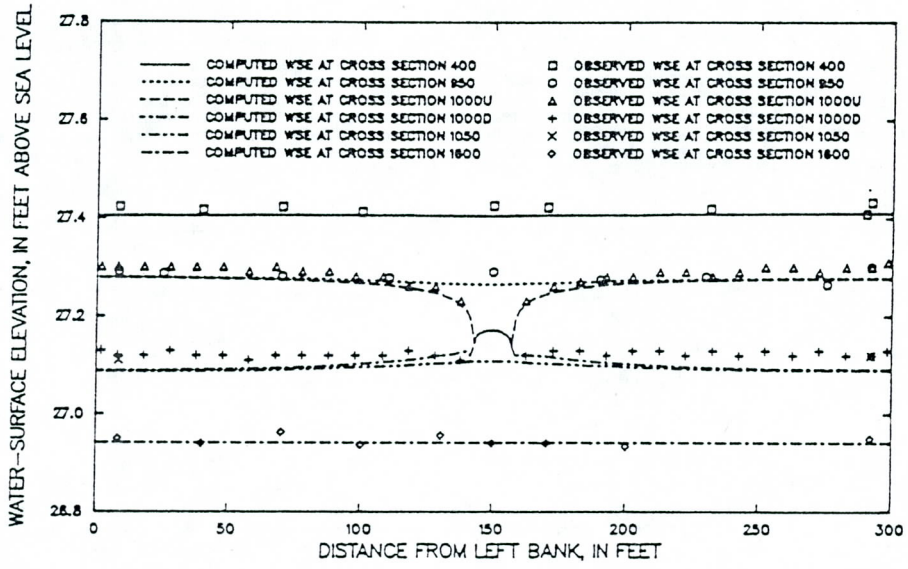

Figure 36. Observed and computed water-surface elevations (WSE) for experiment S6210035, calibrated parameters, network 2. The letters U and D refer, respectively, to the upstream side and the downstream side of the constriction.

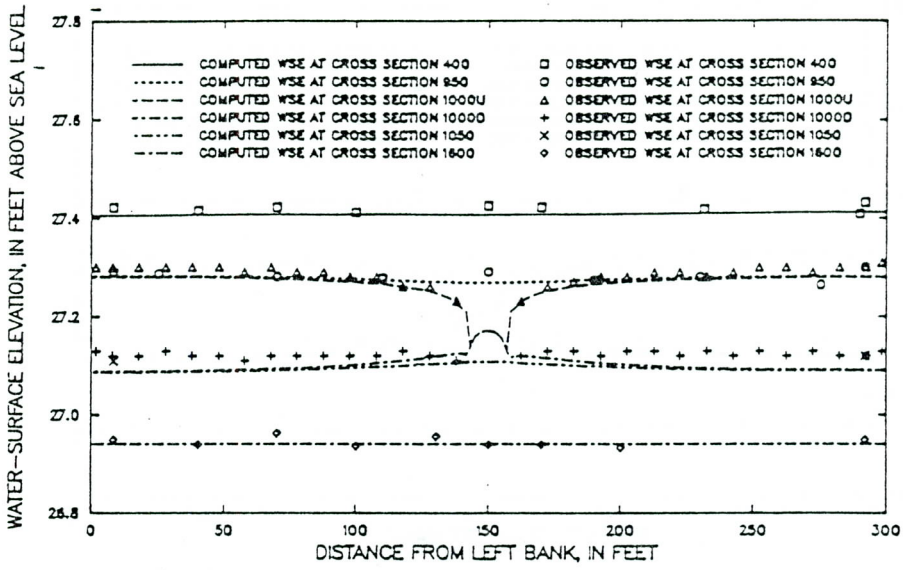

Figure 37. Observed and computed water-surface elevations (WSE) for experiment S6210035, calibrated parameters, network 3. The letters U and D refer, respectively, to the upstream side and the downstream side of the constriction.

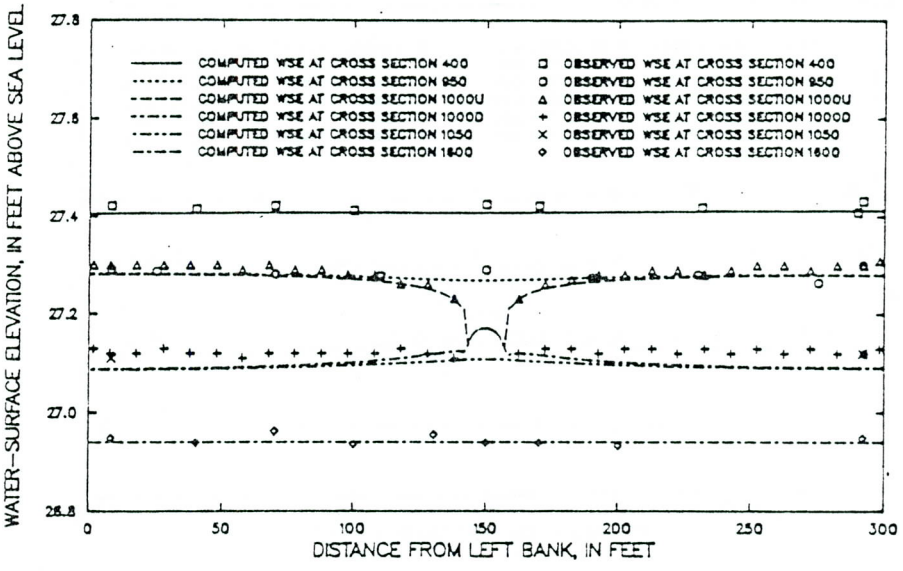

Figure 38. Observed and computed water-surface elevations (WSE) for experiment S6210035, calibrated parameters, network 4. The letters U and D refer, respectively, to the upstream side and the downstream side of the constriction.

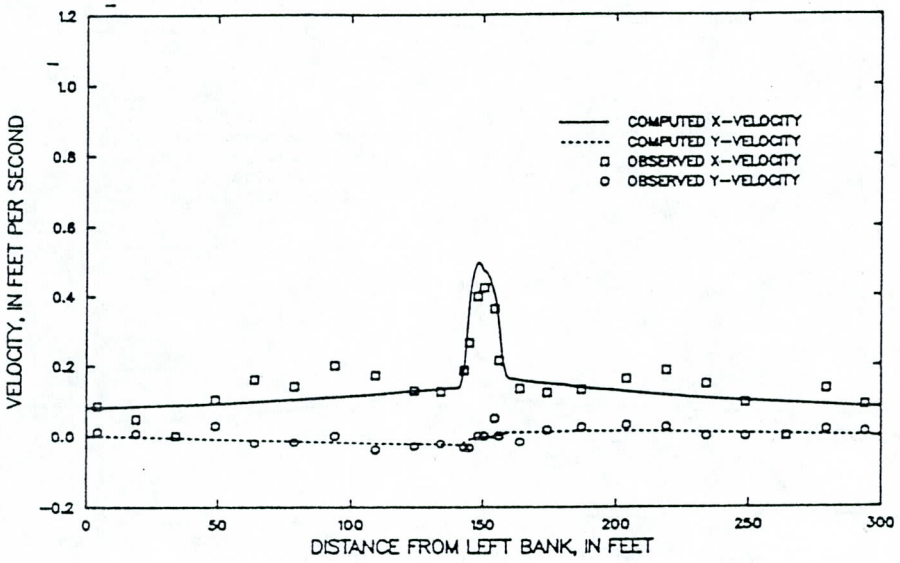

Figure 39. Observed and computed velocity components at cross section 900 for experiment S6210035, calibrated parameters, network 1.

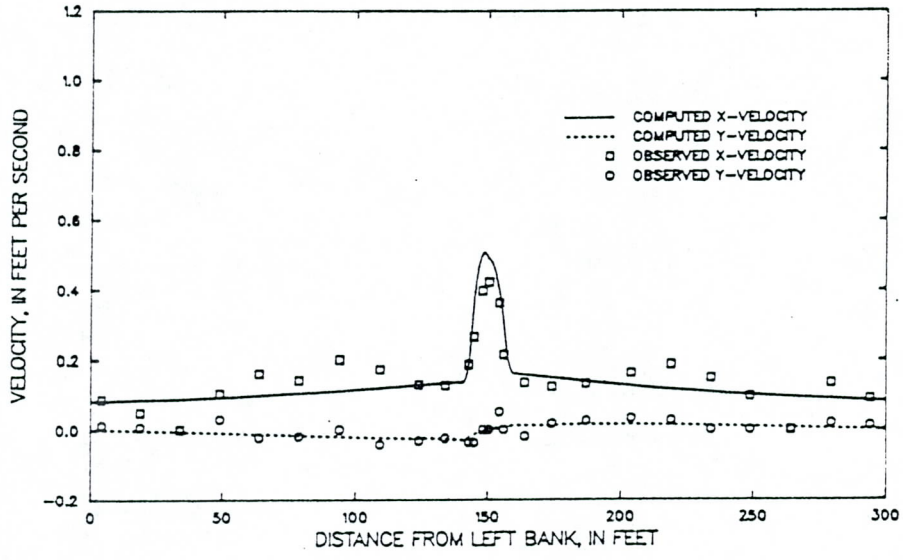

Figure 40. Observed and computed velocity components at cross section 900 for experiment S6210035, calibrated parameters, network 2.

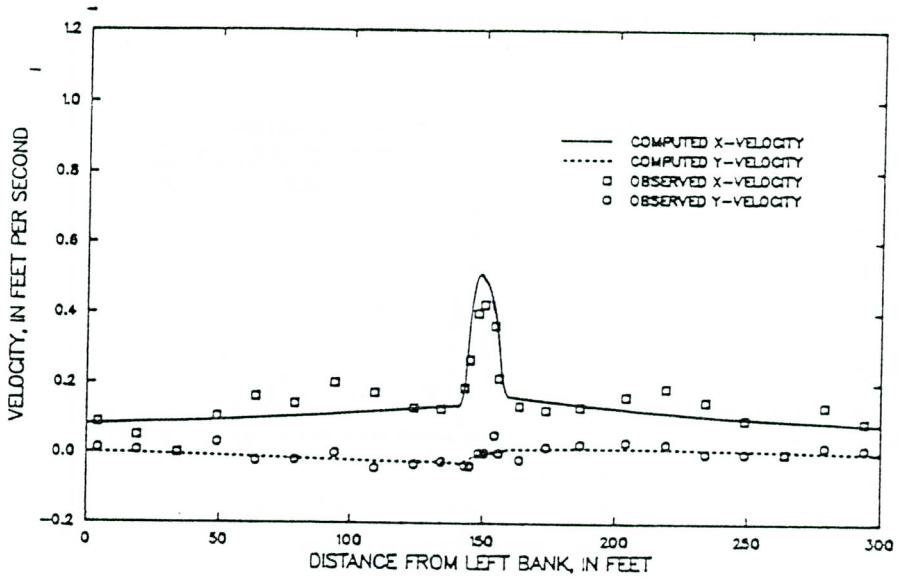

Figure 41. Observed and computed velocity components at cross section 900 for experiment S6210035, calibrated parameters, network 3.

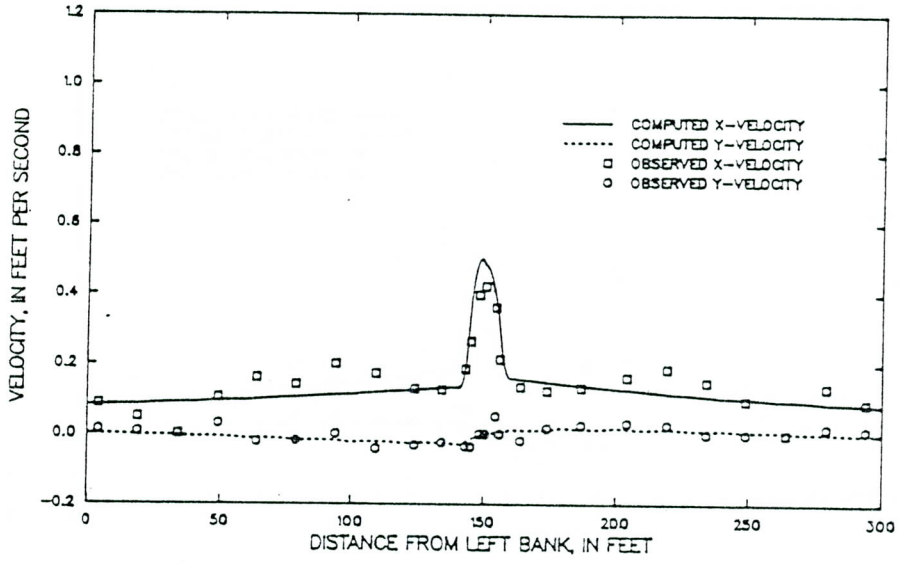

Figure 42. Observed and computed velocity components at cross section 900 for experiment S6210035, calibrated parameters, network 4.

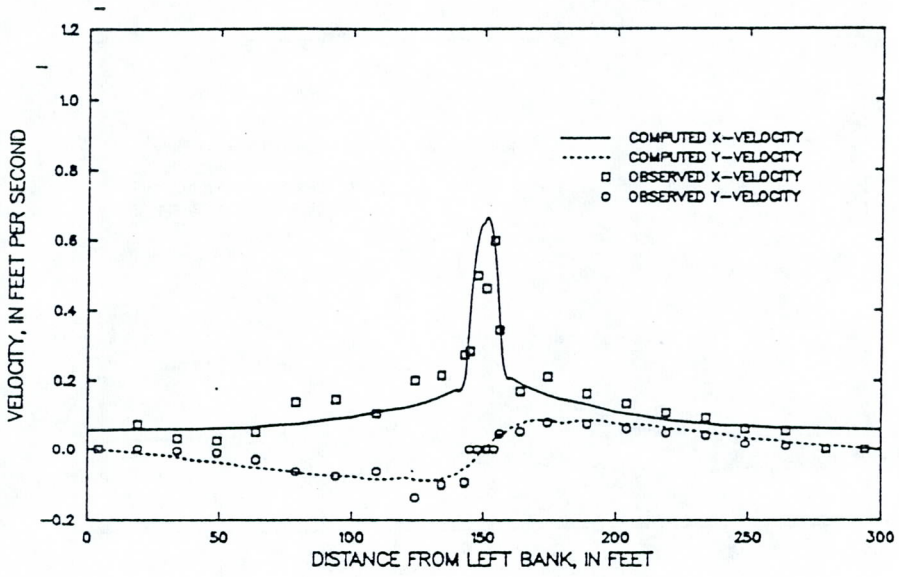

Figure 43. Observed and computed velocity components at cross section 950 for experiment S6210035, calibrated parameters, network 1.

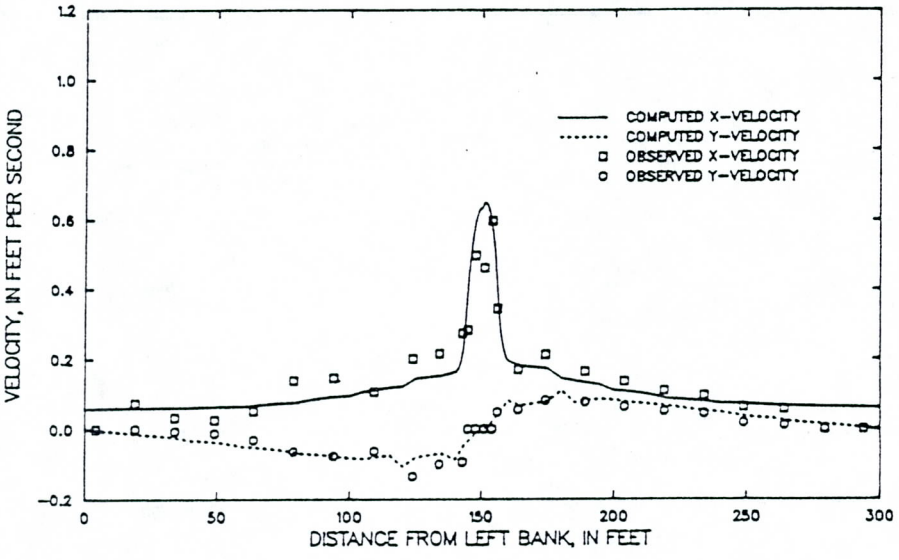

Figure 44. Observed and computed velocity components at cross section 950 for experiment S6210035, calibrated parameters, network 2.

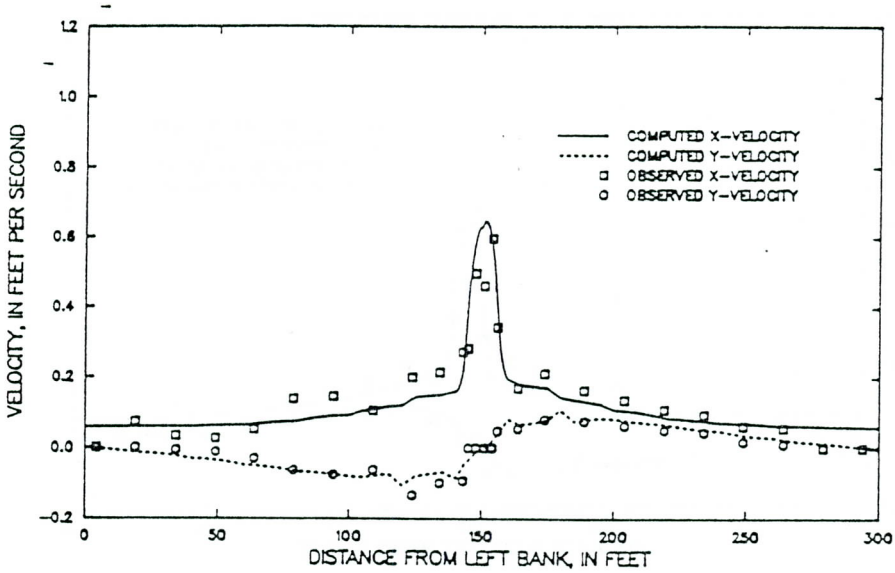

Figure 45. Observed and computed velocity components at cross section 950 for experiment S6210035, calibrated parameters, network 3.

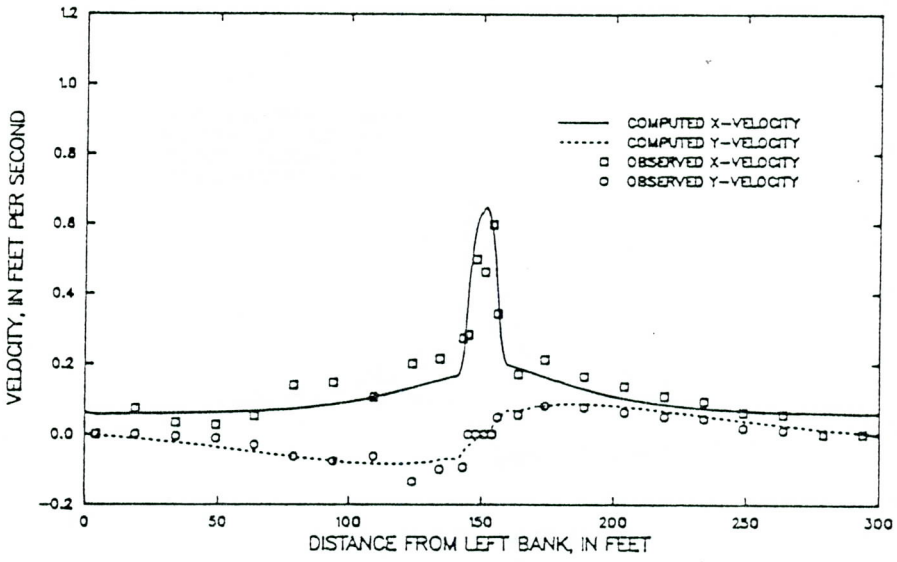

Figure 46. Observed and computed velocity components at cross section 950 for experiment S6210035, calibrated parameters, network 4.

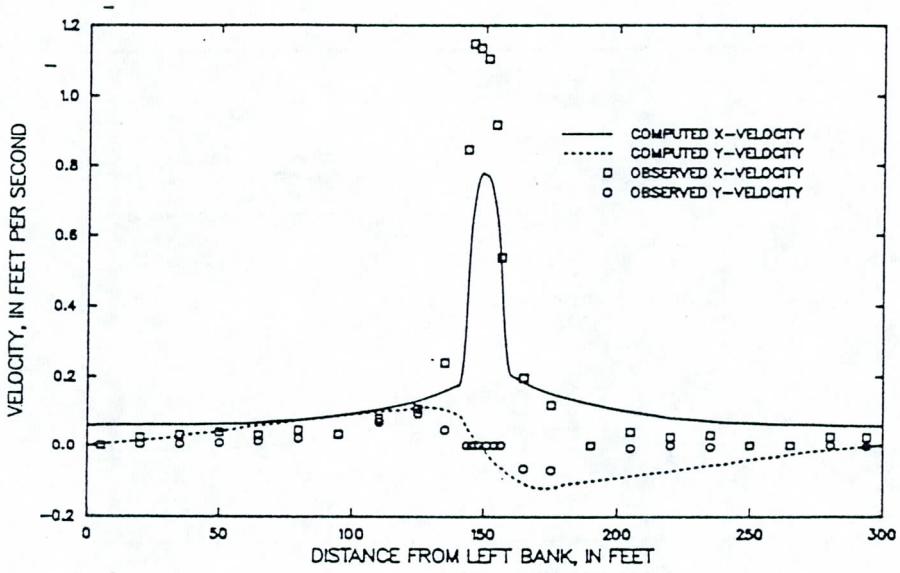

Figure 47. Observed and computed velocity components at cross section 1050 for experiment S6210035, calibrated parameters, network 1.

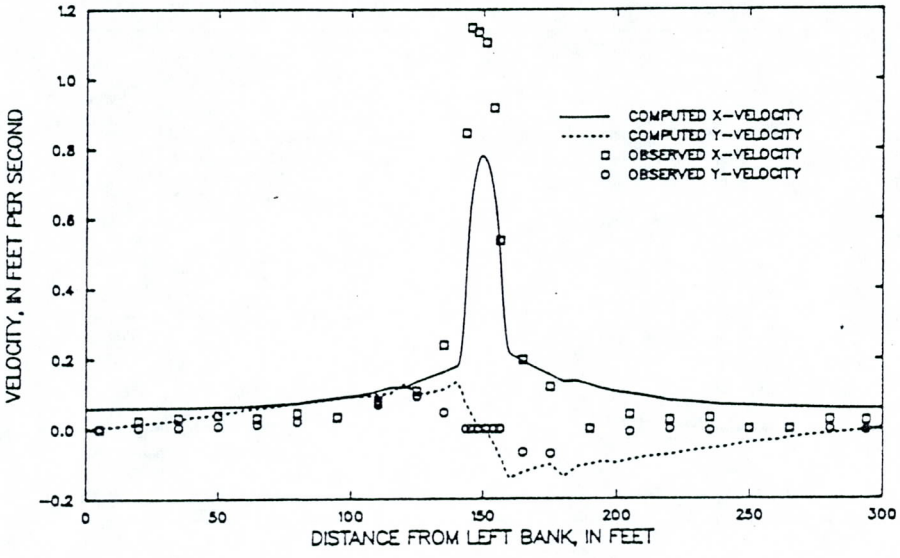

Figure 48. Observed and computed velocity components at cross section 1050 for experiment S6210035, calibrated parameters, network 2.

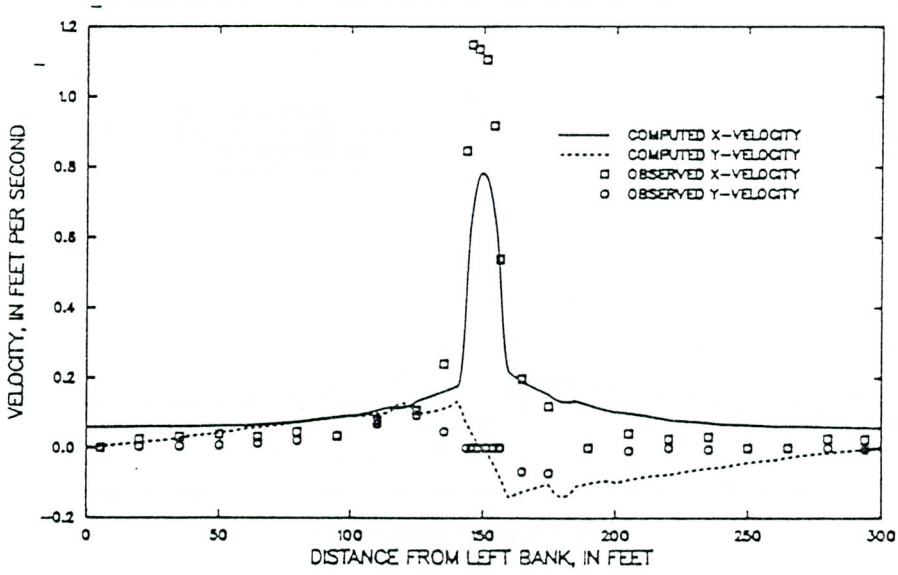

Figure 49. Observed and computed velocity components at cross section 1050 for experiment S6210035, calibrated parameters, network 3.

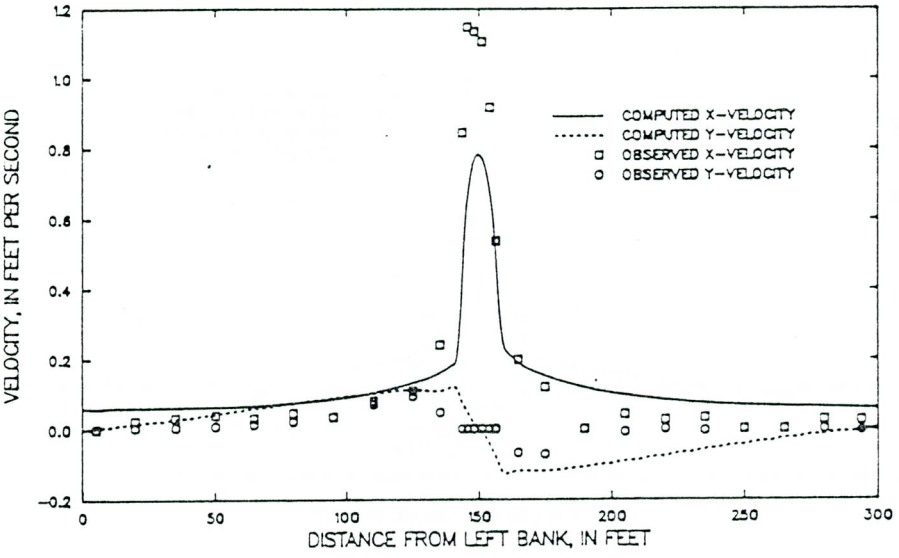

Figure 50. Observed and computed velocity components at cross section 1050 for experiment S6210035, calibrated parameters, network 4.

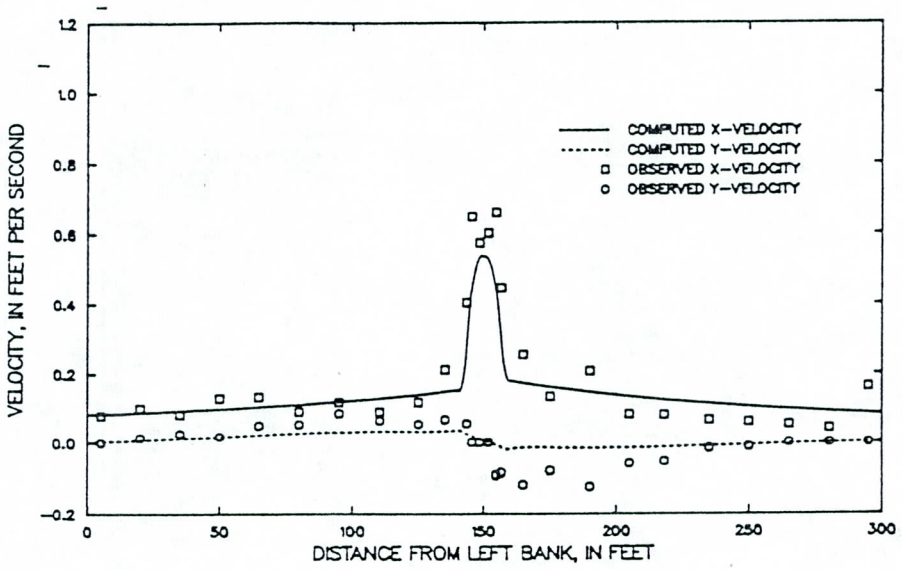

Figure 51. Observed and computed velocity components at cross section 1100 for experiment S6210035, calibrated parameters, network 1.

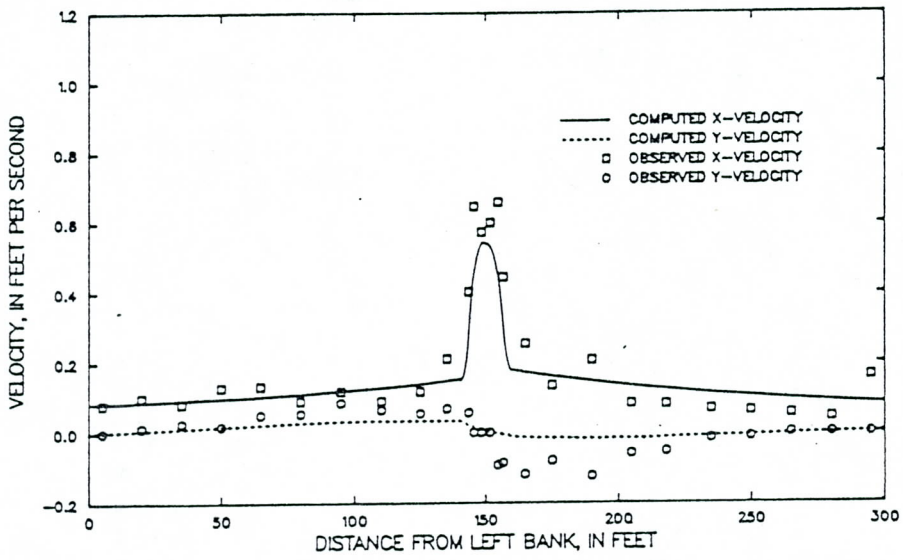

Figure 52. Observed and computed velocity components at cross section 1100 for experiment S6210035, calibrated parameters, network 2.

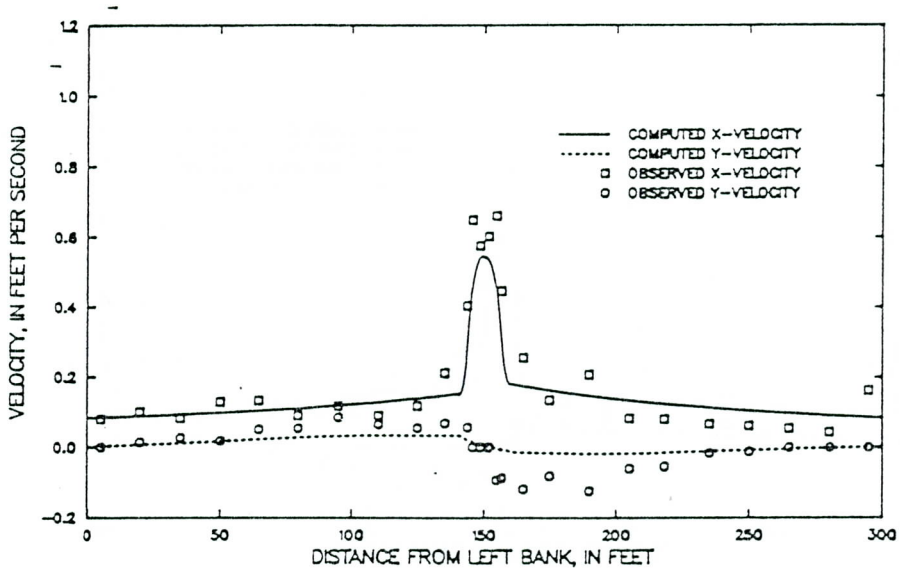

Figure 53. Observed and computed velocity components at cross section 1100 for experiment S6210035, calibrated parameters, network 3.

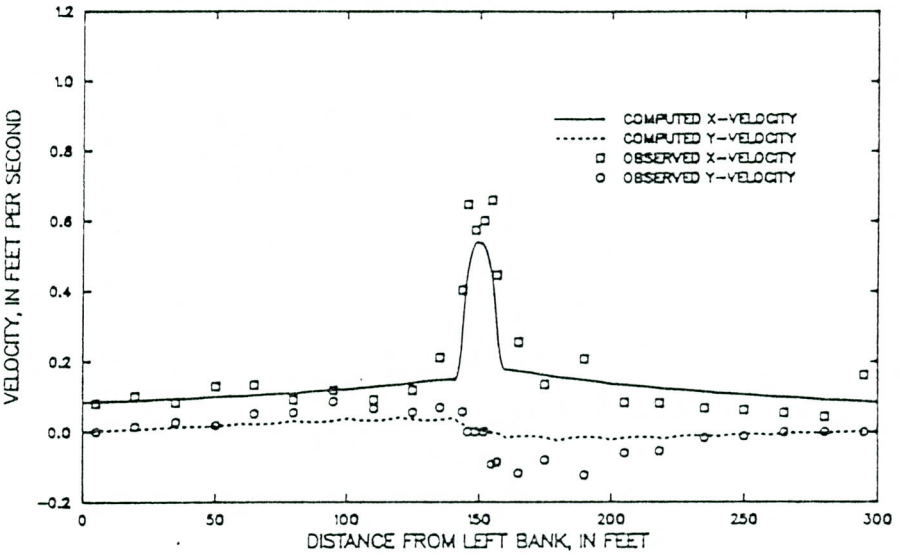

Figure 54. Observed and computed velocity components at cross section 1100 for experiment S6210035, calibrated parameters, network 4.

that the jet downstream from the contracted opening has dissipated too rapidly. The magnitudes of the computed overbank velocity components in both the x- and y-directions are too large at cross section 1050, but the magnitudes of the overbank velocity components in the y-direction are too small at cross section 1100. Network 4 was developed with greater detail farther away from the opening in order to determine whether the jet-dissipation problem was caused in part by an insufficiently fine grid. Figures 50 and 54 show that lack of network detail is not the cause of the problem. We will return to this subject later.

Partial velocity fields for the four networks are shown in figures 55 through 58. These velocity fields extend from the basin centerline 28 ft toward the right bank and from the constriction 20 ft downstream. Few differences are evident except that for networks 3 and 4, there is sufficient detail just downstream of the constriction for a small recirculation zone to appear. The stagnation point on the downstream side of the constriction is located about 138 ft from the right bank for networks 3 and 4.

Water-surface elevations are shown for experiment S6810105 in figures 59 through 62 for the four networks. The improvement in the computed water-surface elevations due to network refinement is more evident in this case than for experiment S6210035. The computed backwater is slightly low for networks 1 and 2 but quite accurate for the more detailed networks 3 and 4. There is virtually no difference between the water-surface elevations for networks 3 and 4. For

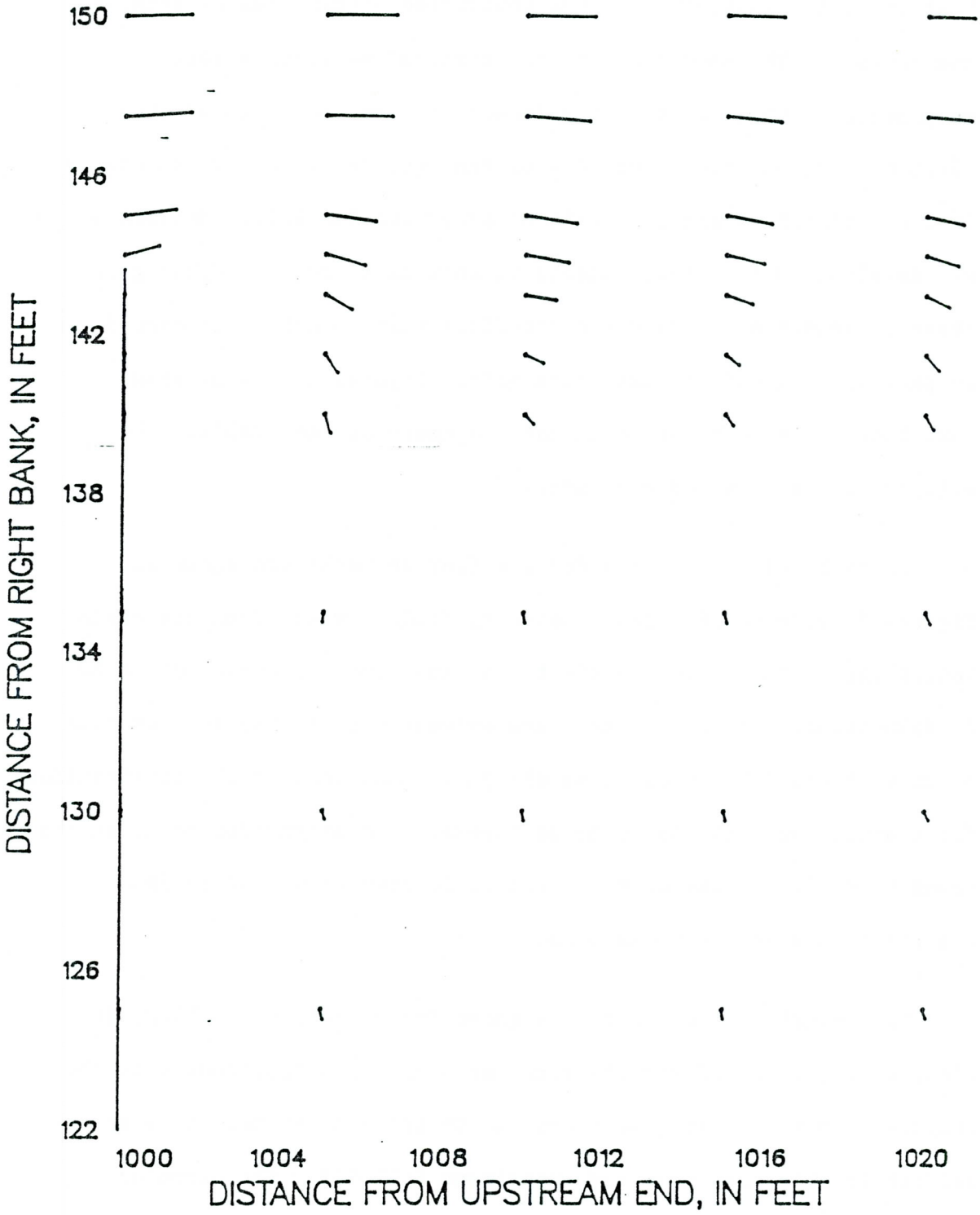

Figure 55. Partial velocity field for experiment S6210035, calibrated parameters, network 1. A vector 1 inch long represents a velocity of 4 feet per second.

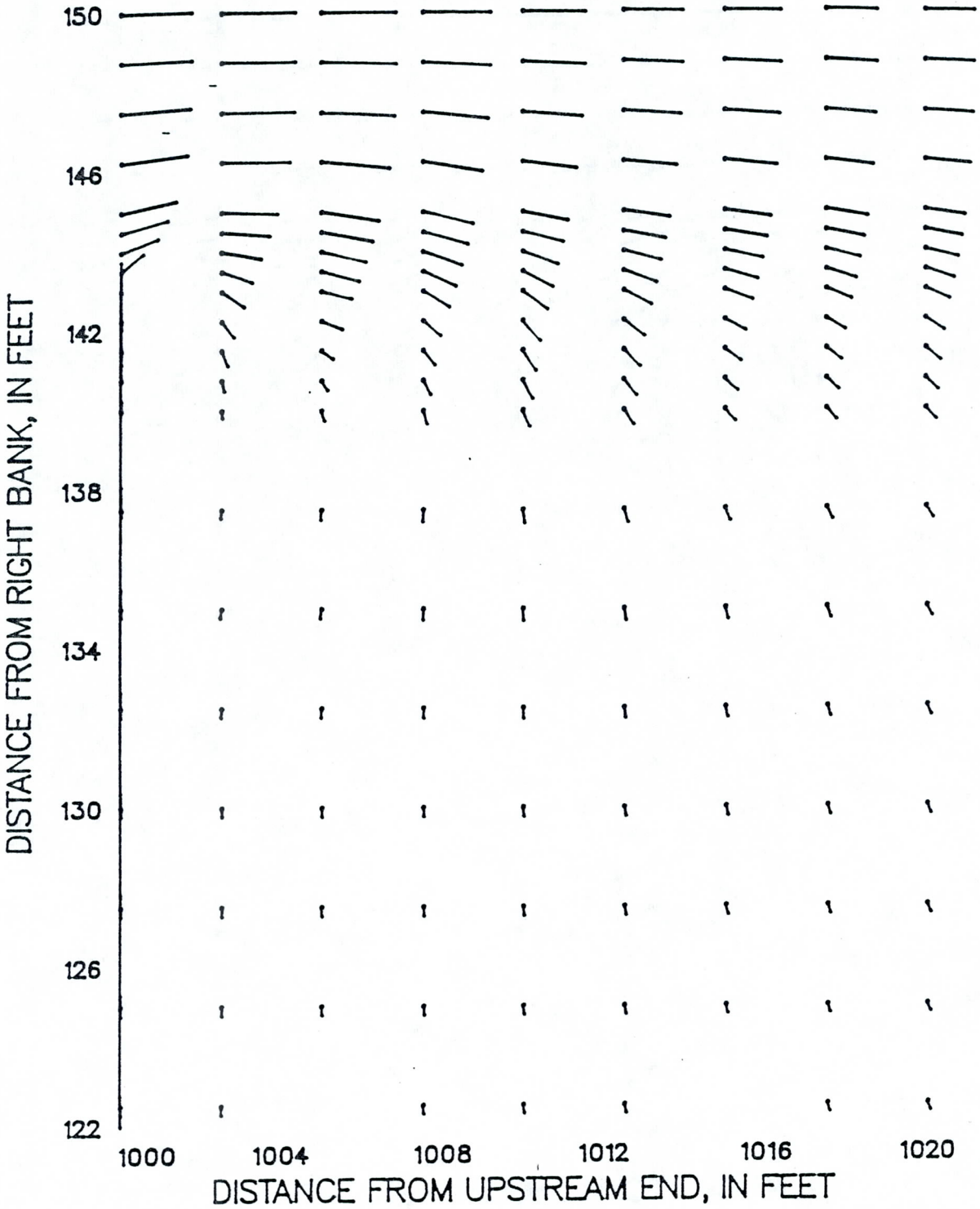

Figure 56. Partial velocity field for experiment S6210035, calibrated parameters, network 2. A vector 1 inch long represents a velocity of 4 feet per second.

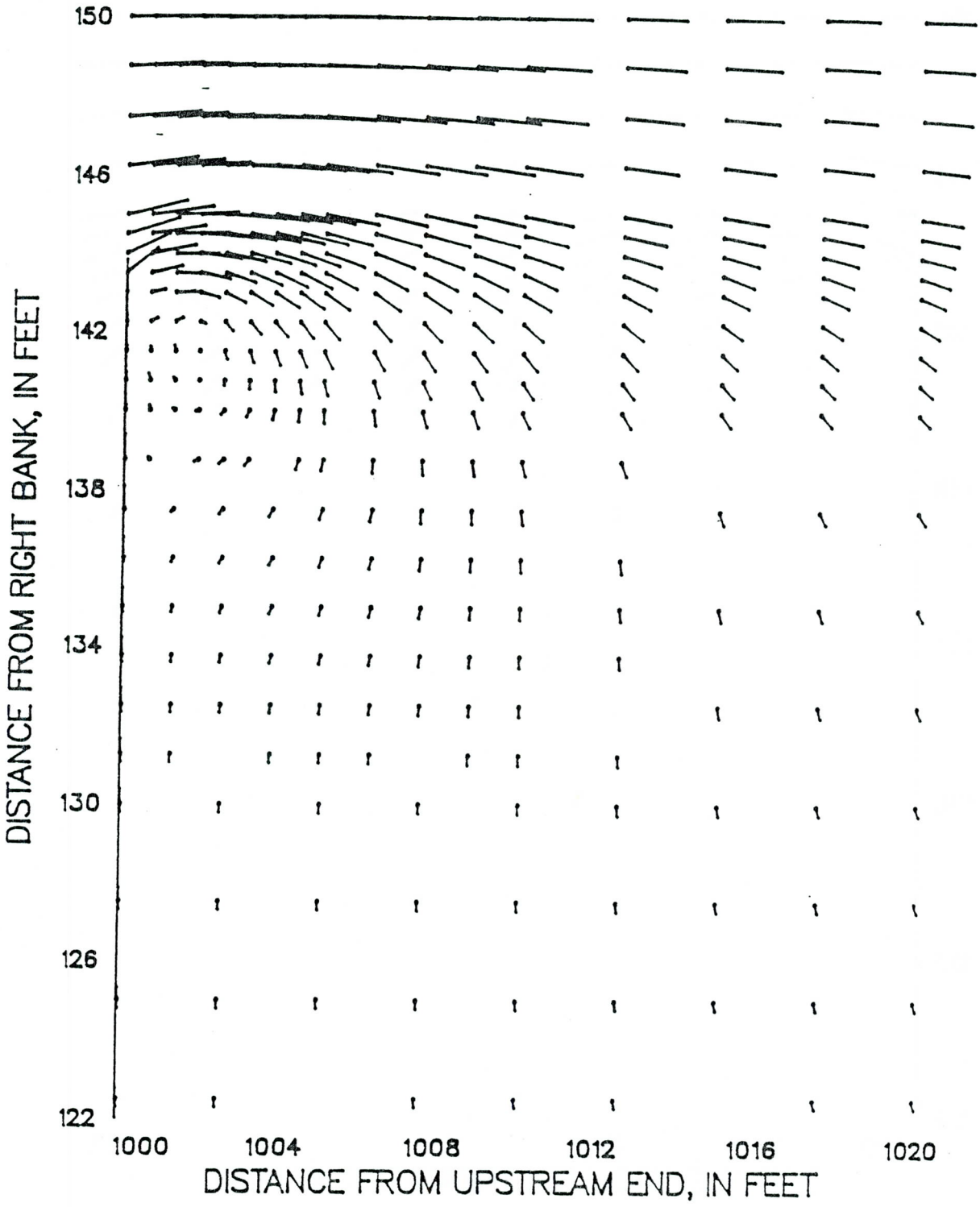

Figure 57. Partial velocity field for experiment S6210035, calibrated parameters, network 3. A vector 1 inch long represents a velocity of 4 feet per second.

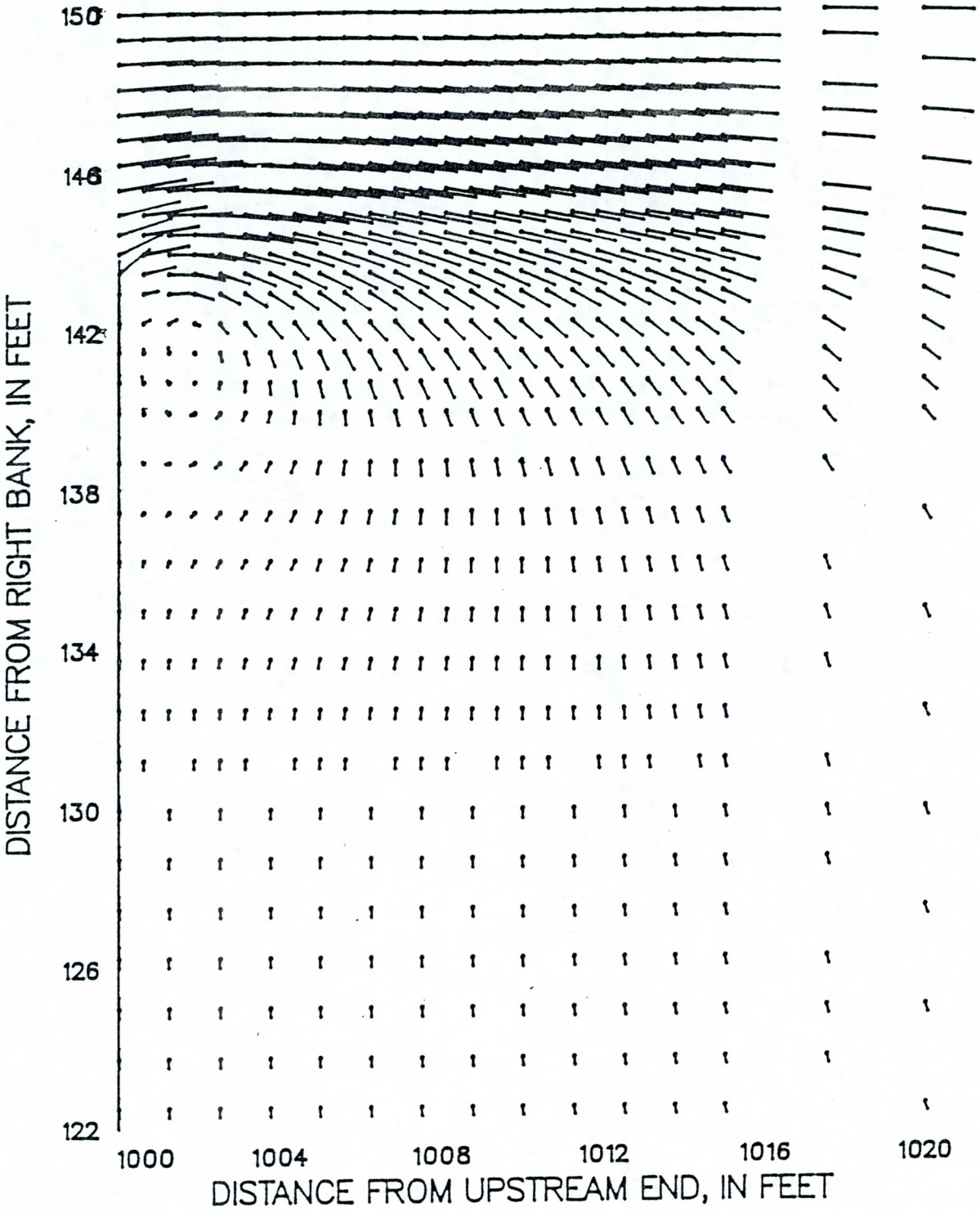

Figure 58. Partial velocity field for experiment S6210035, calibrated parameters, network 4. A vector 1 inch long represents a velocity of 4 feet per second.

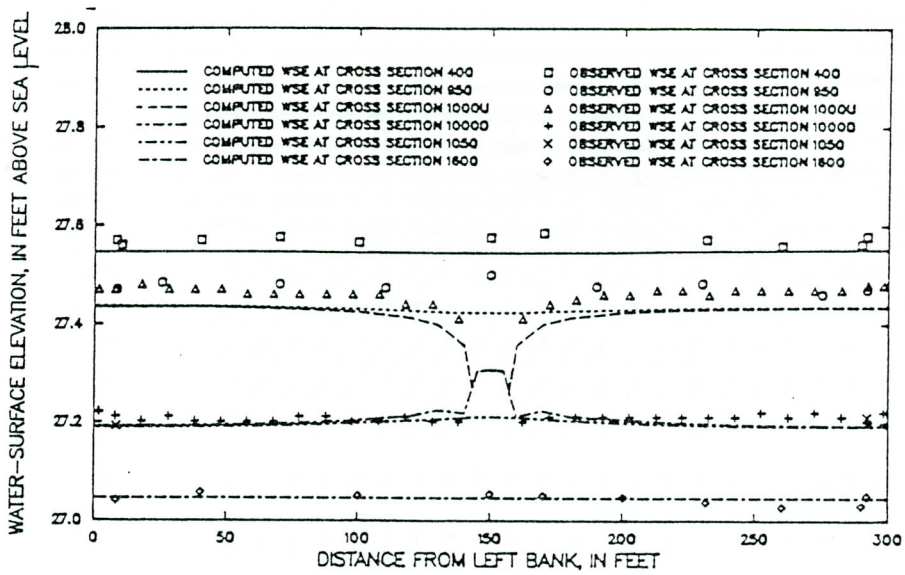

Figure 59. Observed and computed water-surface elevations (WSE) for experiment S6810105, calibrated parameters, network 1. The letters U and D refer, respectively, to the upstream side and the downstream side of the constriction.

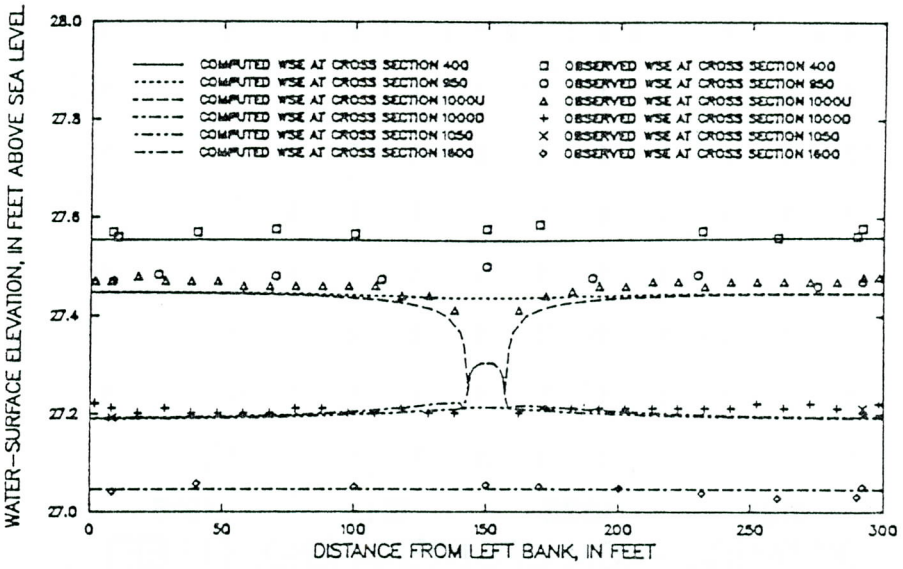

Figure 60. Observed and computed water-surface elevations (WSE) for experiment S6810105, calibrated parameters, network 2. The letters U and D refer, respectively, to the upstream aide and the downstream side of the constriction.

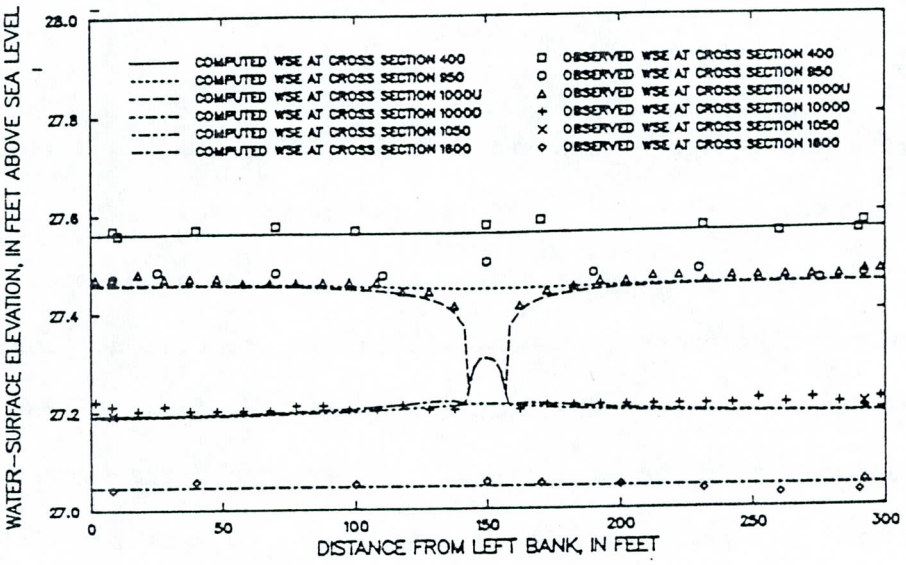

Figure 61. Observed and computed water-surface elevations (WSE) for experiment S6810105, calibrated parameters, network 3. The letters U and D refer, respectively, to the upstream side and the downstream side of the constriction.

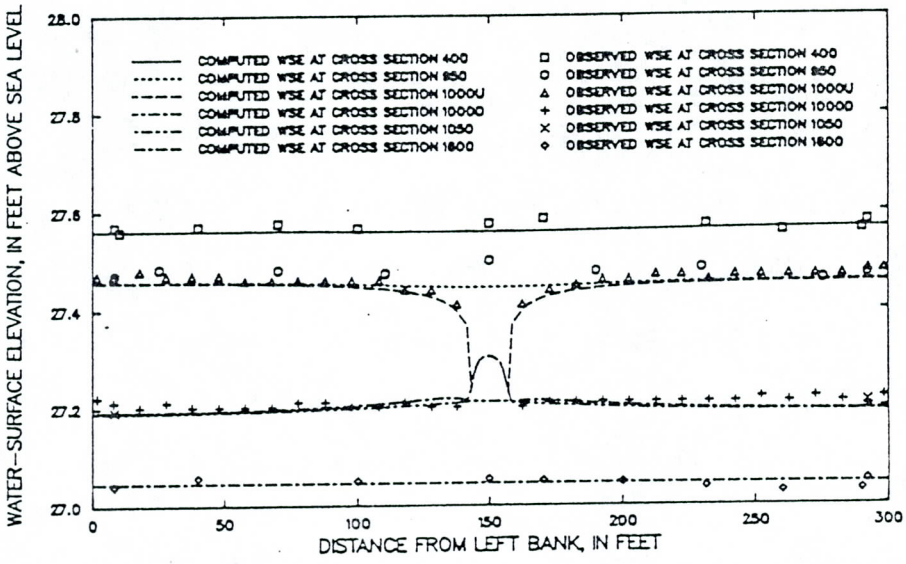

Figure 62. Observed and computed water-surface elevations (WSE) for experiment S6810105, calibrated parameters, network 4. The letters U and D refer, respectively, to the upstream side and the downstream side of the constriction.

these two networks, computed water-surface elevations average about 0.01 ft lower than observed water-surface elevations on both the upstream and downstream sides of the constriction.

Velocity profiles at cross sections 900, 950, 1050, and 1100 are shown in figures 63 through 78. As before, differences among the results for the four networks are minor. The magnitudes of the computed overbank velocity components in the y-direction at cross section 950 are too large. There is no apparent explanation for this. The observations about the dissipation of the jet and the overbank velocity components at cross sections 1050 and 1100 made for the simulations of experiment S6210035 also apply in this case. Downstream from the constriction, the computed peak velocity in the low-water channel is 47 percent low at cross section 1050 and 43 to 44 percent low at cross section 1100.

Partial velocity fields for the four networks are shown in figures 79 through 82. Oscillations due to the coarseness of the network are evident in figures 79 and 80 but disappear in figures 81 and 82. As before, a recirculation zone, larger than that for the S6210035 simulation, appears for networks 3 and 4. The stagnation point on the downstream side of the constriction is located about 133 ft from the right bank for networks 3 and 4.

Water-surface elevations are shown for experiment S7410235 in figures 83 through 86. The improvement in computed water-surface elevations due to network refinement is even more evident in this

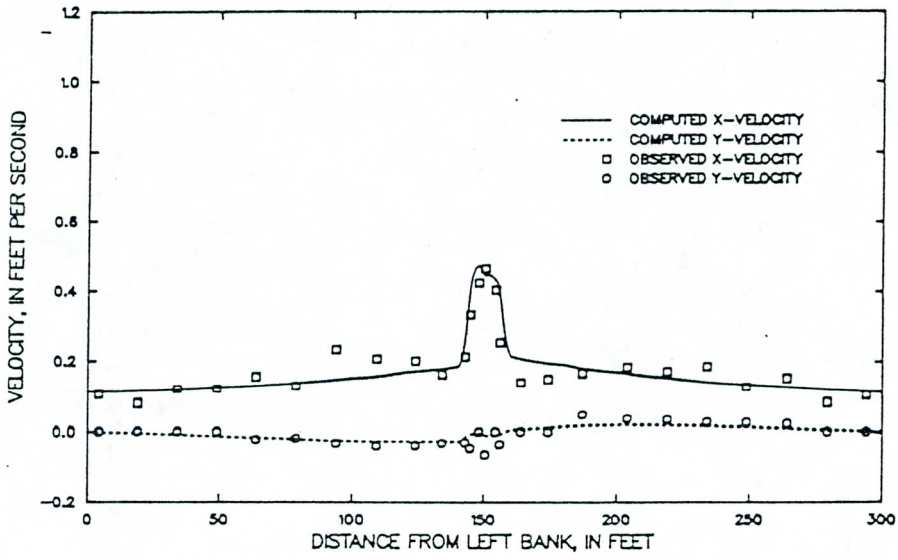

Figure 63. Observed and computed velocity components at cross section 900 for experiment S6810105, calibrated parameters, network 1.

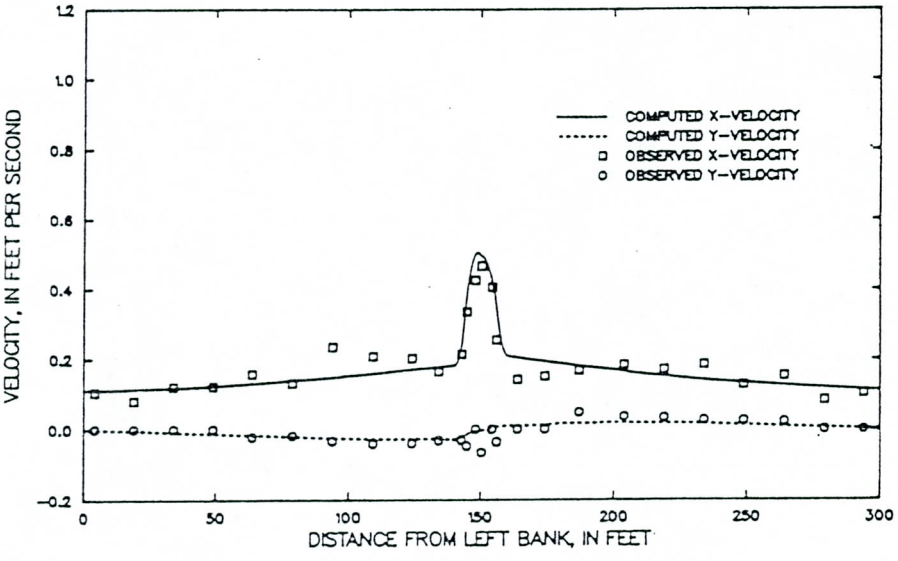

Figure 64. Observed and computed velocity components at cross section 900 for experiment S6810105, calibrated parameters, network 2.

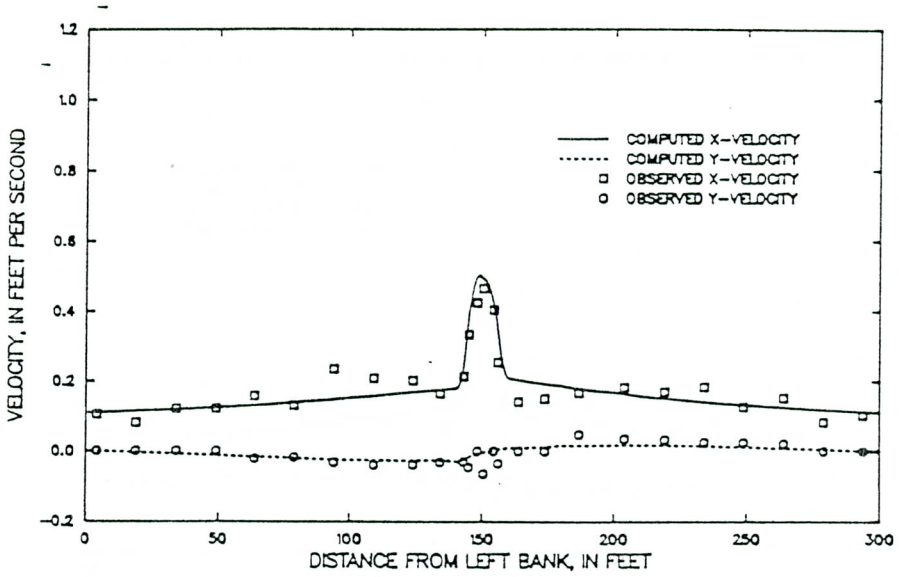

Figure 65. Observed and computed velocity components at cross section 900 for experiment S6810105, calibrated parameters, network 3.

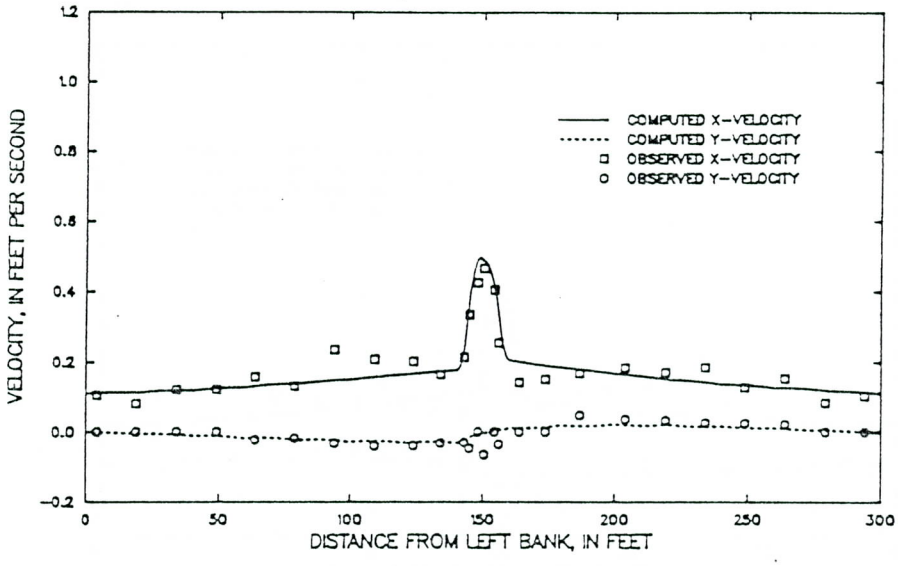

Figure 66. Observed and computed velocity components at cross section 900 for experiment S6810105, calibrated parameters, network 4.

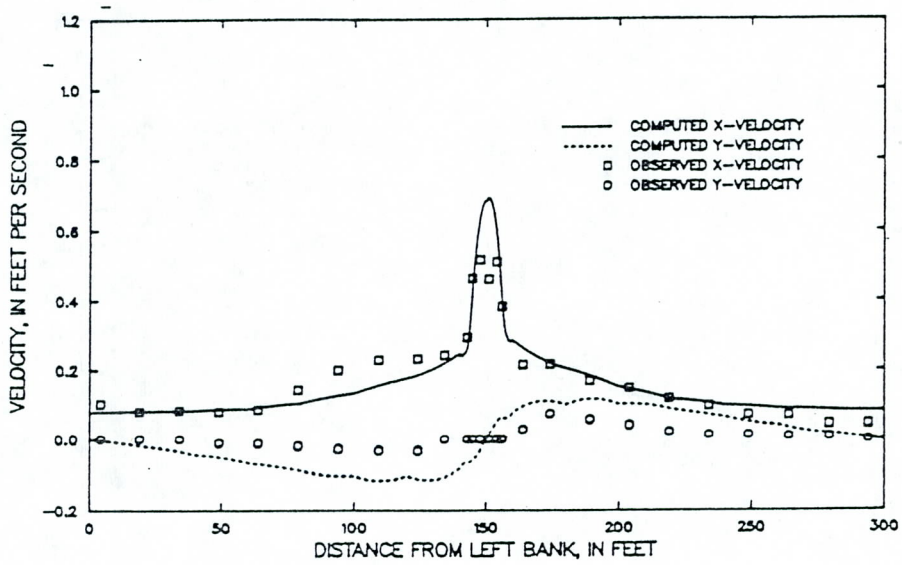

Figure 67. Observed and computed velocity components at cross section 950 for experiment S6810105, calibrated parameters, network 1.

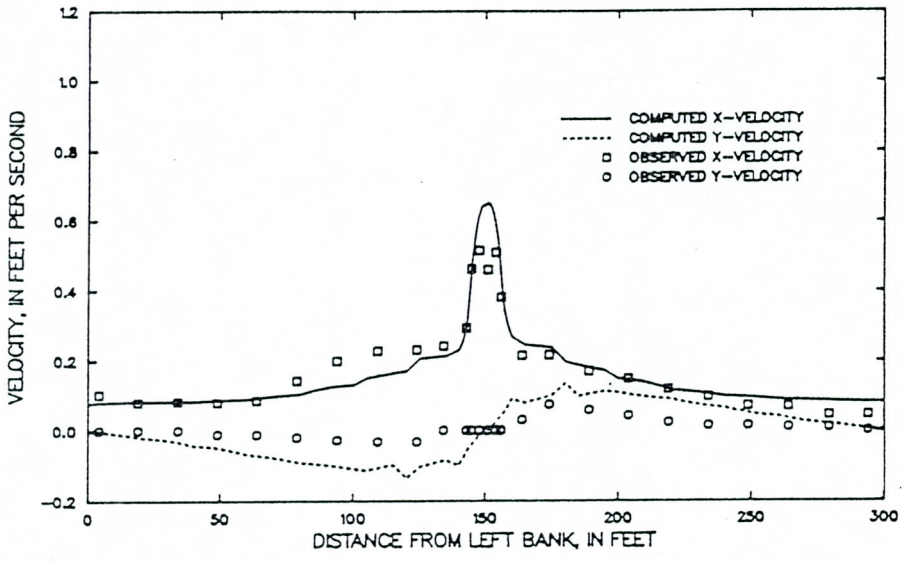

Figure 68. Observed and computed velocity components at cross section 950 for experiment S6810105, calibrated parameters, network 2.

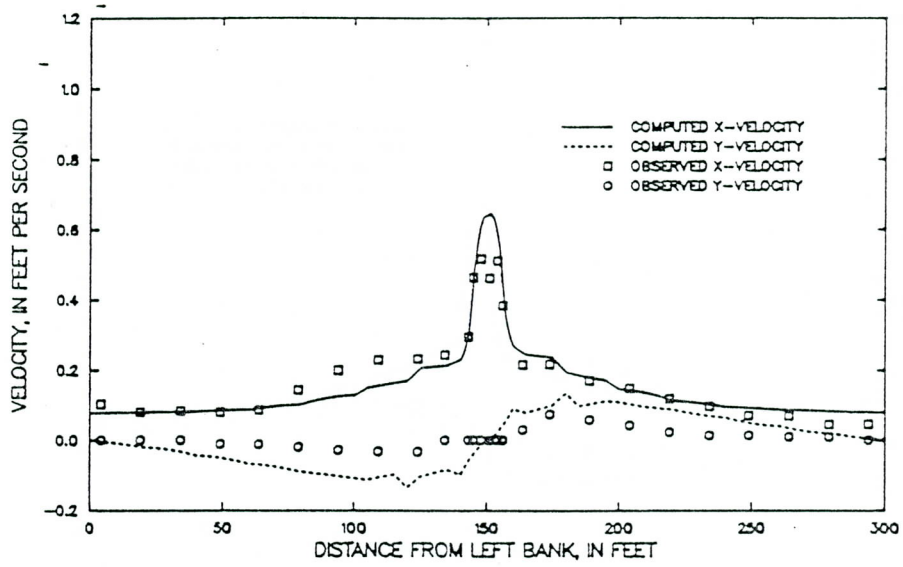

Figure 69. Observed and computed velocity components at cross section 950 for experiment S6810105, calibrated parameters, network 3.

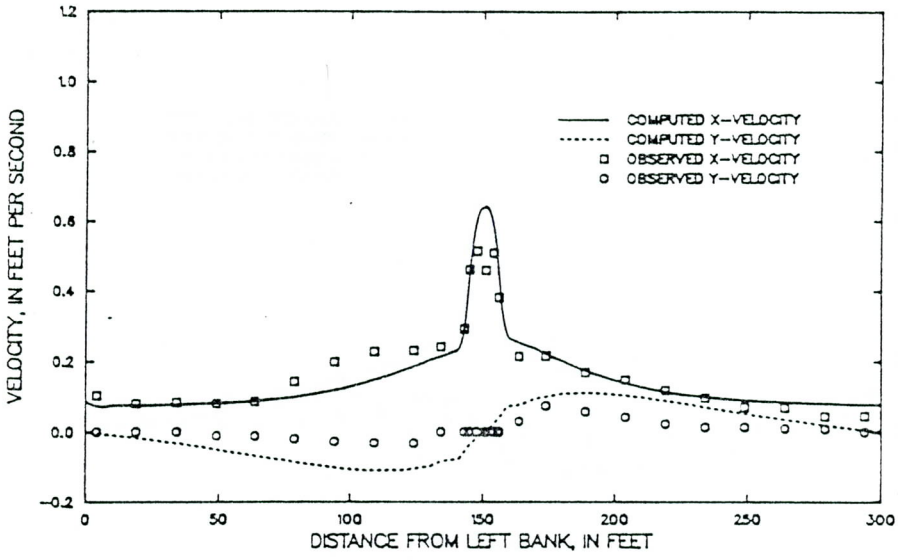

Figure 70. Observed and computed velocity components at cross section 950 for experiment S6810105, calibrated parameters, network 4.

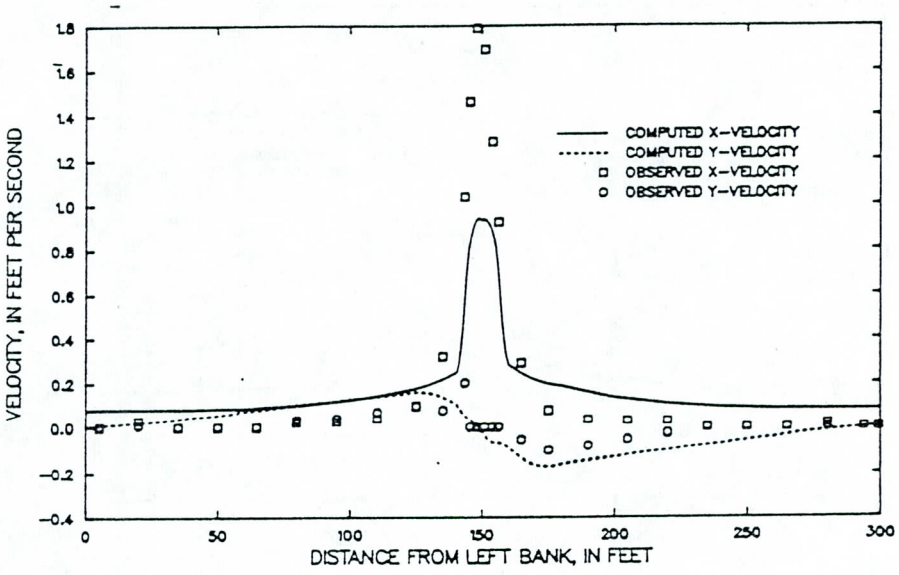

Figure 71. Observed and computed velocity components at cross section 1050 for experiment S6810105, calibrated parameters, network 1.

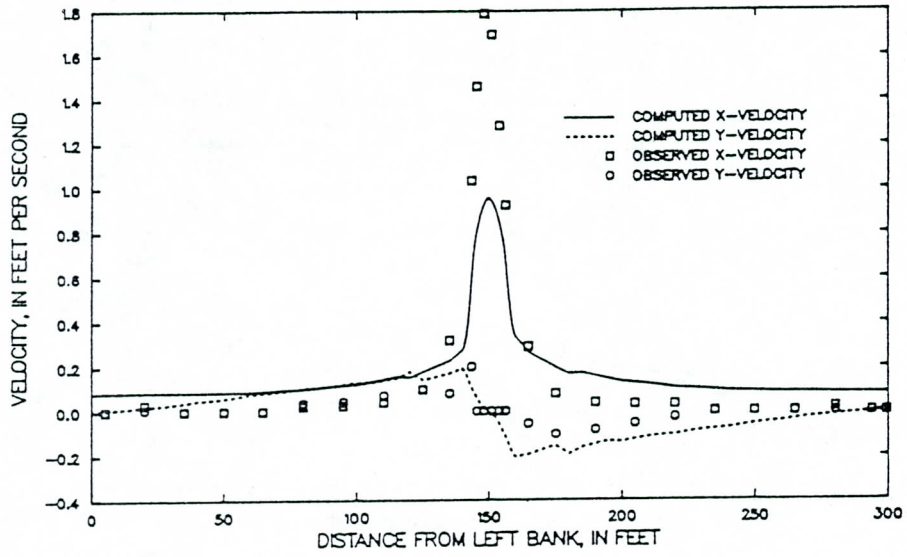

Figure 72. Observed and computed velocity components at cross section 1050 for experiment S6810105, calibrated parameters, network 2.

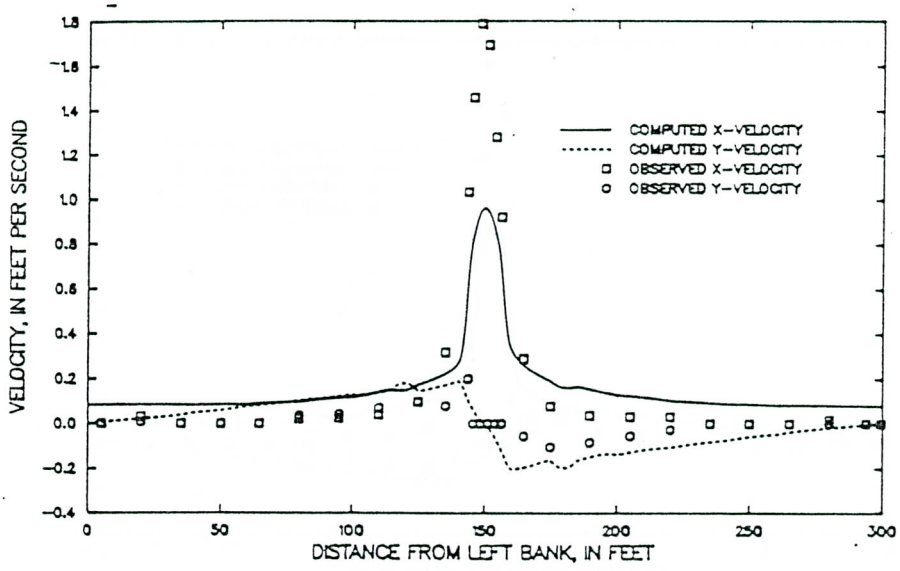

Figure 73. Observed and computed velocity components at cross section 1050 for experiment S6810105, calibrated parameters, network 3.

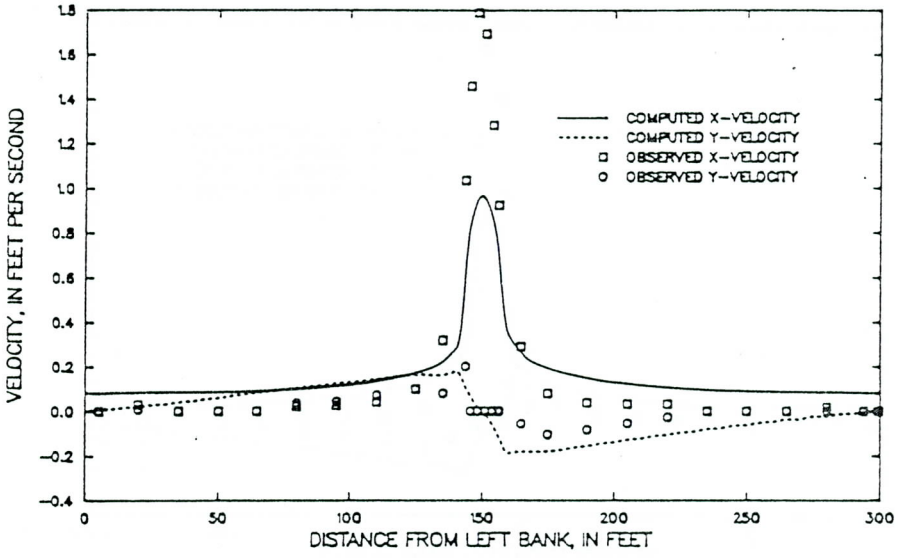

Figure 74. Observed and computed velocity components at cross section 1050 for experiment S6810105, calibrated parameters, network 4.

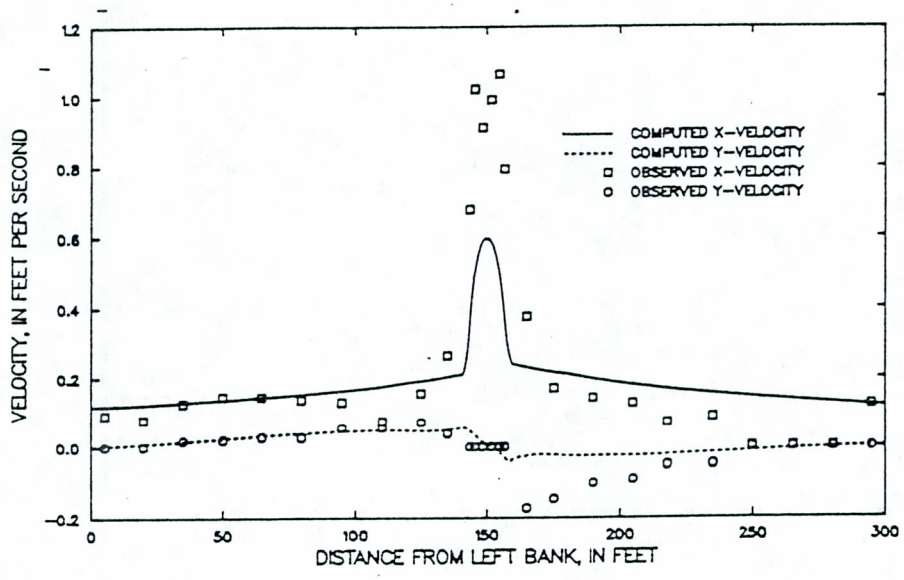

Figure 75. Observed and computed velocity components at cross section 1100 for experiment S6810105, calibrated parameters, network 1.

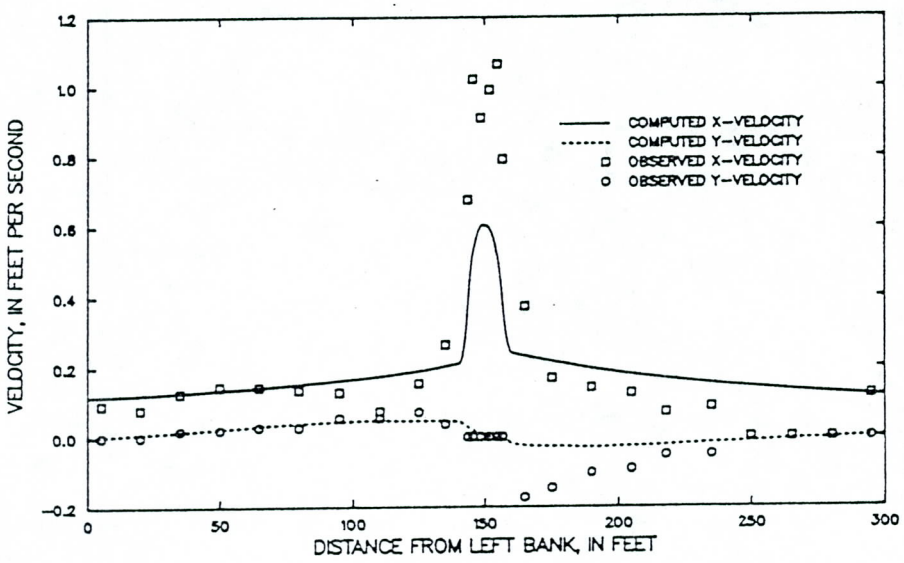

Figure 76. Observed and computed velocity components at cross section 1100 for experiment S6810105, calibrated parameters, network 2.

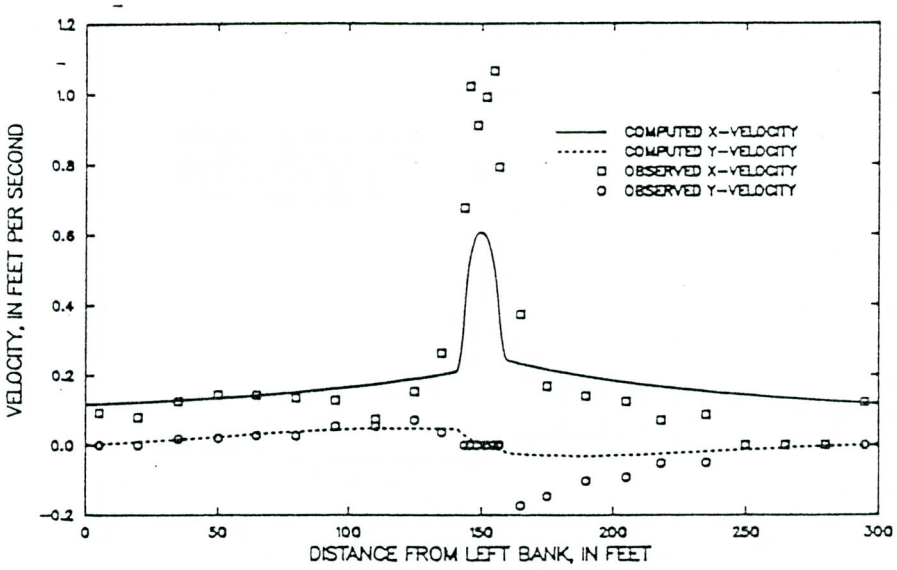

Figure 77. Observed and computed velocity components at cross section 1100 for experiment S6810105, calibrated parameters, network 3.

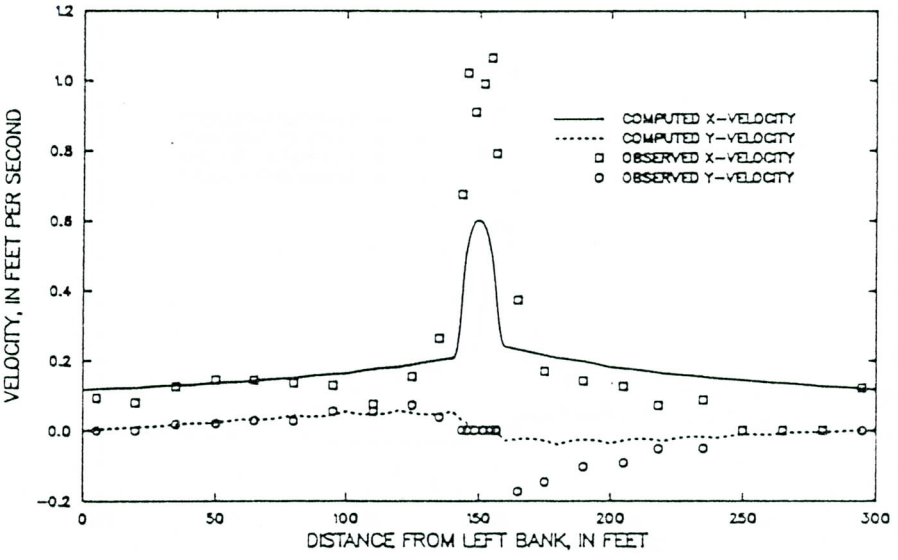

Figure 78. Observed and computed velocity components at cross section 1100 for experiment S6810105, calibrated parameters, network 4.

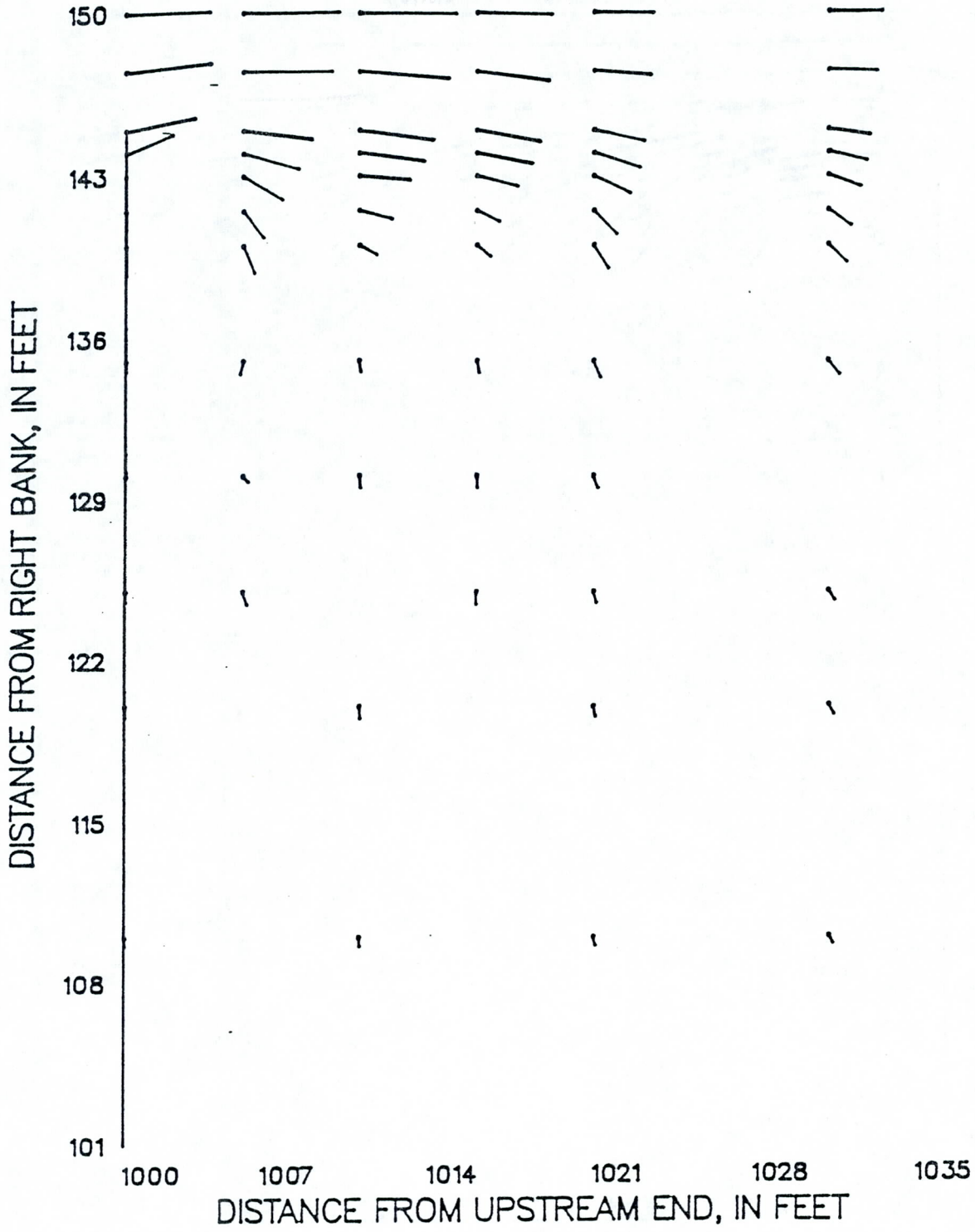

Figure 79. Partial velocity field for experiment S6810105, calibrated parameters, network 1. A vector 1 inch long represents a velocity of 4 feet per second.

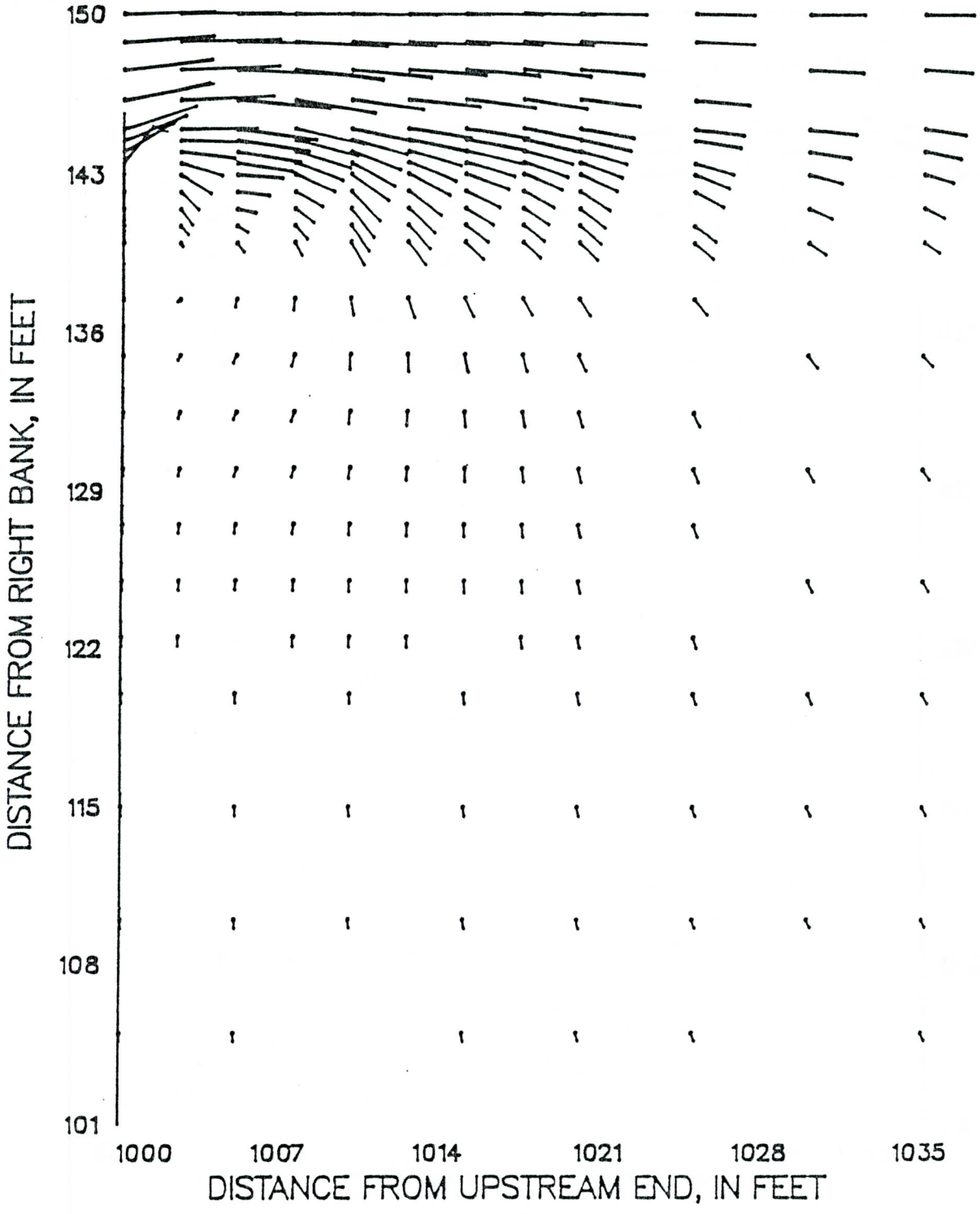

Figure 80. Partial velocity field for experiment S6810105, calibrated parameters, network 2. A vector 1 inch long represents a velocity of 4 feet per second.

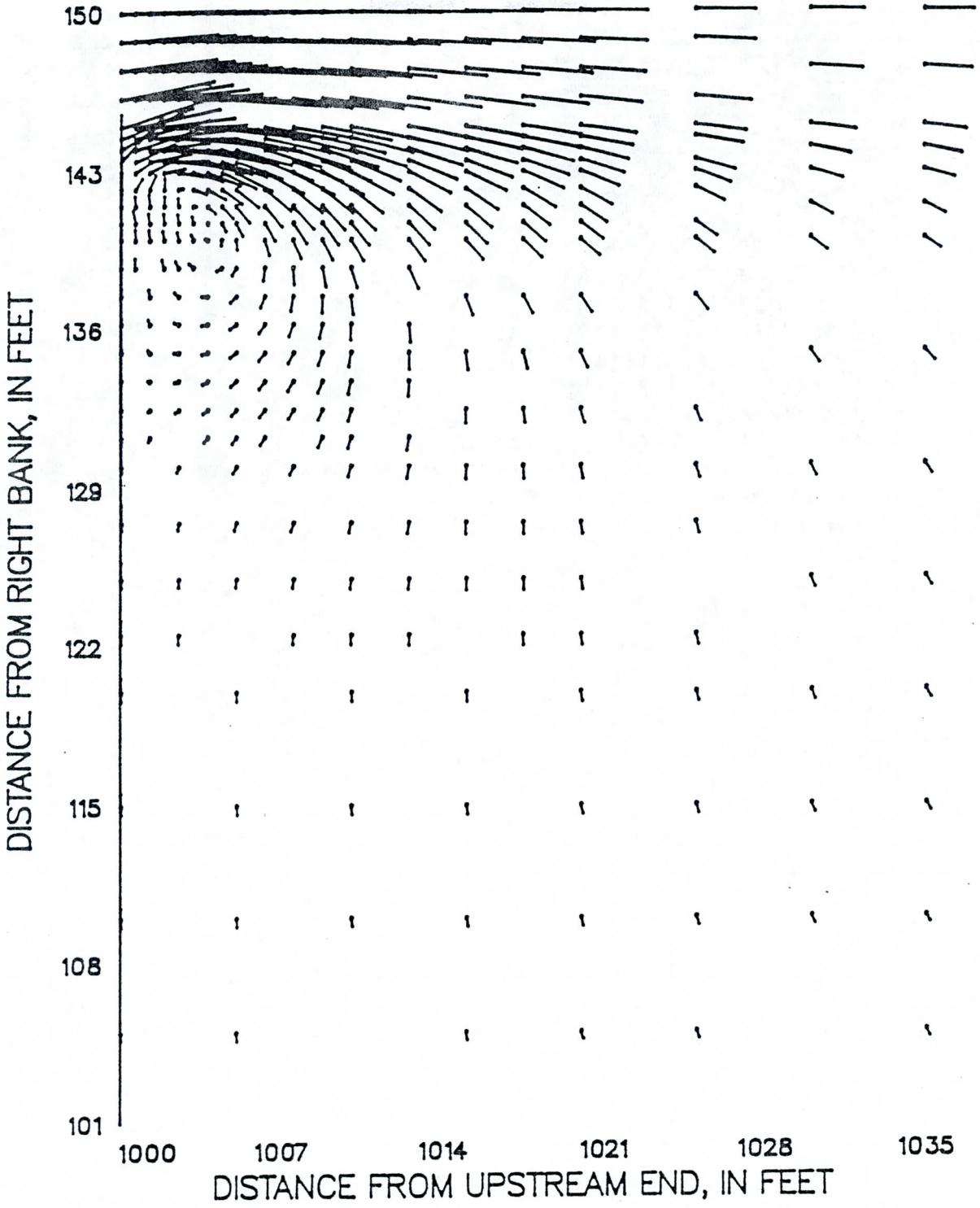

Figure 81. Partial velocity field for experiment S6810105, calibrated parameters, network 3. A vector 1 inch long represents a velocity of 4 feet per second.

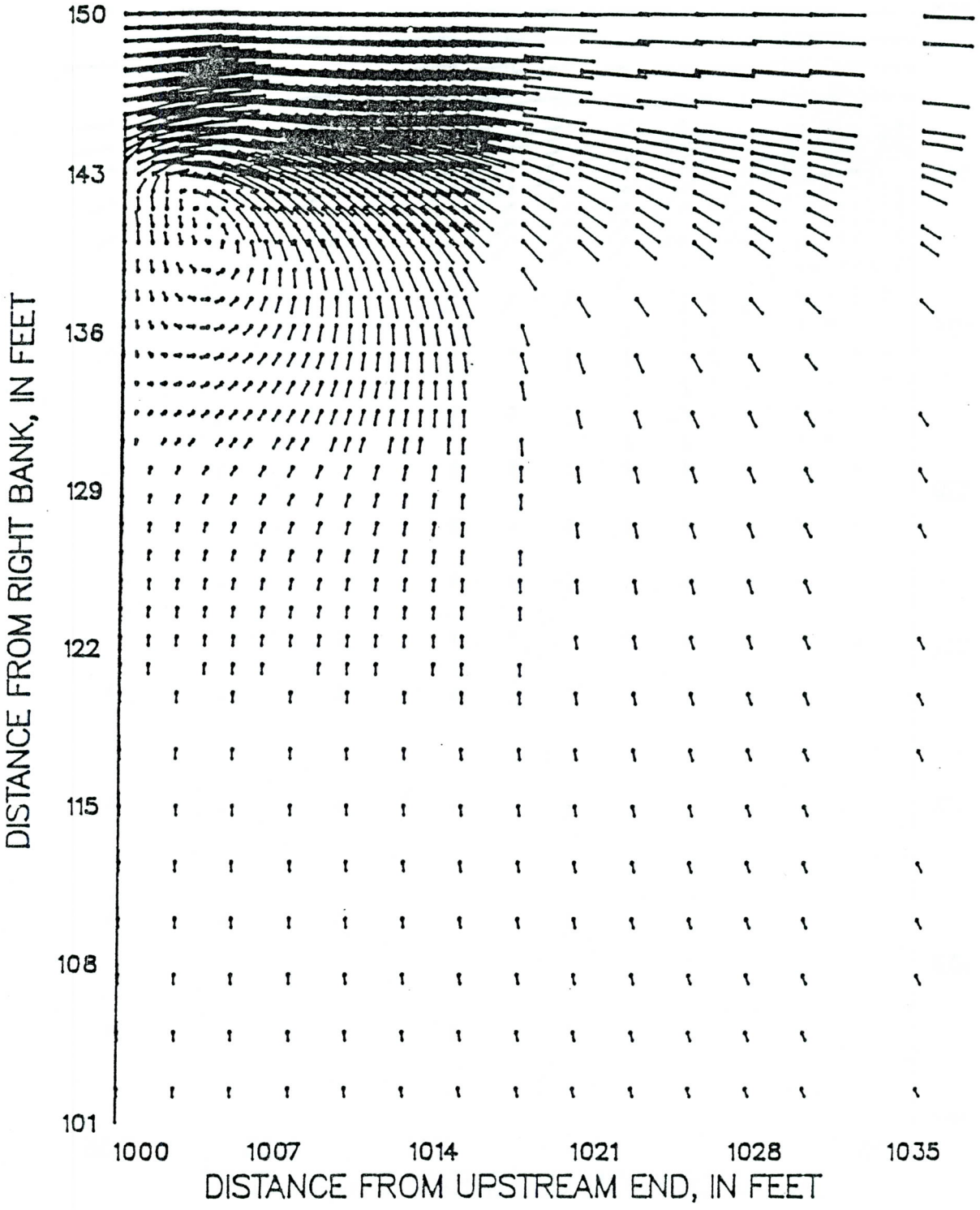

Figure 82. Partial velocity field for experiment S6810105, calibrated parameters, network 4. A vector 1 inch long represents a velocity of 4 feet per second.

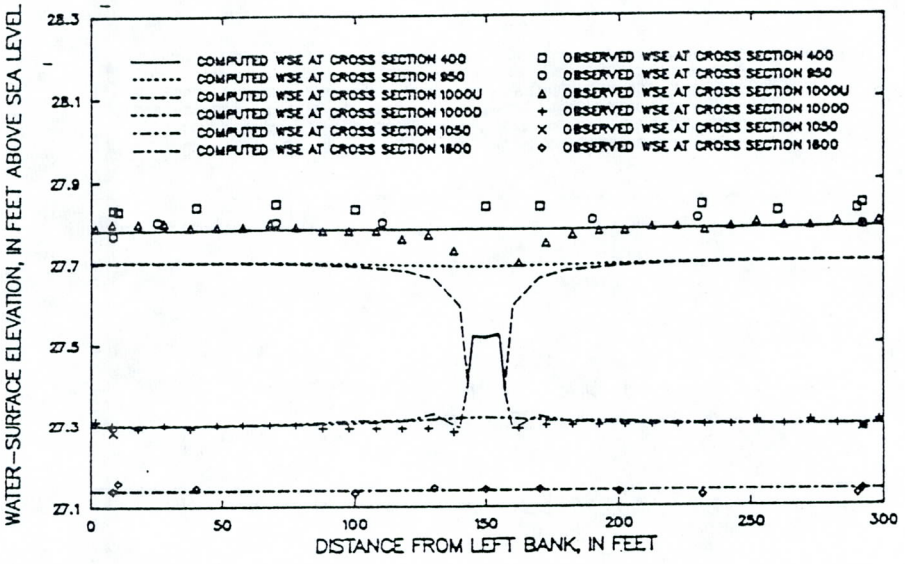

Figure 83. Observed and computed water-surface elevations (WSE) for experiment S7410235, calibrated parameters, network 1. The letters U and D refer, respectively, to the upstream side and the downstream side of the constriction.

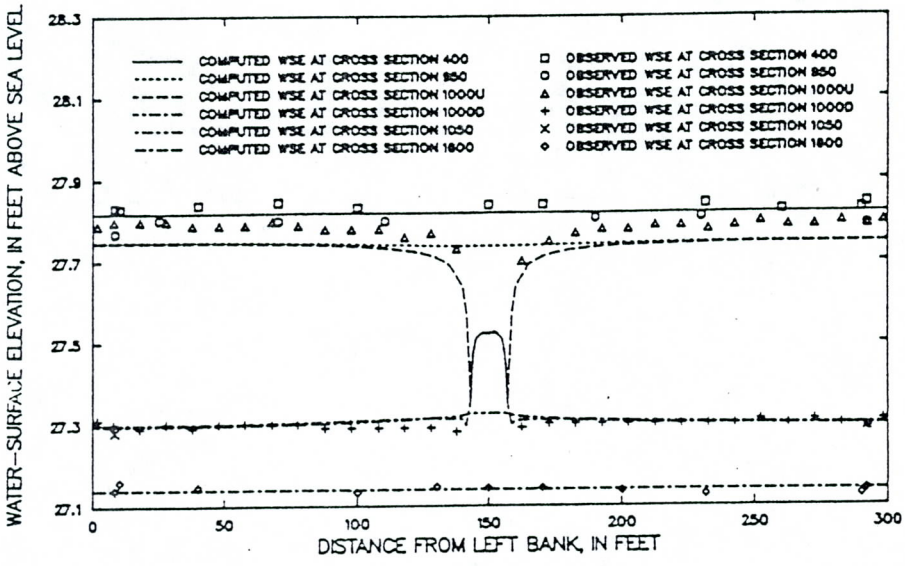

Figure 84. Observed and computed water-surface elevations (WSE) for experiment S7410235, calibrated parameters, network 2. The letters U and D refer, respectively, to the upstream side and the downstream side of the constriction.

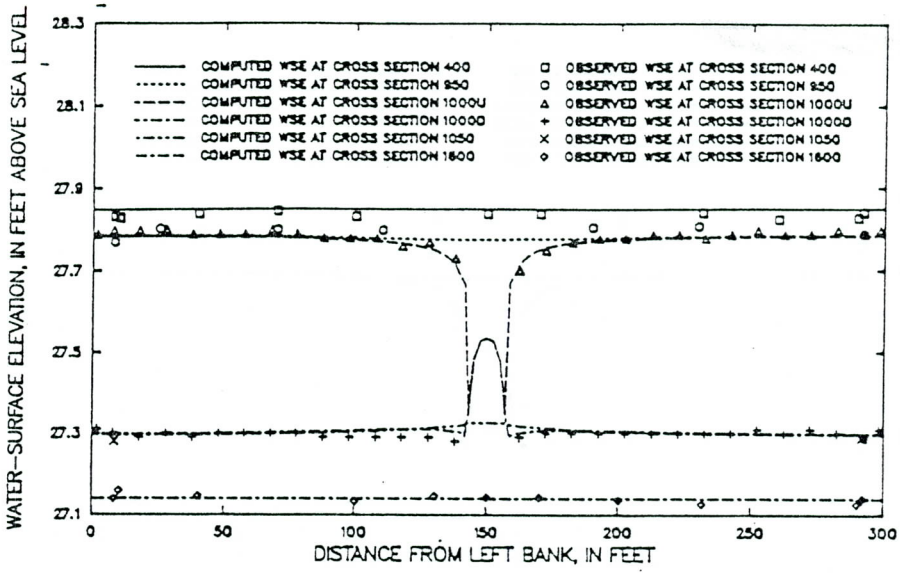

Figure 85. Observed and computed water-surface elevations (WSE) for experiment S7410235, calibrated parameters, network 3. The letters U and D refer, respectively, to the upstream side and the downstream side of the constriction.

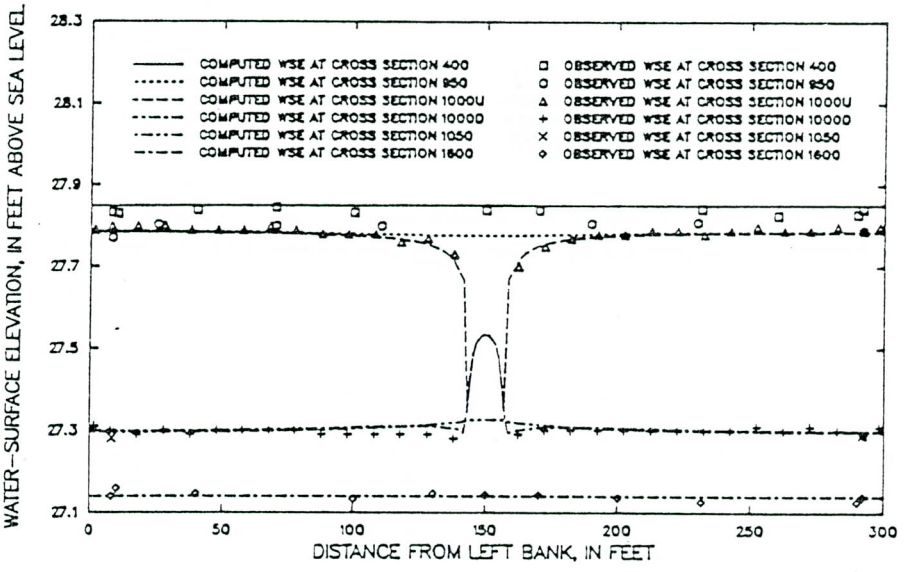

Figure 86. Observed and computed water-surface elevations (WSE) for experiment S7410235, calibrated parameters, network 4. The letters U and D refer, respectively, to the upstream side and the downstream side of the constriction.

case than for experiment S6810105. The computed backwater is low for networks 1 and 2 but very accurate for networks 3 and 4. Again, there is virtually no difference between the results for network 3 and those for network 4.

Velocity profiles at cross sections 900, 950, 1050, and 1100 are shown in figures 87 through 102. Comparing figure 87 with figures 39 and 63 shows that for network 1, oscillations develop as discharge and hence velocity and depth gradients increase. These velocity oscillations disappear for the more refined networks. Differences among the results for networks 2, 3, and 4 are minor. The observations about the dissipation of the jet and the overbank velocity components at cross sections 1050 and 1100 made above apply again. Downstream from the constriction, the computed peak velocity in the low-water channel is 41 to 46 percent low at cross section 1050 and 62 to 64 percent low at cross section 1100.

Partial velocity fields for the four networks are shown in figures 103 through 106. The oscillations seen in the velocity profiles for network 1 are evident in the shear region between the jet and the recirculation zone for both networks 1 and 2. These oscillations are not evident in the results for networks 3 and 4. The stagnation point on the downstream side of the constriction is located about 121 ft from the right bank for network 2, about 117 ft from the right bank for network 3, and about 119 ft from the right bank for network 4. The recirculation zone is substantially larger for this discharge than it was for the smaller discharges.

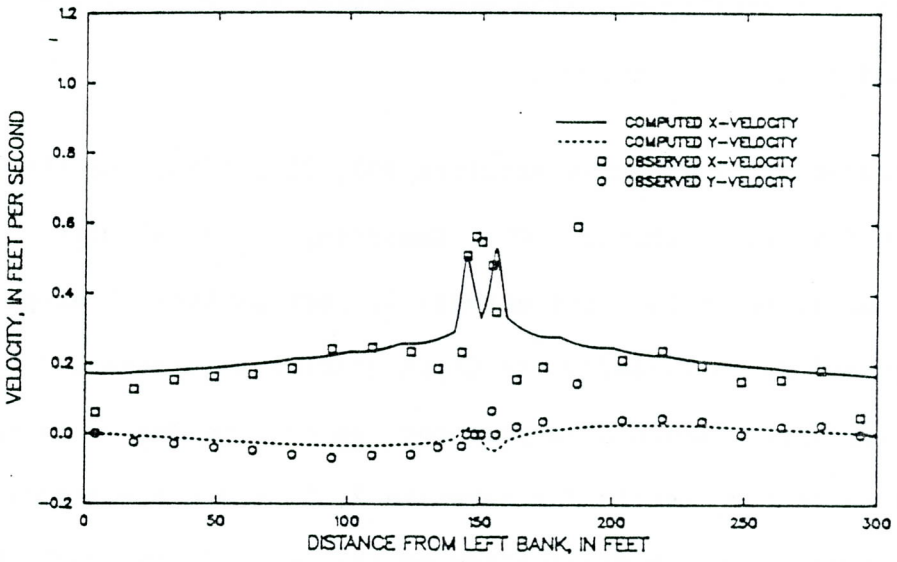

Figure 87. Observed and computed velocity components at cross section 900 for experiment S7410235, calibrated parameters, network 1.

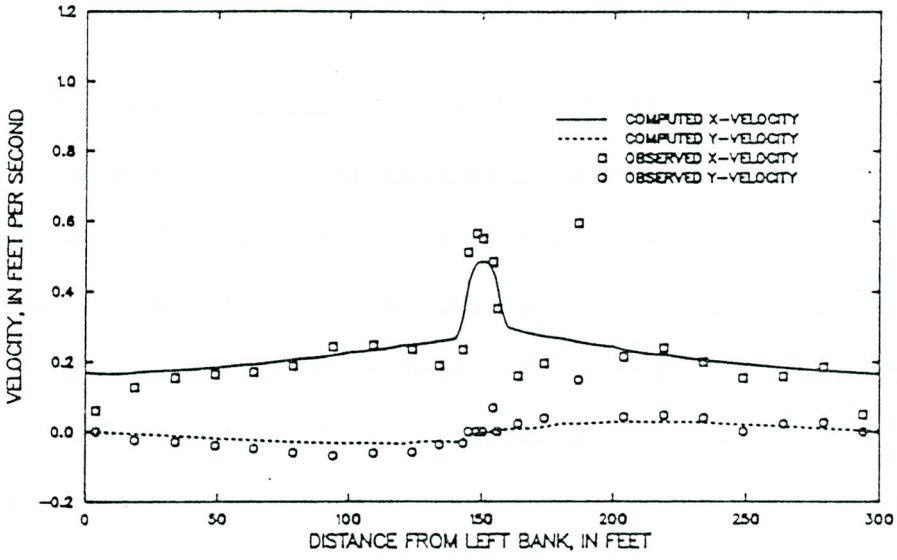

Figure 88. Observed and computed velocity components at cross section 900 for experiment S7410235, calibrated parameters, network 2.

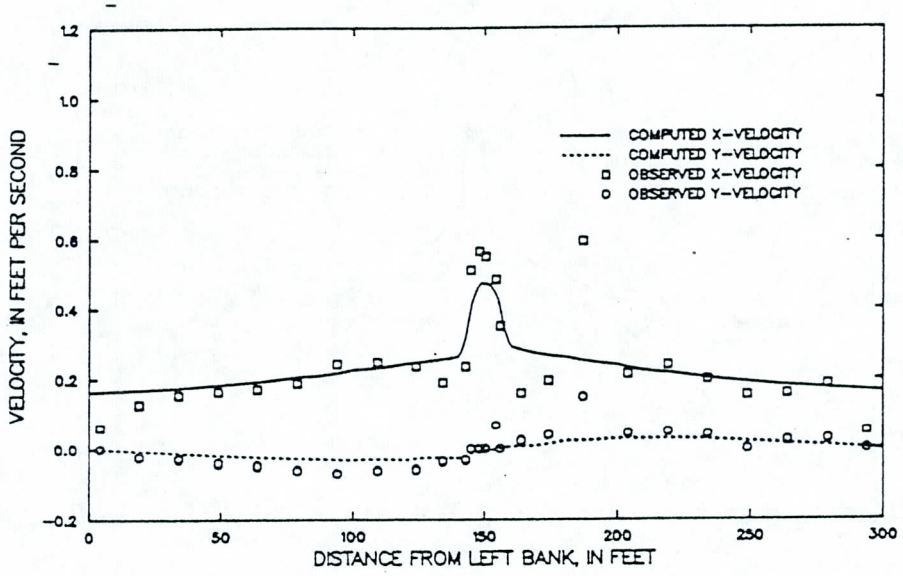

Figure 89. Observed and computed velocity components at cross section 900 for experiment S7410235, calibrated parameters, network 3.

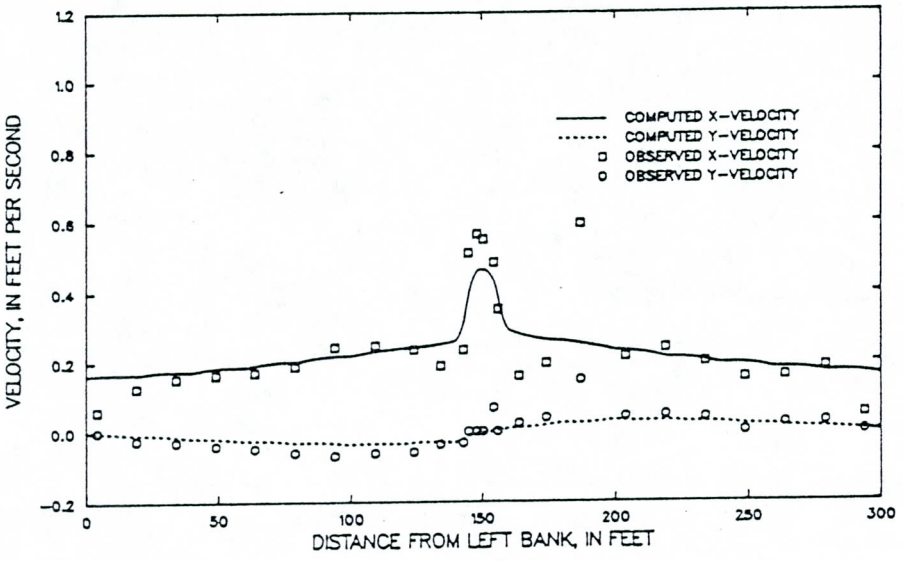

Figure 90. Observed and computed velocity components at cross section 900 for experiment S7410235, calibrated parameters, network 4.

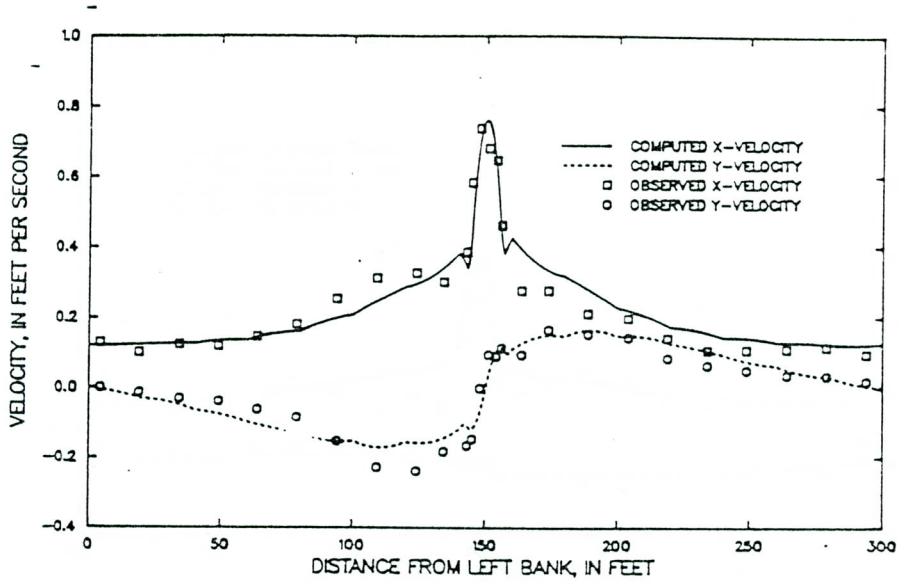

Figure 91. Observed and computed velocity components at cross section 950 for experiment S7410235, calibrated parameters, network 1.

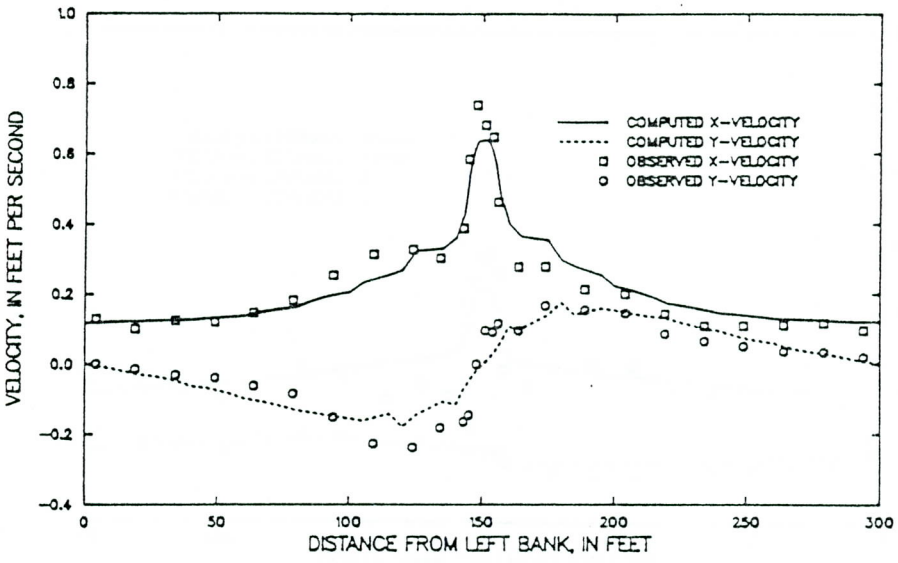

Figure 92. Observed and computed velocity components at cross section 950 for experiment S7410235, calibrated parameters, network 2.

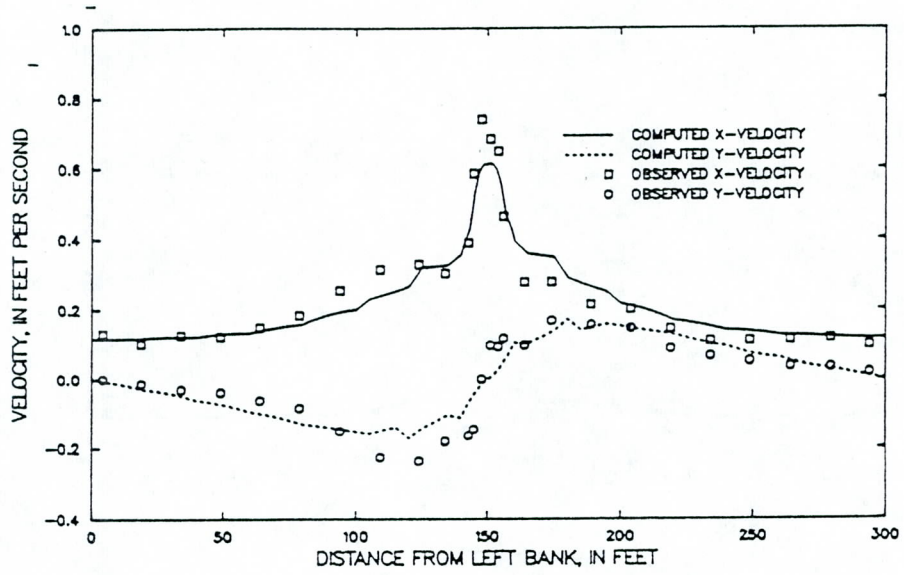

Figure 93. Observed and computed velocity components at cross section 950 for experiment S7410235, calibrated parameters, network 3.

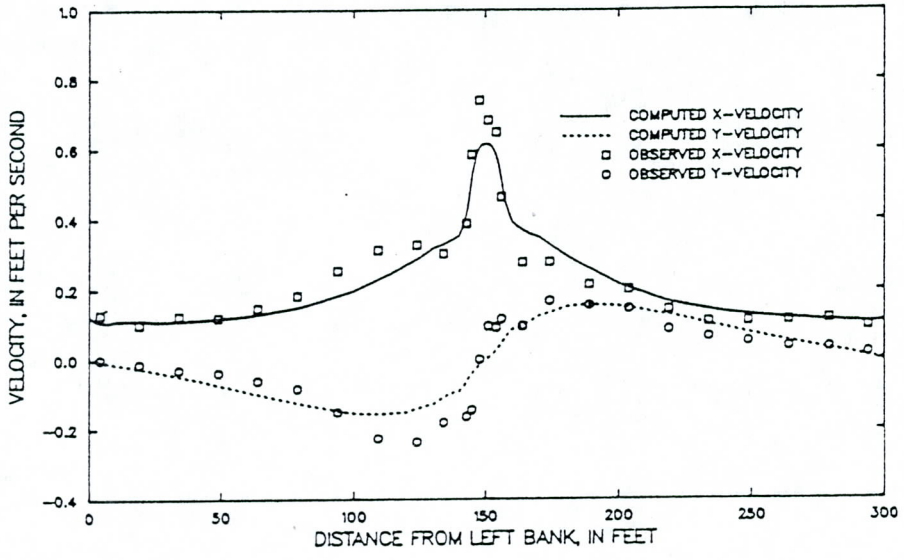

Figure 94. Observed and computed velocity components at cross section 950 for experiment S7410235, calibrated parameters, network 4.

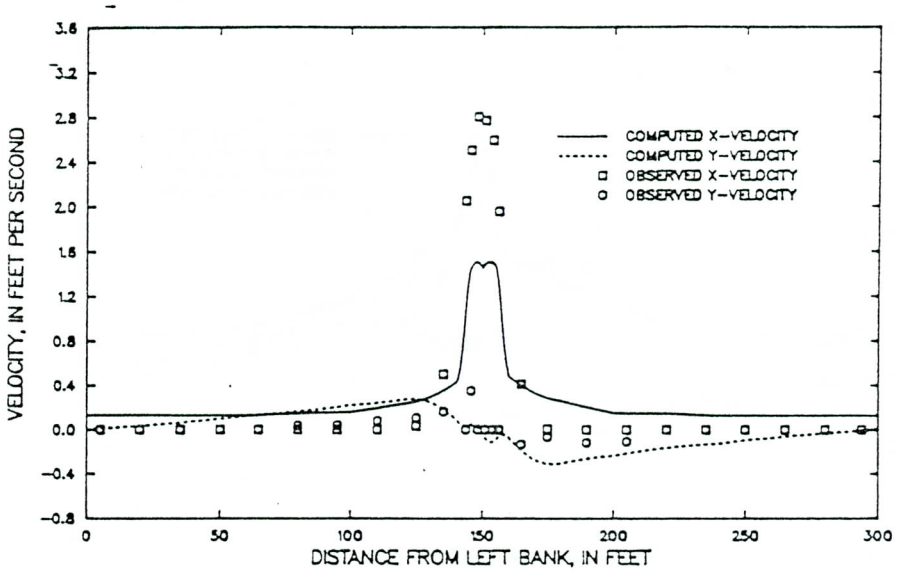

Figure 95. Observed and computed velocity components at cross section 1050 for experiment S7410235, calibrated parameters, network 1.

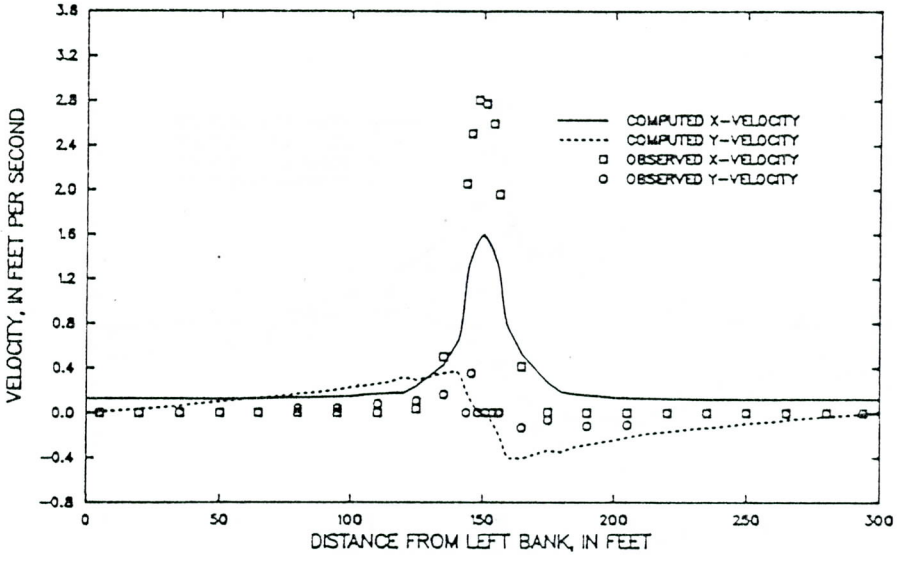

Figure 96. Observed and computed velocity components at cross section 1050 for experiment S7410235, calibrated parameters, network 2.

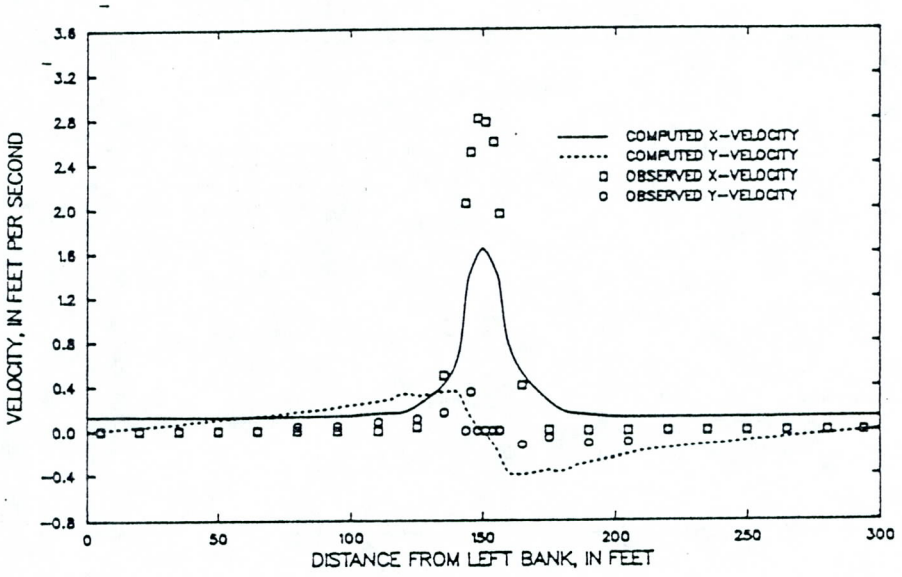

Figure 97. Observed and computed velocity components at cross section 1050 for experiment S7410235, calibrated parameters, network 3.

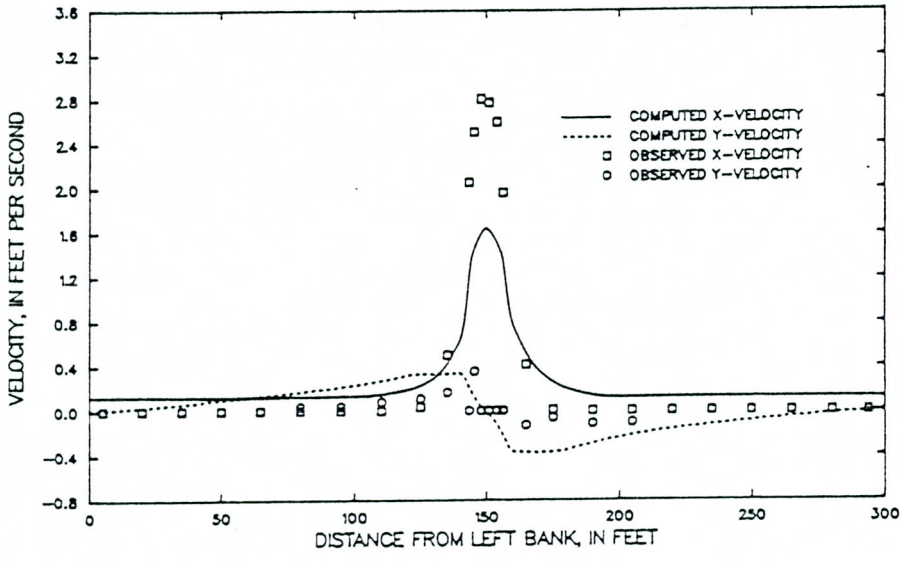

Figure 98. Observed and computed velocity components at cross section 1050 for experiment S7410235, calibrated parameters, network 4.

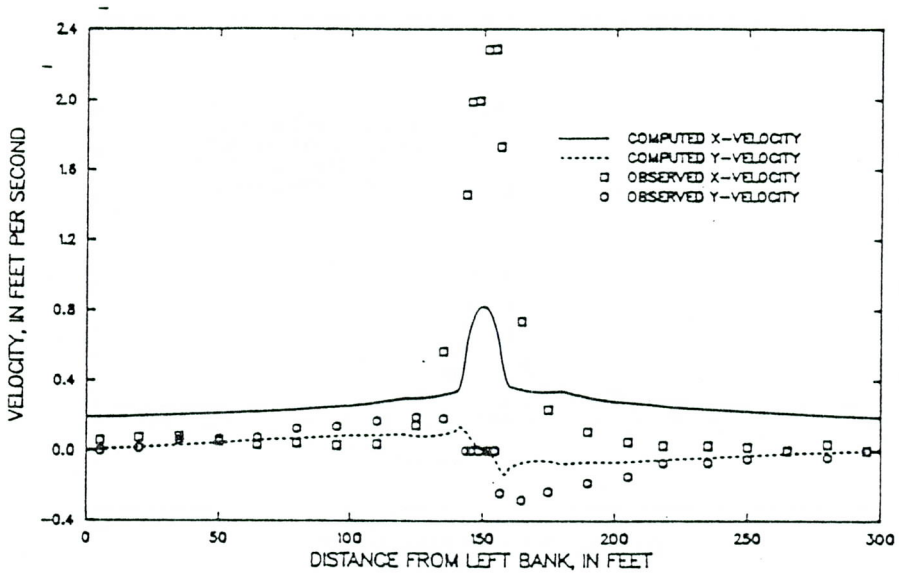

Figure 99. Observed and computed velocity components at cross section 1100 for experiment S7410235, calibrated parameters, network 1.

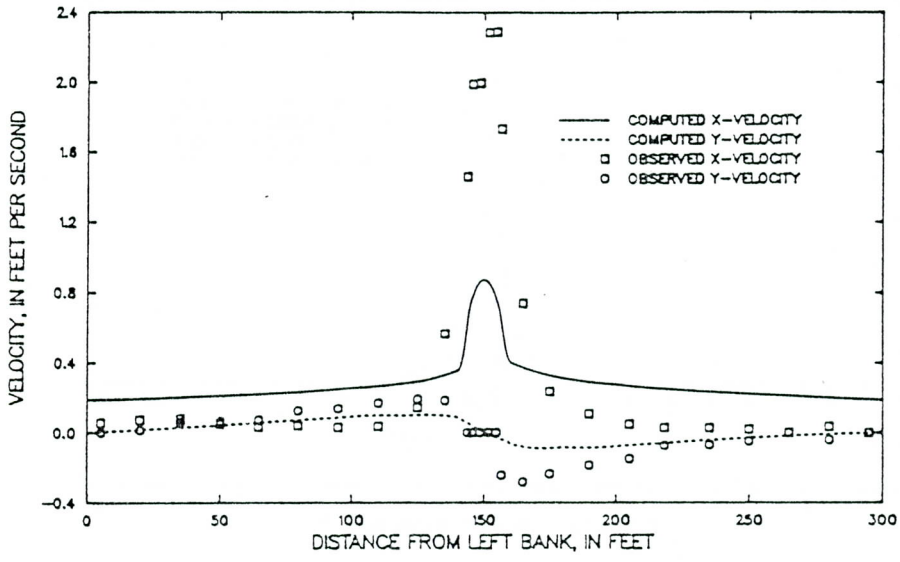

Figure 100. Observed and computed velocity components at cross section 1100 for experiment S7410235, calibrated parameters, network 2.

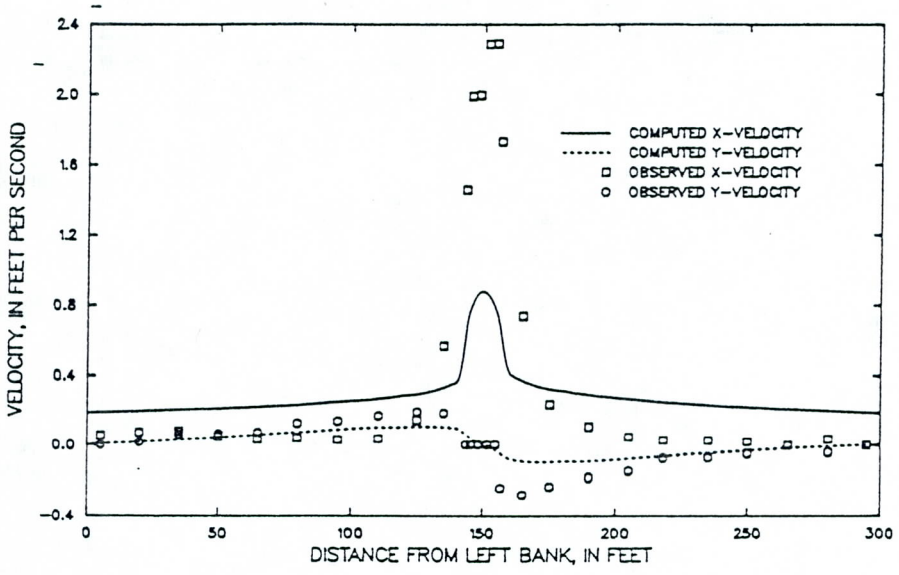

Figure 101. Observed and computed velocity components at cross section 1100 for experiment S7410235, calibrated parameters, network 3.

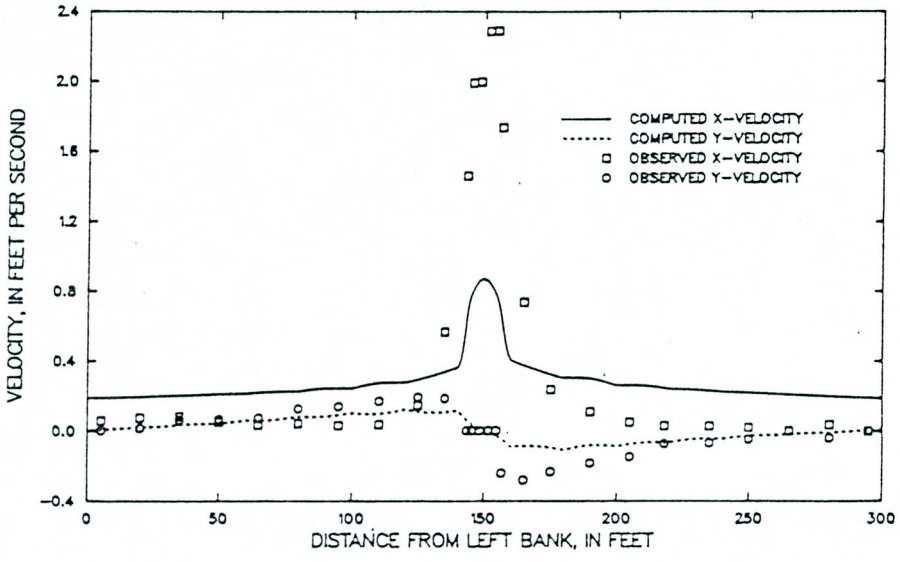

Figure 102. Observed and computed velocity components at cross section 1100 for experiment S7410235, calibrated parameters, network 4.

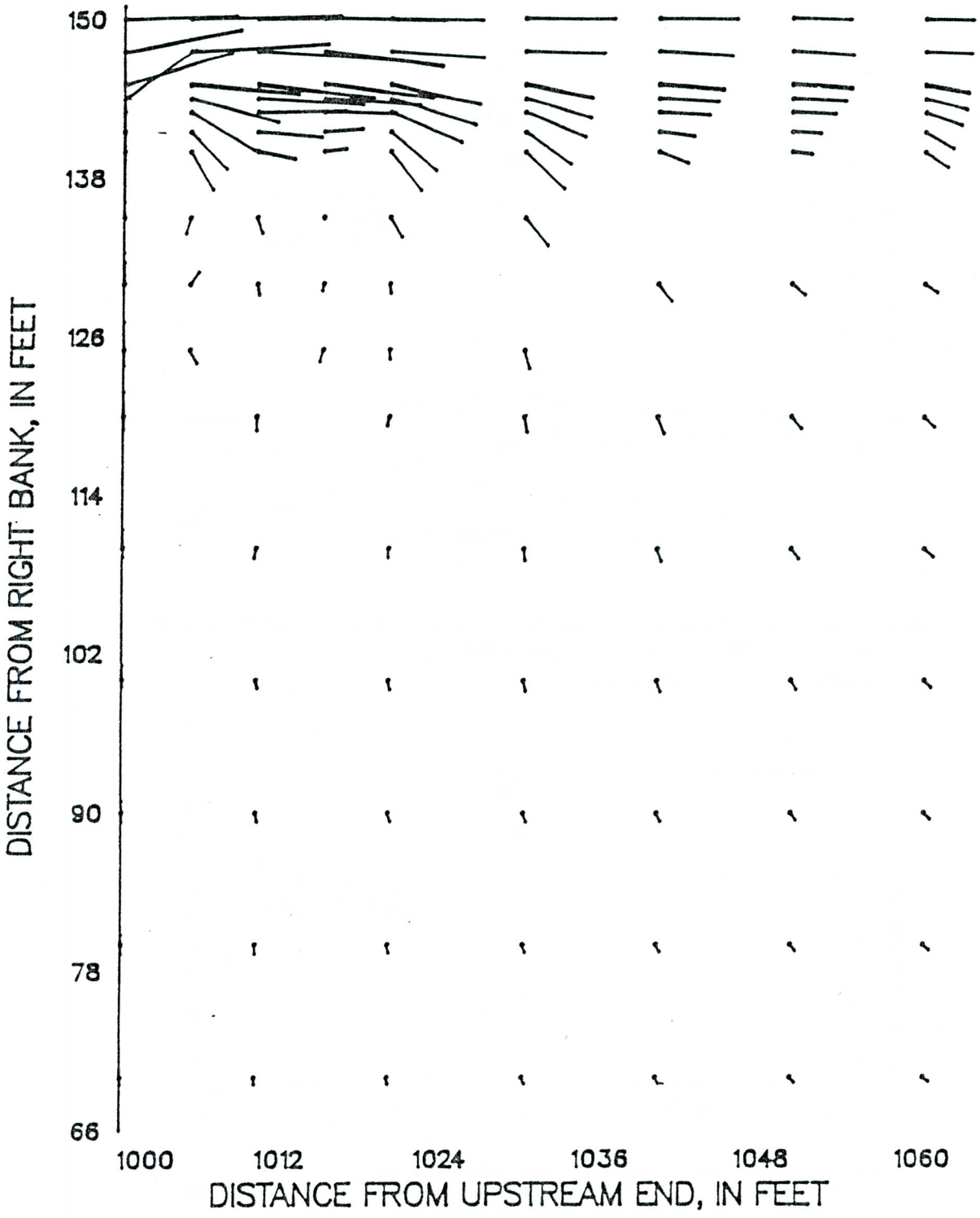

Figure 103. Partial velocity field for experiment S7410235, calibrated parameters, network 1. A vector 1 inch long represents a velocity of 4 feet per second.

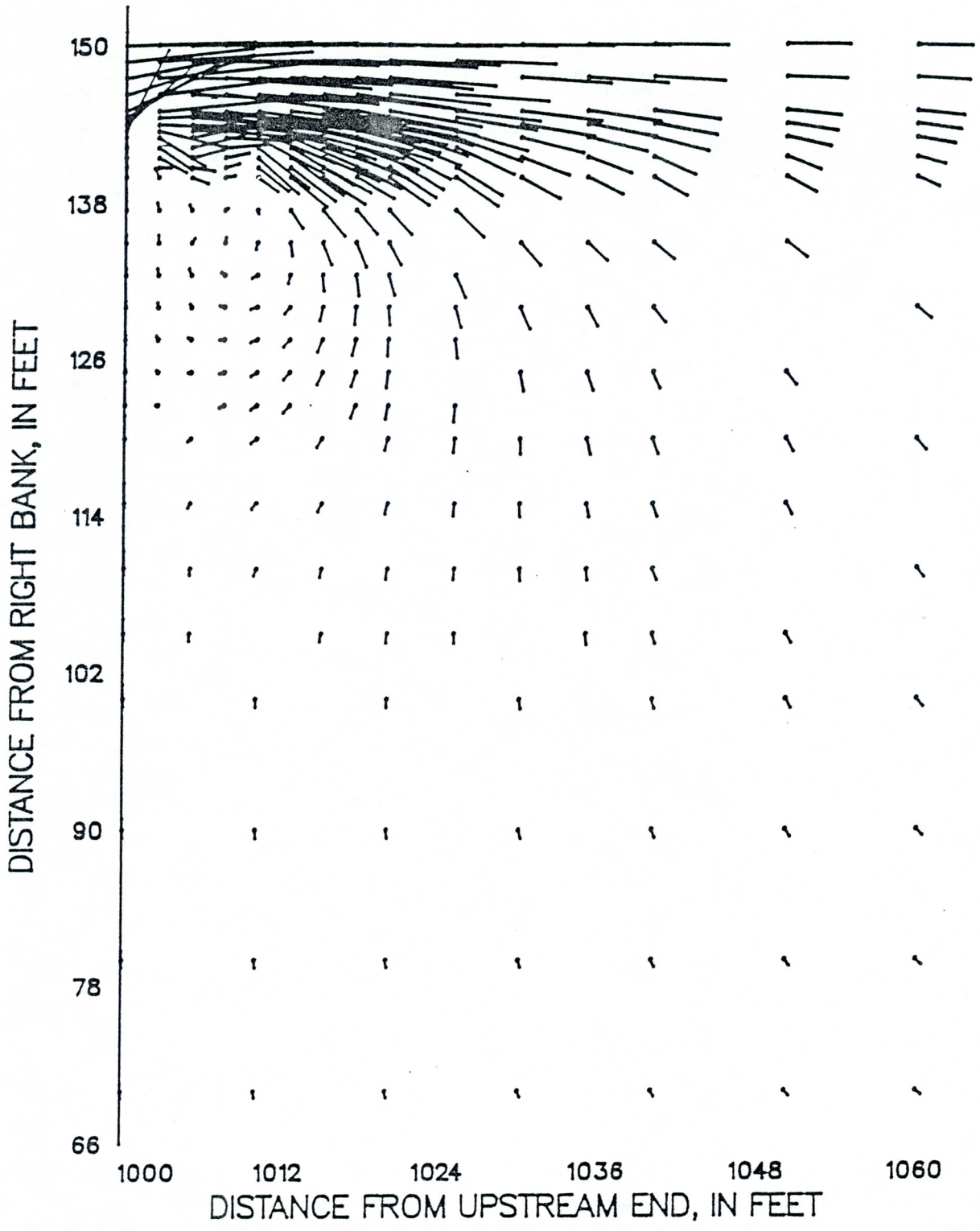

Figure 104. Partial velocity field for experiment S7410235, calibrated parameters, network 2. A vector 1 inch long represents a velocity of 4 feet per second.

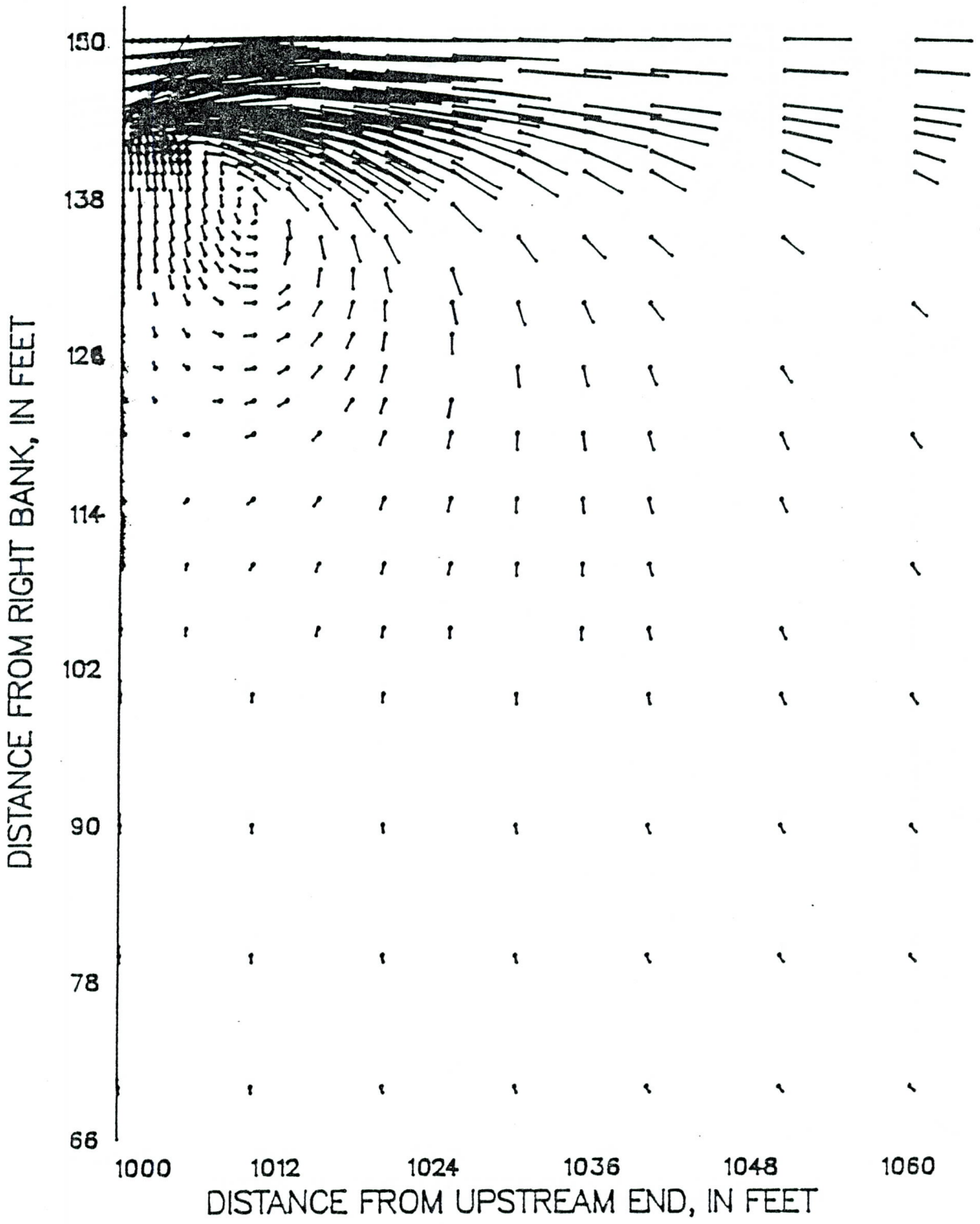

Figure 105. Partial velocity field for experiment S7410235, calibrated parameters, network 3. A vector 1 inch long represents a velocity of 4 feet per second.

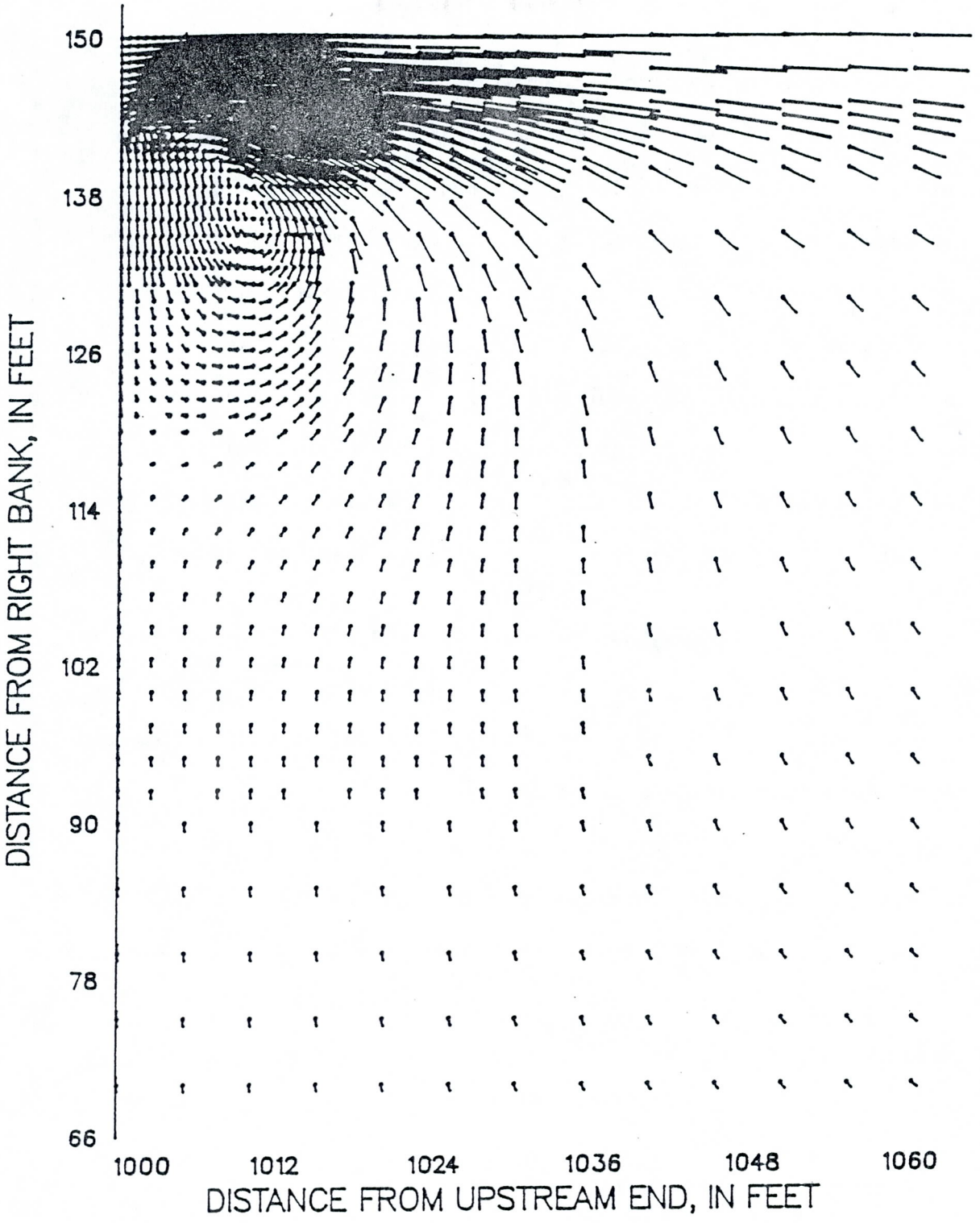

Figure 106. Partial velocity field for experiment S7410235, calibrated parameters, network 4. A vector 1 inch long represents a velocity of 4 feet per second.

The results presented above show that a sufficiently refined network is necessary to compute backwater accurately and to avoid oscillations in the velocity field. For all three discharges modeled, network 3 is sufficiently refined to support converged solutions to the flow equations. For the converged solutions, FLOMOD is able to simulate quite accurately most water-surface elevations throughout the study reach and most velocities upstream from the constriction. However, as discussed above, the jet downstream from the constriction dissipates too rapidly in the model, resulting in peak velocities in the low-water channel that are substantially lower than the corresponding observed values.

It was hypothesized that two major factors contributed to those discrepancies. First, the actual values of the momentum-correction coefficients are substantially larger than unity, the value used in the simulations discussed above. Using more realistic values might improve the results. Second, the values of Manning's n for the jet downstream from the constriction are probably smaller than those determined in the calibration process because the grass in the jet was flattened by the high velocities there. Reducing the values of n in the jet might increase the computed peak velocities there.

Additional simulations using network 3 were carried out to test these hypotheses. First, for each of the three experiments used above, a more realistic value of the momentum-correction coefficient, β, was determined. For each of the 140 vertical

velocity profiles collected during the 1975 experimental series, β was computed from equation 8. This was done by applying to the squares of the point velocities the numerical integration procedure used to integrate the velocity profiles (see p. 111). Because no vertical velocity profiles had been collected for the design discharge of 50 ft^3/s, β was regressed on the measured discharge to give a linear equation which was used to obtain values of β of 1.64, 1.59, and 1.48 for experiments S6210035, S6810105, and S7410235, respectively.

These values were then used in simulations of experiments S6210035, S6810105, and S7410235. In these simulations, all other parameters were the same as in the simulations presented above.

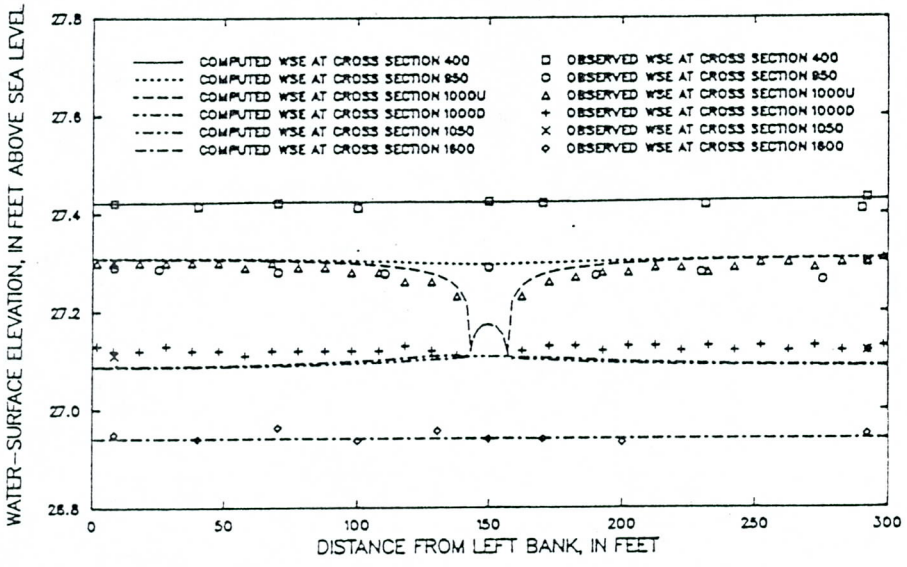

Figure 107. Observed and computed water-surface elevations (WSE) for experiment S6210035, β = 1.64, network 3. The letters U and D refer, respectively, to the upstream side and the downstream side of the constriction.

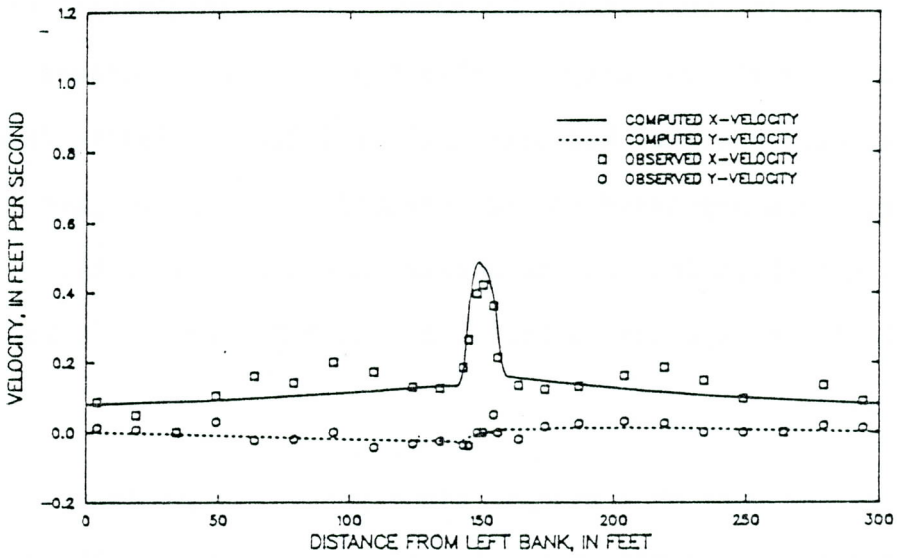

Figure 108. Observed and computed velocity components at cross section 900 for experiment S6210035, β = 1.64, network 3.

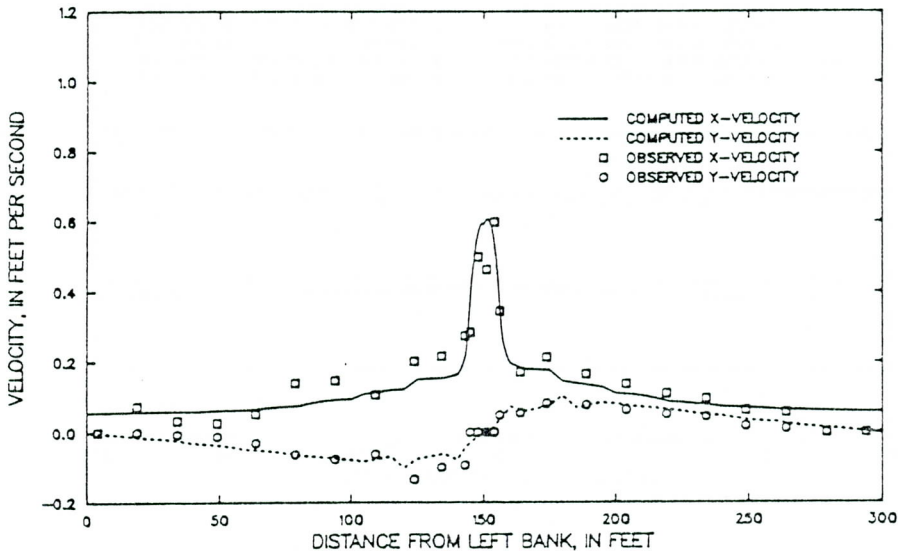

Figure 109. Observed and computed velocity components at cross section 950 for experiment S6210035, β = 1.64, network 3.

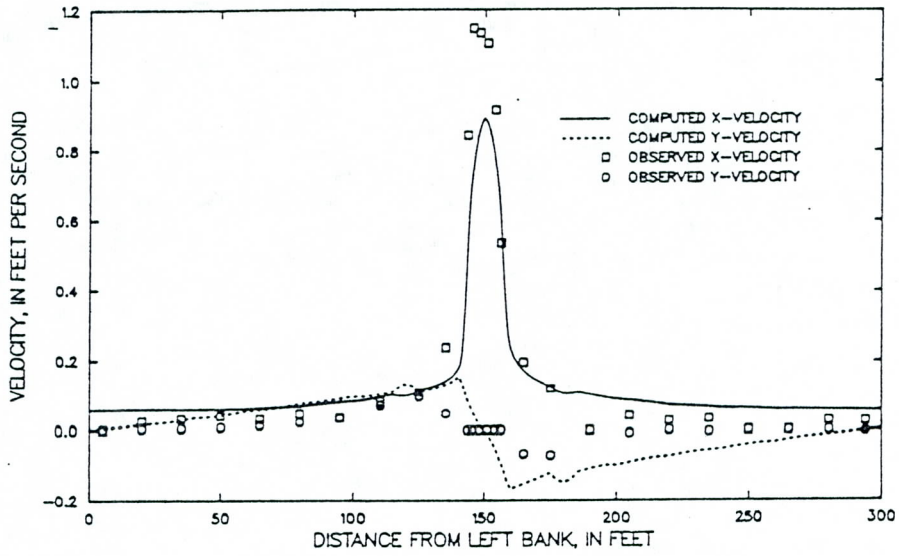

Figure 110. Observed and computed velocity components at cross section 1050 for experiment S6210035, β = 1.64, network 3.

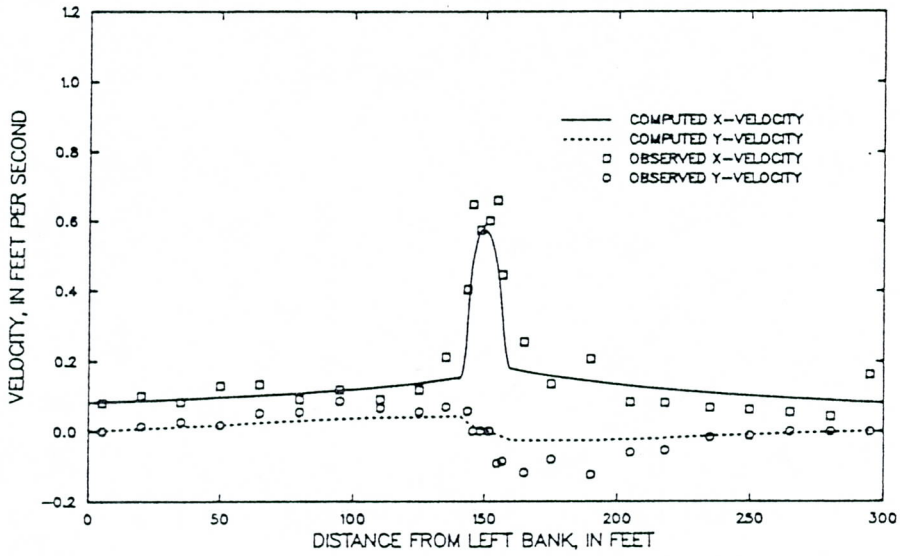

Figure 111. Observed and computed velocity components at cross section 1100 for experiment S6210035, β = 1.64, network 3.

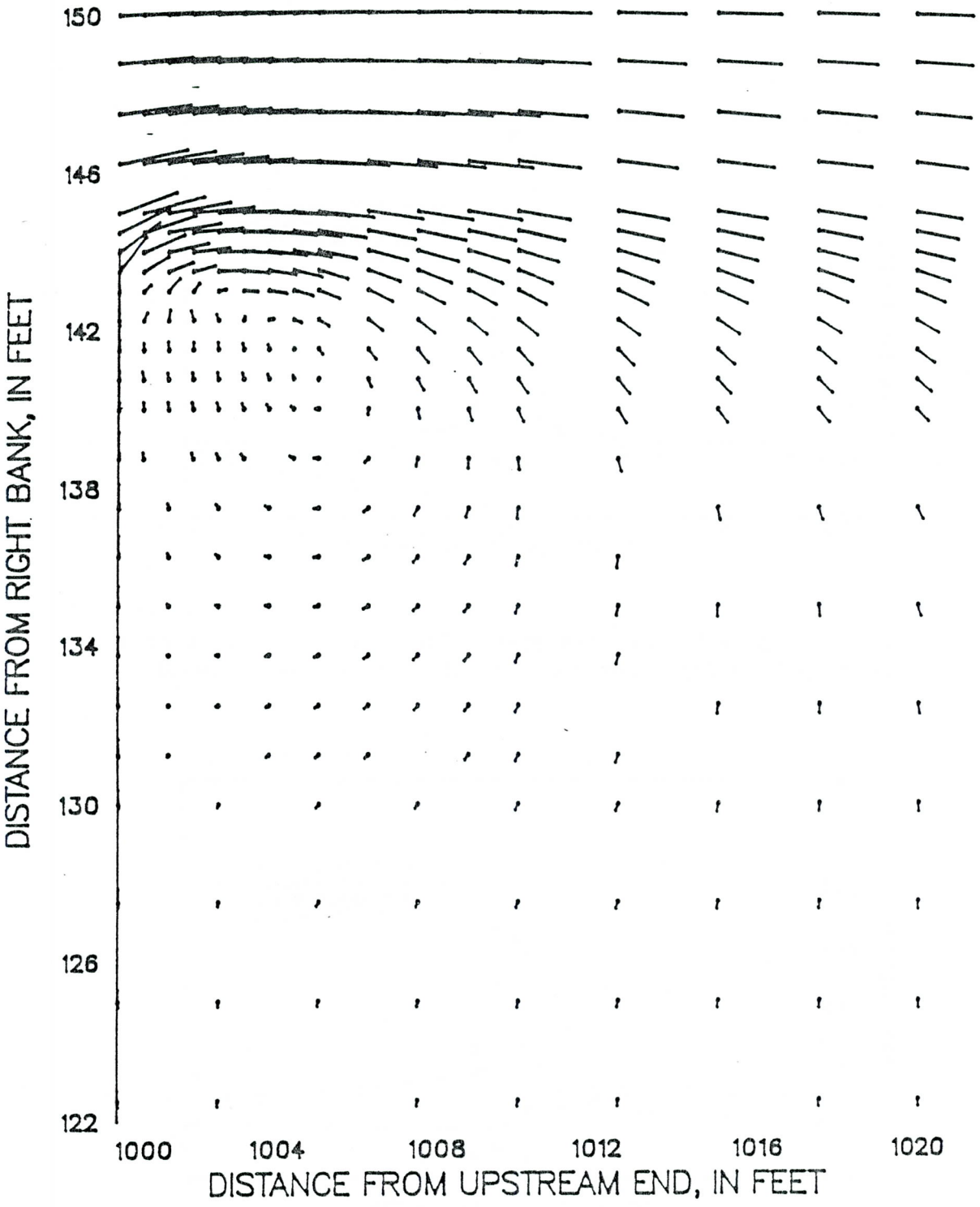

Figure 112. Partial velocity field for experiment S6210035, $\beta = 1.64$, network 3. A vector 1 inch long represents a velocity of 4 feet per second.

Using a value of β greater than unity does not affect the results of the calibration simulations because the convective terms vanish for uniform flows. Water-surface elevations, velocity profiles at cross sections 900, 950, 1050, and 1100, and a partial velocity field for S6210035 are shown in figures 107 through 112; for S6810105 in figures 113 through 118; and for S7410235 in figures 119 through 124.

All three simulations show similar changes. There are small decreases in peak velocities at cross sections 900 and 950 and relatively larger increases in peak velocities at cross sections 1050 and 1100. However, the peak velocities computed at cross sections 1050 and 1100 are still substantially less than the observed

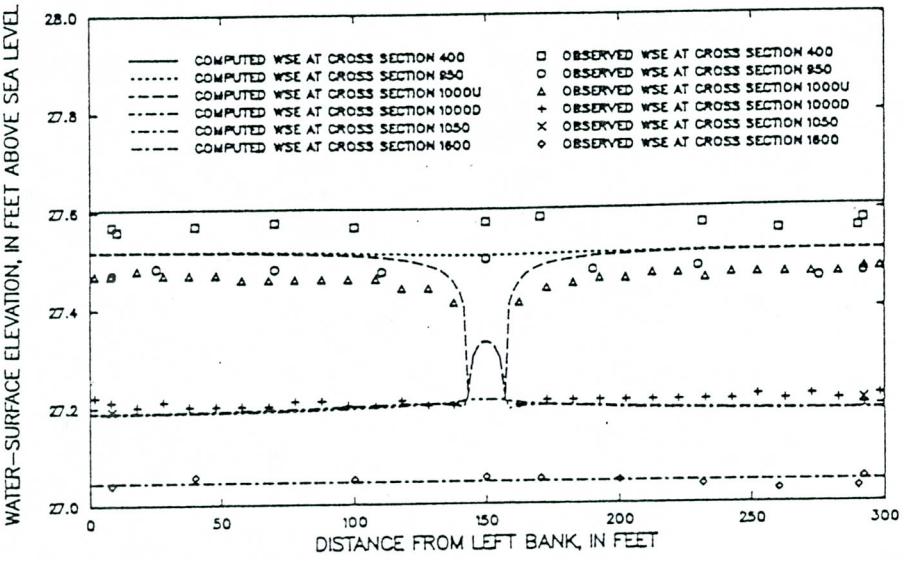

Figure 113. Observed and computed water-surface elevations (WSE) for experiment S6810105, β = 1.59, network 3. The letters U and D refer, respectively, to the upstream side and the downstream side of the constriction.

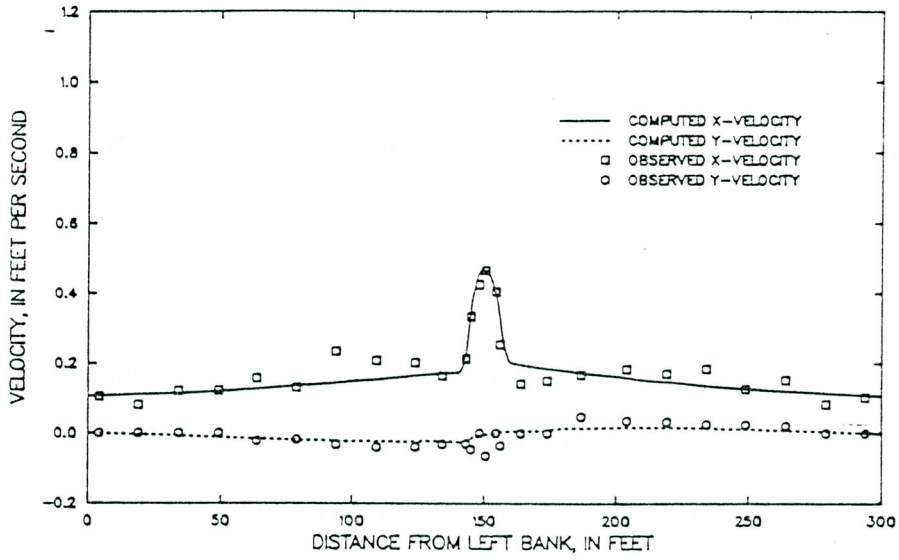

Figure 114. Observed and computed velocity components at cross section 900 for experiment S6810105, β = 1.59, network 3.

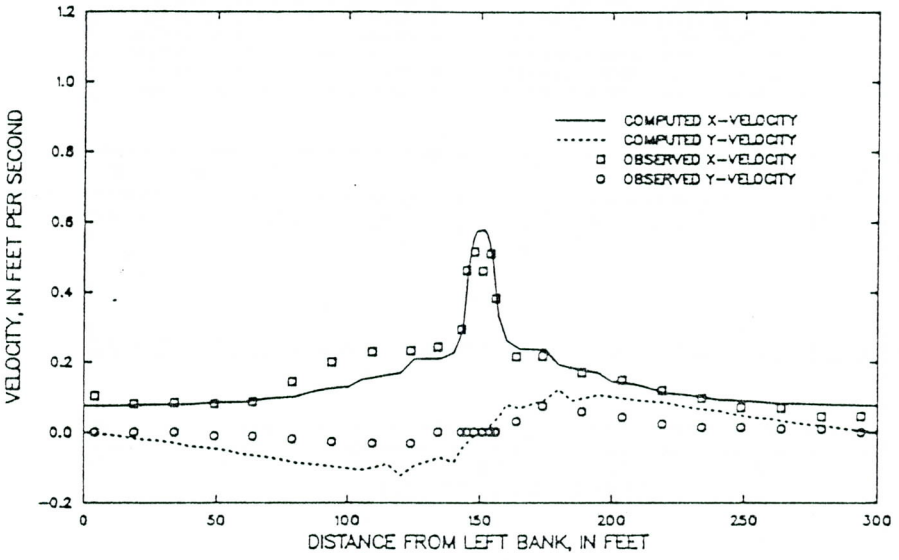

Figure 115. Observed and computed velocity components at cross section 950 for experiment S6810105, β = 1.59, network 3.

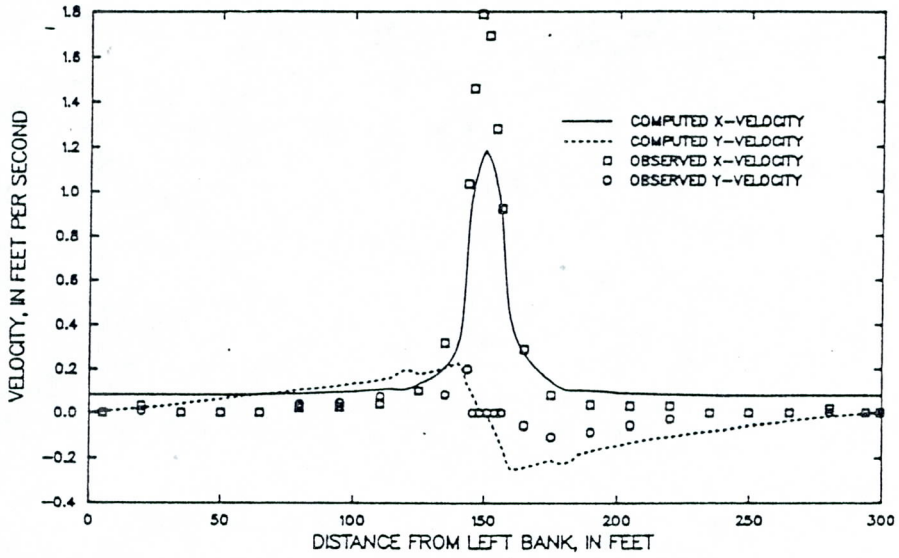

Figure 116. Observed and computed velocity components at cross section 1050 for experiment S6810105, β = 1.59, network 3.

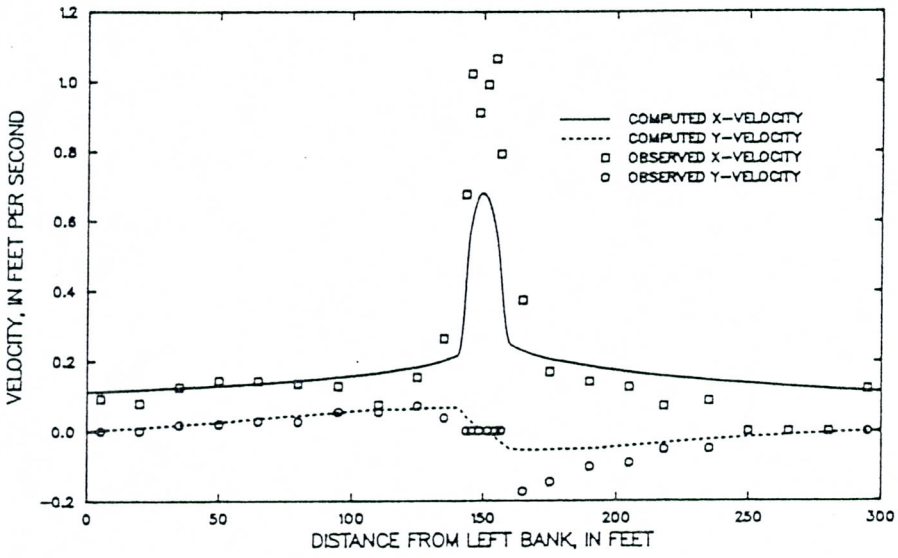

Figure 117. Observed and computed velocity components at cross section 1100 for experiment S6810105, β = 1.59, network 3.

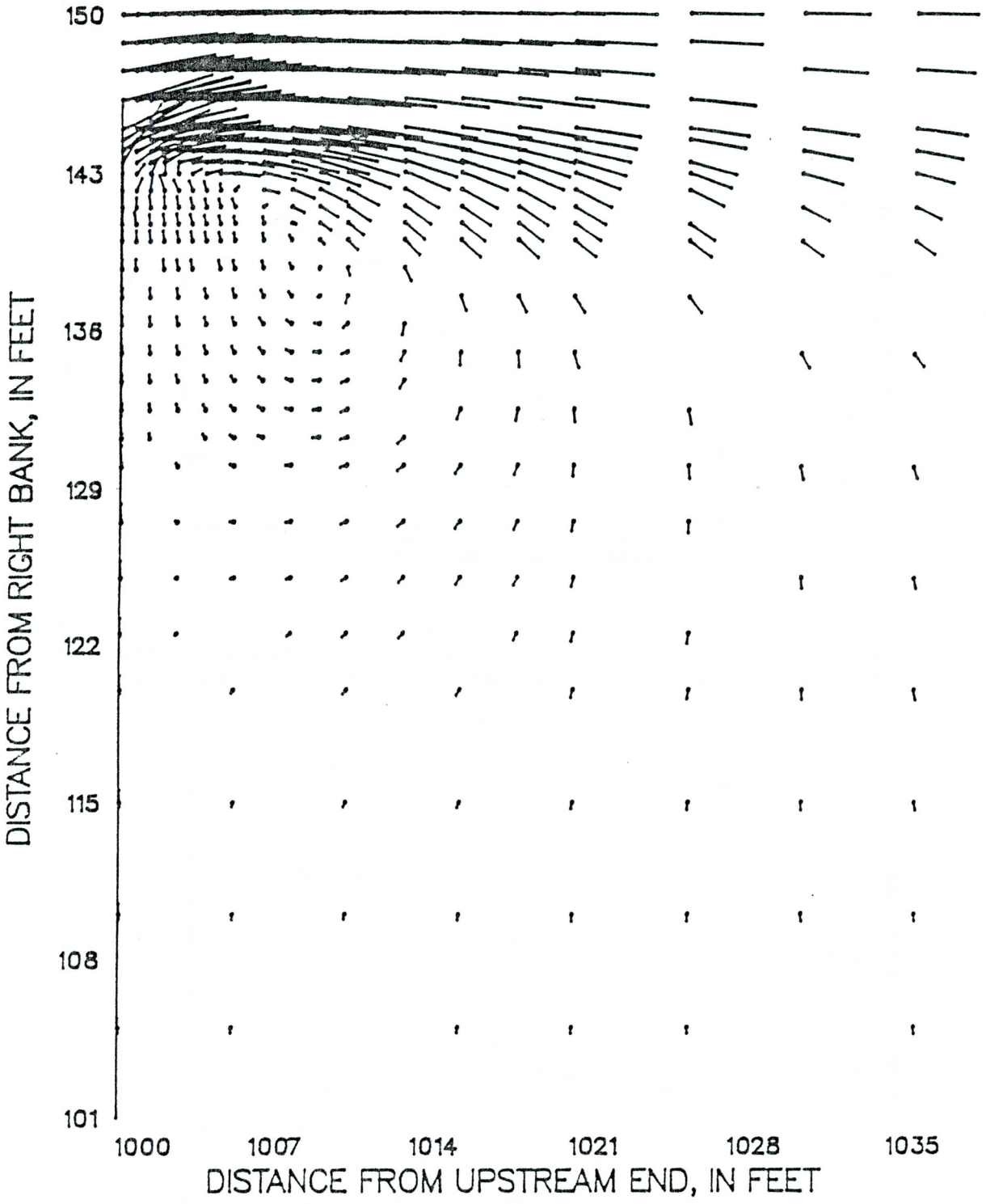

Figure 118. Partial velocity field for experiment S6810105, $\beta = 1.59$, network 3. A vector 1 inch long represents a velocity of 4 feet per second.

values there. Minor improvements are also evident in the velocity components in the y-direction at cross sections 1050 and 1100. The recirculation zones in all three simulations are larger than in the previous simulations. The stagnation point is located about 133 ft from the right bank for this simulation of experiment S6210035, about 124 ft from the right bank for experiment S6810105, and about 102 ft from the right bank for experiment S7410235. Thus, increasing the value of β has moved the stagnation point about 5 ft closer to the right bank for experiment S6210035, about 9 ft closer for experiment S6810105, and about 15 ft closer for experiment S7410235. While the velocity profiles show some improvement, the water-surface elevations are not simulated as

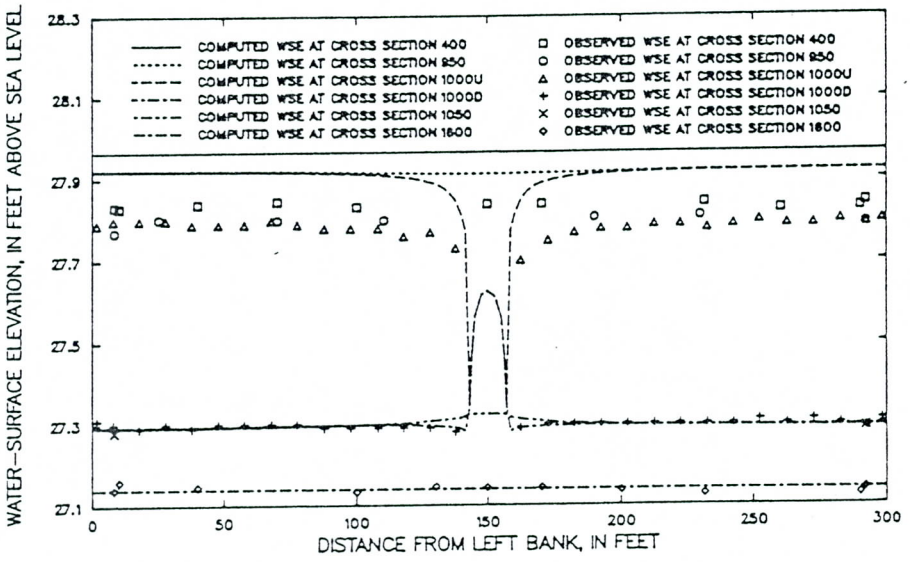

Figure 119. Observed and computed water-surface elevations (WSE) for experiment S7410235, β = 1.48, network 3. The letters U and D refer, respectively, to the upstream side and the downstream side of the constriction.

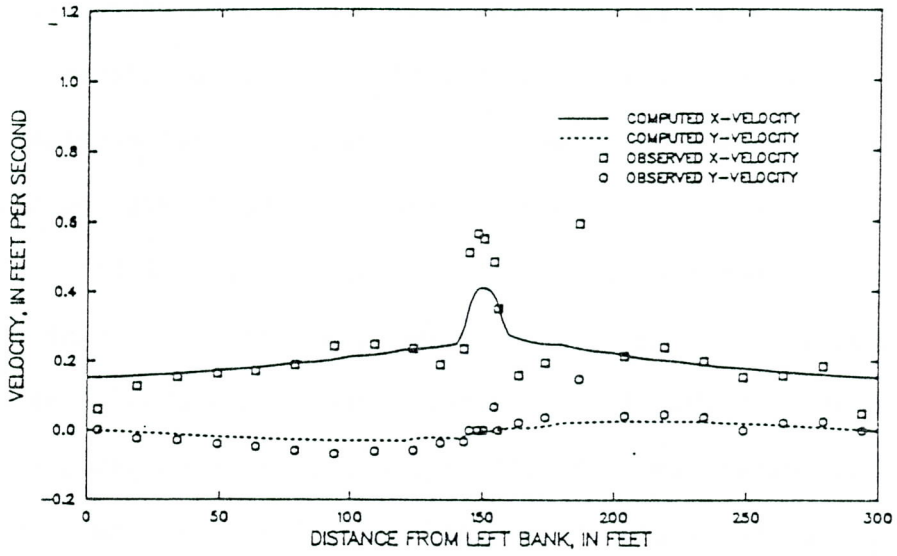

Figure 120. Observed and computed velocity components at cross section 900 for experiment S7410235, β = 1.48, network 3.

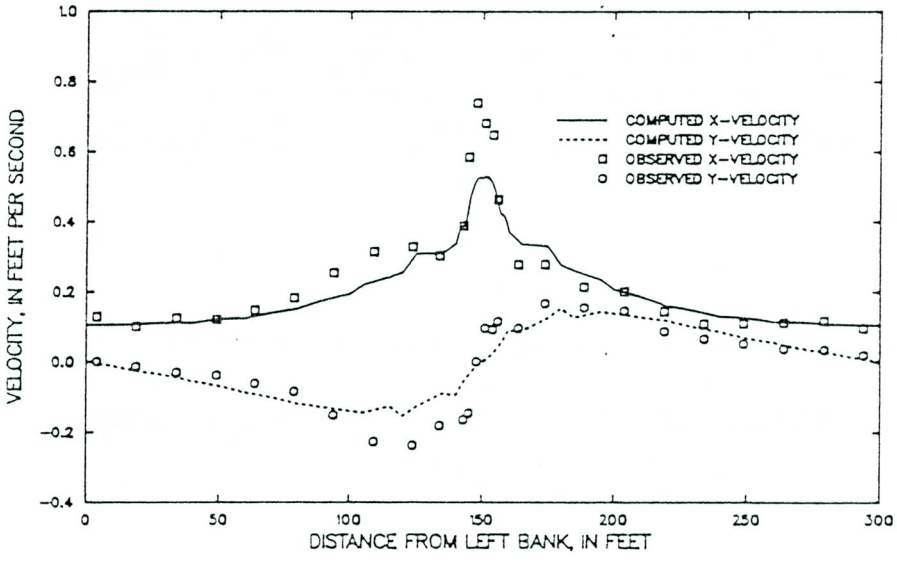

Figure 121. Observed and computed velocity components at cross section 950 for experiment S7410235, β = 1.48, network 3.

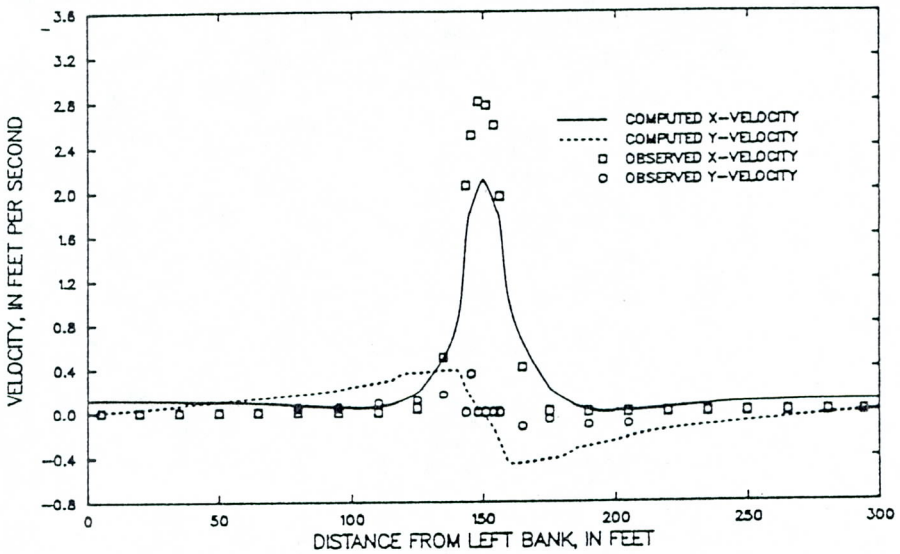

Figure 122. Observed and computed velocity components at cross section 1050 for experiment S7410235, β = 1.48, network 3.

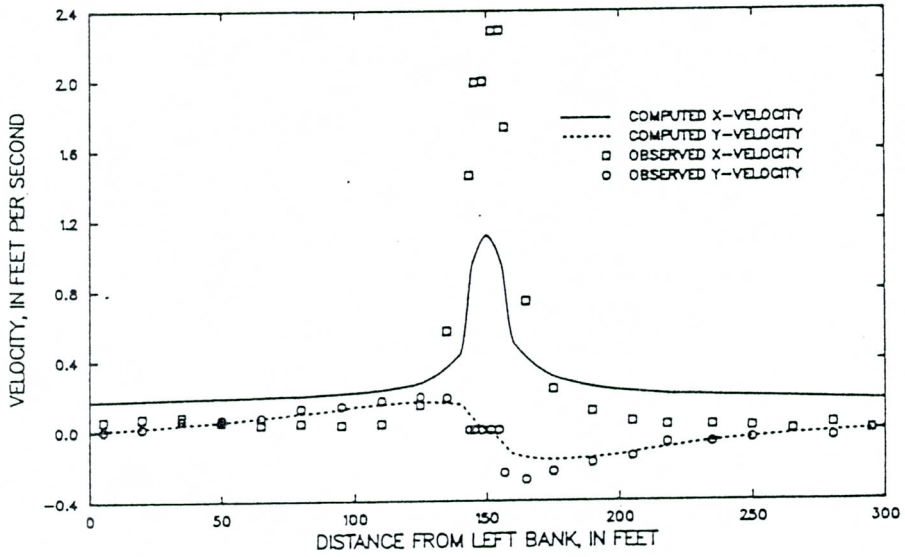

Figure 123. Observed and computed velocity components at cross section 1100 for experiment S7410235, β = 1.48, network 3.

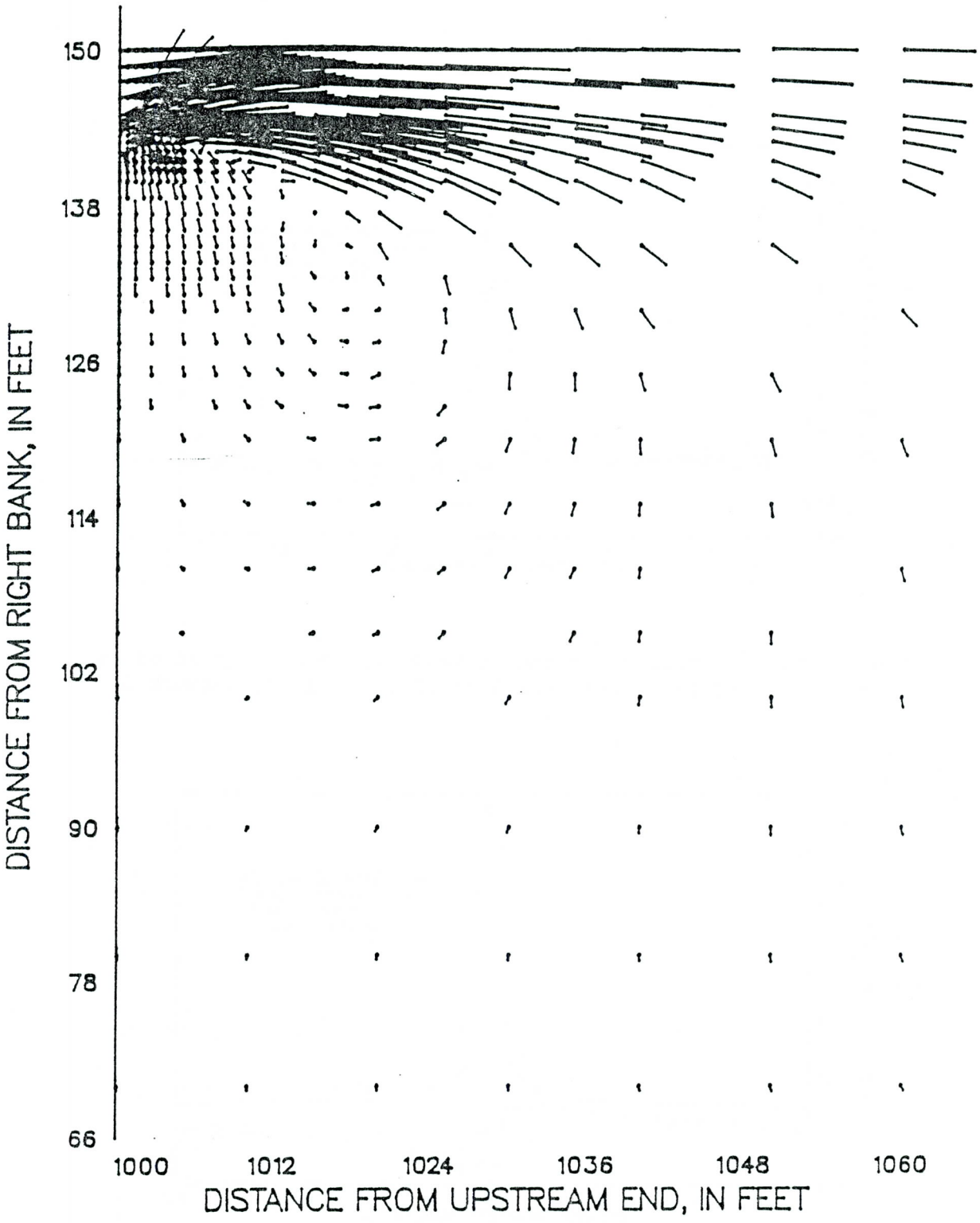

Figure 124. Partial velocity field for experiment S7410235, $\beta = 1.48$, network 3. A vector 1 inch long represents a velocity of 4 feet per second.

well. There is an overestimation of the fall through the opening in all three cases.

These simulations also show that increasing the value of the momentum-correction coefficient has a proportionately greater effect as discharge increases and consequently velocity and depth gradients increase. Thus, improvements in peak velocities and deterioration in water-surface elevations are proportionately greater in the simulation of experiment S7410235 than in the simulation of experiment S6210035.

Next, the effect of reducing the value of Manning's n where the velocities are large was investigated. The values of the momentum-correction coefficient used above were also used in these simulations. For each of the three experiments, an iterative process was performed in which the two values of Manning's n determined in calibration (table 4) were reduced by the same fraction for those elements on which computed velocities initially exceeded 1.0 ft/s. An inner iteration was performed until the computed and observed peak velocities at cross sections 900, 950, 1050, and 1100 were in good agreement. In addition, as velocities changed, an outer iteration was performed during which elements were included in or dropped from the group of elements for which the values of Manning's n were modified.

In all three cases, although Manning's n was reduced independently in each, a 31 percent reduction in the values of Manning's n where

velocities exceeded 1.0 ft/s was required to bring computed and observed peak velocities into agreement. At the end of the iterative process, computed velocities in all three cases exceeded 1.0 ft/s only in the low-water channel. For experiment S6210035, these elements were located between cross sections 985 and 1060; for S6810105, between 982.5 and 1100; and for S7410235, between 982.5 and 1200.

Water-surface elevations; velocity profiles at cross sections 900, 950, 1050, and 1100; and a partial velocity field for S6210035 are shown in figures 125 through 130; for S6810105 in figures 131 through 136; and for S7410235 in figures 137 through 142.

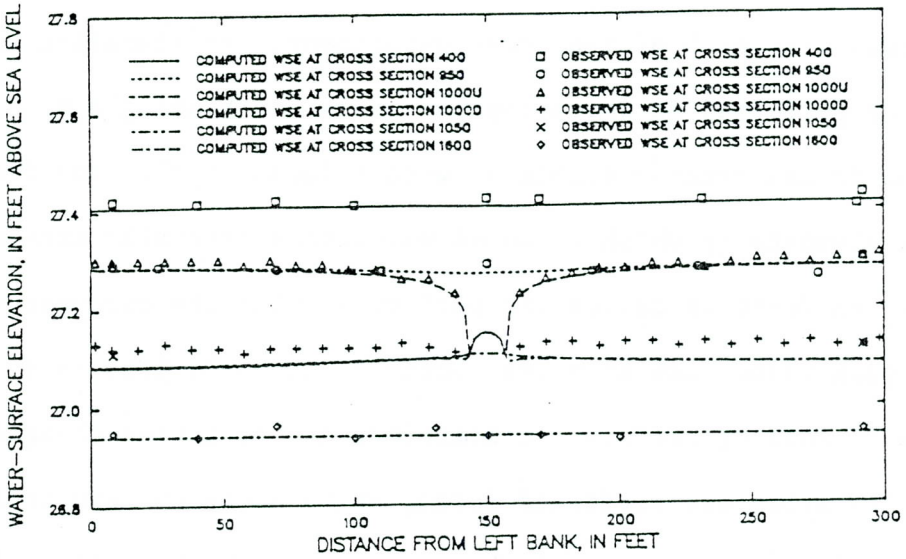

Figure 125. Observed and computed water-surface elevations (WSE) for experiment S6210035, β = 1.64, Manning's n reduced where velocities exceed 1 foot per second, network 3. The letters U and D refer, respectively, to the upstream side and the downstream side of the constriction.

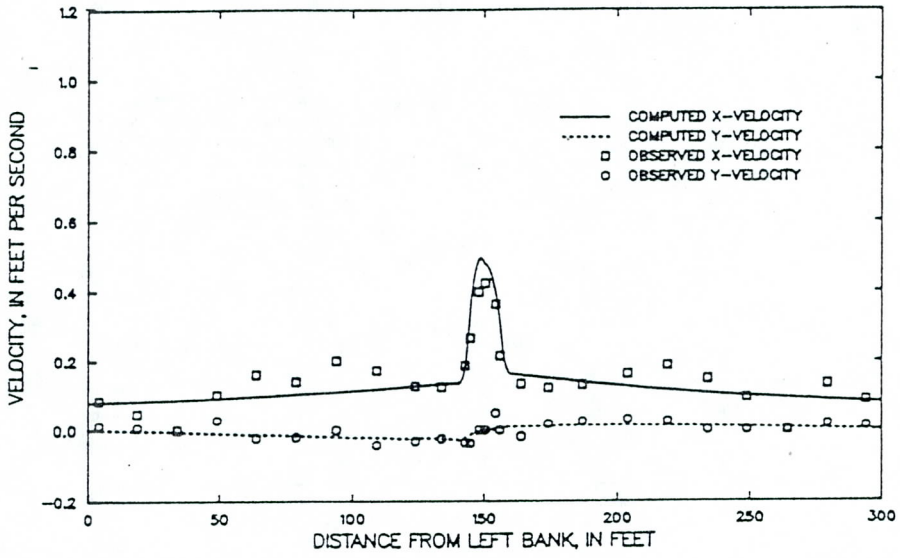

Figure 126. Observed and computed velocity components at cross section 900 for experiment S6210035, β = 1.64, Manning's n reduced where velocities exceed 1 foot per second, network 3.

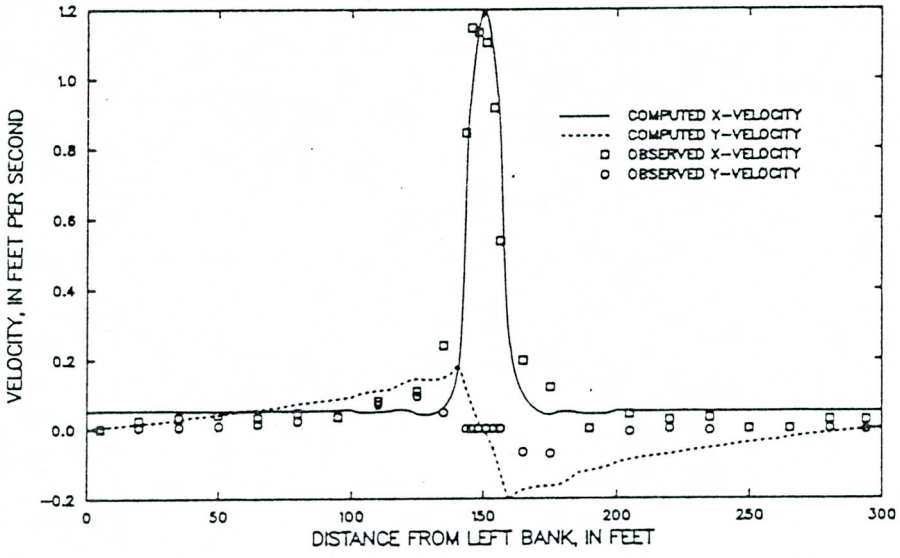

Figure 127. Observed and computed velocity components at cross section 950 for experiment S6210035, β = 1.64, Manning's n reduced where velocities exceed 1 foot per second, network 3.

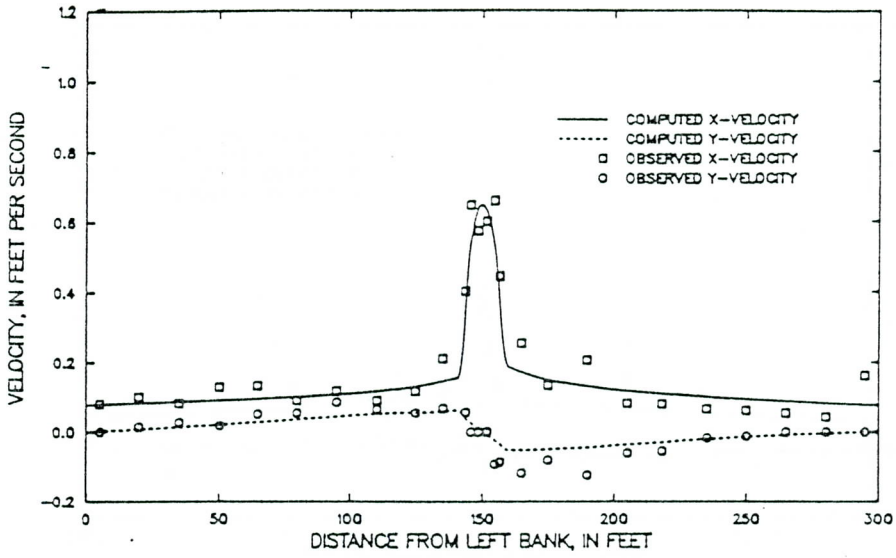

Figure 128. Observed and computed velocity components at cross section 1050 for experiment S6210035, β = 1.64, Manning's n reduced where velocities exceed 1 foot per second, network 3.

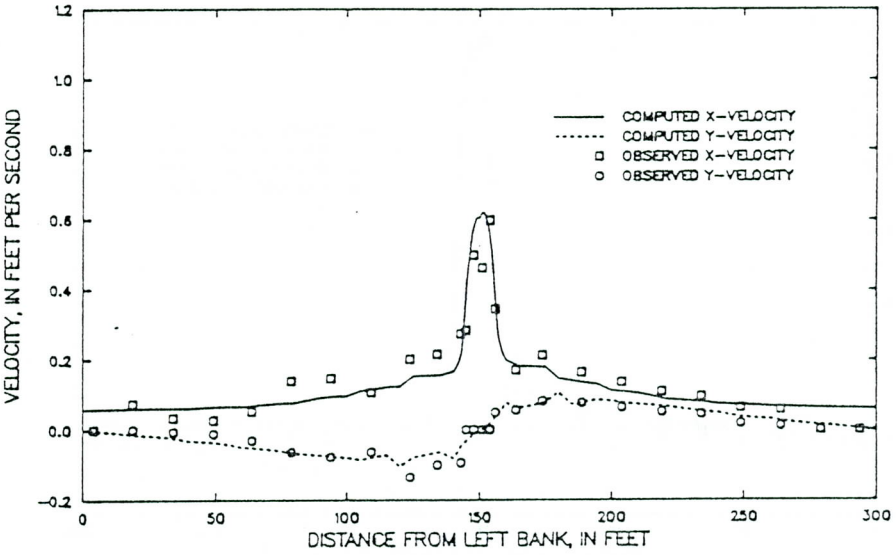

Figure 129. Observed and computed velocity components at cross section 1100 for experiment S6210035, β = 1.64, Manning's n reduced where velocities exceed 1 foot per second, network 3.

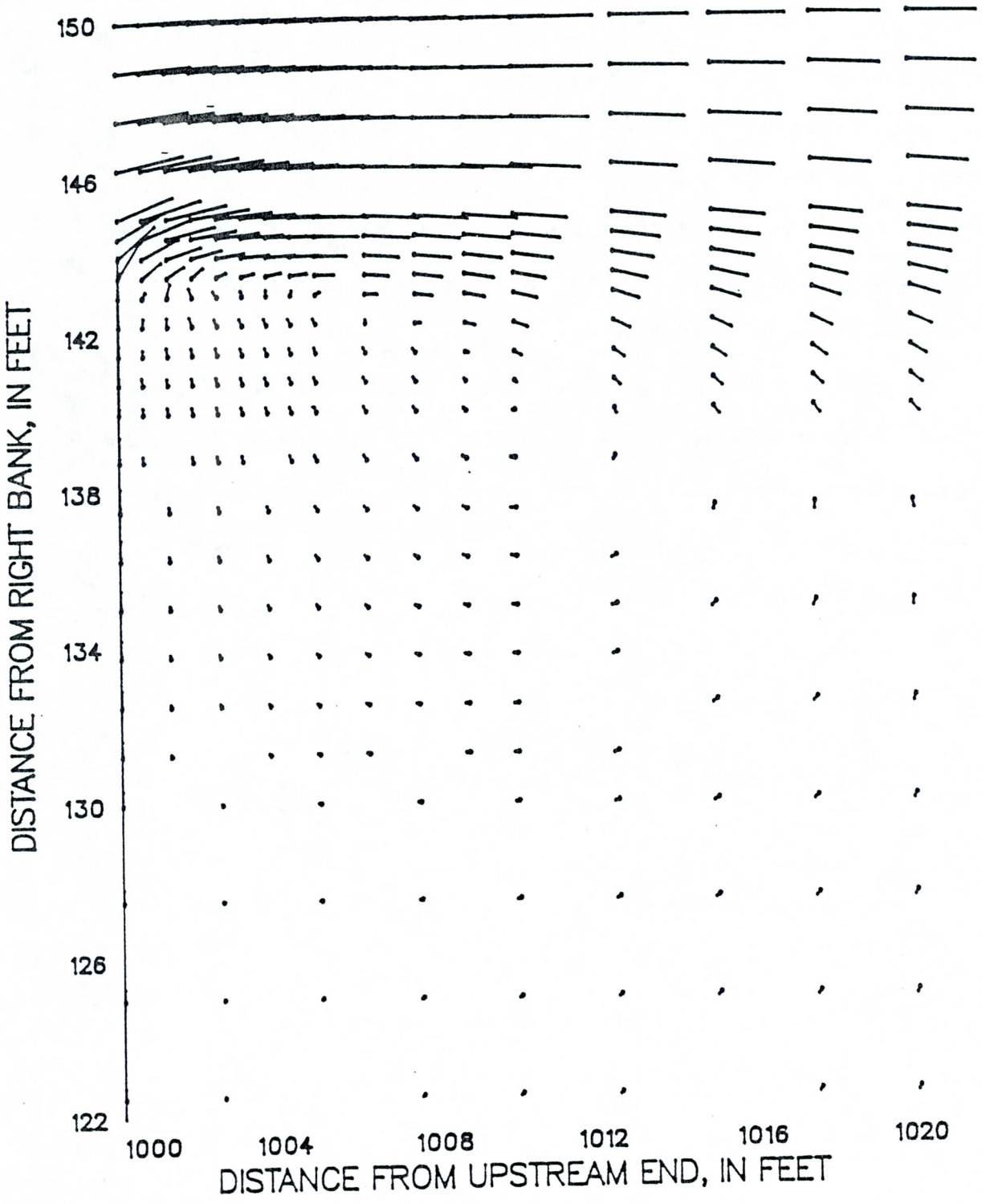

Figure 130. Partial velocity field for experiment S6210035, $\beta = 1.64$, Manning's n reduced where velocities exceed 1 foot per second, network 3. A vector 1 inch long represents a velocity of 4 feet per second.

In all three cases, the computed peak velocities at cross sections 1050 and 1100 are much larger than before and close to the observed values. The peak velocities computed at cross sections 900 and 950 are about the same as in the simulations with the realistic values of the the momentum-correction coefficient. The magnitudes of the computed velocity component in the y-direction are much closer to the observed values at cross section 1100 and, for experiment S7410235, at cross section 1050. For experiments S6210035 and S6810105, the magnitudes of the velocity component in the y-direction are still larger than the observed values at cross section 1050. In all three cases, the recirculation zones are much larger than in both the initial simulations and the simulations

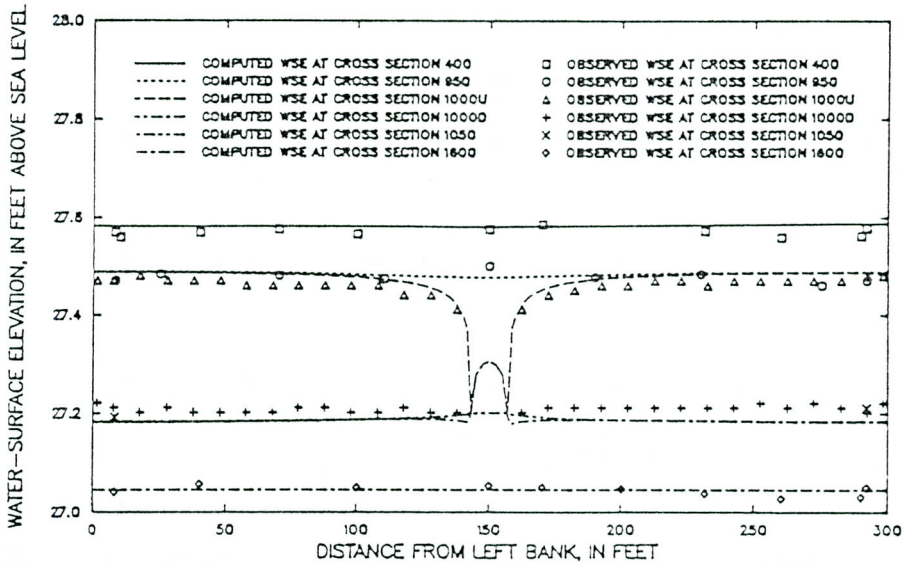

Figure 131. Observed and computed water-surface elevations (WSE) for experiment S6810105, β = 1.59, Manning's n reduced where velocities exceed 1 foot per second, network 3. The letters U and D refer, respectively, to the upstream side and the downstream side of the constriction.

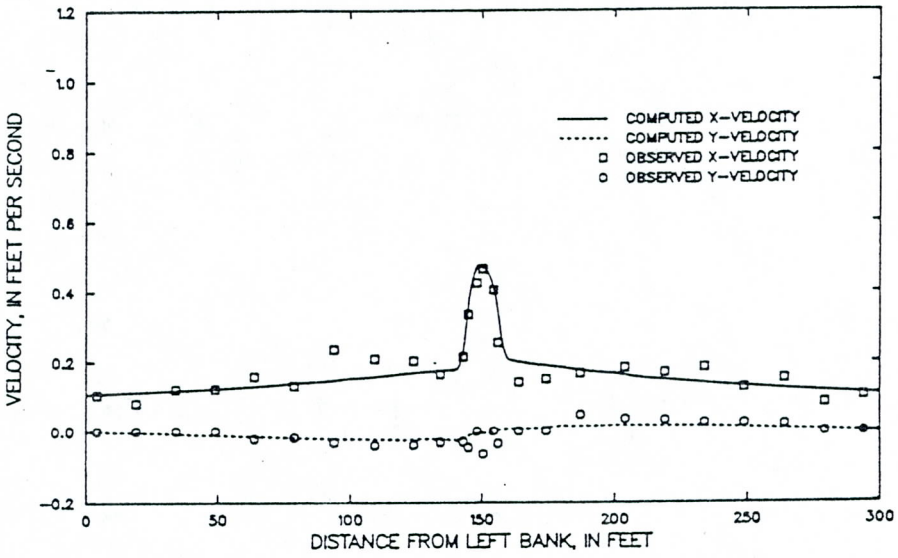

Figure 132. Observed and computed velocity components at cross section 900 for experiment S6810105, β = 1.59, Manning's n reduced where velocities exceed 1 foot per second, network 3.

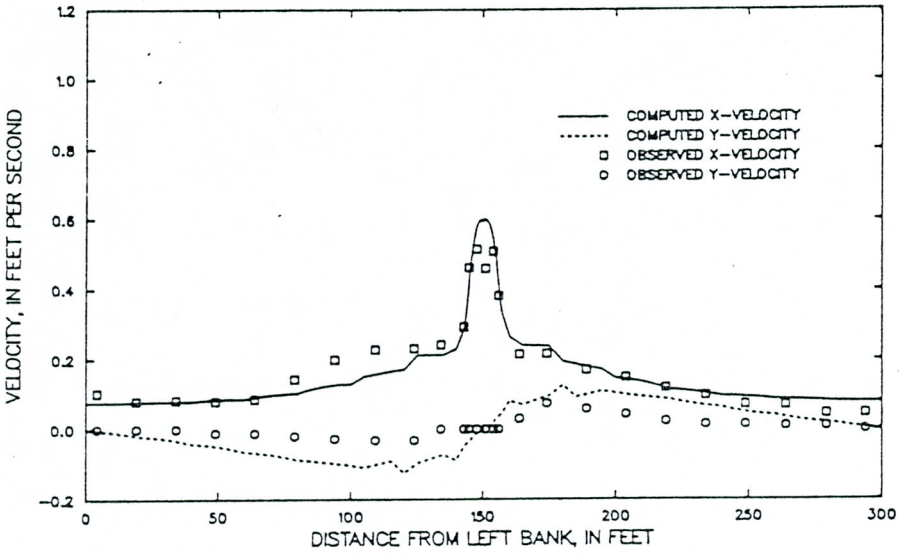

Figure 133. Observed and computed velocity components at cross section 950 for experiment S6810105, β = 1.59, Manning's n reduced where velocities exceed 1 foot per second, network 3.

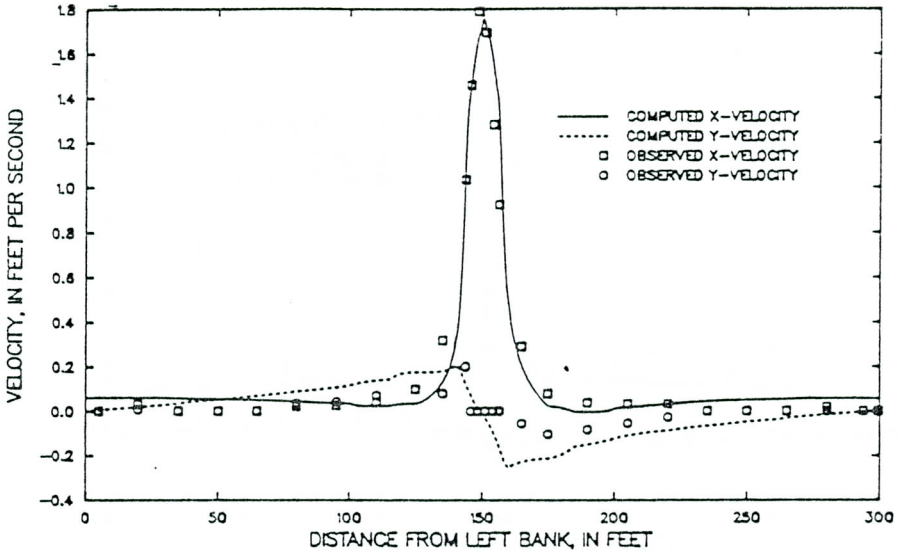

Figure 134. Observed and computed velocity components at cross section 1050 for experiment S6810105, β = 1.59, Manning's n reduced where velocities exceed 1 foot per second, network 3.

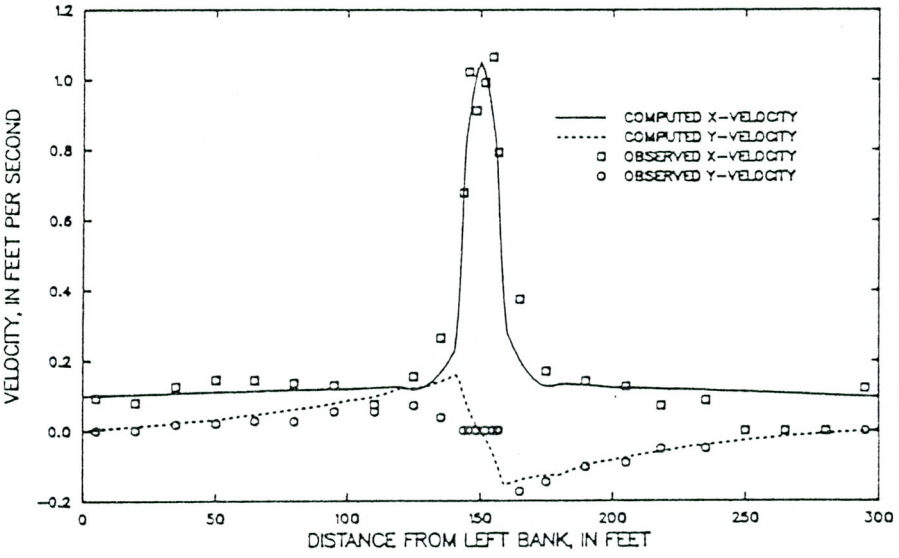

Figure 135. Observed and computed velocity components at cross section 1100 for experiment S6810105, β = 1.59, Manning's n reduced where velocities exceed 1 foot per second, network 3.

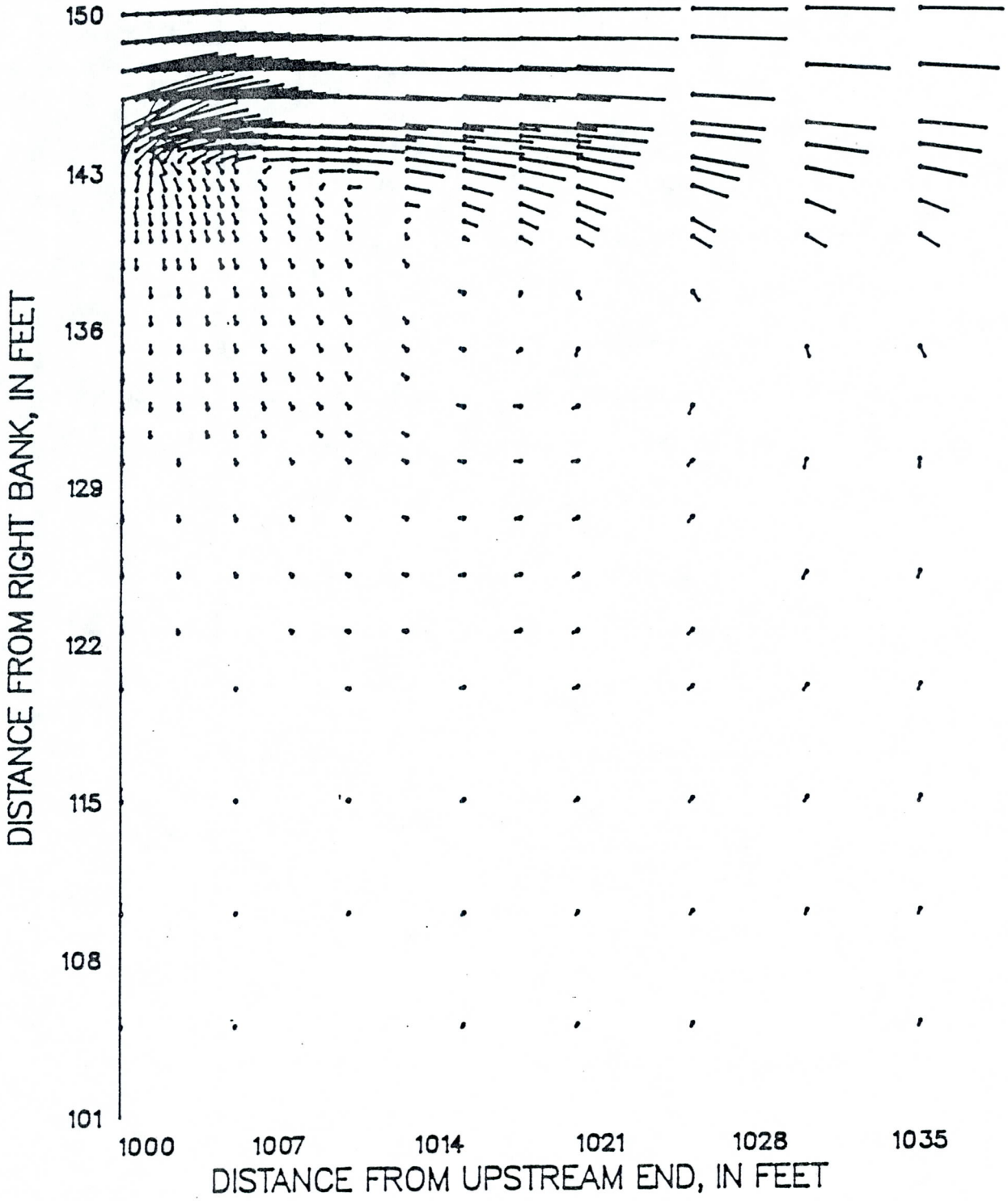

Figure 136. Partial velocity field for experiment S6810105, β = 1.59, Manning's n reduced where velocities exceed 1 foot per second, network 3. A vector 1 inch long represents a velocity of 4 feet per second.

with the larger values of the momentum-correction coefficients. The stagnation point is located about 126 ft from the right bank for this simulation of experiment S6210035, about 112 ft from the right bank for experiment S6810105, and about 75 ft from the right bank for experiment S7410235. Thus, compared with the calibration simulations, using more realistic values of β and reducing Manning's n where velocities exceeded 1.0 ft/s has moved the stagnation point about 12 ft closer to the right bank for experiment S6210035, about 21 ft closer to the right bank for experiment S6810105, and about 42 ft closer to the right bank for experiment S7410235.

Part of the increase in water-surface elevations upstream from the constriction due to increasing the values of the momentum-

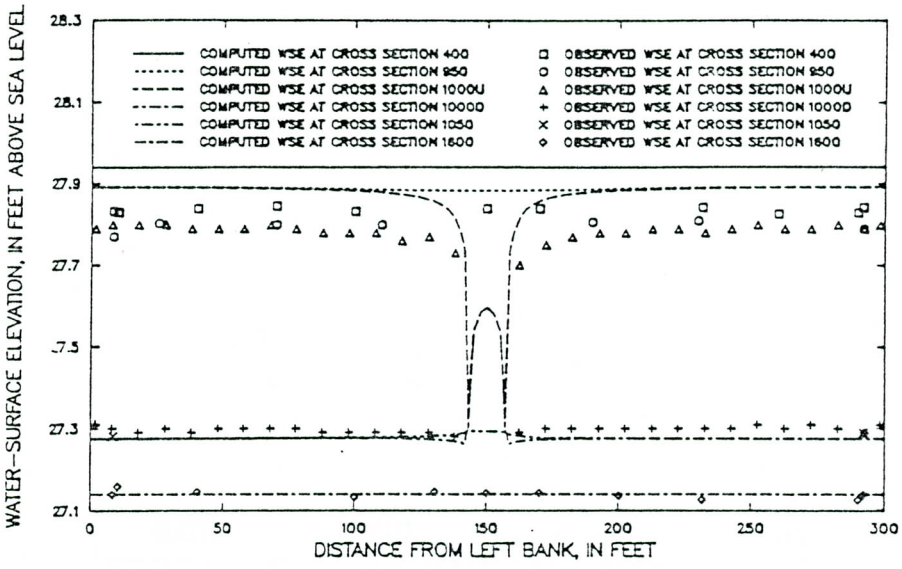

Figure 137. Observed and computed water-surface elevations (WSE) for experiment S7410235, β = 1.48, Manning's n reduced where velocities exceed 1 foot per second, network 3. The letters U and D refer, respectively, to the upstream side and the downstream side of the constriction.

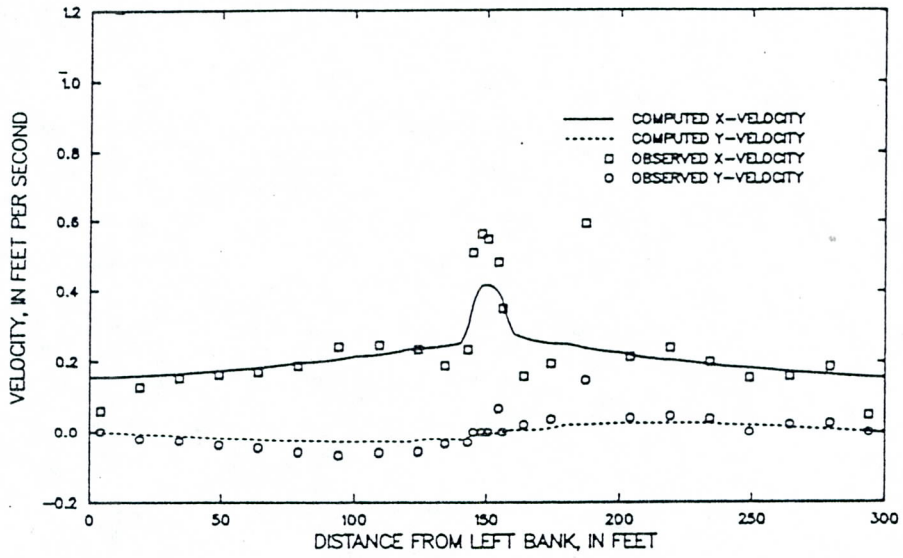

Figure 138. Observed and computed velocity components at cross section 900 for experiment S7410235, β = 1.48, Manning's n reduced where velocities exceed 1 foot per second, network 3.

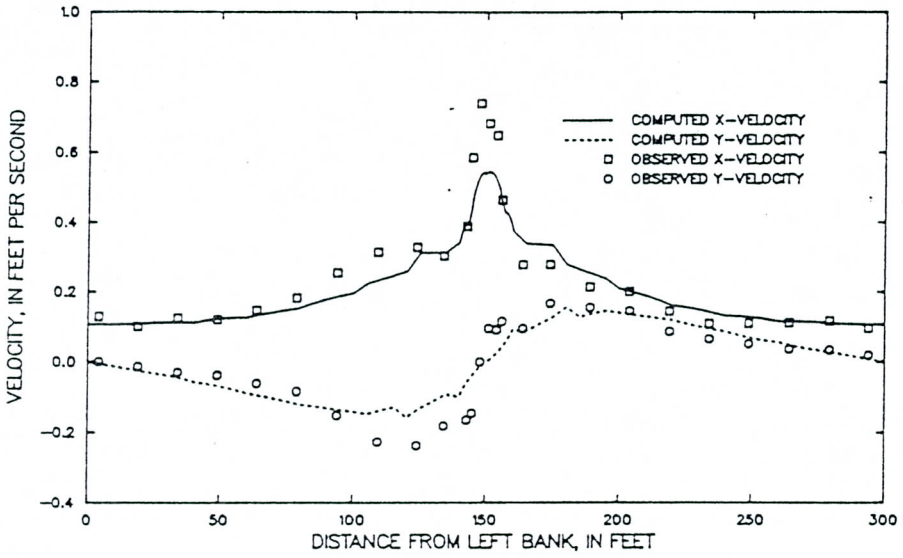

Figure 139. Observed and computed velocity components at cross section 950 for experiment S7410235, β = 1.48, Manning's n reduced where velocities exceed 1 foot per second, network 3.

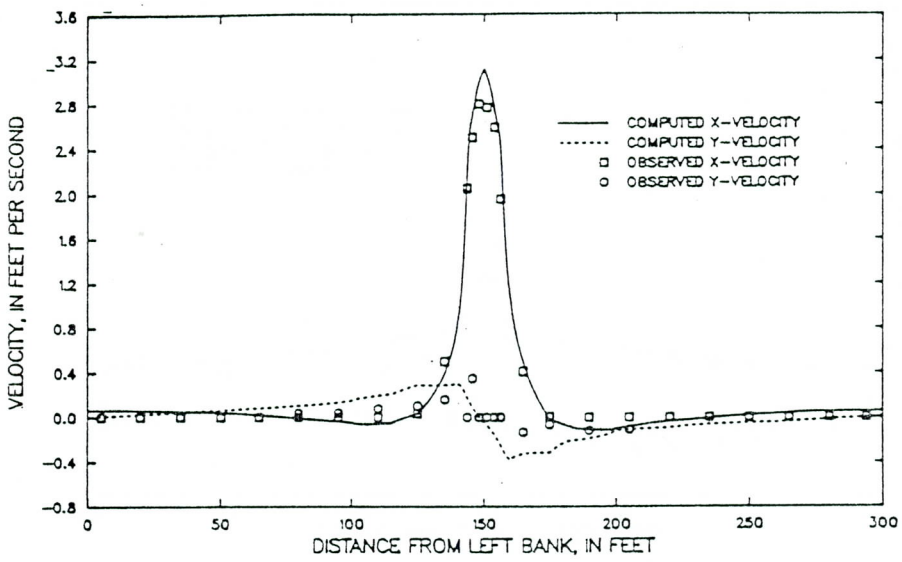

Figure 140. Observed and computed velocity components at cross section 1050 for experiment S7410235, β = 1.48, Manning's n reduced where velocities exceed 1 foot per second, network 3.

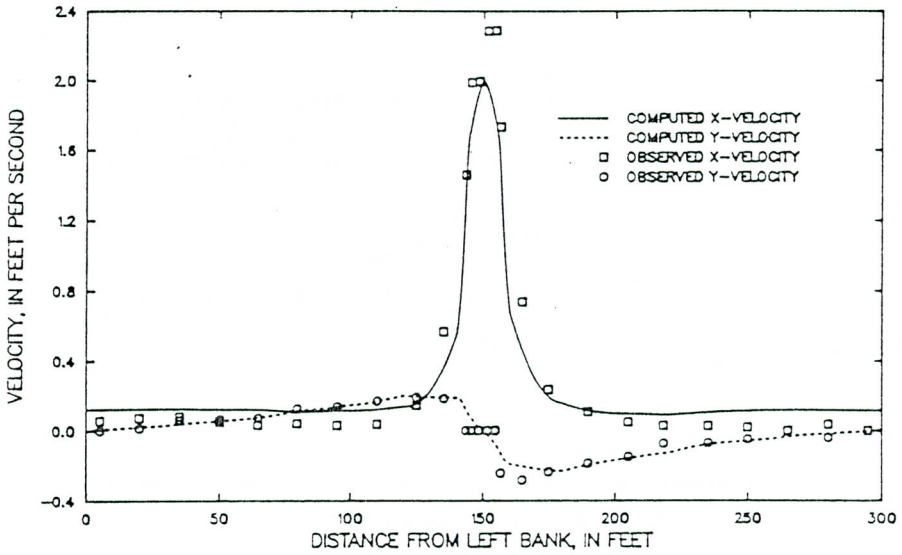

Figure 141. Observed and computed velocity components at cross section 1100 for experiment S7410235, β = 1.48, Manning's n reduced where velocities exceed 1 foot per second, network 3.

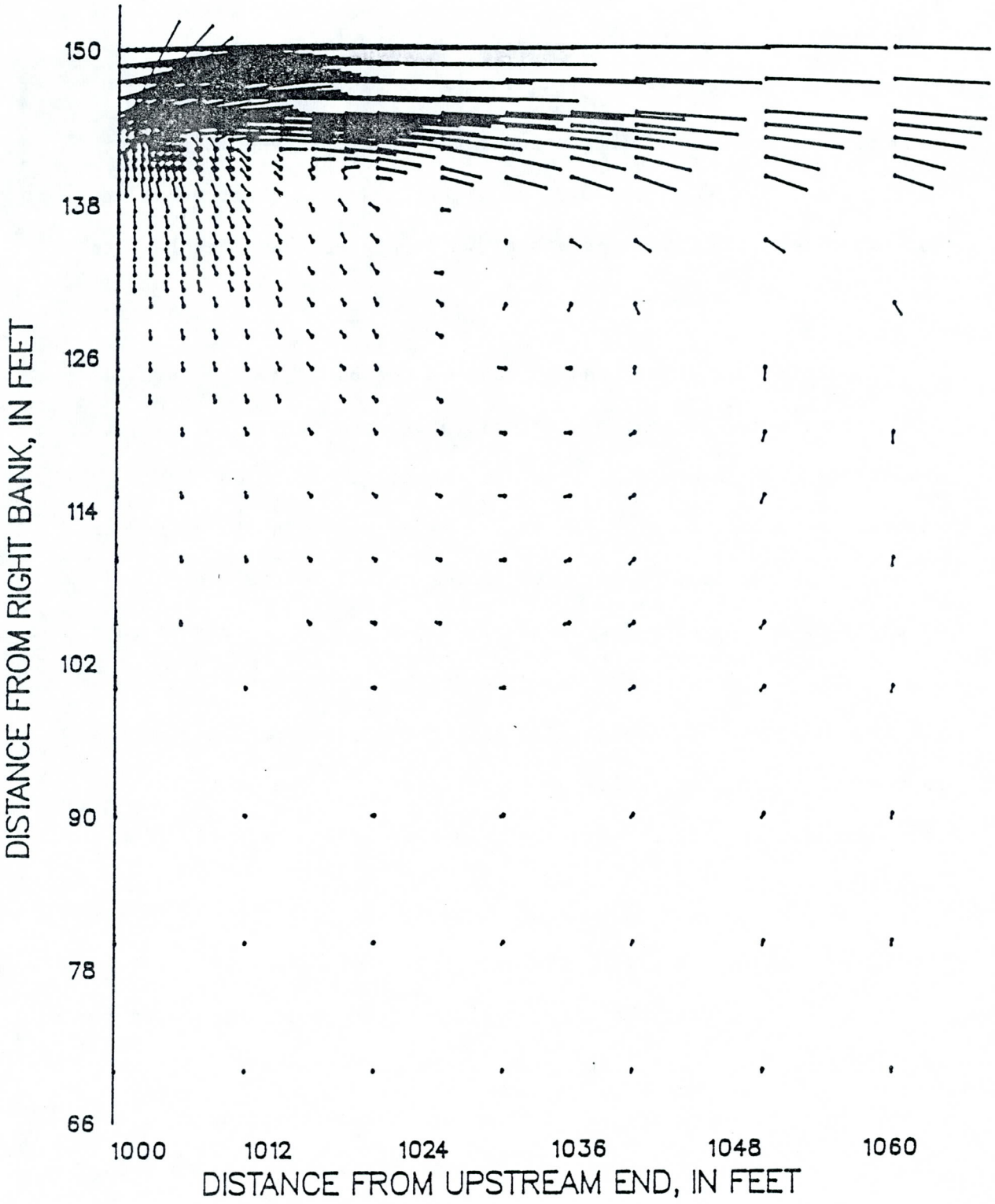

Figure 142. Partial velocity field for experiment S7410235, β = 1.48, Manning's n reduced where velocities exceed 1 foot per second, network 3. A vector 1 inch long represents a velocity of 4 feet per second.

correction coefficient is eliminated in these three simulations. The computed water-surface elevations just upstream from the constriction are about 0.01 ft lower than the observed values for experiment S6210035, about 0.02 ft higher than the observed values for experiment S6810105, and about 0.1 ft higher than the observed values for experiment S7410235.

Several observations can be made on the basis of the results presented above. Decreasing the values of Manning's n in the jet downstream from the constriction has a greater effect on peak velocities than it does on backwater. A decrease in the values of n is partially offset by velocity increases, so losses due to bed friction at the opening decrease only slowly as the values of Manning's n are lowered. On the other hand, when the convective terms are significant near the opening, increasing the value of the momentum-correction coefficient raises peak velocities in the jet without any compensating reduction in the values of n, and backwater increases significantly.

The remaining errors in the calculation of backwater may be due to the likelihood that the single values of the momentum-correction coefficients used in simulating the three experiments may not be correct near the opening. In particular, the overestimation of water-surface elevations just upstream from the constriction for experiment S7412035 (fig. 137) may be due to the fact that the value of the momentum-correction coefficient is based on vertical velocity profiles collected throughout the FPSF. The only place

the momentum-correction coefficient is significant is near the opening, where the convective terms are important. The higher velocities there, which flatten the grass and probably result in smaller values of Manning's n, probably also result in smaller values of the momentum-correction coefficient than the values that are representative of the entire FPSF. Errors in the values of the momentum-correction coefficient would tend to have a proportionately greater effect for the larger discharge of experiment S7410235 than for the smaller discharges of experiments S6210035 and S6810105.

Sensitivity Analyses

A sensitivity analysis was performed for the flow model of experiment S7410235 using network 3. Starting with the base simulation in which the value of the momentum-correction coefficient was unity and the values of Manning's n were those determined in calibration (table 4), the effects of increasing one at a time the values of the kinematic eddy viscosity, Manning's n, and the discharge were determined. These results are not illustrated.

First, the value of the kinematic eddy viscosity was increased from 0.6U*H to 0.66U*H. The results were virtually identical to those with an eddy viscosity value of 0.6U*H.

In the next simulation, the values of Manning's n were increased 10 percent. Compared with the base simulation, water-surface elevations were increased both upstream and downstream from the

constriction. At cross section 400, water-surface elevations rose about 0.04 ft, but the fall through the opening at cross section 1000 increased only about 0.01 ft. Velocities in the low-water channel were reduced slightly both upstream and downstream from the constriction.

Next, the value of the discharge was increased 10 percent. Water-surface elevations rose both upstream and downstream from the constriction. Water-surface elevations at cross section 400 rose about 0.09 ft, and the fall through the opening at cross section increased about 0.08 ft. Velocities increased slightly at all cross sections.

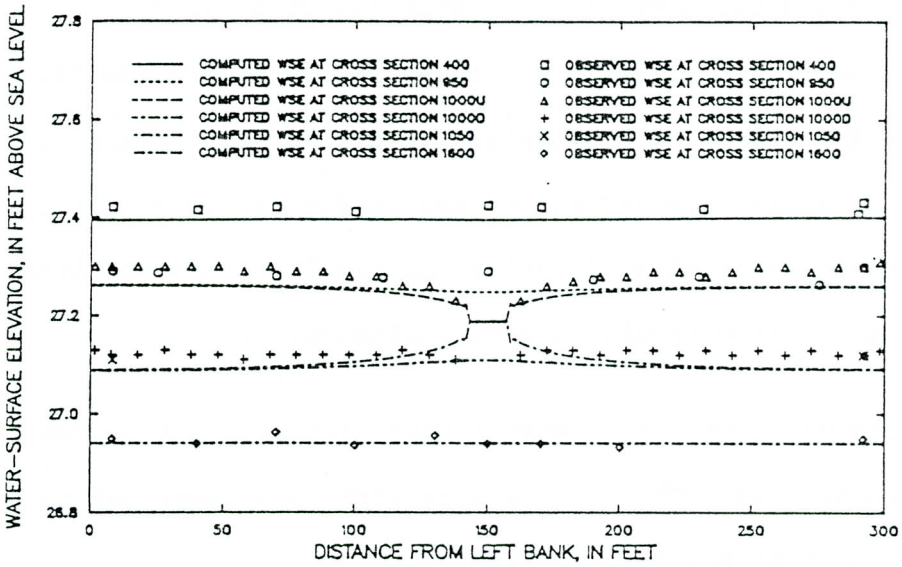

Figure 143. Observed and computed water-surface elevations (WSE) for experiment S6210035, $\beta = 0$, network 3. The letters U and D refer, respectively, to the upstream side and the downstream side of the constriction.

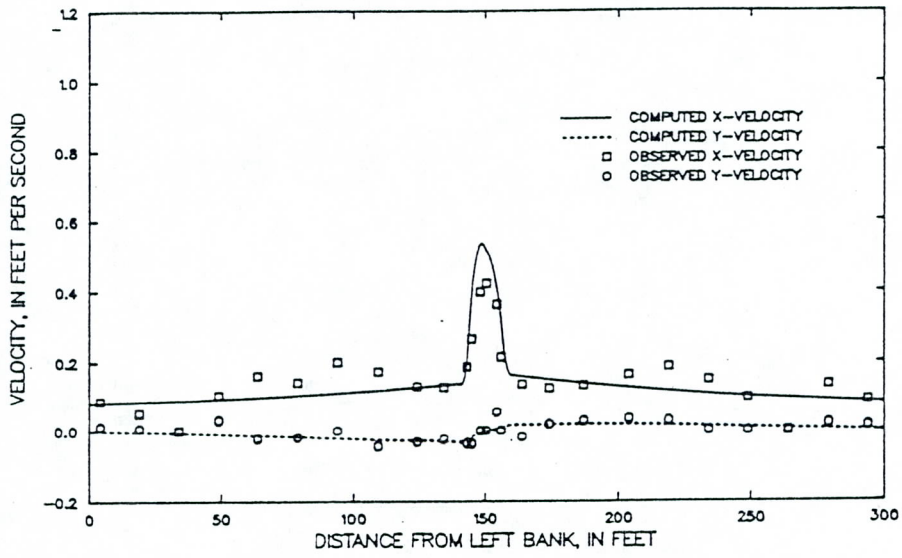

Figure 144. Observed and computed velocity components at cross section 900 for experiment S6210035, β = 0, network 3.

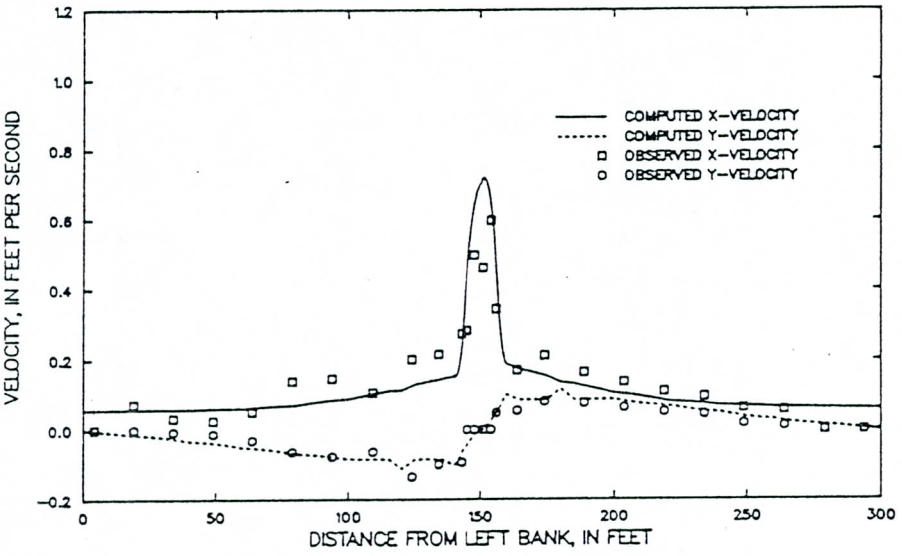

Figure 145. Observed and computed velocity components at cross section 950 for experiment S6210035, β = 0, network 3.

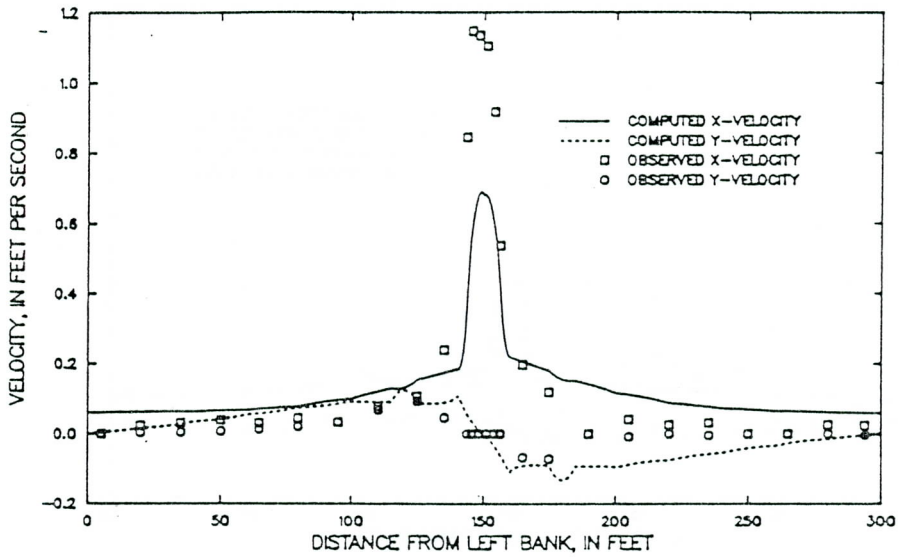

Figure 146. Observed and computed velocity components at cross section 1050 for experiment S6210035, β = 0, network 3.

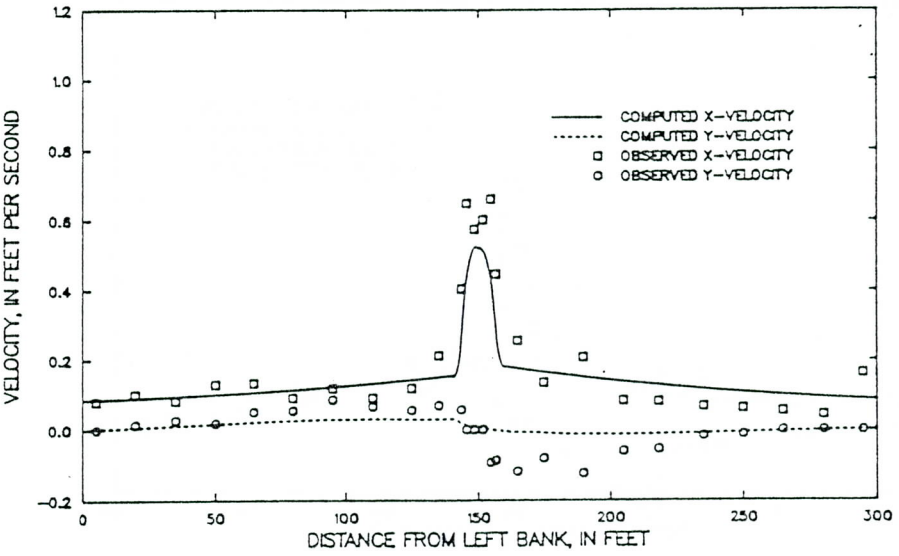

Figure 147. Observed and computed velocity components at cross section 1100 for experiment S6210035, β = 0, network 3.

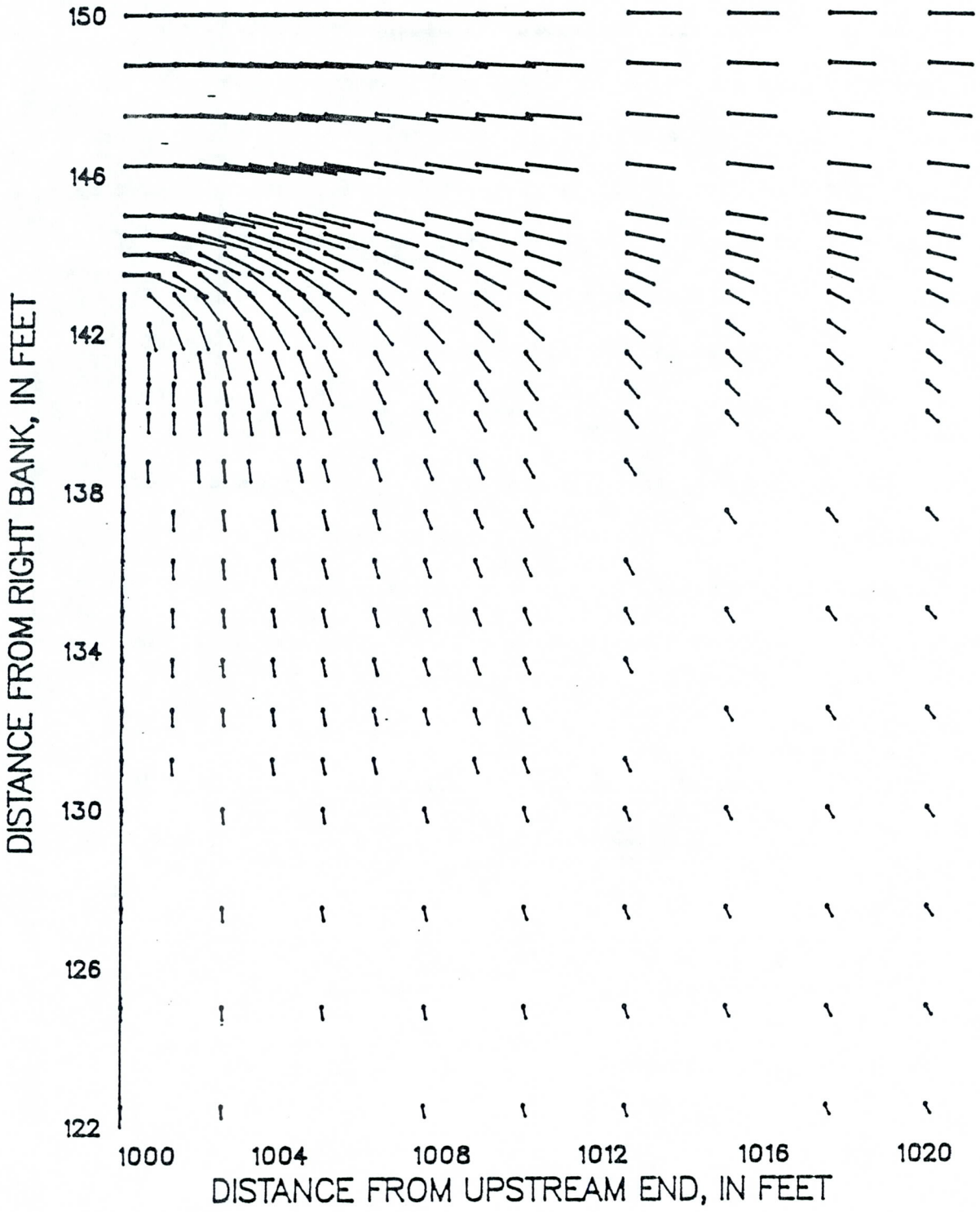

Figure 148. Partial velocity field for experiment S6210035, $\beta = 0$, network 3. A vector 1 inch long represents a velocity of 4 feet per second.

Finally, to evaluate the importance of the convective terms in these simulations, the value of the momentum-correction coefficient, β, was set equal to zero in simulations of experiments S6210035, S6810105, and S7410235. Water-surface elevations, velocity profiles at cross sections 900, 950, 1050, and 1100, and a partial velocity field for S6210035 are shown in figures 143 through 148; for S6810105 in figures 149 through 154; and for S7410235 in figures 155 through 160.

In all three cases, there is a decrease in the computed fall through the opening. The decrease becomes proportionately larger as the discharge increases. The peak velocities upstream from the constriction are higher than those in the calibration simulations,

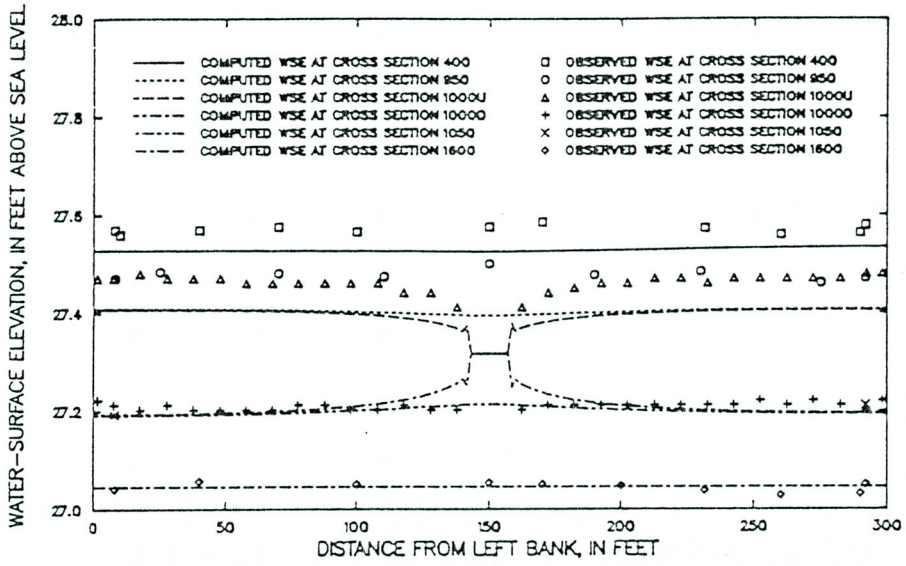

Figure 149. Observed and computed water-surface elevations (WSE) for experiment S6810105, β = 0, network 3. The letters U and D refer, respectively, to the upstream side and the downstream side of the constriction.

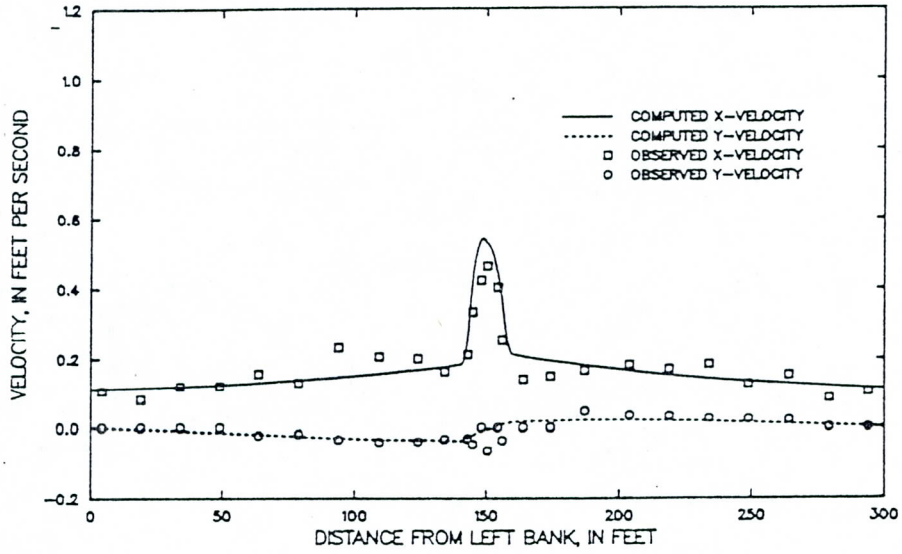

Figure 150. Observed and computed velocity components at cross section 900 for experiment S6810105, β = 0, network 3.

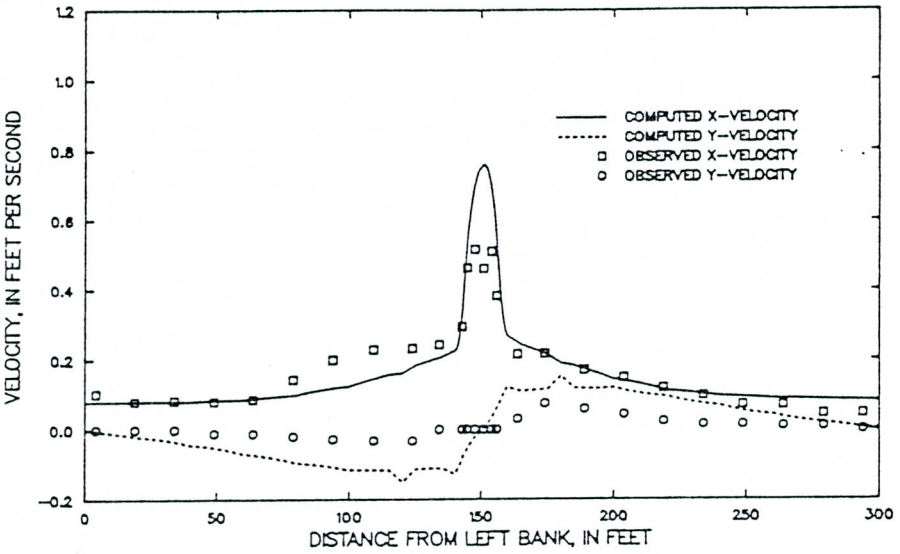

Figure 151. Observed and computed velocity components at cross section 950 for experiment S6810105, β = 0, network 3.

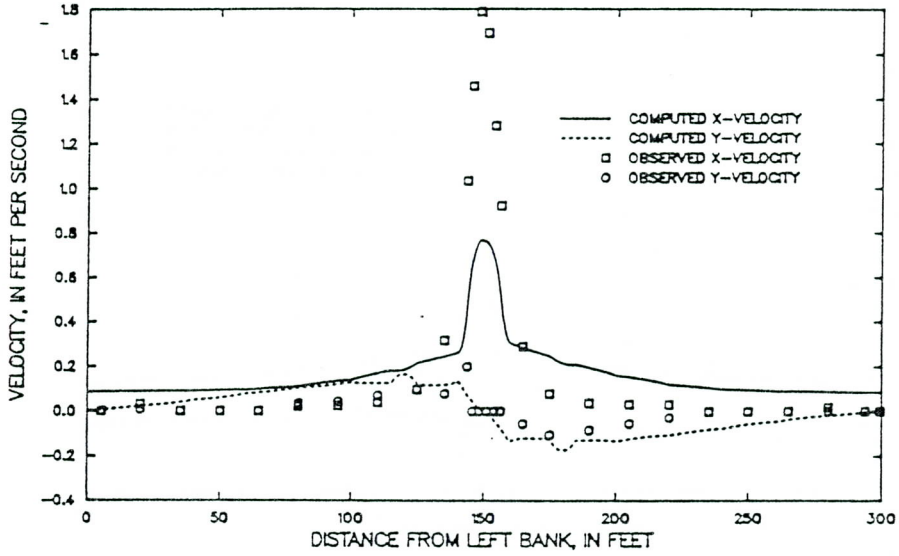

Figure 152. Observed and computed velocity components at cross section 1050 for experiment S6810105, $\beta = 0$, network 3.

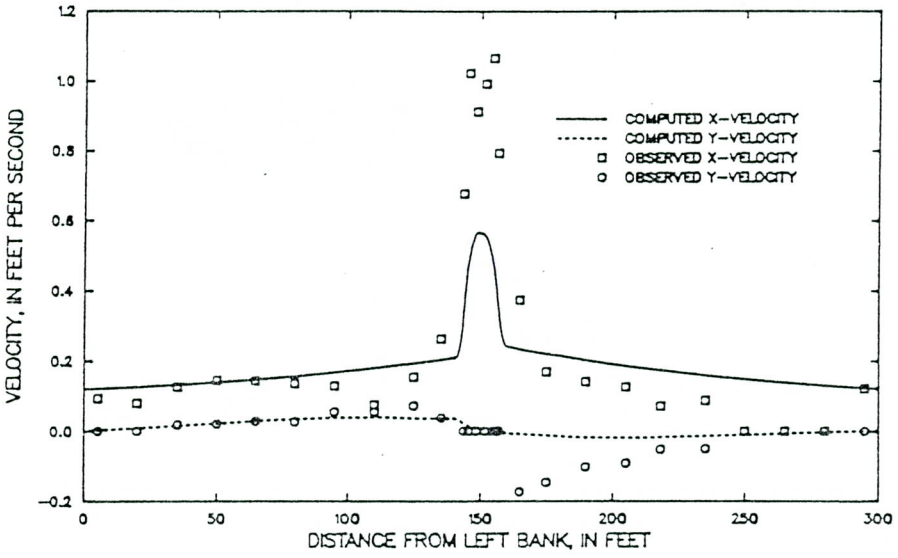

Figure 153. Observed and computed velocity components at cross section 1100 for experiment S6810105, $\beta = 0$, network 3.

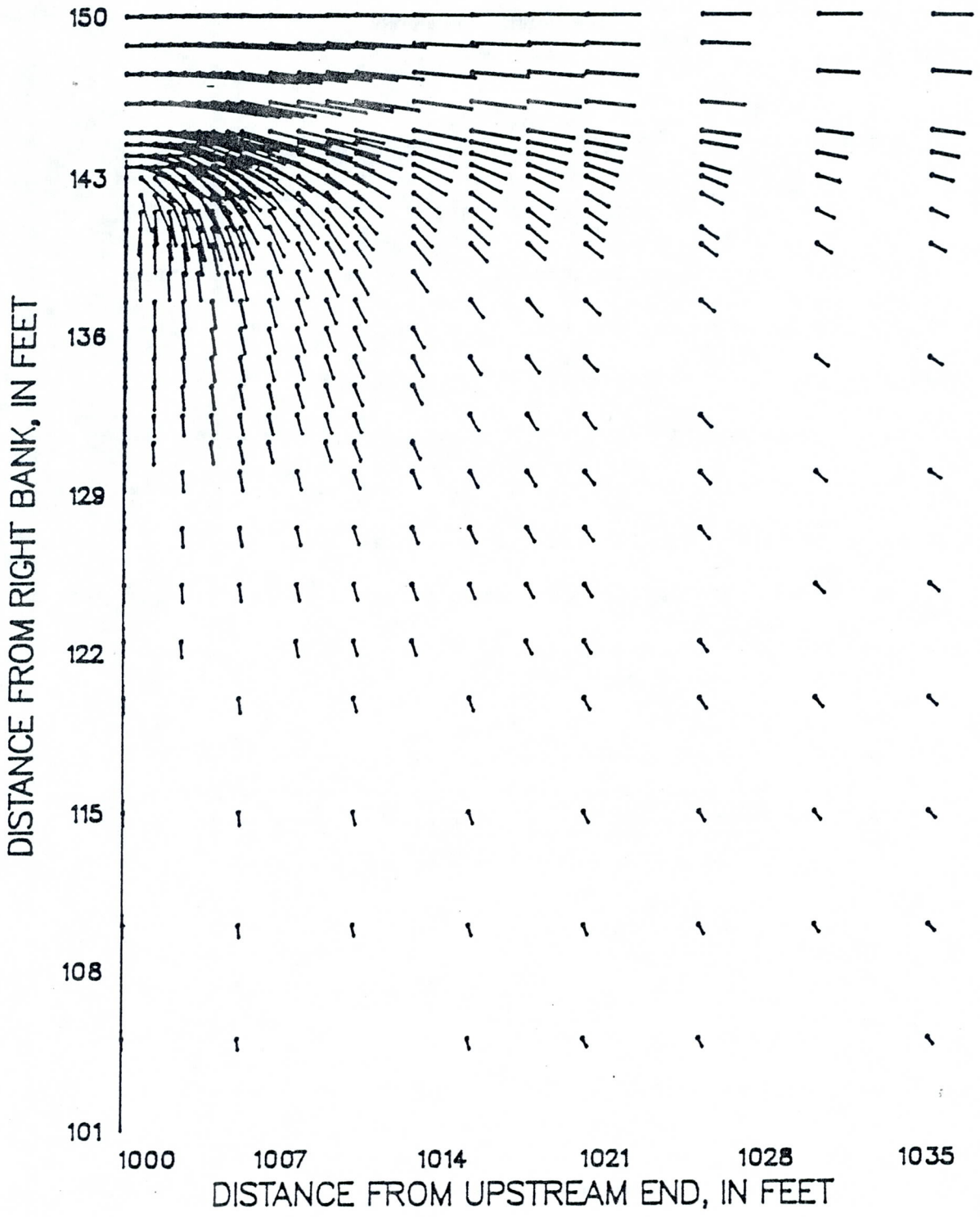

Figure 154. Partial velocity field for experiment S6810105, $\beta = 0$, network 3. A vector 1 inch long represents a velocity of 4 feet per second.

and the peak velocities downstream are lower. The jet and recirculation zones downstream from the constriction are not present.

Conclusions from the Application of FESWMS-2DH to Flood Plain Simulation Facility Data

The following conclusions can be drawn from the application of FESWMS-2DH to data from the FPSF. Backwater associated with steady flow through a contracted opening in the FPSF can be accurately simulated with FESWMS-2DH using a simple representation of the kinematic eddy viscosity, a momentum-correction-coefficient value of unity, and a single linear representation of Manning's n as a function of depth determined during normal flow at the same discharge. Adequate representation of the flow distribution,

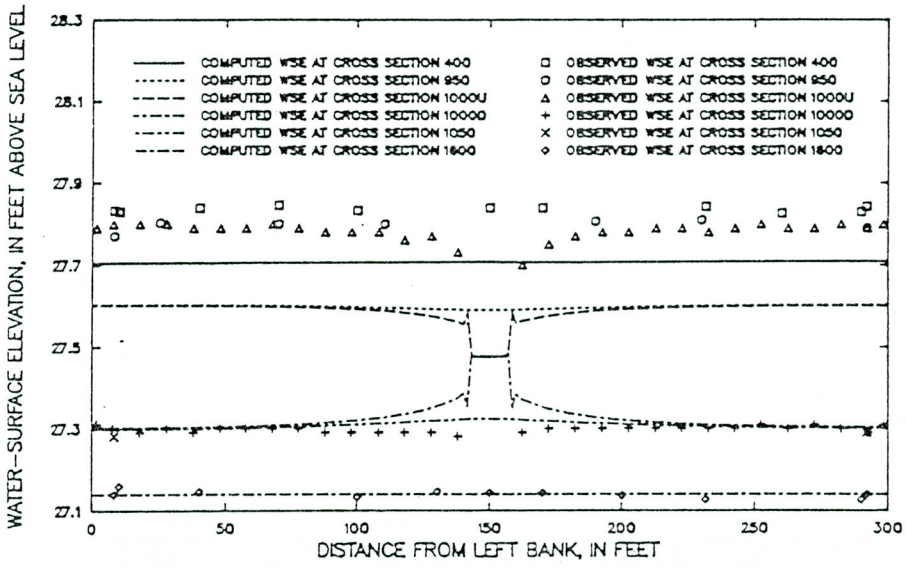

Figure 155. Observed and computed water-surface elevations (WSE) for experiment S7410235, $\beta = 0$, network 3. The letters U and D refer, respectively, to the upstream side and the downstream side of the constriction.

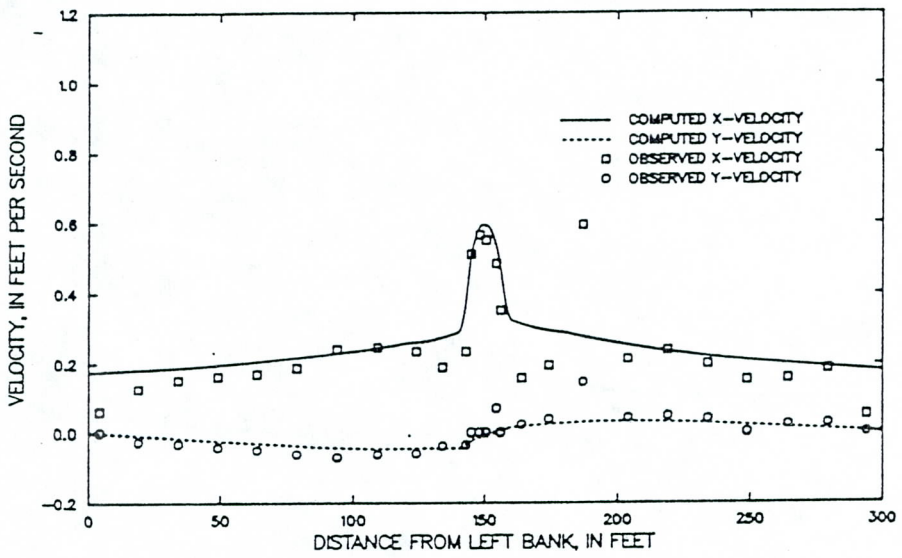

Figure 156. Observed and computed velocity components at cross section 900 for experiment S7410235, β = 0, network 3.

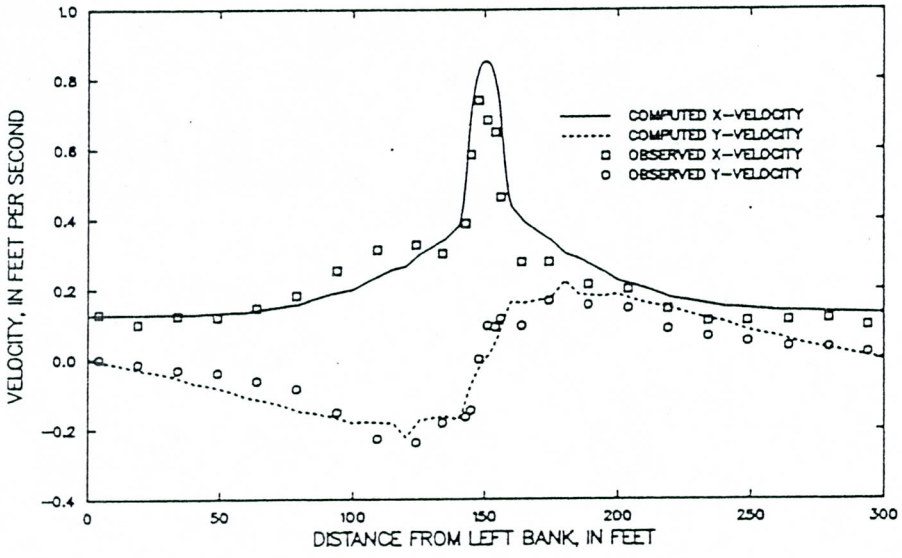

Figure 157. Observed and computed velocity components at cross section 950 for experiment S7410235, β = 0, network 3.

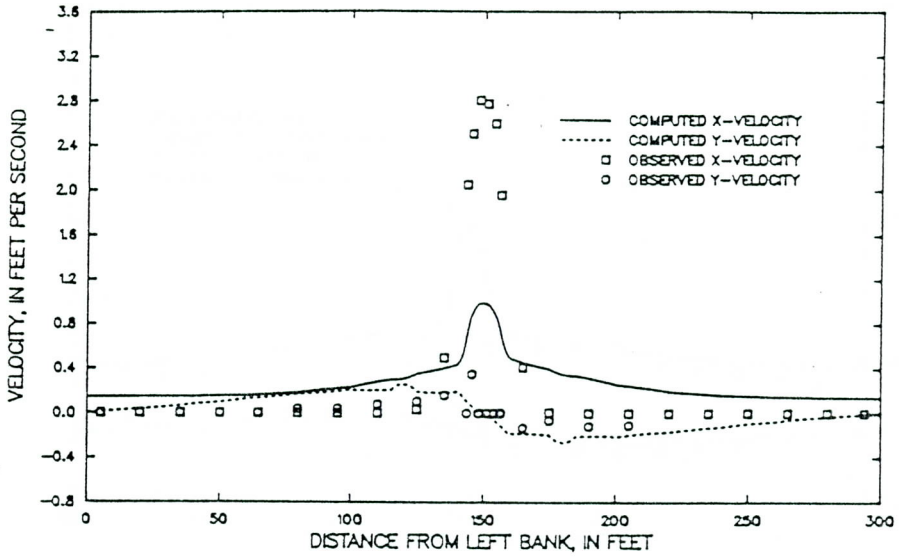

Figure 158. Observed and computed velocity components at cross section 1050 for experiment S7410235, β = 0, network 3.

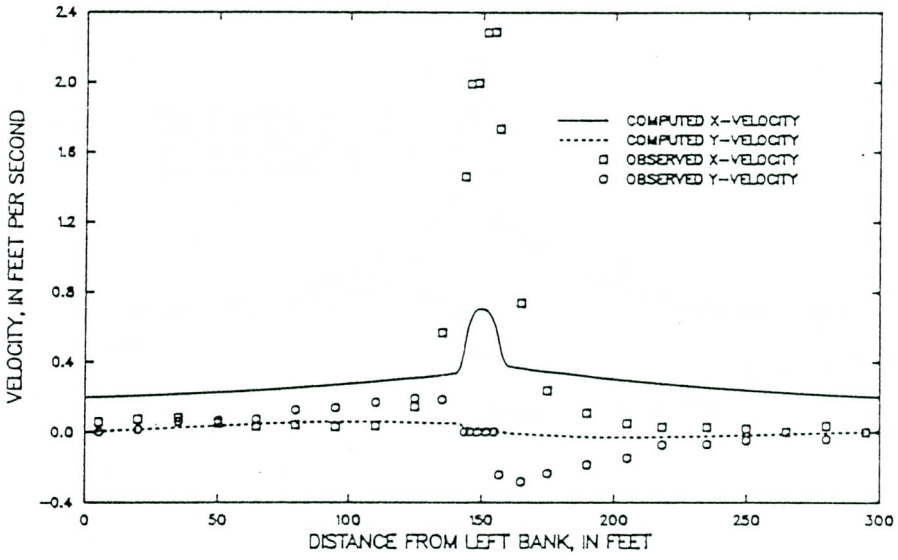

Figure 159. Observed and computed velocity components at cross section 1100 for experiment S7410235, β = 0, network 3.

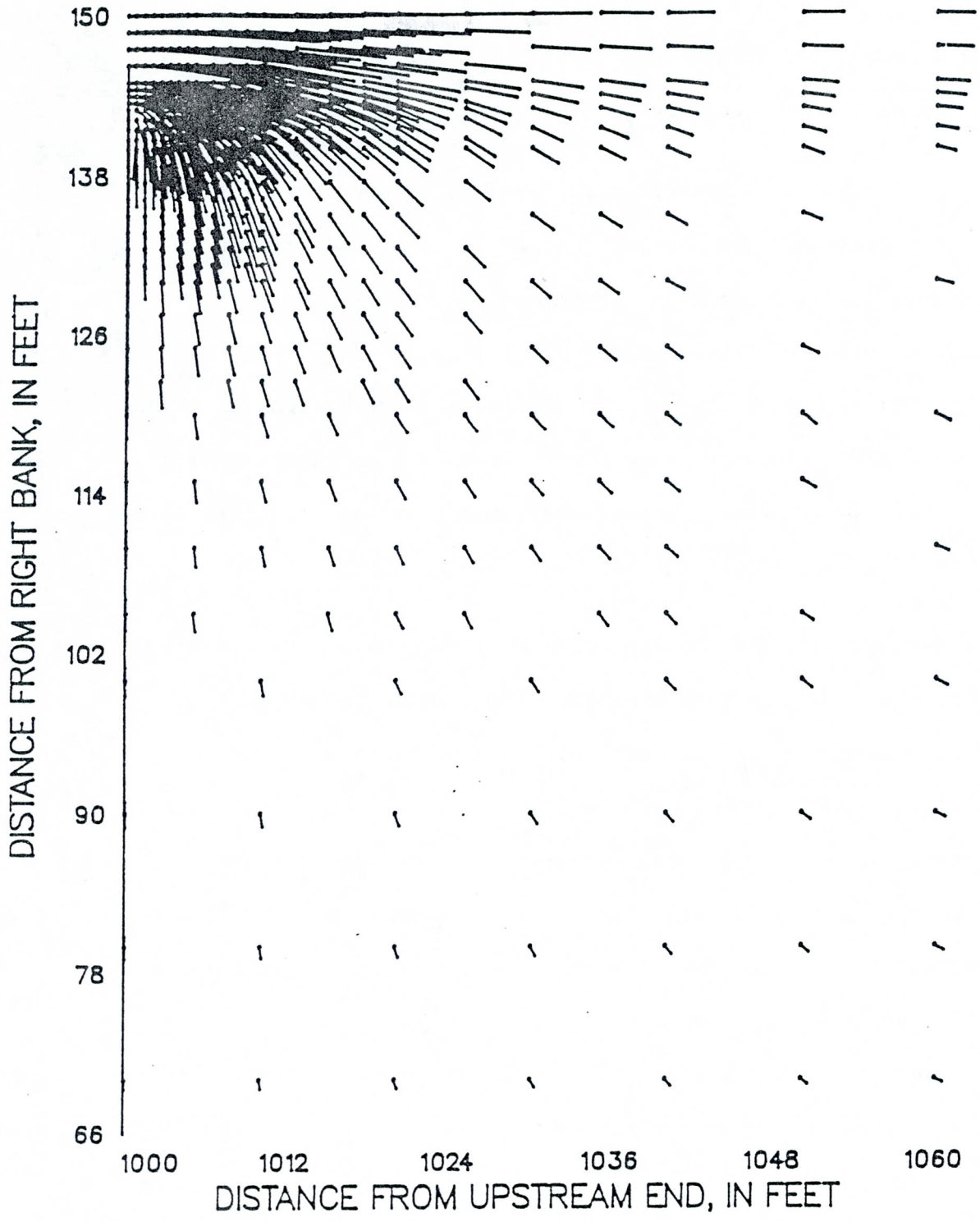

Figure 160. Partial velocity field for experiment S7410235, $\beta = 0$, network 3. A vector 1 inch long represents a velocity of 4 feet per second.

including the jet and recirculation zones downstream from the constriction, requires more information about the values of the momentum-correction coefficient and Manning's n near the opening.

A fairly coarse network provides good results when depth and velocity gradients are not too large. As depth and velocity gradients increase, network refinement is necessary to avoid underestimation of backwater and oscillations in the velocity field. The flux-computation and continuity-norm options in FLOMOD can be used to selectively refine a network to achieve improved accuracy. In all cases, network refinement beyond a certain level provides no improvement in the solution.

In addition, the results illustrate that much more care is required in modeling when the convective terms are significant. Not only is network refinement necessary to avoid velocity oscillations where gradients are large, but also good information about the values of the momentum-correction coefficient and Manning's n near the opening is necessary to avoid large errors in backwater and flow distribution. In particular, if the convective terms are neglected, it is not possible to obtain adequate estimates of backwater and flow distribution when there are large depth and velocity gradients near the contracted opening.

USE AND CALIBRATION OF FESWMS-2DH

From experience with the modeling system FESWMS-2DH in field applications to river-flood-plain systems and in modeling flows in the Flood Plain Simulation Facility (FPSF), discussed in this report, some general guidelines for model users can be deduced. It is recommended that a potential model user read the section in this report on FPSF modeling and the reports by Lee and others (1983), Gilbert and Froehlich (1987), and Wiche and others (1988) on the Pearl River study at Interstate Highway 10 (I-10).

Application of the modeling system requires the collection and analysis of field data, the design of a finite-element network, model adjustment to eliminate deficiencies in the solution, model calibration, and, if possible, model verification.

How well a model reproduces an observed flow depends on the approximations made in the model and on the calibration data. Calibrated model results represent a best fit to the available calibration data.

Network design and adjustment is a process of approximating hydraulically important topographic and vegetative-cover features with a finite number of homogeneous elements. The quality of the approximation depends on the amount and quality of the available topographic and vegetative-cover data. Further approximations are made in assigning model boundary conditions. In addition, the model equations describe the prototype flow process in an approximate

way. The quality of this approximation depends in part on how well such assumptions as steady flow and the eddy-viscosity concept reflect prototype conditions. This approximation also depends on the values of the model's empirical coefficients, determined during calibration. Hence, velocities and water-surface elevations obtained from the calibrated model are approximate values, responses of approximate equations to approximate boundary conditions, topography, and vegetative cover.

Realistic and mutually consistent values of empirical parameters are chosen during calibration to bring model results into as close agreement as possible with observed data. If there is a major discrepancy between model results and observed data, then the approximations made in constructing the model are in error or the observed calibration data are not accurate or are not representative of the general hydraulic situation. The capability of a model to reproduce observed flows and subsequently predict the outcome of future or hypothetical flows depends largely on the amount and quality of the topographic, vegetative-cover, boundary-condition, and calibration data that are available. Thus, improvements in observed data can lead to more accurate simulation.

Data Collection and Analysis

Use of FESWMS-2DH in an actual study requires the collection and analysis of a large amount of hydrographic and topographic data. For example, if an actual flood in a river-flood-plain

system is to be modeled under the assumption of steady flow, high-water marks distributed throughout the study area and discharge measurements at highway crossings should be collected for use in establishing model boundary conditions and calibrating the model. If data from additional floods are available, these data may be used for model verification.

Detailed topographic data must be obtained. For river-flood-plain flows, these data include longitudinal profiles and cross sections for major channels and topographic maps of the inundated flood plain. Special attention must be given to channel and overbank topography at and near bridge openings. Bridge and culvert dimensions must be obtained for use in network layout and the determination of one-dimensional bridge and culvert parameters.

Infrared aerial photographs of the study area are useful in determining vegetative type and density, which in turn determine areas of nearly uniform roughness.

Network Design

To apply the model, the boundaries of the area to be modeled must be determined, and the study area must be represented as an equivalent network of triangular or quadrilateral elements. In modeling a highway crossing of a river-flood-plain system, the lateral boundaries of the area inundated must be approximately determined first. Then the upstream and downstream boundaries should be located at least one flood-plain width distant from the

highway crossing, so that errors in assigning model boundary conditions will not significantly affect flow conditions at the crossing and modifications made to the model at the crossing will have little effect on the boundary conditions.

Elements with curved sides can be used to approximate the lateral boundaries of the system, where tangential flow is specified. The curved sides can better approximate the natural features of the boundary. Curved element sides can also be used to avoid large angles on the boundary where an element side common to two elements intersects the boundary. Although mass is conserved globally regardless of the boundary configuration, minimizing boundary angles also minimizes local mass-conservation errors at the boundary. The use of curved-sided elements to define model boundaries, river channels, and highway embankments is shown in figure 161, a finite-element network near the I-10 crossing of the Pearl River in southeastern Louisiana (adapted from Wiche and others, 1982, p. 264).

If it is not possible to determine the boundaries of the inundated area, the automatic-boundary-adjustment feature of FESWMS-2DH can be used to obtain an initial solution. Then the boundaries can be more precisely located on the basis of preliminary model results, and, if desired, the lateral boundaries can be adjusted for later simulations.

Experience has shown that it is best to locate upstream and downstream model boundaries at approximately right angles to the

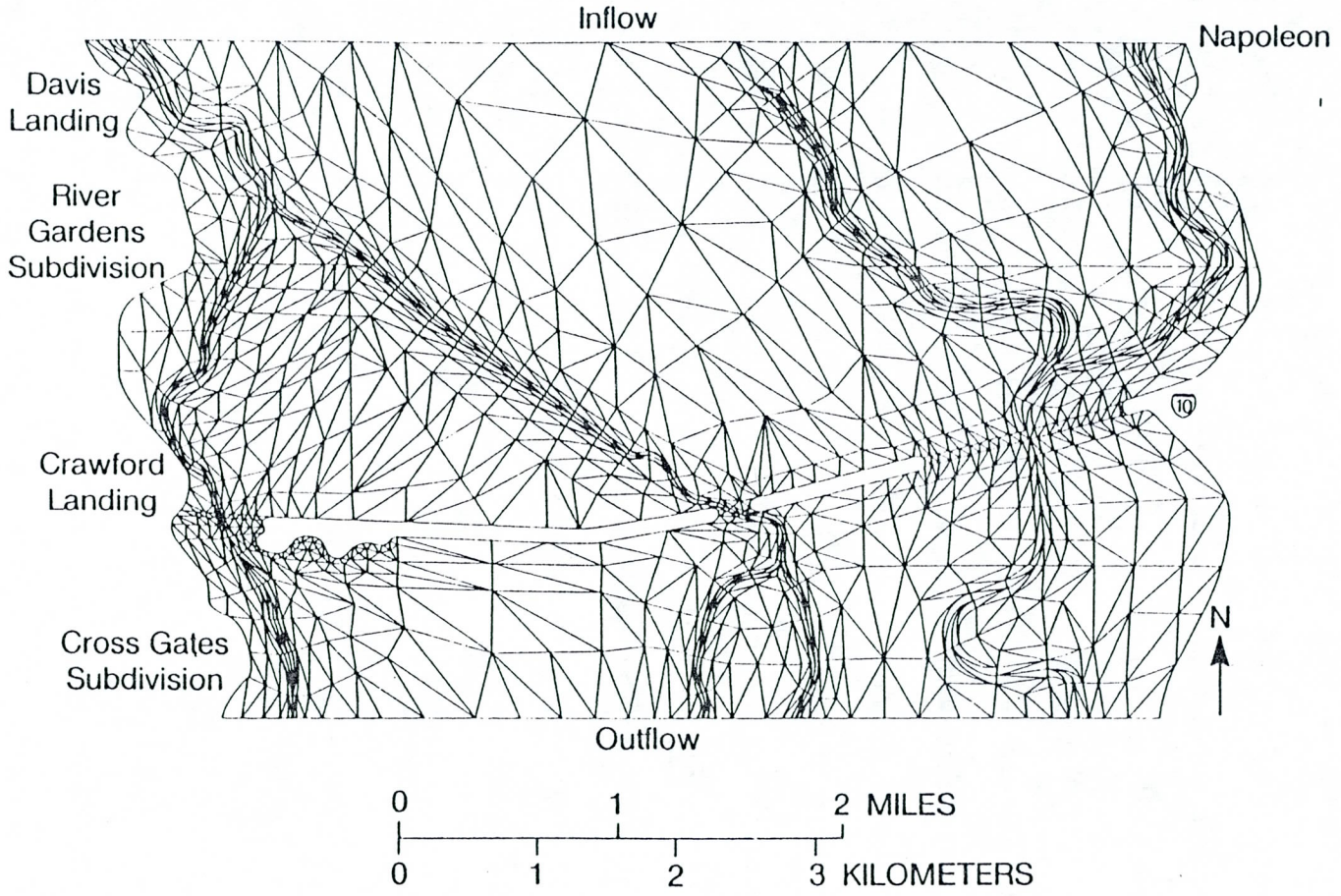

Figure 161. Finite-element network near the I-10 crossing of the Pearl River in southeastern Louisiana (adapted from Wiche and others, 1982, p. 264).

flood-plain axis and to the lateral boundaries of the flood plain or flow domain.

After the boundaries are defined, the study area is subdivided into an equivalent network of triangular or quadrilateral elements. FESWMS-2DH accepts any combination of six-node triangular and eight- or nine-node quadrilateral elements with straight or curved sides. In forming elements, internal angles should be bounded away from zero and 180 degrees. Also, midside nodes of curved element sides should be located within the middle third of the side. Careful placement of nodes and elements is necessary to adequately represent prototype topography and vegetative cover. Subdivision lines between elements are located where abrupt changes in vegetative cover or topography occur. Each element should be designed to represent an area of nearly homogeneous vegetative cover. Automatic network generation can be used in this process after homogeneous subareas of the study area are determined. Elements with curved sides can be used to define channels realistically (fig. 161).

Topographic variations can lead to large velocity and depth gradients that require additional network detail. For example, in field applications, it has been found that local inconsistencies may occur in the solution if the value of the ratio of the maximum depth to the minimum depth on an element exceeds 10. To provide a margin of error, it is suggested that the value of this ratio be kept less than five if possible. Thus, additional network detail may be required in regions where ground-surface gradients, such as

between overbanks and channel bottoms, are large.

Model boundaries, as well as model topography, can lead to flow conditions that vary greatly in a short distance. Thus, at a contracted opening, for example, network detail must be increased for solution accuracy. The discussion of FPSF modeling in this report illustrates the dependence of solution accuracy on network detail in such a situation. It was seen that an increase in discharge can lead to an increase in depth and velocity gradients and thus a decrease in accuracy. Thus, network refinement may be necessary as discharge is increased. It was also shown how the calculation of the mass flux and the element continuity norm can be used to locate and refine parts of the network where solution accuracy is low. In FPSF modeling and steady-flow field applications, it has been found that if the computed discharge at a contracted opening differs from the total inflow by no more than 5 percent, the computed water-surface elevations will be sufficiently accurate for engineering purposes.

The FPSF modeling also showed that network refinement may be necessary to eliminate velocity oscillations and resolve flow features such as recirculation zones.

The use of elements with aspect ratios greater than unity makes it possible to design a network with fewer elements than would be required otherwise. The element aspect ratio is defined as the ratio of the largest element dimension to the smallest. The optimum

aspect ratio for a particular element depends largely on the local velocity and depth gradients. If these gradients can be estimated beforehand, it is possible to align the smallest element dimension with the largest variable change and the largest dimension with the smallest change.

Elements with large aspect ratios are used frequently in defining river channels in a wide flood plain. During network design, the longest element side is aligned with the channel axis, along which velocity and depth changes are typically small. Element aspect ratios should be kept to a maximum of about 10. In channel reaches with significant curvature, however, it may be necessary to use a much smaller value to avoid an unrealistic solution.

The number of elements in a network may also be reduced by other approximations. Only the larger channels in a system need to be included in the network. Less important ones may be ignored. Usually, prototype channel cross sections are represented in the model by either triangular or trapezoidal cross sections with cross-sectional areas equal to the measured areas. Meandrous channel reaches with relatively small flows may be replaced with artificially straightened, but hydraulically equivalent, reaches. For a discussion of this procedure, the reader may refer to Lee and others (1983, p. 26).

Weirs, culverts, and small bridges that are modeled in a one-dimensional sense are treated as point flows along the boundary of

the finite-element network. A point flow is the total discharge that crosses the network boundary due to flow at a specific node point.

One-dimensional weirs and culverts are described by a set of parameters and two boundary node points, one on either side of a weir or on either end of a culvert. Flow over the weir or through the culvert is computed on the basis of the water-surface elevations and velocities at the two node points and the specified parameters. For weirs, the discharge coefficient for free-flow conditions, the length of the weir, and the crest elevation must be specified. For culverts, the discharge coefficient, the cross-sectional area, the hydraulic radius, the length, the Manning roughness coefficient, and the invert elevation are the required parameters.

Flow over roadway embankments is modeled as one-dimensional weir flow. To do this, the finite-element network is designed with solid boundaries following both sides of the embankment. The embankment is divided into a number of weir segments with appropriate parameters assigned to each segment. The number of segments to use depends on the variation of the roadway elevation along the embankment and the spacing of node points on the solid boundaries defining the embankment. The node points chosen to define either side of a weir segment should be located approximately at the center of that weir segment. The location of each weir segment, therefore, should be kept in mind when designing the finite-element network in the vicinity of the embankment.

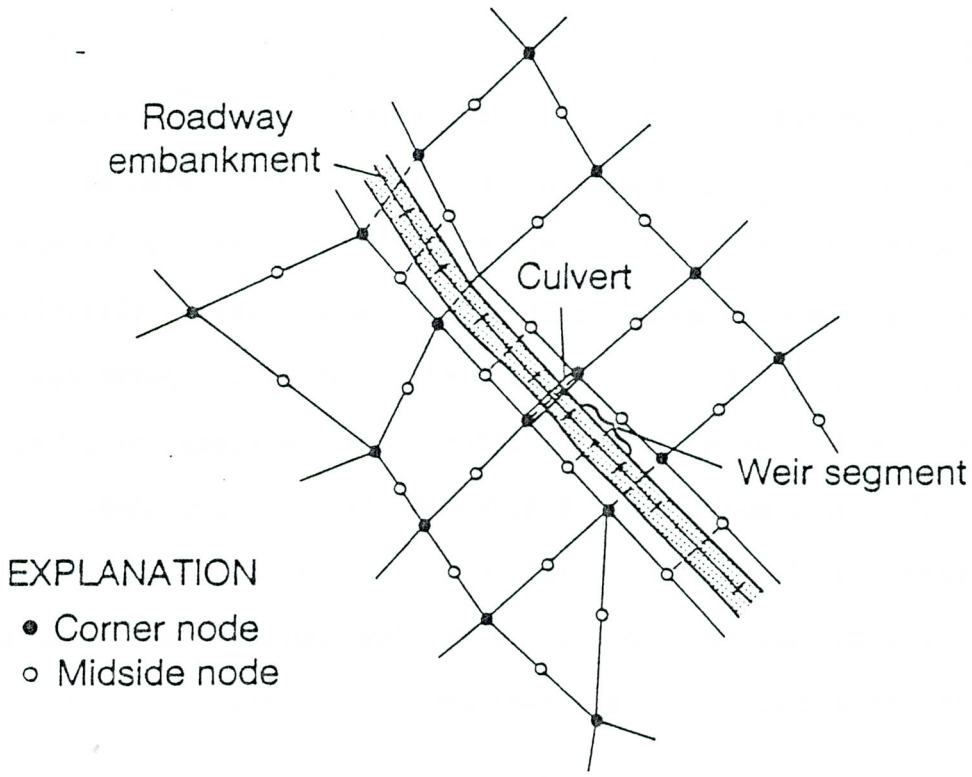

Figure 162. Finite-element network at a roadway embankment that contains a culvert and is divided into weir segments.

The same node can be used to define the side, or end, or both of more than one weir, or culvert, or both. In the case of an overtopped roadway embankment containing a culvert, such as shown in figure 162, the same node points are used to define the culvert and a weir segment.

Two-dimensional flow through a bridge or culvert, when the water surface is not in contact with the top of the bridge or

culvert opening, is modeled exactly as ordinary flow and requires no special consideration. When the water surface is in contact with the top of the opening, however, pressure flow exists. In this case, special consideration must be given to the design of the finite-element network in the vicinity of the bridge opening in order to properly model the flow.

If pressure flow within a bridge opening is to be considered, at least two rows of elements conforming to the bridge deck must be constructed as shown in figure 163. The elevation of the ceiling, or top of the opening (the underside of the bridge deck), must also be specified for each of the corner nodes belonging to the elements describing the opening. More than two rows of elements within the opening may be needed to accurately simulate the confined-flow situation.

Model Adjustment, Including Calibration

After network design is complete, boundary conditions are applied, and the prototype flow is simulated as closely as possible. The model-adjustment process consists of two parts: the adjustment of empirical model coefficients (model calibration) and the adjustment of model boundary conditions, network detail, and ground-surface elevations on the basis of additional information obtained during the study.

The two-dimensional surface-water flow model is based on the formulation and solution of equations which simulate a complex

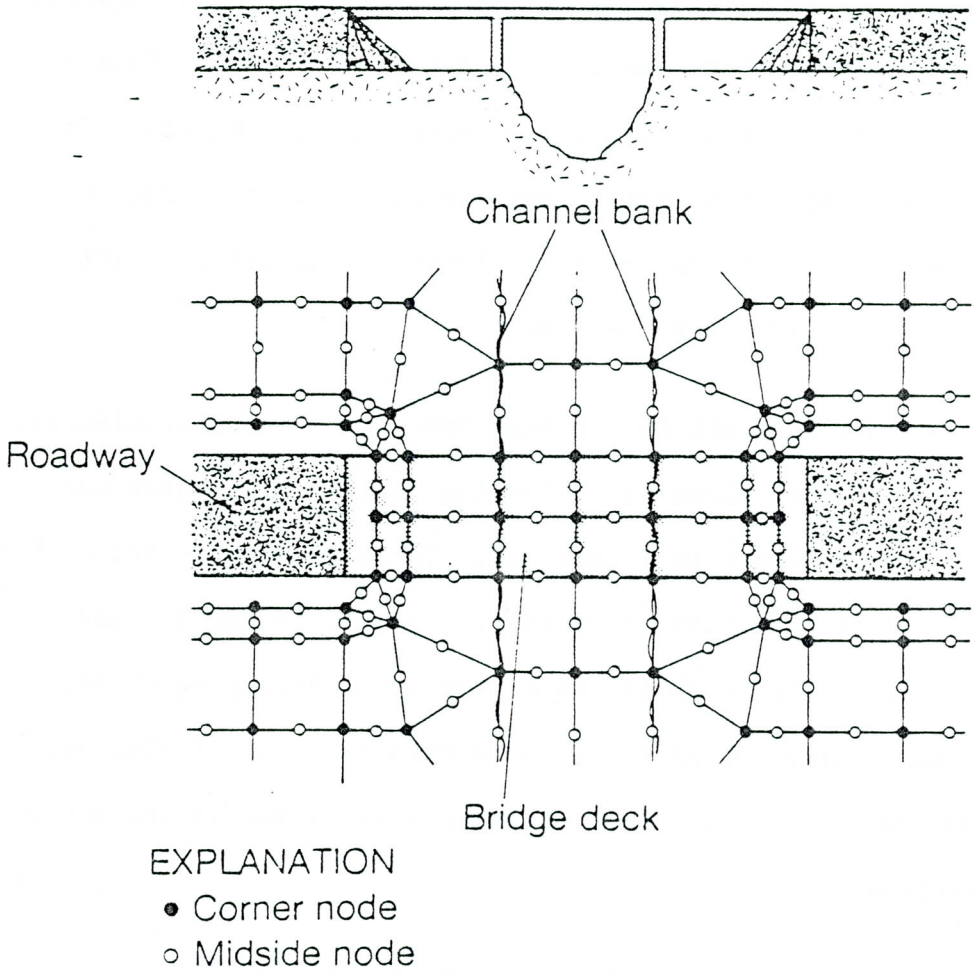

Figure 163. Finite-element network at a bridge where pressure flow within the bridge opening is modeled.

physical flow situation. Since no physical flow system can be completely described or understood, the mathematical formulation involves some level of approximation. Three-dimensional topographic features are represented by two-dimensional elements, and the physics of flow is assumed to obey differential equations in which empirical hydraulic coefficients appear. Model calibration is the process of adjusting the values of the empirical coefficients so

that the model simulates an observed flow as closely as possible. This aspect of model adjustment is discussed in detail below.

The second aspect of the model-adjustment process involves the correction of deficiencies in the model boundary conditions and the representation of flood-plain topography. Often, there are gaps in the data used to estimate model boundary conditions, design the model network, and assign model ground-surface elevations. During model adjustment, it occasionally becomes apparent that these data gaps are causing the model to fail to simulate correctly certain observed features of the flow being studied. A review of existing data or additional data collection is necessary in these instances. Then boundary conditions, network detail, or ground-surface elevations are adjusted on the basis of the additional information. This aspect of model adjustment is also discussed in detail below.

To calibrate a model, the values of the momentum-correction coefficient and the eddy viscosity are usually set first. The momentum-correction coefficient is usually assigned the value unity unless information from vertical velocity profiles is available which indicates that a larger value should be used. The value of the eddy viscosity can be assigned as discussed in the section on eddy viscosities. Often, the value $0.6U_{*}H$ is sufficient, but if it is not possible to obtain convergence for this value, a somewhat larger value may have to be used.

Once the values of the momentum-correction coefficient and the eddy viscosity are fixed, preliminary calibration work can focus on determining the values of the roughness coefficients. Nominal values are selected for initial use on the basis of available data such as infrared aerial photographs of the flood plain and field inspection. In making both the initial estimates of the roughness values and subsequent modifications to them, care should be taken to ensure that the assigned values are reasonable and mutually consistent. Preliminary calibration is based on whatever data are available for the flow being simulated and consists of matching the available data as closely as possible. In the Pearl River study, high-water marks and discharges at bridge openings were available. In the FPSF modeling, discharges, observed water-surface elevations, and the four cross-sectional velocity profiles were used in calibrating the flow model.

At this point, it is useful to examine the flow model's sensitivity to such factors as boundary conditions and model coefficients. For example, in the Pearl River study, it was found that computed water-surface elevations were most sensitive to the roughness values for the wooded flood plain and the channels at and near the bridge openings (Lee and others, 1983, p. 26). This information was useful in fine tuning the model. In the section on FPSF modeling, model sensitivity to the values of the upstream discharge, the Manning n, the momentum-correction coefficient, and the eddy viscosity was discussed.

Appropriate adjustments to the values of the roughness coefficients may give close agreement between computed and observed data in most cases. Often, however, discrepancies between model results and observations make it necessary to obtain additional data or review previously obtained data. Additional field work is occasionally necessary to check the location and elevation of high-water marks and study previously overlooked topographic features. On the basis of the results of the early simulations and the additional observations, modifications are then made to model boundary conditions, network detail, and model ground-surface elevations.

For example, in the Pearl River study, inadequate information for use in establishing the distribution of discharge at the upstream model boundary made it necessary to make adjustments to the upstream boundary condition until observed high-water-mark-elevation data were adequately approximated. Also, it was found that failure to include a short dike in the network near the upstream model boundary and erroneous ground-surface elevations on the overbanks at several I-10 bridge openings were adversely affecting model results (Lee and others, 1983, p. 29-30).

After such adjustments are completed, further fine tuning of model coefficients may be necessary for final calibration.

The values of the Manning n required for two-dimensional model calibration are generally somewhat smaller than the values required to calibrate a one-dimensional model of the same reach. Several

factors contribute to this situation. Wherever lateral flow is significant, streamlines are not parallel to the axis of the flood plain. Thus, flow paths are generally longer in a two-dimensional model than in a one-dimensional model, and it is possible to account for a given loss of energy with a smaller roughness coefficient than is needed in a one-dimensional model. In addition, some energy loss is accounted for by the turbulent-stress terms in the two-dimensional momentum equations. This loss must be accounted for by bottom friction in a step-backwater model.

If data from another flood are available, the calibrated flow model can be verified. Verification involves determining how well the already calibrated model simulates the second flood. Although changes usually have to be made in boundary conditions and perhaps the location of the lateral boundaries, the values of the empirical coefficients are unchanged. If there is good agreement between the computed and observed data for the second flood, the modeler has more confidence in results obtained during the use of the model to study hypothetical flows or flood-plain alterations other than the one for which the model was calibrated.

USE OF FESWMS-2DH BY THE HIGHWAY INDUSTRY

The FESWMS-2DH modeling system is a versatile tool for steady-flow analyses at highway crossings where the flow is two dimensional. Examples of such situations are given in the reports on the Congaree and Pearl Rivers discussed below. Wide distribution within the highway industry of reports on FESWMS-2DH and its application as well as documents such as the executive summary of this project will make information about the system available to potential users. Participation in training courses by potential model users will lead to effective use of the model. Future model enhancements and software maintenance will ensure growing model capabilities with time.

Operational Potential of FESWMS-2DH

The use of FESWMS-2DH and its predecessors in several complex modeling projects, including the analysis of highway crossings of the Congaree River in South Carolina (Lee, 1980; Lee and Bennett, 1982) and the Pearl River between Louisiana and Mississippi (Lee and others, 1982; Wiche and others, 1982; Lee and others, 1983; Gilbert and Froehlich, 1987; Gilbert and Schuck-Kolben, 1987; Wiche and others, 1988), has already demonstrated the operational potential of the modeling system. In these studies, backwater and drawdown caused by highway embankments with multiple openings across wide wooded flood plains were determined. The studies have shown that the finite-element model can be used to simulate both

lateral and longitudinal velocities and variations in water-surface elevation, highly variable flood-plain topography and vegetative cover, and geometric features such as highway embankments, dikes, and channel bends. Geometric features of widely varying sizes were easily accommodated within a single finite-element network.

In the Congaree study, the modeling system was used to study a multiple-opening crossing of a flood plain with a single channel. The rapid expansion of the flood plain of the river upstream from the crossing, an extensive dike system, and highly variable roughness combined to cause significant lateral velocities and variations in stage during floods. A major accomplishment of the study was the demonstration of the model's capability to simulate flows on a flood plain with large roughness variations and large changes in depth with distance.

In the Pearl River study, the capability of the modeling system to simulate the significant features of steady flow in a complex multichannel river-flood-plain system with variable topography and vegetative cover was successfully demonstrated. These features included lateral variations in discharge distribution and backwater and drawdown. Gilbert and Froehlich (1987) and Gilbert and Schuck-Kolben (1987) demonstrated the use of FESWMS-2DH to model flow over highway embankments (weir flow).

Training

Making the model useful to those involved in the design of river and flood-plain highway crossings requires a training program. Two possible methods for providing training in the use of FESWMS-2DH are presented below.

A 1-week FESWMS-2DH workshop is planned in the Southeastern Region of the Geological Survey. The workshop is planned for a class size of about 20 and will involve roughly equal parts of lectures and student exercises. A tentative workshop outline is given in table 6. The course will be available to Geological Survey personnel and cooperating FHWA and State highway agency hydraulic engineers.

A second possible training program involves small teams working on real problems with the assistance of an instructor. Two or three problems would be identified in different locations. A team consisting of, for example, Geological Survey, Federal Highway Administration, State highway agency, and possibly other public works agency personnel would be assembled for each problem. Each team would study the FESWMS-2DH users manual, obtain field data necessary to do the project, and attempt to design a preliminary network. Then all the teams would meet with the instructor for 2 days for comments on their preliminary network designs and lectures on the use of FLOMOD. In the weeks following the 2-day workshop, each team would continue to work on its problem, improving the

Table 6. Outline for a 1-week workshop on finite-element surface-water flow modeling using FESWMS-2DH.

Day	Time	Subject
Monday	Morning	Introduction to two-dimensional flow modeling Review of shallow-water equations Data requirements Sample applications of FESWMS-2DH (finite-element surface-water modeling system)
	Afternoon	Use of data-input module DINMOD (network preparation) Student exercises with DINMOD
Tuesday	Morning	Computational aspects of surface-water flow simulation using flow module FLOMOD
	Afternoon	More student exercises with DINMOD
Wednesday	Morning	Use and operation of flow module FLOMOD
	Afternoon	Student exercises with FLOMOD
Thursday	Morning	Use and operation of the analysis-of-output module ANOMOD
	Afternoon	Student exercises with ANOMOD
Friday	Morning	Discussion of flow-simulation results Questions and answers Quiz and evaluation

network, running FLOMOD, and applying ANOMOD to display the results graphically. Consultation with the instructor would be by telephone. After 1 or 2 months, the teams would meet again with the instructor. Each team would present its results to the other teams and the instructor. Problems encountered and questions raised during the modeling would be discussed. After the teams returned home, they

would complete their modeling projects with consultation with the instructor by telephone.

Future Possible Improvements to FESWMS-2DH

Several future improvements are possible for FESWMS-2DH.

Although many interpolation and weighting functions and several forms of the flow equations were studied during this project, it is possible that more efficient and accurate schemes based on other such functions, or equations, or both may be discovered in the future. If this happens, such a scheme should be incorporated into FLOMOD.

Model efficiency could be increased if it was not necessary to simulate channels in a two-dimensional sense. Simulating channels one dimensionally would increase model efficiency because of the reduction in the number of computational nodes. It would also allow consideration of channels that would be omitted in a two-dimensional network for reasons of computational efficiency and permit the connection of a two-dimensional model with one-dimensional models upstream and downstream.

Most bridge hydraulic engineers are quite familiar with one-dimensional river-hydraulics models (such as WSPRO and HEC-2). These engineers can quickly assemble the data needed as input to these one-dimensional models and rapidly obtain results. However, even in cases where hydraulic conditions are not very complex, it

may be useful to have results from a two-dimensional flow analysis. For example, a detailed description of a two-dimensional flow field may be useful in determining local scour around bridge piers and abutments and in designing erosion protection measures at approach embankments, abutments, and piers. By using one-dimensional input data (cross sections and bridge geometry), a two-dimensional input data file could be created automatically, thus greatly simplifying operation of the two-dimensional model. In fact, a combined one-dimensional/two-dimensional steady-flow model could be developed for evaluating long river reaches where short reaches, such as around bridges, could be simulated in two dimensions.

The addition of the capability to model sediment transport would allow evaluation of erosion and deposition of sediment in river channels, expecially around structures such as dikes and bridges. Although an extremely accurate prediction of scour, or deposition, or both may not be possible without calibrating such a model using prototype measurements, the capability to simulate sediment transport would help detect conditions where a problem is likely to occur. Some examples of such situations are:

- Erosion, or deposition, or both in reaches of relocated or "improved" river channels.
- Erosion, or deposition, or both around dikes used to stabilize channel banks.
- Constriction scour at bridges (both live-bed and clear-water scour conditions could be readily evaluated).

Although it is possible now to simulate pressure flow through a bridge opening (flow in contact with the top of the opening), it is not yet possible to simulate pressure flow through the opening combined with weir flow over the top of the opening. Such a model enhancement could be added in the future.

Permeable spur dikes often are used to protect channel banks. FESWMS-2DH currently cannot be used to simulate flow around, through, and over such dikes. Empirical relations could be added to the model so that such structures could be simulated accurately. Physical hydraulic model studies are needed to determine empirical coefficients used to simulate flow through permeable spur dikes.

Software Maintenance

Experience has shown that most of the problems encountered during use of the FESWMS-2DH programs are due to incorrect input data. Individuals experienced in the application of the model, either in the Geological Survey, the Federal Highway Administration, of State highway departments, can be consulted when such problems arise. For further information regarding assistance, contact the U.S. Geological Survey, Water Resources Division, 430 National Center, 12201 Sunrise Valley Drive, Reston, VA 22092.

Maintenance of FESWMS-2DH software by the Geological Survey, the Federal Highway Administration, or other organizations is dependent on the availability of funds. Such software maintenance could include the correction of conceptual or coding errors; the

communication to users of necessary code changes; the publication of improved versions of the codes and supporting documentation; and response to general correspondence on the modeling system.

SUMMARY AND CONCLUSIONS

In this report were presented the results of the project "Two-Dimensional Finite-Element Hydraulic Modeling of Bridge Crossings," conducted by the Geological Survey in cooperation with the Federal Highway Administration. The finite-element surface-water flow modeling system, FESWMS-2DH, developed under this project, consists of three programs: a data input module, DINMOD; a hydrodynamic flow module, FLOMOD, and an analysis-of-output module, ANOMOD. The features of each program were discussed in this report.

The preprocessor, DINMOD, generates a two-dimensional finite-element network for use by FLOMOD. In particular, DINMOD edits input data, plots the finite-element network, and orders elements to permit an efficient solution. DINMOD is also capable of automatic network generation and refinment.

FLOMOD is capable of simulating steady or unsteady two-dimensional flow in the horizontal plane. The vertically integrated equations of motion and continuity are solved for the depth-integrated velocity components and depth at the node points of the finite-element network. The model takes into account bed friction, turbulent stresses, wind stresses, and the Coriolis force. Flow over weirs (such as highway embankments) and through culverts can be simulated. The effects of vertical nonuniformity of the flow may be taken into account by the use of momentum-correction coefficients. Mass-flux and continuity-norm options may be used to locate areas

where network refinement is needed to improve accuracy.

The postprocessor, ANOMOD, uses output from FLOMOD to generate plots of velocity or unit-discharge vectors and ground-surface-elevation or water-surface-elevation contours. ANOMOD also generates time-history plots at node points or cross-section plots at a specified time of velocity, unit discharge, or water-surface elevation.

Also discussed were initial and boundary conditions, the application of the finite-element method to the flow equations to give a system of nonlinear algebraic equations, and the solution of the resulting system of equations.

A major part of the report was devoted to the application of FESWMS-2DH to data from the Geological Survey's Flood Plain Simulation Facility. It was shown that backwater associated with steady flow through a contracted opening in the FPSF could be simulated without difficulty. On the other hand, adequate representation of the jet and recirculation zones downstream from the constriction required information about local values of the momentum-correction coefficient and Manning's n. As discharge and consequently velocity and depth gradients increased, network refinement was necessary to avoid velocity oscillations and underestimation of backwater. The results also illustrated the importance of the convective terms when large depth and velocity gradients occur near the contracted opening.

The report also discussed the use and calibration of FESWMS-2DH (data collection and analysis, network design, and model adjustment, including calibration) and the use of FESWMS-2DH by the highway industry (operational potential of FESWMS-2DH, training, future possible improvements to FESWMS-2DH, and software maintenance).

The FESWMS-2DH modeling system is a versatile tool for steady-flow analyses at highway crossings where the flow is two dimensional. Its wide range of capabilities were presented in this report and have been demonstrated in applications to the Flood Plain Simulation Facility and several field problems.

REFERENCES

Arcement, G. J., Jr., and Schneider, V. R., 1984, Guide to selecting Manning's roughness coefficients for natural channels and flood plains: McLean, Va., Federal Highway Administration, Report FHWA-TS-84-204, 68 p.

Atkinson, K. E., 1978, An introduction to numerical analysis: New York, John Wiley, 587 p.

Barnes, H. H., Jr., 1967, Roughness characteristics of natural channels: U.S. Geological Survey Water-Supply Paper 1849, 213 p.

Becker, E. B., Carey, G. F., and Oden, J. T., 1981, Finite elements: An introduction: Englewood Cliffs, N.J., Prentice-Hall, 258 p.

Bodhaine, G. L., 1968, Measurement of peak discharge at culverts by indirect measurements: U.S. Geological Survey Techniques of Water-Resources Investigations, Book 3, Chapter A3, 68 p.

Bradshaw, P., Ferriss, D. H., and Atwell, N. P., 1967, Calculation of boundary-layer development using the turbulent energy equation: Journal of Fluid Mechanics, v. 28, pt. 3, p. 593-616.

Buell, W. R., and Bush, B. A., 1973, Mesh generation—A survey: Transactions of the American Society of Mechanical Engineers, Journal of Engineering for Industry, ser. B., v. 95, no. 1, p. 332-338.

Carey, G. F., and Oden, J. T., 1983, Finite elements: A second course: Englewood Cliffs, N.J., Prentice-Hall, 301 p.

Chow, V. T., 1959, Open-channel hydraulics: New York, McGraw-Hill, 680 p.

Elder, J. W., 1959, The dispersion of marked fluid in turbulent shear flow: Journal of Fluid Mechanics, v. 5, pt. 4, p. 544-560.

Engelman, M. S., Strang, Gilbert, and Bathe, K.-J., 1981, The application of quasi-Newton methods in fluid mechanics: International Journal for Numerical Methods in Engineering, v. 17, no. 5, p. 707-718.

Falconer, R. A., 1980, Numerical modeling of tidal circulation in harbors: Proceedings of the American Society of Civil Engineers, v. 106, no. WW1, p. 31-48.

Fischer, H. B., List, E. J., Koh, R. C. Y., Imberger, Jörg, and Brooks, N. H., 1979, Mixing in inland and coastal waters: New York, Academic Press, 483 p.

Flokstra, C., 1977, The closure problem for depth-averaged two-dimensional flow, in Friedrich, R., ed., Hydraulic engineering for improved water management: Congress of the International Association for Hydraulic Research, 17th, Baden-Baden, Germany, 1977, Proceedings: International Association for Hydraulic Research, v. 2, p. 247-256.

Franques, J. T., Jr., 1971, A finite element model for two-dimensional steady flow through contractions in natural channels: Baton Rouge, La., Louisiana State University, Department of Civil Engineering, unpublished dissertation, 120 p.

Franques, J. T., and Yannitell, D. W., 1974, Two-dimensional analysis of backwater at bridges: Proceedings of the American Society of Civil Engineers, v. 100, no. HY3, p. 379-392.

Garratt, J. R., 1977, Review of drag coefficients over oceans and continents: Monthly Weather Review, v. 105, no. 7, p. 915-929.

Gee, D. M., and MacArthur, R. C., 1978, Development of generalized free surface models using finite element techniques, in Brebbia, C. A., and others, eds., Finite elements in water resources: International Conference, 2d, London, 1978, Proceedings: London, Pentech Press, p. 2.61-2.79.

-----1982, Evaluation and application of the generalized finite element hydrodynamics model, RMA-2, in MacArthur, R. C., and others, eds., Two-dimensional flow modeling: National U.S. Army Corps of Engineers-Sponsored Seminar, 1st, Davis, Calif., 1981, Proceedings: Davis, Calif., U.S. Army Corps of Engineers, Hydrologic Engineering Center, p. 97-113.

Gilbert, J. J., and Froehlich, D. C., 1987, Simulation of the effect of U.S. Highway 90 on Pearl River floods of April 1980 and April 1983 near Slidell, Louisiana: U.S. Geological Survey Water-Resources Investigations Report 85-4286, 52 p.

Gilbert, J. J., and Schuck-Kolben, R. E., 1987, Effects of proposed highway embankment modifications on water-surface elevations in the lower Pearl River flood plain near Slidell, Louisiana: U.S. Geological Survey Water-Resources Investigations Report 86-4129, 40 p.

Gray, W. G., 1984, On normal flow boundary conditions in finite element codes for two-dimensional shallow water flow: International Journal for Numerical Methods in Fluids, v. 4, no. 1, p. 99-104.

Gray, W. G., and Kinnmark, Ingemar, 1982, QUIET: A quadratic isoparametric explicit in time finite element model for tidal circulation: User's manual: Princeton, N.J., Princeton University, Department of Civil Engineering, 106 p.

Gray, W. G., and Lynch, D. R., 1979, On the control of noise in finite element tidal computations: A semi-implicit approach: Computers and Fluids, v. 7, no. 1, p. 47-67.

Haney, R. L., and Wright, J. M., Jr., 1975, The relationship between the grid size and the coefficient of nonlinear lateral eddy viscosity in numerical ocean circulation models: Journal of Computational Physics, v. 19, no. 3, p. 257-266.

Hasbani, Yitzhak, and Engelman, M. S., 1979, Out-of-core solution of linear equations with non-symmetric coefficient matrix: Computers and Fluids, v. 7, no. 1, p. 13-31.

Hicks, B. B., 1972, Some evaluations of drag and bulk transfer coefficients over water bodies of different sizes: Boundary-Layer Meteorology, v. 3, p. 201-213.

Hicks, B. B., Drinkrow, R. L., and Grauze, G., 1974, Drag and bulk transfer coefficients associated with a shallow water surface: Boundary-Layer Meteorology, v. 6, no. 1/2, p. 287-297.

Hood, P., 1976, Frontal solution program for unsymmetric matrices: International Journal for Numerical Methods in Engineering, v. 10, no. 2, p. 379-399.

-----1977, Note on frontal solution program for unsymmetric matrices: International Journal for Numerical Methods in Engineering, v. 11, no. 6, p. 1055.

Jamart, B. M., and Winter, D. F., 1982, Finite element solution of the shallow-water wave equations in Fourier space, with applications to Knight Inlet, British Columbia, in Gallagher, R. H., and others, eds., 1982, Finite elements in fluids, v. 4: New York, John Wiley, p. 157-177.

Katapodes, N. P., 1984, A dissipative Galerkin scheme for open-channel flow: Journal of Hydraulic Engineering, v. 110, no. 4, p. 450-466.

King, I. P., and Norton, W. R., 1978, Recent applications of RMA's finite element models for two dimensional hydrodynamics and water quality, in Brebbia, C. A., and others, eds., Finite elements in water resources: International Conference, 2d, London, 1978, Proceedings: London, Pentech Press, p. 2.81-2.99.

Kraichnan, R. H., 1967, Inertial ranges in two-dimensional turbulence: Physics of Fluids, v. 10, no. 7, p. 1417-1423.

Launder, B. E., and Spalding, D. B., 1972, Mathematical models of turbulence: London, Academic Press, 169 p.

-----1974, The numerical computation of turbulent flows: Computer Methods in Applied Mechanics and Engineering, v. 3, p. 269-289.

Lean, G. H., and Weare, T. J., 1979, Modeling two-dimensional circulating flow: Proceedings of the American Society of Civil Engineers, v. 105, no. HY1, p. 17-26.

Lee, J. K., 1980, Two-dimensional finite element analysis of the hydraulic effect of highway bridge fills in a complex flood plain, in Wang, S. Y., and others, eds., Finite elements in water resources: International Conference on Finite Elements in Water Resources, 3rd, University, Miss., 1980, Proceedings: University, Miss., University of Mississippi, School of Engineering, p. 6.3-6.23.

Lee, J. K., and Bennett, C. S., III, 1982, A finite-element model study of the impact of the proposed I-326 crossing on flood stages of the Congaree River near Columbia, South Carolina: U.S. Geological Survey Open-File Report 81-1194, 65 p.

Lee, J. K., and Froehlich, D. C., 1986, Review of literature on the finite-element solution of the equations of two-dimensional flow in the horizontal plane: U.S. Geological Survey Circular 1009, 65 p.

Lee, J. K., Froehlich, D. C., Gilbert, J. J., and Wiche, G. J., 1982, Two-dimensional analysis of bridge backwater, in Smith, P. E., ed., Applying research to hydraulic practice: Conference of the Hydraulics Division of the American Society of Civil Engineers, Jackson, Miss., 1982, Proceedings: New York, American Society of Civil Engineers, p. 247-258.

-----, 1983, A two-dimensional finite-element model study of backwater and flow distribution at the I-10 crossing of the Pearl River near Slidell, Louisiana: U.S. Geological Survey Water-Resources Investigations Report 82-4119, 66 p.

Leendertse, J. J., and Liu, S.-K., 1977, A three-dimensional model for estuaries and coastal seas: Volume IV, Turbulent energy computation: Santa Monica, Calif., Rand Corporation, Report R-2187-OWRT, 59 p.

Leith, C. E., 1968, Diffusion approximation for two-dimensional turbulence: Physics of Fluids, v. 11, no. 3, p. 671-673.

Leschziner, M. A., and Rodi, Wolfgang, 1979, Calculation of strongly curved open channel flow: Proceedings of the American Society of Civil Engineers, v. 105, no. HY10, p. 1297-1314.

Lynch, D. R., and Gray, W. G., 1979, A wave equation model for finite element tidal computations: Computers and Fluids, v. 7, no. 3, p. 207-228.

-----1980, An explicit model for two-dimensional tidal circulation using triangular finite elements: WAVETL user's manual: U.S. Geological Survey Water-Resources Investigations Report 80-42, 70 p.

McGuirk, J. J., and Rodi, Wolfgang, 1978, A depth-averaged mathematical model for the near field of side discharges into open-channel flow: Journal of Fluid Mechanics, v. 86, pt. 4, p. 761-781.

National Bureau of Standards, 1986, Graphical kernel system (GKS): National Bureau of Standards, Federal Information Processing Standards Publication 120, 3 p.

Nee, V. W., and Kovasznay, L. S. G., 1969, Simple phenomenological theory of turbulent shear flows: Physics of Fluids, v. 12, no. 3, p. 473-484.

Norton, W. R., 1980, EBMUD hydrodynamic and water quality models for San Francisco Bay. User's manual and program documentation: Lafayette, Calif., Resource Management Associates, 266 p.

Norton, W. R., and King, I. P., 1973, A finite element model for Lower Granite Reservoir. Computer application supplement and uers's guide: Walnut Creek, Calif., Water Resources Engineers, Inc., 90 p.

Norton, W. R., King, I. P., and Orlob, G. T., 1973, A finite element model for Lower Granite Reservoir: Walnut Creek, Calif., Water Resources Engineers, Inc., 138 p.

Pinder, G. F., and Gray, W. G., 1977, Finite element simulation in surface and subsurface hydrology: New York, Academic Press, 295 p.

Platzman, G. W., 1981, Some response characteristics of finite-element tidal models: Journal of Computational Physics, v. 40, no. 1, p. 36-63.

Pritchard, D. W., 1971, Two-dimensional models, in Ward, G. H., Jr., and Espey, W. H., Jr., eds., Estuarine modeling: An assessment: Washington, D.C., Environmental Protection Agency, Water Quality Office, Water Pollution Control Research Series 16070DZV, p. 22-33.

Rastogi, A. K., and Rodi, Wolfgang, 1978, Predictions of heat and mass transfer in open channels: Proceedings of the American Society of Civil Engineers, v. 104, no. HY3, p. 397-420.

Reynolds, W. C., 1976, Computation of turbulent flows, in Van Dyke, M., and others, eds., Annual Review of Fluid Mechanics, v. 8: Palo Alto, Calif., Annual Reviews, p. 183-208.

Rodi, Wolfgang, 1980a, Turbulence models and their application in hydraulics—A state of the art review: Delft, The Netherlands, International Association for Hydraulic Research, 104 p.

-----1980b, Turbulence models for environmental problems, in Kollmann, W., ed., Prediction methods for turbulent flows: Washington, D.C., Hemisphere Pub. Corp., p. 259-349.

-----1982, Hydraulics computations with the k-ε turbulence model, in Smith, P. E., ed., Applying research to hydraulic practice: Conference of the Hydraulics Division of the American Society of Civil Engineers, Jackson, Miss., 1982, Proceedings: New York, American Society of Civil Engineers, p. 44-54.

Schaffranek, R. W., 1976, Some observations on the open-channel flow equations for turbulent surface-waterbodies: Washington, D.C., George Washington University, School of Engineering and Applied Science, unpublished thesis, 51 p.

Schlichting, Hermann, 1968, Boundary-layer theory (6th ed.): New York, McGraw-Hill, 748 p.

Sokolnikoff, I. S., and Redheffer, R. M., 1966, Mathematics of physics and modern engineering (2d ed.): New York, McGraw-Hill, 752 p.

Teeter, A. M., and McAnally, W. H., 1981, Application of a two-dimensional finite element model for shallow water computations, in MacArthur, R. C., and others, eds., Two-dimensional flow modeling: National U.S. Army Corps of Engineers-Sponsored Seminar, 1st, Davis, Calif., 1981, Proceedings: Davis, Calif., U.S. Army Corps of Engineers, Hydrologic Engineering Center, p. 253-265.

Tracy, F. T., 1976, Graphical pre- and post-processor for 2-dimensional finite element method programs: Computer Graphics, v. 10, no. 1, p. 8-12.

Tseng, M.-T., 1975a, Evaluation of flood risk factors in the design of highway stream crossings. V. III. Finite element model for bridge backwater computation: Washington, D.C., Federal Highway Administration, Report FHWD-RD-75-53, 176 p.

-----1975b, Finite element model for backwater computation, in American Society of Civil Engineers, ed., Symposium on modeling techniques: Annual Symposium of the Waterways, Harbors and Coastal Engineering Division of the American Society of Civil Engineers, 2d, San Francisco, 1975, Proceedings: New York, American Society of Civil Engineers, v. 2, p. 1448-1466.

Walters, R. A., 1980, The frontal method in hydrodynamics simulations: Computers and Fluids, v. 8, no. 2, p. 265-272.

-----1986, A finite element model for tidal and residual circulation: Communications in Applied Numerical Methods, v. 2, p. 393-398.

Walters, R. A., and Cheng, R. T., 1978, A two-dimensional hydrodynamic model of a tidal estuary, in Brebbia, C. A., and others, eds., Finite elements in water resources: International Conference, 2d, London, 1978, Proceedings: London, Pentech Press, p. 2.3-2.21.

-----1980, Accuracy of an estuarine hydrodynamic model using smooth elements: Water Resources Research, v. 16, no. 1, p. 187-195.

Wang, J. D., and Connor, J. J., 1975, Mathematical modeling of near coastal circulation: Cambridge, Mass., Massachusetts Institute of Technology, Department of Civil Engineering, Ralph M. Parsons Laboratory for Water Resources and Hydrodynamics, Report 200, 272 p.

Wiche, G. J., Gilbert, J. J., Froehlich, D. C., and Lee, J. K., 1988, Analysis of alternative modifications for reducing backwater at the Interstate Highway 10 crossing of the Pearl River near Slidell, Louisiana: U.S. Geological Survey Water-Supply Paper 2267, 54 p.

Wiche, G. J., Gilbert, J. J., and Lee, J. K., 1982, Analysis of alternatives for reducing bridge backwater, in Smith, P. E., ed., Applying research to hydraulic practice: Conference of the Hydraulics Division of the American Society of Civil Engineers, Jackson, Miss., 1982, Proceedings: New York, American Society of Civil Engineers, p. 259-269.

Withum, D., Holz, K.-P., and Meissner, Udo, 1979, Finite element formulations for tidal wave analysis: Computer Methods in Applied Mechanics and Engineering, v. 17/18, p. 699-716.

Zienkiewicz, O. C., 1977, The finite element method (3d ed.): London, McGraw-Hill, 787 p.